

**MAGNETIC RESONANCE IMAGING
HAEMODYNAMIC MODELLING
IN CHRONIC LIVER DISEASE:**

**DEVELOPMENT, VALIDATION
AND TRANSLATION**

MANIL CHOUHAN

*A dissertation submitted
in partial fulfilment of the requirements
for the degree of*

**Doctor of Philosophy
of
University College London**

2014

DECLARATION OF ORIGINALITY

I, Manil Chouhan, confirm the work presented in this thesis is my own. Where information has been derived from other sources, I confirm that this has been indicated in the thesis.

Manil Chouhan

ABSTRACT

Though haemodynamic changes underpin the pathophysiology of chronic liver disease, there are currently no robust non-invasive methods available for their assessment.

I propose 'caval subtraction' phase contrast MRI (PCMRI) a novel method to measure total liver blood flow (TLBF) and hepatic arterial (HA) flow using PCMRI measurements of caval and portal venous (PV) flow. I validate this method at 9.4T and 3.0T to demonstrate: agreement between preclinical PCMRI and invasive transit-time ultrasound (TTUS) and fluorescent microsphere measurements of flow parameters; good consistency between clinical caval subtraction PCMRI and independent direct PCMRI measurements; encouraging correlations between PCMRI and invasive ICG clearance in patients; and good seven-day reproducibility of PCMRI derived haemodynamic parameters in normal volunteers.

Using dynamic contrast enhanced (DCE) MRI on a 3.0T system, I demonstrate improved seven-day reproducibility using dual input single compartment pharmacokinetic modelling with a novel method for obtaining physiological vascular input function delays, correction of arterial input functions using PCMRI aortic flow and use of PCMRI estimations of TLBF to correct DCE MRI quantification. I also implement arterial spin labelling (ASL) at 9.4T and demonstrate a tendency for ASL to underestimate PCMRI hepatic parenchymal perfusion.

Using bile-duct ligated (BDL) rats to study cirrhosis, I demonstrate that these have reduced TLBF and HA fraction at baseline, impaired HA regulation and buffer response, cirrhotic cardiomyopathy, and a failure to match hepatic circulatory demands with increased liver:body mass ratio. Acute-on-chronic liver failure (simulated using endotoxaemia) demonstrates reductions in TLBF, HA flow, absence of normal sepsis-induced hepatic hyperaemia and blunted cardiac systolic response. Studies in cirrhotic patients demonstrate increased TLBF and HA flow in higher risk portal hypertensive patients; that HA flow, HA fraction and cardiac output are important correlative parameters with hepatic venous pressure gradient and that caval subtraction PCMRI has potential in evaluating treatments for portal hypertension.

ACKNOWLEDGEMENTS

ACADEMIC

Firstly, I would like to thank my supervisors, Stuart Taylor, Raj Mookerjee and Mark Lythgoe without whom this project would not have been possible. Stuart's approachability, guidance, goal-orientated focus and constant, (sometimes almost instant!) feedback by email have been a true inspiration to my academic development and given this project the necessary momentum to drive it forward to this stage. From foundation to summit, this project was defined and shaped by Raj's close supervision, whose essential insight into Hepatological applications, enthusiasm for the use of imaging methods to address important clinical questions and extensive (often impromptu) discussions on portal hypertension and hepatic vascular physiology, gave the necessary direction that so many liver imaging projects lack. Finally, I am grateful for Mark's generosity and patience, without which the essential preclinical portion of this project could not have taken place.

This project is grounded in highly technical aspects of MR physics that would not have been accessible without the help of Alan Bainbridge. The support acquiring data, developing MR sequences and troubleshooting MR problems was indispensable in catalysing early phases of this project. A special mention must also be given to Shonit Punwani whose enthusiasm helped establish this project and whose guidance on more technical MR aspects has proven vital.

I owe much to Nathan Davies who helped plan animal experiments, facilitated logistics and informed the development many of the preclinical protocols used in this thesis. His work along with the fastidious organisation of Abe Habtieson and unparalleled surgical dexterity of Val Taylor, were essential to all the preclinical work.

My work at CABI would not have been possible without the support of Simon Walker-Samuel and the very significant contribution from Raj Ramasawmy. Raj's generosity, patience and enthusiasm made the incorporation of ASL data into this project possible.

All my colleagues – PhD students at CABI and ILDH – many of which took part in normal volunteer studies and without whose help many experiments simply couldn't take place: to you I am grateful.

Lastly, I must thank the Wellcome Trust for funding this Fellowship and for putting their faith in me to deliver this project and my ultimate goal to improve outcomes for patients.

PERSONAL

Throughout this project, I have stood on the shoulders of giants. My grandmother, Nirmala Chouhan, who taught me the value of faith and perseverance in the face of adversity; my father Dinesh Chouhan, who has always driven me to seek practical solutions and taught me that concepts that change the world are those where simplicity and elegance are inseparable; and my mother, Kaushalya Chouhan, for teaching me to be fearless in the pursuit of my ambitions, inspiring me with a passion for knowledge and introducing me at a young age to the beauty of mathematics.

The past three years, particularly the past few months required to complete this thesis, have exacted tremendous sacrifices from those around me. To my wife, Aachal, who has patiently supported me through this process, listened to my rambling discussions, filled in for my absences and accepted without question countless nights and weekends to the sound of my keyboard typing, I am grateful. My brother Prem, has also endured me through this experience – his wisdom beyond his years in demonstrating to me the importance of single-mindedness and resolve in achieving my goals has been truly inspirational. I must also thank my sister and brother-in-law, Poonam and Milesh Patel, who supported and encouraged me throughout this process.

I dedicate this thesis to my late grandfathers, Baloo and Harjivan Chouhan, who never completed secondary school education, but built my family from nothing. For me, they are forever a testament that real knowledge is not defined by the letters after one's name.

CONTENTS

Declaration of Originality.....	1
Abstract.....	2
Acknowledgements	3
Academic.....	3
Personal.....	4
Preface/Structural Overview	11
Abbreviation list	14
1. VASCULAR ASSESSMENT OF LIVER DISEASE - TOWARDS A NOVEL PARADIGM IN LIVER IMAGING	
1.1 Introduction.....	16
1.2 Liver Imaging – Unmet needs	17
1.2.1 Multiple inputs, multiple compartments - the challenge of vascular imaging in the liver.....	17
1.2.2 Pressure, flow and resistance – the diseased liver	18
1.2.3 “Not-so-golden” gold standards	19
1.3 Approaches to Haemodynamic Imaging in the Liver	22
1.3.1 Scintigraphy.....	22
1.3.2 Ultrasound.....	23
1.3.3 Computerised Tomography	27
1.3.4 Dynamic Contrast Enhanced MRI	30
1.3.5 Dynamic Hepatocyte-specific Contrast Enhanced MRI	34
1.3.6 Phase-Contrast MRI.....	38
1.3.7 Four-Dimensional Phase-Contrast MRI	47
1.3.8 Arterial spin labelling MRI.....	49
1.3.9 Functional MRI	51
1.3.10 Biomechanical Imaging	52
1.4 Conclusion.....	60
1.5 Thesis hypothesis	60
2. DCE MRI - EARLY PRECLINICAL STUDIES OF FEASIBILITY, REPEATABILITY, VALIDATION AND MEASUREMENT OF THE HEPATIC ARTERIAL BUFFER RESPONSE	
2.1 Introduction.....	62
2.2 Author contributions.....	62
2.3 Background	63
2.4 Materials and Methods	64
2.4.1 Experimental subjects	64
2.4.2 Sample size.....	64

2.4.3 Imaging cohort	64
2.4.4 Validation cohort.....	64
2.4.5 Dynamic Contrast Enhanced MRI.....	65
2.4.6 T1 measurements.....	66
2.4.7 Contrast Agent concentration measurements.....	66
2.4.8 Perfusion parameter estimation.....	68
2.4.9 Image analysis	69
2.4.10 Statistical analysis	70
2.5 Results	71
2.5.1 Signal Intensity Calibration.....	71
2.5.2 Cohort features.....	73
2.5.3 DCE MRI feasibility	74
2.5.4 Repeatability	76
2.5.5 Portal venous ligation.....	78
2.5.6 Validation.....	81
2.6 Discussion	82
2.6.1 Dynamic contrast enhanced MRI.....	83
2.6.2 T1 measurements.....	85
2.6.3 Perfusion parameter estimation.....	86
2.6.4 Physiological factors	87
2.6.5 Future developments.....	88
2.7 Conclusions	89
2.8 Closing comments.....	90
3. TROUBLESHOOTING FOR PRECLINICAL DCE MRI	
3.1 Introduction	92
3.2 Author contributions.....	92
3.3 Alternative T1 measurement strategies.....	93
3.3.1 Background.....	93
3.3.2 Materials and methods.....	94
3.3.3 Results.....	97
3.3.4 Discussion.....	101
3.3.5 Conclusion	103
3.4 Bolus protocols	104
3.4.1 Background.....	104
3.4.2 Materials and methods.....	105
3.4.3 Results.....	107
3.4.4 Discussion.....	112
3.4.5 Conclusion	114
3.5 DCE modelling.....	115

3.5.1 Background.....	115
3.5.2 Materials and methods.....	119
3.5.3 Results.....	122
3.5.4 Discussion.....	130
3.5.5 Conclusions.....	134
3.6 Closing comments.....	135
4. PRECLINICAL PCMRI - EARLY ATTEMPTS	
4.1 Introduction.....	138
4.2 Author contributions.....	138
4.3 Sequence optimisation and challenges with PCMRI.....	139
4.3.1. Background.....	139
4.3.2 Velocity encoding settings.....	143
4.3.3 Vessel orthogonality and misalignment.....	150
4.3.4 Spatial resolution and matrix size.....	151
4.3.5 Pulsation artefacts and spatial misregistration.....	152
4.3.6 Intravoxel phase dispersion and velocity compensation.....	153
4.3.7 Phase offset errors.....	153
4.3.8 Temporal resolution.....	154
4.3.9 Discussion and conclusions.....	154
4.4 Repeatability, reproducibility and invasive validation studies.....	155
4.4.1 Background.....	155
4.4.2 Methods.....	155
4.4.3 Results.....	156
4.4.4 Discussion and conclusions.....	157
4.5 Early studies in the modulation of PV flow in chronic liver disease.....	158
4.5.1 Background.....	158
4.5.2 Material and methods.....	159
4.5.3 Results.....	161
4.5.4 Discussion.....	163
4.5.5 Conclusion.....	164
4.6 Implementation of cardiac gating.....	165
4.6.1 Background.....	165
4.6.2 Methods.....	168
4.6.3 Results.....	169
4.6.4 Discussion.....	174
4.6.5 Conclusion.....	175
4.7 Closing comments.....	176

5. PCMRI - NEW TECHNIQUES AND METHODS	
5.1 Introduction	178
5.2 Author contributions.....	179
5.3 Conceptual development.....	180
5.4 Preclinical validation, repeatability and studies of the hepatic arterial buffer response	184
5.4.1 Background.....	184
5.4.2 Methods.....	186
5.4.3 Results.....	193
5.4.4 Discussion.....	203
5.4.5 Conclusion	210
5.5 Clinical translation, validation, reproducibility and studies of the negative hepatic arterial buffer response.....	211
5.5.1 Background and clinical protocol development.....	211
5.5.2 Methods.....	216
5.5.3 Results.....	219
5.5.4 Discussion.....	236
5.5.5 Conclusion	241
5.6 Closing comments.....	242
6. CLINICAL DCE MRI	
6.1 Introduction	244
6.2 Author contributions.....	245
6.3 Clinical DCE MRI feasibility and approaches to handling vascular input function delays	246
6.3.1 Background.....	246
6.3.2 Methods.....	251
6.3.3 Results.....	259
6.3.4 Discussion.....	275
6.3.5 Conclusion	283
6.4 Alternative approaches to DCE modelling.....	284
6.4.1 Background.....	284
6.4.2 Methods.....	286
6.4.3 Results.....	287
6.4.4 Discussion.....	300
6.4.5 Conclusion	302
6.5 Combined DCE and PCMRI – part I – arterial input function correction	303
6.5.1 Background.....	303
6.5.2 Methods.....	305
6.5.3 Results.....	306
6.5.4 Discussion.....	330

6.5.5 Conclusion	331
6.6 Combined DCE and PCMRI – part II – tissue perfusion correction	332
6.6.1 Background	332
6.6.2 Methods	335
6.6.3 Results	336
6.6.4 Discussion	361
6.6.5 Conclusion	365
6.7 Closing comments	366
7. BLOOD FLOW STUDIES IN CHRONIC LIVER DISEASE - PRECLINICAL STUDIES	
7.1 Introduction	368
7.2 Author contributions	369
7.3 Arterial spin labelling – methodology, validation and T1 studies	370
7.3.1 Background	370
7.3.2 Methods	374
7.3.3 Results	378
7.3.4 Discussion	382
7.3.5 Conclusion	385
7.4 Haemodynamic stress in chronic liver disease	386
7.4.1 Background	386
7.4.2 Methods	387
7.4.3 Results	389
7.4.4 Discussion	405
7.4.5 Conclusion	410
7.5 Closing comments	411
8. BLOOD FLOW STUDIES IN CHRONIC LIVER DISEASE - CLINICAL STUDIES	
8.1 Introduction	413
8.2 Author contributions	413
8.3 Background	414
8.4 Methods	418
8.4.1 Subjects and preparation	418
8.4.2 Sample size	418
8.4.3 Two-dimensional cine PCMRI	418
8.4.4 Volumetric assessment and bulk flow normalisation	419
8.4.5 Caval subtraction PCMRI consistency studies	419
8.4.6 Invasive validation studies	419
8.4.7 Haemodynamic characterisation studies	420
8.4.8 Baseline and post-treatment studies	420
8.4.9 Statistical analysis	421

8.5 Results	422
8.5.1 Cohort features.....	422
8.5.2 PCMRI feasibility	423
8.5.3 Caval subtraction PCMRI consistency.....	425
8.5.4 Caval subtraction PCMRI validation	427
8.5.5 Non-invasive and invasive haemodynamic parameter relationships	428
8.5.6 Haemodynamic characterisation studies	432
8.5.7 Post-treatment haemodynamic response	436
8.6 Discussion	440
8.6.1 Feasibility	440
8.6.2 Consistency and validation.....	441
8.6.3 Haemodynamic parameter relationships.....	444
8.6.4 Haemodynamic characterisation studies	445
8.6.5 Post-treatment studies.....	448
8.6.6 General criticisms.....	449
8.6.7 Future directions	449
8.7 Conclusion.....	452
8.8 Closing comments.....	453
 SUMMARY OF FINDINGS.....	 454
 Appendix A - L-NAME and terlipressin dosage regime experiments	 461
Appendix B - Terlipressin dosage regime experiments	464
Appendix C - Preclinical validation, repeatability and studies of the hepatic arterial buffer response – subject participation details.....	466
Appendix D - Normal volunteer study ethics.....	468
Appendix E - Blood flow studies in chronic liver disease – preclinical studies – Subject participation details.....	477
Appendix F - Patient study ethics.....	479
Appendix G - Oral presentations.....	489
 REFERENCES.....	 491

PREFACE/STRUCTURAL OVERVIEW

This thesis demonstrates the development, validation and translation of MRI techniques for haemodynamic assessment of chronic liver disease. The concept of ‘haemodynamics’ is broad, including the assessment of flow, pressure and resistance. Because of peculiarities of the liver organ, comprehensive measurement of any of these parameters cannot be undertaken directly. The notion of ‘modelling’ therefore refers to methods that utilise direct measurements to derive meaningful preclinical and clinical hepatic haemodynamic parameters. This thesis addresses the evaluation of flow and perfusion, framing these measurements in the context of pressure and resistance during clinical translation, presented at the end of the thesis.

The arguments that form this thesis have been structured around eight chapters, but are essentially separated into two main sections: Section I, covering Chapters 2 to 6, includes all the preclinical and clinical developmental work. Section II, covering Chapters 7 and 8, applies previously developed MR methods to study haemodynamic phenomena in chronic liver disease.

In Chapter 1, we outline the clinical challenge in the context of the known vascular pathophysiology of chronic liver disease, review the strengths and weakness of existing imaging methods and use these to frame the overall hypothesis of the thesis. In the second chapter, we present early preclinical work, demonstrating the development, validation and application of DCE MRI. The challenges identified from this work form the basis for Chapter 3, in which several approaches are used to troubleshoot and address these issues.

Faced with difficulties surrounding the preclinical use of DCE MRI in Chapter 3, we develop an alternative strategy in Chapter 4, using preclinical PCMRI. In this chapter, we demonstrate sequence and protocol development, alongside preliminary repeatability and invasive validation. We introduce preclinical models of chronic liver disease and address the need for cardiac gating.

In Chapter 5, we present a novel method for estimating total liver blood flow and hepatic arterial flow. We then apply this method preclinically in healthy and diseased animals, demonstrating feasibility and invasive validation before studying differences in the haemodynamic response after pharmacological stress. We then translate the method using normal volunteers and assess feasibility, consistency and reproducibility of measurements, before using PCMRI to evaluate post-prandial changes in hepatic haemodynamics.

Building on translational work, we develop DCE MRI on a clinical MRI scanner in Chapter 6 and study the effects of progressive post-processing refinements on quantification using normal volunteers. This chapter culminates in the use of PCMRI measurements derived from our novel method to improve accuracy and correct DCE MRI perfusion estimates.

In Chapter 7, we introduce preclinical ASL for the measurement of tissue perfusion. We investigate haemodynamic differences in chronic liver disease and study haemodynamic changes in sepsis. Full clinical translation is presented in Chapter 8. Using PCMRI in portal hypertensive patients, we assess consistency and preliminary invasive validation before investigating differences in MR haemodynamic parameters in patients with varying severity of portal hypertension. In the final part of Chapter 8, we demonstrate the potential of novel PCMRI methods in the investigation of treatments for portal hypertension.

In writing this thesis, I have chosen to report findings entirely in the third person, using 'we', rather than 'I'. Although this deliberately recognises the collective effort of the team involved in this project, it in no way implies that the research presented in this thesis was designed, executed, analysed and reported by anyone else other than myself. By way of clarification, at the start of each Chapter, specific author contributions are listed alongside those of any other members of the research team.

Given the length of the thesis and in order to facilitate perusal, each Chapter has been written in such a way as to enable standalone review. To this effect, although cross-chapter references are included, methods, figure and tables are occasionally repeated, to avoid the need to consult Chapter 2 for example, while reading Chapter 7. Where figures and tables are repeated, the legend is used to indicate that this is the case. In line with the concept of 'reduction' as part of the 3Rs of animals research, developmental preclinical data from the same animal is occasionally used toward the investigation of different developmental hypotheses (Chapters 2-4). Where data has been re-used, note is made in the methods that this is the case. Preclinical experimental reports have been formulated to broadly match criteria specified in the NC3Rs Animal Research: Reporting of *In Vivo* Experiments (ARRIVE) guidelines [1].

A considerable amount of developmental and validation work throughout this thesis is reliant on analysis of agreement, whether in the context of repeatability, reproducibility or validation. This has always been undertaken using Bland-Altman analysis accompanied with the correlative analysis. The latter has been included to visualise the relationship between measurements under investigation, with correlations coefficients used to demonstrate the strength of relationship rather than agreement

between methods. All numerical data are quoted to an accuracy of four significant figures, as appropriate and where cohort averages are quoted, these are given \pm the sample standard error. Lastly, most chapters are subdivided into sections, each with their own aims and objectives, results, discussion and conclusions. Criticisms and potential future work are also explored towards the end of each section. For added clarity, a final 'Summary of findings' is given at the end of the thesis.

In conclusion, this thesis is the culmination of a fully translational project, presenting developmental challenges, the strategies used to successfully overcome these difficulties, implementation, validation, repeatability and reproducibility studies in the preclinical and clinical setting and full translation into patients with early investigation of the potential clinical value of the methods proposed.

ABBREVIATION LIST

AIF	Aortic input function
ASL	Arterial Spin Labelling
BOLD	Blood-Oxygen Level Dependent
CA	Contrast Agent
CASL	Continuous Arterial Spin Labelling
CEUS	Contrast-enhanced Ultrasound
CI	Congestion Index
CT	Computerised Tomography
DCE	Dynamic Contrast Enhanced
DHCE	Dynamic Hepatocyte-specific Contrast Enhanced
DI	Damping Index
DV	Distribution Volume
FAIR	Flow Attenuated Inversion Recovery
FHVP	Free Hepatic Venous Pressure
fMRI	functional Magnetic Resonance Imaging
GSA	Galactosyl Serum Albumin
HA	Hepatic Artery
HABR	Hepatic Arterial Buffer Response
HV	Hepatic Vein
HVAT	Hepatic Venous Arrival Time
HVPG	Hepatic Venous Pressure Gradient
ICG	Indocyanine Green
IDA	Iminodiacetic Acid
IR	Inversion Recovery
IVC	Inferior Vena Cava
LPS	Lipopolysaccharide
MELD	Model for End-stage Liver Disease
MFA	Multi-Flip Angle
MRI	Magnetic Resonance Imaging
MTT	Mean Transit Time
OCA	Obeticholic Acid
PASL	Pulsed Arterial Spin Labelling
PCASL	Pseudo-continuous Arterial Spin Labelling
PCMRI	Phase-Contrast Magnetic Resonance Imaging
PC-VIPR	Phase-Contrast Vastly undersampled Isotropic Projection Reconstruction
PDR	Plasma Disappearance Rate
PET	Positron Emission Tomography
PH	Partial Hepatectomy
PI	Pulsatility Index
PV	Portal Vein
PVL	Portal Venous Ligation
RF	Radio frequency
RI	Resistive Index
ROI	Region-Of-Interest
SAR	Specific Absorption Ratio
SPECT	Single Photon Emission Computerised Tomography
SR	Saturation Recovery
TIPSS	Transjugular Intrahepatic Porto-Systemic Shunt
TJ	Transjugular
TR	Repetition time
TS	Saturation recovery Time
TTUS	Transit-Time Ultrasound
US	Ultrasound
VIF	Vascular Input Function
WHVP	Wedge Hepatic Venous Pressure

CHAPTER 1

VASCULAR ASSESSMENT OF LIVER DISEASE – TOWARDS A NOVEL PARADIGM IN LIVER IMAGING

“...there, inside,
you filter
and apportion,
you separate
and divide,
you multiply
and lubricate,
you raise
and gather
the threads and the grams
of life, the final
distillate:
the intimate essences.”

- Ode to the liver [2].

1.1 INTRODUCTION

Chronic liver disease encompasses a range of pathological processes, with clinical manifestations including portal hypertension that occur in association with profound changes in hepatic vascular parameters. The pathophysiology of chronic liver disease is complex, and further complicated by the dual portal venous and hepatic arterial blood supply received by the liver. The clinical course and progression of chronic liver disease is heterogeneous and can be unpredictable. Routine clinical assessment of liver disease is based on the assimilation of the results of serological, non-invasive and invasive tests [3, 4].

It is well recognised amongst hepatologists that histological assessment of invasive liver biopsy specimens is of limited prognostic value [5-7], however to date, it is non-invasive imaging based assessment of liver fibrosis that has attracted the most attention from the academic imaging community [8-12]. The most robust and well-documented index of chronic liver disease prognosis is however, the hepatic venous pressure gradient (HVPG). The relationship between this invasive surrogate of portal pressure and clinical outcomes is an urgent reminder of the importance of the vascular pathophysiology of liver disease [13-16]. It would therefore seem that non-invasive imaging based assessment of hepatic vascular parameters would be a well-grounded approach to develop meaningful biomarkers for chronic liver disease. In this chapter, we aim to (a) provide a brief overview of vascular sequelae of chronic liver disease amenable to imaging and (b) describe existing imaging methods, including their applications and challenges, in the assessment of hepatic vascular parameters. Against this back drop, we will in the final part of the chapter define the overall hypothesis for this thesis.

1.2 LIVER IMAGING – UNMET NEEDS

Liver disease is the fifth most common cause of death in the UK [17] and there are an estimated 8000 new diagnoses of cirrhosis in the UK each year [18]. The American Association for the Study of Liver Disease/European Association for the Study of the Liver consensus stratifies chronic liver disease into two phases: compensated disease, followed by decompensated cirrhosis. The presence of ascites, variceal haemorrhage, encephalopathy and/or jaundice characterise the latter phase, with both ascites and variceal haemorrhage as recognised direct sequelae of vascular derangements and portal hypertension [19]. Crucially, the median survival of compensated cirrhotics is over 12 years, however for the 5-7% of patients that become decompensated each year, median survival shrinks to a mere 2 years [20, 21]. The difference in clinical outcome and mortality of these two phases is impressive, and serves to underline the importance of vascular phenomena and the measurement of hepatic vascular parameters in defining prognostic outcomes.

Estimation of portal pressure with the HVPG has become the mainstay of vascular assessment of liver disease and is traditionally within the remit of interventional radiologists around the UK. Although we review the methodology and challenges facing this method later, it is the use of HVPG to inform prognosis and management of chronic liver disease that is of particular interest. So-called ‘clinically significant portal hypertension’ is defined as an HVPG of 10 mmHg or more [19]. In compensated patients, the HVPG has been shown to be the strongest predictor for the development of varices and subsequent decompensation [22]. The HVPG is also used to monitor efficacy of medical treatments for portal hypertension and is used at some centres as a definitive indication for a transjugular intrahepatic portosystemic shunt (TIPSS) procedure [23, 24]. Perhaps most notably, in patients with a known diagnosis of cirrhosis, a HVPG rise of 1 mmHg leads to a 3% increase in mortality risk [25].

1.2.1 MULTIPLE INPUTS, MULTIPLE COMPARTMENTS - THE CHALLENGE OF VASCULAR IMAGING IN THE LIVER

The healthy liver receives 75-80% of its total blood supply from the portal vein, with the remainder arriving via the hepatic artery. The hepatic artery is a vessel of resistance: it is a smaller vessel delivering a smaller volume of blood, but at higher pressure, while the portal vein is a lower pressure, higher volume vessel of capacitance. The liver parenchyma is organised into functional units or ‘acini’ (figure 1.1), where afferent portal venous and hepatic arterial blood mix at the capillary level, within the hepatic sinusoid. The sinusoid is a tubular space, lined with fenestrated endothelium draining distally into

an efferent hepatic venule. The sinusoids are flanked almost entirely by hepatocytes, but these are physically separated from the endothelial cells by the 'space of Disse', a separate anatomical compartment into which plasma and low molecular weight compounds (including common extra-cellular contrast agents) can circulate freely. On the opposite surface of the hepatocytes but parallel to the sinusoids, lie bile canaliculi. The canaliculi drain bile and products of hepatocyte bile transporters (including hepatocyte-specific contrast agents) proximally into biliary ductules (figure 1.1). The healthy liver preserves low pressure within the sinusoids, but is tasked with the challenge of being interposed between a mixed high and low pressure input and a low pressure venous output [26, 27].

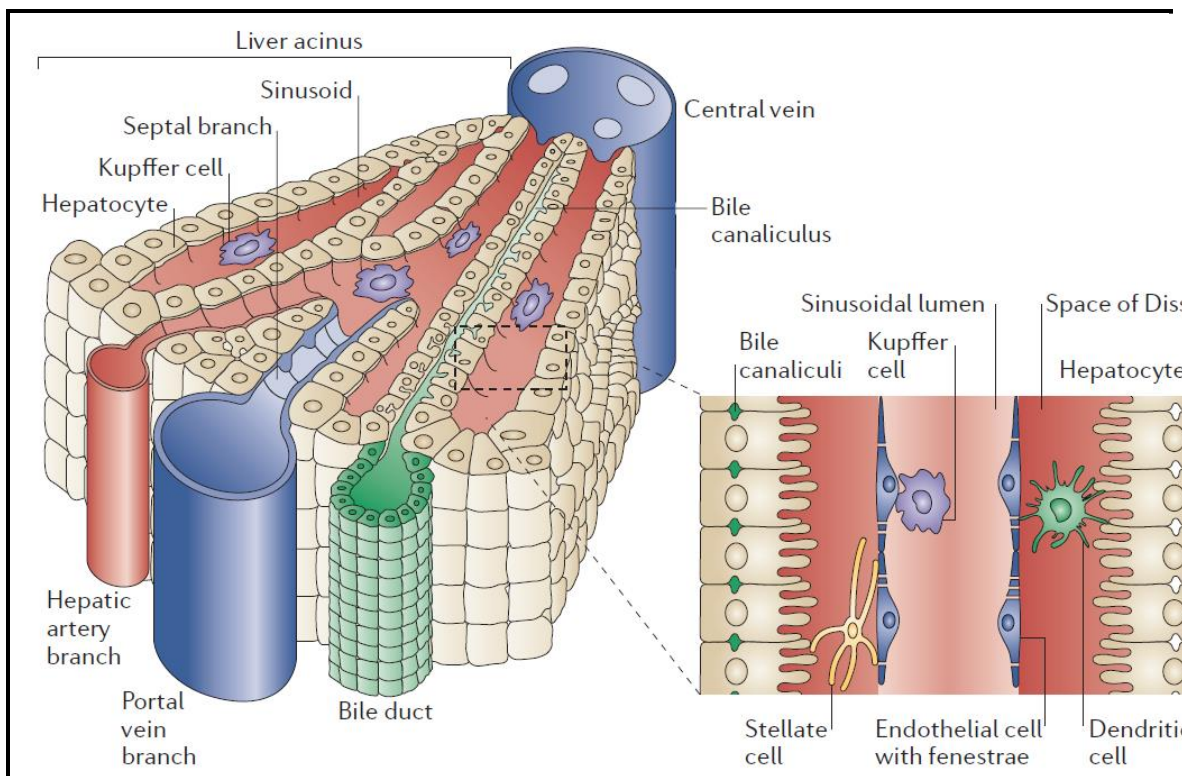


Figure 1.1: Functional anatomy of the liver

Schematic illustration of the functional organisation of the liver acinus (left). Magnified diagram illustrating the arrangement of sinusoid and space of Disse is shown in the right lower corner. (obtained from reference [28])

1.2.2 PRESSURE, FLOW AND RESISTANCE – THE DISEASED LIVER

Chronic liver injury triggers progressive substitution of healthy parenchyma with scar tissue and while fibrosis is a recognised pathological end point, it is recognised that vascular stimuli including angiogenic changes underpin this process [29]. Collagen deposition in the space of Disse and distortion of the sinusoidal architecture as a result of contractile factors, including changes in vascular smooth muscle cells, contraction of activated hepatic stellate cells and sinusoidal endothelial dysfunction act in conjunction to increase intrahepatic parenchymal resistance [30].

As a result of these changes, portal venous blood flow is reduced and the high resistance imposed by the diseased liver is bypassed by shunting of splanchnic blood via the porto-systemic anastomoses, known as 'extra-hepatic shunting' [26]. Reductions of portal venous flow of as much as 60% can be compensated for by rises in hepatic arterial blood flow in the healthy liver – the so-called 'hepatic arterial buffer response' (HABR), but this response is impaired in liver disease, so that reductions in portal venous flow are met with an inadequate response from the hepatic artery and an overall reduction in total liver blood flow [27, 31].

With the evolution of fibrosis into cirrhosis, there is progressive deposition of collagen, leading to reductions in the volume of the extra-cellular, extra-vascular compartment. Microvascular thrombi are commonly seen and the mean transit time (average time for a compound to traverse the parenchyma) for low molecular weight compounds is increased. Neovascularisation of perisinusoidal fibrotic tissue and progressive occlusion of the space of Disse combine to reduce effective hepatocyte perfusion and result in so-called 'intra-hepatic shunting' [32, 33].

Although measurements of these vascular changes are of clear value, the difficult and invasive nature of the methods employed to study them has limited our understanding of their role in the pathophysiology of liver disease and inhibited their development as biomarkers for liver disease.

1.2.3 "NOT-SO-GOLDEN" GOLD STANDARDS

So-called 'gold standards' are essential to the development of well validated imaging-based quantitative methods, however these are rarely used in the clinical setting. The main methods of assessment of vascular parameters of liver disease are the HVPG and indocyanine green (ICG) clearance.

Described originally over sixty years ago, the HVPG is measured routinely by passing a pressure transducer under fluoroscopic guidance into a hepatic vein until it cannot be advanced further. Once the transducer is 'wedged' in the liver parenchyma, a balloon is inflated at the catheter tip so that a continuous column of venous blood is formed between the transducer tip and the sinusoid. The pressure readings from the transducer can then be used to measure the HVPG (figure 1.2) [34]. There is substantial evidence to suggest that the HVPG correlates well with portal pressure in cirrhosis of any aetiology [15, 35, 36], however appropriate and well calibrated equipment is needed in addition to technical expertise to obtain the measurement [15, 34]. Differences in HVPG values have been demonstrated when the catheter is wedged in different hepatic veins and intra-individual variability of HVPG measurement in specialist centres has been estimated to be as much as 8% [37, 38].

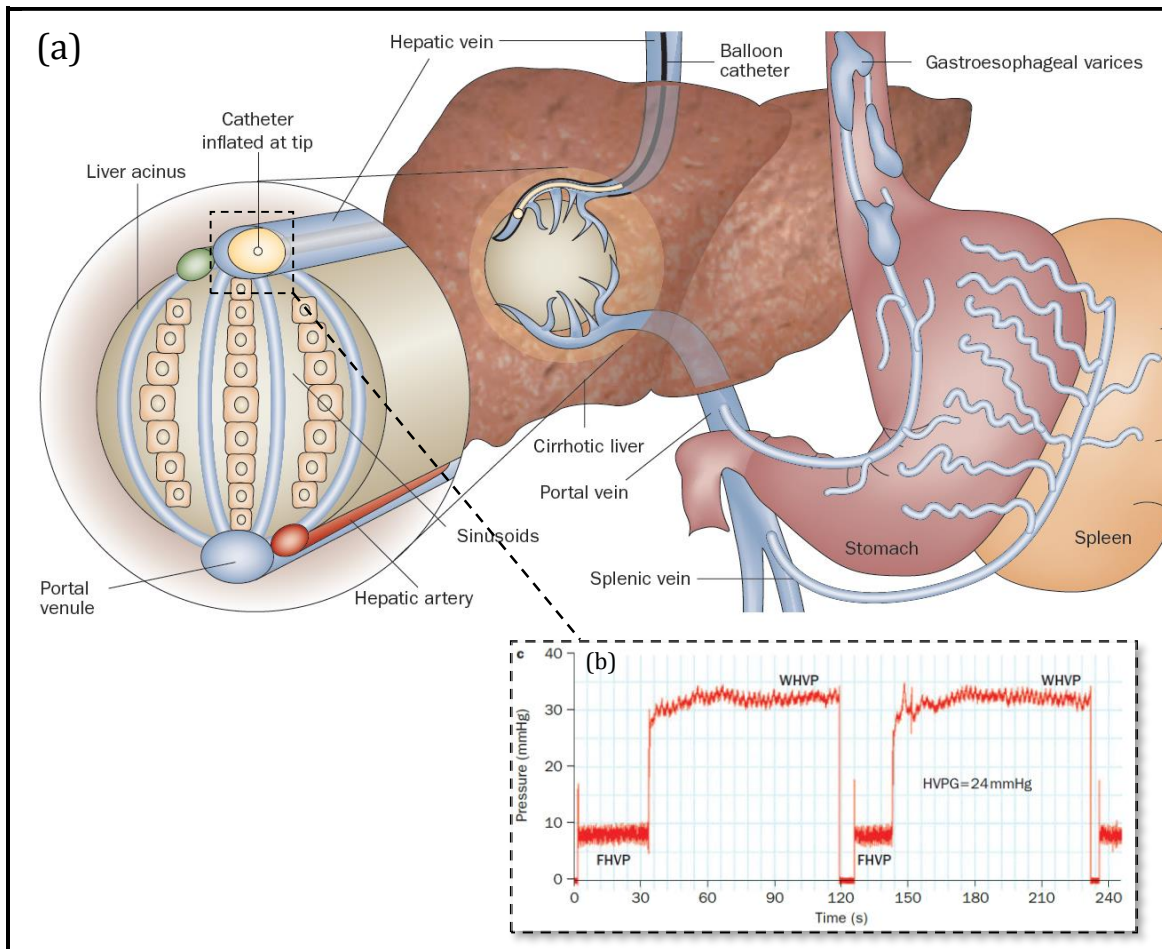


Figure 1.2: Measurement of the hepatic venous pressure gradient

(a) A pressure transducer is advanced via the jugular vein, into the hepatic vein. (b) The pressure recorded from the transducer (WHVP, wedge hepatic venous pressure) will equate to sinusoidal pressure (recognised to be slightly lower than, but directly related to portal venous pressure). The balloon is then deflated, the transducer slightly withdrawn and a reading is obtained of 'free' hepatic venous pressure (FHVP). Although both of these measurements are subject to variations in intra-abdominal pressure, the difference of the two – the HVPG – eliminates this source of error. (Adapted from reference [23])

ICG dye is selectively taken up by hepatocytes and is cleared via bile transporters exclusively into bile. Formal ICG clearance studies utilise the Fick principle, and require peripheral access for an ICG infusion, peripheral arterial access for peripheral 'blood pool' sampling and transjugular hepatic venous catheterisation for hepatic venous sampling. The infusion is run for a fixed time period in which the patient is likely to reach a steady-state concentration in the blood, after which hepatic venous and peripheral arterial samples are obtained. By comparing the concentrations of ICG in these two samples, ICG clearance can be measured, which when combined with blood haematocrit can be used to estimate effective liver blood flow [39, 40]. While well within the remit of research applications, the requisite of hepatic venous sampling (normally performed by interventional radiologists) has restricted routine clinical use. The exclusive hepatic extraction of ICG combined with its spectrophotometric properties has however been used

to derive simpler, less invasive surrogates of formal ICG clearance and these have found favour in routine clinical assessment, particularly in the intensive care setting. These single bolus methods of ICG clearance, such as ICG plasma disappearance rate (ICG-PDR) and ICG 15 minute retention rate (ICG-R15)[41] provide measurements linked to liver blood flow but in alternative units, dependent on other additional factors and subject to error[42].

Measurement of hepatic clearance can also be achieved using other substrates taken up by the liver, including sorbitol[43], lignocaine[44] and galactose[45]. Of note, cholate clearances have been reported to be of particular value in the assessment of liver disease. By measuring clearance of oral and serum cholate, Everson et al have proposed a method of estimating portal hepatic filtration rate (comparable to blood flow), porto-systemic shunting and a composite metric known as 'disease severity index'[46]. The group have demonstrated relationships with fibrosis, complications of portal hypertension and clinical outcomes in hepatitis C virus (HCV) patients [47, 48].

A final and important challenge to both gold standards and the non-invasive methods developed to emulate these methods is the intrinsic physiological variability of haemodynamic parameters. Blood flow, tissue perfusion, pressure and tissue resistance have the physiological potential to vary significantly within an individual in a short time frame. Coupled to this, differences in methods and the units of parameters measured from each method make reliable comparisons between measurements cumbersome, complicated and error prone.

1.3 APPROACHES TO HAEMODYNAMIC IMAGING IN THE LIVER

1.3.1 SCINTIGRAPHY

The earliest accounts of perfusion imaging were by scintigraphic methods, described in 1970s [49]. Tracers such as sulphur colloid, albumin or tin, usually conjugated with ^{99m}Tc were administered, with progressive accumulation of counts monitored using a gamma camera positioned over the liver. Later techniques were able to separate hepatic arterial and portal venous contributions by dynamic imaging and assuming predominantly portal venous perfusion once peak renal tracer accumulation was noted. Rises in activity during arterial and portal venous phases of tracer accumulation could then be used to infer the hepatic arterial perfusion index (HPI - a measure of relative hepatic arterial perfusion), which attracted considerable interest for the characterisation of arterialised liver lesions [50-52].

With the advent of single photon emission computerised tomography (SPECT/CT) the development of more complex quantification methods paved the way for tracers with the potential for both functional and volumetric assessment. Although ^{99m}Tc -Iminodiacetic acid (IDA) compounds have been in use since the 1970s for evaluation of the biliary system, analogues such as ^{99m}Tc -mebrofenin have attracted renewed interest in the development of functional parameters based on quantification of hepatic uptake [53-55]. These tracers, much like ICG and their gadolinium based hepatocyte-specific counterparts for MRI imaging (discussed later), are endocytosed by hepatocyte bile transporters [56, 57]. Importantly, quantification of uptake of IDA analogues has been shown to be highly correlated with ICG clearance [58]. Commercially available in Japan, ^{99m}Tc -Galactosyl Serum Albumin (GSA), binds to the asialoglycoprotein receptors distributed in high concentrations on functional hepatocytes [59, 60]. Accumulation of the tracer is proportional to blood flow and correlations with ICG clearance [61-63] and post-hepatectomy clinical outcomes have been demonstrated [64-66]. The tracer has also been shown to be of value in assessing functional liver volumes [67].

Experimental hepatic scintigraphic tracers have also produced several interesting studies that underline the value of cell-specific agents in quantitative imaging. Of note Iwasa et al. demonstrated that ^{99m}Tc -(Sn)-N-pyridoxyl-5-methyltryptophan - a hepatocyte-specific tracer - could be used to estimate intrahepatic and extrahepatic shunted blood flow and that these parameters could demonstrate changes in cirrhotic patients which were more significant with more advanced Child-Pugh class [68, 69]. Similarly, extrahepatic shunting was evaluated using intrasplenic injection of ^{99m}Tc -

phytatein to demonstrate increased levels of extrahepatic shunting in patients with more advanced Child-Pugh class [70].

More recent development of positron emission tomography (PET) methods, have demonstrated the potential for use of 2-18-fluorodeoxy-galactose as a measure hepatic metabolic function with PET/CT [71, 72], and in demonstrating changes in function post-PV ligation in rats using PET/MR [73].

Although scintigraphic quantification is amenable to a more simplified analysis, the biggest disadvantage of radionuclide imaging is the lack of anatomical resolution. Combined methods such as SPECT/CT do address this challenge, but bring the added hazard of significantly higher doses of ionising radiation. Although quantitative scintigraphy has a defined place in current clinical practice, the appetite for higher quality anatomical over functional imaging is reflected in imaging practices at liver centres in the UK and elsewhere.

1.3.2 ULTRASOUND

Doppler ultrasound (US) studies can be used to study the haemodynamic status of the liver: colour Doppler US can be used to demonstrate flow and flow directionality, while spectral Doppler waveforms can be used to investigate the pattern and flow velocity within a vessel [74]. Rough estimations of bulk vessel flow can be calculated by multiplying the mean flow velocity within a vessel and its cross-sectional area [75]. Numerous studies in patients with chronic liver disease are present in the literature, although findings are variable and data quality heterogeneous.

Colour Doppler US can be used to reliably study flow directionality and the identification of hepatofugal portal venous flow is a recognised discrete biomarker for portal hypertension and chronic liver disease. Flow quantification with US is however much less conclusive. Composite measurements based on velocities recorded from Doppler spectral traces include the resistive index (RI), pulsatility index (PI), congestion index (CI) and damping index (DI), to name but a few of those reported in the literature (figure 1.3, table 1.1) [76]. These parameters have been studied in the hepatic artery, portal vein and hepatic veins with varying success [77].

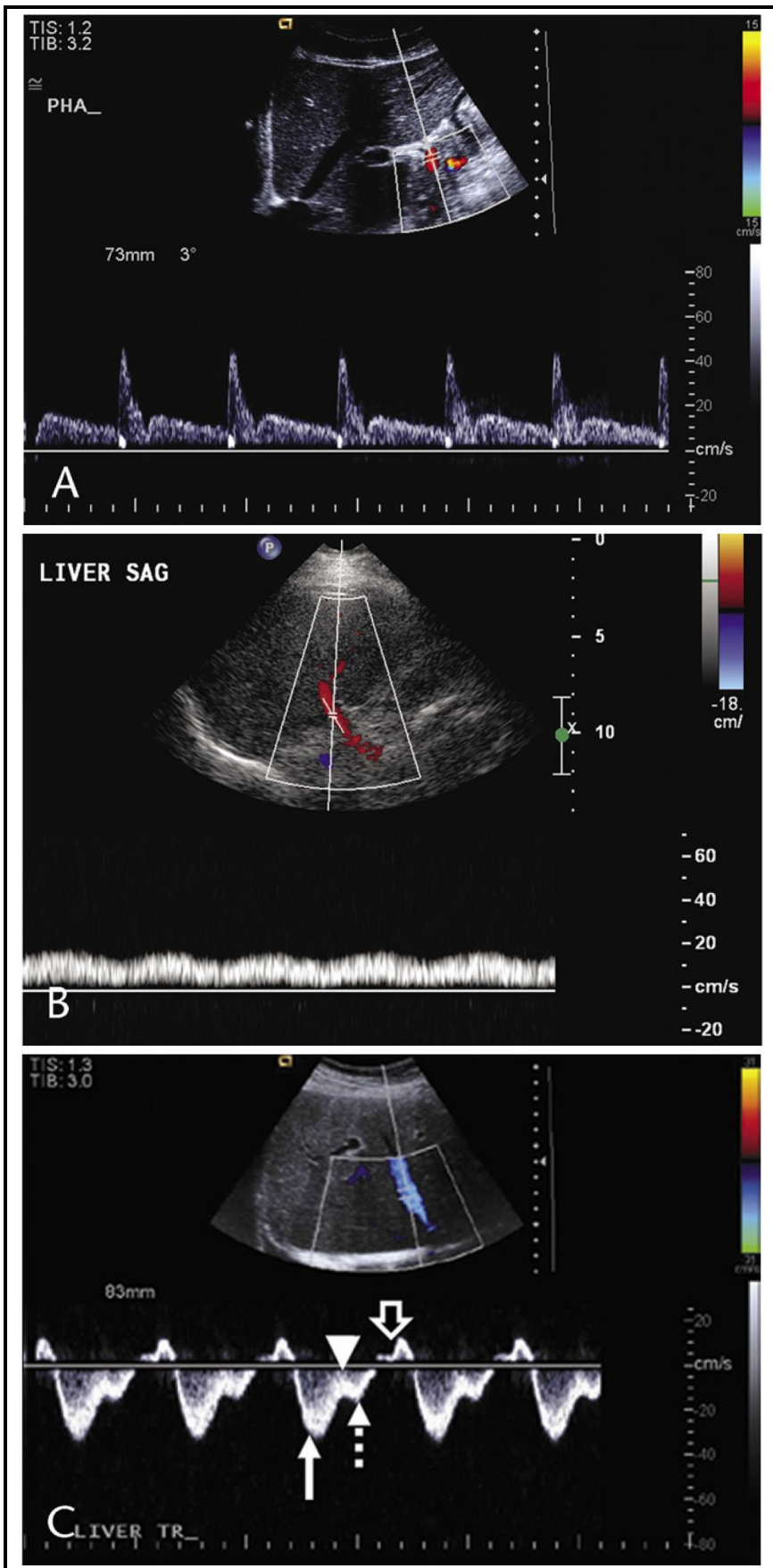


Figure 1.3:
Normal spectral
traces for liver
vessels

(a) Hepatic artery – note the pulsatile waveform with sharp systolic peak, (b) portal vein – continuous hepatopetal flow, with subtle sinusoidal variation through the cardiac cycle and (c) hepatic vein – note the physiological triphasic wave form, with antegrade flow in systole (solid arrow) and diastole (dashed arrow) and retrograde flow due to valvular closure (triangle, wide arrow). (Adapted from reference [78])

Table 1.1: Quantitative indices for Doppler US of hepatic vessels

Resistive Index (RI) = $\frac{\text{peak systolic velocity (cm/s)} - \text{end diastolic velocity (cm/s)}}{\text{peak systolic velocity (cm/s)}}$
Pulsatility Index (PI) = $\frac{\text{trough velocity (cm/s)}}{\text{peak velocity (cm/s)}}$
Congestion Index (CI) = $\frac{\text{portal venous cross sectional area (cm}^2\text{)}}{\text{portal venous velocity (cm/s)}}$
Damping Index (DI) = $\frac{\text{peak hepatic venous outflow during ventricular systole (cm/s)}}{\text{trough hepatic venous outflow during ventricular systole (cm/s)}}$

The hepatic artery is a normally pulsatile, low resistance vessel such that the normal range for the hepatic arterial RI is approximately 0.55-0.81. When studied in the context of chronic liver disease, the picture is ambiguous – cirrhosis itself has the potential to drive up the RI, while the presence of distal shunting will have the opposite effect. Overall hepatic arterial RI has consequently been shown to be unhelpful in predicting cirrhosis or severity of liver disease [74].

The portal venous PI has also been well-investigated with lower PIs corresponding to higher pulsatility. Higher pulsatility is seen in cirrhosis where there is arteriportal shunting. The CI has also been shown to be raised in portal hypertension, but correlation with invasive portal pressure measurements are weak [79]. Reduced portal venous velocity (with eventual flow reversal), increased vessel size and presence of abnormal/re canalised extrahepatic shunts are also sonographic features of portal hypertension, but quantitation of these features is less well correlated with severity of disease [75, 80-82].

The normal hepatic venous spectral trace occurs because of transmitted cardiac flow changes. In cirrhosis, there is flattening of the flow profile as result of non-compliance from surrounding fibrotic tissue, such that is decreased phasicity of the spectral trace and spectral broadening. These changes in theory could be reflected in the DI, however diagnostic performance and correlations between the DI and HVPG though present, are however weak [82-86].

Although transcutaneous approaches to using US for quantitative evaluation of liver blood flow are attractive because of their simplicity and non-invasive nature, invasive approaches have also been reported. Transit-time US probes placed directly on the vessels intra-operatively not only provide more robust quantification, but have enabled studies in which direct physical manipulation of portal flow can be used to study the HABR [87-89]. Presence of the HABR in patients without liver cirrhosis has been demonstrated and impairment of the HABR in cirrhosis has also been shown [31]. Similarly, intra-vascular Doppler US probes have been used to study hepatic arterial flow

[90]. Studies of the HARR, have demonstrated differences in hepatic arterial flow and flow reserve (as assessed by intra-hepatic arterial adenosine infusion) across varying severities of liver disease [91, 92]. Although the findings of these studies are promising, the invasive nature of these studies has limited their translation into regular clinical practice.

Contrast-enhanced US (CEUS) using microbubble contrast media has shown potential for quantitative assessment of liver disease. Like most contrast-based imaging methods, it has been rapidly translated into the clinical setting for qualitative use in characterisation of liver lesions. Microbubble contrast media enhance the Doppler signal by approximately 20dB, with quantitative imaging based on deriving Doppler signal time-intensity curves after administration of the contrast agent intravenously followed by a flush. The Doppler signal over a vessel (typically hepatic vein) is then monitored for several minutes and time-series signal data is then recorded. The Doppler signal correlates well with microbubble concentration, and this can then be used to derive quantitative parameters [93, 94].

The time taken for peripherally administered contrast agent to be detected in the hepatic vein (hepatic venous arrival time or HVAT) has been demonstrated by several groups to be reduced in the context of chronic liver disease. This is thought to be due to intrahepatic shunting and arterialisiation of hepatic capillary beds [93, 95, 96]. Others have measured the time difference between contrast agent arrival time in the hepatic vein and hepatic artery/portal vein – so-called ‘intra-hepatic circulating time’ or ‘hepatic arterial-venous transit time’ and reported encouraging correlations of these parameters with fibrosis scores [97-99]. A small-scale multi-centre trial ($n = 99$) has also reported correlation with fibrosis score and a cut-off value of 13 seconds for the HVAT diagnosis of severe fibrosis (specificity of 78.5%, sensitivity of 78.95%; positive predictive value of 78.33%, negative predictive value of 83.33%)[100]. Of note, a single-centre study has reported statistically significant correlations between the HVPG and HVAT ($r = 0.7470$, $p < 0.001$, $n = 71$) quoting a cut-off value of 14 seconds for the HVAT diagnosis of clinically significant portal hypertension (specificity of 86.7%, sensitivity of 92.7%, positive predictive value of 90.5%, negative predictive value of 89.7%) [101]. The relationship between HVPG and HVAT has however not been confirmed at other centres ($r = 0.276$; $p = 0.041$, $n = 44$) [102]. While these findings are encouraging, concerns over the reproducibility and repeatability of US derived quantitative parameters remain. Studies have reported high inter-equipment variance and poor inter-scan agreement [103, 104]. Additionally, while availability of the contrast agents and hardware is good, the specific software requirements have presented a barrier to widespread clinical use [94].

1.3.3 COMPUTERISED TOMOGRAPHY

By recording serial measurements of mean attenuation of a region-of-interest (ROI) after the administration of contrast agent, Axel was the first to propose in 1980 a novel CT method of quantifying perfusion using so-called 'dynamic contrast enhanced' (DCE) CT [105]. It was not however until the early nineties when this method was first demonstrated by Miles et al in the liver [106-108]. Much like in CEUS, post-contrast attenuation on CT is linearly related to contrast agent concentration. Using the 'direct slope method', perfusion can be estimated from the ratio of the maximum rate of change of parenchymal enhancement post-contrast to the peak attenuation from an ROI over the aorta [107]. Relative hepatic arterial and portal venous contributions can then be separated using peak splenic enhancement as a marker for the start of predominantly portal venous perfusion [108]. This method was subsequently refined as the 'subtraction slope method', which aims to provide a more robust assessment of portal venous perfusion by subtracting the splenic (arterial) enhancement from the hepatic parenchymal enhancement curve and assessing the ratio of the maximum rate of change of enhancement of the 'corrected' enhancement curve to the peak attenuation from an ROI over the portal vein. Using this method, Blomley et al estimated hepatic arterial and portal venous hepatic parenchymal flow to be 19 ± 11 ml/min/100g and 93 ± 26 ml/min/100g in control subjects and demonstrated a statistically significant alteration in these parameters to 25 ± 12 ml/min/100g and 43 ± 26 ml/min/100g in cirrhotic patients [109]. Employing this same method, Tsushima et al correlated wedge hepatic venous pressure (but not HVPG) with splenic perfusion in a small cohort of patients (figure 1.4) and went on to demonstrate that splenic perfusion as calculated by this technique was decreased in patients with known chronic liver disease [110].

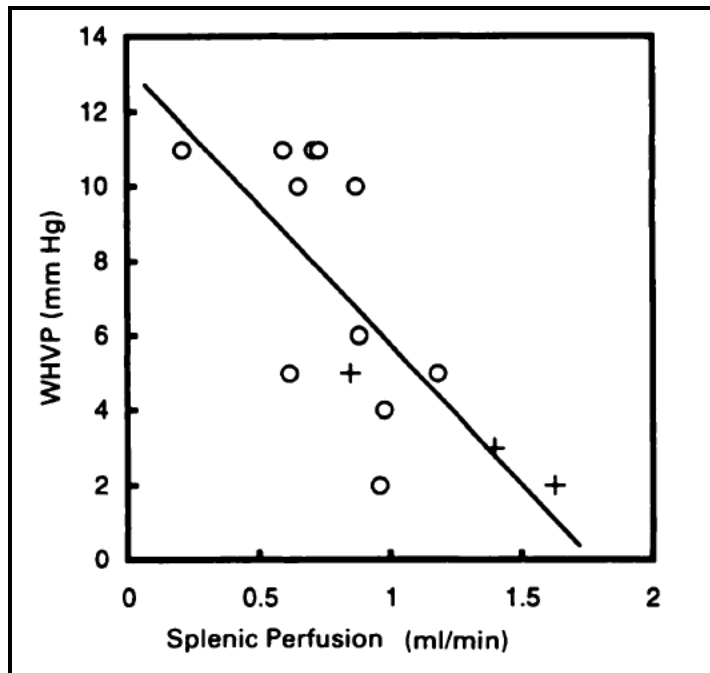


Figure 1.4: DCE CT studies of splenic perfusion and wedge hepatic venous pressure (WHVP)
 Scatterplot demonstrating correlation between WHVP and DCE CT splenic perfusion ($r = 0.724$, $p < 0.0024$; \circ = chronic liver disease, $+$ = normal liver). (Obtained from reference [110]).

Although original validation of the slope technique was based upon assessment of the hepatic arterial fraction using colloid scintigraphy in seven patients, a 2012 study aiming to validate these CT perfusion methods in pigs using TTUS demonstrated disappointing estimation of absolute and relative hepatic arterial and portal perfusion values. More worryingly, the authors also described alterations in bulk vessel flow as measured by TTUS as a result of contrast agent administration [108, 111]. Encouragingly, a more recent study looking at non-modelled parameters such as ‘time-to-peak’ parenchymal enhancement demonstrated good correlations with ICG-R15 ($r = 0.789$, $p < 0.0001$) and ICG-PDR ($r = -0.790$, $p < 0.0001$) in patients with hepatobiliary malignancy [112].

An alternative model initially developed for PET imaging has also been developed for DCE CT [113]. The ‘dual-input single compartment’ (Chapter 2, figure 1.3), models the hepatic parenchymal enhancement with enhancement curves from ROIs placed over the aorta and portal vein. Initial validation with radio-labelled microspheres demonstrated encouraging correlations but weak agreement between methods (Figure 1.5) [114]. Van Beers et al correlated DCE CT perfusion parameters with disease severity in cirrhotic patients and demonstrated a fall in overall perfusion in cirrhotic patients, with a statistically significant rise in arterial fraction and mean transit time ($41 \pm 27\%$ and 51 ± 79 seconds in cirrhotic patients compared with $17 \pm 16\%$ and 16 ± 5 seconds in healthy controls) [115].

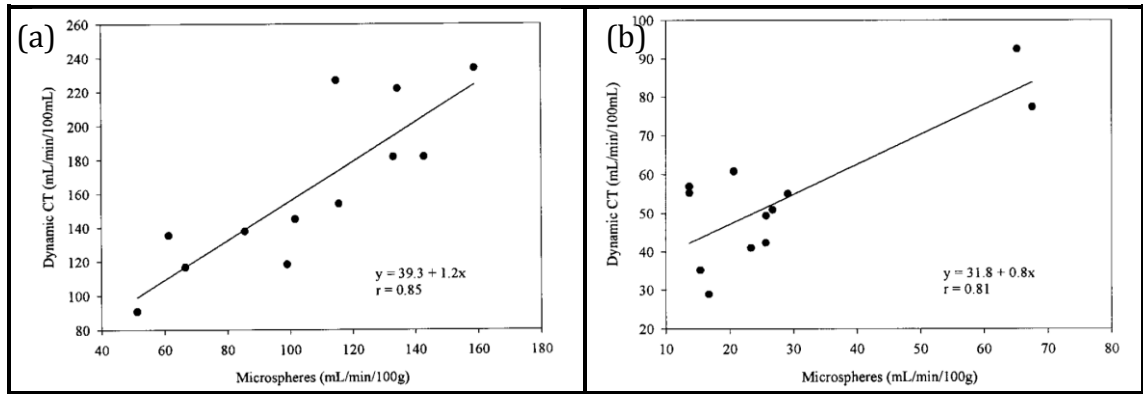


Figure 1.5: Validation of (a) portal venous and (b) hepatic arterial perfusion estimated using DCE CT and the dual input single compartment model with radio-labelled microspheres

Encouraging correlations for (a) portal venous perfusion ($r = 0.85$) and (b) hepatic arterial perfusion ($r = 0.81$) were demonstrated between the two methods. (Obtained from reference [114]).

Building on this work, Materne et al went on to use DCE CT with both low and high molecular weight contrast agents to study differences in modelled perfusion parameters in the normal rabbits and rabbits with histologically verified fibrosis. While standard commercial (lower molecular weight) extracellular contrast agents would easily distribute through the extra-vascular interstitial space, the deposition of fibrotic tissue in the space of Disse (figure 1.1(b)), as seen in liver fibrosis, was thought to restrict the distribution of the higher molecular weight contrast agent, thereby accounting for observed reductions in DCE CT distribution volume (32.0 ± 6.7 to $22.2 \pm 4.8\%$) and mean transit time (12.0 ± 1.2 to 10.0 ± 1.8 seconds), both of which were not significantly different in control animals [116]. A more recent study, evaluating DCE CT in rats with thioacetamide-induced acute liver injury, demonstrated increases in HA perfusion (26.9 ± 4.3 to 44.3 ml/min/100g), reductions in PV perfusion (251.9 ± 6.4 to 107.6 ± 12.4 ml/min/100g) and increases in mean transit time (0.085 ± 0.005 to 0.228 ± 0.035 minutes) and distribution volume (23.6 ± 0.5 to $31.2 \pm 2.0\%$) between control and acutely-injured subjects [117].

While the absolute quantification of flow using DCE CT with either modelling method remains contentious, the real strength of cross-sectional imaging is in the development of regional high resolution parametric maps to study regional differences in perfusion [118]. Consistent alterations in regional contrast enhancement have been reported with DCE CT both in normal patients and those with established portal hypertension [119, 120]. In the context of lesion characterisation, the ability of 'slope methods' to separate arterial and portal venous contributions has been used to aid in the detection of arterialised lesions [121, 122]. The ability of DCE CT to detect gross alterations in perfusion parameters in livers with occult micro-metastases has also

heralded the potential for flow quantification as means to detect evolving metastatic disease before macroscopic lesions are even seen on imaging [123, 124].

While scanner availability is high and overall costs are low, concerns over the ionising radiation dose from DCE CT, particularly in protocols requiring repeated acquisitions of a single axial slice remain the biggest barrier to widespread use in the clinic. Protocols have been suggested where once a standard simple structural CT is performed, further characterisation of identified lesions could be undertaken using single-slice DCE CT at the site of concern [118]. It is however, difficult to envisage such a protocol in the clinical setting especially if there are multiple lesions that require slices at different levels. Additionally DCE CT requires the use of iodinated contrast media which carry the risk of contrast-induced nephropathy. In patients with chronic liver disease and superadded renal complications, a purely diagnostic study therefore has the potential to adversely affect clinical outcomes [125].

1.3.4 DYNAMIC CONTRAST ENHANCED MRI

The principles of DCE MRI are identical to those underpinning DCE CT. DCE MRI is typically undertaken using gadolinium chelated with diethylene triamine pentaacetic acid (Gd-DTPA) as a contrast agent. The paramagnetic properties of gadolinium ensure striking shortening of T1 times and chelation to DTPA ensures rapid distribution within the extracellular space, with exclusive renal clearance [126]. Unlike DCE CT and CEUS however, contrast agent concentration is not linearly related to MRI signal intensity (SI) change, but linearly related to the reciprocal of a given concentration's T1 relaxation time [126, 127]. Formal quantitation therefore requires three sets of data: (i) dynamic T1-weighted images yielding serial mean ROI signal intensities, (ii) measurement of the intrinsic T1 of the tissue within the ROI and (iii) measurement of the contrast agent T1 relaxivity (so-called 'r1' measurement)[128-131]. As with CT, these methods were originally developed for applications in the brain and it was not until the late nineties when the first attempts at translating these methods into the liver were made [132, 133].

Early single slice studies were performed in pigs by Scharf et al. with quantification based on a linear one-compartment open model (figure 1.6). This model is not designed to yield absolute estimates of tissue perfusion but rather 'K_p', a pharmacokinetic parameter related to perfusion, based upon blood flow and intravascular volume. The model is also used to estimate 'A' (amplitude), a term reflecting the degree of relative contrast enhancement. Correlations between K_p and invasive thermal diffusion probe measurements of perfusion in pigs were encouraging ($r = 0.91$, $p < 0.01$), but were much poorer once translated into patients ($r = 0.39$, $p = 0.17$)[134, 135]. Unlike later models, this model does not require the measurement of vascular input functions, nor is

there any attempt to quantify signal intensity change with intrinsic tissue T1 or contrast agent T1 relaxivity.

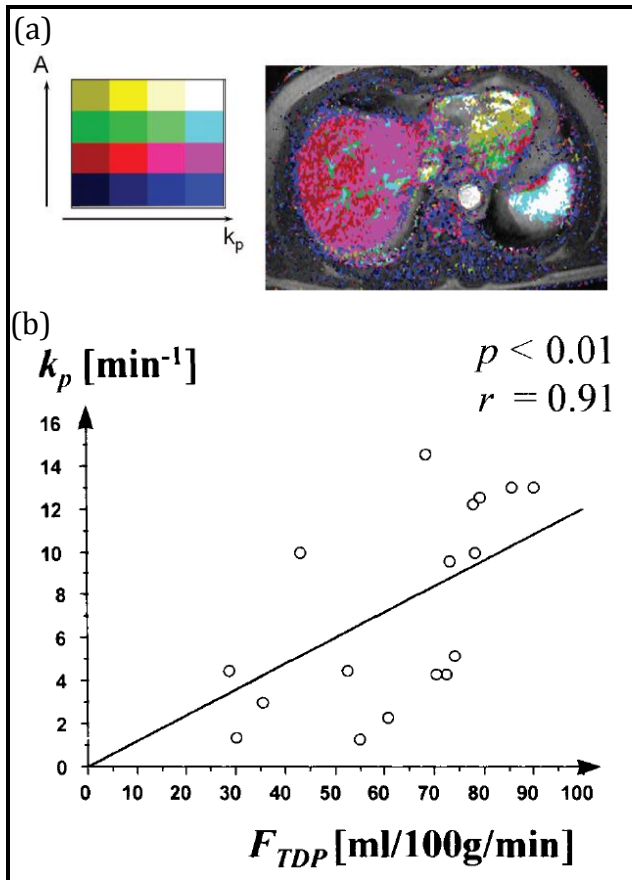


Figure 1.6: DCE MRI flow quantification using the Scharf et al. model

(a) Axial image with overlaying perfusion map of parameters 'A' and 'K_p' in a patient, demonstrating predominantly right liver. (b) Encouraging correlation between 'K_p' and thermal diffusion probe perfusion measurements in pigs. (Obtained from references [135] and [134]).

The first more comprehensive attempts at contrast agent pharmacokinetic modelling in the liver were in the context of developing high resolution parametric maps with a view to lesion characterisation. Jackson et al demonstrated utility in hepatocellular carcinoma characterisation and reproducibility of these parameters in small cohort of patients [136]. An alternative approach was also developed by White et al from adapting early CT based methods [108, 109] to measure 'hepatic perfusion index' (a measure of hepatic arterial fraction within a region of interest) for lesion characterisation [137-139].

The dual input single compartment model was also successfully adapted and applied to DCE MRI. Validation with invasive microsphere measurements in rabbits demonstrated strong correlation and ostensibly better agreement than that seen with CT (figure 1.7, compared with figure 1.5)[140].

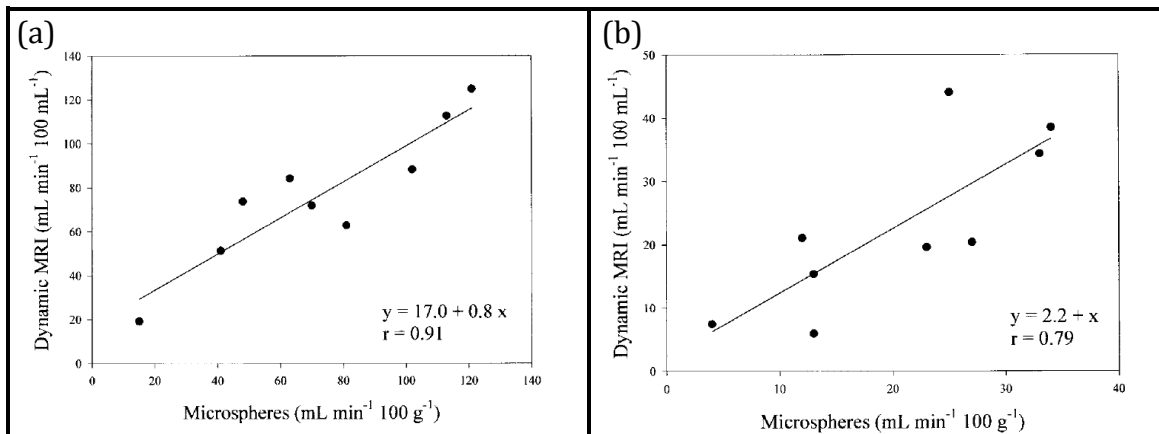


Figure 1.7: Validation of (a) portal venous and (b) hepatic arterial perfusion estimated using DCE MRI and the dual input single compartment model with radio-labelled microspheres

Encouraging correlations for (a) portal venous perfusion ($r = 0.91$) and (b) hepatic arterial perfusion ($r = 0.79$) were demonstrated between the two methods. (Obtained from reference [140]).

The same group proceeded to do a larger study in cirrhotic patients ($n = 46$), demonstrating significant differences in bulk and relative portal flow in normal (56.39 ± 27.82 ml/min/100g and $82.58 \pm 14.88\%$) and cirrhotic patients (16.23 ± 15.22 ml/min/100g and $43.81 \pm 31.97\%$). In the same study DCE MRI parameters were matched with HVPG measurements, and encouraging correlations were demonstrated with portal fraction ($r = -0.769$, $p < 0.001$). Interestingly, this study also collected Doppler US derived flow parameters in the same cohort of patients, which demonstrated much poorer (and non-significant) correlations with both HVPG and Child-Pugh class [82]. The dual input single compartment model parameters were also correlated with invasive fibrosis scores using a three dimensional volumetric (rather than single slice) acquisition, to demonstrate that distribution volume, arterial fraction and mean transit time were the best model derived parameters to predict Batts-Ludwig fibrosis score 3 and above (area under receiver operating characteristic curves of 0.824, 0.791 and 0.775, respectively) [141]. A large animal cohort study in cirrhotic rats ($n=52$) also demonstrated significant but modest correlations between duration of treatment with carbon tetrachloride (a liver fibrotic agent) and distribution volume, mean transit time and portal fraction ($r = -0.483$, $r = -0.664$ and $r = 0.414$, $p < 0.01$) [142]. Additionally, a recent study in seventeen patients with hepatocellular carcinoma undergoing radiotherapy demonstrated significant correlations between dual input single compartment PV perfusion and ICG $T_{1/2}$ (minutes) ($r = 0.7$, $p < 0.0001$) [143].

There have also been a number of clinical studies since the original work by Annet et al. [82], proposing methodological refinements for hepatic DCE MRI. These include correction of arterial input functions (AIFs) [144], evaluation of quantification effects of

changes in temporal resolution [145], evaluation of alternative approaches to conversion of signal intensity into contrast agent concentration [146] and the use of alternative breath holding strategies [147].

As with CT the concept of using contrast agents of higher molecular weight to measure alterations in contrast agent distribution volume in fibrotic subjects was also tested. Using a different contrast agent to their previous CT study, Van Beers et al used a 52 kDa gadolinium based contrast agent in rabbits to demonstrate significant reductions in distribution volume (6.2 ± 2.1 vs $9.7\pm 1.6\%$), but also correlated this with ICG clearance ($r = 0.857$, $p = 0.007$) and collagen content on biopsy ($r = -0.833$, $p = 0.010$) [148]. Based on this work an argument can be made for refining the dual input single compartment model into a dual input dual compartment model, in which the Space of Disse can be accounted for as separate compartment in the model. This more complex model has had limited evaluation in small cohort of mice, with no validation [149]. Further studies have applied the model in the context of evaluation of hepatic metastatic lesions, where a second compartment would be appropriate in the context of anomalous lesional vascularity [150, 151]. Although the extension of the model in microcirculatory terms is interesting, the dual input dual compartment model estimates more parameters from the same data, thereby subjecting the model to a higher risk of error.

1.3.5 DYNAMIC HEPATOCYTE-SPECIFIC CONTRAST ENHANCED MRI

The use of gadolinium based contrast agents chelated with hepatocyte-specific receptor ligands has been rapidly translated into clinical practice for lesion characterisation, but has also generated novel opportunities for flow quantification. Much like their extracellular counterparts, these agents cause T1 shortening but also produce a progressive rise in hepatocyte T1-weighted signal intensity as these agents are taken up by basolateral cell membrane transporters and excreted at the apical surface into the biliary system. Dynamic hepatocyte-specific contrast enhanced (DHCE) MRI studies can also therefore in theory be used to generate other quantitative parameters that may relate to hepatocyte function [152, 153].

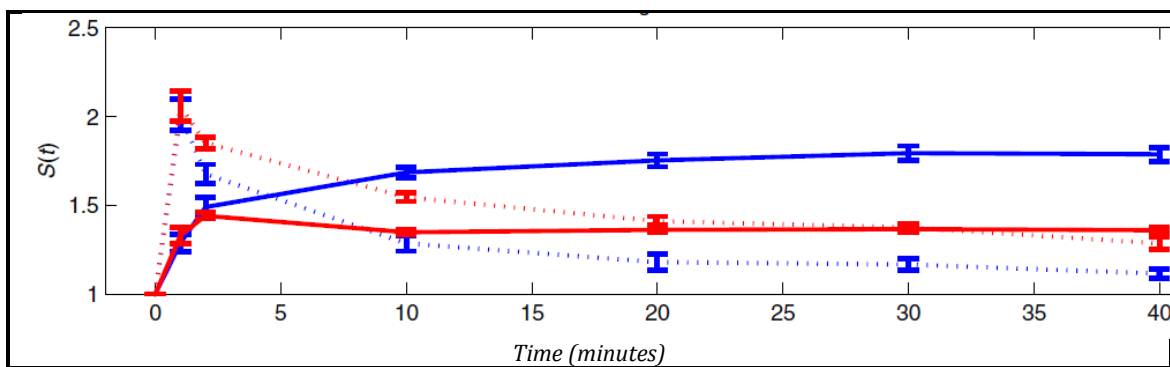


Figure 1.8: Baseline normalised signal intensities for ROI enhancement with hepatocyte-specific contrast agents in healthy volunteers

Hepatic ROI (solid) and splenic ROI (dashed) enhancement with gadobenate dimeglumine (red) and gadoxetic acid (blue). Note how after an initial vascular-phase peak, hepatic gadobenate dimeglumine enhancement slowly rises, with peak enhancement (not shown on this chart) after 45 minutes. Conversely peak enhancement with gadoxetate acid is achieved after 20 minutes. Overall enhancement is much higher with gadoxetic acid. (Obtained from reference [154]).

Two agents have been licensed for clinical use – gadobenate dimeglumine (Multihance, Bracco) and gadoxetic acid (Primovist, Bayer). Following injection, both these agents distribute in the extracellular space before entering into hepatocytes. Five percent of gadobenate dimeglumine undergoes hepatobiliary excretion, compared with 50% of gadoxetic acid. The remainder is excreted renally. Peak hepatobiliary uptake is seen at 45-120 minutes for gadobenate dimeglumine compared with 20 minutes for gadoxetic acid (figure 1.8) [155-157]. Quantitative studies with gadobenate dimeglumine have been limited and only undertaken in the preclinical setting. In an isolated perfused rat liver model, alterations in gadobenate dimeglumine uptake have been demonstrated in cirrhotic bile-duct ligated rats [158]. Complex pharmacokinetic modelling has been developed to quantify differences in hepatocellular uptake in the isolated perfused model, with validation using scintigraphic methods. Unfortunately this is yet to be translated into the *in vivo* or clinical setting[159, 160].

Quantitative studies with gadoxetic acid have been more extensive. Early studies in rabbits before and after induction of cirrhosis using carbon tetrachloride showed alterations in relative 'hepatic extraction fraction' - a modelled parameter from deconvolution analysis. These changes also demonstrated encouraging correlations with rises in ICG-R15 measurements before and after induction of cirrhosis [161]. Building on this work Nilsson et al translated this method into the clinical setting (figure 1.9) [162]. In studies involving predominantly Child-Pugh class A primary biliary cirrhosis and primary sclerosing cholangitis patients, significant differences in 'hepatic extraction fraction' and 'mean transit time' (but not 'input relative blood flow') were observed [163, 164].

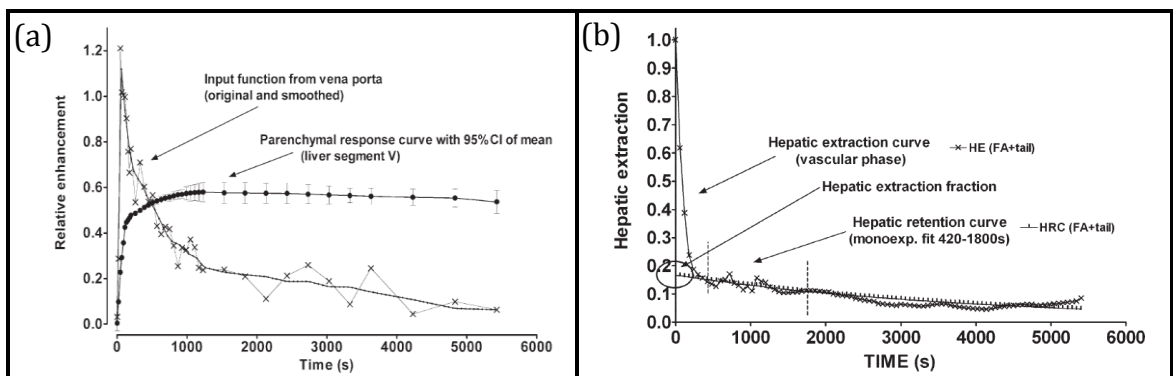


Figure 1.9: Quantitative studies with gadoxetic acid – deconvolution analysis

Enhancement curves obtained from ROIs placed on the portal vein (the vascular input function) and hepatic parenchyma (tissue response function) are shown in (a). Deconvolution analysis was used to generate the curve shown in (b), which was then used to estimate 'hepatic extraction fraction', 'input relative blood flow' and 'mean transit time'. (Obtained from reference [162]).

In a larger scale study ($n = 79$) Chen et al also demonstrated that the dual input single compartment model could be applied for analysis of the first 60 or 100 seconds post-gadoxetic acid, to demonstrate significant differences between hepatic arterial and portal venous flow between normal and chronic hepatic patients. Correlations between these parameters and invasive biopsy fibrosis scores were disappointing [165]. A dual input *dual* compartment model was shown by Sourbron et al to be superior to the single compartment model for gadoxetic acid enhancement in normal liver tissue, but also in focal hepatic parenchymal lesions with abnormal vascular configuration (figure 1.10)[166]. More recently, Saito et al have utilised enhancement from five phases of standard clinical DHCE protocols (baseline, early arterial, arterial, portal venous and hepatocellular phases) with a dual-input Patlak model to study differences in 'uptake rate' and 'extracellular volume' across a large cohort of non-cirrhotic and Child-Pugh Class A and B patients ($n = 119$). Although this study failed to properly quantitate enhancement as no T1 measurements were made, significant differences in uptake rate were demonstrated between non-cirrhotic and between Child-Pugh A and B patients. Attempts

at using this method to quantify arterial fraction did not yield physiologically reasonable estimates [167].

An alternative much coarser approach based on the ratio of liver and splenic enhancement 20 minutes post-gadoxetic acid administration has also been shown to correlate well with ICG-PDR in normal and cirrhotic patients [168]. DHCE quantification by measuring peak signal intensity in the biliary tree relative to adjacent muscle signal intensity has also been attempted, with significant reported correlations with ICG-R15 measurements [169]. Since these studies, a multitude of authors have correlated relative peak hepatobiliary uptake SI (normally to muscle, spleen or baseline SI) with outcomes including liver function tests, MELD scores [170, 171], presence of steatosis [172], fibrosis scores [173, 174], occurrence of liver failure after major resection [175] and post-resection hepatocyte damage [176].

A more scientifically sound approach is based on measurement of baseline and peak hepatobiliary phase T1, to generate a 'T1 relaxation time index' or then just the raw peak hepatobiliary phase T1. This is likely to be more useful, especially in the context of defining diagnostic thresholds that are transferable between institutions. These studies have demonstrated changes in T1-based quantification in the presence of disease and correlations with MELD scores [177, 178].

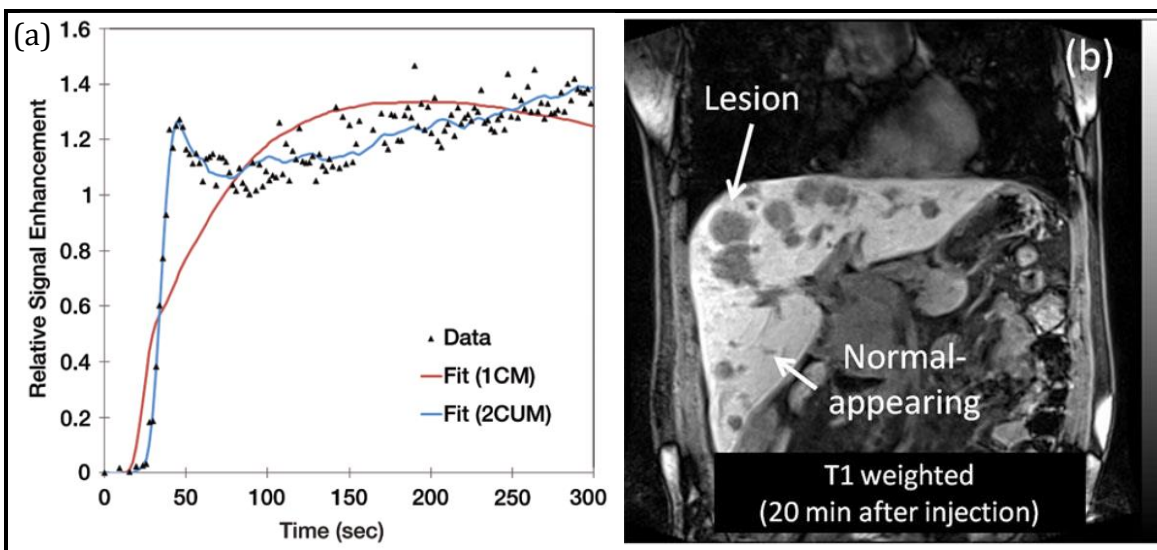


Figure 1.10: Dual input dual compartment modelling for DHCE MRI

(a) Enhancement curve for ROI placed over normal hepatic parenchyma, with markedly improved fitting using a dual input dual compartment model (shown in blue) when compared with a dual input single compartment model (shown in red). (b) T1 weighted coronal image in patient with multiple hepatic metastatic lesions, 20 minutes after gadopentetate administration. Note the striking uptake of contrast agent in normal parenchyma compared to lesional enhancement. (Obtained from reference [166]).

As both hepatocyte-specific contrast agents and ICG enjoy hepatic extraction, it is unsurprising that DHCE-MRI model derived parameters and ICG clearance surrogates have been encouraging. Although studies correlating formal ICG clearance with DHCE-

MRI model derived parameters have yet to be performed, the prospect of absolute quantification of hepatic clearance using DHCE-MRI models is exciting.

Both DCE and DHCE-MRI face similar challenges. At the heart of any contrast-based quantitative imaging method, the relationship between contrast enhancement and contrast agent concentration needs to be defined and approaches to achieve this vary between methods and authors. The absence of a linear relationship between signal intensity and contrast agent concentration and the requirement for additional measurements is cumbersome. Additionally, high concentrations of contrast agent can lead to signal drop out (via T2* effects), a phenomenon which is exacerbated when imaging at higher field strengths [179, 180]. Failure to overcome this combined with poor temporal resolution, particularly for sampling of vascular input functions, can lead to major errors in measurements.

Even once these issues have been addressed, common to MRI, scintigraphic, US and CT methods, is the need to apply an appropriate model to derive useful and relevant haemodynamic parameters. These parameters must also be robust, reproducible and amenable to validation if the method is to gain clinical acceptance.

Despite these challenges, MRI offers unparalleled anatomical image resolution, without compromising patient safety through exposure to ionising radiation or to large volumes of contrast media and the adverse effects that these may cause. DCE and DHCE-MRI quantification studies to-date have been encouraging and with improved rigour and understanding, both approaches have the potential to yield more robust quantification in the future.

1.3.6 PHASE-CONTRAST MRI

All spins in a magnetic field gradient are subject to shifts in their phase of rotation, however moving spins experience a phase shift that, in a linear gradient is proportional to their velocity. By applying opposing magnetic field gradients, the phase shift observed in stationary tissue can be eliminated so that a velocity vector map can be constructed purely of the moving spins passing through the area being imaged (figure 1.11)[181]. Applying this concept to flowing blood in stationary tissue, an image can therefore be produced based upon the velocity vectors of flowing blood. Summing these vectors over the cross-sectional area of a vessel can then yield an estimate of bulk vessel flow. The phase shift is measured in degrees and the amount of shift experienced by a spin moving at a given velocity is dependent on the flow sensitising gradients. To ensure that the phase shift does not exceed 180° , the user must calibrate the gradients by specifying the expected peak velocity (in cm/s) – the so called ‘velocity encoding’ setting. This setting specifies the velocity capable of producing a phase shift of 180° . In two-dimensional phase-contrast MRI (PCMRI), the imaging plane must also be as perpendicular as possible to the direction of flow in the vessel of interest [182].

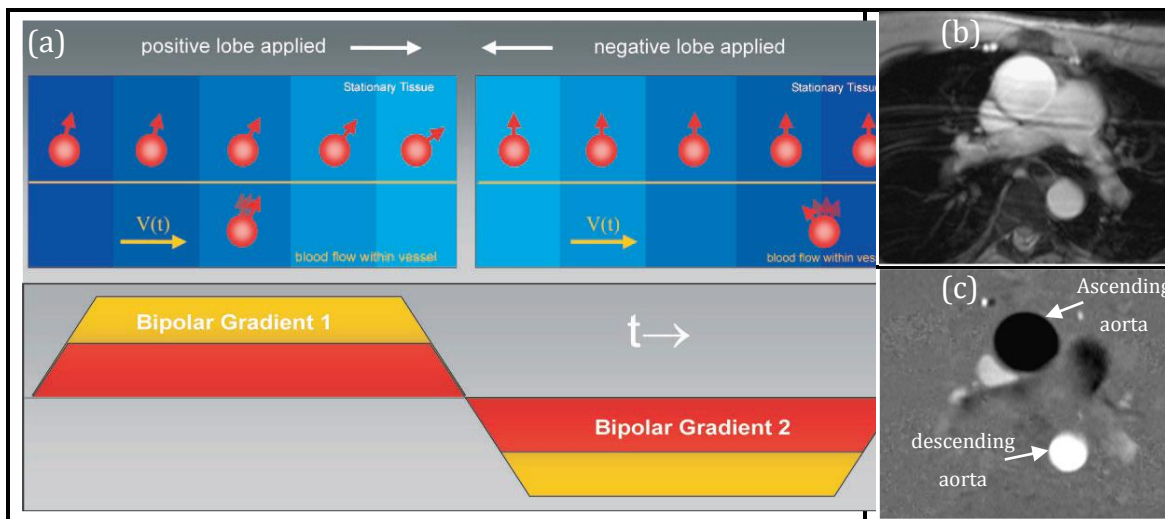


Figure 1.11: PCMRI – (a) schematic diagram of sequence and (b), (c) example of phase contrast acquisition images

(a) Bipolar gradients (lower images) induce phase shift in both stationary and moving spins (upper images), but ultimately cancels out the phase shift seen in stationary tissue. (b) Anatomical axial ‘magnitude’ image through cardiac outflow tracts with (c) corresponding phase contrast map. Note the opposing flow directionality (black versus white) in the ascending and descending aorta (labelled). (Obtained from reference [182]).

The principles underpinning phase-contrast MRI (PC-MRI) have been recognised since the late 1950s, however it was only in the early nineties when the first studies involving measurement of portal venous blood flow were undertaken [183]. Early studies confirmed the ability of PC-MRI to measure directionality of flow and peak portal venous flow velocity, validating these with Doppler ultrasound directionality and velocity

measurements [184-188]. Studies in normal volunteers were able to demonstrate rises in portal venous blood flow post-prandially[189] and it was also apparent early on that patients with portal hypertension had altered portal venous flow [190]. Since then, there have been multiple studies aiming to measure bulk portal venous, hepatic arterial, hepatic venous and azygous flow, and study changes that occur in the setting of chronic liver disease and/or portal hypertension. These are summarised in Table 1.2.

Table 1.2: Summary of studies aiming to measure bulk vessel flow with PC-MRI in the context of liver disease

AUTHORS, YEAR	CONTROL SUBJECTS MEAN VESSEL FLOW \pm SD	TEST COHORT	TEST COHORT MEAN VESSEL FLOW \pm SD	VALIDATION
a) PORTAL VEIN				
Burkart DJ. et al., 1993 [190].	1206 \pm 303 ml/min (n = 5)	Patients with known chronic liver disease and gastro-oesophageal varices	505 \pm 66 ml/min* (n = 6)	Flow phantom PCMRI measurements (r = 0.995, p = 0.0001) Transcutaneous Doppler bulk vessel flow (n = 11, r = 0.94, p = 0.0003)
Burkart DJ. et al., 1993 [191].		Known portal hypertension, varices and referred for liver transplant. Child-Pugh class A and class B (n = 6); class C (n = 26).	Child-Pugh class A and B: 23.8 \pm 7.6 ml/min/kg Child-Pugh class C: 10.4 \pm 8.4 ml/min/kg (measurements normalised to body mass)	None
Kashitani N. et al., 1995 [192].	720 \pm 198 ml/min (n = 20)	Known liver cirrhosis but no ascites (n = 15); chronic hepatitis (n = 5); idiopathic portal hypertension (n = 1)	870 \pm 289 ml/min [†] (n = 21)	Flow phantom PCMRI measurements (r = 0.997) Transcutaneous Doppler US bulk vessel flow (normal volunteers only - no statistically significant difference)
Kuo PC. et al., 1995 [193].		Known end-stage liver disease awaiting transplant (n = 39).	Child-Pugh class A (n = 13): 26 \pm 4 ml/min/100g Child-Pugh class B (n = 10): 46 \pm 6 ml/min/100g Child-Pugh class C (n = 16): 105 \pm 14 ml/min/100g	None

~
40
~

AUTHORS, YEAR	CONTROL SUBJECTS MEAN VESSEL FLOW \pm SD	TEST COHORT	TEST COHORT MEAN VESSEL FLOW \pm SD	VALIDATION
a) PORTAL VEIN (continued)				
Debatin JF. et al., 1996 [194].	Not recorded (n = 10)	Known liver cirrhosis, for elective TIPSS placement. Child-Pugh class A (n = 4); class B (n = 10); class C (n = 6). Chronic Hepatitis C (n = 15) and chronic alcoholic liver disease (n = 2). Child-Pugh class A (n = 10); class B (n = 5); class C (n = 2).	Pre-TIPSS: (n = 20) 996 \pm 618 ml/min [†]	Flow phantom PCMRI measurements (r = 0.997)
Sugano S. et al., 1999 [195].	1300 \pm 200 ml/min (n = 12)		Post-TIPSS: 1946 \pm 910 ml/min [†]	
Nanashima A. et al., 2006 [196].		Surgical cohort - hepatocellular carcinoma (n = 41), biliary tumours (n = 8), metastatic disease (n = 9).	1000 \pm 100 ml/min [†] (n = 17) Child-Pugh class A: 1100 \pm 100 ml/min Child-Pugh class B: 900 \pm 100 ml/min Child-Pugh class C: 700 \pm 100 ml/min	None
Jin N. et al., 2009 [197].	937 \pm 195 ml/min (n = 8)	Normal volunteer breath hold versus free breathing gated study.	Peak velocity, not flow recorded. (n = 58)	Trancutaneous Doppler US vessel peak velocity (n = 17, r = 0.435, p = 0.071)
Yzet T. et al., 2010a [198].	1006 \pm 210 ml/min (n = 20)			None
Yzet T. et al., 2010b [199].	986 \pm 212 ml/min (n = 9)	Reproducibility study with measurements on same subject one year later		Transcutaneous Doppler US bulk vessel flow (1374 \pm 530 ml/min, statistically significantly different from PCMRI)

AUTHORS, YEAR	CONTROL SUBJECTS MEAN VESSEL FLOW ± SD	TEST COHORT	TEST COHORT MEAN VESSEL FLOW ± SD	VALIDATION
a) PORTAL VEIN (CONTINUED)				
Gouya H. et al., 2011 [200].	631±232 ml/min (n = 25)	Known liver cirrhosis (n = 59), chronic liver disease without cirrhosis (n = 12), nodular regenerative hyperplasia (n = 11)	610±389 ml/min† (n = 82) Cirrhotics: 581±405 ml/min Chronic liver disease without cirrhosis: 734±370 ml/min Nodular regenerative hyperplasia: 629±323 ml/min	PCMRI measurements in two flow phantoms of varying size. Statistically significant correlations with actual flow demonstrated.
Stankovic Z. et al., 2012 [201, 202].	640±190 ml/min (n = 20)	Mixed aetiology liver cirrhosis patients. Child-Pugh class A (n = 16); class B (n = 3); class C (n = 1).	790±320 ml/min† (n = 20)	Transcutaneous Doppler US bulk vessel flow (moderate but statistically significant correlations).
Morisaka H. et al., 2013 [203].	734±207 ml/min (n = 60)	Chronic liver disease undergoing endoscopic evaluation for varices – no varices (n = 85), mild varices (n = 62), severe varices (n = 48)	713±298 ml/min† (n = 195)	None
Jajamovich G. et al., 2014 [204].	930±252 ml/min fasting; 1626±612 ml/min post-prandially (n = 11)	Chronic Hepatitis C (n = 19)	960±366 ml/min fasting; 1392±510 ml/min post-prandially (n = 19)	None

AUTHORS, YEAR	CONTROL SUBJECTS MEAN VESSEL FLOW \pm SD	TEST COHORT	TEST COHORT MEAN VESSEL FLOW \pm SD	VALIDATION
b) HEPATIC ARTERY				
Jin N. et al., 2009 [197]. (common hepatic artery)	272 \pm 44 ml/min (n = 8)	Normal volunteer breath hold versus free breathing gated study.		
Wilson DJ. et al., 2009 [205]. (proper hepatic artery)		Mixed conditions - group 1 - cirrhosis, colorectal metastases, PV occlusion (n = 8); group 2 - Pancreatic disease, biliary disease or benign liver conditions (n = 9); Uncategorized (n = 5).	323 ml/min [†] * (n = 22) Group 1: 435 ml/min* Group 2: 235 ml/min*	None
Yzet T. et al., 2010a [198]. (proper hepatic artery)	250 \pm 120 ml/min (n = 20)	Normal volunteer study.		None
Yzet T. et al., 2010b [199]. (proper hepatic artery)	285 \pm 101 ml/min (n = 9)	Reproducibility study with measurements on same subject one year later		Validated with transcutaneous Doppler US (542 \pm 272 ml/min, statistically significantly different from PC-MRI)
c) HEPATIC VEIN				
Nanashima A. et al., 2006 [196].		Surgical cohort - hepatocellular carcinoma (n = 41), biliary tumours (n = 8), metastatic disease (n = 9).	Peak velocity, not flow recorded (n = 58).	Trancutaneous Doppler US vessel peak velocity (n = 17, r = 0.433, p = 0.093)

AUTHORS, YEAR	CONTROL SUBJECTS MEAN VESSEL FLOW \pm SD	TEST COHORT	TEST COHORT MEAN VESSEL FLOW \pm SD	VALIDATION
d) AZYGOUS VEIN				
Lomas DJ. et al., 1995 [206].	171 \pm 65 ml/min (n = 7)	Biopsy proven chronic liver disease, portal hypertension and varices.	628 \pm 220 ml/min (n = 5)	Flow phantom PCMRI measurements (r > 0.99)
Debatin JF. et al., 1996 [194].	86 \pm 21 ml/min (n = 10)	Known liver cirrhosis, for elective TIPSS placement. Child-Pugh class A (n = 4); class B (n = 10); class C (n = 6).	Pre-TIPSS: (n = 20) 424 \pm 238 ml/min [†] Post-TIPSS: 238 \pm 187 ml/min [†]	Flow phantom PCMRI measurements (r = 0.997)
Sugano S. et al., 1999 [195].	139 \pm 43 ml/min (n = 11)	Known liver cirrhosis with portal hypertension. Pre and post-variceal ligation study (n = 10).	519 \pm 249 ml/min [†] (n = 15) Pre-variceal ligation: 530 \pm 301 ml/min Post-variceal ligation: 368 \pm 197 ml/min	None
Ng WH. et al., 2004 [207].	Not recorded (n = 15).	Known liver cirrhosis (n = 32) with endoscopically proven varices. Child-Pugh class A (n = 5); class B (n = 15); class C (n = 12).	Breath hold: (n = 32) 392 \pm 90 ml/min Non breath-hold: 500 \pm 65 ml/min	None
Gouya H. et al., 2011 [200].	40 \pm 33 ml/min (n = 25)	Known liver cirrhosis (n = 59), chronic liver disease without cirrhosis (n = 12), nodular regenerative hyperplasia (n = 11)	179 \pm 182 ml/min [†] (n = 82) Cirrhotics: 220 \pm 197 ml/min Chronic liver disease without cirrhosis: 63 \pm 53 ml/min Nodular regenerative hyperplasia: 101 \pm 83 ml/min	PCMRI measurements in two flow phantoms of varying size. Statistically significant correlations with actual flow demonstrated.

* Data standard deviations not published; [†] Pooled average across entire cohort.

Although the technical quality of PCMRI studies has improved significantly over time, a clear message has yet to emerge for the value of PCMRI derived flow measurements in clinical hepatological practice. Early studies have shown that elevated portal venous flow is associated with previous variceal haemorrhage, however studies correlating portal venous flow with gastro-oesophageal variceal grade have been disappointing [191, 200, 203]. Extra-hepatic shunting in portal hypertension commonly results in the formation of gastro-oesophageal varices and consequently increased azygous venous flow. The latter has emerged as a more useful biomarker in several studies (table 1.2), with correlations demonstrated with gastro-oesophageal variceal grade, presence of cirrhosis, Child-Pugh class [193, 200] and reduction in azygous venous flow post-TIPSS [194].

There are several challenges that need to be overcome for accurate flow quantification with 2D PCMRI, which have to date restricted implementation into routine clinical practice. Misalignment of the flow encoding axis with the direction of flow in the vessel produces errors in bulk flow estimation which are compounded in smaller vessels or in the presence of turbulent flow [208]. Different researchers have applied varying protocols for determining imaging slice-to-vessel orthogonality and even where these are applied in the consistent fashion, turbulent flow even in large vessels such as the portal vein, often seen in chronic liver disease as a result of thrombus or shunting, will only make misalignment errors worse. It is an even bigger challenge for smaller vessels with more variable anatomy, such as the hepatic artery and azygous vein [191, 198, 200]. These studies require a Radiologist or individual trained at identifying these vessels to position the imaging slice, which because of the inherently aberrant anatomy in chronic liver disease can on occasion extend scanning time.

Imaging smaller vessels with PCMRI also introduces the risk of partial voluming errors. The lower spatial resolution of smaller vessels will imply that voxels covering the lumen may also include vessel wall, with errors exacerbated as the ratio of edge to luminal voxels increases. A minimum resolution of 16 pixels over the vessel of interest has been defined as suitable for PCMRI quantification, which may well explain why 2D PCMRI studies of the hepatic artery have only emerged recently as a result of progressive technical improvements to clinical MR systems [209, 210].

Aliasing occurs when the velocity encoding setting has been set to below the maximum velocity in the vessel of interest. Observed phase-shift can then exceed 180° (usually the central portion of the lumen in laminar flow), which without corrective measures will lead to erroneous estimates of flow. Specifying a velocity encoding setting well above the maximum velocity however introduces noise into the measurement thereby also degrading the quality of the measurement [182, 211]. Some studies pre-

specify the velocity encoding for the vessel across all the subjects, thereby subjecting some subjects to more noisy measurements than others [198, 199]. Other studies opt to collect data at multiple velocity encoding settings, discarding data where this is set too low or too high [200]. Not only does this increase the scanning time, but it also requires review of the data while the patient is in the scanner to identify if the velocity encoding setting needs to be modified.

Validation of PCMRI measurements in the liver has to date been patchy and the lack of robust validation is a genuine challenge to clinical translation. Many studies (table 1.2) have opted to use flow phantoms for validation, often presenting excellent correlations with impressive (and minimal) errors in PCMRI flow measurements [190, 192, 194, 200, 206]. Unfortunately, phantoms fail to replicate many of the challenges of imaging in the liver, not least the motion artefact, pulsatile flow and complex orientation of the vessels and adjacent tissue susceptibilities. Trans-abdominal Doppler US has been used by many researchers as a validation tool, but once again this will only record velocity, which in combination with vessel size and certain assumptions can be used to estimate bulk flow. Velocity based comparisons with Doppler US have also been reported, but data on validation with Doppler US has been variable and unimpressive (table 1.2), and it remains contentious as to whether this is due to variability of the Doppler US measurement or the PCMRI measurement itself [190, 196, 199, 202].

Blood flow when studied as a physiological parameter is classically normalised to organ mass, as the volume of tissue perfused will be an important determinant of bulk inflow. The situation is more complex in liver disease as a result of shunting, however few studies make any attempt to normalise liver PCMRI measurements. Studies that normalise flow parameters to whole body mass have been published, but this approach is flawed particularly in liver disease, where whole body mass is often distorted by the presence of ascites [191]. Liver volume can be determined relatively easily from anatomical imaging and correlates well with mass on surgical resection ($r = 0.954$, $p < 0.001$) [193]. It is likely that normalised PCMRI flow values would yield more meaningful biomarkers for liver disease, as demonstrated by Kuo et al.

Bulk flow derived biomarkers from 2D PCMRI are of particular interest because they enable reduction of a large volume of data to a single parameter. This is particularly attractive clinically, where faced with large numbers of complex parameters, clinicians seek simple parameters to stratify patients and inform clinical decision making.

1.3.7 FOUR-DIMENSIONAL PHASE-CONTRAST MRI

By acquiring 2D PCMRI in multiple flow-encoding directions, a three-dimensional image of blood flow can be constructed. Acquiring this data over time can then be used to derive (blood) particle motion streamlines through the cardiac cycle in three-dimensions – thereby enabling more complex analysis of flow (figure 1.12).

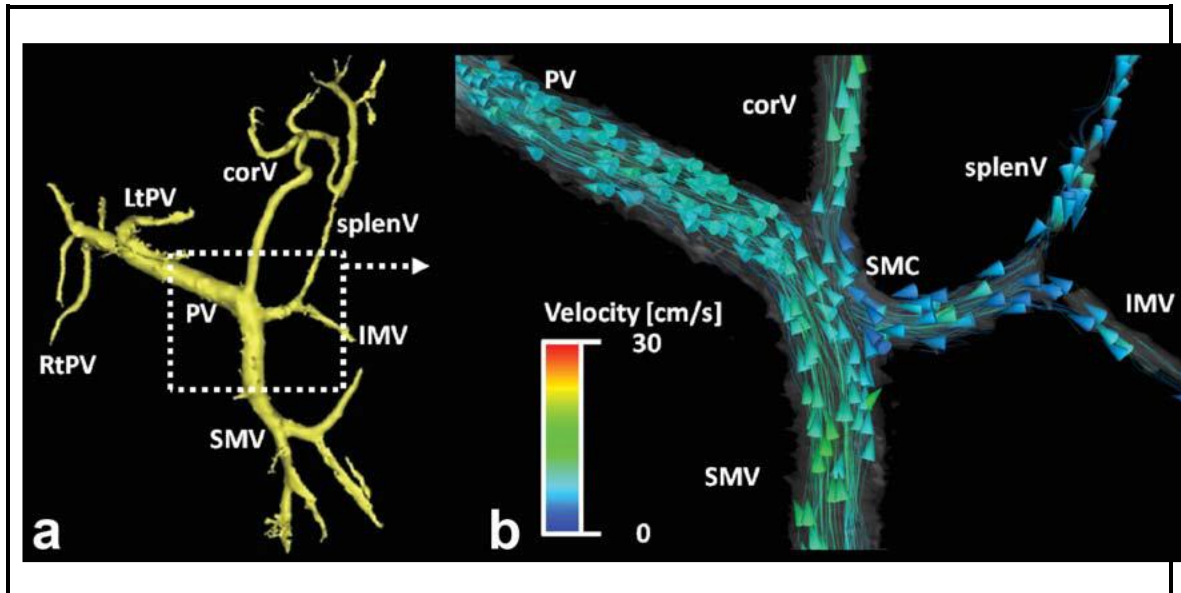


Figure 1.12: Example of 4-Dimensional PCMRI of the hepatic vasculature

Anatomical reconstruction of the venous vasculature in a cirrhotic patient is shown on the left (a), with corresponding 4D PCMRI reconstruction on the right (b). Directionality of velocity vectors is shown by the arrows with colour pertaining to velocity. (Obtained from reference [212]).

Given the larger volume of data required, scanning times are substantially increased, and there have been two alternative approaches to tackle this, particularly in relation to the large volumes of potentially motion corrupted data required for assessing abdominal vasculature [213]. The first of these is a Cartesian approach to sampling k -space, which in its most recent form has been termed the “4 point method”. For each single line of k -space, one reference scan and three velocity encoded acquisitions (each along perpendicular dimensions) are obtained and subsequently reconstructed [214]. The alternative approach known as vastly undersampled isotropic projection reconstruction (PC-VIPR), involves radial k -space sampling, so that each acquired line of raw data passes through the centre of k -space. PC-VIPR accelerates the overall acquisition time, enabling larger volume coverage, high spatial resolution and reduced sensitivity to motion artefact [215, 216]. Conversely, it also has the potential to introduce streak artefacts and an overall reduction in signal-to-noise ratio [213].

Application of 4D PCMRI for liver blood flow quantitation was first demonstrated by Stankovic et al in 2010. Although they successfully demonstrated feasibility, including collecting data on a small number of known cirrhotic patients, their validation with 2D

PCMRI and Doppler US peak velocity was in their words “significant, but modest” ($r = 0.46$; $r = 0.35$, respectively). They also found that both 4D and 2D PCMRI consistently estimated a higher portal venous area than US [201]. A follow-up study in 2012 confirmed modest correlations and acknowledged that flow volumes tended to be underestimated with 4D PCMRI (normal volunteer mean portal venous flow was 670 ± 540 ml/min, for example)[202]. Studies using PC-VIPR have also provided disappointing quantitation. Early studies in a cohort of cirrhotic patients ($n = 22$) confirmed that visualisation was acceptable but did not demonstrate any correlation with model for end-stage liver disease (MELD) scores [212]. A subsequent study claimed to ‘validate’ measurements by assessing consistency of the aggregate flow measurement at different points in the porto-splanchnic system. Consistency was demonstrated, but failed to show any significant difference in blood flow in patients with known portal hypertension [217].

There is little doubt that 4D PCMRI is where the future lies for assessing hepatic vasculature bulk flow, but there remain some key challenges that must be overcome if it is to gain acceptance in the clinical setting. Like all techniques, good validation data (not merely consistency) is essential. Validation attempts with flawed methods such as transcutaneous Doppler US may have hampered attempts so far but it is unclear if the disappointing data has instead been the result of issues inherent with the 4D PCMRI methods. Undersampling k -space using PC-VIPR might yield acceptable imaging and indeed particle motion streamlines, but the impact on actual flow quantification is uncertain. Four dimensional PCMRI faces an even bigger challenge than 2D PCMRI when dealing with selection of a suitable velocity encoding settings. This is a particular challenge in abdominal imaging, where the optimal velocity encoding settings vary so widely (e.g. for arterial vessels when compared to the portal vein). Different strategies to overcome this have been proposed (e.g. five point Cartesian k -space sampling, dual velocity-encoding, to name a few)[214], but this remains a source of error in flow quantification [218]. Scanning time in all published protocols has never exceeded 20 minutes, but this reduced time frame has been obtained through several trade-offs that inherently compromise the quality of the data obtained [219, 220]. Additionally, all accounts of 4D PCMRI highlight the very complex and time-consuming post-processing solutions required to extract useful data. Computational flow dynamics has the ability to use this data to extract new and previously unmeasured blood flow parameters, including estimations of pressure gradient and wall shear stress [213, 218]. While this data is offering new and previously unseen insights into blood flow, the clinical significance of these large volumes of data awaits determination.

1.3.8 ARTERIAL SPIN LABELLING MRI

Arterial spin labelling (ASL) is an exciting method that to date has had very little application in the liver. The basic protocol underpinning ASL is the generation of two images – a control image containing static signal and a ‘labelled’ or flow-sensitised image, possessing signal from both static tissue and magnetised inflowing blood. The subtraction of these two data sets results in a signal difference that reflects local perfusion. By applying an inversion or saturation pulse to a volume containing blood supplying the imaged region and then imaging the area of interest after a delay (to allow time for labelled spins to arrive in the imaging slice), perfusion dependent signal changes can be recorded. The overall ASL signal is dependent on intrinsic tissue and blood T1, which as with DCE MRI, must be measured for formal quantification [221, 222]. There are a variety of labelling techniques including pulsed ASL (PASL), continuous ASL (CASL), and pseudo-continuous ASL (PCASL). In PASL, the labelling slab is positioned just proximal to the imaging slice. To mitigate magnetisation transfer effects, various protocols have been proposed including flow-sensitive alternating inversion recovery (FAIR). With CASL, a gradient is applied in the direction of arterial flow at the same time as a slice selective inversion pulse. This has the effect of selectively inverting moving (arterial) spins that can be imaged in a slice just distal to the slice where the inversion pulse is applied. PCASL breaks the continuous pulse into smaller discrete gradient pulses and can result in improved labelling efficiency while reducing the specific absorption rate (SAR) dose [223, 224].

There is a growing body of literature describing abdominal ASL, specifically in the kidneys [222]. Reports of hepatic ASL however, remain sparse. The earliest reports of liver ASL describe early use of CASL in humans, with inversion planes positioned axially in the supraceliac aorta for arterial labelling and just lateral to the IVC for portal venous labelling [225]. Hirschberg et al. used PASL to investigate changes in the liver perfusion at baseline and during hyperglycaemia in healthy volunteers and type I diabetics [226]. Studies in mice with multi-slice FAIR ASL have demonstrated feasibility with reasonable quantitation of parenchymal perfusion (figure 1.13) [227]. The same group have gone on to use ASL to study perfusion in a model of colorectal carcinoma liver metastases and demonstrate changes after the administration of vascular disrupting agents [228].

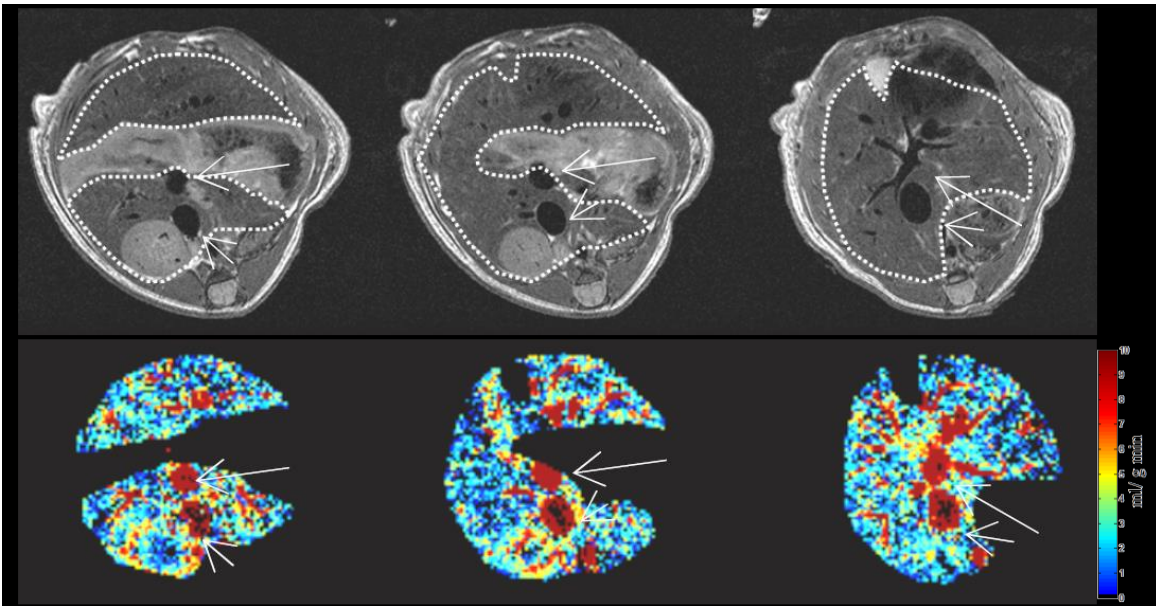


Figure 1.13: Liver ASL in mice at 9.4T

(a) Anatomical axial images of the liver, with (b) corresponding ASL perfusion maps. Note high flow seen in major vessels relative to the parenchyma. (Obtained from reference [227]).

Nonetheless, there is a paucity of high quality validation studies of ASL perfusion measurements in the liver. A study comparing DCE CT perfusion and ASL demonstrated “fair” correlation ($r = 0.794$, $p < 0.01$; $n = 5$)[229]. Correlations with PCMRI and ASL have also been presented. In a clinical study with $n = 30$ subjects, Hoad et al. compared bulk non-normalised PV flow with tissue perfusion (correlation statistics not given) and in a smaller scale preliminary preclinical study, we have demonstrated encouraging agreement between FAIR ASL perfusion measurements and liver weight normalised PCMRI bulk PV flow (mean difference 1.8 ml/min/g, $p < 0.05$)[230, 231]. Finally, a larger scale clinical study ($n = 60$) measuring liver perfusion in Child-Pugh class A compensated cirrhotics demonstrated significant reductions in ASL measured hepatic parenchymal perfusion ($p = 0.002$)[232].

ASL is a complex technique, with specific challenges at each stage of the process, whether labelling, imaging, measuring T1 or modelling signal. Rather than provide an exhaustive discussion, we review some of the broader challenges specific to implementation in the liver. Firstly, unlike in the brain where ASL was first developed, inflowing vessels have an oblique and variable orientation in relation to the tissue they are supplying. Any robust method of quantitation will therefore require a consistent labelling strategy, especially if ASL is to separate the arterial and portal venous contributions. Dealing with dual inputs may also require an alternative approach to modelling perfusion, although this remains to be seen. The resulting subtracted ASL signal is small, such that artefact (particularly motion artefact in the case of the liver), can easily corrupt the data. Motion correction strategies are likely to play an important role in avoiding extended scanning times and high SAR doses required for multiple averages and/or multiple slices.

Formal studies of validation and reproducibility will also need to be undertaken if the method is to gain widespread acceptance. This will also pave the way for a more uniform, consensus based approach to labelling and ASL imaging protocols across different centres.

1.3.9 FUNCTIONAL MRI

Blood oxygen level-dependent (BOLD) MRI, also known as functional MRI (fMRI) utilises the altered tissue susceptibility adjacent to vessels containing paramagnetic deoxygenated haemoglobin to derive signal intensity changes with T2*-weighted imaging. Altered BOLD/fMRI signal is observed with changes in oxygen saturation, blood volume but also importantly with blood flow. Although BOLD/fMRI has been applied more extensively in the brain, there have been several studies implementing this approach in the liver. The liver is suitable for BOLD/fMRI studies because of its high vascularity [233]. Studies typically involve inducing hyperoxia and hypercapnia – increases in tissue oxygenation for example, lead to reductions in deoxyhaemoglobin and consequent prolongation of T2* times with resultant increases in signal intensity. These changes in the signal can then be used to infer perfusional changes.

Early studies in chronically ethanol fed rats (a model of chronic injury secondary to moderate alcohol consumption) demonstrated the feasibility of measuring hepatic BOLD signal, and showed a significantly dampened response to hyperoxia ($22\pm 5\%$ signal increase) relative to control animals ($48\pm 6\%$ signal increase). Increases in signal intensity were observed with hypercapnia ($15\pm 4\%$ in control animals) but not found to be significantly altered in diseased animals ($5\pm 3\%$)[233]. This study was followed up by an elegant study of BOLD signal in healthy rat livers, in the context of hypoperfusion induced through hypovolaemia and portal vein ligation. Barash et al. were able to demonstrate significant rises and reductions in T2* signal intensity during hyperoxia and hypercapnia respectively. Both hyperoxic and hypercapnic BOLD responses were dampened in hypovolaemic or portal vein ligated rats underlining the contribution of perfusion to the signal intensity changes [234]. In a later study, the degree of hypovolaemia was shown to correlate relative change in BOLD signal in both hyperoxia and hypercapnia. Studies in fibrotic animals also demonstrated alterations in BOLD signal in the early stages, corresponding to histological inflammatory change, which subsequently settled in later stages (figure 1.14) [235]. Contrastingly, diethylnitrosamine induced hepatic fibrosis in rats demonstrated progressive alterations in relative BOLD signal ($r = -0.773$; $p < 0.001$)[236]. Of interest, segmental hypoperfusion of foetal ovine liver in response to hypoxia has been demonstrated, a phenomenon thought to be caused by increased ductus venosus shunting [237].

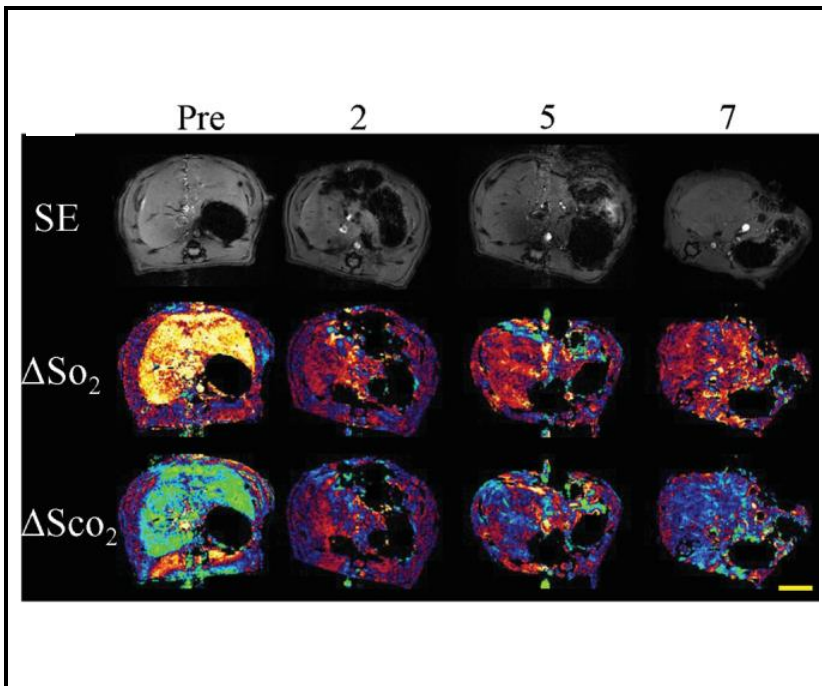


Figure 1.15: BOLD studies after partial hepatectomy (PH)

Axial images through rat liver before (pre) and at 2, 5 and 7 days post-PH (upper row). Regeneration post-hepatectomy can be seen on the anatomical images, with altered post-PH perfusion parameters in hyperoxia (middle row) and hypercapnia (bottom row). Note how once regeneration starts to occur (after day 4). BOLD signal starts to recover. (Obtained from reference [235]).

Human studies have been able to demonstrate altered BOLD signal in the context of gas cycling but also in hyperglycaemia alone, although both published studies have been of small size [238, 239]. There has also been a growing interest in the application of fMRI/BOLD for the evaluation of primary liver tumours, given the potential of BOLD signal to detect neoplastic vascular changes [240, 241].

The extensive vascularity of the liver makes it a good candidate for fMRI/BOLD studies but there are many challenges awaiting resolution. Performing gas challenges in the clinical context can be challenging especially in patients with liver disease [238]. Underpinning alterations in BOLD signal are changes in perfusion, oxygenation and blood volume, each of which can occur as result of very separate biological phenomena, but remain individually indistinguishable on fMRI alone. Quantification of BOLD signal also remains topical – although relative changes can be studied, absolute quantification is problematic and of possible but unknown value. Furthermore, validation of BOLD signal is often presented as correlations of signal relative to measured oxygen saturations but formal validation in terms of absolute quantification in the liver has never been undertaken [235]. fMRI/BOLD holds much promise for generating useful biomarkers of liver disease, however larger cohort studies in humans are required to assess the true potential of the technique.

1.3.10 BIOMECHANICAL IMAGING

Biomechanical imaging methods measure the tissue response to an applied physical stress. The tissue response is dependent on the physical properties of the tissue, such as viscosity, elasticity and stiffness. Haemodynamic factors such as tissue perfusion, bulk

vessel flow and pressure are likely to affect these mechanical properties. Measurements of mechanical properties of the tissue therefore have the potential to make non-invasive inferences about haemodynamic parameters.

1.3.10.1 Ultrasound elastography

Biomechanical imaging methods were first developed for US, with earliest reports dating back to the work of Lerner and Parker in the late 1980s [242, 243]. The principle of 'sonoelasticity' was based upon applying an external vibration at low frequency to induce oscillatory motion in soft tissues. These could then be detected using Doppler ultrasound. These methods were progressively refined, overcoming complexities of quantification. The major challenge of having a single probe incorporating both vibrator and transducer into a single practical unit was overcome by Sandrin et al [244, 245], who formed part of the larger group that setup Echosens™, the organisation that produces and commercialises FibroScan®. FibroScan® devices are standalone units developed purely for the assessment of liver stiffness. A single transducer is used as an ultrasonic emitter, receiver and piston-like vibrator to generate transient low frequency (50 Hz) vibrations. Rather than produce an image of the tissue deformation, elasticity is measured in one dimension at a single instant (approximately 100 ms), thereby termed 'transient elastography'. The devices return a single measurement of Young's modulus (a measure of stiffness calculated as the pressure applied divided by the ratio of the change in length of the stressed tissue). The final units are given in kilopascals (kPa) [244].

An alternative approach to US quantification of tissue stiffness has been through the use of 'acoustic radiation force impulse' (ARFI) imaging. The concept of acoustic radiation force is based on the principle that all wave motion (including sound waves) exert unidirectional (radiation) force on absorbing and reflecting obstacles in their path. By focussing acoustic beams, the energy from absorbed acoustic waves can be converted from compressional waves to shear waves, thereby exerting mechanical stress on the tissues being interrogated. The application to medical imaging was first postulated by Torr in the 1980s [246] and first implemented for diagnostic purposes by Nightingale et al in breast tissue [247]. The lack of a requirement for an external vibrator facilitated translation, but progressive refinements to the technique and quantification methods, resulted in only more recent availability on clinical US imaging systems. ARFI imaging has the advantage being able to deliver localised biomechanical stress under standard B-mode US imaging guidance. As the force is delivered directly to the region of interest, smaller physical stresses are used than those used by transient elastography. The user positions a sampling region on the tissue of interest before a large acoustic impulse is delivered to the

region (figure 1.16). Diagnostic B-mode US images are used to then track the motion of the tissue within the sampling region. The tissue displacement is then quantified as shear wave velocity (m/s), rather than elasticity as estimated by Young's modulus [248].



Figure 1.16: Positioning of sampling regions for splenic ARFI
(Adapted from reference [249]).

Early studies were directed mainly at the elastographic evaluation of fibrosis [250], but recognition of the role of haemodynamics in liver stiffness was first reported in patients with HCV recurrence after transplant using transient elastography. Carrion et al reported a strong positive correlation between liver stiffness and HVPG ($r = 0.854$, $p < 0.001$) and impressive area under receive operating curve (AUROC) values for portal hypertension (HVPG > 6 mmHg) and clinically significant portal hypertension (HVPG > 10 mmHg) as 0.93 and 0.94 respectively [251]. This data was confirmed in a smaller study of chronic (non-transplanted) HCV patients ($r = 0.871$, $p < 0.0001$; AUROC for HVPG > 10 mmHg = 0.99; AUROC for HVPG > 12 mmHg = 0.92), which also underlined poorer correlations between liver stiffness and HVPG in patients with more severe portal hypertension (figure 1.17) [252].

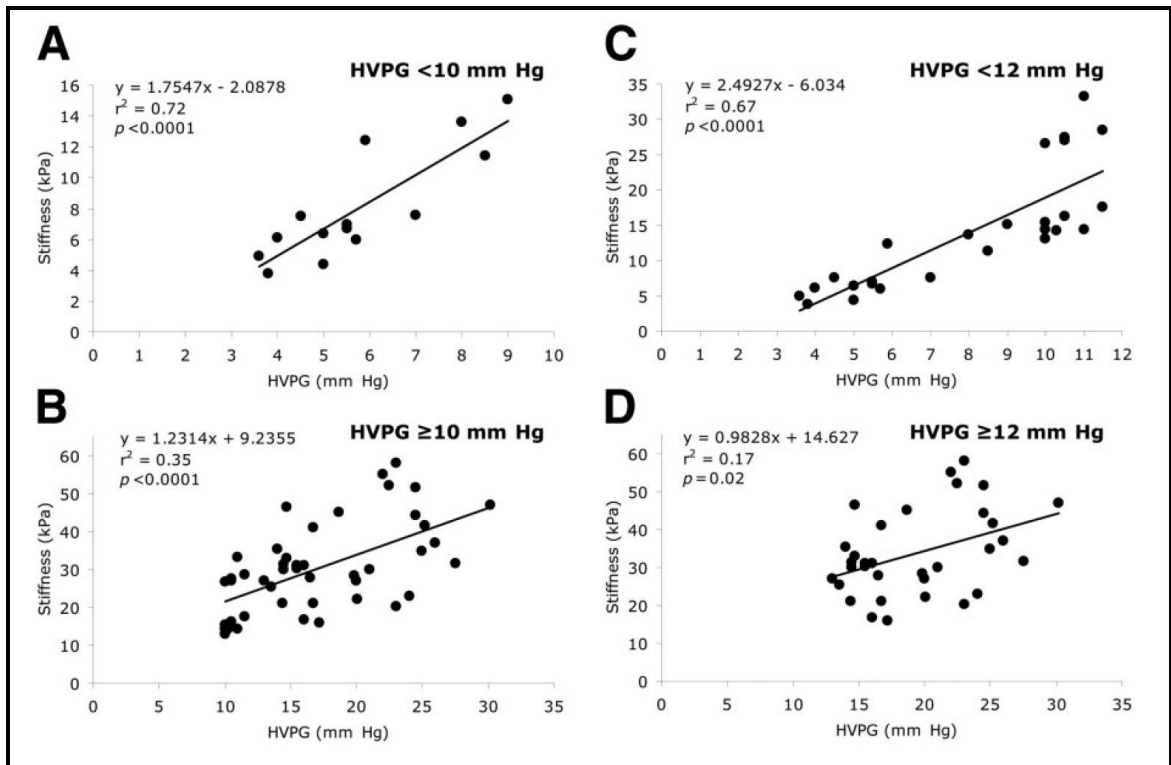


Figure 1.17: Correlations between transient elastography liver stiffness and HVPG in HCV cirrhotics

Positive correlations between transient elastography liver stiffness and HVPG were as high as $r = 0.85$ (A), but poorer correlations were observed in patients with more advanced portal hypertension ($r = 0.41$), (D). (Obtained from reference [252]).

A number of subsequent studies have demonstrated encouraging data evaluating the relationship between HVPG and transient elastography liver stiffness [253-258], including a meta-analysis of 18 studies with data from 3644 cases. Sensitivity and specificity of clinically significant portal hypertension (HVPG > 10 mmHg) in this meta-analysis was given as 90% and 79% respectively [259].

Building on the use of liver stiffness, there has also been interest in the use of splenic stiffness, measured with transient elastography for the assessment of portal hypertension and varices. Colecchia et al proposed a model combining both liver and splenic stiffness, demonstrating improved correlations with HVPG in HCV cirrhotics ($r = 0.922$, $p < 0.0001$) than when each measurement was used correlated with HVPG in isolation [260]. The use of transient elastography splenic stiffness has also been reported to offer superior correlation with HVPG than liver stiffness alone [261].

Studies have also evaluated transient elastography liver and splenic stiffness in determining the presence and severity of oesophageal varices [252, 259, 262-266] and complications of portal hypertension (gastro-intestinal bleeds, decompensation, mortality, etc.) [257, 267, 268]. The data has been positive, albeit less conclusive. In spite of the volume of encouraging data and favourable opinions in the literature [269, 270], there are a number of important limitations which have been highlighted by several studies.

Transient elastography can yield inaccurate or invalid results in patients who are obese or have ascites. Studying a cohort of Child-Pugh A patients with potentially resectable tumours, Llop et al suggested that in as many as half of all cases, transient elastography failed to provide any meaningful quantification of liver stiffness [271]. Other authors also cite difficulties with non-diagnostic values, and call for stratification of patients based on pre-test likelihood of reliable transient elastography liver stiffness measurement [258] and in the longer-term the development of better non-invasive tools for the assessment of portal hypertension [14].

ARFI can be used to overcome some of the limitations of transient elastography: the ability to use two-dimensional B-mode US to visualise the tissue undergoing assessment can ensure that stiffness measurements derive from the organ of interest, even in the presence of ascites/substantial subcutaneous fat. A clear message however, has yet to emerge from studies comparing the performance of ARFI and transient elastography measurements of liver and splenic stiffness for the assessment of portal hypertension. Some authors have reported ARFI as superior to transient elastography [272, 273], others as weaker [274, 275], while others have found no significant difference between the methods [276].

The measurement of splenic stiffness with ARFI for the assessment of HVPG and the presence of oesophageal varices has also been of interest. Studies demonstrating the use of ARFI pre- and post-TIPSS both to evaluate response and monitor function have been encouraging [277, 278]. The ratio of ARFI liver to splenic stiffness has also been used to identify patients more likely to have idiopathic portal hypertension [279]. Much like transient elastography, the value of ARFI in the assessment of oesophageal varices and bleeding has been less conclusive, with probable value in determining the presence, but not necessarily severity of varices [280-283]. Technical challenges remain with ARFI, including standardisation of imaging protocols. Splenic stiffness measurements have been shown to vary significantly for example, with respiratory manoeuvres [284].

Finally, for both transient elastography and ARFI liver and splenic stiffness, there are a paucity of studies evaluating the relationship between stiffness and haemodynamic parameters beyond HVPG, such as flow. Han et al for example, measured Doppler mean PV velocity and splenic indices at the same time as ARFI splenic stiffness, to demonstrate significant but weak correlations, attributing this to the wide variance of a Doppler flow parameters [282]. Such studies, with alternative quantification, perhaps using ICG or alternative imaging methods may yield important insight into factors affecting tissue elasticity and would be important in establishing the role of ultrasound elastography in the assessment of liver haemodynamics.

1.3.10.2 MR Elastography

The first reports of MR elastography (MRE) emerged in the mid-nineties soon after US elastography was first proposed [285, 286]. Much like transient elastography, MRE is based on propagation of low frequency mechanical waves through tissues. The shear waves are propagated through tissues and imaged using a modified PCMRI sequence with so-called 'motion-encoding gradients'. Data generated from these PCMRI sequences can then be used to generate parametric maps of mechanical properties. In order to generate the mechanical stress, a 19 cm plastic disc with a drum membrane is strapped to the patient surface over the right upper abdominal quadrant, under the surface coil. The disc serves as a passive pneumatic driver, connected with plastic tubing to an active acoustic driver outside the scanner room. Vibrations are delivered at 60 Hz and data acquisition is synchronised with the passive driver oscillations. Processing occurs at the time of acquisition, with mapping of data reliability and generation of shear stiffness maps (Young's modulus, kPa) at source. Original acquisitions were designed to acquire data over four axial slices, but newer 3D methods for whole liver coverage are under investigation. Absolute quantification of liver stiffness can then be undertaken using ROIs or from liver parenchymal segmentation with reporting of mean values [287-291]. The sequences, drivers and post-processing technology are commercialised by Resoundant®, an organisation setup by the research group that originally proposed the method. Recently, an alternative approach, termed 'compression-sensitive MRE' has been proposed, based on the use of an alternative driver system and the derivation of alternative quantitative parameters [292-295].

Much like transient elastography, evaluation has largely been directed towards using MRE as a non-invasive alternative to biopsy. Studies assessing the relationship between MRE parameters and portal hypertension first emerged in animal models. In a serial study with two canine subjects, Nedredal et al report significant correlations ($r = 0.95$ and 0.93 ; $p < 0.01$) for liver and splenic stiffness respectively. The raw data (figure 1.18) is an excellent example of how misleading correlative statistics can be [296].

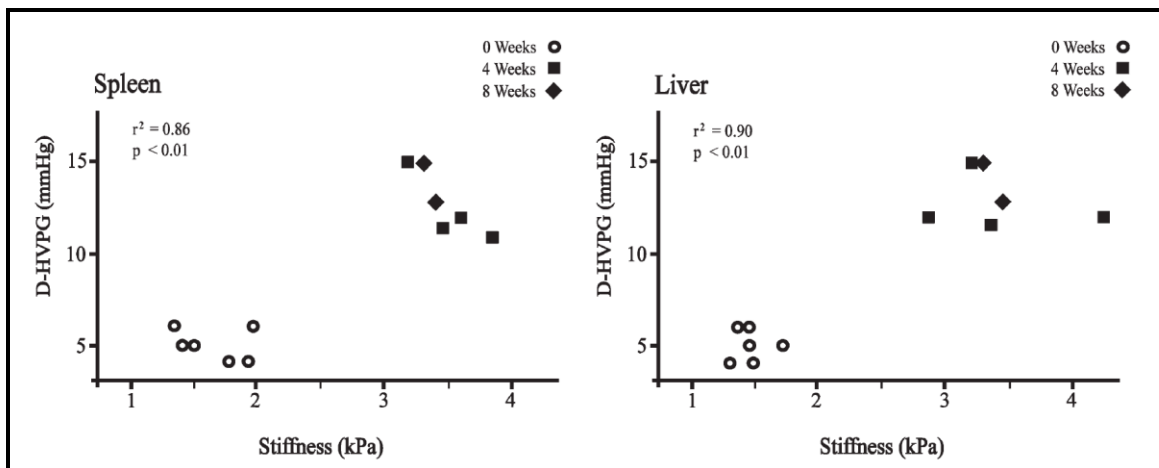


Figure 1.18: Correlations between MRE splenic (left) and hepatic (right) stiffness and HVPG in canine bile-duct ligated models of cirrhosis

Impressive HVPG correlations with MRE liver stiffness ($r = 0.95$) and splenic stiffness ($r = 0.93$) were quoted by this study, but review of the scatterplot is less convincing. (Obtained from reference [296]).

In another study, three pigs were subjected to colloid infusions with controlled rises in systemic and portal pressure. MRE hepatic and splenic stiffness demonstrated more convincing correlations with invasive measurements of systemic and portal pressure ($r = 0.86$ and $r > 0.90$) – of note the analysis was reported in an unconventional manner with no quoting of significance values [297].

The first clinical studies correlated MRE with cirrhotic pre-transplant cirrhotic HVPG ($n = 36$) demonstrating significant but modest correlations between hepatic ($r = 0.44$, $p = 0.017$) and splenic ($r = 0.57$, $p = 0.002$) loss modulus [298]. Using compression-sensitive MRE, correlations were demonstrated in a small cohort ($n = 13$) of pre- and post-TIPSS between hepatic ‘volumetric strain’ and HVPG ($r = 0.852$, $p < 0.0001$) but no correlation with shear modulus [295]. In a similar pre- and post-TIPSS compression-sensitive MRE study, Guo et al found the change in splenic viscoelastic constant modulus (G^*) to be correlated with relative changes in HVPG ($r = 0.659$, $p = 0.013$) [299].

Much like transient elastography and ARFI, several studies have evaluated the relationship between MRE, the presence and severity of oesophageal varices [203, 298, 300-302] and decompensation [303]. Just as with US methods, the data for both liver and splenic stiffness has been positive, but a clear message in terms of clinical value and application has yet to emerge from the literature.

Finally, unlike transient elastography and ARFI, there has been a much greater interest in investigating the contribution of other haemodynamic parameters such as flow and perfusion in MRE quantification. The notion that liver stiffness is derived from inherent structural properties but also haemodynamic factors has driven the hypothesis of several of these studies. Assuming inherent post-prandial rises in portal venous inflow, more marked post-prandial increases MRE liver stiffness have been demonstrated in

patients with chronic liver disease ($21.24 \pm 14.98\%$), compared with normal volunteers ($8.08 \pm 10.33\%$) [304]. A similar study with PCMRI measurements of PV flow and MRE demonstrated significant changes in post-prandial PV flow and MRE liver stiffness. The correlation in this study between PV flow change and MRE stiffness change (Spearman's $\rho = 0.48$, $p = 0.013$) was however disappointing [204]. Shin et al used 3D MRE and DCE MRI to show that combining data from both of these methods resulted in improved detection and assessment of the severity of oesophageal varices [305]. The use of MRE combined with PCMRI PV flow has also been shown to be of value in the prediction of oesophageal varices [203, 300].

Although MRE is clearly at early stage of the exploration of its utility in the evaluation of the haemodynamic factors, there are a number of important challenges that need to be addressed. While both US and MR methods utilise assumptions in the quantification process, the number of these assumptions and complexity of the post-processing is undoubtedly greater in MRE owing to the output of 2D maps. There are a range of theoretical and physical parameters which can be estimated using MRE and all are related to 'stiffness' – Young's modulus, loss modulus, shear modulus, viscoelastic constants, decomposed curl and divergence strain, volumetric strain, to name a few quoted in the literature, cited previously. The nomenclature is confusing and some parameters are abstract, particularly in the hands of clinicians less familiar with biomechanical quantification. Moreover, we have yet to understand the potential clinical value of many of these parameters, some of which may be of greater value in estimation of fibrosis, while others may be of greater value in the estimation of haemodynamic parameters.

Ultimately, the biggest challenge to MRE is competition from US elastography methods. Two-dimensional parametric mapping is MRE's main advantage, but cost, time required and simplicity of use will always favour sonographic approaches. Studies that demonstrate superiority for clinical applications will be vital to clarifying the role of each biomechanical imaging modality as tools in the assessment of liver haemodynamics.

1.4 CONCLUSION

Chronic liver disease is a complex pathophysiological process with significant and consequential vascular sequelae that to date remain poorly understood. A plethora of ionising and non-ionising radiation based imaging techniques have been developed over the years for non-invasive assessment of liver haemodynamics, some more successful than others and each with their strengths and weaknesses. MRI based assessment of liver haemodynamics, be this with DCE, DHCE, 2D phase contrast, 4D phase contrast, ASL or functional MRI each remain at varying stages of infancy. Robust methods, validated systematically in large cohorts of clinical and preclinical subjects will pave the way for a much greater role of each of these modalities in clinical practice. The future of MRI holds much more, as experience with techniques aimed at quantifying fibrosis, biomechanical properties and haemodynamics combine to yield multimetric imaging strategies that yield even more useful and meaningful noninvasive biomarkers for clinical decision making.

1.5 THESIS HYPOTHESIS

The development of methods to assess hepatic vascular parameters are likely to yield (a) novel insights into the pathophysiology of chronic liver disease and (b) potential biomarkers for chronic liver disease.

We have chosen to develop MRI as this non-ionising radiation based modality possesses combined quantitative and anatomical capabilities beyond other functional imaging modalities.

Quantitative methods such as DCE MRI and PCMRI in particular have already shown potential in the evaluation of hepatic vascular parameters. DCE MRI is logistically feasible as contrast-enhanced studies are usually part of standard clinical MRI protocols. Development of this protocol would form a sound foundation for implementation of other quantitative methods.

Preclinical studies have better potential for much needed invasive validation, and enable investigation of pathological phenomena in better controlled studies. Clinical translation is essential to securing the clinical credibility of the method, and overcoming logistical factors that may represent barriers to widespread use.

With this in mind, this overriding aim of this thesis is to study the vascular pathophysiology of chronic liver disease, through the development and validation of modelled preclinical and clinical quantitative MR methods.

CHAPTER 2

DCE MRI – EARLY PRECLINICAL STUDIES OF FEASIBILITY, REPEATABILITY, VALIDATION AND MEASUREMENT OF THE HEPATIC ARTERIAL BUFFER RESPONSE

“...Submerged
viscus,
measurer
of the blood,
you live
full of hands
and full of eyes,
measuring and transferring
in your hidden
alchemical
chamber.”

- Ode to the Liver [2].

2.1 INTRODUCTION

Dynamic contrast enhanced (DCE) MRI has the advantage of being conceptually simple and readily translatable, as the use of contrast enhancement is typically part of clinical MRI protocols. In this chapter we develop and implement preclinical DCE MRI on a 9.4T system in rats. We assess feasibility, conduct repeatability studies, validate measured perfusion parameters and investigate the hepatic arterial buffer response.

2.2 AUTHOR CONTRIBUTIONS

In fulfilment of the aims in this chapters, I: (a) prepared and conducted all animal scanning experiments; (b) developed preclinical DCE MRI protocols; (c) refined Matlab code for DCE MRI quantification; (d) performed surgery for portal venous ligation (PVL); (e) developed protocols and collected invasive TTUS measurements of PV flow; (f) collected and analysed all the data; and (g) prepared all the material contained within this chapter.

Alan Bainbridge developed MR sequences, helped with scanning and developed the original Matlab code for DCE MRI quantification. For establishment of small animal intravenous access, I received help from Nathan Davies.

2.3 BACKGROUND

In health, maintenance of total hepatic blood flow is achieved via close regulation of relative contributions from the hepatic artery (HA) and portal vein (PV). Reductions in portal flow are matched by compensatory increases in hepatic arterial flow – the so-called “hepatic arterial buffer response”. DCE MRI has been used to measure hepatic perfusion parameters noninvasively[82, 116, 140, 148], but there have been no studies to date quantifying changes in global perfusion after therapeutic or physical interventions affecting liver blood flow. An animal model in which such changes could be noninvasively assessed could provide a model in which invasive validation could be undertaken but would also represent a platform for the development of therapeutic agents to improve liver perfusion in the context of liver disease.

The credibility of such a noninvasive method would rest upon three key features:(i) consistency as assessed by repeated measurements, (ii) the ability to detect expected alterations of hepatic perfusion parameters in response to a controlled insult and (iii) validation of obtained measurements using gold-standard invasive methods. PVL is a well-established simple physical method for gross modulation of PV flow. Previous rodent studies have demonstrated post-PVL haemodynamic changes and that sole arterial perfusion of the liver is possible without causing immediate demise[306, 307].Validation of PV perfusion can be assessed using transit-time US (TTUS) probes. These probes are placed directly onto vessels intra-operatively and have been used previously to demonstrate changes in portal blood flow before and after pharmacological manipulation [31, 308]. Under the assumption that there is homogeneous distribution of bulk PV flow throughout the liver, estimations of PV perfusion can be made that can be used to validate DCE MRI parenchymal measurements.

In this study we assess the potential of DCE MRI with dual input compartment modelling, and assess the ability of the method to measure changes in perfusion as a result of portal venous ligation (PVL) in healthy rodents. The specific aims of this study are to (a) determine if DCE MRI is feasible in healthy rodents using high-field strength MRI, (b) assess if estimated hepatic perfusion parameters are repeatable, (c) determine if post-PVL reductions in portal venous perfusion and rises in hepatic arterial perfusion as a result of the hepatic arterial buffer response can be measured and (d) to validate hepatic perfusion parameters measured with DCE MRI using invasive TTUS.

2.4 MATERIALS AND METHODS

2.4.1 EXPERIMENTAL SUBJECTS

All experiments were conducted according to the Home Office guidelines under the UK Animals in Scientific Procedures Act 1986. Animals were maintained as per guidelines and approval of the ethical committee for animal care of University College London. Experiments were performed on healthy male Sprague-Dawley rats ($n = 19$, Charles River UK, Margate, UK) with normal liver function. Animals were housed in cages at 22-23°C, ~50% humidity and with 12 hours of light and ad libitum access to water and rat feed. Within each cohort, subjects were randomly selected at the time of removal from the cage. Any adverse events and subsequent protocol modifications were recorded and reported in the results.

2.4.2 SAMPLE SIZE

A pragmatic approach to sample size was used given that data collection during these studies was undertaken alongside protocol development. As parameter variability with our protocol was unknown and studies with DCE MRI had not previously been undertaken in PVL subjects, data was evaluated incrementally with a view to preliminary characterisation of parameters for future planning of adequately powered studies.

2.4.3 IMAGING COHORT

After induction of anaesthesia with isoflurane, a catheter was sited in a carotid vessel. Laparotomy was performed and a silk ligature was placed loosely around the PV. The laparotomy was closed and the animal was placed in the scanner for initial imaging. After imaging with a patent PV, animals were removed from the scanner and randomised into two subgroups. For animals undergoing repeatability studies the laparotomy wound was re-opened but the previously placed ligature was not instrumented. For animals undergoing PVL, the laparotomy wound was re-opened and the previously placed ligature was tightened maximally around the portal vein. The animal was then returned to the scanner for a second study. A 45 minute delay was adhered to between the first and second DCE studies to allow for adequate washout of contrast agent and recovery of tissue and vascular pool T1. Subjects were terminated after the second scan.

2.4.4 VALIDATION COHORT

TTUS measurements were performed with a 2mm probe (Transonic Systems, Ithaca, USA). After induction of anaesthesia with isoflurane, laparotomy was performed and the PV was

dissected. A silk ligature was placed loosely around the PV and the TTUS probe was placed just distal to this. Repeatability and PVL studies were performed in the same cohort of animals. PV flow measurements were then recorded. The probe was then removed and the animal was allowed to settle for 45 minutes. The TTUS probe was then re-sited in a similar position to the first time without instrumenting the previously placed ligature, and a second PV flow measurement was recorded. After this, the previously placed ligature was tightened maximally around the portal vein. A final PV flow measurement was then recorded before terminating the animal. For all TTUS measurements, the animal was allowed to stabilise for at least 3 minutes and only at a time when a consistent reading was demonstrated, was the portal flow recorded. Bulk flow was normalised to estimated liver mass before data analysis [309].

2.4.5 DYNAMIC CONTRAST ENHANCED MRI

DCE MRI is based upon serial imaging of an area-of-interest over time before and after intravenous administration of a bolus of extracellular contrast agent. Measurement of hepatic perfusion parameters with DCE MRI therefore requires (i) dynamically acquired T1-weighted images, (ii) measurement of the baseline T1 values of hepatic parenchyma and blood, (iii) measurement of the contrast agent T1 relaxivity and (iv) modelling of the derived contrast agent concentration curves for each region of interest (ROI).

Imaging was performed using a 9.4T Agilent scanner (Oxford, UK). Data was acquired using a respiratory-gated T1 weighted, saturation-recovery, spoiled gradient-echo sequence with centric-ordered k -space filling. A single axial slice was selected from initial anatomical images that enabled good visualisation of the portal vein, aorta and a large volume of hepatic parenchyma. A slice was acquired at each respiration trigger point (figure 2.1). The saturation-recovery time (TS) was set to enable each slice acquisition to be completed within a single respiratory cycle. In-flow effects into the slice were minimised using a global saturation pulse. Flow artefacts in vessels perpendicular to the acquisition slice were minimised by using velocity-compensated slice-select gradients. For the dynamic acquisition, the following parameters were used: TR = 6.2 ms, TE = 3.4 ms, flip angle (α) = 15°, 128 x 96 (frequency encoding x phase encoding) acquisition matrix and TS = 250 ms. After initial baseline T1 measurements (see below), dynamic imaging was commenced. Ten seconds after dynamic imaging began, a 500 μ L bolus of 0.025 mmol/L Gd-DOTA (gadoteratedimeglumine, Dotarem®, Guerbet, Roissy, France) was administered over 5-10 seconds by hand injection. Sequential dynamic images were obtained for a total of 3 minutes.

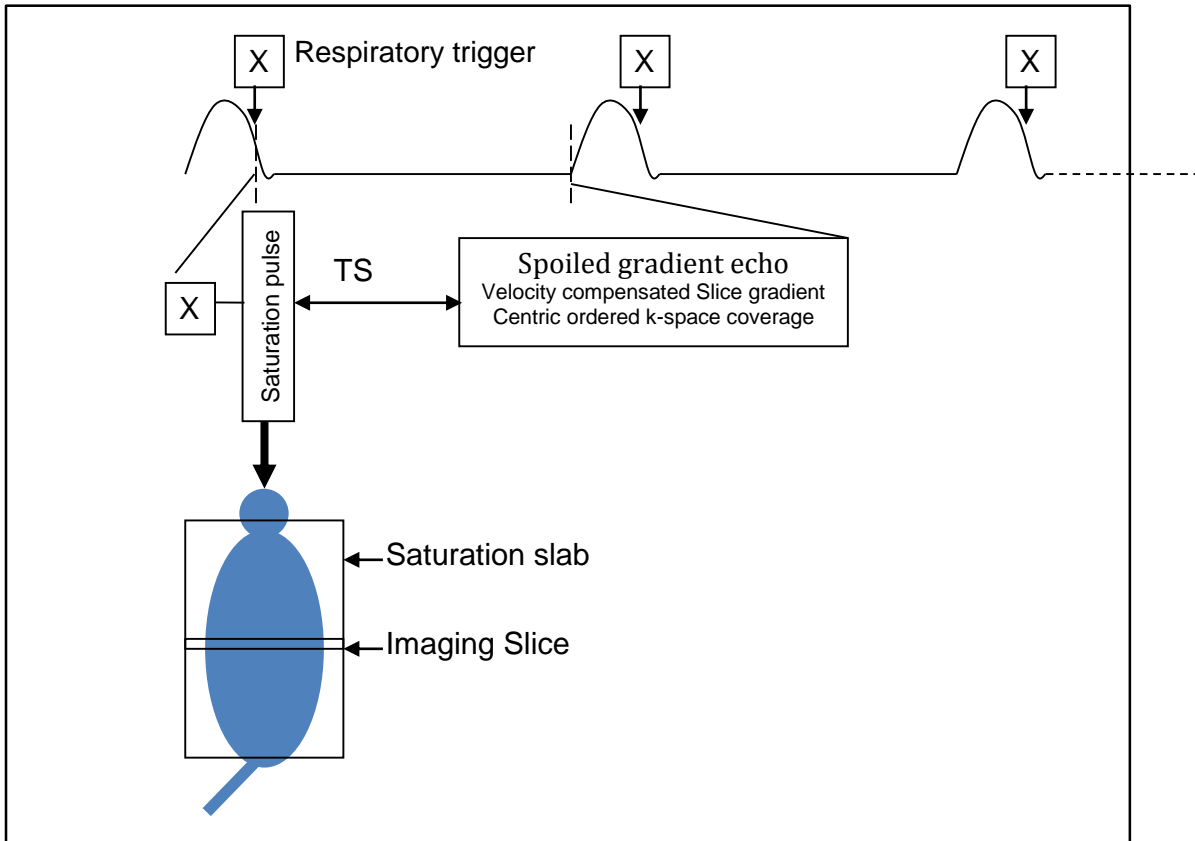


Figure 2.1: Schematic diagram of imaging protocol and gating

The rat is depicted in blue in the lower left corner. Respiratory motion was used to trigger the sequence, which would begin with a saturation pulse to minimise inflow effects, followed by spoiled gradient echo imaging of the imaging slice.

2.4.6 T1 MEASUREMENTS

T1 measurements were obtained using the saturation recovery method. Briefly, the selected slice was imaged using a range of saturation times (TS) from 100 ms, with 200 ms increments to 10100 ms. Any motion corrupted images were discarded from the data set. Curves of signal intensity and TS were then plotted for each ROI. The signal intensity was then modelled using equation 1:

$$M_{xy} = M_0(1 - e^{-\frac{TS}{T1}})$$

(Equation 2.1)

Baseline ROI T1 was then determined by fitting the curve with the function above.

2.4.7 CONTRAST AGENT CONCENTRATION MEASUREMENTS

Contrast agent T1 relaxivity was determined using a phantom composed of tubes with contrast agent diluted with varying quantities of normal saline (0.9% NaCl/H₂O). Nine

dilutions were prepared, ranging from 0.1 ml/L to 25.6 ml/L of contrast agent, in addition to two tubes containing pure water (figure 2.2). T1 measurements were performed using the saturation recovery method (above). Contrast agent concentration was then plotted against the reciprocal of the T1 value at each concentration and the relaxivity (r_1) was then determined using linear regression. Once intrinsic tissue T1 was measured and r_1 was defined, signal intensity from dynamic images was converted into contrast agent concentration using the following equation:

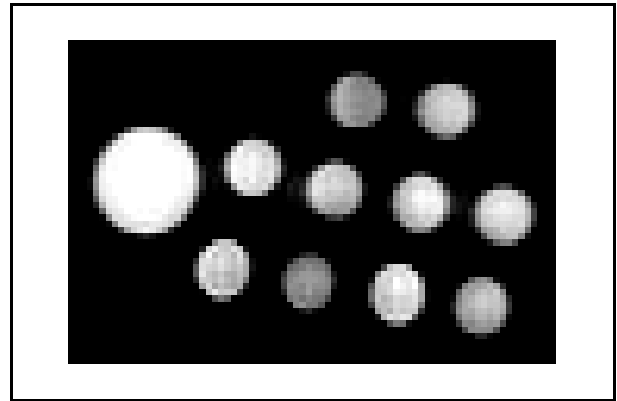
$$\frac{1}{T1_{post}} = \frac{1}{T1_{pre}} + r_1[\text{contrast agent}]$$

(Equation 2.2)

Where $T1_{pre}$ represents the intrinsic ROI T1 and $T1_{post}$ represents the ROI T1 after administration of contrast agent.

Figure 2.2: Contrast agent phantom

MR image of axial section through tube phantom containing Gd-DOTA diluted with normal saline at concentrations of 0.1, 0.2, 0.4, 0.8, 1.6, 3.2, 6.4, 12.8 and 25.6 ml/L. Two additional tubes containing pure water were also included.



2.4.8 PERFUSION PARAMETER ESTIMATION

Hepatic perfusion parameters can be estimated using a dual-input single compartment model. This model is described schematically in figure 2.3. The contrast agent concentration in the liver parenchyma is determined by the concentrations in the supplying vessels (PV and HA) and appropriate rate constants for the transfer of contrast agent from blood plasma to tissue parenchyma. The HA is often very small and can be difficult to resolve on imaging, resulting in partial voluming with surrounding tissues. Thus, in order to determine the HA input function, it is assumed that the HA enhancement curve will be similar to that of the aorta.

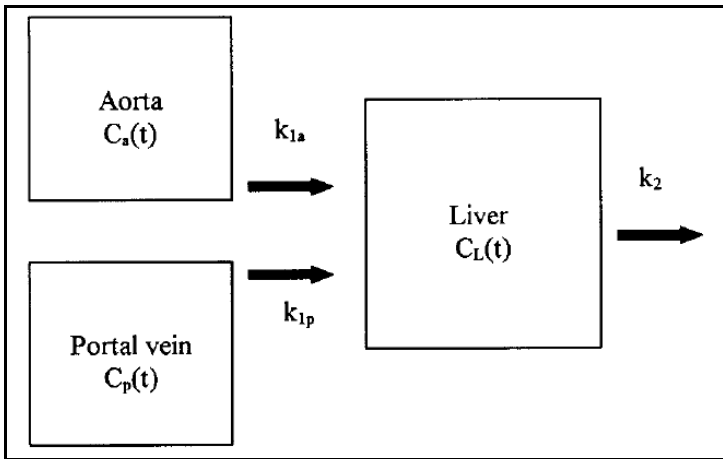


Figure 2.3: Schematic illustration of the dual-input single compartment model

The variables k_{1a} and k_{1p} represent inflow constants, k_2 is the outflow rate constant and $C_a(t)$, $C_p(t)$ and $C_L(t)$ represent contrast agent concentration in ROIs placed over the aorta, portal vein and liver parenchyma respectively (obtained from reference [114]).

The dual input, single compartment model can be described mathematically using the following equation:

$$\frac{dC_L(t)}{dt} = k_{1a}C_a(t) + k_{1p}C_p(t) - k_2C_L(t) \quad (\text{Equation 2.3})$$

The model describes the rate of change in concentration in the liver parenchyma ($C_L(t)$), as being the rate of the inflow (where $C_a(t)$ and $C_p(t)$ represent concentrations in the aorta and portal vein respectively) minus the rate of outflow, where k_{1a} represents the arterial inflow constant, k_{1p} represents the portal venous inflow constant and k_2 represents the outflow constant. Solving for $C_L(t)$ then yields:

$$C_L(t) = \int_0^t [k_{1a}C_a(t) + k_{1p}C_p(t)]e^{-k_2(t)} dt' \quad (\text{Equation 2.4})$$

The signal derived from vascular input function (VIF) ROIs is related to the blood-plasma contrast agent concentration. Thus the calculation of whole-blood concentration must take into account the presence of red blood cells. To account for this, $C_a(t)$ and $C_p(t)$ must

be divided by one minus the haematocrit, so that k_{1a} and k_{1p} represent that transfer constants for the aortic and portal venous plasma contrast agent concentration to the liver parenchyma. The assumption then is that the liver parenchymal ROI represents a single compartment containing a negligible volume of vascular tissue.

The rate constants are then directly related to perfusion by the following relationship:

$$k_{1a} + k_{1p} = F \cdot E \quad (\text{Equation 2.5})$$

Where ' F ' represents perfusion and ' E ' represents the fraction of contrast agent extracted by from the inflow. Additionally F needs to be corrected for small vessel red blood cells so that finally:

$$F_{\text{Arterial perfusion}} (\text{ml/s/g}) = \frac{k_{1a}}{E(1 - Hct_{SV})}$$

and:

$$F_{\text{PV perfusion}} (\text{ml/s/g}) = \frac{k_{1p}}{E(1 - Hct_{SV})} \quad (\text{Equations 2.6 and 2.7})$$

Where Hct_{SV} represents small vessel haematocrit (assumed to be 0.25)[ref 31]. ' E ' is assumed to be 1.0 in the normal liver, as the contrast agent can pass freely through the vascular endothelium to the interstitium and space of Disse. Strictly speaking, the units of perfusion are ml/s per ml (volume unit) of tissue. Assuming the specific tissue gravity of liver to be 1.0, we can assume the more familiar unit of 'ml/s/g', which can then be multiplied through to yield usual perfusion unit quoted in physiology manuscripts of 'ml/min/100g'.

Arterial and portal fraction can then be easily determined by assessing rate constant ratios, where portal fraction is $100 [k_{1p}/(k_{1a} + k_{1p})]$. The distribution volume (DV; %) is then calculated as $100 (k_{1a} + k_{1p})/k_2$, while the mean transit time (MTT; seconds) is calculated as $1/k_2$.

2.4.9 IMAGE ANALYSIS

ROIs were drawn on the imaging slice over the aorta, PV and hepatic parenchyma. Care was taken to select hepatic parenchymal ROIs that did not contain any overt vessels. Equation 2.1 was fitted to saturation recovery data with varying TS, using the solver tool in Microsoft Excel 2010 (Redmond, USA), to determine baseline T1 values. Baseline (pre-contrast agent) signal intensity data was subtracted from the post-contrast data sets to

determine the change in signal intensity over time after contrast agent administration. The r_1 determined from phantom experiments was then used to determine ROI contrast agent concentration as a function of time. Dual-input single compartment fitting was then performed, with the parameters k_{1a} , k_{1p} and k_2 as free variables, using in-house developed Matlab code.

2.4.10 STATISTICAL ANALYSIS

Kolmogorov-Smirnov tests were used to confirm normality of variable distributions. Repeatability studies were assessed using paired t-tests or Wilcoxon matched-pairs signed rank tests where appropriate, Bland-Altman analysis of agreement with calculation of the coefficient of repeatability and assessment of correlation between repeated measurements using Pearson's correlation coefficient. Portal venous ligation studies were of small size ($n = 4$), and were paired data assessed using Wilcoxon matched-pairs signed rank tests while unpaired data was assessed using Mann-Whitney U tests where specified. As separate subject cohorts were used, validation studies were assessed using unpaired t-tests. The threshold of statistical significance was defined to be $p < 0.05$.

2.5 RESULTS

2.5.1 SIGNAL INTENSITY CALIBRATION

The contrast agent phantom was scanned using saturation times between 110 to 3910 milliseconds with 100 ms increments (figure 2.4(a)). The signal intensity was then plotted against saturation time curves, which were then fitted to equation 2.1, using least squares regression, to derive a T1 estimate for each dilution. Based on these results, a saturation time of 250 ms was selected for DCE experiments, to optimise the dynamic range for assessment of contrast agent concentration. Signal drop out was observed with contrast agent concentrations above or equal to 12.8 ml/L of normal saline. These were excluded from the r_1 calculation.

Using concentrations up to 6.4 ml/L, an almost linear relationship between the Gd-DOTA dilution and the reciprocal of T1 was identified. This was then fitted using linear regression to determine $r_1 = 0.0031$ (figure 2.4(b)). Having determined r_1 in this way, all subsequent concentrations are quoted in units of 'ml/L' rather than 'mmol/L'.

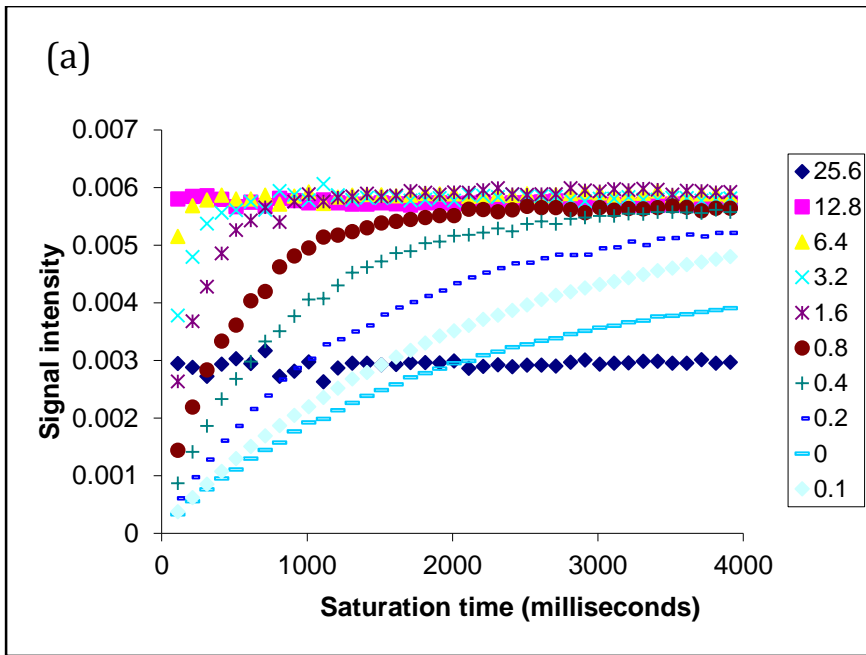
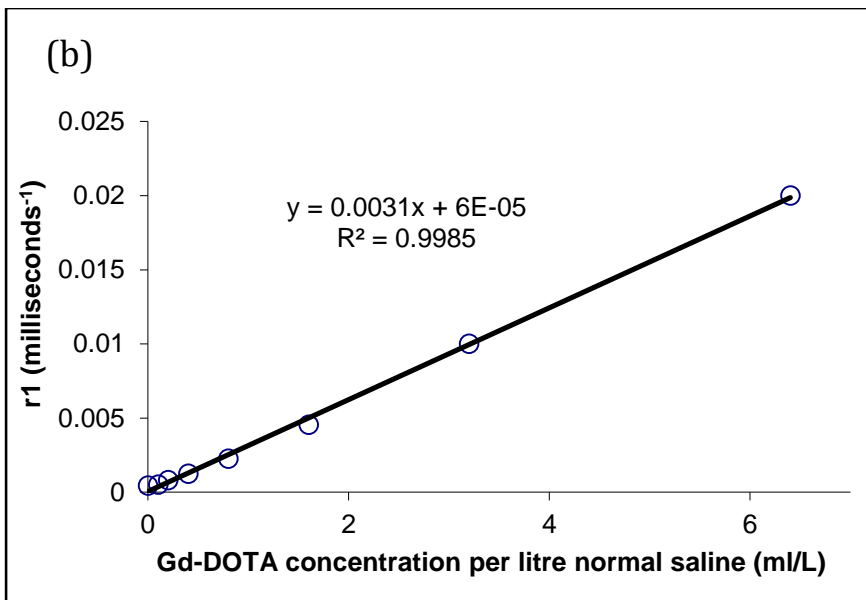


Figure 2.4: T1 phantom measurements and r1 estimation

(a) The phantom shown in figure 2.3 was imaged at a variety of saturation times to determine the T1 for each concentration of contrast agent. Note how at concentrations above 6.4 ml/L, the T1 was either too short to measure (12.8 ml/L) or signal drop out was noted (25.6 ml/L). (b) r1 was then determined using linear regression.



2.5.2 COHORT FEATURES

Data for the experimental subjects is summarised in table 2.1. Estimated liver weights are given for both cohorts.

Table 2.1: Cohort features

	IMAGING COHORT	VALIDATION COHORT
	<i>n</i> = 13	<i>n</i> = 6
Body weight	280.30±4.37g	443.80±38.31g*
Estimated liver weight	14.34±0.19g	20.43±1.39g*
Repeatability study	<i>n</i> = 5	<i>n</i> = 4
PV ligation study	<i>n</i> = 4	<i>n</i> = 4

(all weights given as mean ± standard error of the mean); *(unpaired t-test, $p < 0.05$)

Animals in the validation cohort were significantly different in body and estimated liver weight. To mitigate these effects, validation analysis was performed with flow data normalised to estimated liver weight.

Although a total of $n = 13$ were scanned in the imaging cohort, data for one subject was discarded due to poor fitting of the data with the dual input single compartment model (see discussion). A further $n = 3$ underwent only an initial imaging study due to time constraints - this data was utilised for unpaired comparisons. In the imaging cohort, repeatability ($n = 5$) and PV ligation studies ($n = 4$) were performed in separate animals. In the validation cohort, $n = 2$ animals were lost after the initial measurement as a result of gross intra-abdominal haemorrhage from traumatic placement of the TTUS probe. As the initial baseline PV flow was still recorded, data from these subjects was utilised for unpaired t-tests. Repeatability and PV ligation studies were performed in the same animals in this cohort. This information is summarised below in figure 2.5.

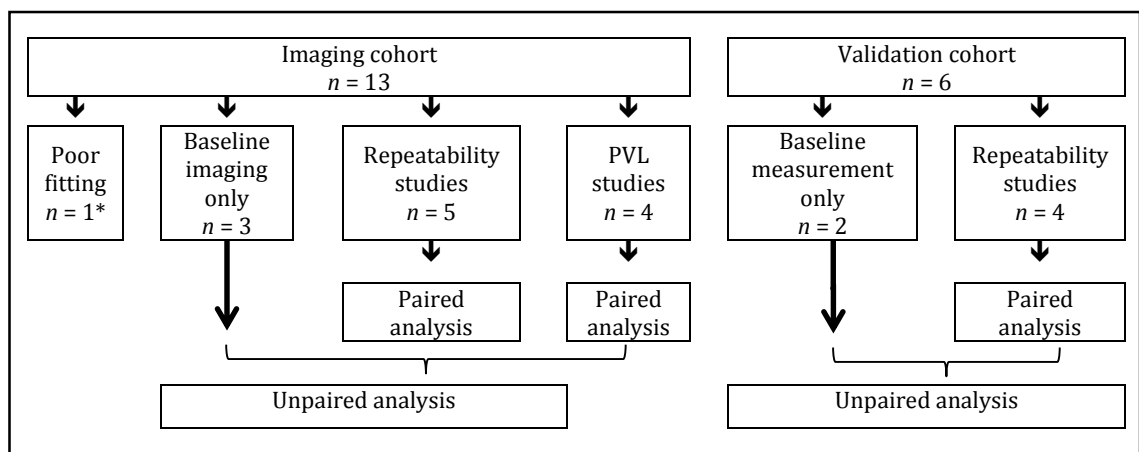


Figure 2.5: Schematic diagram of planned statistical analyses

Given the small numbers involved, incomplete data sets were used for unpaired analyses where possible. *The poorly fitted subject data ($n = 1$) was excluded from analyses.

2.5.3 DCE MRI FEASIBILITY

Regions of interest were drawn over the aorta, portal vein and hepatic parenchyma as shown in figure 2.6. An example of the curve fitting procedure to determine T1 measurements using the saturation recovery method is illustrated in figure 2.7.

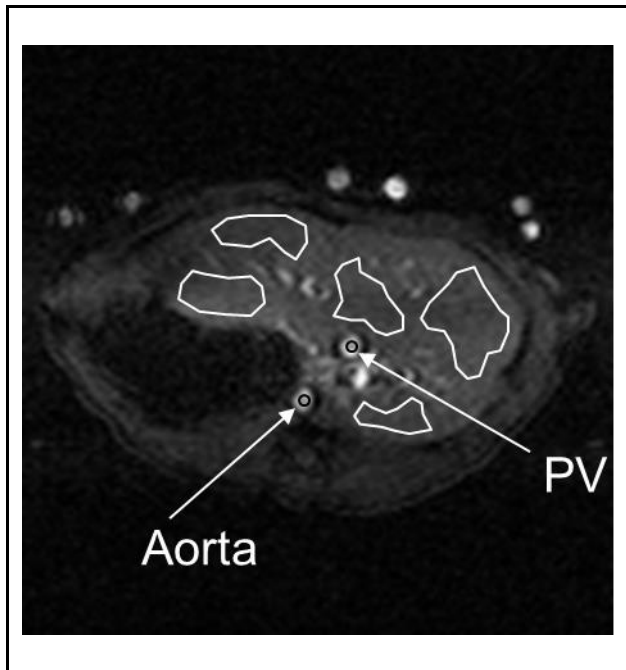


Figure 2.6: Example of ROI placement for DCE MRI quantification

Aortic and portal venous ROIs as shown. Parenchymal data was averaged across the ROIs shown in white

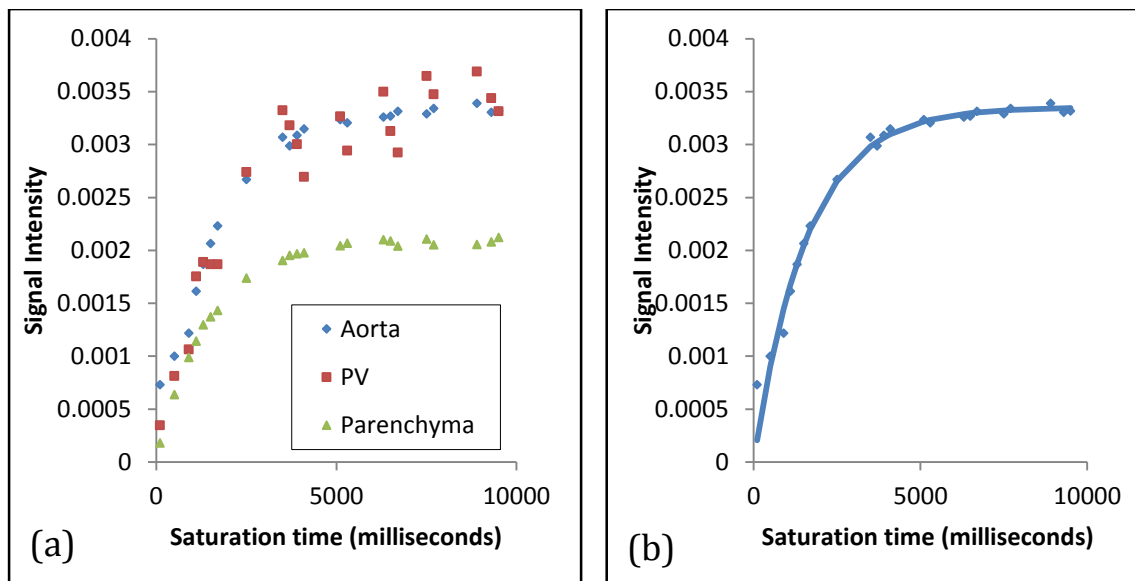


Figure 2.7: (a) Measurement of ROI T1 times, with (b) specific example of aortic ROI fitting to determine T1

(a) The slice shown in figure 2.5 was imaged at a variety of saturation times to determine the T1 for each ROI. The curve fit for the aortic ROI data is shown in (b) (T1 = 1587 milliseconds).

Signal intensity-time curves from similar ROIs were then converted using the previously described method into Gd-DOTA concentration-time curves. Modelling was then undertaken using the dual-input single compartment model. An example of the contrast

agent concentration curves, their corresponding fits and modelled hepatic perfusion parameters are illustrated in figure 2.8.

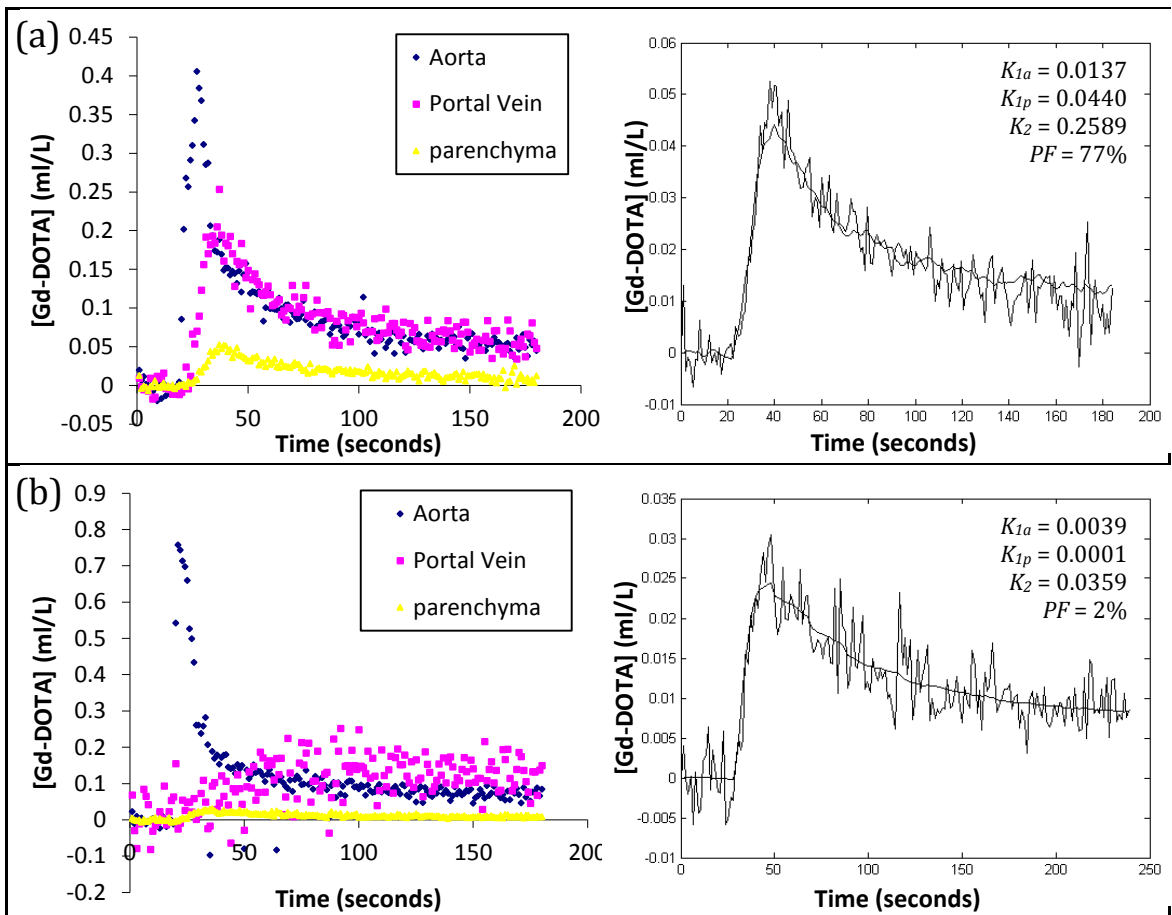


Figure 2.8: Example of contrast agent concentration curves at corresponding fits.

Baseline (a) and post-PVL (b) enhancement curves. Corresponding model fits for $C_L(t)$ and estimated hepatic perfusion parameters (upper right corners) can be found on the right; (n.b. PF = portal fraction).

2.5.4 REPEATABILITY

Repeatability of all five hepatic perfusion parameters obtained from DCE MRI imaging and normalised bulk PV flow as measured by TTUS were assessed (summarised in table 2.2). All perfusion parameters were normally distributed with the exception of TTUS PV flow.

Table 2.2: Summary of repeatability statistics

	MEAN DIFFERENCE BETWEEN REPEATED MEASUREMENTS	P-VALUE	COEFFICIENT OF REPEATABILITY
DCE MRI			
Arterial perfusion (ml/min/100g)	-6.40±9.61	0.541	42.10
PV perfusion (ml/min/100g)	-86.88±89.41	0.386	391.8
Portal fraction (%)	-2.19±6.80	0.764	29.82
DV (%)	0.53±0.55	0.387	2.403
MTT (s)	0.31±1.02	0.775	4.469
TTUS			
Normalised PV flow (ml/min/100g)	0.3904*	>0.999	38.71

(all parameters given as mean ± standard error of the mean)
*(median value given as non-normally distributed)

No significant differences in the repeated measurements were demonstrated in any parameters. Graphical analysis of agreement is depicted in figure 2.9. With the exception of arterial perfusion ($r = 0.92$, $p < 0.05$; figure 2.9(b)) and distribution volume ($r = 0.946$, $p < 0.05$; figure 2.8(h)), correlations between repeated measurements were poor and non-significant.

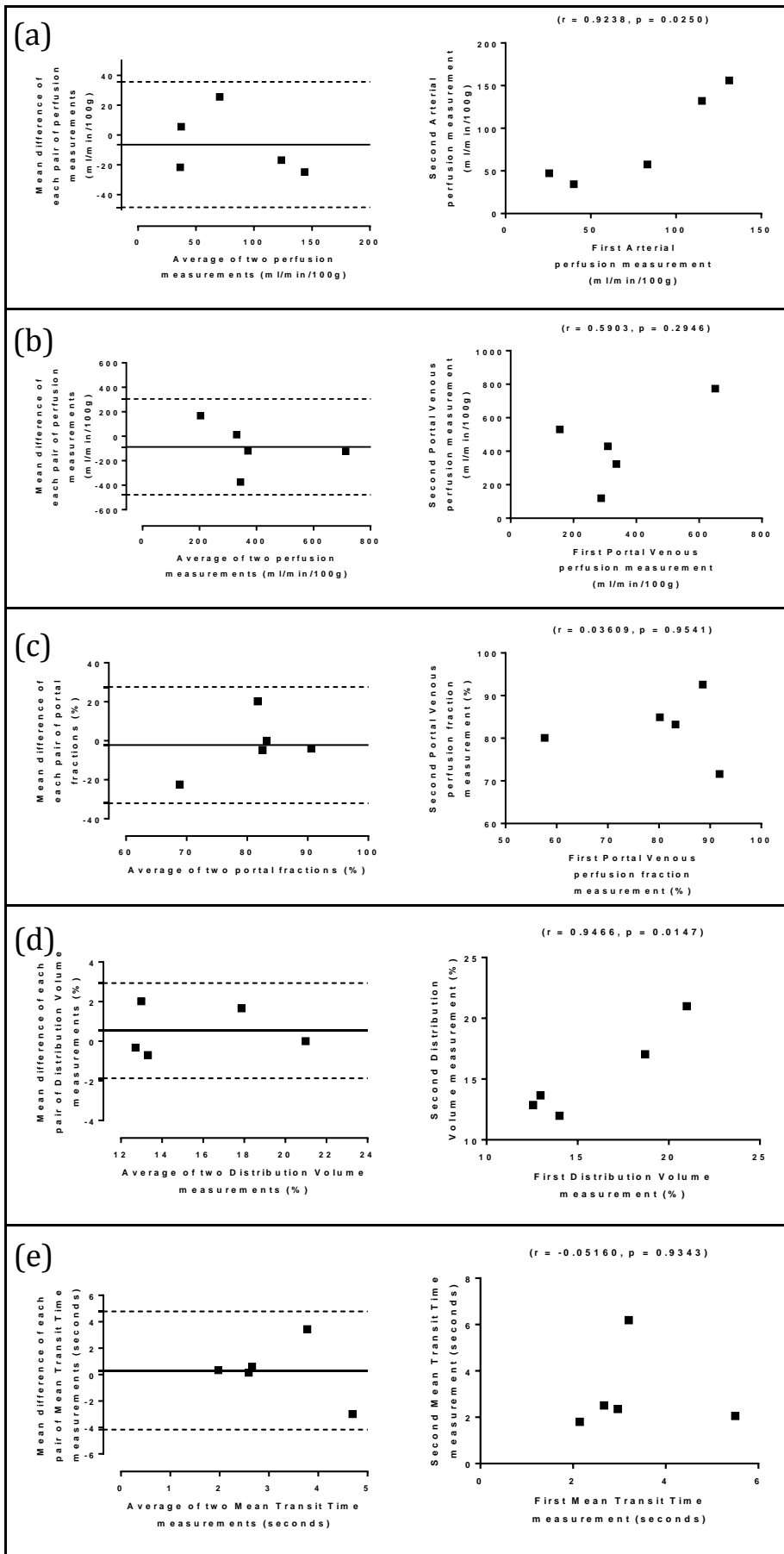


Figure 2.9: Analysis of agreement of repeated hepatic perfusion measurement
S Bland-Altman and regression analysis of (a) arterial perfusion, (b) portal venous perfusion, (c) portal fraction, (d) distribution volume and (e) mean transit time.

2.5.5 PORTAL VENOUS LIGATION

All five hepatic perfusion parameters obtained from DCE MRI imaging were assessed before and after PVL (summarised in table 2.3). Paired analysis was performed, but unpaired tests using the larger cohort of baseline data are also presented to improve the power of the statistical interpretation.

Table 2.3: Summary of DCE MRI hepatic perfusion changes post-PVL

(a) Paired analysis

	BASELINE (n = 4)	POST-PVL (n = 4)	MEDIAN DIFFERENCE
Arterial perfusion (ml/min/100g)	108.2±8.91	37.60±11.44	75.20
PV perfusion/normalised bulk PV flow (ml/min/100g)	290.8±46.73	1.6±1.35	321.2
Portal fraction (%)	71.54±4.70	10.35±9.53	65.71
Distribution Volume (%)	18.91±1.48	12.21±1.84	6.845
Mean Transit Time (seconds)	4.00±0.61	28.94±5.66	21.05

(b) Unpaired analysis

	BASELINE (n = 12)	POST-PVL (n = 4)	MEDIAN DIFFERENCE
Arterial perfusion (ml/min/100g)	79.47±11.29	37.60±11.44	43.20
PV perfusion/normalised bulk PV flow (ml/min/100g)	321.2±43.95	1.6±1.35	302.8*
Portal fraction (%)	77.75±3.72	10.35±9.53	77.90*
Distribution Volume (%)	16.49±1.06	12.21±1.84	4.135
Mean Transit Time (seconds)	3.58±0.30	28.94±5.66	21.45*

(all parameters given as mean ± standard error of the mean)

*(significant differences on Wilcoxon matched-pairs signed rank/Mann-Whitney testing $p < 0.05$)

Changes post-PVL are illustrated with charts in figure 2.10. Expected reductions in PV perfusion/normalised bulk PV flow, portal fraction and rises in MTT were found to be statistically significantly different (on unpaired analysis) after PVL when compared to baseline. Paired analysis of arterial perfusion demonstrated a non-significant reduction (rather than the expected rise) after PVL. Unpaired analysis of arterial perfusion (median difference after PVL = 43.20 ml/min/100g, $p = 0.0742$) approached significance. No significant changes in DV were observed after PVL using both paired (median difference after PVL = 6.845%, $p = 0.1250$) and unpaired analyses (median difference after PVL = 4.135%, $p = 0.0956$).

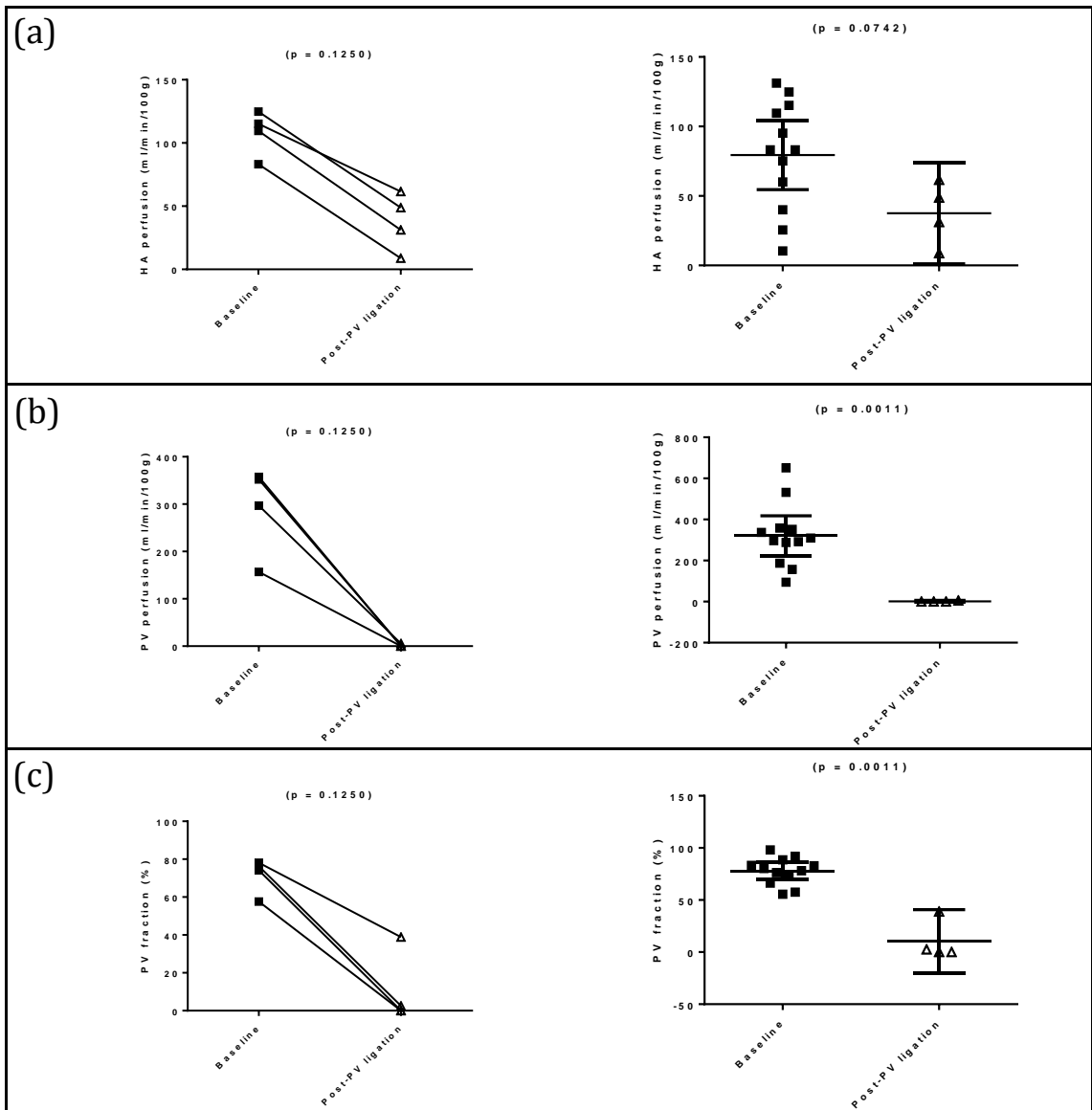


Figure 2.10: Baseline and post-PVL changes in hepatic perfusion parameters obtained with DCE MRI

Paired analysis ($n = 4$) (shown on the left) and unpaired analysis ($n = 12$), (shown on the right) for (a) arterial perfusion, (b) portal venous perfusion, (c) portal fraction, (d) distribution volume and (e) mean transit time (continued on next page).

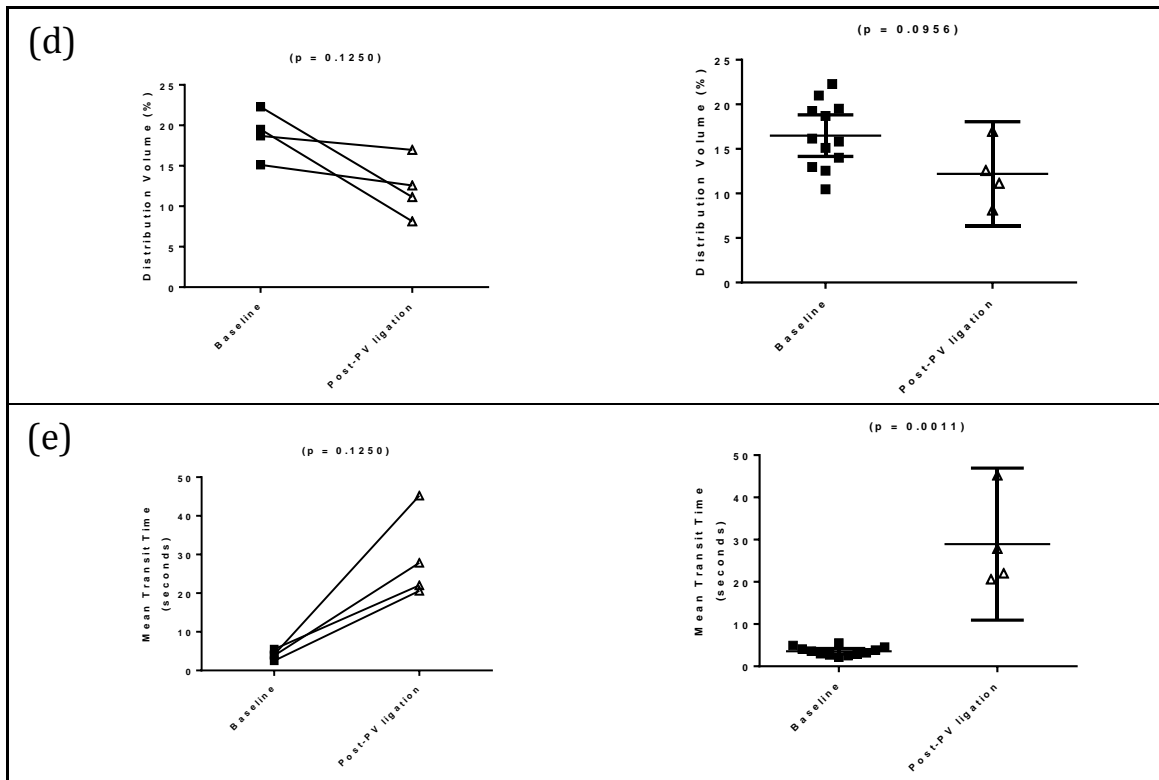


Figure 2.10: Baseline and post-PVL changes in hepatic perfusion parameters obtained with DCE MRI (continued).

Paired analysis ($n = 4$) (shown on the left) and unpaired analysis ($n = 12$), (shown on the right) for (a) arterial perfusion, (b) portal venous perfusion, (c) portal fraction (on previous page); (d) distribution volume and (e) mean transit time.

2.5.6 VALIDATION

Baseline DCE MRI PV perfusion (321.2 ± 43.95 ml/min/100g, $n = 12$) was compared with TTUS normalised bulk PV flow (150.1 ± 7.73 ml/min/100g, $n = 6$). A significant difference was demonstrated (171.1 ± 63.34 ml/min/100g, $p < 0.05$) illustrated with figure 2.11.

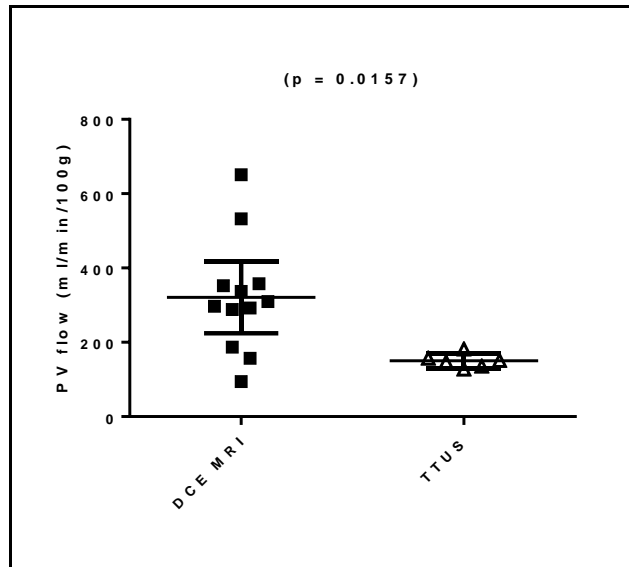


Figure 2.11: Baseline DCE MRI portal venous perfusion compared with TTUS normalised bulk portal venous flow

Reductions in DCE MRI PV perfusion (median -321.2 ml/min/100g, $p < 0.05$) and TTUS bulk PV flow (median -149.20 ml/min/100g, $p < 0.05$) were demonstrated after PVL (figure 2.12).

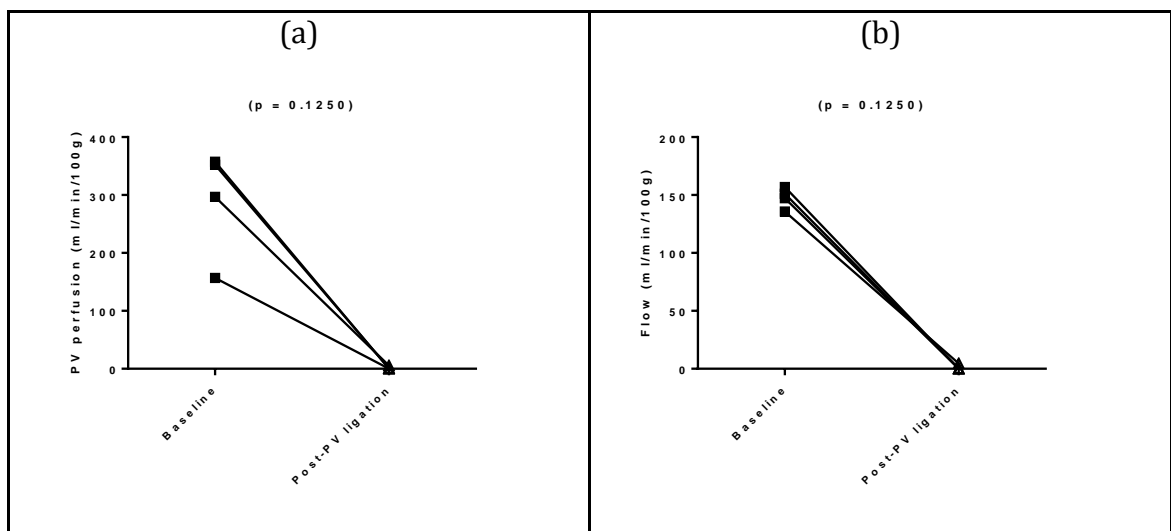


Figure 2.12: Post-PVL reductions in (a) DCE MRI portal venous perfusion and (b) TTUS portal venous bulk flow

2.6 DISCUSSION

Our data has shown that rat liver DCE MRI is feasible at 9.4T and can be used to estimate hepatic perfusion parameters. Although numbers were small, no significant difference in repeat measurements was demonstrated. The coefficient of repeatability statistics are high and generally poor correlations between repeat measurements were seen, with the exception of arterial perfusion and DV measurements.

Post-PVL studies were encouraging. Firstly, expected gross reductions in PV perfusion and portal fraction were demonstrated. Unfortunately, no significant change in arterial perfusion was observed. Although one would expect the HABR to become manifest in PVL, there are no published studies measuring hepatic arterial perfusion in the context of total PVL – the significance of this finding is therefore uncertain. A rise in MTT was observed post-PVL, which would theoretically be expected given the lower perfusing volumes in PVL. Significant changes were demonstrated in all parameters except DV. Although the p-value approaches significance in both paired and unpaired analysis, the non-significant difference is encouraging as one would expect the DV to remain constant regardless of PVL.

DCE MRI PV perfusion measurements demonstrated gross over-estimation of absolute PV perfusion. While absolute quantification of perfusion may be inaccurate, it is encouraging that the mean portal fraction ($77.75 \pm 3.72\%$; $n = 12$) matches generally accepted values in physiology texts of approximately 75%. Expected reductions in TTUS measured bulk PV flow were demonstrated post-PVL thereby validating the PVL procedure.

To assess DCE MRI perfusion parameters better, we have compared our absolute perfusion measurements with other DCE MRI measurements in the literature.

Table 2.4: Absolute perfusion measurements with DCE MRI compared with literature reported values

STUDY	SPECIES	ARTERIAL PERFUSION (ml/min/100 g)	PV PERFUSION (ml/min/100 g)	PORTAL FRACTION (%)	DV (%)	MTT (seconds)
<i>Our study</i>						
DCE MRI	Sprague-Dawley rats	79.47±11.29	321.2±43.95	77.75±3.72	16.49±1.06	3.58±0.30
TTUS		-	150.1±7.73	-	-	-
<i>Kim et al. [142]</i>						
DCE MRI	Wistar rats	340.54 [†]	1021.62 [†]	75	63	3.7
<i>Materne et al. [140]</i>						
DCE MRI	New Zealand White rabbits	23±13	84±32	78.50	13.0±3.7	8.9±4.1
Microspheres		20±10	73±35			
<i>Annet et al. [82]</i>						
DCE MRI	Humans, non-cirrhotic	8.78±5.38	56.39±27.82	82.58±14.88	11.43±4.48	12.7±8.6
Doppler US	chronic liver disease	-	644.9±213.2	-	-	-
<i>Hagiwara et al. [141]</i>						
DCE MRI	Humans, non-fibrotic chronic liver disease	6.0±5.1	126.3±66.7	92.4±7.9	17.3±3.9	9.3±4.3

[†](Unpublished values. These were calculated from published values of DV, MTT and portal fraction).

Published DCE MRI data with dual input single compartment modelling in healthy rats is sparse. In the Kim et al. study only portal fraction, DV and MTT are quoted, however when using these to infer the inflow constants (see above), unreasonable estimates of hepatic perfusion parameters are generated. The validation data from the first DCE MRI study using the dual input single compartment model in rabbits, including microsphere validation is included for comparison. Derived relative perfusion parameters (portal fraction, DV and MTT) are also presented, as is human data.

Eye-balling data in figure 2.10(a) and 2.10(b), a significant issue with DCE MRI derived perfusion parameters is the large variance of measurements, specifically absolute parameters such as k_{1a} , k_{1p} and k_2 . This is striking when compared with TTUS, for example (figure 2.11). DCE MRI is a complex process and small errors introduced at each stage in the methodology are likely to propagate into more significant overall errors in estimates of hepatic perfusion parameters. Methodological considerations at each stage are reviewed below in turn.

2.6.1 DYNAMIC CONTRAST ENHANCED MRI

Accurate measurement of enhancement over the vascular ROIs to derive consistent VIFs is essential for precise pharmacokinetic quantitation. This has however been shown to be challenging because of (i) the sensitivity of gradient echo imaging to inflow effects [310] and (ii) the rapid changes in contrast agent concentration that occur during the first pass peak of the bolus injection, both of which are particular issues for ROIs placed over high flow vessels such as the aorta. The compromise between the higher temporal resolution required for the VIF and the high spatial resolution required for an accurate parenchymal

enhancement curve represents an even bigger challenge in small animals particularly when imaging at higher field strengths.

To minimise inflow effects, a global saturation pulse was applied before each saturation-recovery measurement and each DCE imaging acquisition. Although inflow effects will have been minimised, measured signal will still have been degraded by inflow effects thereby affecting the quality of both baseline vascular ROI T1 measurements but also measured DCE VIFs.

As previously demonstrated (figure 2.4(a)), a loss of signal intensity is observed at higher contrast agent concentrations when T2* effects predominate in their contribution to the signal intensity. By way of illustration, in an early experiment in which an undiluted bolus of Gd-DOTA was given, no rise in signal intensity was seen after administration, furthermore circulating high concentrations of blood pool contrast agent thereafter ensured persistent low aortic ROI signal intensity (figure 2.13).

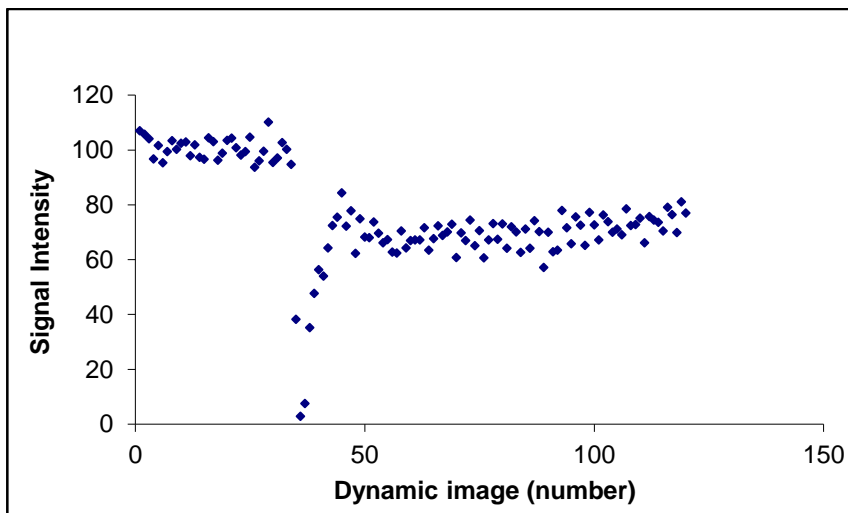


Figure 2.13: Aortic ROI signal intensity after administration of undiluted contrast agent

No rise in signal intensity is recorded, indeed high concentrations of circulating contrast agent after the bolus is given ensure that T2* effects predominate in their contribution to post-bolus ROI signal intensity.

A more dilute bolus would mitigate these effects (figure 2.14), but a bolus that would be too dilute would compromise the signal-to-noise ratio, especially at lower concentrations as observed in ROIs over the liver parenchyma. Additionally the rate of bolus administration will also affect maximal aortic contrast agent concentration. A rapidly administered bolus will result in a higher peak first-pass contrast agent concentration and (if the temporal resolution is insufficient) result in inadequate sampling of the VIF peak. A slowly administered bolus will result in a lower maximal concentration, but will spread/smear the VIF. A smeared VIF is acceptable as long as (a) the VIF is not distorted by second and third passes of the bolus and (b) the arterial and portal venous VIFs are of

sufficiently different form, thereby optimising pharmacokinetic modelling (discussed later in the “perfusion parameter estimation” section). The “ideal bolus” would therefore be of small volume, high concentration and administered as rapidly as possible.

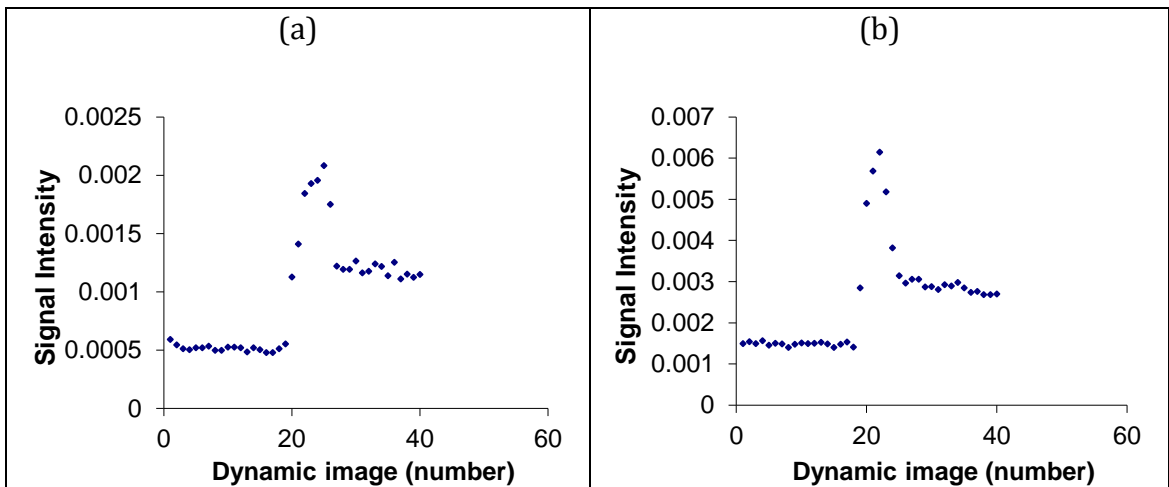


Figure 2.14: Aortic ROI signal intensity after administration of (a) 1:20 dilution and (b) 1:40 dilution of Gd-DOTA

Note how the peak ROI enhancement appears clipped in (a) compared to (b), presumably due to T2 effects from the higher aortic ROI concentrations observed in (a).

To optimise the bolus protocol, several pilot data sets were collected to finalise the protocol before collecting the data presented in this study. The final protocol reflects these challenges and compromises – a dilute bolus (1:40 dilution of Gd-DOTA) was administered slowly (over 5-10 seconds). For practical reasons, a hand injection was used – this was suboptimal and will have introduced variation in both inter- and intra-bolus rate of administration.

Additionally, although imaging acquisitions were respiratory gated, some corruption from motion artefact will still have occurred. Motion artefact is best appreciated (and corrected for) on images obtained in the coronal or sagittal plane. Our data was obtained with axial imaging and any motion correction procedures were not therefore possible.

2.6.2 T1 MEASUREMENTS

For precise absolute quantitation, especially between different subjects, signal intensity calibration and the process of calculating absolute ROI contrast agent concentration, must be robust and accurate. R1 is fixed across all experiments, so any errors introduced at this stage will impact absolute quantification, but are unlikely to account for the wide inter-subject variation. ROI-based T1 measurements must however be accurate and it is here that there is the biggest potential for error. We have used the saturation-recovery method to estimate T1, which relies on the accurate application of a 90° pulse to efficiently eliminate any longitudinal magnetisation affecting the measured signal. When imaging a

volume such as the liver, any variations in B_1 will alter the precision of the pulse angle applied thereby producing errors in T1 measurements in certain parts of the imaging slice.

Additionally, steady-state magnetisation has the potential to be affected by respiratory triggering, thereby affecting both T1 quantification and T1 signal in respiratory gated post-contrast images. Finally, errors in T1 measurements have the potential to propagate into perfusion parameters estimated from pharmacokinetic modelling [311].

2.6.3 PERFUSION PARAMETER ESTIMATION

We elected to use the dual input single compartment model to estimate perfusion parameters from DCE MRI data, limitations of which were exposed by some of our data sets. Dual input single compartment modelling was achieved using a non-linear least squares fitting algorithm, by convolving each VIF with the residue function:

$$C_L(t) = k_{1a} \cdot C_a(t) \otimes e^{-k_2 t} + k_{1p} \cdot C_p(t) \otimes e^{-k_2 t} \quad (\text{Equation 2.8})$$

Good fits were obtained with both pre and post-PVL DCE data sets, although data ($n = 1$) was discarded due to unreasonable fitting (figure 2.15). Our experience from this and pilot data was that this phenomenon was more likely to occur when both $C_a(t)$ and $C_p(t)$ were not sufficiently morphologically distinct from one-another, thereby underlining the importance of optimising the contrast agent bolus protocol.

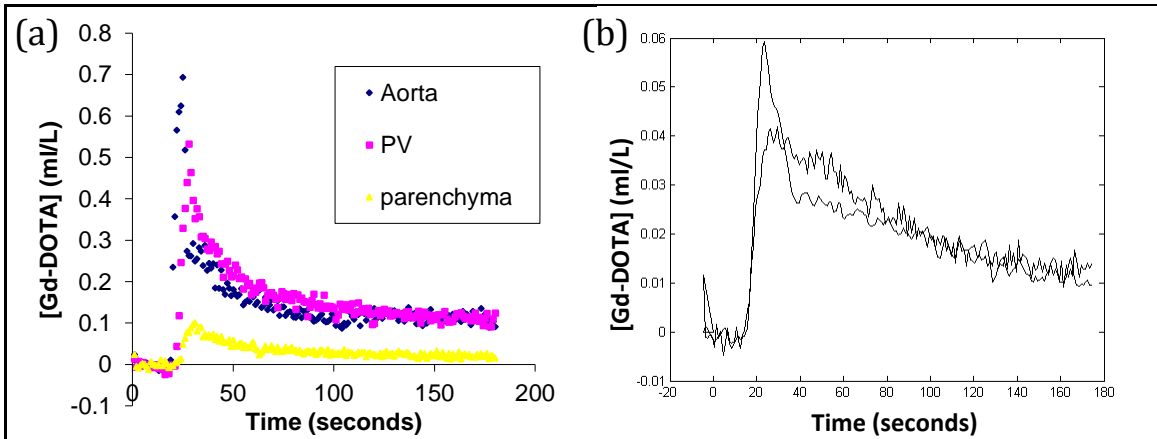


Figure 2.15: Failure of the dual-input single compartment model

Contrast agent concentration curves on the left (a), with corresponding model fit for $C_L(t)$ on the right (b). Note how the fitted curve on the right is visibly discrepant from the observed parenchymal enhancement.

Of course, to accurately model the parenchymal enhancement, both vascular input functions (VIFs) need to be shifted in time to account for the delay between the enhancement in the aortic ROI and arrival of the contrast in the hepatic parenchymal ROI. To incorporate this delay, we modify the model so that $C_L(0) = 0$:

$$C_L(t) = \int_0^t [k_{1a}C_a(t' - \tau_a) + k_{1p}C_p(t' - \tau_p)]e^{-k_2(t-t')} dt' \quad (\text{Equation 2.9})$$

In this study, the parameters τ_a and τ_p were assumed to be negligible and therefore equal to zero, but a variety of different approaches to τ_a and τ_p have been adopted in the literature. Some studies have chosen to fix τ_a and τ_p as equal constants across all subjects (e.g. two seconds)[140], others have chosen to model only τ_a [141]and others have included both τ_a and τ_p as variables to fit in the model[142]. Several authors have concluded that even small changes in the delay factors (especially τ_a), can result in major alterations of the estimated hepatic perfusion parameters[312, 313]. What is also clear is that the more parameters are estimated from the same data, the higher the risk of errors and unreasonable model-derived values of estimated perfusion parameters. The decision to set both delay parameters to zero in this study was made to simplify the modelling process, however any robust attempt at dual input single compartment modelling must find a consistent and scientifically acceptable method of dealing with these delay parameters.

Finally, the dual input single compartment model itself was originally developed to demonstrate regional differences in perfusion parameters, specifically in the context of lesion characterisation. This is a more sound application of the model, reliant on the ability to detect relative regional changes in hepatic perfusion parameters, without the need for accurate absolute quantification. Several studies measuring absolute bulk parenchymal perfusion have been performed, but as our study demonstrates – absolute quantification is fraught with difficulty. The application of the model in the context of PVL is also new and untested. The model coped well measuring reductions in PV perfusion post-PVL. But post-PVL, the model would have had to fit data from a theoretically similar aortic VIF to a smaller parenchymal enhancement curve. This modelling peculiarity may well explain the observed reduction in estimated parenchymal arterial perfusion (rather than the expected hepatic arterial buffer response).

2.6.4 PHYSIOLOGICAL FACTORS

Both HA and PV blood flow are also dependent on systemic mean arterial pressure and cardiac output, both of which were not evaluated in this study. Laparotomy for example, is associated with an unavoidable decline in mean arterial pressure (although both baseline and post-PVL data were recorded after laparotomy). Anaesthesia itself is known to have profound systemic and liver-specific haemodynamic effects. Inhaled anaesthesia over extended time periods, as administered in this study will lead to increased insensible

losses and almost all anaesthetic agents including injectable agents, are associated with reductions in mean arterial pressure. Agents such as halothane for example, are known to precipitate reductions in both arterial and portal venous flow in humans, rodents and rodent models of cirrhosis [314-317]. Isoflurane (used in this study) has been demonstrated both in humans and rodent models of cirrhosis to be less disruptive to hepatic blood flow than other inhaled and injectable anaesthetics [315, 318, 319].

2.6.5 FUTURE DEVELOPMENTS

There are a number of strategies that can be taken to overcome the issues identified above. With regards to the imaging protocol, improved VIF measurements can be achieved by minimising inflow effects through better quality global saturation pulses and improvements in the bolus protocol. Intra- and inter-bolus variation can be eliminated by using a syringe driver to deliver the bolus at a fixed rate. To determine this, experiments optimising bolus concentration and rate need to be performed. Secondly the compromise between improved VIF measurement and poor parenchymal SNR can be overcome using a so-called “dual-bolus” approach[179, 180, 320, 321]. An initial dilute bolus can be administered quickly to obtain the VIFs. A second higher concentration bolus can then be administered to optimise the SNR of parenchymal enhancement data. The dilute bolus VIF can then be scaled to match the expected VIF from the higher concentration parenchymal bolus, before modelling the data.

There are also a number of alternative approaches to measuring the intrinsic T1 relaxivity of the tissues and vascular ROIs. The “inversion-recovery” method for example, widely accepted to be the more robust, “gold-standard” approach to measuring T1 could be used.

Alterations to the modelling process may also help yield more consistent, accurate absolute quantification of perfusion. A protocol for the estimation of the delay parameters (τ_a and τ_p) in a scientifically acceptable way will need to be developed. Alternatively, there are several alternative models in the literature, such as the Scharf et al. model[134, 135], the “hepatic perfusion index” model[138, 139], and not least the dual input dual compartment model[149, 150], all of which may yet yield more robust, useful and repeatable parameters in the context of global perfusion.

Finally, future experiments could include some measurement of systemic haemodynamics, ideally through monitoring mean arterial pressure (via carotid catheterisation) or by measuring cardiac output, potentially using MR methods.

2.7 CONCLUSIONS

This is the first study to our knowledge that has used DCE MRI with dual input single compartment modelling to measure hepatic perfusion parameters in rodents at 9.4T and the first study of *in vivo* repeatability and changes post-complete PVL. Our early studies have shown that DCE MRI is feasible in healthy rodents at high MR field strength and that estimated hepatic perfusion parameters are repeatable, but show large variance. PVL elicited reductions in measured PV perfusion and combined arterial and PV parenchymal perfusion. The hepatic arterial buffer response however, was not observed post-PVL. Finally, absolute quantification of PV perfusion with current DCE MRI protocols did not agree with invasive TTUS validation.

2.8 CLOSING COMMENTS

DCE MRI was an ideal method to initiate studies of haemodynamic assessment, having the important advantage of being based upon standard anatomical imaging sequences and therefore mitigating the need for development of new and more complex MRI sequences at this early stage. While conceptually simple, our experience of DCE MRI has highlighted some of the major challenges associated with the method. Moving forward, protocol refinements are required to tackle the challenges identified in this chapter. We have proposed several strategies that could be used to address these challenges, which once implemented would be important in establishing DCE MRI as a robust preclinical method for the quantification of hepatic perfusion.

CHAPTER 3

TROUBLESHOOTING FOR PRECLINICAL DCE MRI

“...And every feeling
or impulse
grew in your machinery,
received some drop
of your tireless
elaboration...”

- Ode to the liver [2].

3.1 INTRODUCTION

In Chapter 2, it was demonstrated that in vivo dynamic contrast enhanced (DCE) MRI with dual input single compartment modelling was feasible in rodents at 9.4T. DCE MRI derived perfusion parameters demonstrated a large variance and invasive validation with transit-time ultrasound (TTUS) found absolute quantification with DCE MRI to be inaccurate. To address these challenges, a number of potential strategies were evaluated. These broadly fell into the following 3 categories: (a) alternative methods for T1 measurement, (b) novel bolus protocols and (c) modifications and alternative approaches to the DCE MRI pharmacokinetic modelling. In the final part of this chapter we review why the DCE MRI approach was ultimately abandoned in favour of other, less error prone approaches.

3.2 AUTHOR CONTRIBUTIONS

In fulfilment of the aims given for each section in this Chapter, I: (a) prepared and conducted all animal scanning experiments; (b) developed Matlab code for quantification of inversion recovery and multi-flip angle T1 acquisitions; (c) developed and built the syringe driver arrangement; (d) developed the protocols and conducted the experiments for alternative contrast agent bolus protocols; (e) conceptualised novel methods for handling VIF delays; (f) developed all the Matlab code for alternative methods of pharmacokinetic quantification, including alternative methods of handling VIF delays; (g) collected and analysed all the data; and (h) prepared all the material contained within this chapter.

Alan Bainbridge developed MR sequences and helped with scanning. He developed the quantification method for saturation recovery T1 quantification and the original Matlab code for dual input single compartment modelling using no VIF delays. For establishment of small animal intravenous access, I received help from either Val Taylor, Nathan Davies or Abe Habtieson. Multi-flip angle T1 quantification was adapted from Matlab code originally written by Catherine Morgan.

3.3 ALTERNATIVE T1 MEASUREMENT STRATEGIES

3.3.1 BACKGROUND

T1 refers to the relaxation time for recovery of magnetisation along the *z*-axis. The recovery time is dependent on the chemical composition and environment of protons in a given tissue, such that each tissue (arterial blood, portal venous blood, liver parenchyma, etc.) will have a specific T1. These values are likely to change in pathology as a result of secondary alterations in the chemical composition of tissues. Although there has been some interest in evaluating alterations in intrinsic tissue T1 in the context of hepatic fibrosis [322-324], a reliable measurement of T1 is essential in any DCE MRI experiment to accurately quantify the signal intensity change once a gadolinium based contrast agent has been administered. This is because raw pre-contrast signal intensity reflects tissue T1 and any calculation of subsequent contrast agent concentration would need to take this into account.

There are several approaches to measuring T1, including using saturation recovery described in section 2.4.5, inversion recovery and gradient-echo multi-flip angle methodologies. The aim of this section was to apply each of these approaches to the rat liver *in vivo* at 9.4T and to compare absolute T1 measurements from each approach with literature derived values, with a view to finalising a robust protocol for baseline T1 measurements as part of a DCE MRI protocol.

3.3.2 MATERIALS AND METHODS

3.3.2.1 Experimental subjects

All experiments were conducted according to the Home Office guidelines under the UK Animals in Scientific Procedures Act 1986. Animals were maintained as per guidelines and approval of the ethical committee for animal care of University College London. Experiments were performed on healthy male Sprague-Dawley rats (Charles River UK, Margate, UK) with normal liver function. Animals were housed in cages at 22-23°C, ~50% humidity and with 12 hours of light and ad libitum access to water and rat feed. Within each cohort, subjects were randomly selected at the time of removal from the cage. Any adverse events and subsequent protocol modifications were recorded and reported in the results.

3.3.2.2 Sample size

A pragmatic approach to sample size was used given that data collection during these studies was undertaken for the purpose of protocol development. As T1 measurements were undertaken before each DCE MRI study, data for this section was accrued from other experiments (figure 3.1).

3.3.2.3 Animal preparation

After induction with isoflurane, a catheter was sited in either the carotid or jugular vessel. The anaesthetised animal was then sited in a 9.4T Agilent scanner (Oxford, UK) with a rectal probe for temperature monitoring. Core body temperature was maintained between 36 and 38°C using circulating warm water pipes and warm air.

3.3.2.4 Saturation recovery T1 measurement

Sixteen subjects underwent saturation recovery (SR) T1 measurements. These measurements were undertaken as described in section 2.4.5. After initial anatomical imaging, a single axial slice was selected that enabled good visualisation of the portal vein (PV), aorta and a large volume of hepatic parenchyma. The selected slice was imaged repeatedly following a global saturation pulse with a 90° pulse gradient echo sequence at a range of different saturation times (TS), from 100 ms to 10100 ms, with 200 ms increments. Centric-ordered k -space sampling was used. Any motion corrupted images were discarded from the data set. For each region-of-interest (ROI), mean signal intensity (M_{xy}) was plotted against each TS before modelling using least-squares fitting with equation 3.1 to estimate M_0 and T1.

$$M_{xy} = M_0(1 - e^{-\frac{TS}{T1}})$$

(Equation 3.1)

Liver parenchymal T1 was recorded as the average T1 from each of the parenchymal ROIs.

3.3.2.5 Inversion recovery T1 measurement

Seventeen subjects underwent inversion recovery (IR) T1 measurements. After initial anatomical imaging, a single axial slice was selected that enabled good visualisation of the portal vein, aorta and a large volume of hepatic parenchyma. The selected slice was imaged repeatedly following a global saturation pulse using a 180° inversion pulse, followed by a 90° pulse separated by varying delays/inversion times (TI), ranging from 50 ms to 3000 ms. Centric-ordered k -space sampling was used. Between each acquisition, a ten second delay was introduced to ensure magnetisation had fully recovered and that imaged spins were fully relaxed at the start of each acquisition. A total of 17 images were obtained and any motion corrupted images were discarded from the data set. For each ROI, mean signal intensity (M_z) was plotted against each TI before modelling using least-squares fitting with equation 3.2 to estimate M_0 and T1.

$$M_z = M_0(1 - 2e^{-\frac{TI}{T1}}) \quad (\text{Equation 3.2})$$

Liver parenchymal T1 was recorded as the average T1 from each of the parenchymal ROIs.

3.3.2.6 Gradient echo multi-flip angle T1 measurement

Five subjects underwent gradient echo multi-flip angle (MFA) T1 measurements. Respiratory-gated 3D spoiled gradient echo images were obtained repeatedly over the entire abdominal volume at flip angles of 2, 4, 6, 8, 10, 12, 14, 16, 18, 20, 25, 30 and 40°, with a constant repetition time (TR) of 2.796 ms. Slices were then selected that enabled good visualisation of the portal vein, aorta and a large volume of hepatic parenchyma. For each ROI, mean signal intensity (M_{xy}) was plotted against each flip angle (θ) before modelling using non-linear Levenberg-Marquardt fitting [325] with the Ernst function (equation 3.3) to estimate M_0 and T1.

$$M_{xy} = M_0 \sin \theta \left(\frac{1 - e^{-\frac{TR}{T1}}}{1 - \cos \theta e^{-\frac{TR}{T1}}} \right) \quad (\text{Equation 3.3})$$

Liver parenchymal T1 was recorded as the average T1 from each of the parenchymal ROIs.

3.3.2.7 Statistical analysis

Kolmogorov-Smirnov tests were used to confirm normality of variable distributions. One-way analysis of variance (ANOVA) was used to compare mean aortic, portal venous and liver parenchymal T1 values. Unpaired t-tests were used to compare T1 measurement methods with SR derived values, as this was the original method used. One-sample t-tests were then used to compare each T1 measurement method with averaged 9.4T T1 values obtained from published literature [326-328]. The threshold of statistical significance was defined to be $p < 0.05$.

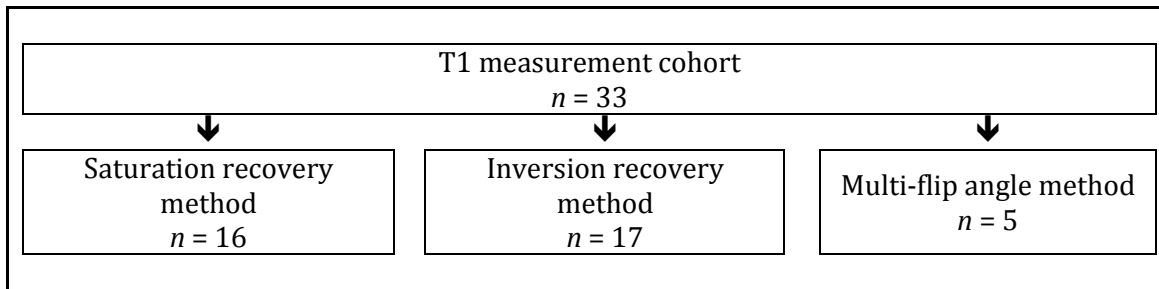


Figure 3.1: Schematic diagram demonstrating cohort sizes

Data for T1 measurement, included saturation recovery datasets from previous T1 measurements underpinning quantification presented in Chapter 2 ($n = 13$). The multi-flip angle data ($n = 5$) was measured in the subjects which were undergoing inversion recovery T1 measurement. The large inversion recovery method sample size is justified by developmental work that was taking place for methods not presented in this thesis.

3.3.3 RESULTS

Regions of interest were drawn over the aorta, portal vein and hepatic parenchyma as shown in figure 3.2 (SR and IR methods) and figure 3.5 (MFA method). An example of the curve fitting procedure to determine T1 measurements using the SR, IR and MFA methods is illustrated in figures 3.3, 3.4 and 3.6.

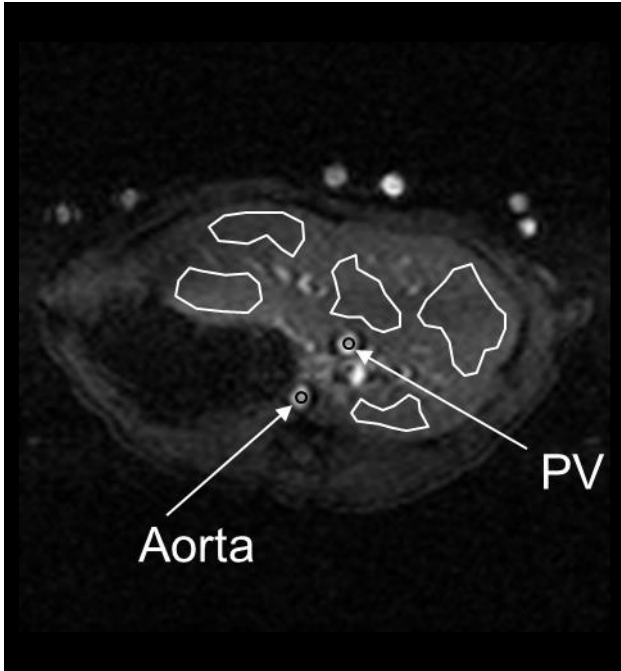


Figure 3.2: Example of ROI placement for T1 measurement using the saturation recovery and inversion recovery method

Aortic and portal venous ROIs as shown. Parenchymal data was averaged across the ROIs shown in white. This figure was replicated from figure 2.6.

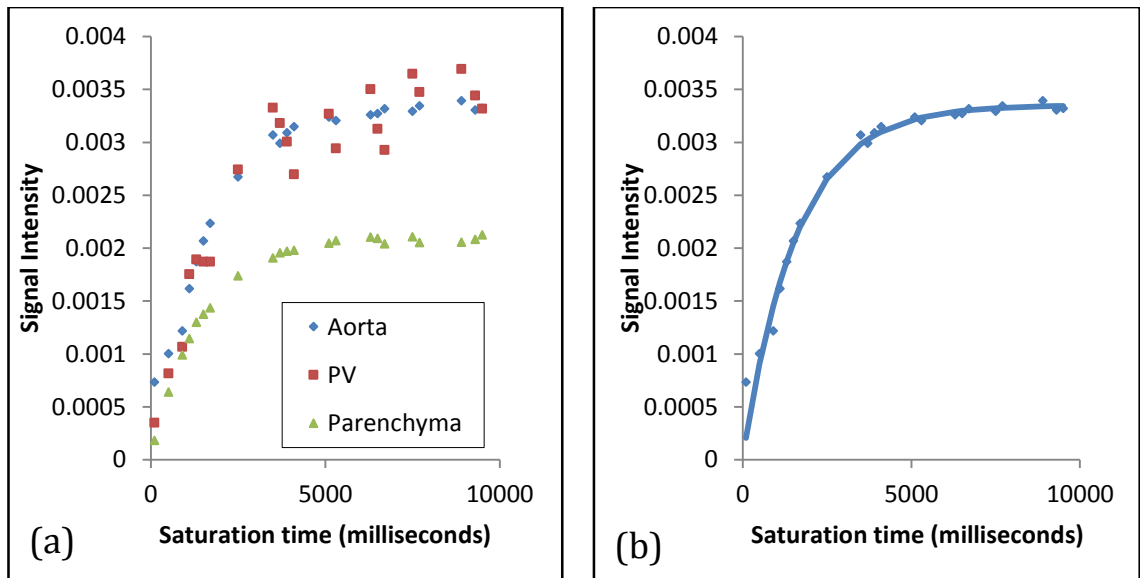


Figure 3.3: (a) Measurement of ROI T1 times using the saturation recovery method, with (b) specific example of aortic ROI fitting to determine T1

(a) The slice shown in figure 3.2 was imaged at a variety of saturation times to determine the T1 for each ROI. The curve fit for the aortic ROI data is shown in (b) (T1 = 1587 milliseconds). These diagrams were replicated from figure 2.7.

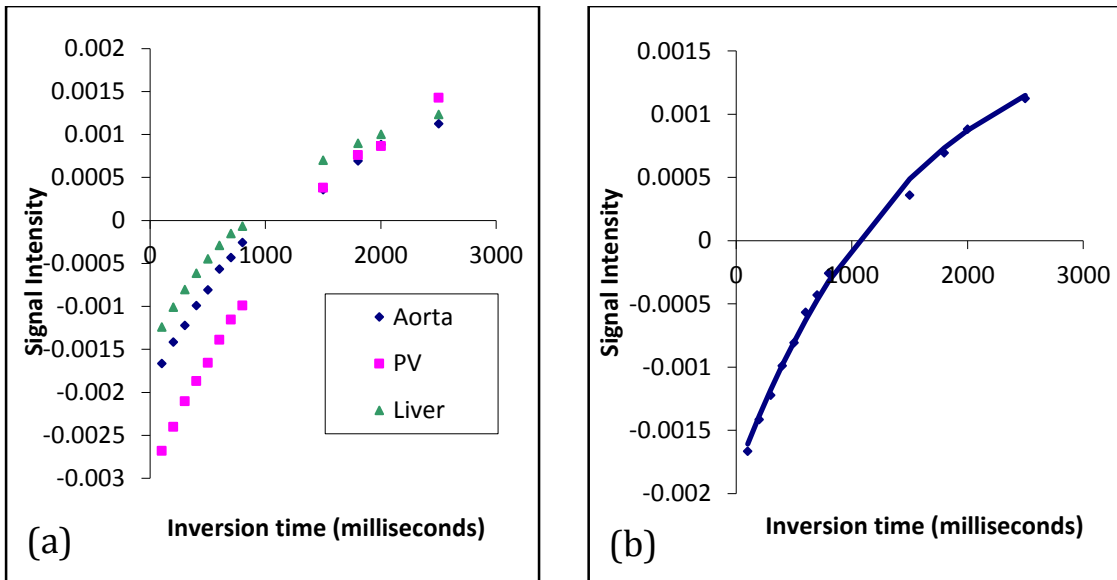


Figure 3.4: (a) Measurement of ROI T1 times using the inversion recovery method, with (b) specific example of aortic ROI fitting to determine T1

(a) A slice similar to that shown in figure 3.2 was imaged at a variety of inversion times to determine the T1 for each ROI. The curve fit for the aortic ROI data is shown in (b) (T1 = 1500 milliseconds).

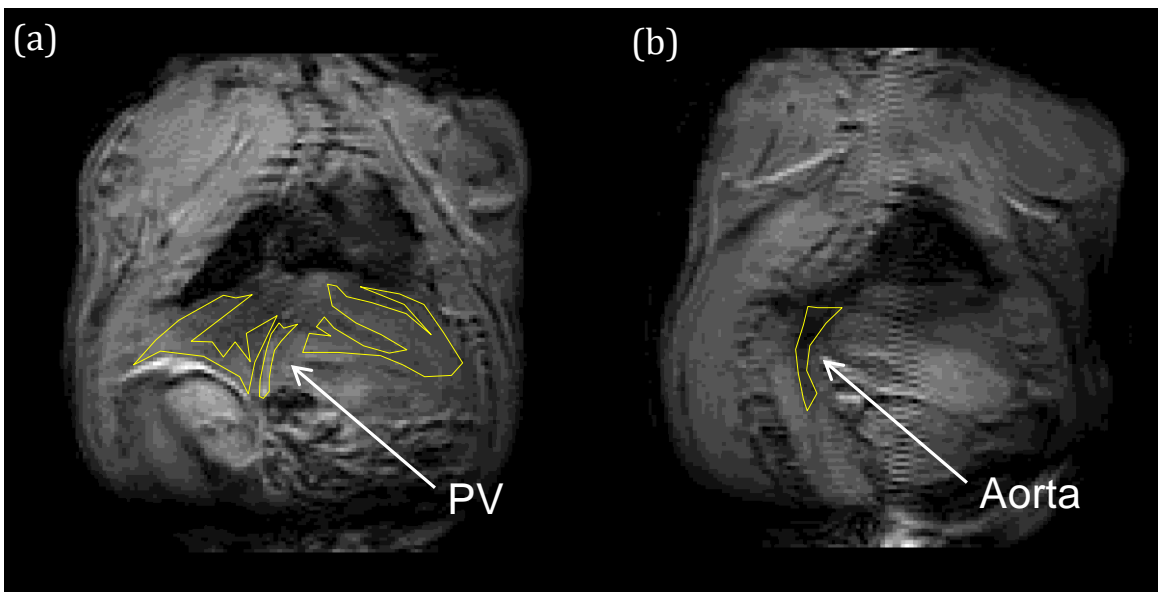


Figure 3.5: Example of ROI placement for T1 measurement using the gradient echo multi-flip angle method

Separate slices were selected for placement of ROIs for the (a) hepatic parenchyma, portal vein and (b) aorta. Parenchymal data was averaged across the parenchymal ROIs.

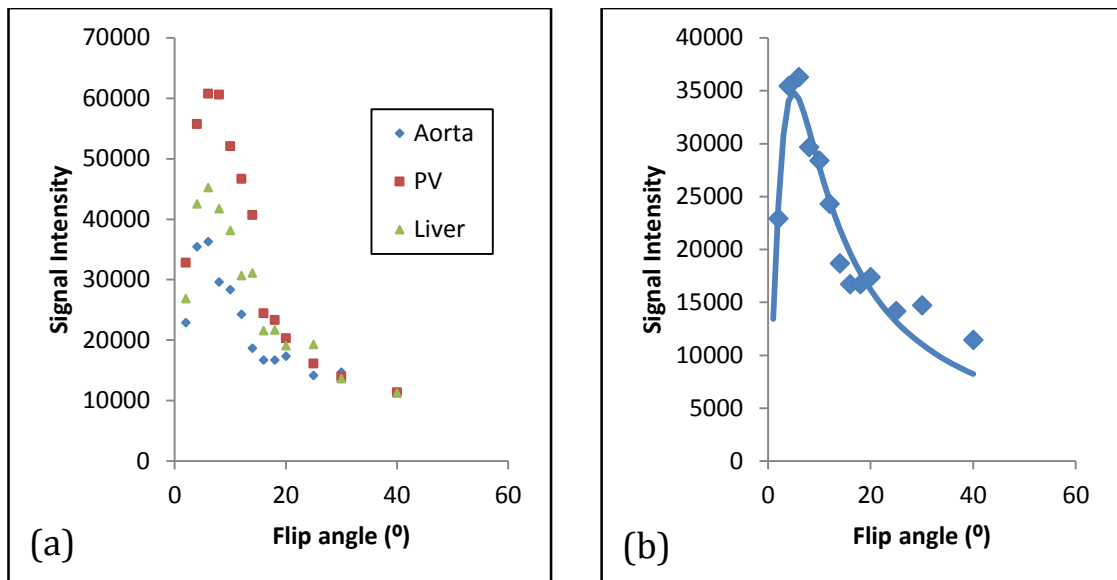


Figure 3.6: (a) Measurement of ROI T1 times using the gradient echo multi-flip angle method, with (b) specific example of aortic ROI fitting to determine T1

(a) The slices shown in figure 3.5 were imaged with a variety of flip angles to determine the T1 for each ROI. The curve fit for the aortic ROI data is shown in (b) (T1 = 723 milliseconds).

3.3.3.1 Comparative analysis

Significant differences were demonstrated between measurements methods for all 3 ROIs ($F = 29.99$; $p < 0.0001$) (figure 3.7). Mean SR aortic T1 (1622 ± 42.88 ms) was just significantly different from IR aortic T1 (1444 ± 72.80 ms; $p = 0.0408$) and MFA aortic T1 (506.5 ± 108.8 ms; $p < 0.0001$). Aortic T1 values obtained with any of the three methods were significantly different from literature derived mean values for blood T1 (2365 ms). Mean SR PV T1 (1711 ± 39.89 ms) was not significantly different from IR PV T1 (1622 ± 93.04 ms; $p = 0.6248$) but was significantly different from MFA PV T1 (898.7 ± 135.2 ms; $p < 0.0001$). PV T1 values obtained with any of the three methods were significantly different from literature derived mean values for blood T1 (2365 ms). Mean SR liver T1 (1312 ± 37.46 ms) was significantly different from IR liver T1 (1124 ± 30.59 ms; $p = 0.0005$) and MFA liver T1 (395.9 ± 136.2 ms; $p < 0.0001$). Liver T1 values obtained with the IR method were not significantly different from literature derived mean values for hepatic parenchymal T1 (1075 ms; $p = 0.1266$), but were significantly different when using SR and MFA methods. These data are summarised in table 3.1.

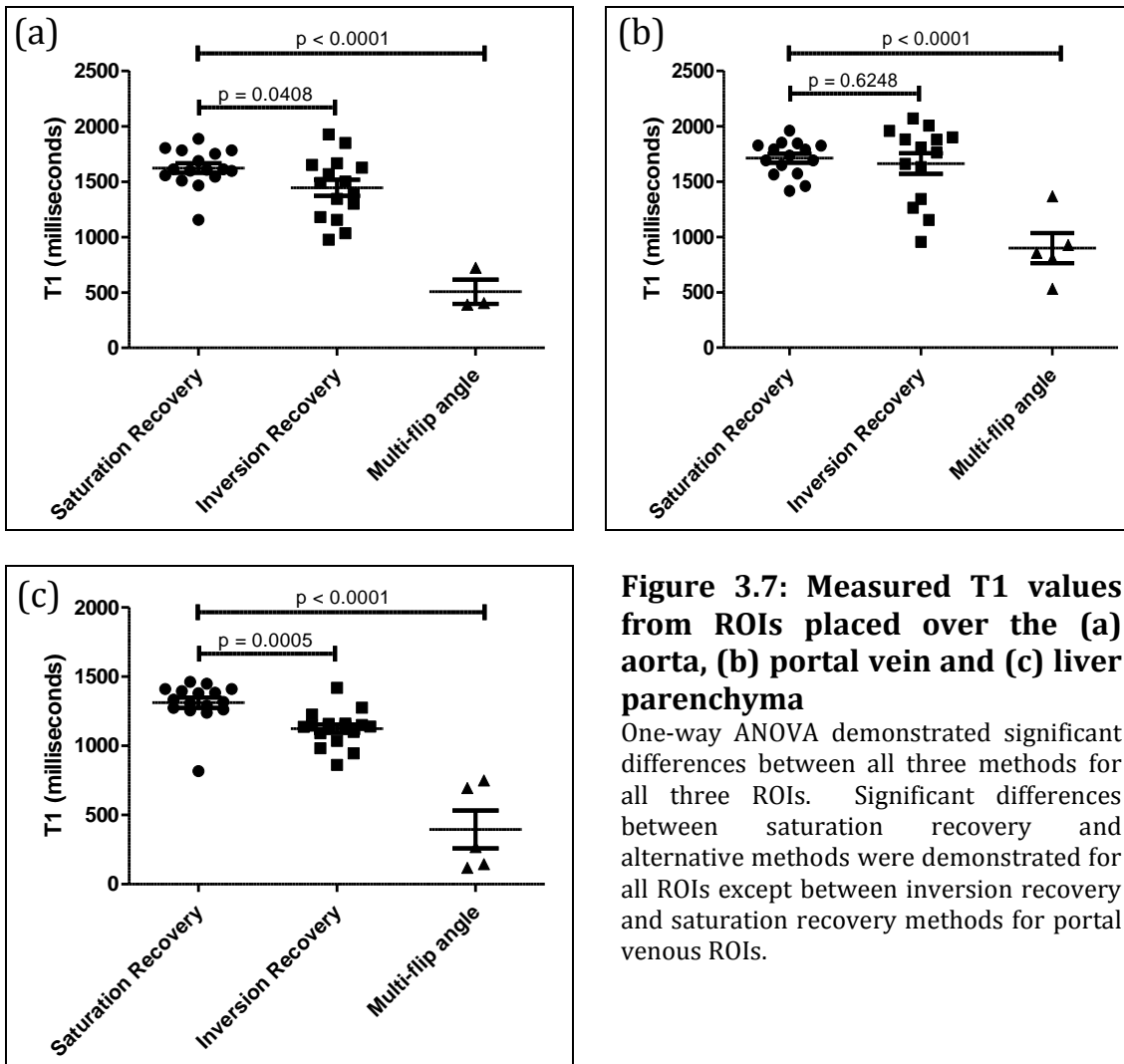


Figure 3.7: Measured T1 values from ROIs placed over the (a) aorta, (b) portal vein and (c) liver parenchyma

One-way ANOVA demonstrated significant differences between all three methods for all three ROIs. Significant differences between saturation recovery and alternative methods were demonstrated for all ROIs except between inversion recovery and saturation recovery methods for portal venous ROIs.

Table 3.1: Summary of T1 measurement statistics and literature comparison

	SATURATION RECOVERY METHOD (MILLISECONDS)	INVERSION RECOVERY METHOD (MILLISECONDS)	GRADIENT ECHO MULTI-FLIP ANGLE METHOD (MILLISECONDS)	LITERATURE DERIVED T1 AVERAGES (MILLISECONDS)
Aorta	1622±42.88*	1444±72.80*	506.5±108.8*	2365
PV	1711±39.89*	1662±93.04*	898.7±135.2*	2365
Liver	1312±37.46*	1124±30.59	395.9±136.2*	1075

(all parameters given as mean ± standard error of the mean; *p < 0.05 against literature derived average value)

3.3.4 DISCUSSION

We have demonstrated the potential for T1 measurements with alternative approaches and shown variation in their T1 estimates for different tissues at 9.4T. Different approaches all estimate T1 with varying degrees of accuracy and possess differing strengths and weaknesses. SR methods are relatively simple, but data collection can be more time consuming, particularly relative to gradient echo MFA methods. This is of course, less of an issue in a preclinical context. Inhomogeneity in B_1 particularly at high field strength, will result in flip angles other than 90° being applied in some parts of the imaging slice, thereby resulting in inaccuracies in SR T1 estimation. IR methods are considered the “gold-standard” approach to T1 measurement and while even slower than SR methods, are able to overcome issues of B_1 inhomogeneity by using two repeated pulses separated by the TI. Finally gradient echo MFA methods have the advantage of being able to collect large volumes of data quickly (hence 3D volumes were obtained in our study), but are especially susceptible to B_1 errors. Important features of raw MFA data are obtained at smaller flip angles where B_1 errors are likely to be more pronounced, which may well account for the poor data fits that were observed. This may also explain why SR data obtained at higher flip angles, though subject to B_1 error appeared more robust. The difficulties with MFA fitting were apparent early on and it was for this reason that this approach was abandoned after only $n = 5$ data sets were obtained.

Interestingly, the variance of SR T1 measurements was comparable or superior to the so-called “gold-standard” IR T1 measurements. Although mean values were significantly different for liver parenchyma and just significant for aortic blood, there was no statistically significant difference between the methods for estimation of PV blood T1. Perhaps even more surprisingly, comparison with literature derived values for blood T1, though significantly different are still less different than IR method derived T1 values.

Striking and disappointing differences between our estimates and literature derived blood T1 values were recorded [326, 328]. Both studies that have published similar blood T1 values at high field strength have done so in different species (bovine and human), both *in* and *ex vivo*, and at different field strengths to demonstrate a linear relationship between blood T1 and B_0 field strength. It is has been demonstrated that blood T1 is dependent on temperature and haematocrit but not oxygenation [326, 329]. Our experience however, demonstrated consistent differences between aortic and PV blood T1 values, across all three methods, where both temperature and haematocrit would have remained constant. An important consideration with *in vivo* imaging is presence of inflow effects [310, 330, 331]. Fresh blood flowing into the imaging slice has the potential to alter the signal intensity and actual flip angle experienced in the ROI.

Blood in the aorta and PV also have blood flowing at very differing velocities thereby introducing different errors into each vessel measurement. Although a global saturation pulse was applied before each SR/IR acquisition to address this issue, inflow effects may well have contributed to the intra-subject discrepancy between vessel T1 values and the observed difference between these and literature based T1 values.

Finally, a formal assessment of repeatability and reproducibility would be an important part of determining which method of T1 measurement to favour. Accuracy of SR and gradient echo MFA methods could be improved with B₁ mapping and approaches to improve the efficiency of the global saturation pulse could go some way to producing more robust and accurate T1 measurements.

3.3.5 CONCLUSION

The decision was made to use the IR method for T1 measurement. This method was favoured because of its ability to avoid inaccuracies introduced by B₁ errors. Although potentially more time consuming, this was deemed less of an issue for preclinical experiments.

3.4 BOLUS PROTOCOLS

3.4.1 BACKGROUND

Accurate sampling of the vascular input functions (VIFs) is essential to successful pharmacokinetic modelling, but is especially challenging with high field strength imaging. The ideal bolus maximises VIF recorded signal/concentration, is administered quickly to maximise the distinction between the arterial input function (AIF) and portal venous input function (PVIF) and delivers parenchymal contrast agent (CA) concentrations that maximise parenchymal signal-to-noise ratio (SNR). In our previous attempts, a small, very dilute bolus (1:40 dilution of Gd-DOTA) was administered over 5-10 seconds with a hand injection. Manual injections introduce both inter- and intra-bolus variation in administration rate and undermine controlled experiments to determine the optimal bolus concentration. To address this, a syringe driver was introduced into the protocol. From previous experiments described in chapter 2, the occurrence of T2* effects at higher concentrations (figure 2.13) called for the use of very dilute CA boluses for AIF measurement, while the maximisation of parenchymal SNR would call for more concentrated CA boluses. A possible strategy to address these conflicting requirements is the use of a dual-bolus approach: an initial more dilute bolus can be administered for optimal VIF sampling and a second more concentrated bolus can be administered for optimising the SNR from parenchymal enhancement [179, 180, 320, 321, 332, 333]. The dilute bolus can then be scaled to match the expected VIF from the higher concentration parenchymal bolus before pharmacokinetic modelling.

The aim of this section was to setup a syringe driver arrangement to deliver CA boluses and determine the optimum Gd-DOTA bolus protocol for DCE MRI at 9.4T, specifically determining the optimum bolus (i) infusion rate, (ii) concentration and (iii) the potential for dual-bolus methods.

3.4.2 MATERIALS AND METHODS

Experimental subjects and animal preparation was as described in section 3.3.2.

3.4.2.1 Sample size

A pragmatic approach to sample size was used given that data collection during these studies was undertaken for the purpose of protocol development. As parameter variability with our protocol on our scanning system was unknown, data was evaluated incrementally with a view to inform protocol development and provide preliminary characterisation of parameters for future planning of adequately powered studies.

3.4.2.2 Dynamic Contrast Enhanced MRI

Imaging was performed using a 9.4T Agilent scanner (Oxford, UK). Data was acquired as described in section 2.4.4. After initial baseline T1 measurements using the IR method (see above), a bolus of diluted Gd-DOTA (gadoteratedimeglumine, Dotarem®, Guerbet, Roissy, France) was primed into a 0.58 mm internal diameter fine bore polyethylene line (Portex, Smiths Medical, Kent, England) as shown in figure 3.7. Ten seconds after dynamic imaging began, a 300 μ L heparinised saline flush was administered using an MRI compatible syringe driver (Harvard Apparatus, Kent, England). Sequential dynamic images were obtained for a total of 3 minutes. CA concentration was measured using methods described in section 2.4.6.

3.4.2.3 Bolus protocols

Experiments were performed in $n = 5$ subjects. The first four subjects underwent experiments with progressively increasing CA bolus concentrations (0.0001, 0.005, 0.01, 0.02, 0.03, 0.04, 0.05, 0.06, 0.07 and 0.1 mmol/kg, based on a 250g animal). The bolus size was fixed at 100 μ L, and a 20-40 minute delay was used between subsequent DCE studies to allow adequate CA washout and recovery of tissue and vascular pool T1. The delay was determined by assessment of T1 maps obtained at regular intervals after a bolus had been administered. To prevent physiological disruption as a result of large volume of CA administration and extended periods of anaesthesia, no more than four boluses were administered to each subject. Experiments were conducted with an infusion rate of 4 ml/min (a 4.5 second injection) and 2 ml/min (a 9 second injection) for CA bolus concentrations above 0.04 mmol/kg.

3.4.2.4 Dual-bolus DCE MRI

The potential for the dual bolus approach was assessed in two ways. The first involved upscaling of more diluted CA bolus VIFs [333], to compare these with recorded higher concentration VIFs in the same subject. The second involved analysing data from the final

two subjects who received a lower concentration pre-bolus for VIF sampling and a higher concentration bolus for parenchymal enhancement. VIF data obtained after the pre-bolus was linearly up-scaled by the ratio of pre-bolus to main bolus CA concentration. Pharmacokinetic modelling using the dual-input single compartment was then applied using the methods described in section 2.4.7.

3.4.2.5 Statistical analysis

Manual delays were added to VIFs to take into account varying contrast bolus arrival delays to allow VIF comparisons. Given the non-parametric data, Kruskal-Wallis tests were used when more than two VIFs were being compared. Direct comparisons between two VIFs were performed using the Mann-Whitney U-test. The presence of T2* effects was determined by visual inspection. Wilcoxon matched-pairs signed rank tests were performed to assess the consistency between observed higher CA bolus concentration VIFs and upscaled dilute CA bolus VIFs. Upscaled dilute CA bolus VIFs were then modelled with parenchymal enhancement obtained after higher concentration CA bolus using the dual input single compartment model. The threshold of statistical significance was defined to be $p < 0.05$.

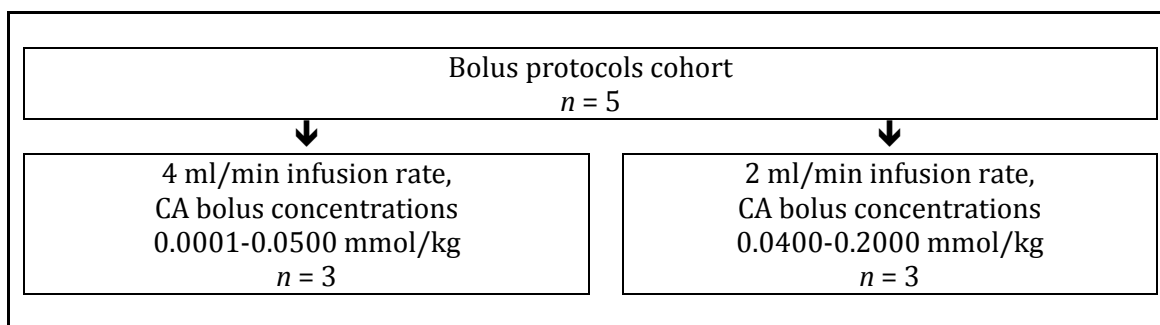


Figure 3.8: Schematic diagram demonstrating cohort sizes

Single data sets were obtained at each of the CA bolus concentrations except for concentrations of 0.01, 0.04 and 0.05 mmol/kg where three datasets were obtained. Data for inversion recovery T1 measurements derived from the five subjects that participated in this experiment were used in section 3.3.

3.4.3 RESULTS

3.4.3.1 Syringe driver arrangement

Unlike clinical power injectors which have two syringe drivers to deliver a CA bolus and a flush, we were limited to a single syringe driver that did possess some ferromagnetic components thereby limiting proximity to the scanner. To overcome this issue and ensure the CA bolus was delivered at constant rate, the final most consistent arrangement involved placing a single long continuous line primed with heparinised saline, interrupted by a 3-way tap a short distance from the scanner, depicted in figure 3.9. An essential consideration was the length of the line between the 3-way tap and the animal: the line had to be of sufficient length for this portion of the line to be primed with the CA bolus, without any entering the animal. The rate of delivery could then be controlled by the syringe driver which could be at any length away from the scanner, activated at the time of each DCE MRI experiment.

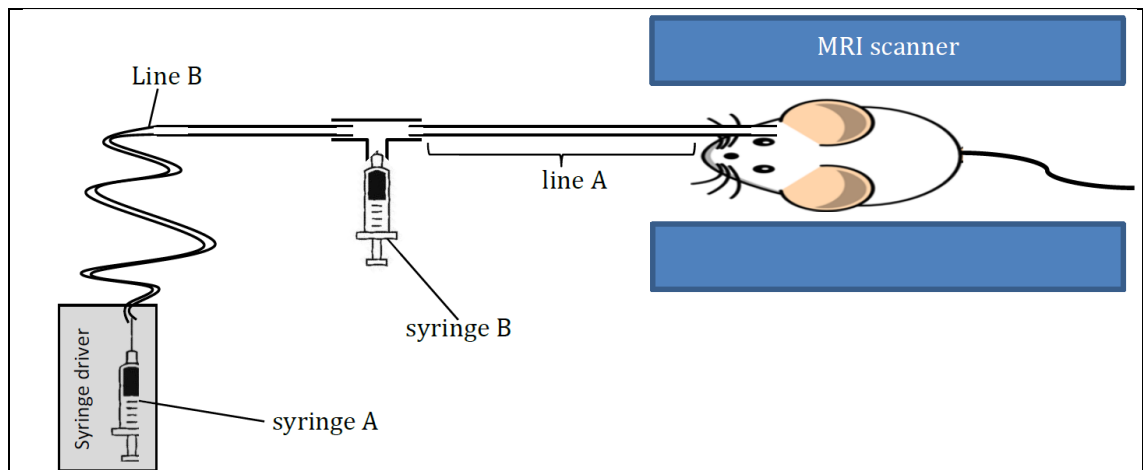


Figure 3.9: Schematic diagram of syringe driver arrangement

Line A was of fixed length, so that it could be primed with CA (syringe B) at the 3-way tap, without any CA entering the animal. Syringe A and line B were primed with heparinised saline, so that the CA bolus could then be pushed into the animal followed by a heparinised saline flush at a fixed rate determined by the syringe driver settings. Line B could be of any length, and enabled the syringe driver to be positioned at a safe distance from the scanner.

3.4.3.2 Bolus infusion rate and concentration

In the first subject, experiments conducted with CA bolus concentrations of 0.0001 and 0.005 mmol/kg produced no discernable VIFs or parenchymal enhancement. Experiments with bolus concentrations of 0.01 mmol/kg produced AIFs, but the concentration was too low for any discernable PVIF.

Subsequent data was collected at bolus concentrations at and above 0.01 mmol/kg, with experiments conducted at both bolus infusion rates (figure 3.10). At 4 ml/min (figure 3.10a), a dose-dependent increase in AIF was not observed (excluding 0.01 mmol/kg, no statistically significant difference was demonstrated between AIFs ($H =$

1.513, $p = 0.6792$). AIFs derived from the same concentration bolus, demonstrated that infusion rates of 4 ml/min did not yield consistent results even at low 0.01 mmol/kg concentrations, but this difference was found to be non-significant (figure 3.10b; $H = 1.542$; $p = 0.4625$). Infusion rates of 2 ml/min demonstrated a dose-dependent response (figure 3.10c) that was consistent within (0.04 mmol/kg data; $U = 48.00$, $p = 0.4307$) and across subjects (0.05 mmol/kg data; $U = 51.00$, $p = 0.5545$) for each given bolus. At concentrations above 0.05 mmol/kg (figure 3.10d), T2* effects predominated resulting in AIF derangements.

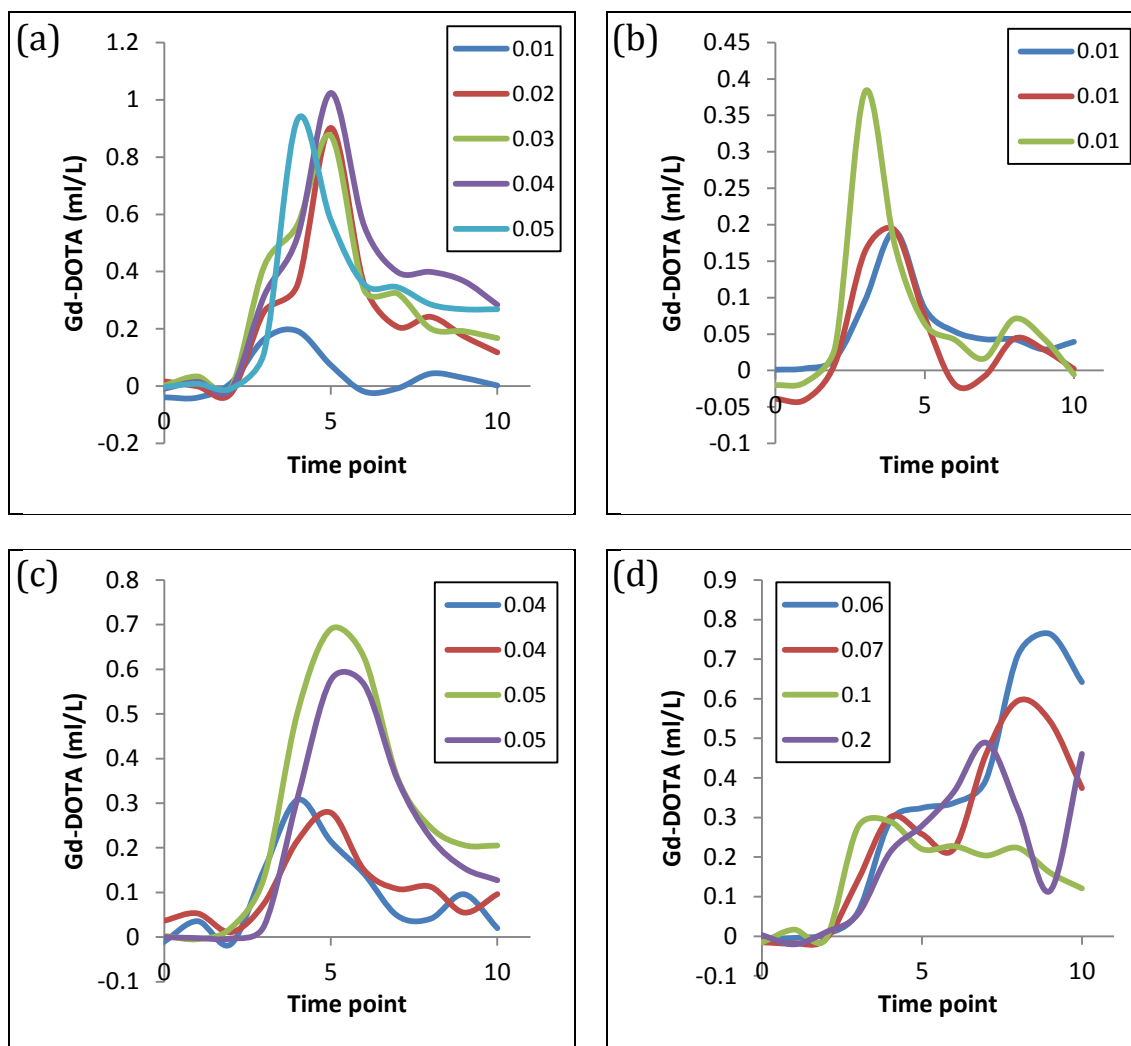


Figure 3.10: Aortic input functions at different bolus infusion rates and contrast agent bolus concentrations

CA boluses were administered at 4 ml/min - (a),(b); and 2 ml/min - (c),(d). **(a)** At 4 ml/min dose-dependent increases in AIF were not observed. **(b)** AIFs derived from the same concentration bolus, lacked consistency even at low CA bolus concentrations. **(c)** Infusion rates of 2 ml/min demonstrated a consistent and dose-dependent response. **(d)** T2* effects were noted in CA bolus concentrations above 0.05 mmol/kg.

Unlike AIFs, statistically significant dose-dependent changes in PVIFs were observed with CA boluses infused at 4 ml/min (figure 3.11a; $H = 18.54$; $p = 0.0003$) and at 2 ml/min

(figure 3.11b; $H = 9.571$, $p = 0.0084$). Infusion rates of 2 ml/min demonstrated a consistent dose-dependent response within (0.04 mmol/kg data; $U = 113.0$, $p = 0.5847$) and across subjects (0.05 mmol/kg data; $U = 100$, $p = 0.300$) for each given bolus. At concentrations above 0.06 mmol/kg (figure 3.11d), T2* effects predominated resulting in PVIF derangements.

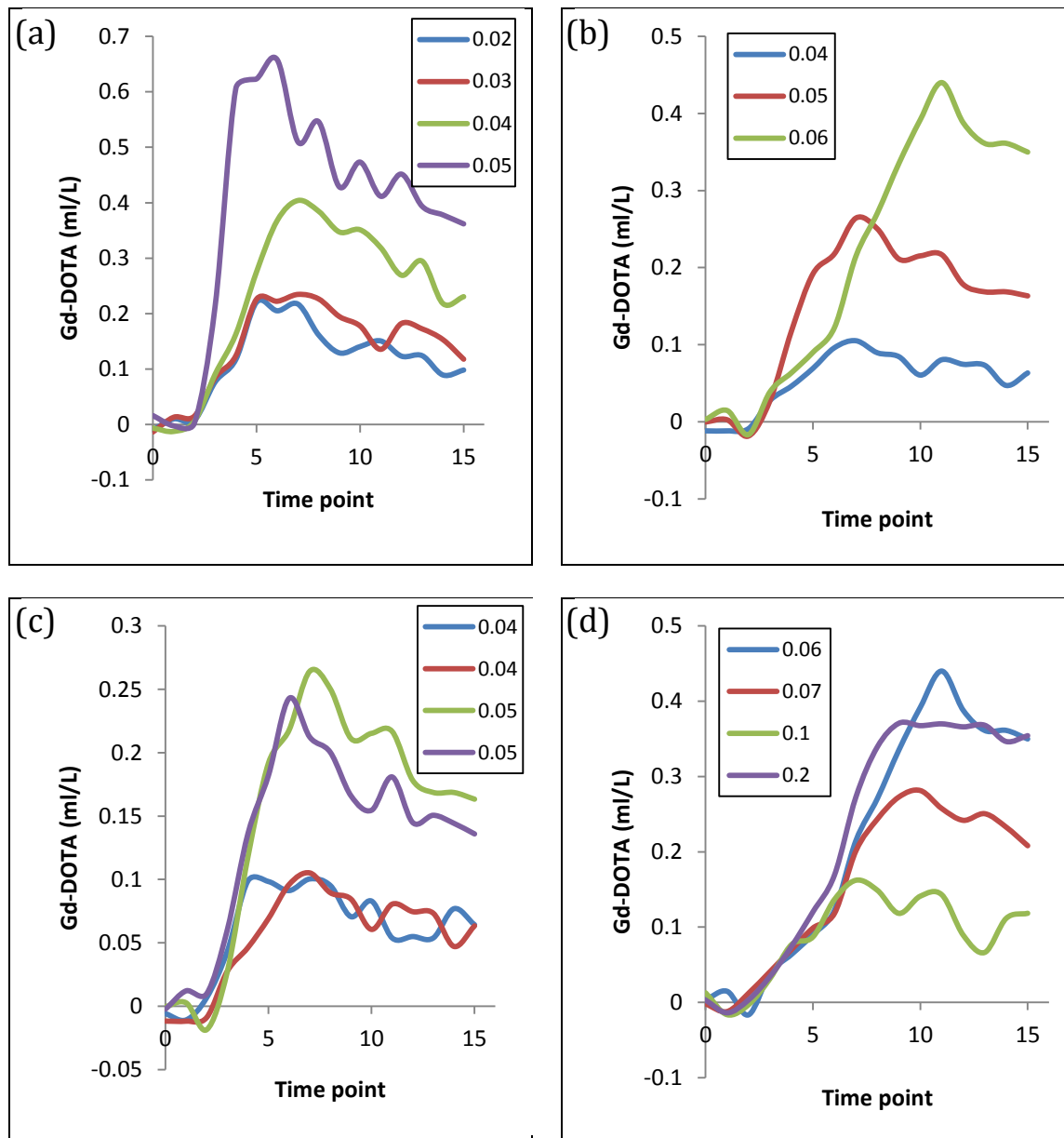


Figure 3.11: Portal Venous input functions at different bolus infusion rates and contrast agent bolus concentrations

CA boluses were administered at 4 ml/min - (a); and 2 ml/min - (b), (c), (d). Dose-dependent changes in PVIF were observed at 4 ml/min (a) and at 2 ml/min (b). (c) Infusion rates of 2 ml/min demonstrated a consistent and dose-dependent response. (d) T2* effects were noted in CA bolus concentrations above 0.06 mmol/kg.

The bolus infusion rate and concentration optimisation data is summarised in table 3.3.

3.4.3.3 Dual-bolus DCE MRI

For CA boluses infused at 2 ml/min, scalable non-T2* artefacted VIFs were only available at concentrations of 0.04 and 0.05 mmol/kg. AIFs and PVIFs obtained from 0.04 mmol/kg boluses were scaled to 0.05 mmol/kg and compared with observed 0.05 mmol/kg boluses (figure 3.12).

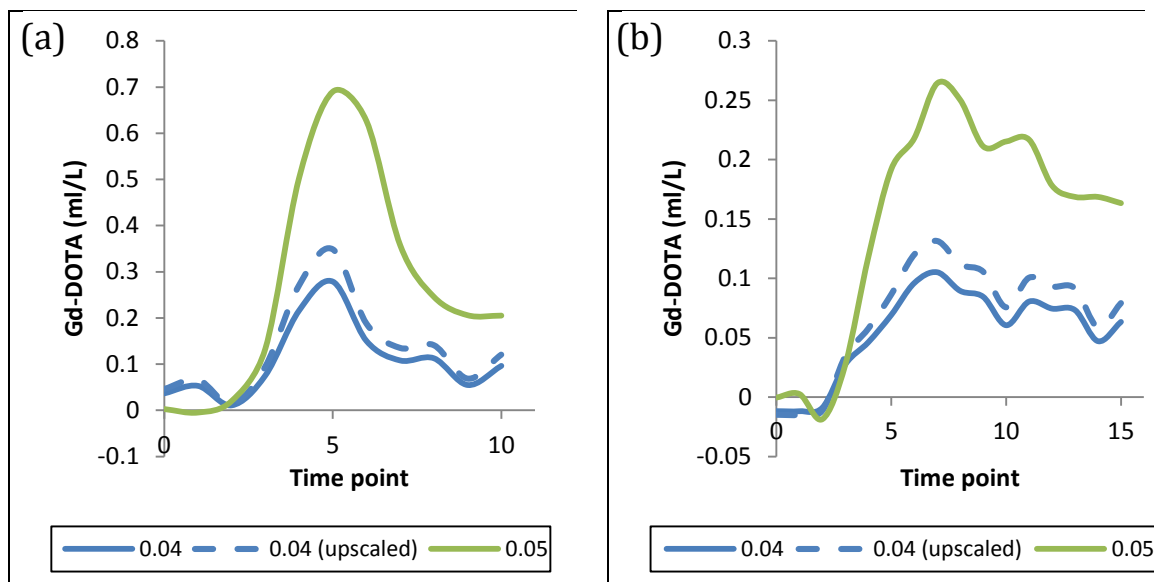


Figure 3.12: Scaled and observed arterial and Portal Venous input functions

VIFs derived from 0.04 mmol/kg CA boluses were upscaled to 0.05 mmol/kg and compared with observed 0.05 mmol/kg CA bolus data.

Even on visual inspection of both AIF and PVIF up-scaled boluses, there is poor agreement with the observed 0.05 mmol/kg bolus. This was confirmed with statistically significant differences between upscaled and observed AIFs ($W = -52.00$, $p = 0.0186$) and PVIFs ($W = -130.0$, $p = 0.0009$).

Two subjects underwent formal dual-bolus protocol studies. Based on earlier CA bolus concentration and infusion rate data, a pre-bolus of 0.05 mmol/kg CA was administered at 2 ml/min, followed by a main bolus of 0.2 mmol/kg at 2 ml/min. Pharmacokinetic modelling of pre-bolus and dual bolus data (figure 3.13) revealed comparable estimates of k_{1a} and k_{1p} , but differences in k_2 . Fit residuals were smaller with single (pre) bolus methods.

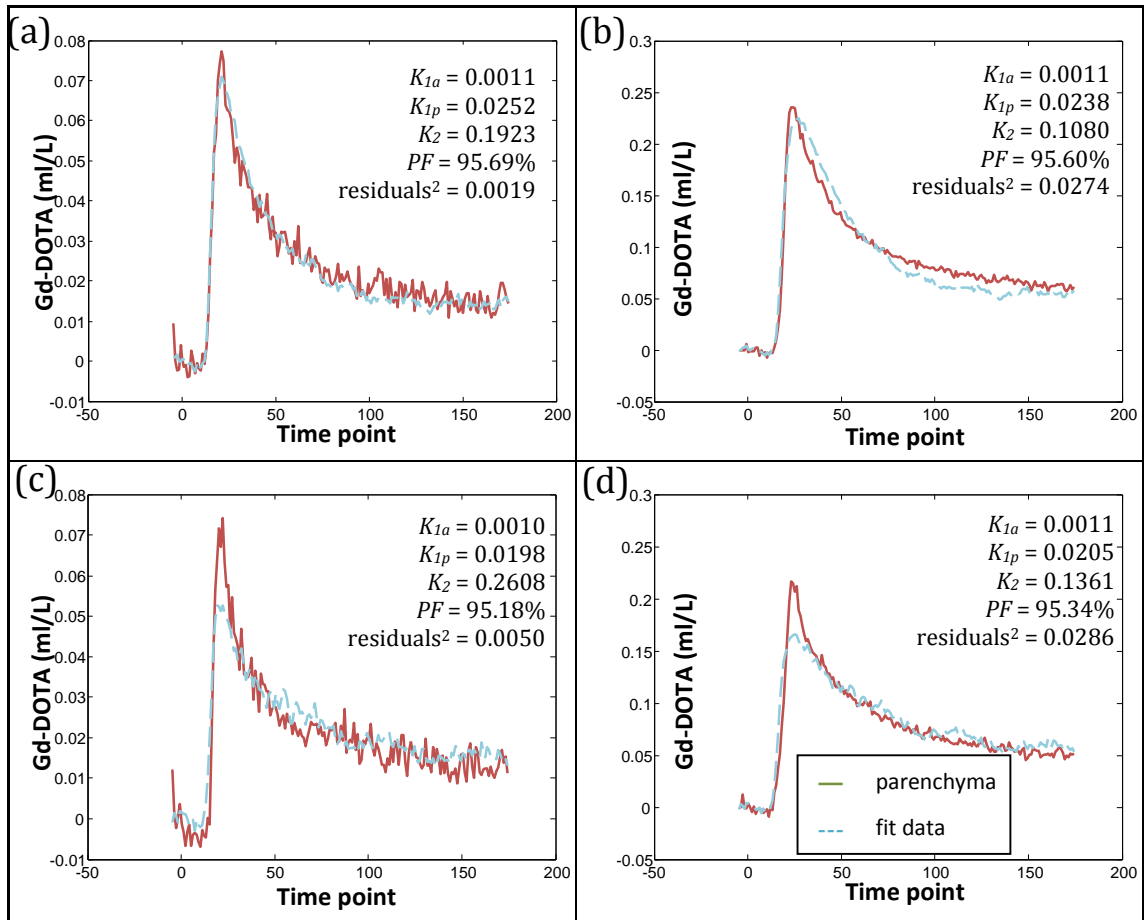


Figure 3.13: Parenchymal enhancement curves and corresponding fits using a single bolus (left) or dual bolus (right) methods for vascular input function measurement

Data from subject 1 (a and b) and subject 2 (c and d). Raw data is shown in red and fit data is shown by the dashed line. Note the y-axis scale differences between each method.

Pharmacokinetic data derived from both methods was then converted into hepatic perfusion parameters before comparison in table 3.3. Absolute perfusion parameters and portal fraction show good between method concordance (reflective of k_{1a} and k_{1p}), with differences in k_2 accounting for divergent distribution volume and mean transit time estimates.

Table 3.2: DCE MRI hepatic perfusion parameters with the single and dual bolus methods

	SUBJECT 1		SUBJECT 2	
	SINGLE BOLUS*	DUAL BOLUS†	SINGLE BOLUS*	DUAL BOLUS†
Arterial perfusion (ml/min/100g)	8.8	8.8	8.0	8.0
PV perfusion (ml/min/100g)	201.6	190.4	158.4	164.0
Portal fraction (%)	95.82	95.58	95.19	95.35
Distribution Volume (%)	13.68	23.06	7.98	15.80
Mean Transit Time (seconds)	5.20	9.26	3.83	7.35

(*0.05 mmol/kg; †0.05 mmol/kg and 0.2 mmol/kg)

3.4.4 DISCUSSION

The development of a safe and simple syringe driver arrangement to allow consistent, robust, controlled delivery of CA boluses was an essential first step to optimising bolus protocols. The results of infusion rate and CA bolus concentration experiments are summarised in table 3.3.

Table 3.3: Summary of bolus infusion rate and concentration data

CA BOLUS CONCENTRATION	INFUSION RATE (ML/MIN)	ARTERIAL INPUT FUNCTION	PV INPUT FUNCTION
0.0001	4	-	-
0.005	4	-	-
0.01	4	✘	-
0.02	4	✘	✓
0.03	4	✘	✓
0.04	4 and 2	(✘ - not consistent at 4 ml/min)/✓	✓
0.05	2	✓	✓
0.06	2	✘	✓
0.07	2	✘	✘
0.1	2	✘	✘
0.2	2	✘	✘

(- = no discernable enhancement; ✓ = usable VIF – normal VIF morphology, dose appropriate response, consistent VIF size; ✘ = erroneous VIF)

Although the ideal bolus protocols deliver CA as quickly as possible to maximise distinction between the AIF and PVIF, these gains are restricted by the temporal resolution of the DCE MRI sequence and the sensitivity to T2* effects (particularly at high field strength), generated by the higher AIF bolus concentrations. Our data demonstrated that AIFs obtained at higher infusion rates lacked CA dose sensitivity and consistency even at low CA bolus concentrations. This was not apparent with PVIFs, presumably as bolus dispersal would have resulted in (a) a more ‘spread-out’ input function thereby less susceptible to temporal resolution limitations and (b) lower peak CA concentrations thereby less susceptible to T2* effects. Despite limited data, dose-responsive AIFs and PVIFs were observed with slow infusion rates (2 ml/min). This combined with consistent VIFs both within and between subjects would favour the use of the slower infusion rate in a refined dose protocol. Even when using a slower infusion rate, bolus concentrations above 0.05 mmol/kg for AIFs and above 0.06 mmol/kg for PVIFs resulted in measurement errors, likely due to secondary to T2* effects. Non-corrupted parenchymal enhancement data was observed even when using a 100 µL undiluted bolus of Gd-DOTA (0.2 mmol/kg) and it was decided that a final dual-bolus protocol could then be attempted using a more dilute pre-bolus of 0.05 mmol/kg for VIF assessment, followed by a 30 minute period to

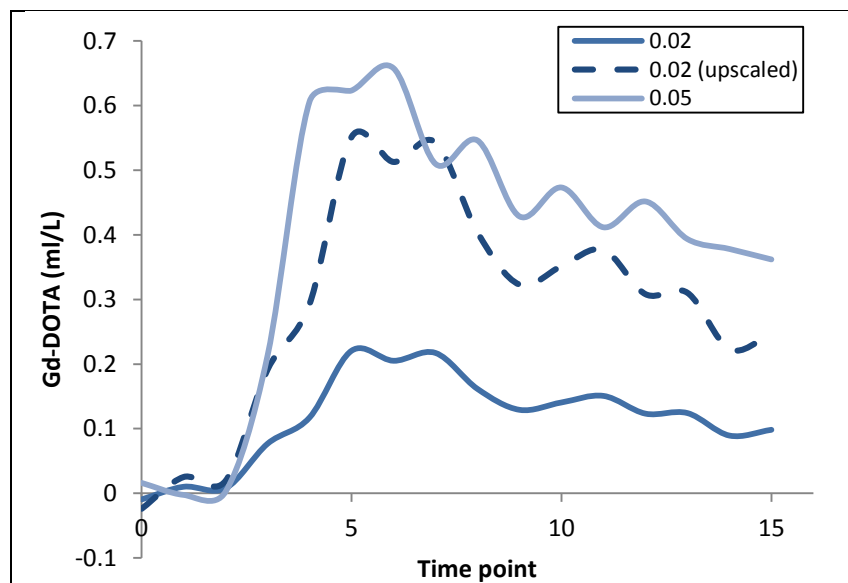
allow blood pool T1 recovery and a subsequent 0.2 mmol/kg bolus for evaluation of parenchymal enhancement.

Upscaling of dilute boluses demonstrated poor concordance with recorded higher CA concentration boluses thereby undermining the entire dual bolus method. More dilute VIFs (0.04 mmol/kg CA boluses) were upscaled linearly, based on the principal that observed CA concentrations would remain within a range where a linear relationship between signal intensity and CA r_1 was maintained. Although this could plausibly explain why linear upscaling was unsuccessful, it would be expected that upscaling of lower concentration VIFs (such as the PVIF) should theoretically be more successful – a difference which was not demonstrated by the data (figure 3.12).

An alternative explanation could be that lower SNR obtained from more dilute boluses could produce underestimated VIFs, resulting in erroneous upscaled data. In support of this explanation, upscaling PVIFs obtained at lower CA bolus concentrations from 4 ml/min infusion rates demonstrated better concordance with their higher concentration counterparts (figure 3.14; $W = -120.0$, $p = 0.0021$).

Figure 3.14:
Upscaled and
observed PV input
functions obtained
at 4 ml/min
infusion rates

Upscaled curves demonstrate better concordance than in figure 3.10b, but still remain statistically significantly different from observed higher CA bolus concentration data.



Pre-bolus upscaling and pharmacokinetic modelling of dual bolus data was possible using our methods and capable of delivering similar estimates for some (but not all) of the pharmacokinetic parameters. Divergent estimates of k_2 are suggestive of modelling issues with the impulse residue function, particularly during the CA wash-out phase (curve tail). This is apparent when inspecting the wash-out phase curve fits in figure 3.131, and could certainly account for the larger residuals obtained from the dual bolus method. The cause of this divergence is unclear: scaling difficulties with this portion of the VIFs would be counterintuitive as the ROI concentrations would be lower (and less affected by T2*

effects) and less vulnerable to sampling issues secondary to temporal resolution limitations.

Data obtained using syringe driver single and dual bolus methods is compared with baseline manual injection data from Chapter 2 in table 3.4

Table 3.4: Summary of DCE MRI hepatic perfusion changes with manual contrast agent bolus injection, and syringe driver single and dual bolus methods

	MANUAL INJECTION (<i>n</i> = 12)	SINGLE BOLUS (<i>n</i> = 2)	DUAL BOLUS (<i>n</i> = 2)
Arterial perfusion (ml/min/100g)	79.47±11.29	8.4±0.4	8.4±0.4
PV perfusion (ml/min/100g)	321.2±43.95	180±21.6	177.2±13.2
Portal fraction (%)	77.75±3.72	95.50±0.313	95.47±0.117
Distribution Volume (%)	16.49±1.06	10.83±2.85	19.43±3.63
Mean Transit Time (seconds)	3.58±0.30	4.517±0.683	8.303±0.956

Although the portal fractions obtained from both syringe driver methods appear high, this may related to pharmacokinetic modelling issues discussed later. Encouragingly, PV perfusion obtained by both syringe driver methods was closer to transit-time US normalised bulk PV flow (150.1±7.73 ml/min/100g, *n* = 6).

Data in this section has been modelled using large area-based parenchymal ROIs. Although reasonable pharmacokinetic modelling with data from the more dilute pre-bolus (0.05 mmol/kg) alone is feasible, the real value of dual bolus high SNR parenchymal data is in obtaining more robust pixel-based data for modelling to derive anatomical maps of pharmacokinetic parameters. Finally, samples for single and dual bolus methods are small (*n* = 2), and while too small to make global and generalisable conclusions, are justifiable on the basis of informing our protocol development.

3.4.5 CONCLUSION

Consistent Gd-DOTA bolus delivery was achieved using a syringe driver. To overcome difficulties sampling VIFs, we defined a dual bolus protocol, with a 100µL 0.05 mmol/kg pre-bolus delivered at 2 ml/min followed by a 100 µL 0.2 mmol/kg main bolus delivered at the same rate. Although scaling issues may exist, we have demonstrated that dual input single compartment modelling is possible with a dual bolus approach.

3.5 DCE MODELLING

3.5.1 BACKGROUND

Although methodological refinements in the acquisition process improve data quality, the ultimate determinant of measured perfusion parameters is the model used to fit the data. There are a variety of models for hepatic perfusion described in the literature, each providing a mathematical description for how the contrast agent is handled by liver tissue. The choice of model must be based on the parameters the researcher is interested in measuring and the description offered by the model should match the physiological principles underpinning the pharmacodynamics of how the contrast agent is handled in the tissue.

Herein lie three important consequences which must be considered by the researcher: (i) a model can be constructed that may 'fit' the data, but that is physiologically inaccurate, (ii) a model is a simplification of physiological system: to match the true complexity of a physiological system parameters can be added to the model but that (iii) in adding these variables, the quality of the 'fit' may improve, but that the model will determine these variables indiscriminately of physiological limitations, with the potential to derive good mathematical 'fits' using non-physiological, (effectively meaningless) estimates of the parameters themselves.

The criteria for evaluating the true adequacy of a model must therefore include an assessment of model fit (residual sum of squares), but also look beyond this - specifically at invasive validation, with variance of model-derived parameters matching physiological variance in addition to measures of repeatability and reproducibility. To investigate the effects of alternative DCE models, the dual input single compartment, dual input dual compartment and hepatic perfusion index models were studied.

3.5.1.1 Dual input single compartment modelling

In section 2.4.7, we introduced the dual input single compartment model, which described the rate of change of CA concentration in the liver parenchyma ($C_L(t)$), as being equal to the rate of the inflow (where $C_a(t)$ and $C_p(t)$ represent concentrations in the arterial and portal venous supply respectively) minus the rate of outflow, so that k_{1a} represents the arterial inflow constant, k_{1p} represents the portal venous inflow constant and k_2 represents the outflow constant:

$$\frac{dC_L(t)}{dt} = k_{1a}C_a(t) + k_{1p}C_p(t) - k_2C_L(t)$$

(Equation 2.3)

Solving for $C_L(t)$ then yields:

$$C_L(t) = \int_0^t [k_{1a}C_a(t) + k_{1p}C_p(t)]e^{-k_2(t)} dt' \quad (\text{Equation 2.4})$$

The model given in equation 2.4 is dependent on measuring the arterial and portal venous CA concentrations in the same physical location as the parenchymal ROI. In practical terms, the most reliable site for measuring $C_a(t)$ and $C_p(t)$ is in the aorta and portal vein respectively. The model assumes that the true parenchymal $C_a(t)$ and $C_p(t)$, adopt the same morphology as the aortic $C_a(t)$ and portal venous $C_p(t)$, but to account for the VIF ROIs receiving CA before the parenchyma, we must alter the parenchymal enhancement so that $C_L(0) = 0$ and delays for each VIF (τ_a and τ_p) are added to the model:

$$C_L(t) = \int_0^t [k_{1a}C_a(t' - \tau_a) + k_{1p}C_p(t' - \tau_p)]e^{-k_2(t-t')} dt' \quad (\text{Equation 2.9})$$

In section 2.4.7, the parameters τ_a and τ_p were assumed to equal zero, but this assumption is physiologically incorrect. A variety of approaches to τ_a and τ_p have been adopted in the literature, with some studies choosing to fix τ_a and τ_p as equal constants across all subjects (e.g. two seconds)[140], others choosing to model only τ_a [141]and others have including both τ_a and τ_p as variables to fit in the model[142]. Several authors have shown that small changes in the delay factors (especially τ_a), can result in major alterations of the estimated hepatic perfusion parameters [312, 313] and it is therefore essential that any robust attempt at dual input single compartment modelling must find a consistent and scientifically acceptable method of dealing with these delay parameters.

3.5.1.2 Dual input dual compartment modelling

The dual input dual compartment model is based on the principle that once in the parenchyma, extracellular CAs can only occupy either the vascular or interstitial space. This is a potentially useful model to apply to the study liver haemodynamics because of the unique anatomical configuration of the hepatic parenchyma (figure 1.1). CA passing into the parenchyma enters into the vascular space of the sinusoid, but will also pass through endothelial fenestrae into the perisinusoidal Space of Disse. The potential to study haemodynamic changes in each of these compartments is of significance in chronic liver disease, not only because of collagen deposition in the Space of Disse but also because of intrahepatic shunting that arises in chronic liver disease as a result of neovascularisation of this space. Assuming good mixing between the compartments, the

dual input single compartment model can be expressed using the following system of equations [149, 150]:

$$v_1 \frac{d}{dt} C_{L1}(t) = F\rho(C_{in}(t) - C_{L1}(t)) - PS\rho(C_{L1}(t) - C_{L2}(t)) \quad (\text{Equation 3.4})$$

$$v_2 \frac{d}{dt} C_{L2}(t) = PS\rho(C_{L1}(t) - C_{L2}(t)) \quad (\text{Equation 3.5})$$

where,

v_1	Fractional vascular volume (%)
v_2	Fractional interstitial volume (%)
$C_{L1}(t)$	CA concentration in the vascular compartment (mmol/L)
$C_{L2}(t)$	CA concentration in the interstitial compartment (mmol/L)
$C_{in}(t)$	CA input function (mmol/L) – this term is represented by equation 3.6
F	Total blood inflow/tissue perfusion (ml/min/100g)
ρ	Tissue density (assumed to be 1 g/ml)[149]
PS	Permeability surface-area product (measure of endothelial permeability; ml/min/100g)

Given the need for inclusion of both the AIF ($C_a(t)$) and VIF ($C_p(t)$) in the input term, $C_{in}(t)$ can be expressed as:

$$C_{in}(t) = \alpha C_a(t) + (1 - \alpha)C_p(t) \quad (\text{Equation 3.6})$$

where α represents the hepatic arterial fraction. Parenchymal enhancement can then be described as the product of tissue perfusion and equation 3.6 convolved with the impulse residue function:

$$C_L(t) = FC_{in}(t) \otimes [Ae^{s_1 t} + (1 - A)e^{s_2 t}] \quad (\text{Equation 3.7})$$

where s_1 and s_2 are solutions for s in the following quadratic equation:

$$s^2 + \left(\frac{PS\rho}{v_1} + \frac{PS\rho}{v_2} + \frac{F\rho}{v_1} \right) s + \left(\frac{PS\rho}{v_2} \frac{F\rho}{v_1} \right) = 0 \quad (\text{Equation 3.8})$$

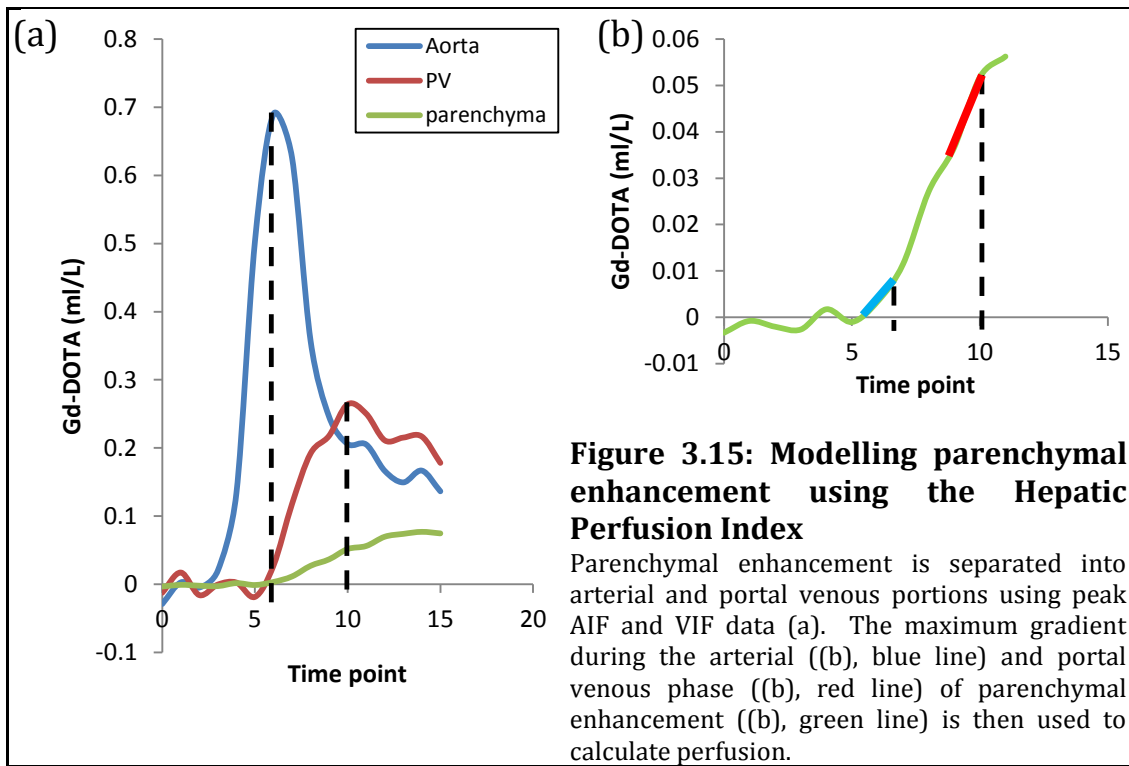
and:

$$A = \frac{\left(s_1 + \frac{PS\rho}{v_1} + \frac{PS\rho}{v_2} \right)}{s_1 - s_2} \quad (\text{Equation 3.9})$$

Alternative, more complex methods for deriving the impulse residue function with this model have been described [150, 151], but a full exploration of these methods has not been undertaken as part of this thesis.

3.5.1.3 Hepatic perfusion index modelling

The hepatic perfusion index is a much simpler model that aims to only measure hepatic arterial and portal venous perfusion and their relative ratios [107]. Once MRI signal has been converted into CA concentration, the parenchymal enhancement curve ($C_L(t)$) can be separated into predominantly arterial ($C_{La}(t)$) and portal venous ($C_{Lp}(t)$) portions using the timings for the peak aortic and portal venous enhancement curves respectively (figure 3.15a).



The peak gradient during the arterial ($\Delta C_{La}(t)'$) and portal venous phase ($\Delta C_{Lp}(t)'$) is then used to estimate perfusion using the maximum AIF CA concentration ($C_a(t)'$) [138, 139]:

$$F_{\text{Arterial perfusion}} (\text{ml/s/g}) = \frac{\Delta C_{La}(t)'}{C_a(t)'}$$

and:

$$F_{\text{PV perfusion}} (\text{ml/s/g}) = \frac{\Delta C_{Lp}(t)'}{C_a(t)'}$$

(Equations 3.10 and 3.11)

Developments of this method have proposed using splenic enhancement to correct the liver parenchymal enhancement curve to represent portal venous enhancement alone, but this modification was not included as splenic enhancement data was not available [108].

In this section, we use data obtained after applying the methodological refinements in T1 measurement and bolus protocols, to firstly explore the dual input single compartment model used in Chapter 2. Different approaches are then used to measure AIF and PVIF delay parameters to determine the optimum approach when using this model. Secondly, we study the parameters derived from application of the dual input dual compartment model to the same data and finally we study the parameters derived from the much simpler hepatic perfusion index model.

3.5.2 MATERIALS AND METHODS

Experimental subjects and animal preparation was as described in section 3.3.2. Experiments were performed in $n = 7$ subjects. DCE MRI was performed as described in section 3.4.2. A 100 μ L CA bolus of 0.05 mmol/kg (based on a 250g animal) concentration was infused at 2 ml/min as described previously. ROIs over the aorta, portal vein and liver parenchyma were used to obtain signal-intensity-time curves which were then converted to CA concentration using methods described in section 2.4.6.

3.5.2.1 Sample size

A pragmatic approach to sample size was used given that data collection during these studies was undertaken for the purpose of protocol development. DCE MRI data sets obtained from other experiments were therefore collated for inclusion in this section.

3.5.2.2 Dual input single compartment modelling

Method 1

Dual input single compartment modelling was undertaken assuming zero-delays between the vascular input functions and parenchymal enhancement (as in section 2.4.7).

Method 2

AIF and PVIF delays (τ_a and τ_p) were modelled freely to optimise the fit quality by minimising residual sum of squares.

Method 3

A zero delay is assumed for the PVIF, with free modelling of the AIF delay.

Method 4

A zero delay is assumed for the AIF, with free modelling of the PVIF delay.

Method 5

Delays were pre-estimated by measuring approximate CA arrival time for the AIF, PVIF and liver parenchyma. For the AIF and PVIF, the maximum gradient during the upstroke of each VIF was identified and this portion of the VIF enhancement curve was then modelled using linear regression to derive an estimate for VIF CA arrival time ($t_{C_a arrival}$ and $t_{C_p arrival}$) (figure 3.16).

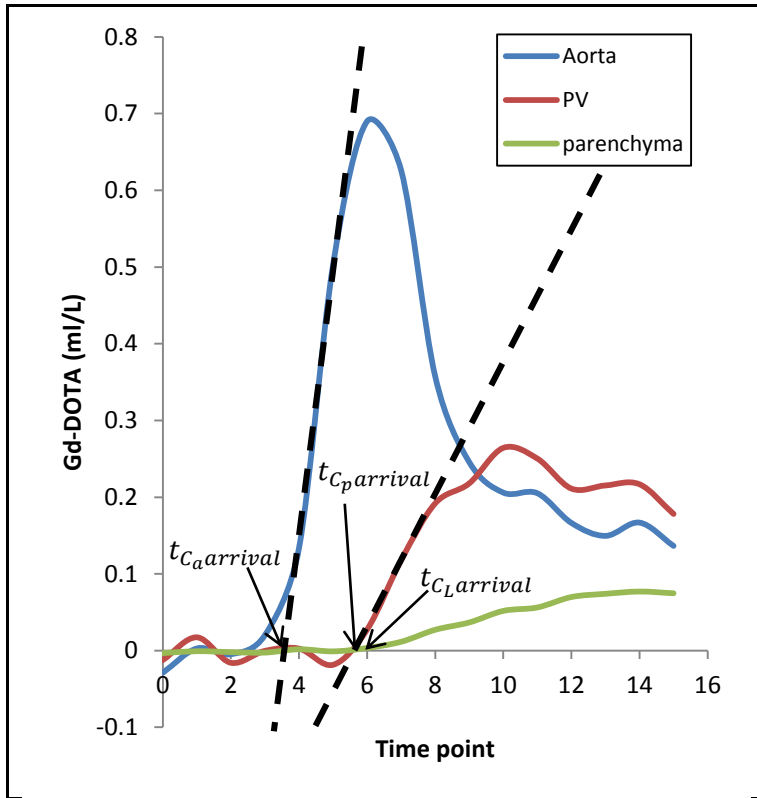


Figure 3.16: Pre-estimation of τ_a and τ_b to constrain free modelling of delay parameters

The maximum gradient of the upstroke for each VIF was modelled using linear regression to estimate $t_{C_a arrival}$ and $t_{C_p arrival}$. Parenchymal CA arrival time was determined using the 95% upper limit confidence interval of baseline data.

CA arrival in the parenchymal ROI ($t_{C_L arrival}$) was determined as the time of the last point before parenchymal CA concentration exceeded the upper limit of the 95% confidence interval of the baseline (pre-contrast) data (figure 3.16). Estimates for τ_a and τ_p were then determined:

$$\tau_a' = t_{C_L arrival} - t_{C_a arrival}$$

$$\tau_p' = t_{C_L arrival} - t_{C_p arrival}$$

(Equations 3.12 and 3.13)

As τ_a' and τ_p' represented estimates of VIF delays, limited by temporal resolution and SNR, the pre-estimates were then used to constrain the range in which free modelling of τ_a and τ_p could occur, to one time point before and one time point after each estimate.

3.5.2.3 Dual input dual compartment modelling

Free modelling of parameters using the dual input dual compartment model was undertaken with limited success. Fractional interstitial volume (v_2) was then constrained to between zero and twenty percent to determine more physiological estimates of perfusion parameters.

3.5.2.4 Hepatic perfusion index

Hepatic perfusion index parameters of absolute and relative perfusion were derived.

3.5.2.5 Statistical analysis

Kolmogorov-Smirnov tests were used to confirm normality of variable distributions. Repeated measures one-way analysis of variance (ANOVA) with corrections for non-sphericity were used to compare perfusion parameters from dual input single compartment modelling using each of the five approaches to VIF delay estimation, with post-hoc Tukey's test where significant differences were identified. Where variables were found not to be normally distributed, the Kruskal-Wallis test was used followed by post-hoc Dunn's test where significant differences were identified. As method 5 represented an evolved approach to enable free modelling within physiological constraints, common absolute and relative perfusion parameters were compared using paired t-tests with dual input dual compartment and hepatic perfusion index models derived data. For validation, unpaired t-tests were used to compare PV perfusion derived with each method to invasive TTUS data obtained from experiments described in Chapter 2. The threshold of statistical significance was defined to be $p < 0.05$. T1 measurement data from all seven subjects was used in section 3.3 and data from two subjects was used in section 3.4.

3.5.3 RESULTS

3.5.3.1 Dual input single compartment modelling

A sample data set was used to demonstrate the VIFs and parenchymal enhancement curves obtained with corresponding curve fits in figure 3.17, using each of the five approaches. In this instance, pre-estimation of delays with constrained fitting yielded the same estimates as free modelling. Alternative delays resulted in effective shifts of the VIF as shown in the charts on the left in figure 3.17. The effects of these shifts on estimated parameters resulted in profound differences in estimated perfusion parameters for each method, as shown by the data overlaying the charts on the right (figure 3.17).

Data for each of the perfusion parameters is plotted for each method in figure 3.18 and tabulated in table 3.5. Hepatic arterial (HA) perfusion and PVIF delay parameters demonstrated a non-normal distribution and therefore underwent Kruskal-Wallis testing. Significant differences were demonstrated between the five methods for PV perfusion ($F(2.197, 13.18) = 12.99$; $p = 0.0006$), HA perfusion ($H = 10.57$; $p = 0.0319$), PV fraction ($F(1.531, 9.185) = 10.04$; $p = 0.0068$) and residual sum of squares ($F(1.118, 6.708) = 6.656$; $p = 0.0357$). Post-hoc tests on PV perfusion measurements, showed all methods differed from Method 1 except Method 4, and differences in PV fraction were demonstrated between Method 1 and Method 2. No post-hoc significant differences were demonstrated in HA perfusion or residual sum of squares.

Validation against TTUS derived cohort means demonstrated significant differences with dual input single compartment derived PV perfusion using Method 3 (mean difference -41.91 ± 16.90 ml/min/100g; $p = 0.0306$) and Method 5 (mean difference -39.90 ± 16.12 ml/min/100g; $p = 0.0308$), with the possibility of the type II error for Method 2 (mean difference -39.12 ± 17.98 ml/min/100g; $p = 0.0522$).

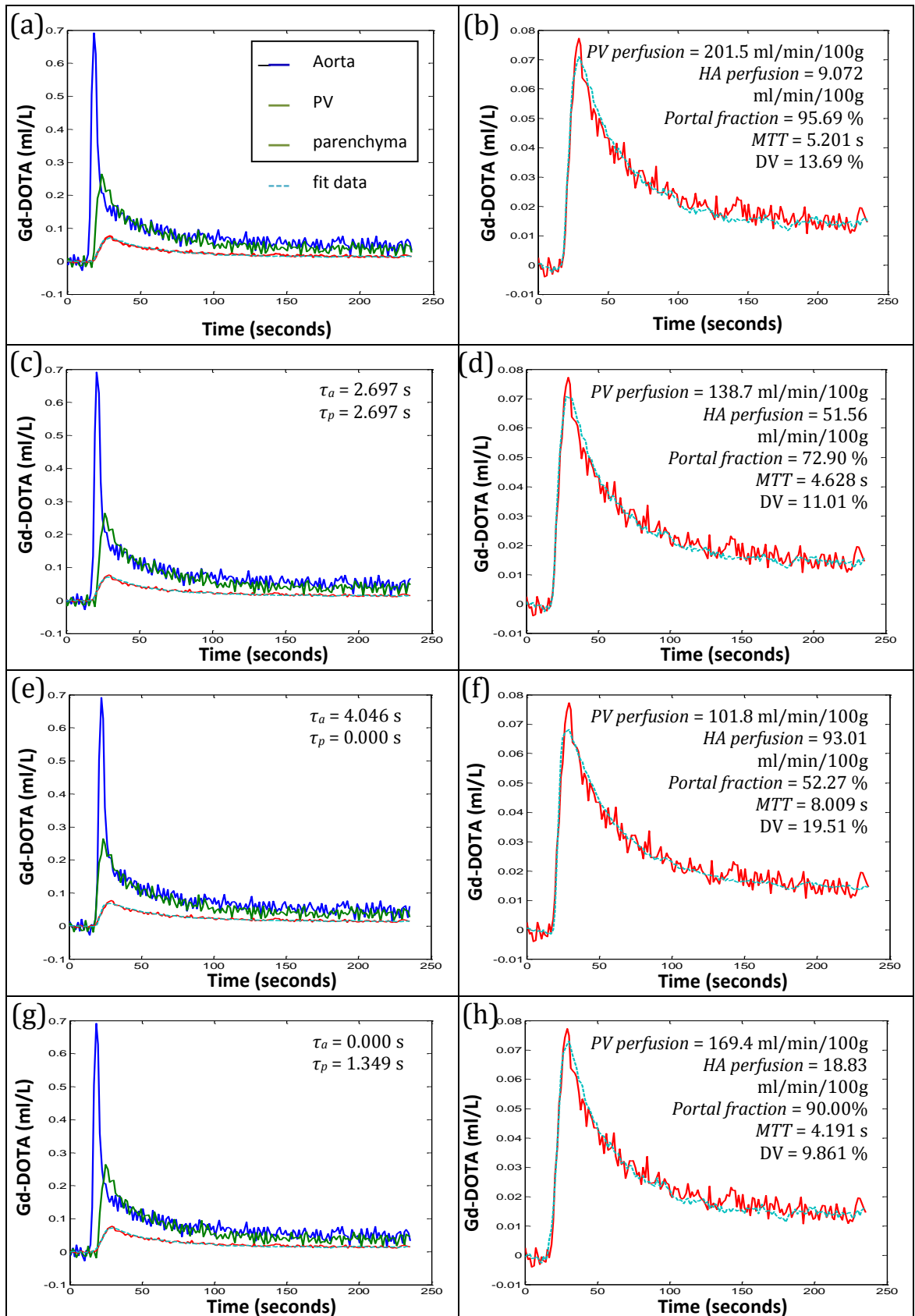


Figure 3.17: Dual input single compartment modelling VIFs and parenchymal enhancement curves with fitted parenchymal enhancement curves

Data assuming τ_a and τ_p are zero - (a) and (b), free modelling of τ_a and τ_p - (c) and (d), free modelling of τ_a with τ_p set to zero - (e) and (f) and finally free modelling of τ_p with τ_a set to zero - (g) and (h). Data from pre-estimated delays and constrained free modelling was the same as (c) and (d). Mean estimated parameters from each of the approaches are listed in table 3.5.

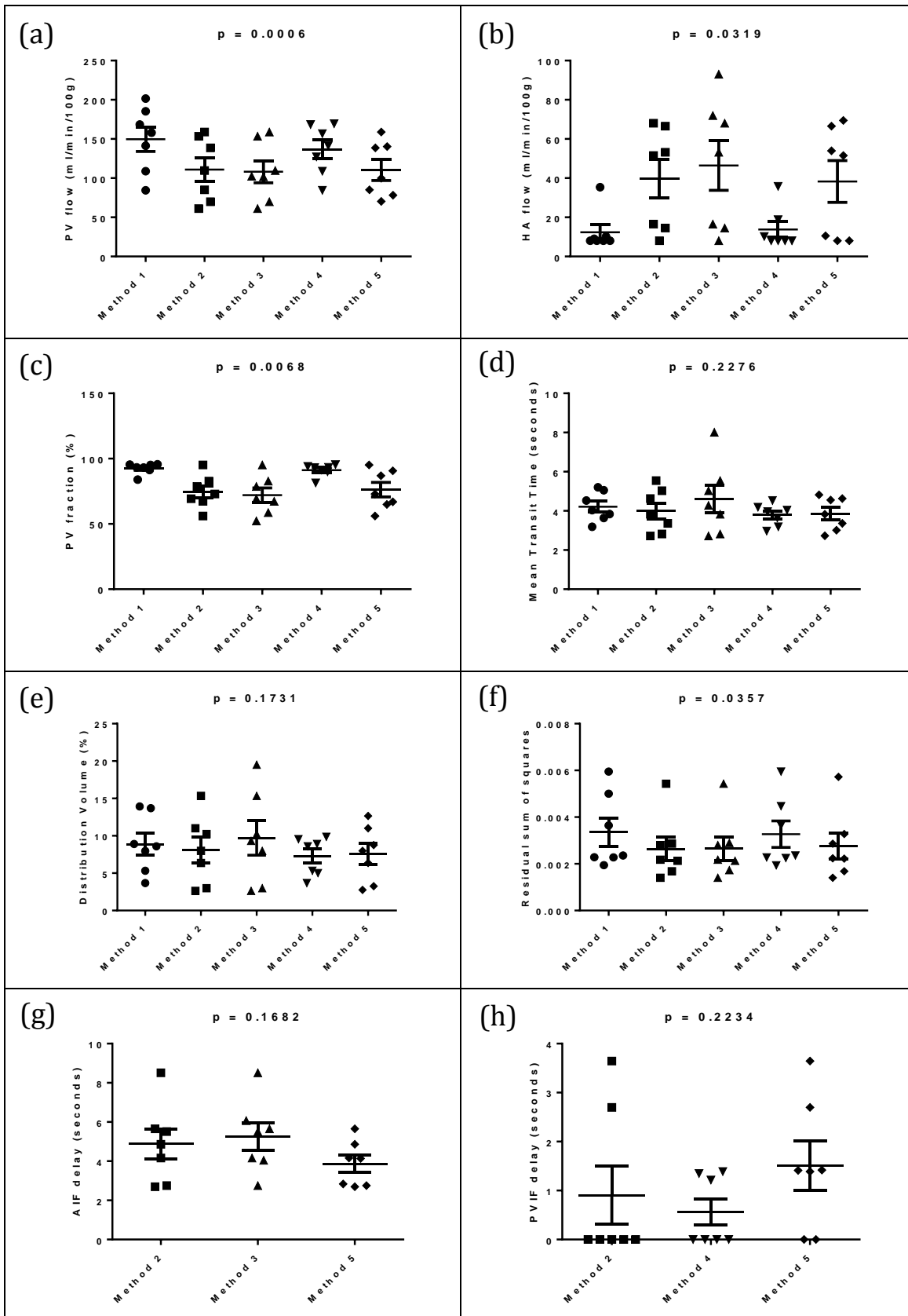


Figure 3.18: Perfusion parameters estimated using the dual input single compartment model, with each method of VIF delay estimation

p-values are quoted for one-way ANOVA/Kruskal-Wallis tests where appropriate. Comparisons of delay parameters were only undertaken when these were freely modelled ((g) and(h)).

Table 3.5: Perfusion parameters estimated using the dual input single compartment model, with each method of VIF delay estimation

	METHOD 1 (no delays)	METHOD 2 (freely modelled delays)	METHOD 3 (freely modelled AIF delay, PVIF delay set to zero)	METHOD 4 (freely modelled PVIF delay, AIF delay set to zero)	METHOD 5 (pre-estimated delays with constrained free modelling)	TTUS (n = 6)
PV perfusion (ml/min/100g)*	149.7±15.71	111.0±15.20 [†]	108.2±14.11 ^{†‡}	136.6±12.05	110.2±13.31 ^{†‡}	150.1±7.73
HA perfusion (ml/min/100g)*	12.37±3.842	39.77±9.781	46.47±12.65	13.83±3.958	38.29±10.68	-
PV fraction (%)*	92.59±1.552	74.62±4.715 [†]	72.04±5.550	91.25±1.775	76.24±5.594	-
Mean Transit Time (seconds)	4.212±0.2818	3.991±0.4168	4.605±0.6915	3.788±0.2107	3.849±0.3179	-
Distribution Volume (%)	8.867±1.458	8.082±1.722	9.717±2.322	7.273±0.9522	7.539±1.401	-
Residuals ^{2*}	0.00351±0.0005944	0.002642±0.0005070	0.002654±0.0005054	0.003270±0.0005645	0.002773±0.0005486	-
τ_a (seconds)	-	4.879±0.7555	5.245±0.6969	-	3.871±0.4362	-
τ_p (seconds)	-	0.9059±0.5938	-	0.5644±0.2668	1.509±0.5013	-

(*one-way ANOVA/Kruskal-Wallis p<0.05; [†] post-hoc Tukey test comparison with Method 1 p<0.05; [‡] unpaired t-test comparison with TTUS p<0.05)

3.5.3.2 Dual input dual compartment modelling

Initial attempts at dual input dual compartment modelling revealed some inherent challenges with the model (figure 3.19 and table 3.6). While fits appeared visually acceptable (figure 3.19a), mean v_2 or fractional interstitial volume was non-physiological at 96.78%. PV perfusion estimates though variable were physiologically feasible, but HA perfusion was low and therefore PV fraction was elevated.

To investigate this further, we assessed the impulse residue functions (figure 3.19b), which would normally be expected to assume the morphology of a negative logarithmic function in keeping with washout of CA in response to the bolus. An example of an expected impulse residue function is demonstrated from dual input single compartment data (figure 3.19e). Instead, the impulse residue function from dual input dual compartment data consistently showed a positive upstroke before dipping below zero and then stabilising. By restricting the upper limit of v_2 , the aberrant impulse residue function could be corrected, but at the expense of restricting an unknown variable of potential pathophysiological significance. The data was re-analysed restricting the upper limit of the fractional interstitial volume to 20%. An example of fitting using this restriction and the corrected impulse residue function are shown in figure 3.19c and d. As would be expected, once v_2 was restricted, all but one data set fitted fractional interstitial volume at 20%. With the application of the restriction, PV perfusion and HA perfusion dropped to non-physiological levels. Data from both unrestricted and restricted data is shown in table 3.6, alongside dual input single compartment modelling and TTUS validation data.

Paired comparison of PV perfusion with dual input single compartment data using Method 5 showed no statistically significant difference with unrestricted dual input dual compartment data (mean difference 13.04 ± 24.64 ml/min/100g; $p = 0.6156$), but significant differences with restricted dual input dual compartment data (mean difference -54.12 ± 19.49 ml/min/100g; $p = 0.0321$). Unpaired comparisons with validation TTUS data demonstrated no significant difference with unrestricted dual input dual compartment data (mean difference -26.86 ± 22.87 ml/min/100g; $p = 0.2649$), but significant differences with restricted dual input dual compartment data (mean difference -94.03 ± 16.64 ml/min/100g; $p = 0.0001$).

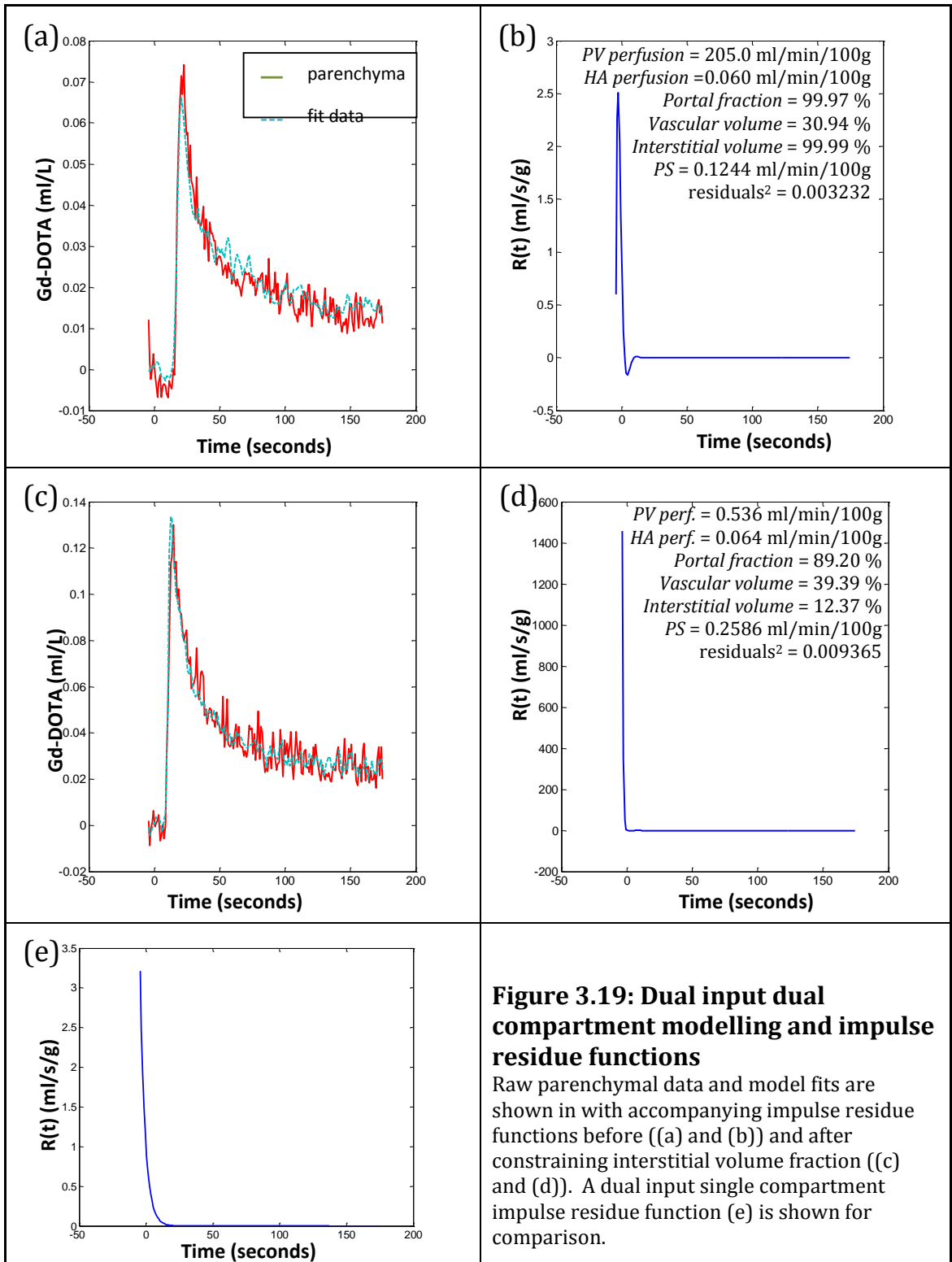


Figure 3.19: Dual input dual compartment modelling and impulse residue functions

Raw parenchymal data and model fits are shown in with accompanying impulse residue functions before ((a) and (b)) and after constraining interstitial volume fraction ((c) and (d)). A dual input single compartment impulse residue function (e) is shown for comparison.

Table 3.6: Perfusion parameters estimated using the dual input dual compartment model

	DUAL INPUT DUAL COMPARTMENT (<i>interstitial fraction unrestricted</i>)	DUAL INPUT DUAL COMPARTMENT (<i>interstitial fraction restricted</i>)	DUAL INPUT SINGLE COMPARTMENT <i>Method 5</i>	TTUS (<i>n = 6</i>)
PV perfusion (ml/min/100g)	123.2±20.00	56.06±13.85*†	110.2±13.31	150.1±7.73
HA perfusion (ml/min/100g)	5.266±2.142	1.706±0.8050	38.29±10.68	-
PV fraction (%)	96.24±0.01259	96.13±0.01508	76.24±5.594	-
Fractional vascular volume (%)	20.63±4.103	13.21±4.815	-	-
Fractional interstitial volume (%)	96.78±3.025	18.91±1.090	-	-
Permeability Surface Area product (ml/min/100g)	0.1023±0.02431	0.09017±0.03316	-	-
Residuals ²	30.02±5.302x10 ⁻⁴	37.54±9.833x10 ⁻⁴	27.73±5.486x1 ⁻⁴	-

(* paired t-test comparison with dual input single compartment Method 5 $p < 0.05$; † unpaired t-test comparison with TTUS $p < 0.05$)

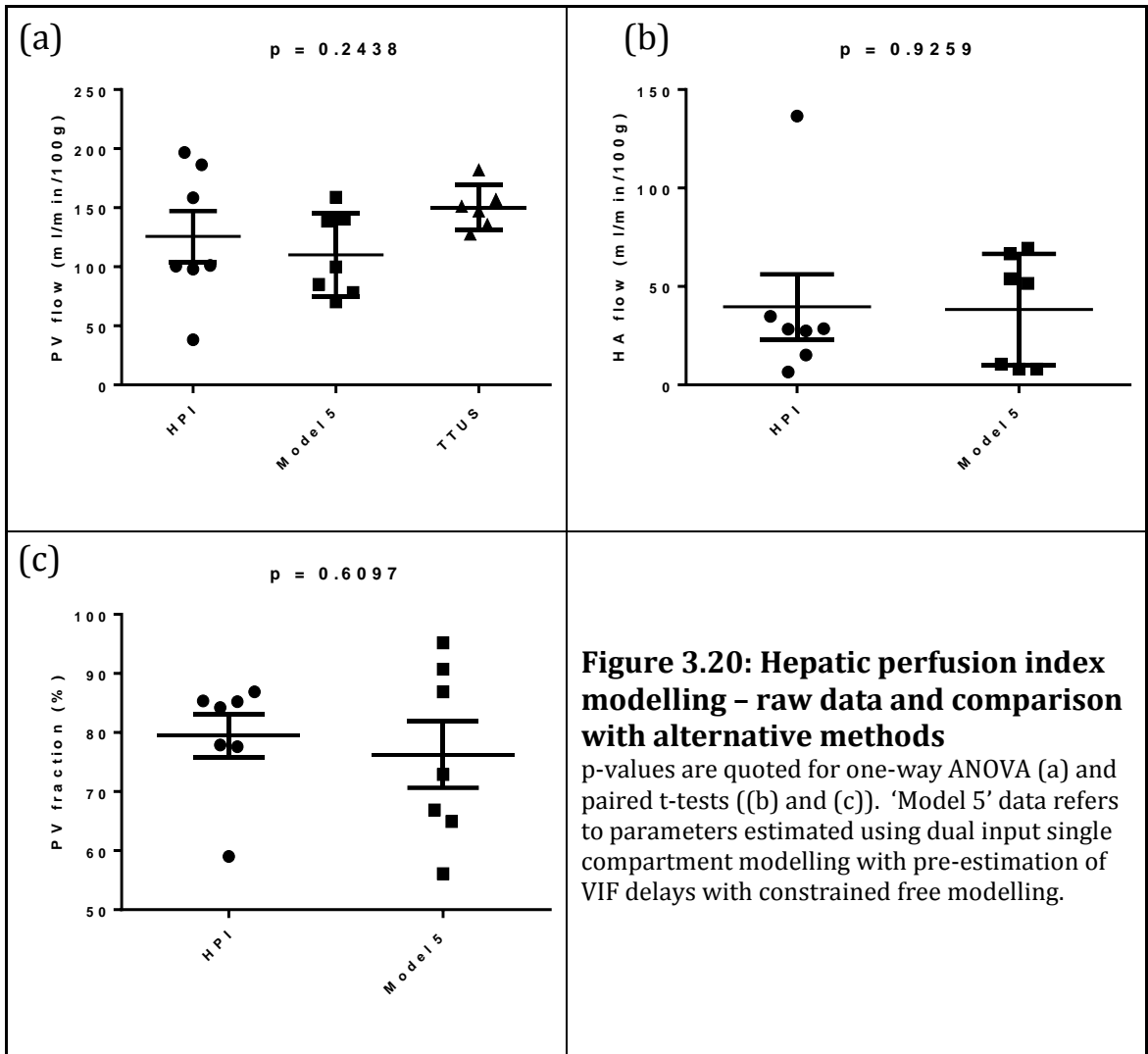
3.5.3.3 Hepatic perfusion index modelling

Perfusion parameters estimated using hepatic perfusion index modelling are shown in table 3.7 and illustrated in figure 3.20. No significant differences were demonstrated between hepatic perfusion index and dual input single compartment modelling using Method 5 for PV perfusion (mean difference 15.47±28.87 ml/min/100g; $p = 0.6113$), HA perfusion (mean difference -1.356±13.99 ml/min/100g; $p = 0.9259$) and PV fraction (mean difference -3.220±5.981 %; $p = 0.6097$). Unpaired comparison with TTUS validation data also revealed no significant difference in PV perfusion (mean difference -24.43±24.46 ml/min/100g; $p = 0.3393$).

Table 3.7: Perfusion parameters estimated using the hepatic perfusion index model

	HEPATIC PERFUSION INDEX	DUAL INPUT SINGLE COMPARTMENT <i>Method 5</i>	TTUS (<i>n = 6</i>)
PV perfusion (ml/min/100g)	125.7±21.53	110.2±13.31	150.1±7.73
HA perfusion (ml/min/100g)	39.64±16.55	38.29±10.68	-
PV fraction (%)	79.46±3.683	76.24±5.594	-

(* paired t-test comparison with dual input single compartment Method 5 $p < 0.05$; † unpaired t-test comparison with TTUS $p < 0.05$)



3.5.4 DISCUSSION

It has been shown previously that alterations in VIF delays can have significant effects on perfusion parameters estimated with dual input single compartment modelling [166, 312, 334]. Researchers who choose to fix VIF delays can argue that this is adequate as it enables comparison of perfusion parameters across cohorts of subjects that are being studied (i.e. control versus disease), but this discards the role of VIF delays in the pathophysiology of perfusion. Changes in VIF delays between subjects, healthy or diseased, may indeed represent underlying pathophysiological sequelae. Failure to include a proper treatment of these parameters in any modelling approach is likely to be flawed.

We have shown that perfusion parameters estimated using the dual input single compartment model are sensitive to both AIF and PVIF delays. To investigate this further, varying combinations of AIF and PVIF delay were applied from zero to twelve to study how perfusion parameter estimates changed. The results from a single data set are shown in figure 3.21, and are broadly similar across different datasets. In this subject, free modelling of delays (Method 2) resulted in an AIF delay of 4.859 seconds and PVIF delay of 3.644 seconds. The delays were pre-estimated as 6.074 seconds for the AIF and 3.644 seconds for the PVIF, with constrained free modelling (Method 5) on this occasion producing the same delays. At small PVIF delays, increasing AIF delay produces an initial rise in HA perfusion, PV perfusion, MTT and DV before causing a decline in these parameters. Conversely a fall in PV fraction is seen with small AIF delays, which is then seen to rise once AIF delays become larger. Increasing PVIF delays generally results in fall in PV perfusion and PV fraction and rise in HA perfusion. At small AIF delays, increasing PVIF delays produces an initial decline followed by a sharp rise in MTT and DV.

It was encouraging to see corroboration between free modelling of delays (Method 2) and constrained free modelling of pre-estimated delays (Method 5). This would suggest that when left to its own devices, the model may have the potential to provide physiologically sensible parameters. Although no statistically significant differences were demonstrated from comparisons of either delay, this was not always found to be the case, with non-physiological AIF delays (suggesting AIF arrival after parenchymal enhancement) being estimated from free modelling in two of the seven data sets. The concern would be that fitting poorer quality, noisier pixel-wise parenchymal enhancement data using free modelling of delays would result in non-physiological estimates of VIF delay parameters much more readily. It is for this reason that constrained free modelling of pre-estimated VIF delays (Method 5) is likely to be a much more physiologically sound approach for future attempts. Pre-estimation ensures that estimated VIF delays are

always physiological, while constrained free modelling allows the fitting process to account for limitations in temporal resolution and SNR.

It is also worth noting that free modelling of VIF delays places heavier processing requirements on the computer fitting the data, which are considerably reduced when using constrained free modelling of pre-estimated VIF delays.

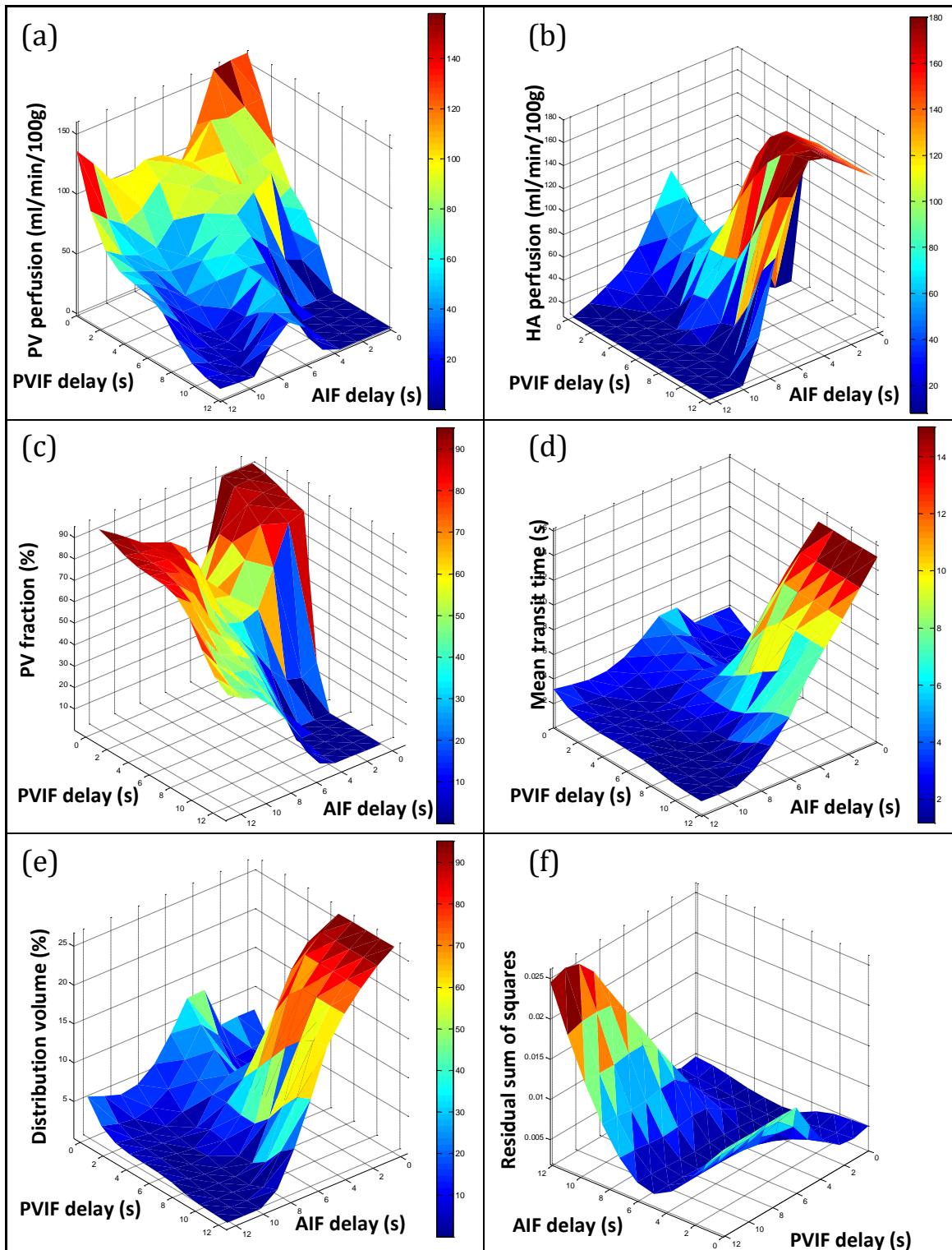


Figure 3.21: Variation of dual input single compartment modelling parameters in a single dataset across different VIF delays

PV perfusion (a), HA perfusion (b), PV fraction (c), Mean Transit Time (d), Distribution Volume (e) and residual sum of squares (f), with modelled parameter values matched to colour scale on the right of each chart. Note the horizontal axes on chart (f) have been swapped for better visualisation of the data.

The dual input dual compartment model is an interesting model because it purports the measurement of interstitial volume, a parameter which would be of potential

significance in liver disease [26]. Unfortunately, our experience failed to generate any meaningful data using this model. The original proponents of the model have in subsequent publications have afforded a more complex mathematical description of the impulse residue function, presumably to address this problem [150, 151]. As the model has been applied specifically in the context of neuro-endocrine tumours and as development has been driven towards this end rather than global assessment of perfusion, implementation of these more complex approaches was not undertaken. The application of the dual input dual compartment model has however been a useful exercise in demonstrating an important principal of pharmacokinetic modelling: estimation of more parameters from the same data (though attractive!), will only result in a higher risk of non-physiological parameter estimates.

It is therefore perhaps a fitting testimony to the elegance of simplicity that the hepatic perfusion index model should have performed so well compared to its more complex dual input single and dual compartment counterparts. Unfortunately, the data required to apply the more complex 'direct' hepatic perfusion index which corrects hepatic parenchymal enhancement using peak splenic enhancement was not available. The spleen is a smaller in relative size to the liver in rodents and therefore not consistently identified on axial slices of the liver, when compared with human subjects. The application of hepatic perfusion index model is also dependent on accurate measurement of the AIF peak. This would not have been possible without the bolus protocol experiments in section 3.4, but also highlights an important vulnerability of the method, especially at higher field strength. Finally, while the estimation of parameters using the hepatic perfusion index model was impressive, an important advantage of the dual input single compartment is the derivation of MTT and DV parameters, both of which are of potential significance in liver disease.

It can be argued that subjecting the same data to alternative modelling methods is of limited value because each model aims to measure different parameters by different methods. In selecting a particular model, a researcher commits to the derived parameters and as long as these are the same across the cohorts of subjects that are being studied (i.e. control vs disease), any comparison is valid. While this may be true of an individual exploratory study, if the work is to inform the development of clinically usable biomarkers, care must be taken to develop image protocols and select models that yield robust parameters both within and between institutions [335]. The work presented in this section is therefore an essential first step towards establishing a modelling protocol for robust parameters on our imaging platform.

3.5.5 CONCLUSIONS

After applying methodological refinements in T1 measurement and bolus protocols, we have demonstrated pharmacokinetic modelling of CA behaviour in the parenchyma to measure perfusion parameters using the dual input single compartment, dual input dual compartment and hepatic perfusion index models.

We have enhanced the dual input single compartment methods demonstrated in Chapter 2 through evaluation of VIF delays and demonstrated significant changes in perfusion parameters by inclusion of these delays. We have tested different methods of measuring these delays and proposed a novel method to derive physiologically meaningful estimates of them. Our studies have shown that our novel method – “constrained free modelling of pre-estimated VIF delays” – is feasible and moving forward has the potential to be superior to alternative strategies proposed in the literature.

Our experience using the dual input dual compartment model highlights the challenges and pitfalls of using more complex mathematical descriptions. The hepatic perfusion index model, though simpler can be used to quantify perfusion comparably to the dual input single compartment model with constrained free modelling of pre-estimated VIF delays.

3.6 CLOSING COMMENTS

In spite of the methodological refinements and developments with post-processing of data, it became apparent that significant inaccuracies were being introduced into experiments as a result of problems with MR signal measurement. Inflow effects from fresh blood flowing into a slice, particularly in vessels coursing perpendicular to axial slices, such as the aorta and PV must be dealt with effectively in any DCE MRI experiment. To minimise inflow effects, a global saturation pulse was applied before each slice acquisition, but the size and duration of the pulse was limited by the respiratory rate, as both the saturation pulse and image acquisition had to take place within a single between-breath interval.

This method appeared effective with the smaller animals used in earlier developmental work (figure 3.22a). Animal models of disease would be larger, as would be their sham counterparts and therefore much more susceptible to these errors (figure 3.22b).

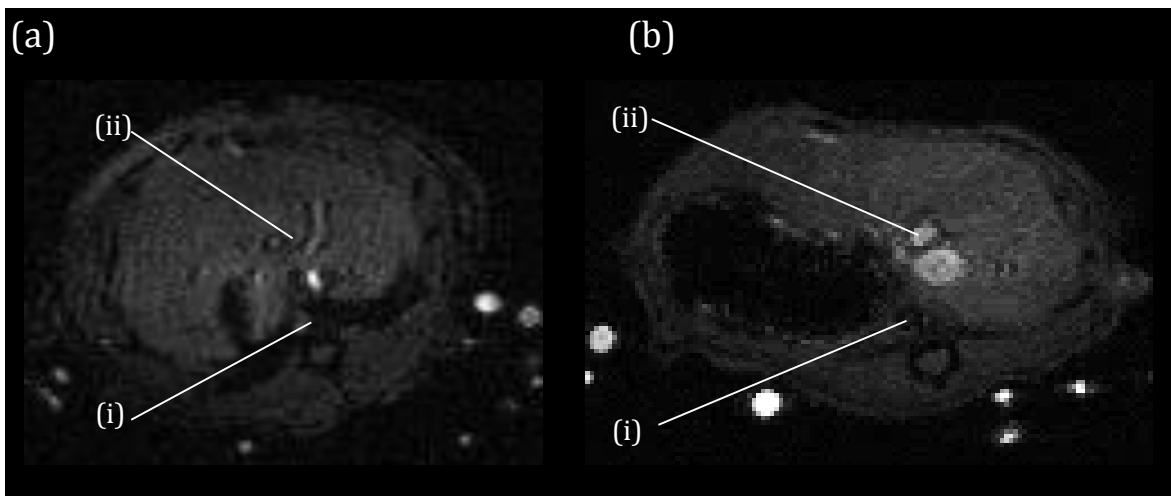


Figure 3.22: Baseline pre-contrast images and inflow effects

Differing vessel inflow effects in (a) 306g and (b) 525g subjects. Baseline signal in the (i) aorta and (ii) PV is demonstrated with inefficient saturation of splanchnic blood in the larger animal (b).

Figure 3.22b demonstrates a baseline pre-contrast image with differential signal in the aorta and PV suggestive of differing vessel inflow effects. Fast flowing blood in the aorta appears efficiently saturated, but slower moving portal venous blood is not, hence the presence of signal in the portal vein. Although signal intensity changes in a DCE MRI experiment are relative to the baseline pre-contrast images, the signal in each of the post-contrast images would also have been altered by the inflow effects. After administration of CA, each frame of the DCE MRI slice would have been corrupted by these effects, resulting in erroneously raised CA concentrations, specifically for ROIs over the PV [310].

Indeed problems with saturation pulse efficiency may well explain differences in baseline aortic and PV T1, as mentioned in section 3.3.

Strategies to address this problem include the development of more efficient saturation pulse and post-processing corrections to account for these effects [310, 336, 337]. Due to time constraints, neither of these approaches was adopted, and DCE MRI work was suspended in favour of alternative quantitative PCMRI methods.

CHAPTER 4

PRECLINICAL PCMRI – EARLY ATTEMPTS

“...Yellow
is the matrix
of your red hydraulic flow,
diver
of the most perilous
depths of man,
there forever hidden,
everlasting,
in the factory,
noiseless...”

- Ode to the liver [2].

4.1 INTRODUCTION

Our previous experience demonstrated that although measurement of tissue perfusion with dynamic contrast enhanced (DCE) MRI was possible, errors introduced before the measurement, during measurement and during post-processing of data had the potential to cause substantial errors in the final estimated perfusion parameters. We attempted to validate our measurements using transit-time ultrasound (TTUS), which although when normalised to liver weight would have been related to tissue perfusion, were in absolute terms measurements of portal venous (PV) vessel bulk flow. Perhaps then a better grounded approach would be to use a quantitative MRI technique which measured bulk vessel flow and did this in a way reliant on the same inflow effects that had been so troublesome with DCE MRI at 9.4T. With this in mind, two-dimensional phase contrast MRI (PCMRI) was developed and tested on a preclinical system.

In this chapter, we look at early sequence development, specifically (a) sequence optimisation and challenges with PCMRI, (b) repeatability and invasive validation studies, (c) early studies in the modulation of PV flow in chronic liver disease and (d) implementation of cardiac gating.

4.2 AUTHOR CONTRIBUTIONS

In fulfilment of the aims in this chapter, I: (a) prepared and conducted all animal scanning experiments; (b) developed preclinical PCMRI protocols; (c) developed Matlab code for PCMRI quantification; (d) performed surgery and collected invasive TTUS measurements of PV flow; (e) conducted bench-top experiments prior to MRI scanning for the development of protocols for the administration of L-N^G-nitro arginine methyl ester (L-NAME) and terlipressin; (f) built the signal processing unit to allow the use of pulse oximetry for cardiac gating; (g) collected and analysed all the data; and (h) prepared all the material contained within this chapter.

Alan Bainbridge developed MR sequences and helped with scanning. He developed the original Matlab code for PCMRI quantification, which was subsequently redesigned and optimised. For establishment of small animal intravenous access, I received help from either Val Taylor, Nathan Davies or Abe Habtieson. Sham-operated and bile-duct ligated rats were prepared by Abe Habtieson. Pharmacological modulation of PV flow was developed under the guidance of Nathan Davies. The signal processing unit was conceptualised by Alan Bainbridge and designed by Aaron Taylor. It was built with Raj Ramasawmy.

4.3 SEQUENCE OPTIMISATION AND CHALLENGES WITH PCMRI

4.3.1. BACKGROUND

MR signal is essentially a vector quantity, possessing both magnitude (often the signal used for the image) but also phase, arising from the spins of nuclei participating in the MR experiment. The frequency of nuclear precession (ω), is given by the Larmor equation, where γ is the gyromagnetic ratio and B_0 is the static main magnetic field:

$$\omega = \gamma B_0 \quad (\text{Equation 4.1})$$

Phase (ϕ) can then be calculated as integral of the Larmor frequency:

$$\phi = \int \omega dt \quad (\text{Equation 4.2})$$

With the application of a linear time-dependent magnetic field gradient ($G(t)$), the precession of a spin at a specified location and time ($x(t)$) can be expressed in terms of Equation 4.1 as:

$$\omega_{x(t)} = \gamma(B_0 + \Delta B_0(x) + G(t).x(t)) \quad (\text{Equation 4.3})$$

Where ΔB_0 represents errors introduced from local field inhomogeneities. The expression for phase in Equation 4.2 is dependent on the duration of $G(t)$ and can then be expressed as:

$$\phi_x = \phi_0(x) + \gamma \int_0^t G(t).x(t) dt \quad (\text{Equation 4.4})$$

Where the terms for initial and background phase at location x are reduced to $\phi_0(x)$. Where the spin at location x is moving, the location of that spin can be expressed as:

$$x(t) = x(0) + v(t) \quad (\text{Equation 4.5})$$

Where v represents the velocity for that spin. Substituting equation 4.5 into 4.4, we can construct an expression for phase that includes velocity:

$$\phi_x = \phi_0(x) + \gamma \int_0^t G(t).(x(0) + v(t))dt$$

$$= \phi_0(x) + \gamma \int_0^t x(0) \cdot G(t) dt + \gamma \int_0^t v(t) \cdot G(t) dt$$

Which under the assumption that the velocity during the application of the magnetic field gradient ($G(t)$), is constant (v) and given that $x(0)$ is fixed, can be simplified to:

$$\begin{aligned} \phi_x &= \phi_0(x) + \gamma x(0) \int_0^t G(t) dt + \gamma v \int_0^t G(t) dt \\ &= \phi_0(x) + \gamma x(0) M_0 + \gamma v M_1 \end{aligned} \quad \text{(Equation 4.6)}$$

Where M_0 and M_1 refer to the gradient moments for stationary and moving tissue. When a second magnetic field gradient of the same magnitude and duration is applied in the opposing direction immediately following the first gradient (bipolar gradients), stationary and moving spins respond differently (figure 4.1).

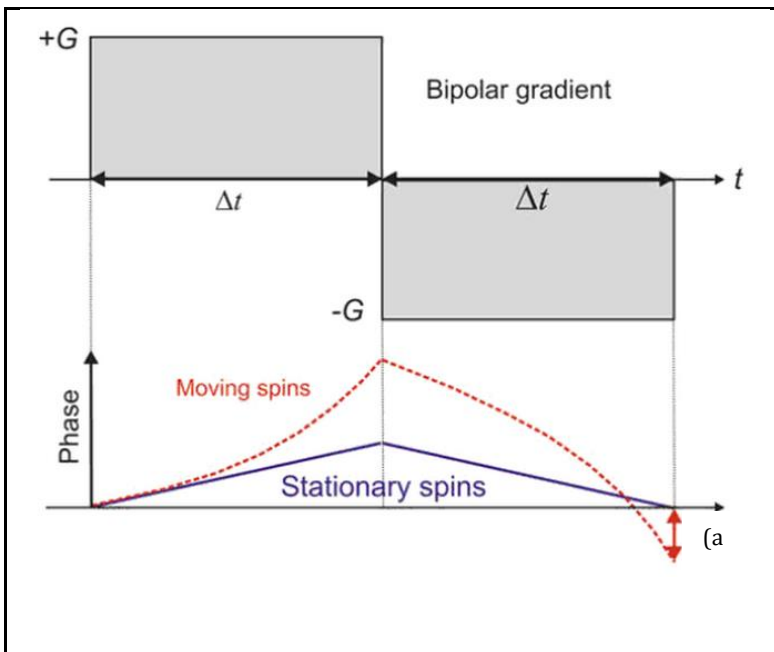


Figure 4.1: Phase shifts in response to bipolar gradients

Time is represented on the x-axis, with gradient magnitude represented on the y-axis in the upper portion of the graph and phase in the lower portion of the graph.

Phase shifts are observed in both stationary and moving spins, but bipolar gradients can be used to cancel out phase shifts in stationary spins, so that the remaining phase shift after the bipolar gradients - (a) - is proportional to velocity of the moving spins.

(Adapted from reference [338]).

Net phase shifts for stationary spins after bipolar gradients are equal to zero, but for moving spins the residual shift is proportional to their velocity. We can express the phase shift at x then as:

$$\phi_x = \phi_0(x) + \phi_{x, \text{positive gradient}} + \phi_{x, \text{negative gradient}} \quad \text{(Equation 4.7)}$$

Where from equation 4.6:

$$\phi_{x, \text{positive gradient}} = \gamma x(0) M_0 + \gamma v M_1 \quad \text{(Equation 4.8)}$$

And for the negative gradient ($G'(t)$):

$$\begin{aligned}\phi_{x, \text{negative gradient}} &= \gamma x(t) \int_t^{2t} G'(t) dt + \gamma v \int_t^{2t} G'(t) dt \\ &= \gamma x(t) M_0' + \gamma v M_1'\end{aligned}\tag{Equation 4.9}$$

By substituting 4.8 and 4.9 into 4.7 (note that the terms M_0' and M_1' are negative):

$$\begin{aligned}\phi_x &= \phi_0(x) + (\gamma x(0)M_0 + \gamma v M_1) + (\gamma x(t)M_0' + \gamma v M_1') \\ &= \phi_0(x) + (\gamma x(0)M_0 + \gamma x(t)M_0') + (\gamma v M_1 + \gamma v M_1')\end{aligned}$$

From figure 4.1, the phase shifts after each gradient are equal for stationary spins but discrepant only for moving spins, so that after a bipolar gradient, the phase shift of x can be expressed as:

$$\begin{aligned}\phi_x &= \phi_0(x) + (\gamma v M_1 + \gamma v M_1') \\ &= \phi_0(x) + \gamma v \Delta M_1\end{aligned}\tag{Equation 4.10}$$

Unfortunately, we are only really truly interested in the portion of the phase shift that is proportional to the spin velocity and therefore we must measure background phase ($\phi_0(x)$), by performing a reference scan without gradients:

$$\Delta\phi_x = \phi_x - \phi_0(x)\tag{Equation 4.11}$$

The resulting phase difference ($\Delta\phi_x$) represents MR signal phase changes attributable to motion in the direction of the so-called 'velocity-encoding gradient'. This can then finally be used to yield the velocity of the moving spin x :

$$v = \frac{\Delta\phi_x}{\gamma\Delta M_1}\tag{Equation 4.12}$$

By adding flow sensitising gradients to a gradient echo sequence, the scheme above can be used to generate PCMRI images of moving spins travelling through a single slice. The velocities of voxels of a known size over a vessel can then be summed to derive an estimate of bulk flow in that vessel (figure 4.2)[338, 339].

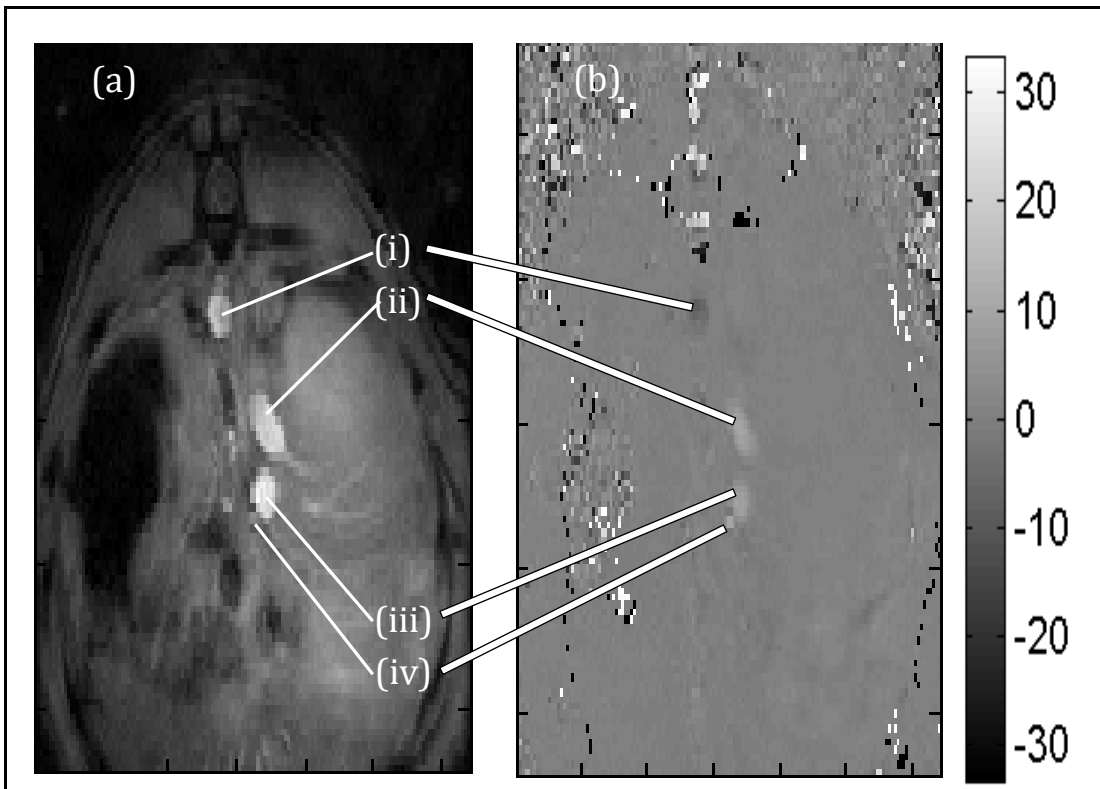


Figure 4.2: Magnitude image (a) and corresponding velocity map (b) from axial abdominal slice

Coherent signal is seen from the (i) aorta, (ii) IVC, (iii) PV and (iv) hepatic artery. Note how the velocity map distinguishes the opposing directionality of flow in the aorta and IVC.

Regions of interest drawn around vessel signal on the velocity map identify velocity vectors that when summed can estimate bulk flow in that vessel. This image was acquired with a 128x128 (PE_xFE) matrix, 2 mm slice thickness, $\alpha = 10^\circ$ and V_{enc} setting of 33 cm/s.

Accurate and robust quantitative PCMRI can only be undertaken with proper attention to the many challenges and settings that define PCMRI protocols. In this section we review the key steps that were taken to optimise early 2D PCMRI experiments at 9.4T. Certain parameters, such as velocity encoding settings, required the collection of empirical data for optimisation. This is reflected in the way the data is presented in this section. Other considerations, such as vessel orthogonality, spatial resolution and spatial misregistration were addressed using experience from one or two acquisitions. In these instances, an account and/or example of the issue is given followed by the strategy developed to overcome it.

4.3.2 VELOCITY ENCODING SETTINGS

Because phase shifts represent rotational motion, $\Delta\phi_x$ can only adopt values between $-\pi$ and π radians (negative values represent flow in the opposite direction to the velocity encoding gradients). The maximum velocity from a given PCMRI experiment that can be recorded (V_{enc}) can then be calculated as:

$$V_{enc} = \frac{\pi}{\gamma\Delta M_1} \quad \text{(Equation 4.13)}$$

There are three important sequelae that arise from this calculation. Firstly, the researcher must be cognizant of the flow velocities in the vessels they are interested in studying. The V_{enc} is essentially determined by ΔM_1 or the size of the velocity encoding gradients. The user will need to modify the size of these gradients in accordance with vessel whose flow they intend to study.

Secondly, that any spin that possesses a velocity that exceeds the V_{enc} will register a phase shift that exceeds π by a quantity of θ radians and will therefore become indistinguishable from a spin travelling in the opposing direction, recording a phase shift of $\pi - \theta$ radians (figure 4.3). This phenomenon results in an artefact known as velocity aliasing or phase wrapping.

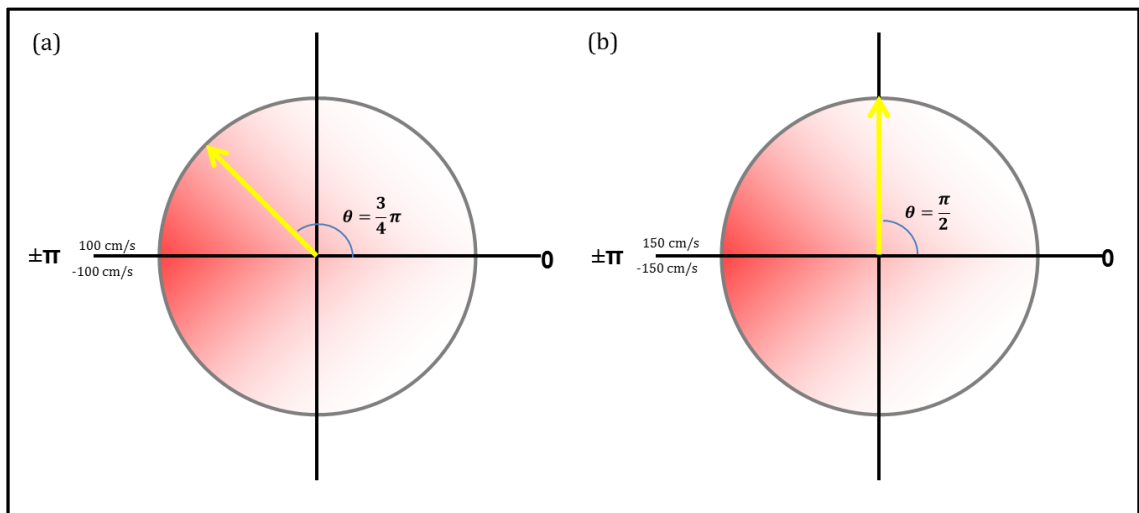


Figure 4.3: Phase shifts, V_{enc} settings and velocity aliasing

Using a V_{enc} setting of (a) 100 cm/s or (b) 150 cm/s restricts the maximal phase shift ($\pm\pi$) to that velocity. A spin travelling at 75 cm/s (yellow arrow), will record a shift of $\frac{3}{4}\pi$ when $V_{enc} = 100 \text{ cm/s}$ (a) and a shift of $\frac{\pi}{2}$ when $V_{enc} = 150 \text{ cm/s}$ (b). Note that a spin travelling at -125 cm/s (a) and -225 cm/s (b) will also record the same phase shift, resulting in aliasing/phase wrapping.

Finally that setting the V_{enc} to exceed the maximum spin velocity can be easily achieved, but occurs at the expense of velocity noise (σ), or random errors of velocity

measurements. The relationship between V_{enc} and the SNR of magnitude image can be expressed as:

$$\sigma \sim \frac{V_{enc}}{SNR} \quad (\text{Equation 4.14})$$

In the interest of obtaining accurate velocity measurements, the researcher must therefore tune the V_{enc} setting to exceed the maximum flow velocity in that vessel, but within a range where not beyond a level where velocity noise compromises the quality of the accuracy of the flow measurement.

The aim of this next subsection was to determine the optimal V_{enc} setting to use for the PV with a view to finalising a 2D PCMRI protocol for flow measurements in these vessels.

4.3.2.1 Methods

4.3.2.1.1 Numerical simulations

Expected values for PV flow were obtained from published values in the literature for Sprague-Dawley rats and previously derived TTUS data (section 2.5). Simulations were performed at 0.01 cm increments using vessel diameters ranging from 0.1-0.2 cm. Expected velocities ($v_{expected}$, cm/s) were calculated assuming plug flow with the following expression:

$$v_{expected} = \frac{Q}{A} \quad (\text{Equation 4.15})$$

Where flow (Q) was converted into ml/s and A (vessel cross-sectional area, cm²) was calculated from the diameter assuming a circular vessel profile.

4.3.2.1.2 Experimental subjects

All experiments were conducted according to the Home Office guidelines under the UK Animals in Scientific Procedures Act 1986. Animals were maintained as per guidelines and approval of the ethical committee for animal care of University College London. Experiments were performed on healthy male Sprague-Dawley rats (Charles River UK, Margate, UK) with normal liver function. Animals were housed in cages at 22-23°C, ~50% humidity and with 12 hours of light and ad libitum access to water and rat feed. For each experiment/cohort, subjects were randomly selected at the time of removal from the cage. Any adverse events and subsequent protocol modifications were recorded and reported in the results.

4.3.2.1.3 Sample size

A pragmatic approach to sample size was used given that data collection during these studies was undertaken for the purpose of protocol development. As parameter variability with our protocol on our scanning system was unknown, data was evaluated incrementally with a view to inform protocol development and provide preliminary characterisation of parameters for future planning of adequately powered studies.

4.3.2.1.4 Animal preparation

After induction with isoflurane, the anaesthetised animal was then sited in a 9.4T Agilent scanner (Oxford, UK) with a rectal probe for temperature monitoring. Core body temperature was maintained between 36 and 38°C using circulating warm water pipes and warm air.

4.3.2.1.5 Two-dimensional PCMRI

Five healthy, naïve subjects underwent 2D PCMRI for optimisation of V_{enc} settings. After initial anatomical imaging, a slice was positioned orthogonal to the PV using Agilent Varian's 3 point planning tool. Respiratory-gated 2D PCMRI was undertaken using 2 mm slice thickness, a 10° flip angle and a 128 x 128 (frequency encoding x phase encoding) acquisition matrix. Data was obtained at a range of velocity encoding settings informed from previous numerical simulations. ROIs were positioned over the portal vein for quantitative analysis.

Table 4.1: Sequence parameters

	PCMRI
<i>TR/TE (milliseconds)</i>	6.3/5.6
<i>Flip angle (°)</i>	10
<i>Matrix size (pixels)</i>	128 x 128
<i>Field-of-view (mm)</i>	40 x 40
<i>Spatial resolution (mm²)</i>	0.3125 x 0.3125
<i>Slice thickness (mm)</i>	2

4.3.2.1.6 Statistical analysis

Bulk flow and peak velocity data was analysed from 2D PCMRI experiments. Kolmogorov-Smirnov tests were used to confirm normality of variable distributions. Repeated measures one-way analysis of variance (ANOVA) with corrections for non-sphericity were used to compare data obtained at different V_{enc} settings, with post-hoc Tukey's test where significant differences were identified. Where variables were found not to be normally distributed, the Kruskal-Wallis test was used followed by post-hoc Dunn's test where significant differences were identified. The threshold of statistical significance was defined to be $p < 0.05$.

4.3.2.2 Results

4.3.2.2.1 Numerical simulations

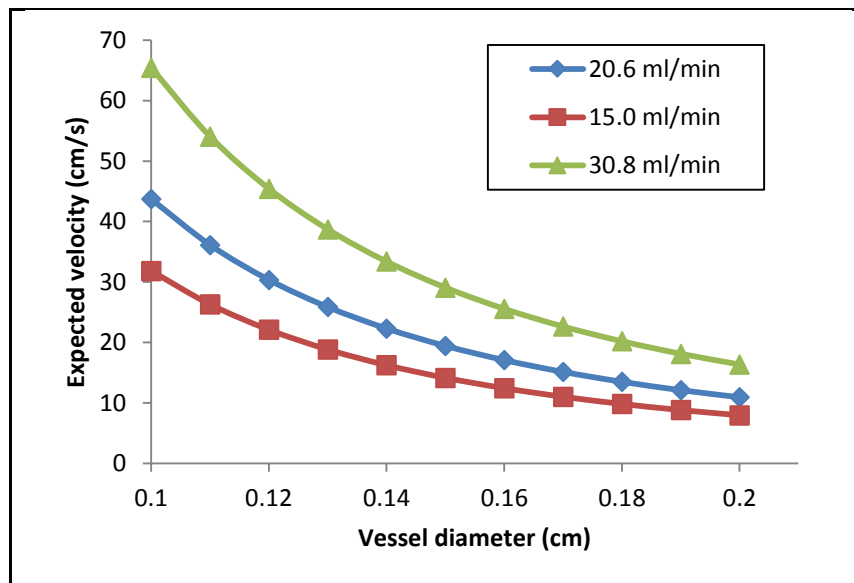
Limited published data for mean PV flow in healthy Sprague-Dawley rats is available from the literature, but this and data from previous experiments is listed in table 4.2. Based on these data, simulations of estimated plug flow velocity were carried out with bulk PV flows of 15.0, 20.6 and 30.8 ml/min (figure 4.4). Mean expected plug flow velocity across all three simulations was 24.09 ± 0.4251 cm/s.

Table 4.2: PV flow data from the literature and previous experiments

STUDY	n	BULK PV FLOW (ml/min)	SUBJECT WEIGHT (g)
Previous data	6	30.83 ± 1.35	444.8 ± 18.77
D'Almeida et al.[308]	10	20.6 ± 2.5	337 ± 16
Richter et al.[340]	18	15.0 ± 1.2	-

Figure 4.4: Simulated expected plug flow velocities

Based on invasive experimental and literature derived bulk flow estimates, expected plug flow velocity was estimated using a range of vessel diameters to determine a reasonable range of velocity encoding settings to test *in vivo*.



4.3.2.2.2 Two-dimensional PCMRI

Given that vessel diameter is likely to be above 0.15 cm, experiments were performed with V_{enc} settings of 11, 16, 22 and 33 cm/s. An example of repeated measurements at different V_{enc} settings is shown in figure 4.5.

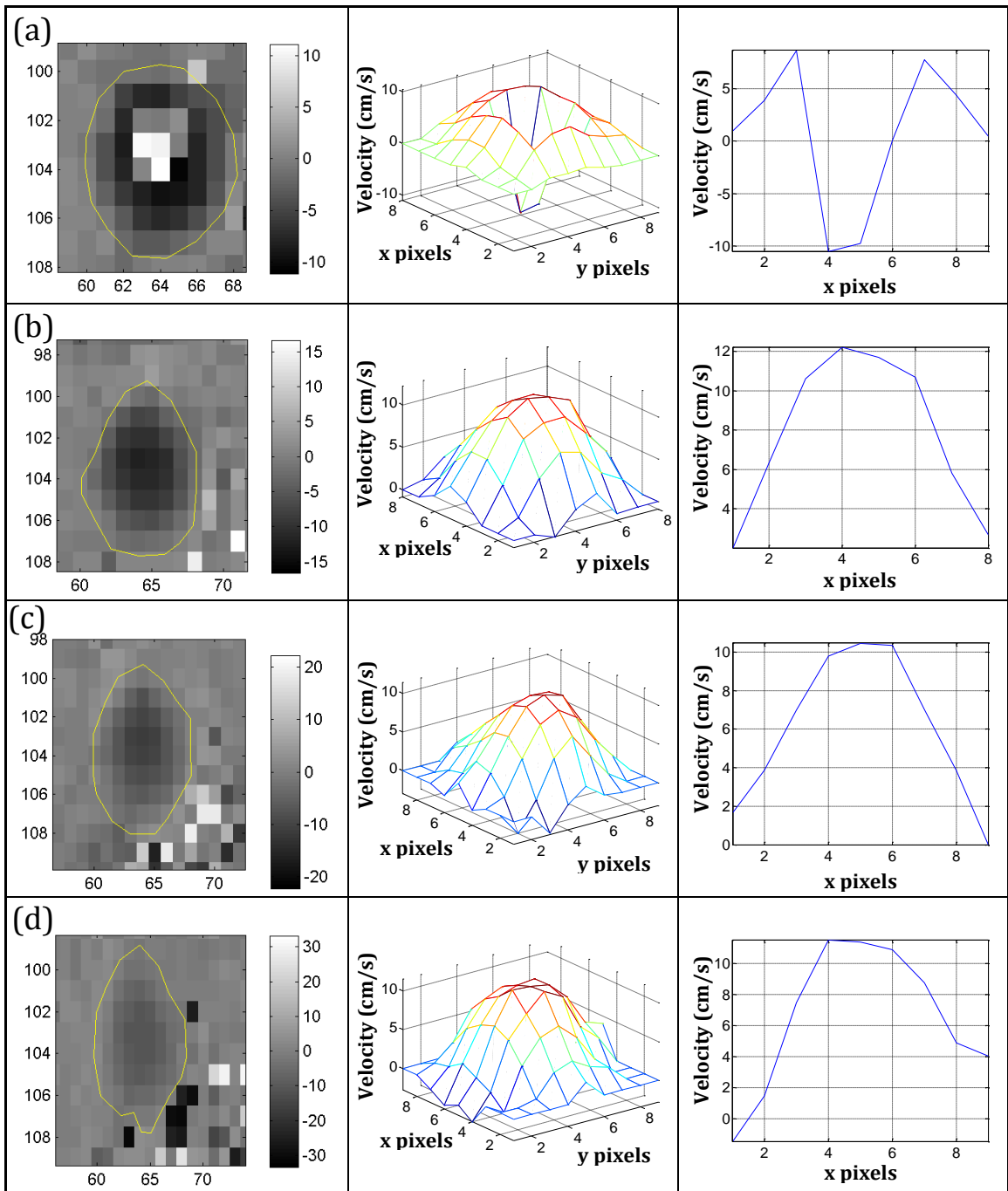


Figure 4.5: Velocity profiles at different V_{enc} settings

PV PCMRI data from the same subject at V_{enc} settings of (a) 11 cm/s, (b) 16 cm/s, (c) 22 cm/s and (d) 33 cm/s. Images on the far left demonstrate the segmented PV on the calculated velocity map. The three-dimensional flow profiles are shown in the middle, with a mid-vessel profile demonstrated on the far right at each of the V_{enc} settings.

Aliasing was consistently seen with bulk flow measurements at 11 cm/s (figure 4.5a), so measurements at this V_{enc} setting were only performed in three subjects. For PCMRI experiments performed with V_{enc} settings above the peak velocity, a dome-like laminar flow profile was demonstrated (middle and far right images, figure 4.5). Data for bulk flow and peak velocity at each of the V_{enc} settings is shown in figure 4.6.

4.3.2.3 Discussion

Numerical simulations have revealed a simple relationship between vessel size and peak velocity at various physiological levels of bulk flow. Simulations were conducted assuming plug flow which would have resulted in underestimation of the peak velocity. The relationship between vessel size and peak velocity is however, likely to be broadly similar for the more physiologically relevant laminar flow and on this basis the numerical simulations yield useful insight into how V_{enc} settings can be adjusted in different physiological contexts.

The range of settings that was tested demonstrated how lower V_{enc} settings could result in aliasing artefact but failed to demonstrate problems arising from velocity noise at higher V_{enc} settings. A larger variance in the data, particularly peak velocity would be expected at these settings, suggesting that velocity noise is not an issue in the PV at $V_{enc} = 33$ cm/s. This phenomenon may yet be an issue at higher V_{enc} settings.

A statistically significant difference in bulk flow was observed at different V_{enc} settings but looking at mean values for non-aliased data (18.49 ± 2.007 , 17.08 ± 2.268 , 17.38 ± 2.165 ml/min for 16, 22 and 33 cm/s respectively), these differences are unlikely to be of physiological significance.

Finally, it is worth noting that there are approaches to dealing with phase wrapping artefact. Although not ideal, wrapped signal can potentially be 'unwrapped' to ensure that meaningful bulk flow estimates are made.

4.3.2.4 Conclusion

PCMRI for bulk PV flow measurement can be lowered to 16 cm/s, but when undertaken with V_{enc} settings of 22 or 33 cm/s are less likely to suffer from velocity aliasing and have not been shown to suffer from noise. A V_{enc} setting of 33 cm/s is therefore appropriate for PCMRI PV flow measurements in Sprague-Dawley rats.

4.3.3 VESSEL ORTHOGONALITY AND MISALIGNMENT

PCMRI sequences can be designed with velocity encoding gradients applied in the in-plane (phase encode or frequency encode directions) or through-plane (slice select direction). Three-dimensional and 4D PCMRI sequences apply velocity encoding gradients in all three directions, but 2D PCMRI sequences apply flow encoding gradients in the slice select direction only. With this in mind, the slice position of any 2D PCMRI experiment must be carefully planned to ensure that the direction of flow is aligned with those of the flow encoding gradients (slice select direction), i.e. that the imaging plane is as orthogonal to the vessel as possible [341]. In order to achieve this, PCMRI studies were planned using a two-step method: Firstly, initial axial anatomical images were used to identify the portal vein. The scanner console software (VnmrJ 3.2, Agilent, Oxford, UK) enabled placement of three markers in the PV lumen, for automated planning of scanning slices through the PV in the coronal plane. The PV was then identified on coronal slices and two markers were placed on either side of the vessel to position an imaging slice that would be orthogonal to the vessel (figure 4.7).

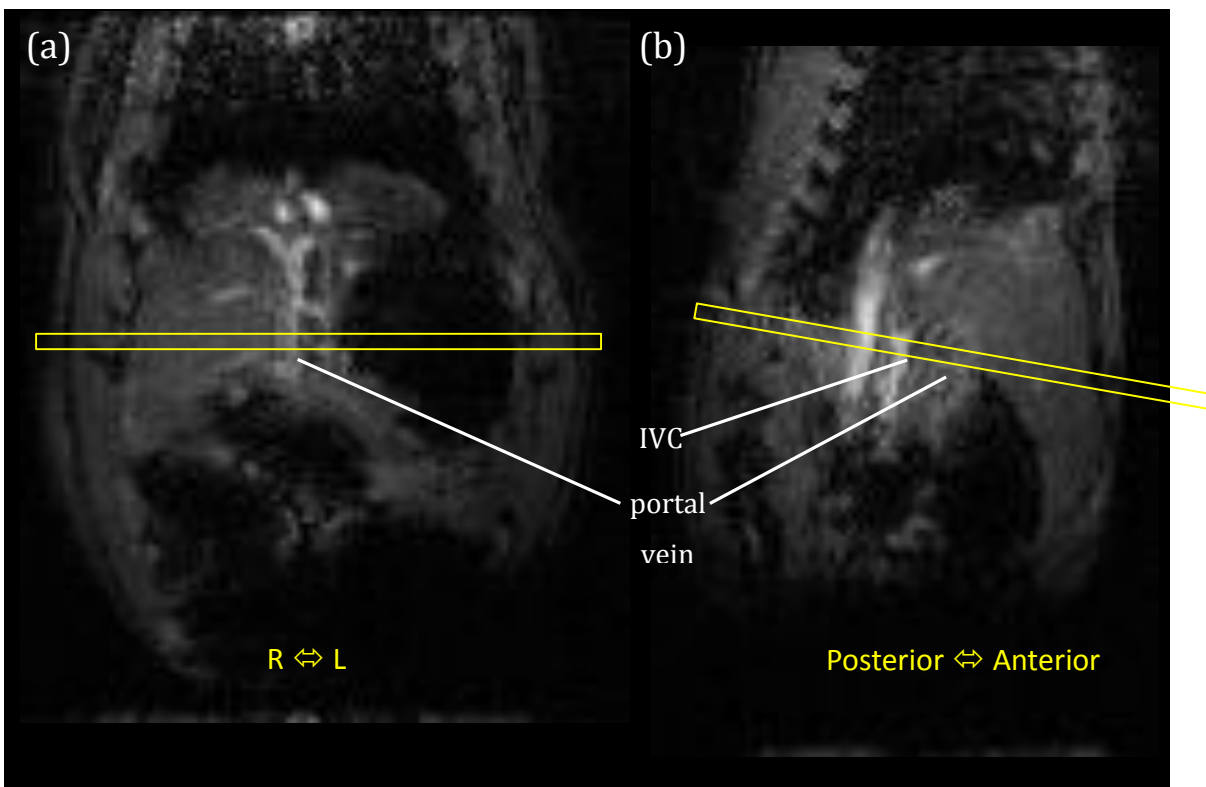


Figure 4.7: PCMRI slice planning for PV flow measurements

Anatomical images were obtained in the (a) coronal plane to identify the portal vein. Sagittal images parallel to the vessel were then obtained (b). The PCMRI slice was positioned to ensure orthogonality to the vessel in two planes. Note PV orthogonality usually also resulted in a suitable plane for IVC quantification.

Deviation from absolute orthogonality can affect data quality, but there is a margin for error within which quantification is still acceptable. Although there are very few studies that have investigated these errors, it has been demonstrated that deviations from the orthogonal plane of as much as 15° can still yield acceptable results [182].

4.3.4 SPATIAL RESOLUTION AND MATRIX SIZE

Spatial resolution is an important consideration and of direct relevance when imaging small vessels in rodents. Partial voluming from smaller vessels can result in significant errors, particularly in view of the reliance on measurements of area for the calculation of bulk flow. Published data suggests that measurements where pixel size exceeds one quarter of the vessel diameter (i.e. less than 16 pixels over a square region of interest (ROI) covering the vessel) are likely to be inadequate [211, 342-344]. From repeated measurements at different V_{enc} settings, PV vessel size ranged from 26-73 pixels (mean 54 ± 3 pixels; $n = 5$). Increasing pixel size may increase the resolution of the images, but compromises the SNR. Although this is particularly pertinent in smaller vessels where the velocity signal may inherently be less, this phenomenon is also known to affect larger vessels.

Initial experiments performed with a 128×128 matrix frequently showed areas of high signal spanning 2-4 pixels adjacent to the portal vein, likely to represent hepatic artery (HA) (figure 4.8a). Because of partial voluming, no accurate flow measurements could be obtained. When resolution was increased using a 256×256 matrix ($n = 1$), the HA was no longer seen indeed PV bulk flow measurements were less and the data was much noisier (figure 4.8b).

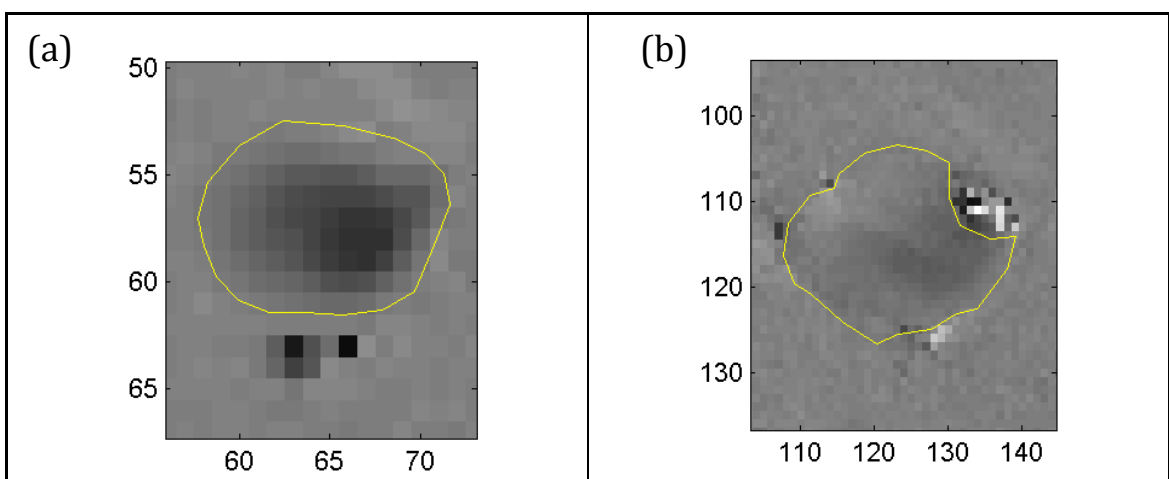


Figure 4.8: Portal venous velocity maps acquired at lower and higher resolution

Data in the same subject over the PV acquired at (a) 128×128 and (b) 256×256 resolution. Note how signal inferior to the PV, outside the yellow ROI, presumed to be hepatic artery (a) is not seen at higher resolution (b). Also note noisier signal, more prone to artefact at higher resolution (b).

The reduction in signal resulted in the adoption of a 128 x 128 matrix for imaging larger vessels such as the PV.

4.3.5 PULSATION ARTEFACTS AND SPATIAL MISREGISTRATION

High volume and pulsatile flow results in vessel motion between acquisitions of successive phase maps. This results in 'pulsation artefact' – a well-documented phenomenon in vessels such as the descending aorta, apparent in the phase-encode direction. While not directly a problem, 2D PCMRI slices through the portal vein include the descending aorta and therefore have the potential to be corrupted if artefact signal is projected over the vessel of interest. This was commonly seen with the inferior vena cava (IVC) adjacent to the aorta (figure 4.9a). When identified, the acquisition was repeated after swapping the phase and frequency encode directions, which usually ensured that the pulsation artefact was not extending over the PV or IVC (figure 4.9b).

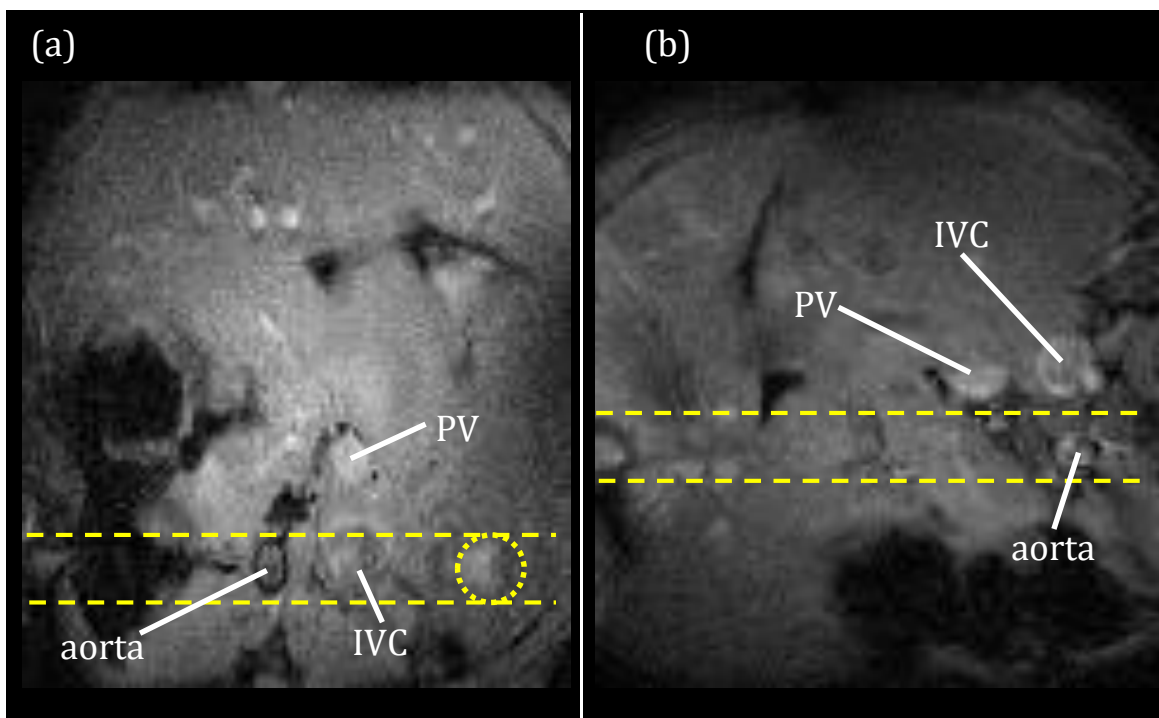


Figure 4.9: Aortic pulsation artefact with corruption of inferior vena caval signal and subsequent correction

Magnitude images from an orthogonal slice through the PV, with phase encoding along the horizontal axis and frequency encoding along the vertical axis. Aortic pulsation artefact is projected over the IVC (a), with reduced IVC signal and erroneous signal (short dashed circle) projected over an area of normal tissue. This was corrected in the same subject by swapping the phase and frequency encode directions so that the persistent aortic pulsation artefact would not be projected over vessels of interest.

Spatial misregistration can also occur because of respiratory, but also cardiac motion. Respiratory gating alone was found to be adequate in avoiding misregistration artefacts at the site of PV PCMRI measurements.

4.3.6 INTRAVOXEL PHASE DISPERSION AND VELOCITY COMPENSATION

Physiological vessel flow adopts a laminar flow profile (figure 4.5, far right) which in vessels that experience high velocity and high bulk flow can be a cause of artefact. This is because the parabolic distribution of flow velocities will result in stationary (zero velocity) spins at the vessel periphery with progressively faster spins towards the centre of the vessel. For voxels towards the periphery of the vessel, the range of velocities is much larger than voxels towards the vessel centre. The wide range of phase shifts at the vessel periphery is prone to measurement errors which can result in reduction or even complete abolition of signal at the vessel periphery. This phenomenon, known as intravoxel phase dispersion can result in erroneous underestimation of vessel size and flow. In combination with pulsatile flow and variations in flow velocities across the repetition time (TR), intravoxel phase dispersion can also cause pulsation artefacts in the phase-encoding direction (figure 4.9)[211, 338, 339].

Intravoxel phase dispersion can be addressed using flow or velocity compensation techniques. Additional bipolar gradients were inserted in the slice select and frequency-encoding directions for velocity compensation to minimise these artefacts.

4.3.7 PHASE OFFSET ERRORS

Phase offset errors affect the measurement of stationary and moving phase shifts. These are the result of local and static magnetic field inhomogeneities but also occur secondary to gradient imbalances and eddy currents [211, 345]. In the interest of increasing the speed of the acquisition, phase shifts are often calculated as simply the difference between positive and negative gradient phases. It can be argued that as background phase data would be collected in both positive and negative gradient phase acquisitions, background phase ($\phi_0(x)$) cancels out as a term in the calculation of phase shift. The more comprehensive description given at the start of this section (equation 4.11), requires a separate measurement of $\phi_0(x)$, with its inclusion in the calculation of phase shift which has the added benefit of addressing some of these errors.

Post-processing correction of phase offset errors can also be addressed using a method known as 'background compensation'. An ROI on the phase shift map is placed on stationary tissue adjacent to the vessel of interest and based on the phase shift observed in this ROI, the vessel signal can then be corrected. The latter has the potential to introduce errors in quantification and was not adopted in the methods used [182, 346, 347].

4.3.8 TEMPORAL RESOLUTION

Adequate temporal resolution is especially important in the context of pulsatile flow. Although PV flow is non-pulsatile, gentle sinusoidal variation in physiological flow has been noted through the cardiac cycle [76, 78]. No cardiac gating was used during these early attempts, but in recognition of temporal resolution errors, three repeated measurements were obtained in succession and averages were recorded for final measurements. Averaging had the added benefit of reducing errors introduced by other technical PCMRI challenges.

There are a number of methods for optimising and accelerating acquisitions to allow the acquisition of multiple PCMRI frames through the cardiac cycle, which are discussed later in this chapter.

4.3.9 DISCUSSION AND CONCLUSIONS

We have demonstrated that 2D PCMRI is feasible for measuring PV flow in the rat at 9.4T and optimised our protocols to address the challenges and settings of the method. In the assessment of PV flow, we have found V_{enc} settings at 22 cm/s or above to be adequate, developed a robust method for ensuring slice to vessel orthogonality, determined a 128x128 matrix size as providing adequate SNR and developed a strategy to deal with pulsation artefacts from the aorta. The use of velocity compensation to deal with intravoxel phase dispersion and background phase subtraction to minimise phase offset errors was also implemented, in addition to recognising the acceptability of using non-cardiac gated studies for the assessment of PV flow and the collection of three successive measurements for averaging of final results.

Early experiments demonstrated signal over the hepatic artery at lower resolution and a considerable amount of development time was invested into trying to adapt the sequence to obtain reliable measurements of hepatic arterial flow. Although the requirement for cardiac gating in the assessment of pulsatile hepatic arterial flow was an immediate hurdle, it was the inability to achieve adequate hepatic arterial SNR at higher resolution that necessitated alternative approaches to direct hepatic arterial PCMRI (Chapter 5).

4.4 REPEATABILITY, REPRODUCIBILITY AND INVASIVE VALIDATION STUDIES

4.4.1 BACKGROUND

We have previously demonstrated that PCMRI measurements of bulk PV flow are possible using the protocol developed in section 4.3.2. In this section we aim to assess the (a) repeatability and reproducibility of PCMRI measurements of bulk PV flow and compare repeatability with that of the TTUS measurements and finally (c) validate PCMRI PV flow measurements with TTUS measurements.

4.4.2 METHODS

Experimental subjects and animal preparation was as described in section 4.3.2.1.

4.4.2.1 Sample size

A pragmatic approach to sample size was used given that data collection during these studies was undertaken alongside protocol development. As parameter variability with our protocol was unknown and PV PCMRI studies had not previously been undertaken in rats, data was evaluated incrementally with a view to preliminary characterisation of parameters for future planning of adequately powered studies.

4.4.2.2 Two-dimensional PCMRI

Subjects underwent PCMRI as described in section 4.3.2.1. Data was acquired using a V_{enc} setting of 22 cm/s.

4.4.2.3 Transit-time US

Invasive TTUS measurements were performed as described previously (section 2.4.3). Briefly, a laparotomy was performed and a 2 mm TTUS probe (Transonic Systems, Ithaca, USA) was placed around the PV. Readings were taken after 10-15 minutes, once the subject was stable.

4.4.2.4 Repeatability

Fourteen healthy, naïve subjects underwent PCMRI or TTUS repeatability studies with repeat data obtained 30-45 minutes after the first measurement. For PCMRI ($n = 9$), the animal remained in the scanner after initial measurements. For TTUS ($n = 5$), the US probe was removed after the initial measurement and the laparotomy was temporarily closed during the interval before the second measurement.

4.4.2.5 Validation and reproducibility

Three subjects underwent invasive validation with TTUS, 4 weeks post-sham operation. After initial PCMRI, the animal was removed from the scanner and a TTUS measurement was recorded. For PCMRI reproducibility, the laparotomy was closed and the animal was then returned to the scanner for a second PCMRI measurement.

4.4.2.6 Statistical analysis

All PV flow measurements were normalised to explanted liver weight. Kolmogorov-Smirnov tests were used to confirm normality of variable distributions. Repeatability studies were assessed using paired t-tests, Bland-Altman analysis of agreement with calculation of the coefficient of repeatability and assessment of correlation between repeated measurements using Pearson's correlation coefficient. Given the small numbers of subjects, validation and reproducibility studies were assessed using the Wilcoxon matched-pairs signed ranks test. The threshold of statistical significance was defined to be $p < 0.05$.

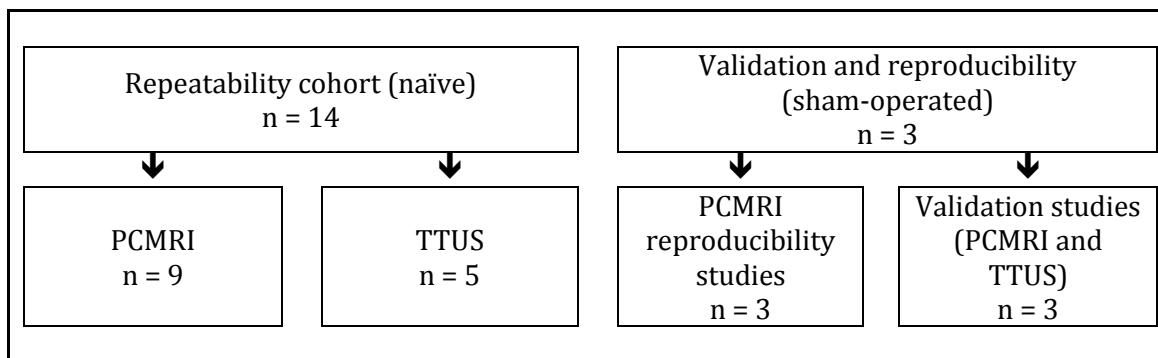


Figure 4.10: Schematic diagram demonstrating cohort sizes

Data for TTUS repeatability included four datasets previously presented in Chapter 2. Reproducibility and validation data was obtained using the same three sham-operated subjects.

4.4.3 RESULTS

No significant differences were demonstrated between repeated PCMRI (mean difference - 1.305 ± 3.973 ml/min/100g, $p = 0.7510$) or repeated TTUS (mean difference - 8.868 ± 9.189 ml/min/100g, $p = 0.3891$) PV flow measurements. The coefficient of repeatability was larger for repeated TTUS measurements (40.27 vs 23.37; TTUS vs PCMRI). Graphical analysis (figure 4.11) shows correlations between repeated PCMRI measurements were just non-significant ($r = 0.6611$, $p = 0.0525$).

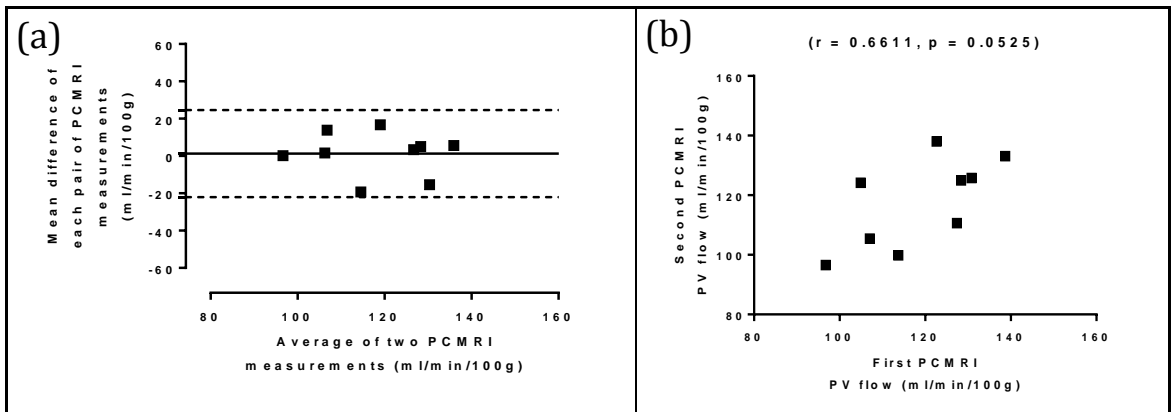


Figure 4.11: Repeatability of PCMRI PV flow measurements

Bland-Altman analysis of agreement (a) and regression analysis (b) for PCMRI. TTUS data is not presented because of the small sample size ($n = 5$).

Reproducibility of PCMRI measurements showed no significant difference between PCMRI measurements (median -19.46 ml/min/100g, $p = 0.2500$). Invasive validation in the same subject demonstrated no significant difference between the methods (median 1.306 ml/min/100g, $p = 0.5000$). Given the small sample size, this raw data is presented in table 4.3.

Table 4.3: Reproducibility and invasive validation of PV flow measured using PCMRI and TTUS

	PCMRI PV FLOW 1 (ml/min/100g)	TTUS PV FLOW (ml/min/100g)	PCMRI PV FLOW 2 (ml/min/100g)
Subject 1	134.3	133.3	166.6
Subject 2	128.3	150.8	116.2
Subject 3	154.0	155.3	173.5

4.4.4 DISCUSSION AND CONCLUSIONS

Our findings have shown that PCMRI measurements of PV flow are repeatable. When compared with a small cohort of TTUS measurements, PCMRI measurements may tentatively possess greater repeatability, as demonstrated by the smaller coefficient of repeatability and narrower mean difference confidence intervals for PCMRI measurements. Reproducibility of a small cohort of PCMRI measurements is encouraging as is direct within-subject inter-technique agreement with invasive TTUS.

4.5 EARLY STUDIES IN THE MODULATION OF PV FLOW IN CHRONIC LIVER DISEASE

4.5.1 BACKGROUND

In previous work presented in Chapter 2, PV ligation was used as a simple method for gross modulation of PV flow. While effective in achieving flow modulation, a method that could be used to achieve controlled graded changes in PV flow would be more advantageous. This would then verify the ability of the method to detect changes which may exist across a spectrum of disease or subtle haemodynamic changes induced by therapeutic agents. Mechanical modulation can be undertaken with vascular occlusion cuffs – these are placed surgically around the vessel and are inflated with air to induce varying degrees of flow restriction. Such methods can be successful with larger vessels in larger animals but based on experience from early experiments, consistent changes in small animals were difficult to achieve. Additionally, a cuff inflated with air in situ in the MR scanner has the potential to introduce significant artefact around the vessel itself, which could ultimately compromise any quantification. Flow changes in smaller vessels including hepatic artery can be achieved using micro-manipulators, but these are invasive, bulky and not available as MR compatible devices.

An alternative approach to flow modulation could be achieved using pharmaceutical agents. These have the advantage of being MR safe and potentially administered to the animal while remaining in situ in the scanner (e.g. by IV route). Dose-dependent responses can also then potentially be used to investigate graded changes in PV flow. In this section, studies of PV flow modulation were undertaken using L-N^G-nitro arginine methyl ester (L-NAME) and terlipressin.

Nitric oxide is an endogenous smooth muscle relaxant which causes physiological vasodilatation and increased blood flow. By inhibiting nitric oxide synthetase, L-NAME is able to reduce nitric oxide levels, thereby triggering vasoconstriction and reduced flow. Even when administered systemically, L-NAME driven reductions in splanchnic blood flow have been observed [348]. Terlipressin is a clinically used long-acting vasopressin analogue acting primarily on vascular, renal and pituitary vasopressin receptors. Action on V1a receptors in the splanchnic vascular bed is thought to reduce PV blood flow, forming the basis of clinical use of terlipressin in the management of variceal bleeds [349].

In this section we aim to assess the ability of PCMRI to detect expected changes in PV flow after (a) L-NAME and (b) terlipressin administration and finally (c) evaluate any differences in the response to terlipressin between normal and diseased rats.

4.5.2 MATERIAL AND METHODS

4.5.2.1 Experimental subjects

Experimental subjects were maintained as described in section 4.3.2.1.

To study differential responses to terlipressin in models of liver disease, subjects weighing 250-300g were randomised to bile-duct ligation (BDL) procedure ($n = 4$) or sham laparotomy ($n = 4$). BDL and sham surgery was conducted as described previously by researchers at our institution [350]. Briefly, a midline abdominal incision was made under 2% isoflurane and intraperitoneal levobupivacaine. For animals undergoing BDL procedure, the common bile duct was isolated, triply ligated with 3-0 silk and sectioned between the ligatures. After closure and recovery, animals were maintained for 5 weeks to allow the development of portal hypertension and features of chronic liver disease. Data from previous validation of the BDL model at our institution is presented in table 4.4, demonstrating deranged liver function tests, reduced plasma oncotic pressure and raised portal pressure in the BDL cohort in keeping with features of chronic liver disease.

Table 4.4: Differences between sham and BDL Sprague-Dawley rats at 5 weeks

	SHAM ($n = 6$)	BDL ($n = 6$)
<i>Weight</i>		
Baseline	325±8g	320±7g
6 weeks	509±16g	453±15g
<i>Liver function</i>		
ALT	108±10 IU/L	161±23 IU/L*
AST	169±16 IU/L	703±113 IU/L*
Bilirubin	3.0±0.3 IU/L	197.3±18 IU/L*
<i>Plasma oncotic pressure</i>	12.8±0.5 mmHg	9.3±1.1 mmHg*
<i>Portal pressure</i>	6.3±0.4 mmHg	15.8±2.2 mmHg*

(all parameters given as mean ± standard error of the mean; * $p < 0.05$)

4.5.2.2 Animal preparation

Animal preparation was as described in section 4.3.2.1.3, with additional siting of a 0.58 mm internal diameter fine bore polyethylene line (Portex, Smiths Medical, Kent, England) in the jugular vein after initial induction with isoflurane and before transfer to the MR scanner.

4.5.2.3 Two-dimensional PCMRI

Subjects underwent PCMRI as described in section 4.4.2.1.

4.5.2.4 L-NAME response

Pilot experiments using TTUS to monitor PV flow were performed on the bench to determine the dosage regime (Appendix A). After baseline PCMRI measurements, four normal subjects received a 10 mg/kg bolus of L-NAME administered intravenously through the previously sited jugular venous line. Repeat PCMRI measurements were performed 10-15 minutes after the drug was given.

4.5.2.5 Terlipressin response

Pilot experiments using TTUS to monitor PV flow were performed on the bench to determine the dosage regime (Appendix A). After baseline PCMRI measurements, sham ($n = 4$) and BDL ($n = 4$) subjects received a 100 μ g/kg bolus of terlipressin acetate (Glypressin, Ferring Pharmaceuticals, UK) administered intravenously through the previously sited jugular venous line. Sequential PCMRI measurements were obtained for 30-40 minutes post-administration.

4.5.2.6 Statistical analysis

All PV flow measurements were normalised to explanted liver weight. Given the small sample sizes, a normal distribution was not assumed and Mann-Whitney U tests were used for unpaired comparisons and Wilcoxon matched-pairs signed rank tests were used for paired comparisons. For sequential flow measurements in sham and BDL animals receiving terlipressin, data was plotted and fitted using smoothed cubic spline interpolation to demonstrate the coarse trend across each cohort. The threshold of statistical significance was defined to be $p < 0.05$.

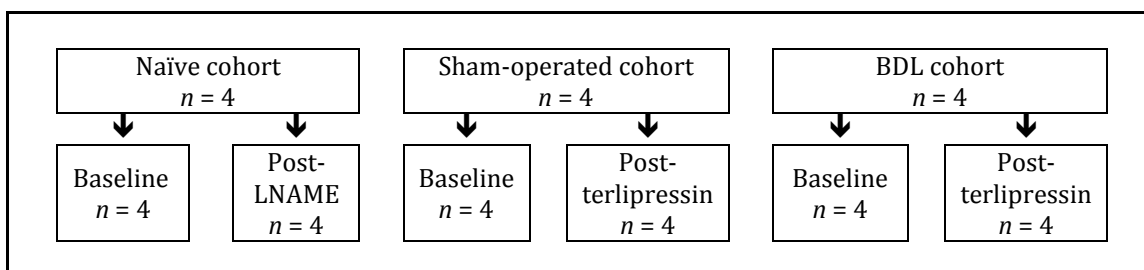


Figure 4.12: Schematic diagram demonstrating cohort sizes

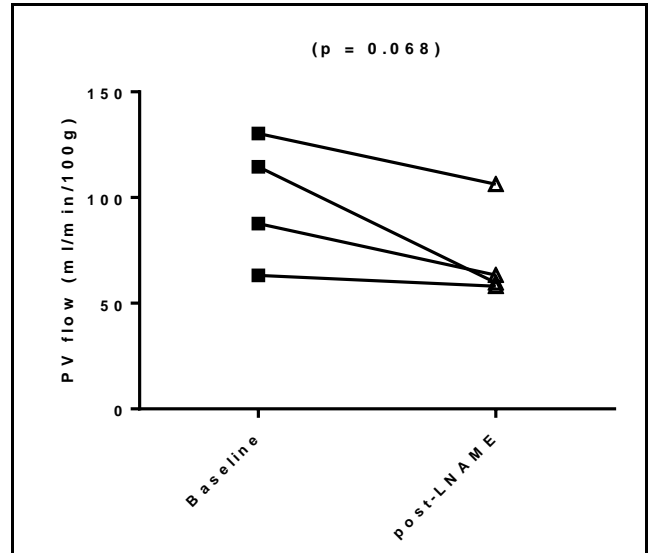
Paired baseline and post-treatment data was obtained for all subjects in each cohort. Unpaired analyses were undertaken between sham and BDL cohorts at baseline and for nadir post-terlipressin PV flow. Reproducibility and invasive validation data was collected for $n = 3$ of the sham operated cohort (presented section 4.4.2).

4.5.3 RESULTS

Mean baseline PV flow in normal rats was 98.95 ± 14.80 ml/min/100g, which dropped to 71.84 ± 11.55 ml/min/100g 10-15 minutes after LNAME administration, but this difference was just above the significance threshold ($W = -10.00$, $p = 0.0680$).

Figure 4.12: Baseline and post-LNAME PCMRI PV flow in normal rats

Reductions in mean PV flow were consistently observed in all subjects post-LNAME, but this was found to be just non-significant.



After 5 weeks, mean sham body weight exceeded BDL body weight (531 ± 38 g vs 427 ± 42 g, $p = 0.0286$), however in keeping with development of chronic liver injury, mean sham liver weight was significantly less than mean BDL liver weight (19 ± 1.4 g vs 32 ± 2.2 g, $p = 0.0286$). Both cohorts responded to terlipressin differently, with sham animals starting with higher baseline flow, dropping PV flow but then generally showing a trend toward returning to baseline. This was not consistently seen in BDL animals (figure 4.13).

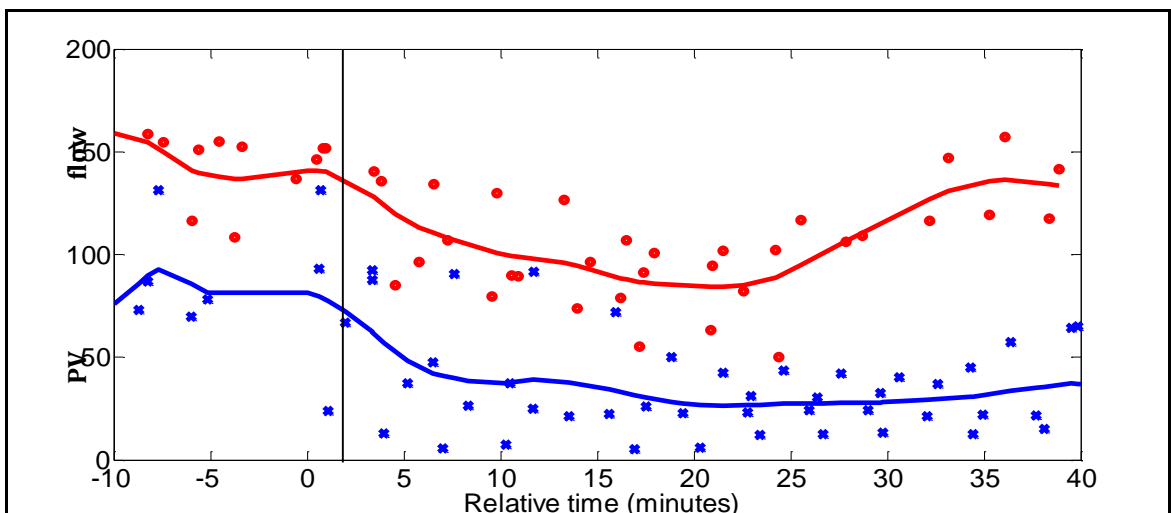


Figure 4.13: Scatter plot of PV flow changes in sham and BDL animals

Sham ($n = 4$) and BDL ($n = 4$) PV flow data plotted on a single chart, with solid lines representing the coarse trend fitted using smoothed cubic spline interpolation. Terlipressin was administered at a relative time of zero minutes.

Mean sham baseline PV flow was higher than in BDL animals (143.5 ± 7.209 vs 79.51 ± 22.37 ml/min/100g, $p = 0.0571$), but this difference was just above the significance threshold (figure 4.14a).

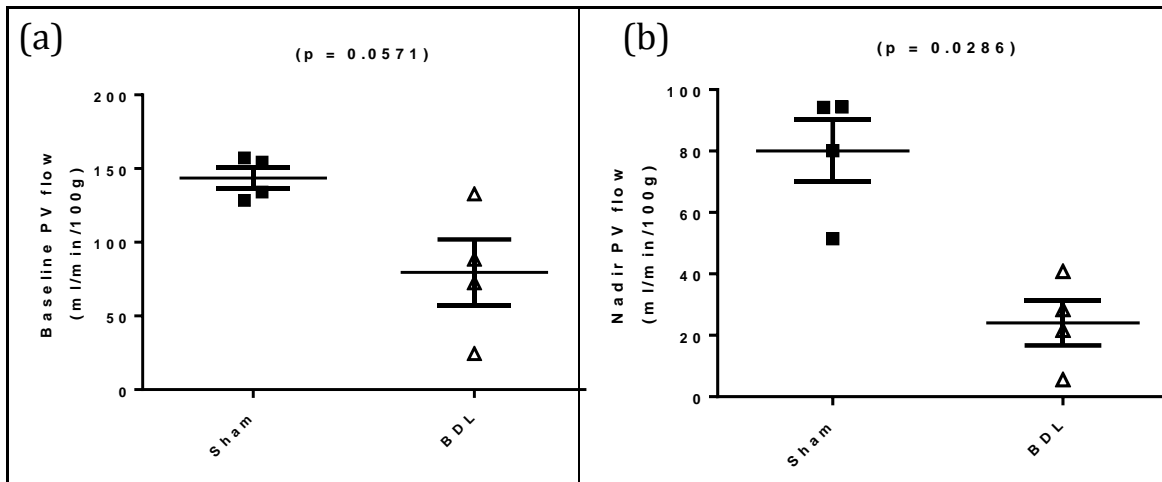


Figure 4.14: Baseline (a) and nadir (b) PV flows post-terlipressin in sham and BDL rats

Mean baseline PV flow was higher in sham operated animals, but this difference was just non-significant. A significant difference in nadir PV flow after terlipressin was demonstrated between sham and BDL cohorts.

Both cohorts responded to terlipressin with reductions in PV flow (figure 4.15), but for both sham (mean difference -63.48 ± 7.138 ml/min/100g, $p = 0.0680$) and BDL cohorts (mean difference -55.44 ± 17.86 ml/min/100g, $p = 0.0680$), these differences were just non-significant. Nadir sham PV flow after terlipressin however, was significantly different to that of BDL animals (80.05 ± 10.09 vs 24.07 ± 7.330 ml/min/100g, $p = 0.0286$) (figure 4.14b).

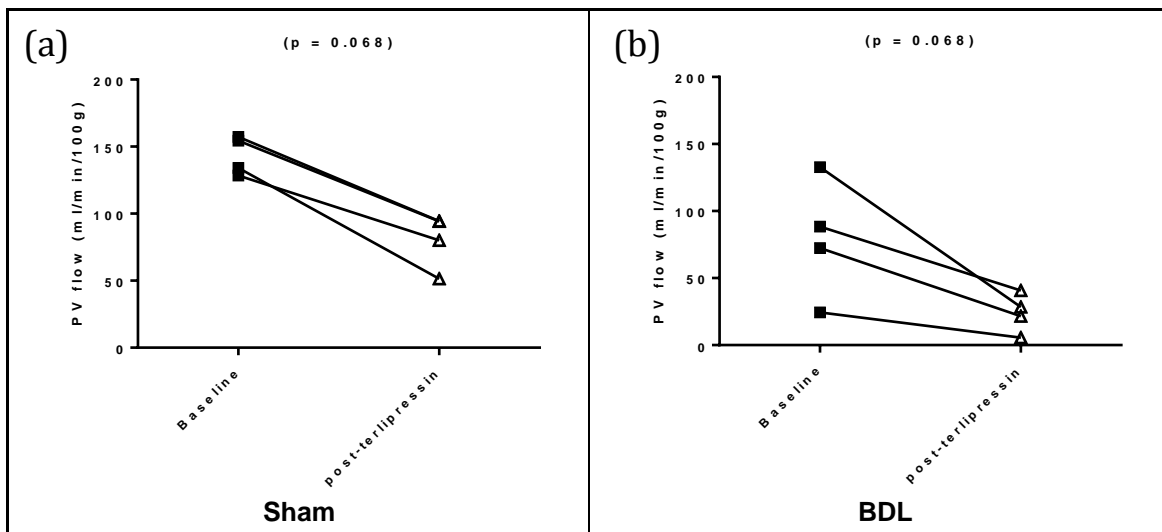


Figure 4.15: Reductions in PV flow after terlipressin in sham (a) and BDL (b) rats

Expected reductions in PV flow were observed in both the sham (a) and BDL (b) cohorts although these differences were just non-significant in both cohorts.

4.5.4 DISCUSSION

The only statistically significant haemodynamic comparison was of nadir PV flow post-terlipressin between sham and BDL cohorts. Reductions in PV flow after L-NAME and terlipressin were however consistently noted in all subjects, though these were all just over the significance threshold. This suggests a potential for type II errors, secondary to small sample size rather than genuine non-significant differences. It is worth noting that if assuming a normal distribution (which would be expected for each of these haemodynamic parameters), the use of Student t-tests would demonstrate significant differences in all of the comparisons undertaken. In view of the likelihood of type II errors, trends from this small sample size early data are encouraging and suggest that PCMRI has potential for evaluation haemodynamic changes in response to pharmacological modulation. Interestingly, our data has also demonstrated haemodynamic differences in between healthy and diseased animals, which though previously described [351-353] has never previously been described using PCMRI.

We have demonstrated the use of pharmacological agents to modulate PV flow. Both sham and BDL cohorts demonstrated reductions in PV flow post-terlipressin, which were more profound in the BDL cohort as shown by significantly lower nadir PV flow. While the use of pharmacological agents to modulate PV flow have the previously mentioned advantage of being non-invasive and easily studied without perturbing the animal in the scanner, our data also underlined some of the disadvantages of using systemic agents. Firstly agents administered into the systemic blood stream will invariably exert effects on other organs, and particularly in the case of vasoactive substances (such as LNAME and terlipressin) the concern would be over confounding effects on the systemic vasculature. Both of these drugs are known to affect mean arterial pressure, and potentially systemic vascular resistance both of which undermine the evaluation of the haemodynamic changes in the context of hepatic rather than systemic factors. In order to make inferences regarding haemodynamic changes secondary to liver disease, attempts must be made to measure and control for these systemic changes. Secondly, pharmacological agents may exert specific and dose-dependent effects, but these effects are much more prone to inter-subject variation than with mechanical flow modulation.

4.5.5 CONCLUSION

Pharmacological agents such as LNAME and terlipressin can be used to modulate PV flow and these changes in PV flow can be measured using PCMRI. BDL can be used to establish pathological features of chronic liver disease and preliminary studies have demonstrated reduced baseline PV flow in disease. Reductions in PV flow elicited by terlipressin can be measured with PCMRI and we have shown a differential response to terlipressin between sham and BDL rats.

4.6 IMPLEMENTATION OF CARDIAC GATING

4.6.1 BACKGROUND

In part (a), we underlined the need for cardiac gating in the assessment of pulsatile blood flow. Findings presented in sections 4.3 and 4.4 were based on non-cardiac gated data which though suboptimal were important in demonstrating the potential of PCMRI for generating repeatable, reproducible, accurate measurements, amenable to the study of flow changes and chronic liver disease. Although the assumption of non-pulsatile flow in the PV may be physiologically acceptable, non-cardiac gated data is likely to be more error prone and inadequate in the assessment of pathological scenarios where PV flow has the potential to become more pulsatile (e.g. portal hypertension, dehydration, sepsis, etc.). Additionally, any attempt to accurately measure hepatic arterial flow with PCMRI would be impossible without cardiac gating.

A cardiac gated PCMRI study would produce multiple velocity maps as part of a single study, each representative of a phase in the cardiac cycle. Bulk flow measurements for a vessel at each stage of the cardiac cycle could then be interpolated so that the area under the interpolated points would then represent bulk vessel flow through the cardiac cycle. For robust cardiac gating, each phase-encoding step needs to be acquired at exactly the same stage in the cardiac cycle and this can only be achieved if there is accurate synchronisation of the pulse sequence with the cardiac cycle.

Monitoring of the cardiac cycle is classically undertaken using an electrocardiogram (ECG) trace. Typically, clinical MR systems usually apply four electrodes to obtain limb lead traces with the main objective being consistent detection of the R-wave and R-R interval (figure 4.16a). The application of magnetic field gradients in the scanner have the potential to induce currents in ECG electrodes thereby corrupting the signal. This effect is minimised by placing the electrodes closer together, but must be traded-off against the physiological improvement in ECG signal obtained by positioning electrodes as far apart as possible [339]. This is a particular problem in preclinical systems, where the small animal and scanner bore-hole size, increased gradient strength and less robust ECG systems can pose a significant challenge.

Radiofrequency interference with the ECG signal poses another challenge to accurate monitoring. Filtering of ECG waveform has been developed on clinical systems to aid with these issues but this is yet another area of difficulty on preclinical systems.

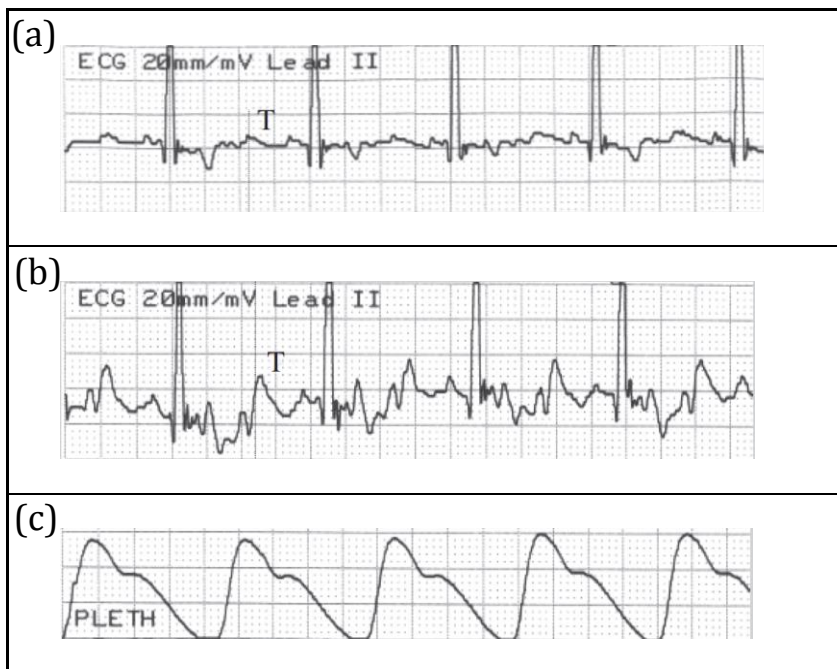


Figure 4.16: Clinical cardiac monitoring with ECG and pulse oximetry

ECG trace (a) was obtained outside the magnet bore while ECG trace (b) was obtained inside the magnet bore. Note the increased baseline artefact. Trace (c) was obtained with a finger pulse oximetry probe in the same patient, while in the magnet bore. (Traces obtained from reference [339]).

Pulse oximetry or photoplethysmography is another method for monitoring the cardiac cycle. A probe is typically placed on a finger tip (clinical system) or paw (preclinical system). Light absorbance fluctuates with the cardiac cycle so that signal peaks are comparable to R-R interval. Because the monitoring occurs at an extremity distal to the heart, it can be argued that there is a delay between pulse oximetry and R-wave peaks, which may compromise the timing of pulse oximetry based gating. Nonetheless, the use of pulse oximetry signals for cardiac gating has been tested on clinical systems and avoids the issues that arise in ECG monitoring from induced currents and/or RF interference [354].

There are a number of approaches to synchronising MR acquisitions with the cardiac cycle, broadly falling into either prospective or retrospective gating strategies. Prospective gating strategies involve acquisitions that only collect data at the required stage of the cardiac cycle. Retrospective strategies usually involve continuous acquisitions with post-acquisition sorting of data into relevant stages of the cardiac cycle and possible discarding of useless or corrupted data [338].

The method applied in this study is prospective and can be described as “fixed delay multiphase cardiac triggering”. The size of the R-R interval can be estimated from the subject’s heart rate. The researcher can then choose to collect data for any number of phases in the cardiac cycle, as long as the interval between successive phases is not less than the repetition time. Upon detection of an open cardiac (and respiratory) gate, the sequence is triggered initially with zero delay, acquiring data all with the same phase

encoding amplitude, followed by data at progressively increasing phase encoding amplitude to complete the data set. To acquire the data from the next phase in the cardiac cycle, a fixed delay is then applied after detection of an open cardiac gate and the process is repeated once again. The delay is incremented progressively, based on predefined heart rate and researcher preference so that multiple phases are thus acquired through the cardiac cycle (figure 4.17)[355].

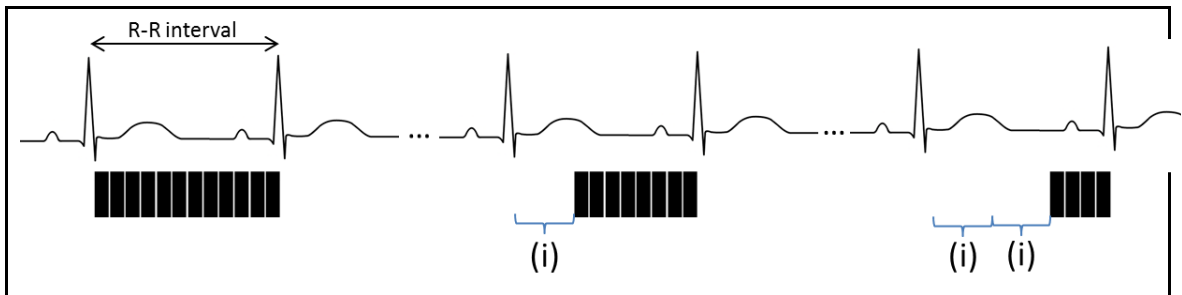


Figure 4.17: Fixed delay multiphase cardiac gating

Acquisitions are triggered by the start of the cardiac cycle, with initial acquisitions obtained with zero delay (far left). After the complete acquisition of a single phase, a successive fixed delays of size (i) were introduced for the acquisition of each subsequent phase. For phases later in the cardiac cycle, acquisition times were much longer because the smaller cardiac gate acquisition window (far right).

From work presented in section 4.5, an assessment of systemic haemodynamics would be useful in the context of contextualising the significance of absolute hepatic flow measurements but also to control for systemic haemodynamic consequences of disease or pharmacological modulation. A possible non-invasive MRI based strategy to address this would be to use cardiac-gated PCMRI to measure aortic root flow and thereby estimate cardiac output.

With this in mind, in this section we aim to (a) implement fixed delay multiphase cardiac gating for PCMRI (b) evaluate portal venous, inferior vena cava and aortic root flow using cardiac gated PCMRI and (c) validate cardiac gated PCMRI PV flow measurements with TTUS measurements in the same subject.

4.6.2 METHODS

4.6.2.1 Experimental subjects

Experimental subjects were maintained as described in section 4.3.2.1.2.

4.6.2.2 Sample size

A pragmatic approach to sample size was used given that data collection during these studies was undertaken for the purpose of protocol development. As parameter variability with cardiac-gated PV PCMRI measurements was unknown, data was evaluated with a view to inform protocol development and provide preliminary characterisation of parameters for future planning of adequately powered studies.

4.6.2.3 Animal preparation

Animal preparation was as described in section 4.3.2.1.3. Healthy, naïve animals were used.

4.6.2.4 Fixed delay multiphase cardiac gated PCMRI

Once positioned in the scanner, anatomical images were obtained to confirm vessel orthogonality as described in section 4.3.3. IVC flow measurements were obtained from the same slice used to measure PV flow ($n = 6$), with dedicated anatomical planning for the aortic root ($n = 5$). PCMRI planning provided time for the animal to settle before evaluating subject heart rate. Because of time constraints, fixed delays were calculated for only six phases through the cardiac cycle. Two-dimensional PCMRI as described in section 4.3.2.1.4 was then performed when cardiac and respiratory gates were both open, with addition of successive fixed delays to obtain data for successive phases in the cardiac cycle. Data for PV and IVC flow was acquired using V_{enc} settings of 33 cm/s (based on the assumption that 33 cm/s would be suitable for the larger vessel size and flow volumes expected in the IVC) and aortic root flow measurements were acquired using V_{enc} settings of 133 cm/s. Single multiphase acquisitions were collected rather than three datasets as previously.

4.6.2.6 Validation

Four subjects under invasive validation with TTUS using methods described in section 4.4.2.2. To control for physiological sequelae of laparotomy and PV instrumentation, laparotomy was performed and the PV was dissected before abdominal closure and initial PCMRI. To match the procedural sequence described previously, the animal was then removed from the scanner and a TTUS measurement was recorded.

4.6.2.7 Statistical analysis

All PV flow measurements were normalised to explanted liver weight. IVC and aortic root bulk flows were not normalised. Given the small sample size of the validation cohort ($n = 4$), a normal distribution was not assumed and a Wilcoxon matched-pairs signed rank tests were used for paired comparisons. The threshold of statistical significance was defined to be $p < 0.05$.

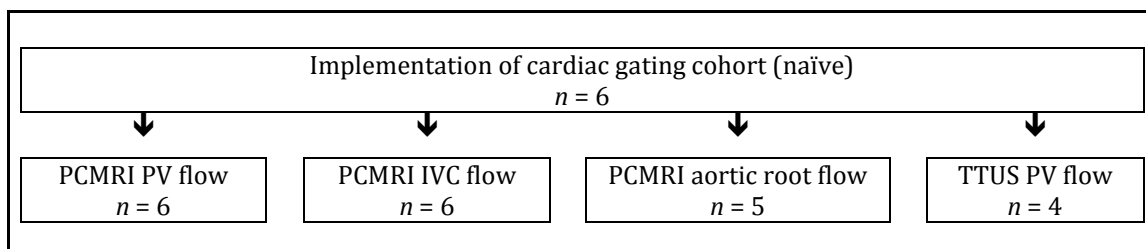


Figure 4.18: Schematic diagram demonstrating cohort sizes

A cohort of six subjects was used in which, five had aortic root flow measured and four had invasive TTUS flow measurements undertaken.

4.6.3 RESULTS

4.6.3.1 Cardiac monitoring

Early cardiac monitoring was attempted using a dual electrode single lead system (SA instruments, New York, USA). Although expected deterioration in the cardiac signal was observed once the animal was sited in the scanner, RF interference introduced artefacts that obscured QRS complexes to the extent that the R-R interval could not be consistently identified once RF pulsing began.

To address this challenge, a small animal pulse oximeter (Starr Lifesciences, Pennsylvania, USA) was used. The pulse oximeter was designed to output a digital trace via USB to a dedicated software package provided by the manufacturer, which while adequate for recording heart rate and oximetry data was not suitable for scanner gating. The signal processing module was returned to the manufacturer for addition of a female Bayonet Neill-Concelman (BNC) connector to enable output of analog signal. This arrangement avoided the added signal processing delay introduced by the computer but the raw signal was still not adequate for cardiac gating and a further step of signal processing was required (figure 4.19).

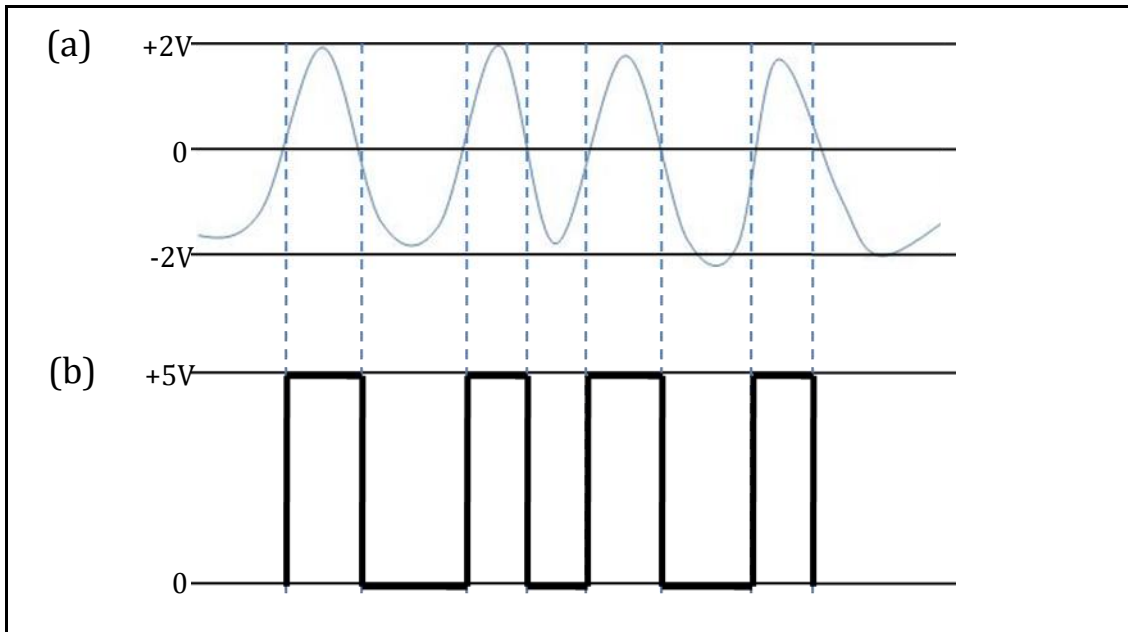


Figure 4.19: Raw analog signal and the required signal form for cardiac gating

Raw analog signal (a), had a sinusoidal alternating current waveform. The required signal form (b) was a positive square wave, with larger amplitude than the raw signal.

Three steps were required to convert the raw analog signal into the required format: firstly the wave had to be converted into a squared wave, secondly a direct current offset would need to be added to the signal to ensure it remained positive and thirdly the signal would need to be scaled to consistently reach the required threshold of five volts.

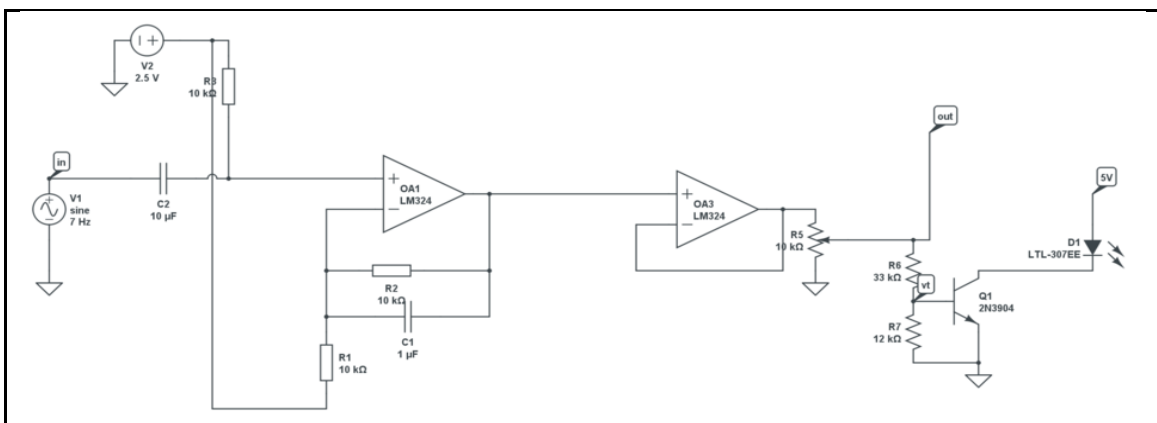


Figure 4.20: Schematic circuit design for the pulse oximetry analog signal processing unit

Input would arrive through a BNC connector in the form of an analog sine wave as shown in figure 4.17a at the far left of the diagram ('in'). Signal would undergo potentiometer driven amplification with signal output through a BNC connector ('out'). An LED would be used as visual indicator of the gated signal (far right of the diagram).

To achieve this, a signal processing unit was developed. A schematic design was produced and simulated online (Circuitlab, Mountain View, USA) (figure 4.20). This was then

constructed on a breadboard (figure 4.21a), tested and then formally set up on a printed circuit board (PCB) with a protective box for more robust day-to-day use (figure 4.21b).

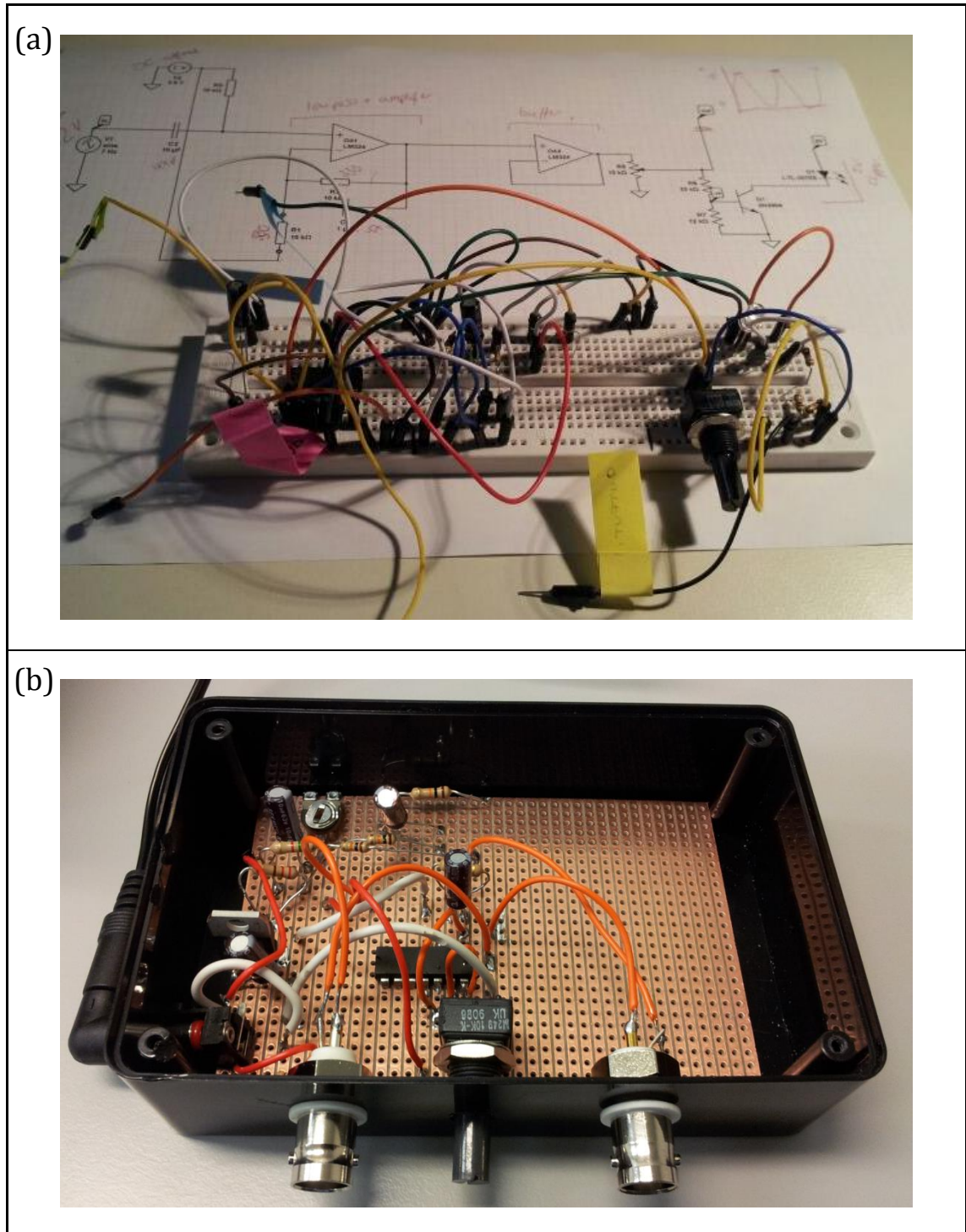
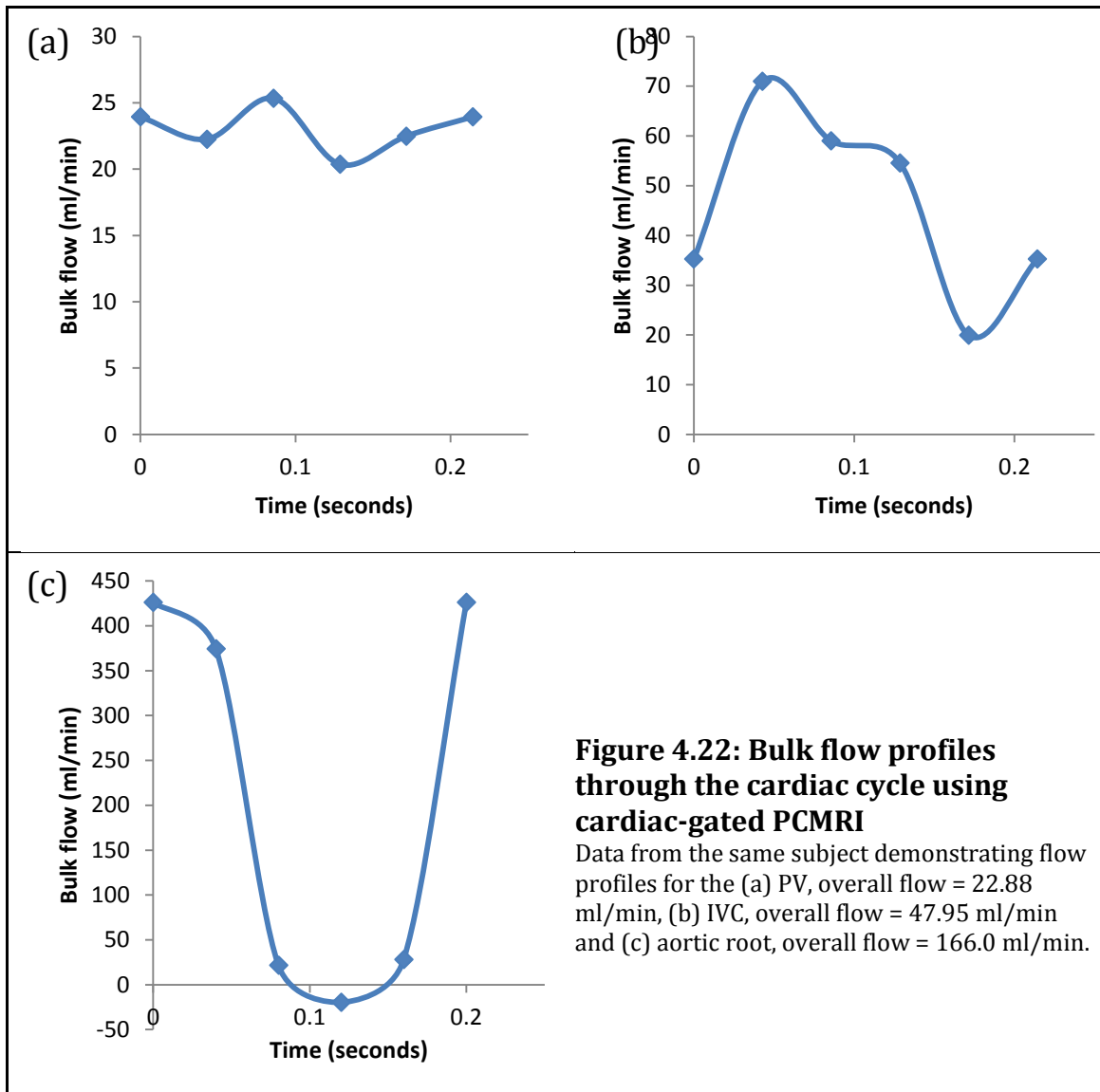


Figure 4.21: Construction of the pulse oximetry analog signal processing unit

Designs were initially structured and tested on breadboard (a) before permanent PCB construction with protective box (b). Input (right) and output (left) BNC connectors are shown with the potentiometer placed between the sockets.

4.6.3.2 Fixed delay multiphase cardiac gated PCMRI

Using pulse oximetry to monitor the cardiac cycle, consistent cardiac-gating using fixed delay multiphase cardiac gated PCMRI was attempted. Waveforms from a single subject for bulk flow through the cardiac cycle in the PV, IVC and aorta are shown in figure 4.22.



Bulk flow measurements in the portal vein (200.1 ± 16.20 ml/min/100g), IVC (44.10 ± 2.628 ml/min) and aortic root (174.5 ± 25.05 ml/min) were calculated from flow profiles and plotted in figure 4.23.

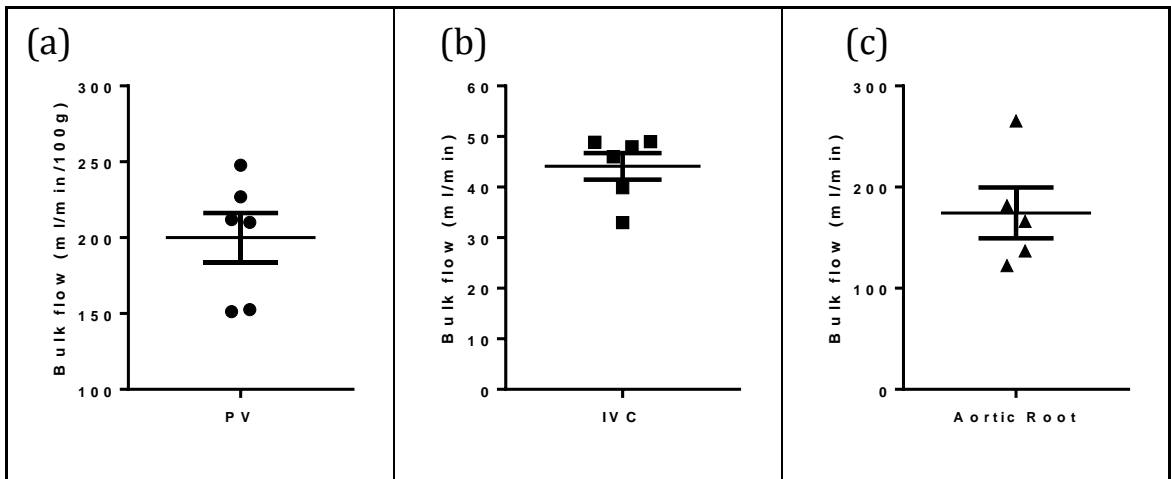
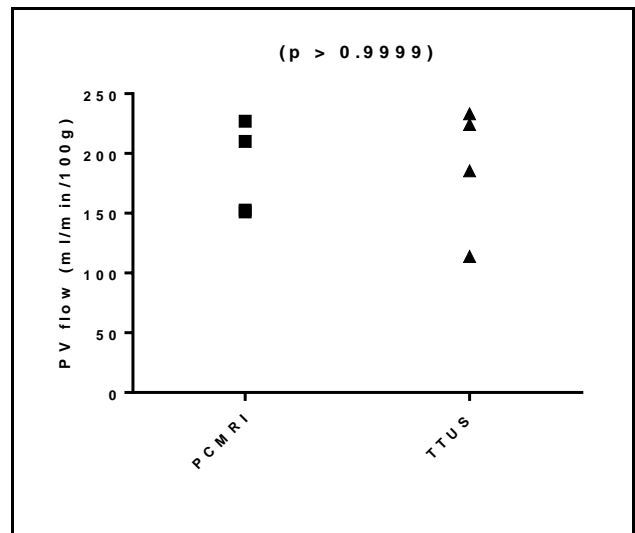


Figure 4.23: Average bulk flow measurements of the (a) PV, (b) IVC and (c) aortic root

Invasive validation in the same subject demonstrated no significant difference between cardiac gated PCMRI and invasive TTUS PV flow measurements (median difference 10.25 ml/min/100g, $p > 0.9999$).

Figure 4.24: Normalised PV flow measured with cardiac-gated PCMRI and invasive TTUS

Paired data from measurements in the same subjects demonstrated a non-significant difference between flow measurements.



4.6.4 DISCUSSION

Any cardiac gating strategy is reliant on accurate monitoring of the cardiac cycle. Faced with the challenges of small animal ECG monitoring, we have developed a system to modify the signal from a small animal pulse oximetry device to provide a useful signal for cardiac gating. Applying this system, we have shown pulse oximetry can be used to collect gated PCMRI data with fixed delay multiphase cardiac triggering in vessels with highly pulsatile and less pulsatile flow. We have also shown encouraging inter-technique agreement between cardiac gated PCMRI and invasive TTUS measurements of PV flow.

An important criticism of pulse oximetry based cardiac gating is the delay between the cardiac contractile events and pulse oximetry signal changes at the periphery. This could explain the morphology of the aortic root flow curve (figure 4.22c), where the first (zero delay) data point is seen to lie at the peak of the flow curve. Errors arising from this can be overcome if the earlier part of the flow curve is sampled later on in the cardiac cycle.

Fixed delay multiphase cardiac triggering has the advantage of being simple to implement, but there are number of weaknesses with this method which can affect quantification. Firstly, the researcher calculates an R-R interval and determines a fixed delay based on the assumption that the R-R interval is constant throughout the experiment. While this is unlikely to affect earlier phases in the cardiac cycle, this can be troublesome for later phases resulting in undersampling of phases through the cardiac cycle (and underestimation of flow) if the R-R interval has extended or overlap of final phases with the start of the next cardiac cycle (and therefore over estimation of flow) if the R-R interval has shortened. A possible strategy to overcome these issues is to intentionally over sample phases to ensure there is overlap with the start of the next cardiac cycle. The researcher can then retrospectively discard overlapped data or use the additional data if R-R prolongation arises [355].

Another important disadvantage is the duration of multiphase acquisitions. Because of sequential cardiac cycle phase acquisitions, the introduction of delays results in wasted, unused time during the acquisition window when both respiratory and cardiac gates are open. This extends acquisition time so that even with only six phases, a single set of measurements on a vessel could take as long as 40 minutes to obtain. Because of the time taken to obtain a single set of cardiac-gated measurements, it was not possible to use multiple averages as a method of eliminating sampling errors. It is also worth noting that while cardiac gated PCMRI is likely to be viable for haemodynamic studies in models of disease, the duration of the fixed delay multiphase acquisition will prove challenging.

Studies involving more delicate diseased models undergoing haemodynamic stress using vasoactive pharmacological agents will require faster acquisition methods as the temporal window for measuring these changes is likely to be short.

Reducing the number of phases inherently reduces the accuracy of the measurement, especially for high velocity, high volume pulsatile vessels such as the aorta. It has also been demonstrated from clinical data that the use of six phases is likely to underestimate bulk flow, by as much as 25% of the measurements made with double the number of cardiac cycle phases [182]. Early validation data would however suggest that six phases through the cardiac cycle is adequate for PV flow measurement. Underestimation is however likely to be more of an issue for more pulsatile vessels such as the aorta and this could certainly account for the wide variance of the aortic root flow measurements (figure 4.22c). The significant difference demonstrated between cardiac gated PCMRI PV flow measurements and previously obtained non-cardiac gated data (section 4.3.2) could also be explained by this phenomenon (figure 4.25).

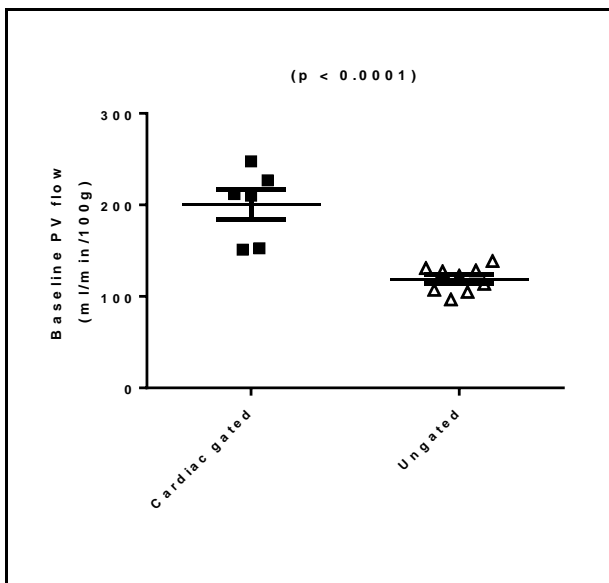


Figure 4.25: PV flow measured using cardiac-gated and non-cardiac gated PCMRI

Cardiac gated PCMRI PV flow (left) (mean 200.1 ± 16.20 ml/min/100g), was significantly different to previously presented respiratory but not cardiac gated PCMRI PV flow data (right) (mean 118.9 ± 4.663 ml/min/100g).

Finally, the drive towards cardiac gated measurements was specifically aimed at attempts to measure hepatic arterial flow. Unfortunately our experience demonstrated that even with cardiac gating, SNR over the hepatic artery was still too low to feasibly measure bulk flow.

4.6.5 CONCLUSION

Fixed delay multiphase cardiac gating can be used with pulse oximetry to evaluate bulk PV, IVC and aortic root flow. We have also demonstrated encouraging preliminary inter-technique agreement of cardiac gated PCMRI bulk PV flow with TTUS.

4.7 CLOSING COMMENTS

We have discussed in this chapter the implementation and optimisation of two dimensional PCMRI to measure PV flow, demonstrating repeatability and invasive intra-subject inter-technique agreement of these measurements. We have shown that the technique can be used to evaluate bulk vessel flow in models of chronic liver disease and have preliminarily demonstrated haemodynamic differences in disease both at baseline and during pharmacological stress. Finally, we have implemented cardiac gating for measurement of pulsatile vessel flow.

Although the PCMRI methods developed in this chapter are promising, measurement of hepatic arterial flow remains elusive. Additionally, the extended acquisition times for fixed delay multiphase cardiac gating are not feasible for studies of pharmacologically induced haemodynamic stress. Moving forward, a practical strategy to tackle both of these challenges will be required for accurate and robust assessment of liver blood flow.

CHAPTER 5

PCMRI - NEW TECHNIQUES AND METHODS

“...it is born
of your invisible
machinery,
it flies
from your tireless
confined mill,
delicate
powerful
entail,
ever alive and dark...”

- Ode to the liver [2].

5.1 INTRODUCTION

Early experience with PCMRI allowed the development of strategies to overcome technical challenges, but failed to deliver a reliable method for measurement of hepatic arterial (HA) flow. Additionally, acquisitions remained time consuming and prohibitive of reasonable haemodynamic studies in animal models of disease or studies of pharmacological stress.

In this chapter we review the conceptual development for strategies to overcome these challenges before implementation, validation and studies of pharmacological stress using a novel approach on a preclinical system. In the final section of this chapter, we translate these methods to a clinical system and investigate hepatic haemodynamic changes in normal human volunteers during physiological stress.

5.2 AUTHOR CONTRIBUTIONS

In fulfilment of the aims in this chapters, I: (a) conceptualised, developed and implemented the novel method presented at the start of this chapter, (b) prepared and conducted all animal scanning experiments; (c) developed preclinical PCMRI protocols; (d) developed Matlab code for PCMRI quantification; (e) performed surgery and collected invasive TTUS measurements of PV flow; (f) performed US guided injections of fluorescent microspheres and conducted all post-processing of samples for quantification; (g) conducted bench-top experiments prior to MRI scanning for the development of protocols for the administration of terlipressin; (g) translated, developed and optimised clinical PCMRI protocols; (h) recruited normal volunteers into validation, reproducibility and post-prandial flow studies; (i) supervised the scanning of all normal volunteer scans; (j) collected and analysed all the data; and (k) prepared all the material contained within this chapter.

Alan Bainbridge developed preclinical MR sequences. Cine sequences originally developed by Tom Roberts and were adapted by Alan Bainbridge for hepatic PCMRI. Matlab code for preclinical PCMRI quantification was based on previous work by Raj Ramasawmy and was subsequently redesigned and adapted using techniques developed in Chapter 4. Cardiac cine MRI sequences were originally developed by Anthony Price and adapted by Alan Bainbridge. For establishment of small animal intravenous access, I received help from Val Taylor. Sham-operated and bile-duct ligated rats were prepared by Abe Habtieson. Pharmacological modulation of PV flow was developed under the guidance of Nathan Davies. Microsphere post-processing was informed by protocols provided by Nathan Davies.

With additional input from David Atkinson, proprietary clinical PCMRI sequences were adapted by Alan Bainbridge for hepatic applications. Normal volunteer recruitment took place using ethical approval originally sought by Margaret Hall-Craggs. All clinical scans were conducted by MRI radiographers. Statistical power calculations were undertaken by Paul Bassett.

5.3 CONCEPTUAL DEVELOPMENT

The assessment of HA flow with PCMRI is challenging in both preclinical and clinical contexts. In rodents, the vessel itself is extremely small – less than 1 mm in diameter – and as a testimony to the challenges of studying small animal HA flow, all published invasive studies have been performed with placement of a transit-time ultrasound (TTUS) probe around the coeliac artery and ligation of the gastric and splenic branches so that coeliac and HA flow are equivalent [340, 356, 357]. Even when imaging with a 9.4T system, obtaining sufficient HA signal-to-noise ratio (SNR) is challenging. At lower resolution, HA signal is often visualised, but this is simply insufficient for reliable visualisation once the matrix size is increased (figure 4.8). The increased matrix size also brings the disadvantage of extended acquisition times, which can be critical during *in vivo* studies. Increasing slice thickness can on occasion be used to improve SNR, but for fine vessels like the hepatic artery, this risks the introduction of further errors. HA tortuosity, branching and anatomical variants all increase orthogonality errors, small region of interest (ROI) size can result in errors from partial voluming and intra-voxel phase dispersion and finally, in the absence of robust cardiac gating strategies, problems with spatial misregistration and errors in the estimation of pulsatile flow. It is also worth noting that although the hepatic artery was visualised at lower resolution, good planning of 2D PCMRI studies requires a good understanding of subject-specific vessel anatomy. The high resolution planning studies required to collect this data were simply beyond the time constraints of feasible *in vivo* work.

The technology to directly measure HA flow on clinical systems with PCMRI has been available for many years but because of challenges associated with the method, very few PCMRI HA flow studies have been published [197-199, 205]. Obtaining adequate SNR is less of an issue given the approximate vessel diameter (4-8 mm), although problems with partial voluming and spatial resolution have been identified as an issue for measurements, particularly with 1.5T systems [205]. Anatomical variants have been cited as a particular problem precluding systematic planning strategies. Incidence of variants have been cited as occurring in anything from 10-40% of the population (figure 5.1) [358-360]. Two-dimensional PCMRI studies that have measured hepatic arterial flow describe several methods for ensuring appropriate planning and vessel orthogonality but all highlight the difficulties associated with anatomical variants, vessel tortuosity and the requirement for good anatomical images combined with radiological expertise for adequate planning to occur. Finally, the measurement of hepatic arterial flow with 2D PCMRI is often complicated by the site of measurement – an issue exacerbated by

confusing nomenclature. The so-called ‘common’ hepatic artery arises directly from the coeliac axis and is the origin of both the ‘proper’ hepatic artery (which provides the definitive arterial supply to the hepatic vascular bed) and the gastroduodenal artery. Authors can therefore claim to measure HA flow at either ‘common’[197] or ‘proper’[198, 199, 205] sites.

Finally it remains to be said that a simple protocol with reduced scope for variation between scanners/sites are important requisites that current PCMRI methods for clinical HA flow assessment fail to meet. Until these challenges are met, widespread investigation and ultimately adoption of HA flow measurements as part of standard clinical assessment remains unlikely.

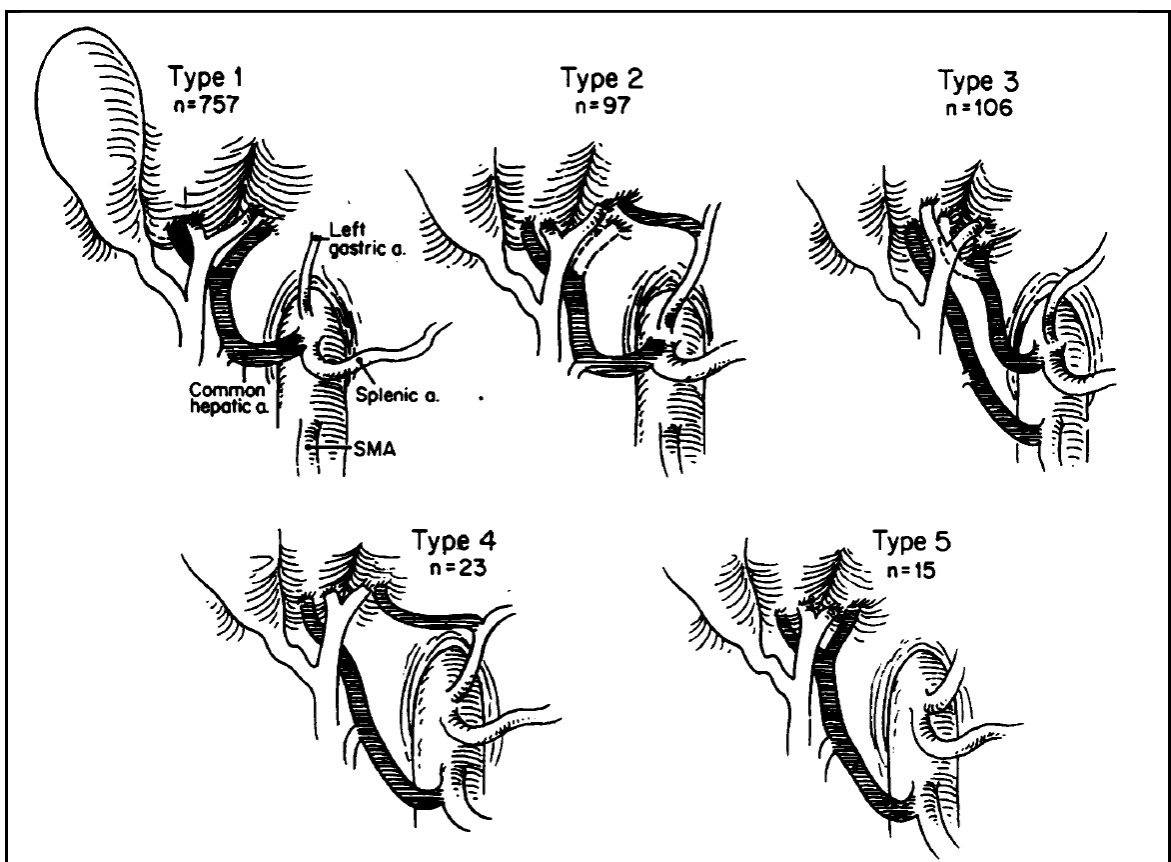


Figure 5.1: Anatomical variations of the hepatic arterial blood supply

In a classification system proposed by Hiatt et al.[359], variations were categorised into 5 subtypes – type 1 (normal anatomy), type 2 variant (accessory left hepatic artery arising from the left gastric artery), type 3 variant (accessory right hepatic artery arising from the superior mesenteric artery), type 4 variant (combined type 2 and type 3 variants) and type 5 variant (common hepatic artery arising from the superior mesenteric artery). Relative incidence in 1000 cases is reported on the diagram below each subtype. (Obtained from reference [359]).

In recognition of these challenges, we propose a novel method for the measurement of total liver blood flow (TLBF) and HA flow.

We know from the application of the principle of conservation of mass to flow (Q) through a given tissue volume (V_{tissue}) that:

$$Q_{in} = Q_{out} + \Delta V_{tissue} \quad \text{(Equation 5.1)}$$

Of course in the context of steady physiological flow through an entire organ, liver volume is fixed so that:

$$Q_{in} = Q_{out} \quad \text{(Equation 5.2)}$$

There have been previous attempts at measuring hepatic venous outflow [196] and while these vessels are of comparable size to the PV at their confluence with the inferior vena cava (IVC), anatomy is variable and the presence of at least three (possibly four) vessels would require separately planned PCMRI studies on each vessel.

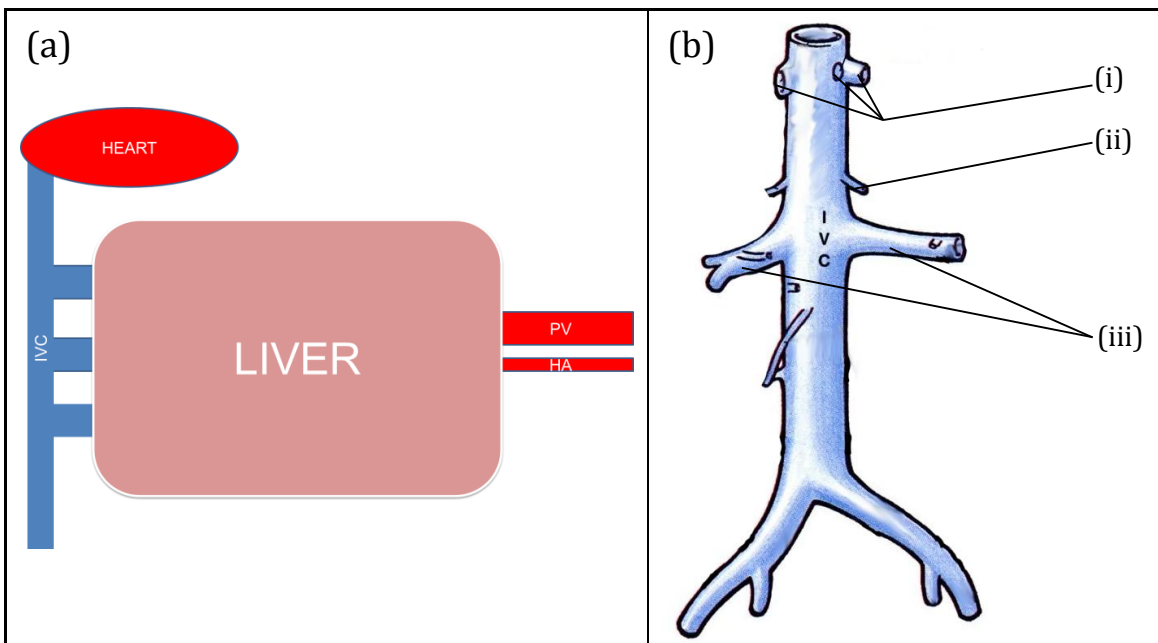


Figure 5.2: Schematic diagram of blood supply and drainage around the liver and anatomical configuration of the IVC

Schematic blood supply and drainage (a) demonstrative of a simple dual input from the PV and HA and outflow through at least three large hepatic veins into IVC. The anatomical configuration of the IVC shown in (b) with only a small contribution between the length between the (i) hepatic and (ii) renal veins, from (ii) the supra-renal vessels. (Adapted from reference [361]).

If we consider the schematic anatomical configuration of the liver (figure 5.2a) and in recognition of the fact that: (a) the IVC enjoys a simpler structure than its aortic counterpart with an extended portion of the vessel fed entirely by hepatic venous blood (figure 5.2b) and (b) that we have previously demonstrated that PCMRI can be used to reliably measure bulk flow in large vessels (PV, IVC and aorta), we propose that a simple and reliable estimation of TLBF can then be made using bulk IVC flow (figure 5.3a).

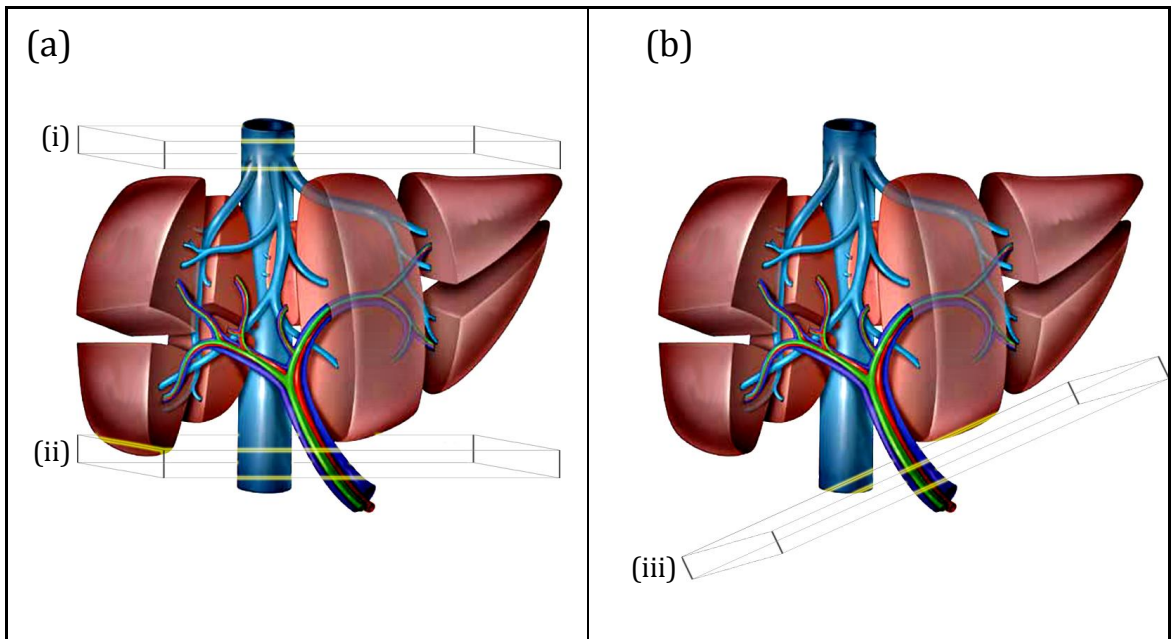


Figure 5.3: Scheme for PCMRI planning for estimation of TLBF and PV flow

These diagrams demonstrate segmental anatomy but were chosen because of the clarity of the structure and orientation of venous vascular structures. TLBF can be estimated by subtracting bulk vessel flow in the IVC measured with 2D PCMRI studies planned at (ii) from IVC flow measured at (i). Finally, an estimation of HA flow can be made by further subtraction of PV flow measured at (iii). (Diagrams adapted and modified from reference [362]).

By measuring bulk flow in the supra-hepatic, but sub-cardiac portion of the (distal) IVC and then subtracting flow from the infra-hepatic, but supra-renal portion of the (proximal) IVC, TLBF can be estimated (Equation 5.2). Given that we have demonstrated PV flow (Q_{PV}) measurements using PCMRI are technically feasible, HA flow (Q_{HA}) could then be estimated by subtracting PV flow from IVC-derived TLBF (figure 5.3b, equation 5.3).

$$Q_{TLBF} = Q_{distal\ IVC} - Q_{proximal\ IVC} \quad \text{(Equation 5.3)}$$

$$Q_{HA} = Q_{TLBF} - Q_{PV} \quad \text{(Equation 5.4)}$$

Armed with this new ‘caval subtraction’ method for measuring TLBF and HA flow, we sought to investigate its potential on both preclinical and clinical systems. Studies were conducted to assess repeatability, reproducibility and the hepatic arterial buffer response.

5.4 PRECLINICAL VALIDATION, REPEATABILITY AND STUDIES OF THE HEPATIC ARTERIAL BUFFER RESPONSE

5.4.1 BACKGROUND

From previous work presented in section 4.6, we successfully implemented fixed delay multiphase cardiac gating. The extended acquisition times resulting from this gating strategy were cumbersome and likely to hinder accurate measurements in animal models of disease or during pharmacological stress. A considerable amount of time is wasted during fixed delay multiphase cardiac gating through addition of delays for acquisition of successive phases of the cardiac cycle, during which both cardiac and respiratory gates are open, but no data is collected. So-called 'cine' MR refers to an alternative group of gating strategies which take advantage of the entire acquisition window during the cardiac cycle [338, 355]. By acquiring as many lines of k -space as possible through the R-R interval and then retrospectively sorting the data into each phase of the cardiac cycle, the entire acquisition window can be exploited. The phase-encoding amplitude can be changed at the start of each R-R interval, so that over a given time-period a multiphase data set can be constructed with potentially more phases through the cardiac cycle than with the previous strategy and using a shorter acquisition period (figure 5.4).

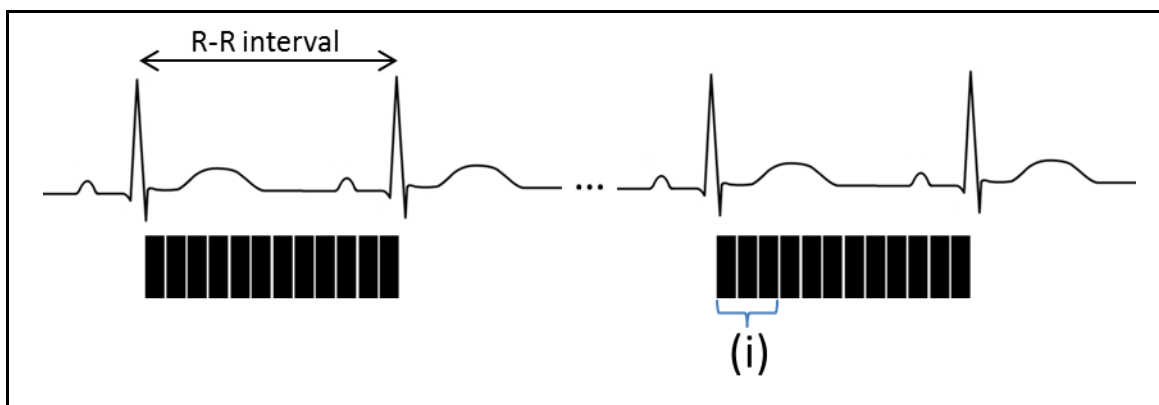


Figure 5.4: Cine-PCMRI cardiac gating

Cine gating strategies exploit the entire R-R window for the duration of the acquisition. For PCMRI sequences, the requirement for measurement of background and successive phase-shifts extend repetition time (i) and imply a smaller number of phases can be sampled through the cycle.

There have been many subsequent refinements to this method, including oversampling of the R-R window with the use of an 'arrhythmia rejection' window to retrospectively account for changes in heart rate and 'view sharing' for interleaved cardiac phase acquisitions [339, 355].

The scheme in figure 5.4 demonstrates the implications of measuring multiple phase-shifts, but also highlights the value of using a cine-gating strategy for acquisition of anatomical images. Cardiac cine MR with short-axis views have been well validated for measurement of stroke volume [363-365] and therefore could be used to validate PCMRI measurements of aortic root flow.

Although validation of PCMRI PV flow measurements can be undertaken with direct within-subject TTUS measurements as previously described, the validation of HA flow measurements with TTUS is problematic. As described in section 5.3, the surgery required to access the coeliac artery would be very invasive (requiring considerable retraction and dissection of the upper abdominal viscera and tissue planes) and non-physiological (requiring ligation of the gastric and splenic branches of the coeliac artery)[340, 356, 357]. An alternative method for measuring HA flow is through the use of microspheres. The administration of microsphere particles that lodge in organ capillary beds can be used to study regional and inter-organ perfusion differences. Classically, these microspheres are radiolabelled, so that once the experiment is complete, organs can be extracted and quantification can be performed using a scintillation counter [366]. Working with radioactive materials provides added, cumbersome, logistical considerations not least area-based restrictions for experimental activity but also added costs for storage and disposal of biological tissues. The use of fluorescent-labelled microspheres provides an alternative well-established non-ionising radiation based method for quantification. Once injected, these microspheres can be recovered using specialist methods and quantified using spectrophotometry [367, 368]. This method can also be used to quantify perfusion at different stages of an experiment using injections of microspheres containing different fluorophores. Differing fluorophore excitation wavelengths enable spectrophotometric perfusion quantification for each injection from the same tissue sample [27].

Finally, the ability to detect expected alterations of hepatic perfusion parameters in response to a controlled insult is an important way of demonstrating the validity of a new method. Having previously demonstrated (section 4.5) that PV flow modulation can be achieved non-invasively using terlipressin, caval subtraction PCMRI could be used to demonstrate changes in PV flow and moreover has the potential to study the hepatic arterial buffer response non-invasively.

With this in mind, in this section we aim to (a) demonstrate the feasibility of using caval subtraction PCMRI to measure TLBF, HA and PV flow, (b) study the repeatability of cine PCMRI measurements of PV flow, (c) validate aortic root, PV and relative HA flow

measurements using short-axis anatomical cine MRI, TTUS and microspheres respectively and (d) investigate haemodynamic changes in response to terlipressin using caval subtraction PCMRI in normal and diseased rats.

5.4.2 METHODS

5.4.2.1 Experimental subjects

All experiments were conducted according to the Home Office guidelines under the UK Animals in Scientific Procedures Act 1986. Animals were maintained as per guidelines and approval of the ethical committee for animal care of University College London. Experiments were performed on healthy male Sprague-Dawley rats (Charles River UK, Margate, UK) with normal liver function. Animals were housed in cages at 22-23°C, ~50% humidity and with 12 hours of light and ad libitum access to water and rat feed.

For studies in models of liver disease, subjects weighing 250-300g were randomised to bile-duct ligation (BDL) procedure ($n = 12$) or sham laparotomy ($n = 13$). BDL and sham surgery was conducted as described previously by researchers at our institution [350]. Briefly, a midline abdominal incision was made under 2% isoflurane and intraperitoneal levobupivacaine. For animals undergoing BDL procedure, the common bile duct was isolated, triply ligated with 3-0 silk and sectioned between the ligatures. After closure and recovery, animals were maintained for 5 weeks to allow the development of portal hypertension and features of chronic liver disease.

For each experiment/cohort, subjects were randomly selected at the time of removal from the cage. Any adverse events and subsequent protocol modifications were recorded and reported in the results.

5.4.2.2 Sample size

Validation of PCMRI PV flow was prioritised for calculation of sample size, as variability of other parameters in our study remained unknown. Experiments were planned based on Bland-Altman analysis of agreement, using preliminary inter-technique agreement data between PCMRI and TTUS PV flow acquired in section 4.6. Power calculations were undertaken for a statistical power of 90% and a 5% significance level. Assuming intra-subject differences between the two techniques of at worst 20% (therefore implying standard deviation for intra-subject differences of approximately 10%), and defining the level of agreement within 7% precision, a sample of $n = 24$ subjects (half of which would have liver disease) would be advised. Projecting a 15% attrition rate, the final sample size would be $n = 28$.

5.4.2.3 Animal preparation

After induction with isoflurane, a 0.58 mm internal diameter fine bore polyethylene line (Portex, Smiths Medical, Kent, England) was sited in the jugular vein. The anaesthetised animal was then transferred to a 9.4T Agilent scanner (Oxford, UK) with a rectal probe for temperature monitoring. Core body temperature was maintained between 36 and 38°C using circulating warm water pipes and warm air. Cardiac monitoring was undertaken using a triple electrode single lead system (SA instruments, New York, USA).

5.4.2.4 Two-dimensional cine PCMRI

Once positioned in the scanner, axial anatomical images were used to identify the vessel of interest. Three markers were placed in the vessel lumen, for automated planning of scanning slices through the vessel in the coronal plane (Vnmrj 3.2, Agilent, Oxford, UK). The vessel was then identified on angled coronal slices and studies were planned to ensure orthogonality to the vessel. Cardiac gated images were used for planning of studies on the distal IVC (figure 5.5) and aortic root (see cardiac cine MRI methods). Proximal IVC flow measurements were obtained from the same slice used to measure PV flow (figure 4.7).

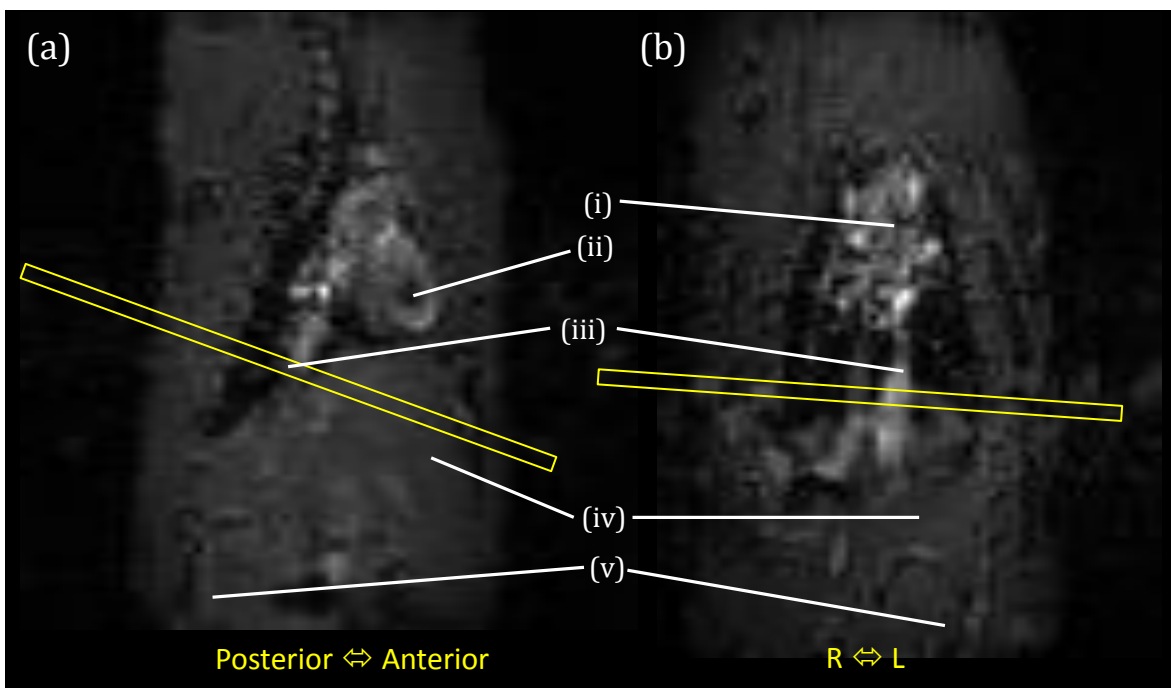


Figure 5.5: PCMRI slice planning for distal IVC flow measurements

Cardiac gated anatomical images were obtained in the (a) sagittal plane to identify the distal IVC (iii). Coronal images parallel to the vessel were then obtained (b). The PCMRI slice was positioned to ensure orthogonality to the vessel in two planes. Anatomical images typically included the great vessels (i), heart (ii), liver (iv) and kidneys (v).

PCMRI planning provided time for the animal to settle before evaluating subject heart rate. Based on the heart rate (R-R interval) and sequence repetition time (TR), the number of frames acquired through the cardiac cycle was set as two less than the maximum number of frames possible, to avoid cycle overlap should heart rate increase. Heart rate was recorded so that the extended interval between the final frame and end of the cycle could be accounted for in flow calculations. All datasets included at least 10 frames through the cardiac cycle.

Cardiac and respiratory-gated 2D cine PCMRI was then undertaken using 2 mm slice thickness, a 10° flip angle and a 192 x 192 (frequency encoding x phase encoding) acquisition matrix. Based on previous work, data was acquired using V_{enc} settings of 33 cm/s for PV and proximal IVC flows, 66 cm/s for distal IVC flows and 133 cm/s for aortic root flows. ROIs were manually positioned on each vessel for each frame of the cardiac cycle and quantitative analysis was undertaken as previously. All PV flow, estimated TLBF and HA flow measurements were normalised to explanted liver weight. Cardiac cine MR derived cardiac output (CO) was used to calculate estimated TLBF as a % of CO and estimated HA flow as a % of CO. Data was analysed using in-house developed Matlab code (MathWorks, Natick, USA).

Table 5.1: Sequence parameters

	PCMRI	CARDIAC CINE MRI
<i>TR/TE (milliseconds)</i>	10/1.2	7.5/1.2
<i>Flip angle (°)</i>	10	15
<i>Matrix size (pixels)</i>	192 x 192	128 x 64
<i>Field-of-view (mm)</i>	40 x 40	40 x 40
<i>Spatial resolution (mm²)</i>	0.208 x 0.208	0.313 x 0.625
<i>Slice thickness (mm)</i>	2	1
<i>Slice gap (mm)</i>	-	0
<i>Cardiac cycle phases</i>	12-15	≥20

5.4.2.5 Repeatability

Thirteen subjects underwent cine PCMRI PV flow repeatability studies, with repeat data obtained 60-100 minutes after the first measurement. All subjects remained in the scanner after the initial measurements.

5.4.2.6 Cardiac cine MRI validation

Cardiac cine MRI was performed as described previously by researchers at our institution [369]. Cardiac and respiratory gated coronal images through the thorax were obtained for planning. Long-axis images were then acquired to ensure accurate short-axis view planning.

Because of the proximity of the mitral valve orifice to the aortic vestibule and obliquity of the cardiac axis (figure 5.5) in the rat, cardiac cine MRI was usually undertaken before aortic root PCMRI measurements so that the short axis slice orientation of slices adjacent to the aortic root could be used to plan aortic root flow PCMRI studies.

Planning provided time for the animal to settle before evaluating subject heart rate. As with cine PCMRI, the heart rate and repetition time were used to determine the maximum number of frames possible through the cardiac cycle. Acquisitions were for two frames less than this number, to avoid cycle overlap should heart rate increase. All datasets included at least 20 frames through the cardiac cycle. Spoiled gradient echo images were obtained with an echo time of 1.2 milliseconds, repetition time of 7.5 milliseconds, 15° flip angle, slice thickness of 1 mm, no slice separation, field of view of 40 x 40 mm² and 128 x 64 (frequency encoding x phase encoding) acquisition matrix. Data was analysed using the freely available software package Segment (Medviso, Lund, Sweden). Automatic segmentation tools were used to identify the endocardial surface, with frame by frame manual review and segmentation correction where appropriate.

5.4.2.7 TTUS validation

Invasive TTUS measurements were performed as described previously in sham-operated animals. Extensive adhesions around the porta hepatis and high risk of traumatic damage and haemorrhage precluded TTUS validation in BDL subjects. To control for the haemodynamic sequelae of laparotomy, all BDL subjects underwent laparotomy and intestinal manipulation.

5.4.2.8 Microsphere validation

Polystyrene fluorescent microspheres (15 µm, FluoSpheres, Life Technologies, UK), were suspended in a 1:10 dilution of heparinised saline. Immediately after vortex mixing, a 1 ml intra-ventricular injection was administered over approximately 10 seconds using a 26G 13 mm needle. To minimise invasive complications, percutaneous intra-cardiac injections were administered trans-thoracically using a portable bench-top US system (Terason, Burlington, USA) with a 1.5 cm 2.5 MHz linear probe (figure 5.6). Validation was undertaken at baseline and after terlipressin using green (450/480 nm excitation wavelength) and carmine (580/620 nm excitation wavelength) microspheres respectively.

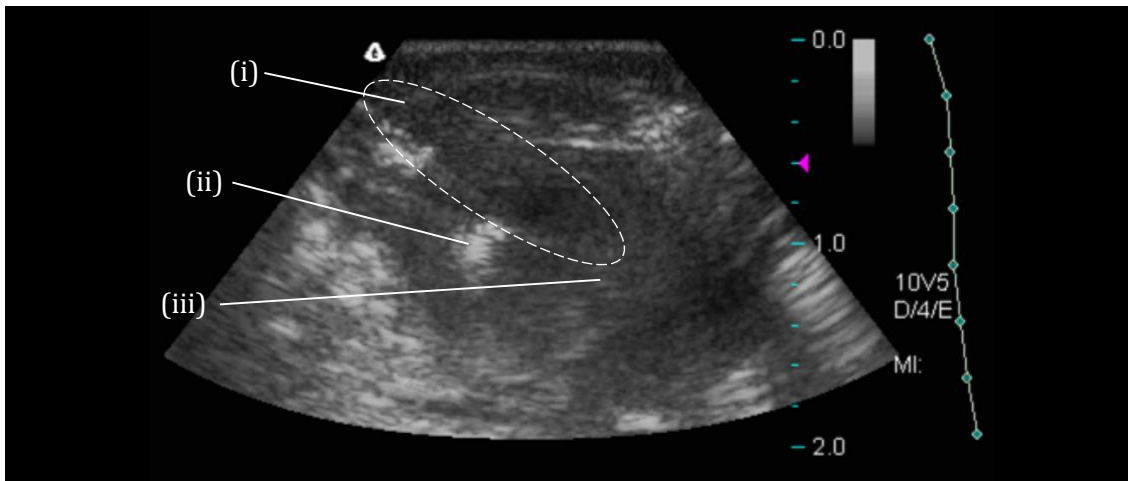


Figure 5.6: Ultrasound guided intra-cardiac microsphere injections

A 26G needle (i) was advanced under US guidance through the myocardium (ii) into the endocardial cavity (iii). Injections were administered over approximately 10 seconds.

Once in vivo experimentation was complete, the animal was terminated and organs were explanted for microsphere processing using a protocol adapted from previously described methods [368]. The liver, spleen, gut, mesentery and both kidneys were explanted and weighed before storage in a falcon tube with saturated potassium hydroxide solution. Samples were stored in a 37°C incubator and manually shaken every 3-4 days to ensure mixing.

Measurement was then performed after 3 weeks. To ensure adequate liquefaction of larger tissue samples (e.g. gut, liver), mechanical tissue homogenisation was undertaken (LabGEN, Cole-Parmer Instrument Co., London, UK). Samples were then filtered using 100 µm pore cell strainers to remove any large solid waste material, before centrifugation for 10 minutes at 3000g. After discarding the supernatant, samples were washed with 0.25% Tween 80 in demineralised water, re-suspended and centrifuged. The washing step was repeated twice before transferring samples to glass tubes for a final washing step with demineralised water alone and centrifugation. Supernatant was discarded but a 1 ml volume was maintained around the pellet. Finally, 2 mls of 2-(2-ethoxyethoxy)ethyl acetate (Sigma-Aldrich, UK) was added to the glass tube to dissolve the polystyrene microspheres and release the fluorescent particles. Samples were then vortexed and stored overnight before repeat vortex mixing and centrifugation. The supernatant was then transferred to a 96-well glass plate for spectrophotometric quantification (FLUOstar Omega, BMG Labtech, Ortenberg, Germany).

To ensure adequate mixing of the microspheres in the central circulation, sample sets with over 20% difference between right and left renal microsphere content were discounted from the final analysis. Microspheres recovered from the gut, mesentery and spleen (splanchnic beds) were considered analogous to portal venous circulation [352,

370], while microspheres recovered from the liver were used for hepatic arterial flow quantification. Because of difficulties processing large whole organ volumes (e.g. gut, liver), 10 ml volumes of homogenised samples were assessed with correction of absolute values to whole organ sample volume for quantification. Hepatic arterial fraction was calculated as follows:

$$HA_{\%} = \frac{M_{\text{liver}}}{M_{\text{liver}} + M_{\text{gut, mesentery}} + M_{\text{spleen}}} \quad (\text{Equation 5.4})$$

Where ‘ M_{organ} ’ refers to the absolute number of microspheres recovered from the respective organ tissue.

5.4.2.9 Terlipressin response

Pilot experiments using TTUS to monitor PV flow were performed on the bench to determine the dosage regime (Appendix B). For a sustained reduction in PV flow for the duration of the experimental protocol, a 100 µg/kg bolus of terlipressin acetate (Glypressin, Ferring Pharmaceuticals, UK) was administered using the previously sited jugular venous line, followed by an infusion of 10 µg/kg/min for 40 minutes.

5.4.2.10 Experimental in vivo protocol

The entire in vivo experimental protocol was split into three phases, in broad terms: (i) pre-terlipressin, pre-MRI bench validation, (ii) MRI measurements pre and post-terlipressin and (iii) post-MRI, post-terlipressin bench validation (figure 5.7).

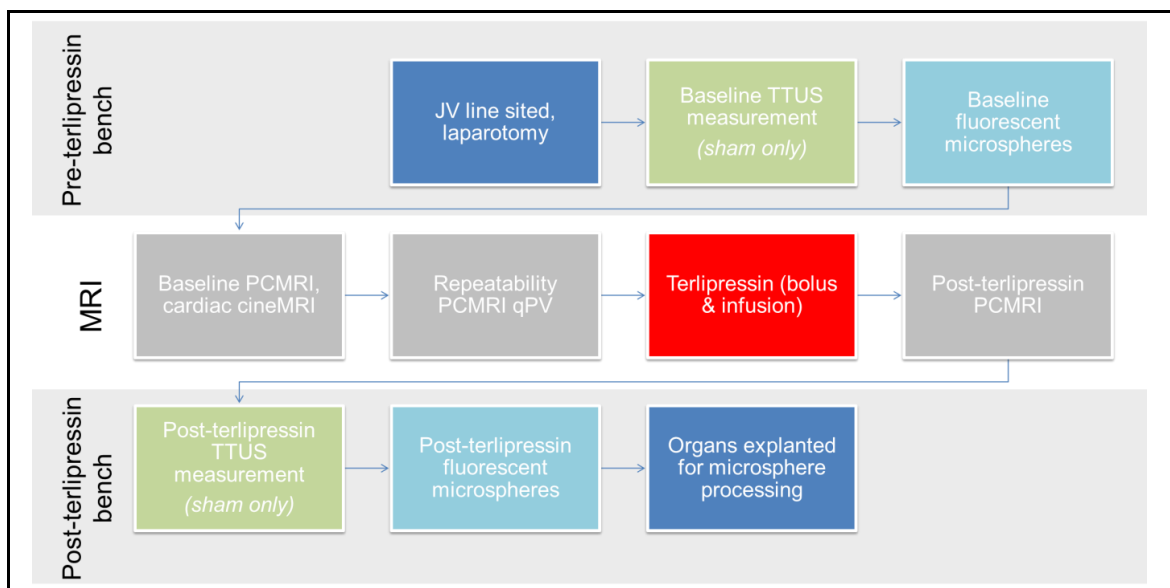


Figure 5.7: Experimental protocol

Validation, repeatability and terlipressin response was assessed invasively and non-invasively in both sham and BDL animals.

5.4.2.11 Statistical analysis

Kolmogorov-Smirnov tests were used to confirm normality of variable distributions. Comparisons between sham and BDL cohorts were undertaken using unpaired and paired t-tests where appropriate. Repeatability and validation studies were assessed using paired t-tests, Bland-Altman analysis of agreement with calculation of the coefficient of repeatability and assessment of correlation between repeated/validated measurements using Pearson's correlation coefficient. Terlipressin response studies were evaluated using paired t-tests in sham and BDL cohorts. The threshold of statistical significance was defined to be $p < 0.05$.

5.4.3 RESULTS

5.4.3.1 Cohort features

Experiments were performed in sham operated ($n = 13$) and BDL ($n = 12$) rats. Four weeks post-surgery, mean BDL body weight ($422.3 \pm 11.10\text{g}$) was lower than mean sham body weight ($484.0 \pm 5.565\text{g}$; $p < 0.0001$). Conversely mean BDL wet liver mass ($32.38 \pm 1.941\text{g}$) was higher than mean sham wet liver mass ($16.09 \pm 0.6558\text{g}$; $p < 0.0001$). Cohort sizes varied for each part of the study, primarily as a result of evolution of the protocol while experiments were conducted, but also because of difficulties with gating and artefact. Overall numbers are summarised in table 5.2, but a detailed summary of subject participation in each stage of the protocol shown in figure 5.7 can be found in Appendix C.

Table 5.2: Cohort numbers for invasive, MRI and terlipressin studies

	SHAM ($n = 13$)	BDL ($n = 12$)
<i>Baseline cardiac cine MRI</i>	13	12
<i>Baseline TTUS and PCMRI PV flow validation</i>	11	-
<i>Baseline aortic root PCMRI validation</i>	8	8
<i>Baseline caval subtraction PCMRI</i>	7	9
<i>PCMRI PV flow repeatability</i>	6	6
<i>Post-terlipressin caval subtraction PCMRI</i>	6	6
<i>Post-terlipressin TTUS and PV PCMRI flow validation</i>	6	-
<i>Microspheres and PCMRI HA fraction validation</i>	6	6

5.4.3.2 Caval subtraction cine PCMRI

ECG and respiratory gated cine PCMRI flow studies through the cardiac cycle demonstrated physiological flow profiles through the PV, proximal IVC, distal IVC and aortic root. Acquisition of a full hepatic haemodynamic data set took on average 28.42 ± 1.422 minutes, with an additional 12.83 ± 0.833 minutes for acquisition of aortic root flow data ($n = 12$, sham and BDL).

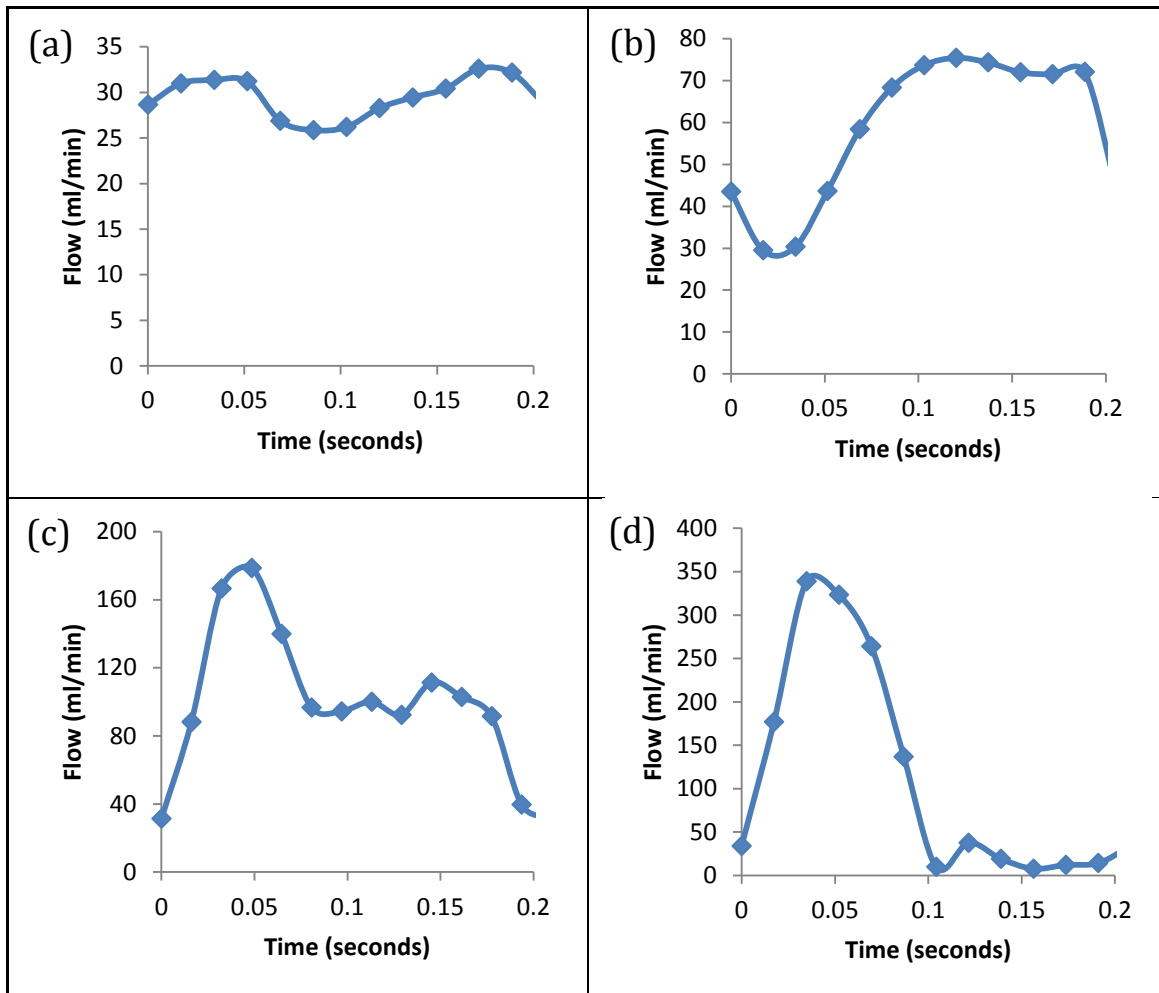


Figure 5.8: Bulk flow profiles through the cardiac cycle using cine PCMRI

Data from the same subject demonstrating flow profiles for the (a) PV (overall flow 29.88 ml/min), (b) proximal IVC (overall flow 59.53 ml/min), (c) distal IVC (overall flow 101.3 ml/min) and (d) aortic root (overall flow 122.7 ml/min).

Caval subtraction methods, applied for example to the dataset above were suitable for estimation of TLBF (41.81 ml/min), HA flow (11.93 ml/min) and %HA flow (28.53%).

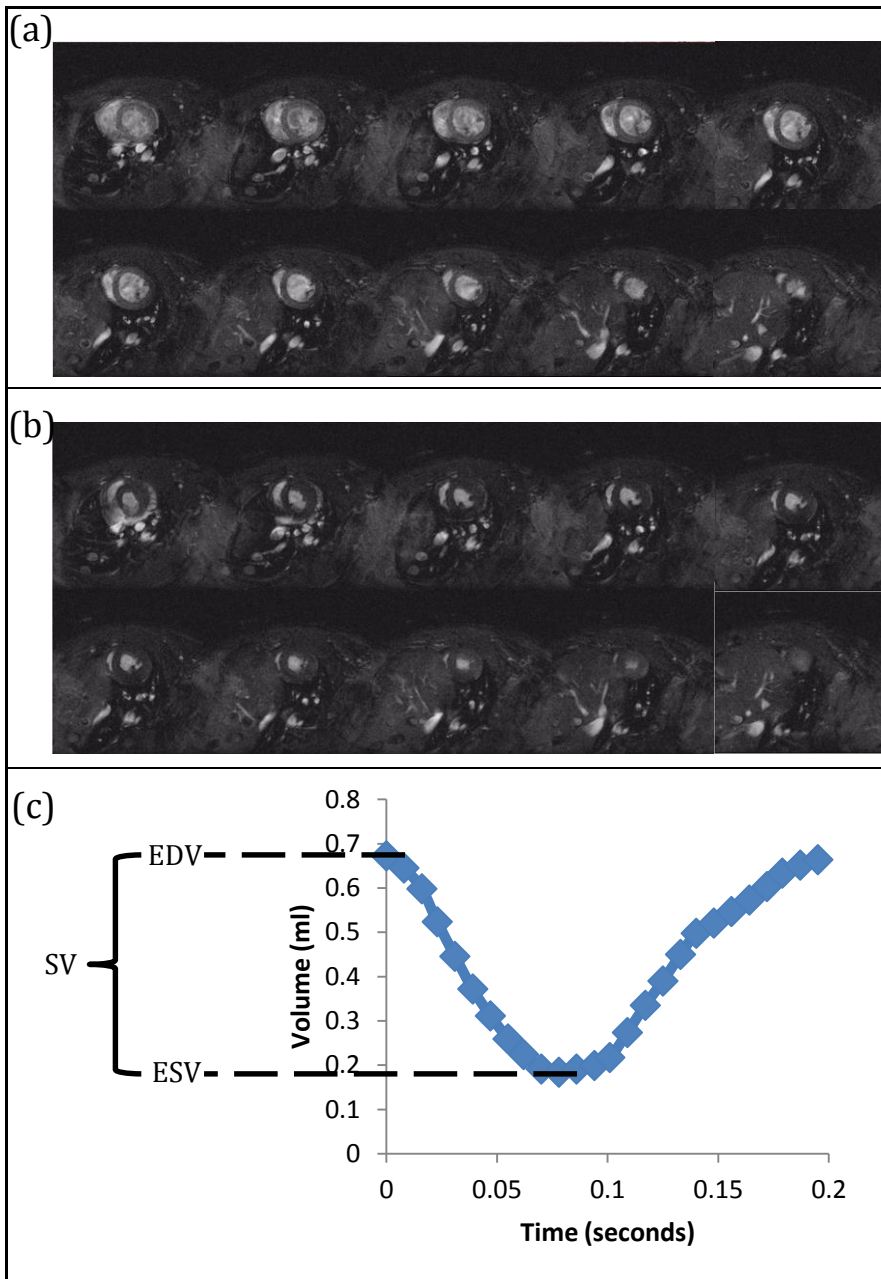


Figure 5.9:
Preclinical
anatomical
cardiac cine MR
and volumetric
quantification

Ten left ventricle short-axis slices (1 mm thickness) extending to the apex (a,b, right lower corner image) are shown from a sham-operated rat. The stroke volume can be calculated from segmentation of endocardial areas at end diastole (a) and end systole (b). Segmentation of ventricular volumes through multiple phases of cardiac cycle can be used to generate volume-time curves (c).

Estimated TLBF can then be normalised to systemic haemodynamics using measurement of cardiac output assessed with cardiac cine MRI (figure 5.9). Cardiac output measured by cine MRI was 156.4 ml/min in this example so that estimated TLBF as a percentage of CO was 26.73% and estimated HA flow as a percentage of CO was 7.628%.

5.4.3.3 Baseline haemodynamic studies

Baseline hepatic haemodynamics were compared in sham ($n = 7$) and BDL ($n = 9$) rats. Baseline mean PV flow in sham operated animals (181.4 ± 12.06 ml/min/100g) was higher than in BDL animals (68.52 ± 10.16 ml/min/100g; $p < 0.0001$) (figure 5.10a). Estimated TLBF measured with the novel caval subtraction method was on average higher in sham rats (214.3 ± 16.68 ml/min/100g) compared with BDL rats (152.3 ± 18.68 ml/min/100g; $p = 0.0308$) (figure 5.10b). Conversely, estimated HA flow was on average higher in BDL rats (83.75 ± 19.12 ml/min/100g) compared with sham counterparts (32.98 ± 11.29 ml/min/100g; $p = 0.0526$), but this difference was just above the stipulated significance level (figure 5.10c). Estimated HA fraction (figure 5.10d) was however significantly different in BDL animals ($51.51 \pm 6.758\%$) compared with sham animals ($14.37 \pm 4.446\%$; $p = 0.0007$).

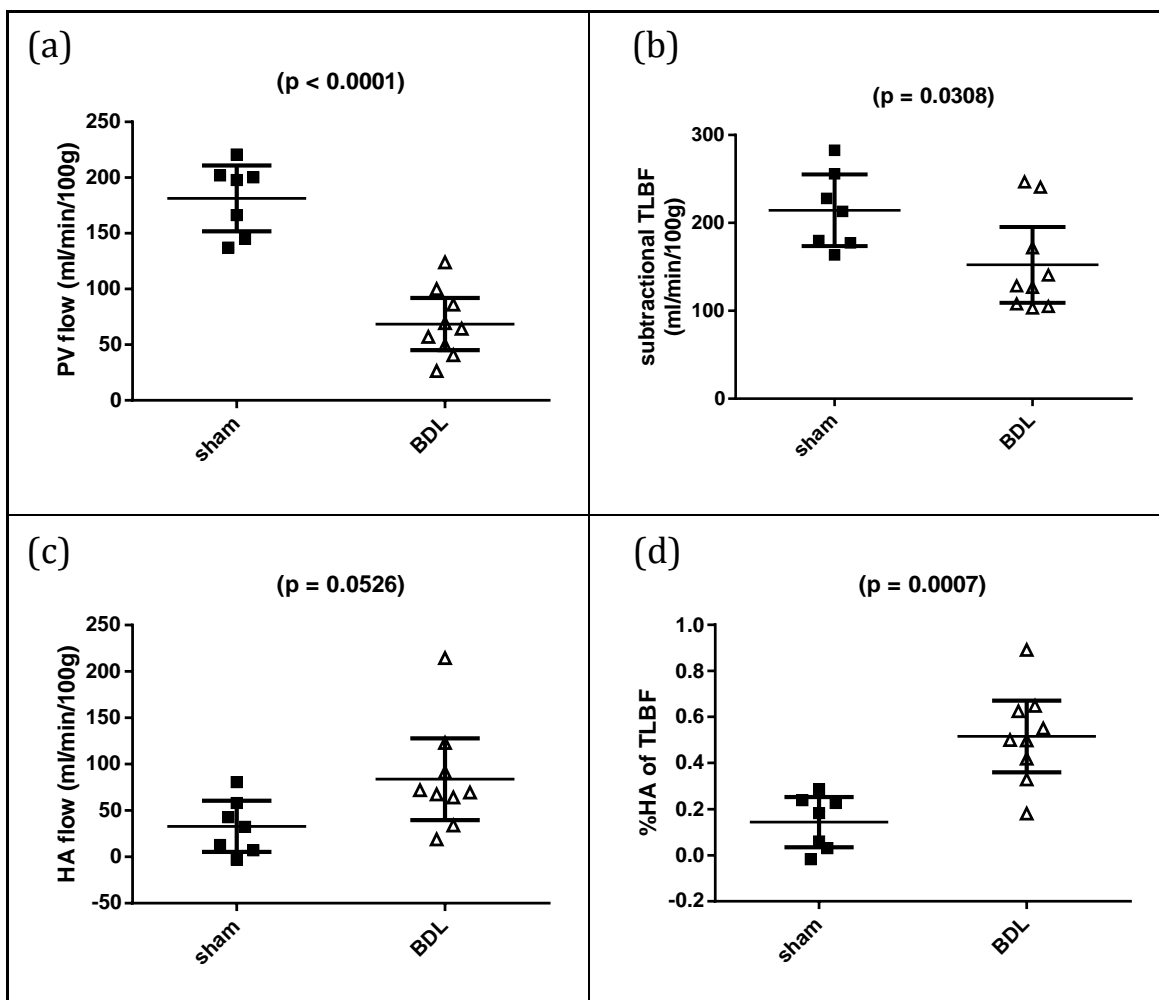


Figure 5.10: Hepatic haemodynamic differences at baseline between sham and BDL rats

Baseline PV flow and estimated TLBF were higher in sham rats. Estimated HA flows and HA fractions were on average higher in BDL animals. Differences were statistically significant except for absolute estimated HA flows, which was found to be just non-significant ($p = 0.0526$).

Cardiac output measurements were used to contextualise absolute hepatic haemodynamic parameters to systemic circulatory factors. BDL subjects had significantly higher HA flow relative to cardiac output ($13.89 \pm 2.370\%$) when compared to their sham counterparts ($3.442 \pm 1.111\%$; $p = 0.0027$) (figure 5.11a), but interestingly demonstrated no significant difference in estimated TLBF relative to cardiac output ($25.66 \pm 2.455\%$ BDL, $24.49 \pm 1.615\%$ Sham, $p = 0.7162$) (figure 5.11b).

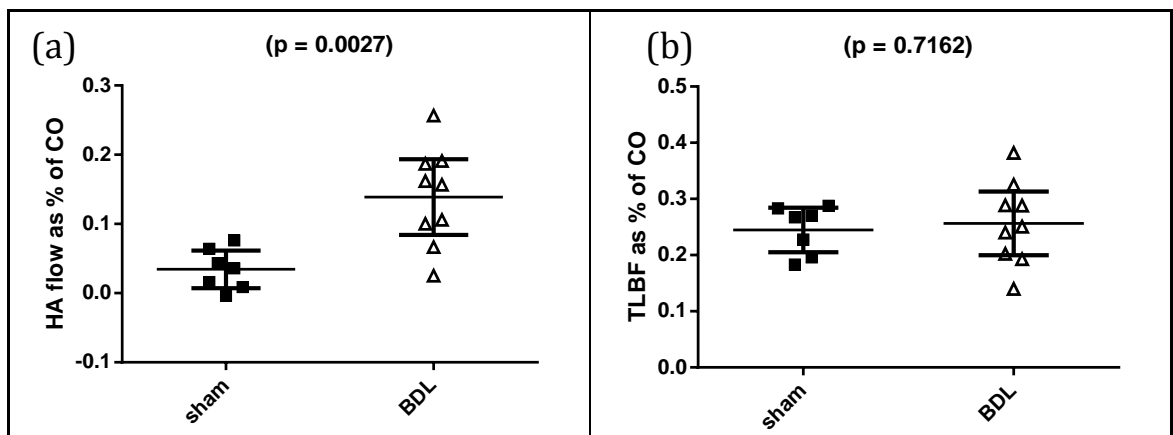


Figure 5.11: Haemodynamic differences relative to cardiac output at baseline between sham and BDL rats

HA flow (a) and TLBF (b) as a percentage of CO. Significant differences between cohorts were shown for HA flow relative to CO, but not TLBF.

5.4.3.4 Repeatability studies

Repeatability of cine PCMRI measurements was assessed using measurements of PV flow in sham ($n = 6$) and BDL ($n = 6$) animals. Average time between repeat measurements across the entire cohort was 83.77 ± 18.97 minutes. No significant differences were demonstrated between repeated PV flows in sham (mean difference -25.46 ± 14.26 ml/min/100g; $p = 0.1342$) or BDL cohorts (mean difference 3.749 ± 5.823 ml/min/100g; $p = 0.5435$). The coefficient of repeatability was higher in sham (68.45 ml/min/100g) than BDL animals (30.20 ml/min/100g). Graphical analysis (figure 5.12) showed correlations between repeated PCMRI PV flow measurements were significant ($r = 0.9041$; $p < 0.0001$).

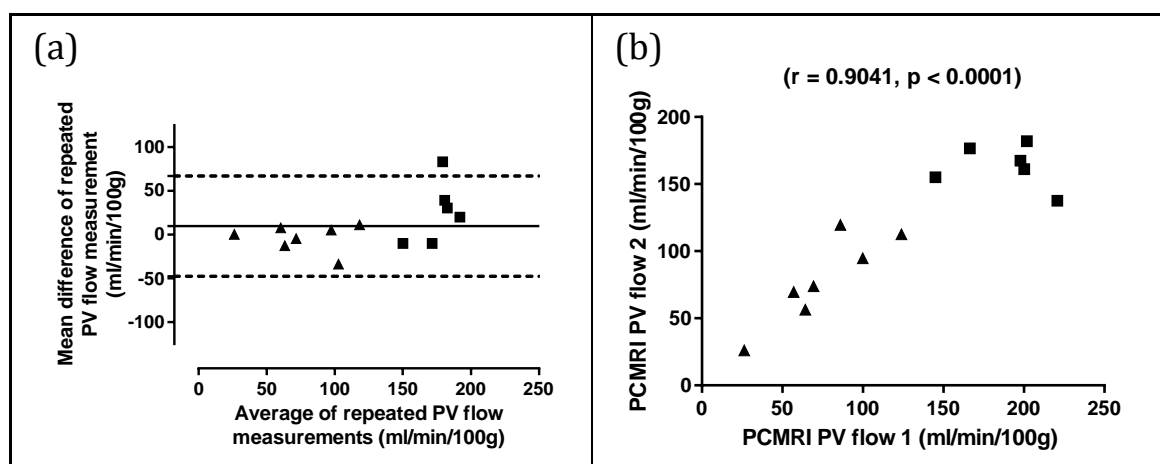


Figure 5.12: Repeatability of PV flow measurements with cine PCMRI

Data from sham (■) and BDL (▲) rats. Repeat measurements were obtained on average 83.77 ± 18.97 minutes apart. The overall cohort coefficient of repeatability was 57.37 ml/min/100g. A strong and significant correlation between repeated measurements was demonstrated.

5.4.3.5 Validation studies

Validation of cine PCMRI measurements of aortic root flow were undertaken using measurements of cardiac output derived from short axis cardiac cine MRI volumetric analysis (figure 5.9) in sham ($n = 8$) and BDL ($n = 8$) animals. Paired t-tests demonstrated non-significant differences between cine PCMRI cardiac output and cardiac cine MRI cardiac output in sham (mean difference 8.856 ± 7.247 ml/min; $p = 0.2613$) and BDL cohorts (mean difference 8.340 ± 15.48 ml/min; $p = 0.6067$). The coefficient of variation was higher for cine PCMRI cardiac output in both sham (23.73% vs 19.12% ; PCMRI vs cardiac cine MRI) and BDL subjects (28.06% vs 24.89% ; PCMRI vs cardiac cine MRI). Graphical analysis (figure 5.13b) showed correlations between PCMRI and cardiac cine MRI derived cardiac output were significant ($r = 0.7554$; $p = 0.0007$).

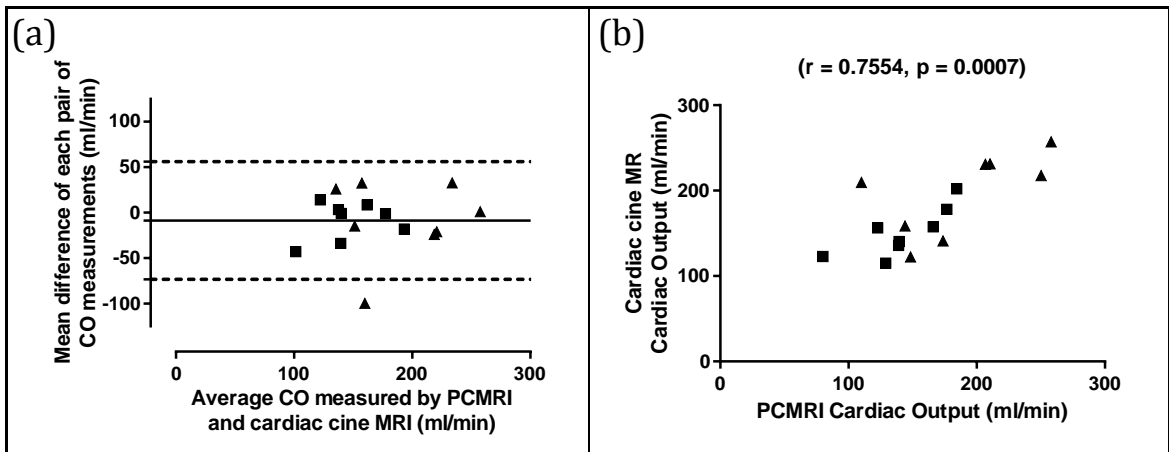


Figure 5.13: Validation of aortic root cine PCMRI using short axis cardiac cine MRI

Data from sham (■) and BDL (▲) rats. Despite encouraging overall correlation, the coefficient of repeatability between measurement methods was large for sham (40.18 ml/min) and even larger for BDL rats (85.8 ml/min).

Validation of cine PCMRI measurements of PV flow were undertaken in sham subjects as previously using invasive TTUS. Measurements were obtained at baseline ($n = 11$) and post-terlipressin ($n = 6$). Paired t-tests demonstrated non-significant differences between TTUS and PCMRI PV flow at baseline (mean difference -3.518 ± 9.426 ml/min/100g; $p = 0.7167$) and post-terlipressin (mean difference -23.01 ± 14.91 ml/min/100g; $p = 0.1834$). The coefficient of variation was higher for TTUS measurements at baseline (21.19% vs 17.92%; TTUS vs PCMRI) and post-terlipressin (33.02% vs 13.91%; TTUS vs PCMRI). Graphical analysis (figure 5.14b) showed correlations between PCMRI and TTUS PV flow were significant ($r = 0.7737$; $p = 0.0003$).

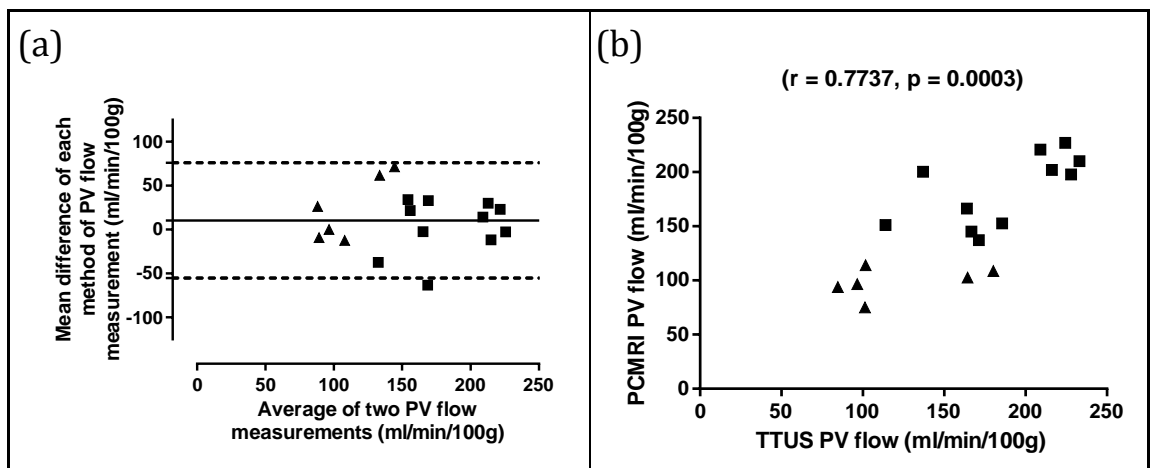


Figure 5.14: Validation of PV flow cine PCMRI using TTUS

Data from sham rats at baseline (■) and post-terlipressin (▲). The coefficient of repeatability between measurement methods was comparable at baseline (61.27 ml/min/100g) and post-terlipressin (71.58 ml/min/100g).

Validation of caval subtraction cine PCMRI estimates of HA fraction was undertaken in sham ($n = 7$) and BDL ($n = 9$) subjects using microspheres at baseline ($n = 16$) and in sham

($n = 3$) and BDL ($n = 2$) rats post-terlipressin ($n = 5$). Because of inadequate mixing, nine microsphere datasets were discarded. Final analysis was based on twelve caval subtraction cine PCMRI estimates of HA fraction from sham ($n = 6$) and BDL ($n = 6$) subjects using microspheres at baseline ($n = 8$) and post-terlipressin ($n = 4$). Paired t-tests across the entire cohort demonstrated a significant difference between PCMRI and microsphere derived HA fraction (mean difference $14.40 \pm 6.372\%$; $p = 0.0450$). The coefficient of variation was higher for PCMRI HA fraction (80.68% vs 75.22%; PCMRI vs microspheres). Graphical analysis (figure 5.15b) showed significant correlations between PCMRI and microsphere derived HA fraction ($r = 0.7944$; $p = 0.0020$).

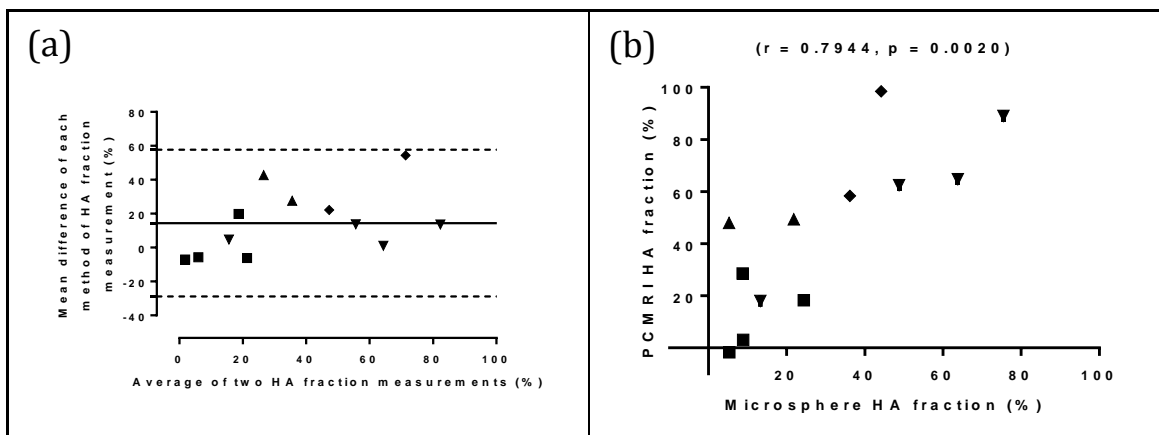


Figure 5.15: Validation of PCMRI HA fraction using microspheres

Data from sham rats at baseline (■), sham rats post-terlipressin (▲), BDL rats at baseline (▼) and BDL rats post-terlipressin (◆). Analysis was pooled across all four cohorts because of small intra-cohort numbers. The coefficient of repeatability between measurement methods was large (43.27%).

5.4.3.6 Haemodynamic response to terlipressin

The response to terlipressin was evaluated in sham ($n = 6$) and BDL ($n = 6$) rats. Post-terlipressin PCMRI flow measurements were acquired on average 15.42 ± 1.305 minutes after the terlipressin infusion was started. Paired t-tests demonstrated expected reductions in sham (mean difference -90.25 ± 11.13 ml/min/100g; $p = 0.0005$) and BDL (mean difference -29.75 ± 6.853 ml/min/100g; $p = 0.0049$) PV flow (figure 5.16a and b). No significant change in estimated TLBF was observed in sham animals (mean difference -2.538 ± 13.97 ml/min/100g; $p = 0.8630$), but contrastingly a reduction in estimated TLBF was observed in BDL animals (mean difference -65.48 ml/min/100g; $p = 0.0006$) (figure 5.16c and d). The changes in estimated TLBF reflect a buffering of the drop in PV flow by a rise in HA flow in sham animals (mean difference 34.43 ± 7.494 ml/min/100g; $p = 0.0059$). This phenomenon was not observed in BDL animals where a decline in HA flow was recorded (mean difference -34.43 ± 7.494 ml/min/100g; $p = 0.0059$) (figure 5.16e and f). Comparison of pre and post-terlipressin HA fraction confirmed relative buffering of the decline in PV flow in sham rats (mean difference $38.78 \pm 6.520\%$; $p = 0.0019$), but stable HA fraction in the face of TLBF decline in BDL rats (mean difference $8.340 \pm 8.305\%$; $p = 0.3614$) (figure 5.16g and h).

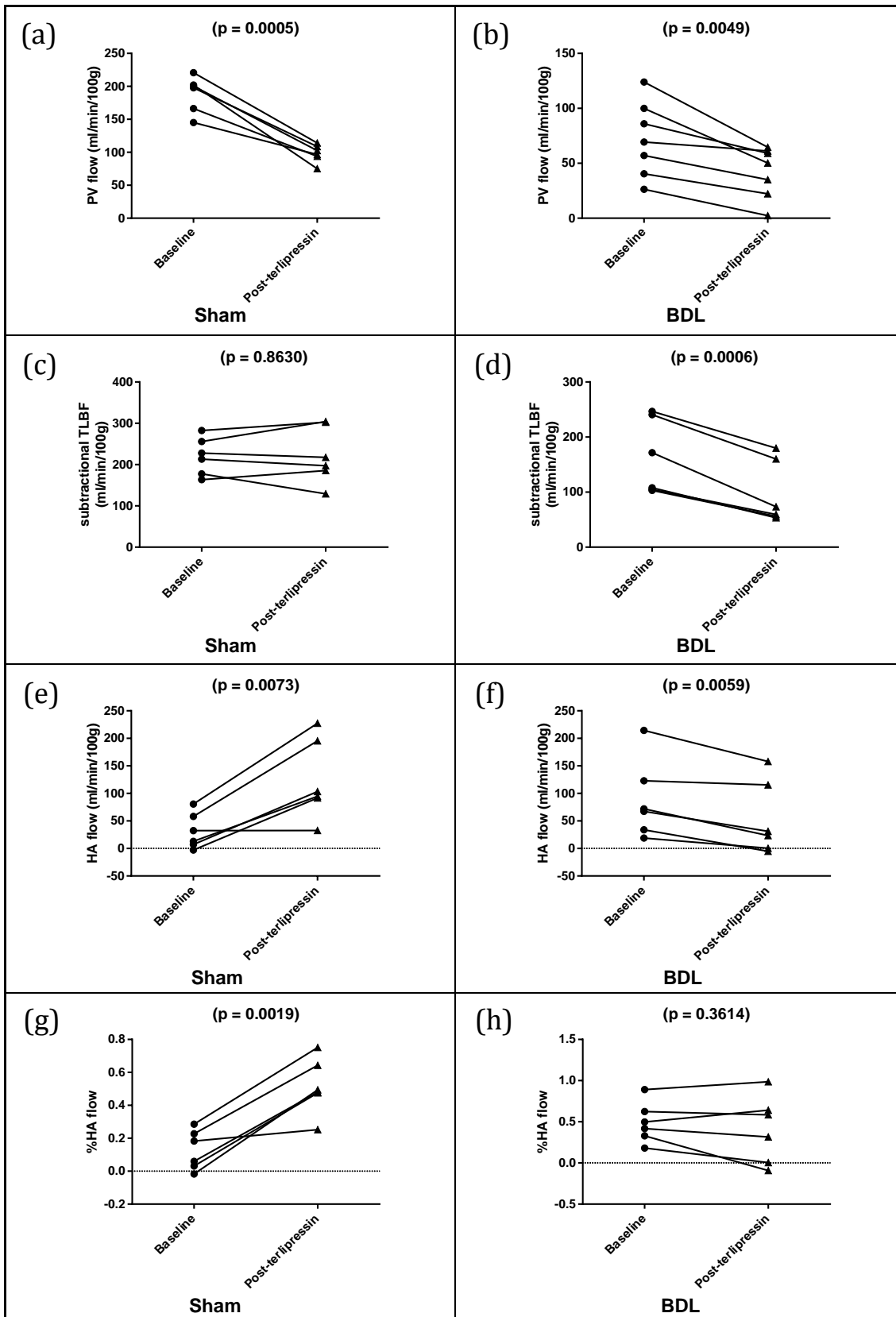


Figure 5.16: Haemodynamic response to terlipressin in sham and BDL rats
 Sham data is shown in the left column and BDL data on the right. Haemodynamic response was assessed using PV flow (a),(b), estimated TLBF (c),(d), estimated HA flow (e),(f) and HA fraction (g),(h).

5.4.4 DISCUSSION

We have demonstrated successful development of cardiac and respiratory gated cine PCMRI to measure pulsatile vessel flow in small animals at 9.4T. The implementation of methods to measure pulsatile flow accurately (as discussed previously and in section 4.6), are dependent on robust systems for cardiac monitoring. Unlike our experience of the dual electrode system available during early developmental work (section 4.6), the triple electrode system was much more robust to radio frequency (RF) interference, with consistent detection of the R-R interval. Because of this, the decision was taken to use triple lead ECG monitoring rather than pulse oximetry and the signal processing unit developed in section 4.6. Our implementation of cine PCMRI gating was however much simpler than contemporary implementations on clinical systems and resulted in under-sampling of data towards the end of the R-R interval. Strategies to account for over or under sampling of data as a result of variations of the R-R interval are especially important for experiments that have extended acquisition times (over ten minutes for a single measurement in our study) as seen with cine PCMRI or short-axis cardiac cine MRI. Additionally, cine PCMRI data was acquired by application and sampling of successive zero, positive and negative gradients through the cardiac cycle. This restricted the number of phases acquired through the cardiac cycle but also incorrectly assumes that flow is constant while each of the three gradients are being applied. Split acquisition methods can overcome this problem, whereby data from successive measurements in a single R-R interval are obtained and compared with data from other R-R intervals where the timing of the gradients has been shifted. This enables data collection from potentially many more phases through the cardiac cycle (restricted only by the repetition time for application of single gradient), but on preclinical system is likely to result in extended acquisition times [371].

While the use of cardiac and respiratory gated cine PCMRI to measure blood flow on a preclinical system is in itself is not novel, we have applied this method to demonstrate that caval subtraction PCMRI can be used to estimate TLBF and HA flow. We have also shown that hepatic flow measurements can be contextualised to systemic circulatory factors non-invasively using cardiac cine MRI measurements of cardiac output. Using these methods, we studied haemodynamic differences at baseline between sham and BDL animals. Our findings confirmed earlier pilot data suggestions of reduced PV flow at baseline (section 4.5) but more importantly also demonstrated reduced estimated TLBF using our novel method in models of chronic liver disease. Our novel proposed method for estimating HA flow also suggests elevated absolute HA flow at baseline in disease, with significantly higher HA fraction in BDL rats. This is the first account to our knowledge of

demonstration of these findings non-invasively, although these findings in themselves are partially corroborated by previously published data from invasive studies using TTUS and/or microspheres. Reduced PV flow for example has been demonstrated in BDL and carbon tetrachloride (CCl₄) models of chronic liver disease [340, 352, 370], and elevated HA flow has also been shown in BDL models [352, 353]. Interestingly, overall reductions in TLBF have been demonstrated in CCl₄ models but not in published BDL data [340, 352, 353]. Analysis of our bulk estimated TLBF (non-normalised to liver volume) supports this claim (figure 5.17).

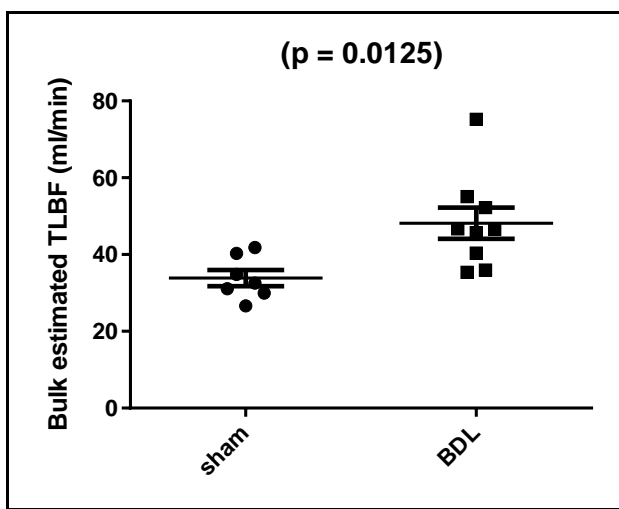


Figure 5.17: Comparison of bulk estimated TLBF in sham and BDL rats

Significant differences ($p = 0.0125$) in bulk estimated TLBF (non-normalised to liver volume) were demonstrated between cohorts suggesting that estimated TLBF in BDL rats (48.15 ± 5.052 ml/min) is higher than in sham counterparts (33.88 ± 2.088 ml/min).

While we have demonstrated that caval subtraction MRI can be used to demonstrate haemodynamic differences in models of chronic liver disease, our experience has also served to highlight several weaknesses in the methodology. Each PCMRI bulk flow measurement (distal IVC, proximal IVC and PV) have associated measurement errors which are propagated in arithmetic calculations. To estimate mean error in PCMRI measurements of PV, aortic root flow and HA fraction (assuming TTUS, cardiac cine MRI derived CO and microsphere derived HA fraction as the respective reference standards), the parameters for the probability distribution of the mean difference between paired measurements can be evaluated as a percentage of the observed mean PCMRI measurements (table 5.3).

Table 5.3: Error estimation for PCMRI derived flow measurements

	GLOBAL MEAN*	MEAN DIFFERENCE TO REFERENCE STANDARD	ESTIMATED PERCENTAGE ERROR
PCMRI PV flow	153.0±12.01 ml/min/100g	10.40±8.116 ml/min/100g [†]	6.8±5.3%
PCMRI aortic root flow	165.0±12.19 ml/min	8.598±8.255 ml/min [‡]	5.2±5.0%
PCMRI HA fraction	29.66±6.909%	14.40±6.372%	49±21%

(*pooled mean across baseline, post-terlipressin, sham and BDL measurements; [†]TTUS reference standard; [‡]cardiac cine MRI derived CO reference standard)

Assuming for example an error of 10% in distal and proximal IVC flow measurements, an estimated TLBF measurement would then be associated with a propagated error of 20%. Estimated HA flow error would also need to include the additional error associated with PV flow measurement (6.797%, table 5.3), raising mean error in this example, to as much as 27%. In demonstration of this, PCMRI derived HA fraction measurements were associated with large errors (table 5.3). Error margins of this magnitude can lead to unexpected and non-physiological results such as negative estimates of HA flow – a phenomenon observed with one dataset.

In spite of these limitations, the presence of such profound haemodynamic differences at baseline has important ramifications for our understanding of the vascular pathobiology of chronic liver disease. The presence of elevated HA fraction suggests that chronic reductions in PV flow are buffered by rises in HA flow in chronic liver disease, but that this is still inadequate in view of the observed reduction in overall TLBF.

At baseline, both sham and BDL animals were under the effects of isoflurane, having been subjected to laparotomy for an extended period of time as part of the experimental protocol. An important method of controlling for changes in systemic factors would be through simultaneous monitoring of mean arterial pressure, but this was not possible because of the complexity of the protocol and requirement for additional equipment not available at the time of the experiment. To provide some sort of contextualisation of hepatic haemodynamic changes, cardiac cine MRI measurements of cardiac output were utilised. An appreciation of the significance of the differences in HA flow and TLBF as a percentage of CO therefore must be considered alongside differences in left-sided systolic function between sham and BDL rats (figure 5.17).

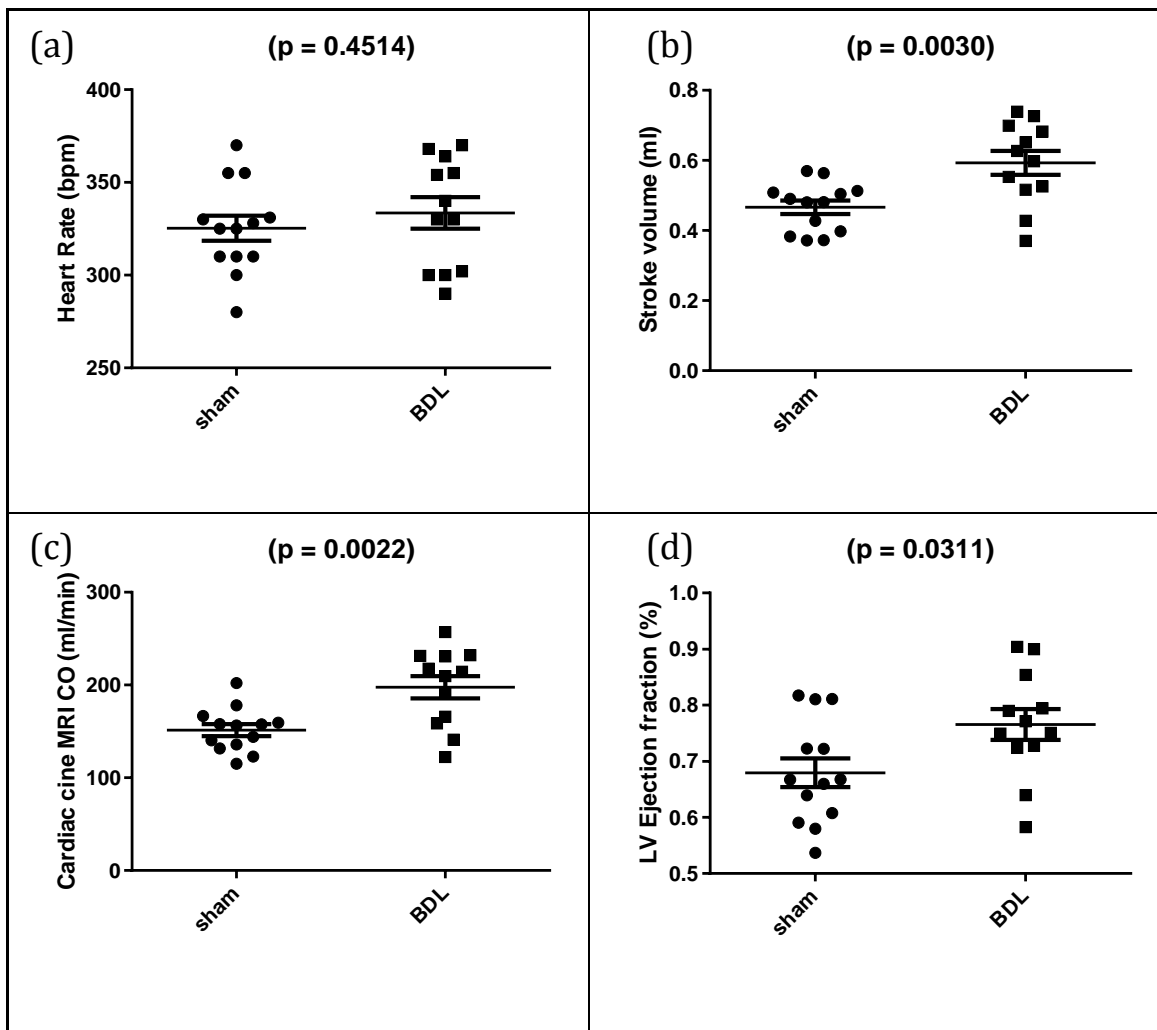


Figure 5.17: Cardiac systolic parameters in sham and BDL rats at baseline

Data from sham ($n = 13$) and BDL ($n = 12$) animals. At baseline, no significant difference in (a) heart rate was demonstrated between sham (325.3 ± 6.803 bpm) and BDL rats (333.6 ± 8.497 bpm; $p = 0.4514$). BDL animals did however demonstrate a larger (b) stroke volume and (c) CO (0.5929 ± 0.03390 mls and 197.6 ± 12.06 ml/min) than their sham counterparts (0.4664 ± 0.01921 mls and 151.4 ± 6.518 ml/min; $p = 0.0030$ and $p = 0.0022$ respectively). Interestingly, (d) ejection fraction at baseline in BDL subjects ($76.57 \pm 2.742\%$) was also greater than in sham subjects ($67.95 \pm 2.567\%$; $p = 0.0311$).

Statistically significant differences between cohorts were demonstrated in all parameters (stroke volume, CO and ejection fraction) except heart rate. These changes highlight the value of cardiac assessment and the growing interest in changes of both systolic and diastolic cardiac function in chronic liver disease. Elevated cardiac output has previously been reported in BDL subjects [370, 372], and it is especially with this in mind that the significance of differences in estimated TLBF and HA flow as percentages of CO are so interesting. Bulk (absolute) estimated TLBF (non-normalised to liver volume) but relative to CO, is unchanged in BDL animals, underlining the importance of normalisation of bulk flow to liver volume in the evaluation of haemodynamic change. Findings also demonstrate that at baseline, BDL livers fail to place a comparable demand on the systemic circulation despite differences in organ:body mass ratios.

Differences in bulk estimated HA flow as a percentage of CO are so profound that even without normalisation to liver volume, they are higher in BDL animals. The CO normalisation thus reveals an inability of BDL HA flow to profit from the systemic hyperdynamic circulation and while this may reflect the advanced disease observed 4-weeks post-BDL procedure, does support the normalisation of bulk HA flow to CO as a potential method of quantifying haemodynamic differences in liver disease.

We have demonstrated that PCMRI measurements of PV flow are repeatable in both healthy and diseased animals. Repeatability over an extended period is advantageous and demonstrates relative stability of haemodynamic factors through the experiment at baseline. Unfortunately repeatability of estimated TLBF and HA flow was not measured, which in hindsight would have been important.

Validation of PCMRI aortic root flow with short-axis cardiac cine MR CO measurements was undertaken to demonstrate the feasibility of PCMRI assessment of large pulsatile vessel flow. Differences in PCMRI measurements at each site caused by (i) scanner factors (the animal was not repositioned during the experiment, so that errors introduced by local inhomogeneities in B_0 and B_1 would have been different at each measurement site) and (ii) animal-specific factors (differing susceptibilities of surrounding tissues at measurement sites, differing quantities of motion artefact and differing errors introduced by V_{enc} settings) imply that reliability of PCMRI IVC flow for example, cannot be inferred through aortic root PCMRI. While we acknowledge that validation of aortic root flow does not in any way enable the validation of hepatic haemodynamic flow parameters, we would argue that this experiment does provide added confidence in the reliability of PCMRI methods. It is also worth noting that validation of PCMRI aortic root flow measurements provides added confidence in the use of these rather than cardiac cine MRI based measurements in the future for calculation of estimated TLBF and HA flow as percentages of CO. As PCMRI data is acquired more quickly (10-15 minutes) than cardiac cine MRI data (20-40 minutes), measuring cardiac output with PCMRI can be advantageous in experimental protocols involving fast-acting drugs or toxins.

Validation of PCMRI PV flow measurements with TTUS was unfortunately only undertaken in sham subjects for reasons mentioned previously. Original power calculations were based on measurement of TTUS PV flow in BDL subjects and we accept this is a major strategic criticism of experimental design. Protocol development also compromised final sample sizes (Appendix C). Validation data however, did corroborate earlier findings (section 4.4), suggestive of good agreement between non-cardiac gated

PCMRI derived PV flow and reference standard TTUS measurements. Validation at baseline and post-terlipressin demonstrated an overall coefficient of repeatability of 65.59 ml/min/100g between methods and while this may seem large (mean PCMRI PV flow across the entire cohort was 153.0 ± 12.01 ml/min/100g), the coefficient of variation of TTUS PV flow measurements was greater than that recorded for PCMRI PV flow measurements both at baseline and post-terlipressin. This would suggest that PCMRI PV flow measurements may indeed be more stable than their 'reference standard' counterparts.

Validation of PCMRI derived HA fraction with microspheres inspired less confidence but was nonetheless encouraging. Because individual sample sizes were small, pooled data from both baseline and post-terlipressin sham and BDL cohorts resulted in large coefficients of variation across PCMRI and microsphere datasets. HA fraction measurements with caval subtraction PCMRI suffer from error propagation (earlier discussion and table 5.3) and this could certainly account for the large coefficient of repeatability (43.27%). More reassuringly, significant correlations between measurements made with microspheres were demonstrated.

Unfortunately, quantification of absolute blood flow with microspheres was not undertaken because of the requirement for simultaneous peripheral arterial sampling. Baseline and post-terlipressin measurements were separated by an extended time period and the technical challenge of timing the intra-cardiac injection with simultaneous rate-controlled (syringe driver) sampling of peripheral arterial blood, proved in pilot experiments error prone and unreliable. The decision was then made to collect technically simpler and less error prone measurements of relative perfusion. Even using this simplified method, multiple ($n = 9$) microsphere datasets were discarded due to inadequate mixing. Although care was taken to ensure diluted preparations of microspheres were well vortexed before injection, published method descriptions advise sonication [373], which was not undertaken because of equipment restrictions.

The measurement of haemodynamic changes in response to terlipressin was an important method of demonstrating the sensitivity of PCMRI methods to PV flow modulation but also in demonstrating the potential of caval subtraction PCMRI to infer changes in estimated TLBF and HA flow. We have demonstrated expected reductions in PV flow and our data is the first to our knowledge to have demonstrated non-invasively in rats the hepatic arterial buffer response and failure of this phenomenon in chronic liver disease using terlipressin. Stable HA fraction in BDL rats post-terlipressin underscores dysfunctional regulation of HA flow but is also suggestive of haemodynamic changes as a

result of systemic rather than hepatic factors. Unfortunately post-terlipressin CO was not measured because of time constraints, and in the absence of these and mean arterial pressure measurements, systemic causes cannot be excluded. It is however worth noting that clinical terlipressin dosing regimes are associated with increases (and not reductions) in mean arterial pressure, systemic vascular resistance and cardiac output [374].

Acquisition of a full hepatic haemodynamic data set (PV, proximal and distal IVC flow) lasted on average 28.42 ± 1.422 minutes ($n = 12$, sham and BDL). The accuracy of estimated TLBF and HA flow measurements would therefore be dependent on stable systemic and hepatic haemodynamics during the entire acquisition. While this would be likely at baseline, post-terlipressin protocols were developed during pilot experiments to maximise the likelihood of an extended window of stable haemodynamics for the measurements to take place. The dose of terlipressin given was also substantially higher than those used clinically. The British National Formulary advises an intravenous dosing regime in acute variceal bleeds of 2 mg over 4 hours (which as an infusion in a 70kg individual would equate to $0.12 \mu\text{g}/\text{kg}/\text{min}$) [375]. Doses used in this study were almost ten-fold higher ($10 \mu\text{g}/\text{kg}/\text{min}$), but comparable to those used in rats published in the literature [376-379].

The changes in estimated TLBF and HA flow post-terlipressin in animal models of chronic liver disease do beg important questions about the clinical value of terlipressin. The use of terlipressin in acute variceal haemorrhage would be justified as hepatic hypoperfusion would be a small price to pay to avoid massive blood loss. The use of terlipressin in hepatorenal syndrome does however merit discussion – improvements in renal perfusion may indeed be beneficial but the long-term sequelae of hepatic hypoperfusion suggested by our data may be counter-productive over an extended treatment period [374, 380].

5.4.5 CONCLUSION

In this section, we have implemented cardiac and respiratory gated cine PCMRI and demonstrated the feasibility of using our novel caval subtraction PCMRI method in the estimation of TLBF and HA flow. Our data has shown significant differences at baseline between sham and BDL rats, with reduced estimated TLBF and HA fraction in chronic liver disease. These findings suggest inadequate baseline hepatic arterial buffer response in BDL subjects. Measurement of CO demonstrates significant differences in estimated HA flow but not TLBF as a percentage of CO. These findings suggest a failure of BDL livers to place a comparable demand on systemic circulation despite increased organ:body mass ratio.

We have demonstrated repeatability of PV flow measurements in the same subject, and validated direct and indirect estimates of measured PCMRI flow using (a) cardiac cine MRI for validation of aortic root PCMRI, (b) TTUS for validation of PV PCMRI and (c) fluorescent microspheres for validation of caval subtraction PCMRI estimated HA fraction. Good agreement with reference methods was demonstrated for aortic root and PV flow PCMRI. Encouraging correlations were demonstrated with microspheres however our data highlights the risks of error propagation in the estimation of HA flow with caval subtraction methods.

Finally, we have investigated the haemodynamic response to terlipressin in sham and BDL animals to demonstrate (a) expected reductions in PV flow, (b) an intact hepatic arterial buffer response in healthy animals and (c) failure of the hepatic arterial buffer response in animals with chronic liver disease.

5.5 CLINICAL TRANSLATION, VALIDATION, REPRODUCIBILITY AND STUDIES OF THE NEGATIVE HEPATIC ARTERIAL BUFFER RESPONSE

5.5.1 BACKGROUND AND CLINICAL PROTOCOL DEVELOPMENT

Cine PCMRI sequences are well established on clinical systems, with primary application in cardiac imaging. A reasonable volume of studies applying PCMRI around the liver can be found in the literature (section 1.3.6). Published methods were evaluated and then used to inform the development of our own protocols. Adaptation of sequences and development of protocols to measure blood flow around the liver was undertaken with specific attention to each of the factors discussed in section 4.3. Methods were developed to maximise (i) accuracy of absolute and caval subtraction measurements in the abdomen/lower thorax, (ii) practicality of the protocol in healthy subjects and importantly in those with disease, (iii) transferability of the protocol to other scanner systems at our institution and beyond.

To determine the optimal velocity encoding settings, the literature review performed in section 1.3.6 was used to identify studies where PCMRI studies of PV, HA, hepatic venous and azygous venous flow were measured. The V_{enc} settings used in these studies (figure 5.18) were then used to guide pilot measurements in normal volunteers.

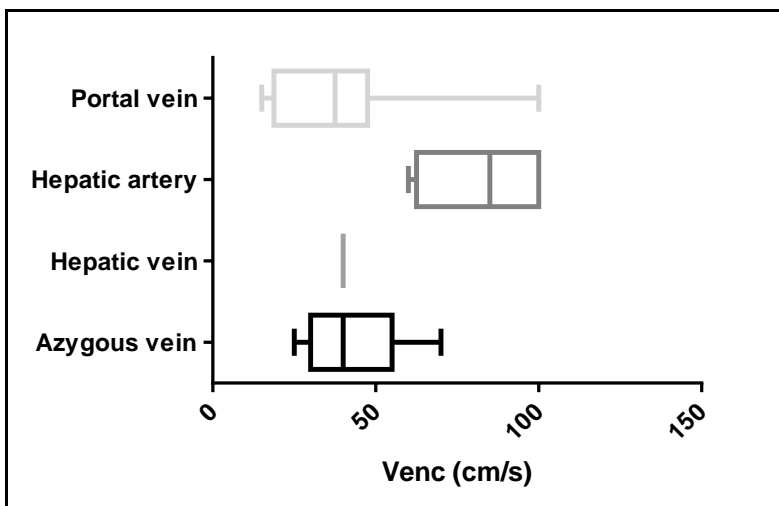


Figure 5.18: Box and whisker plots for published V_{enc} settings for PCMRI studies of hepatic vessels

Data from PCMRI studies in the PV ($n = 12$), HA ($n = 4$), hepatic vein ($n = 1$) and azygous vein ($n = 4$) are shown.

Final protocols were based on V_{enc} settings of 40, 60, 60, 80 and 120 cm/s for PV, HA, proximal IVC, distal IVC and aortic root flow measurements respectively.

As velocity encoding gradients were applied only in the slice select direction, ensuring alignment of vessel flow and flow encoding gradients was important in ensuring

accurate measurements. For PV flow studies, coronal anatomical images were initially obtained on expiratory breath-hold. The scanner console software (Philips MR WorkSpace, Philips Healthcare, Best, Netherlands) then enabled placement of three markers in the PV lumen and images were then obtained parallel to the PV. Two-dimensional PCMRI studies were then planned on these images to ensure vessel orthogonality (figure 5.19).

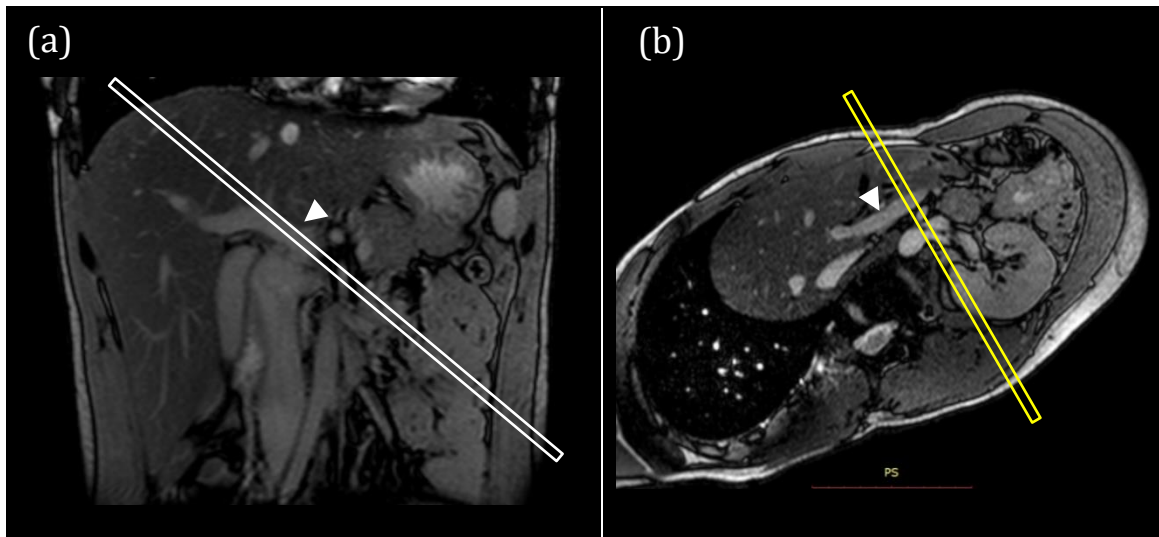


Figure 5.19: Systematised planning for PV PCMRI studies

The portal vein (▲) was identified on coronal images (a) and a slice was planned parallel to the vessel (white slice planning box). Anatomical images obtained in that plane (b), were used to identify the PV (▲) and plan a PCMRI slice perpendicular to the vessel.

For studies of HA, IVC and aortic root flow, expiratory breath-hold sagittal anatomical images were obtained through the upper abdominal and lower thoracic great vessels with the field-of-view adjusted to include tissues approximately 5 cm on either side the vertebral bodies. These images were evaluated in conjunction with coronal images to identify (a) the coeliac axis and common HA, (b) the proximal IVC above the renal veins but below the hepatic IVC, (c) the IVC above the hepatic venous inflow but below the right-atrial junction and (d) the aortic root. For each of the sites, PCMRI studies were planned ensuring orthogonality on coronal and sagittal images (figure 5.20).

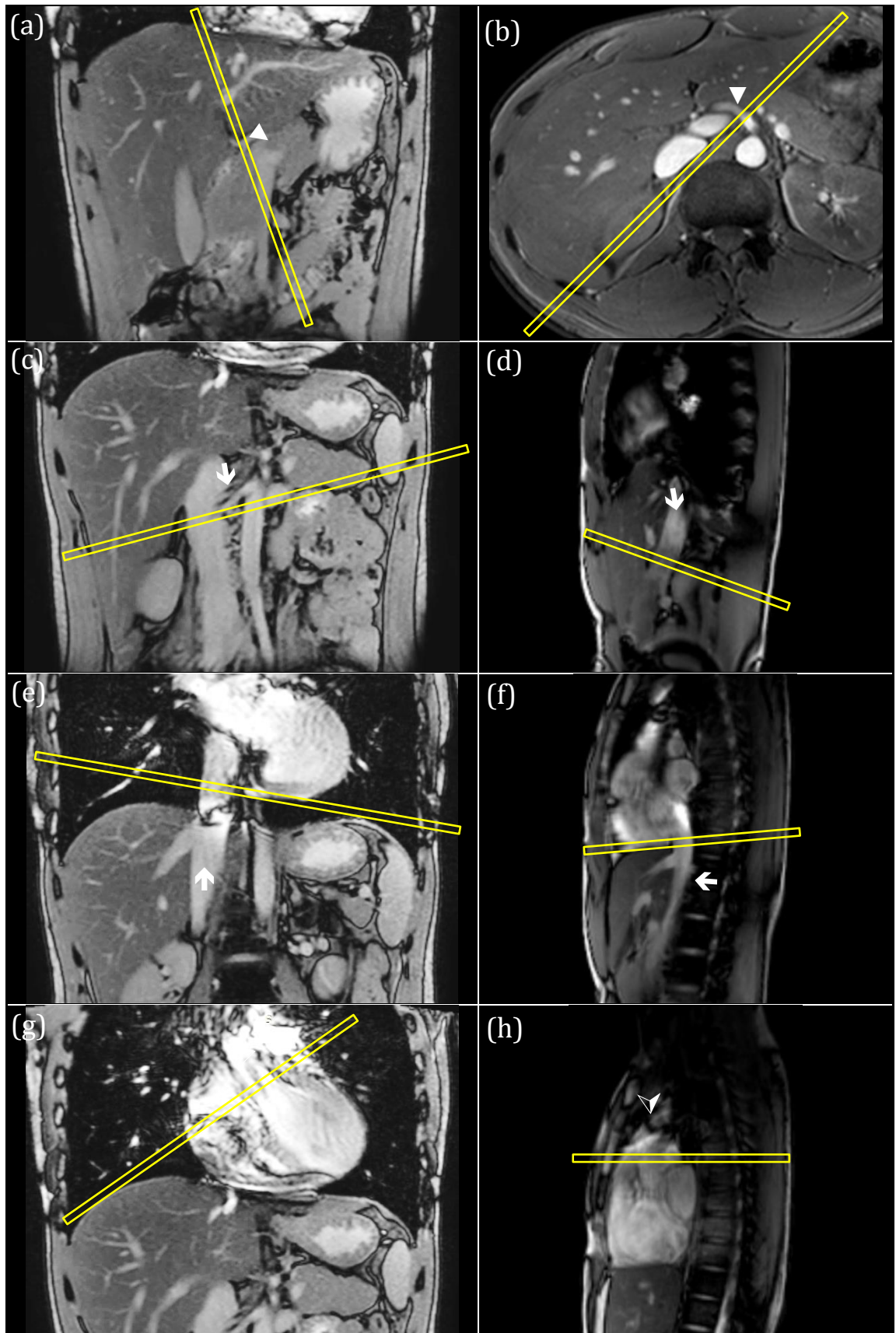


Figure 5.20: Systematised planning for other PCMRI studies

The HA (▲), IVC (↑) and aortic root (△) were identified on coronal images (a, c, e and g), axial (b) and sagittal images (d, f, and h). Slices were planned (yellow planning box) to ensure orthogonality in at least two planes. Note the positioning of the proximal (c, d) and distal (e, f) PCMRI studies.

Ensuring adequate spatial resolution and appropriate matrix size was especially important for measurements in smaller vessels such as the common HA. An important advantage of PCMRI using 3T (relative to lower field strength systems) is the improved SNR at higher resolution [205]. All studies were performed using a 5 mm slice thickness and a 336x336 matrix size. The field of view was 271 x 210 mm so that in-plane spatial resolution was 0.808 x 0.625 mm². At this resolution, a 5 mm diameter vessel would render signal in over 35 pixels. It is worth noting that this resolution is higher than that used in previously published HA flow PCMRI studies [198, 199, 205].

PCMRI data from large, high flow volume pulsatile vessels such as the aorta and IVC are at risk of pulsation artefacts and spatial misregistration. To minimise these effects, all measurements were undertaken in expiratory breath-hold. While this had the advantage of much faster acquisitions (as these were based on cardiac gating alone), the method was also very dependent on the subject's quality and compliance with the breath-hold during the acquisition.

Because the sequences were adapted and optimised from manufacturer PCMRI sequences, velocity compensation and methods to minimise intravoxel phase dispersion and phase offset errors during acquisition and post-processing were included as features of standard sequence design. No additional modification of these settings was introduced in the interest of maximising transferability of the sequence to other scanners and institutions.

All PCMRI studies were cardiac gated using pulse oximetry for cardiac monitoring. Data was collected using a temporal resolution of seven phases through the cardiac cycle. The low temporal resolution was chosen to enable a single measurement to be completed within a single breath-hold (<15 seconds). Pilot work in patients with liver disease demonstrated that sampling of more phases through the cardiac cycle would be unfeasible in a single breath-hold for subjects with more elevated heart rates (>80 beats per minute). In the interest of maximising the practicality of the protocol in patients with liver disease (likely to have higher heart rates and smaller breath-hold capacity), protocols were maintained at low temporal resolution.

Finally, all PCMRI measurements were performed in triplicate and recorded measurements were averaged across the three studies. This had the added benefit of minimising errors introduced by many of the potential challenges to accurate PCMRI quantification, including those introduced by lower temporal resolution measurements.

As discussed in section 1.3.6, validation of PCMRI measurements is a significant challenge on clinical systems. Many researchers have opted to use either flow phantoms or transcutaneous Doppler US, both of which have significant limitations. Validation with transcutaneous Doppler US has been variable and unimpressive (table 1.2), and it is questionable as to whether this is due to variability in Doppler US or PCMRI measurements [190, 192, 199, 201]. Direct validation of hepatic vessel flow can be achieved invasively (ICG clearance methods, section 1.2.3), but as that would be unfeasible in healthy volunteers, we propose instead checking the consistency of hepatic caval subtraction PCMRI measurements. This could be achieved non-invasively by checking the agreement between PCMRI afferent (PV and HA) and efferent (caval subtraction IVC) bulk flow measurements. Validation of aortic root flow measurements with cardiac cine MRI could also be undertaken as previously as a means of verifying the reliability of absolute flow quantification using PCMRI.

The ability to detect expected changes in hepatic haemodynamic parameters in response to a controlled insult would be important in demonstrating the clinical feasibility of caval subtraction MRI. The use of dedicated pharmaceutical agents to demonstrate this phenomenon in patients/healthy volunteers would be difficult to justify. There have been several PCMRI studies demonstrating physiological post-prandial rises in PV flow and in view of this data [381-384], measurements were performed in the fasted and post-prandial state to assess the performance of our novel method.

With this in mind, in this section we aim to (a) demonstrate the feasibility of using caval subtraction PCMRI to measure TLBF, HA and PV flow on a clinical system, (b) assess the consistency of estimated TLBF and HA flow measurements using caval subtraction PCMRI by comparison with directly measured PCMRI flow and validate aortic root flow measurements using short-axis cardiac cine MRI, (c) study the reproducibility of caval subtraction PCMRI measurements performed in the same subject after 7 days, and finally (d) investigate post-prandial hepatic haemodynamic changes in healthy volunteers.

5.5.2 METHODS

5.5.2.1 Subjects and preparation

Local ethics committee approval was obtained and all participants provided informed written consent. Participant information sheets and consent form copies can be found in Appendix D. Healthy volunteers were recruited by means of advertisement. There were seven male (aged 26.5 ± 1.36 years) and six female (aged 31.2 ± 2.62 years) participants. Volunteers were excluded if (a) they had any contraindication to standard MR imaging, (b) if they were taking any long-term medication (excluding the oral contraceptive pill) and (c) if they had any documented history of previous liver or gastrointestinal disease. As subjects also underwent DCE MRI (findings presented in Chapter 6), those with any prior history of renal disease were excluded. One subject was excluded because of claustrophobia. Participants were asked to remain fasted for six hours prior to imaging and were advised to consume water ad libitum, but asked to refrain from the consumption of caffeinated fluids.

5.5.2.2 Two-dimensional cine PCMRI

Imaging was performed using a 3.0T scanner (Achieva, Philips Healthcare, Best, Netherlands) with a 16 channel body coil (SENSE XL-Torso, Philips Healthcare, Best, Netherlands). The coil was positioned over the lower thorax and upper abdomen and subjects were monitored using digital pulse oximetry and bellows.

Initial scouts were performed to ensure inclusion of the entire cardiac and liver volume within the field-of-view. Coronal images of the upper abdomen and lower thorax, and sagittal images including the abdominal great vessels were obtained with successive expiratory breath-holds using a gradient echo sequence (table 5.4). Localisation of the vascular structures of interest was performed as described earlier, with additional anatomical imaging through the PV. PCMRI studies were planned through the PV, common HA, proximal IVC, distal IVC and aortic root in succession. Where HA anatomical variations were noted ($n = 2$), measurements were made as close as possible to the aortic origin and measurements were obtained from more than one vessel where necessary. Studies were performed in expiratory breath-hold and cardiac gated using peripheral pulse oximetry and settings listed in table 5.4. Before each scan, subject heart rate was adjusted on the scanner console software to optimise the arrhythmia rejection window. Acquisition time for each measurement was less than 20 seconds. Each PCMRI study was repeated three times in succession. All PCMRI measurements, including planning time were usually completed within 20 minutes. Quantification was performed using the freely available software package, Segment (Medviso, Lund, Sweden).

5.5.2.3 Cardiac cine MRI validation

Long-axis anatomical images were planned using previously acquired coronal image data. Short-axis cardiac cine MRI studies were then planned checking correct orientation on both coronal and long-axis images. Before scanning, subject heart rate was adjusted on the scanner console software to optimise the arrhythmia rejection window. Contiguous slice datasets were obtained, each with 30 frames through the cardiac cycle. Images were obtained in expiratory breath-hold, using a spoiled gradient echo sequence (table 5.4). Most acquisitions were complete within 7 breath-holds. Quantification was performed using the freely available software package, Segment (Medviso, Lund, Sweden). Automatic segmentation tools were used to identify the endocardial surface, with frame by frame manual review and segmentation correction where appropriate.

Table 5.4: Sequence parameters

	ANATOMICAL IMAGES	PCMRI	CARDIAC CINE MRI
<i>TR/TE (seconds)</i>	2.47/1.23	8.70/5.22	3.40/1.70
<i>Flip angle (°)</i>	45	10	45
<i>Matrix size (pixels)</i>	352 x 352	336 x 336	256 x 256
<i>Field-of-view (mm)</i>	350 x 350	271 x 210	320 x 320
<i>Spatial resolution (mm²)</i>	0.994 x 0.994	0.808 x 0.625	1.25 x 1.25
<i>Bandwidth (Hz/pixel)</i>	1640	210	1243
<i>Slice thickness (mm)</i>	5	5	8
<i>Slice gap (mm)</i>	5.5	-	8
<i>Cardiac cycle phases</i>	-	7	30

5.5.2.4 Volumetric assessment and bulk flow normalisation

All PCMRI bulk flow measurements were normalised to liver volume. Liver volume was measured using 5 mm slice thickness gradient echo coronal anatomical images. Segmentation was performed manually using Amira (Amira Resolve RT, Visage Imaging, Berlin, Germany). A tissue density of 1.0 g/ml was assumed [193].

5.5.2.5 Caval subtraction PCMRI consistency studies

To measure the consistency of estimated TLBF using subtracted PCMRI IVC flows, comparison was made with bulk inflow PCMRI measurements at the PV and common HA. Comparisons between caval subtraction PCMRI estimated and directly measured HA flow and HA fractions were also studied.

5.5.2.6 Reproducibility studies

To measure reproducibility, subjects were scanned using the same MRI protocol 7 days later. As with the initial study, subjects were asked to remain fasted for at least 6 hours

prior to the study and were advised to consume water ad libitum, but refrain from the consumption of caffeinated fluids. Care was taken to ensure subjects were scanned at a comparable time of the day to the original study.

5.5.2.7 Physiological stress studies

Post-prandial changes in liver haemodynamics were studied using a meal challenge. After the initial scan, subjects were removed from the scanner and given 440 mls of Ensure Plus® (Abbot Laboratories, Illinois, USA) for oral ingestion, compatible with 660 kcal (2780 kJ) of prandial stress. During this time, subjects remained seated outside the scanner, to minimise any cardiovascular changes. Approximately 45-60 minutes after ingestion, the MRI protocol was repeated.

5.5.2.8 Statistical analysis

Kolmogorov-Smirnov tests were used to confirm normality of variable distributions. Reproducibility, consistency and validation studies were assessed using paired t-tests, Bland-Altman analysis of agreement with calculation of the coefficient of repeatability and assessment of correlation between measurements using Pearson's correlation coefficient. Post-prandial hepatic haemodynamic changes were evaluated using paired t-tests. The threshold of statistical significance was defined to be $p < 0.05$.

5.5.3 RESULTS

5.5.3.1 Cohort features

Cohort features are shown in table 5.5.

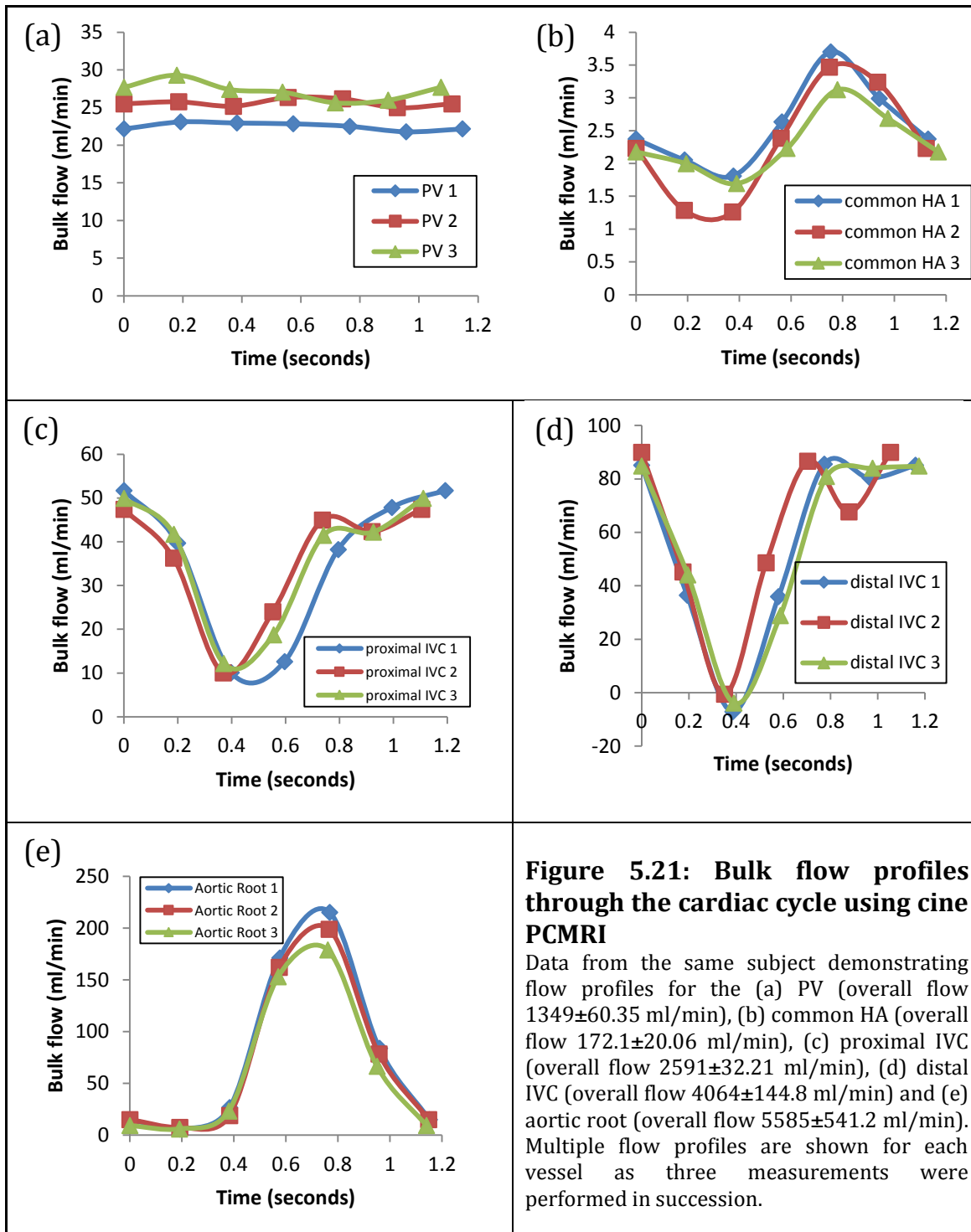
Table 5.5: Cohort numbers for normal volunteer studies

	MALE (<i>n</i> = 7)	FEMALE (<i>n</i> = 6)
<i>Age (years)</i>	26.7±1.55	30.2±2.37
<i>Liver volume (mls)</i>	1215±66.5	1207±91.3

(all parameters given as mean ± standard error of the mean)

5.5.3.2 Caval subtraction PCMRI

Pulse oximetry and respiratory gated cine PCMRI flow studies through the cardiac cycle demonstrated physiological flow profiles through the PV, common HA, proximal IVC, distal IVC and aortic root.



Caval subtraction methods, applied for example to the dataset above were suitable for estimation of TLBF (1473 ml/min), estimated HA flow (124 ml/min) and estimated %HA

flow (8.418%). Note some agreement with directly measured HA flow (172 ml/min) and %HA flow (11.31%).

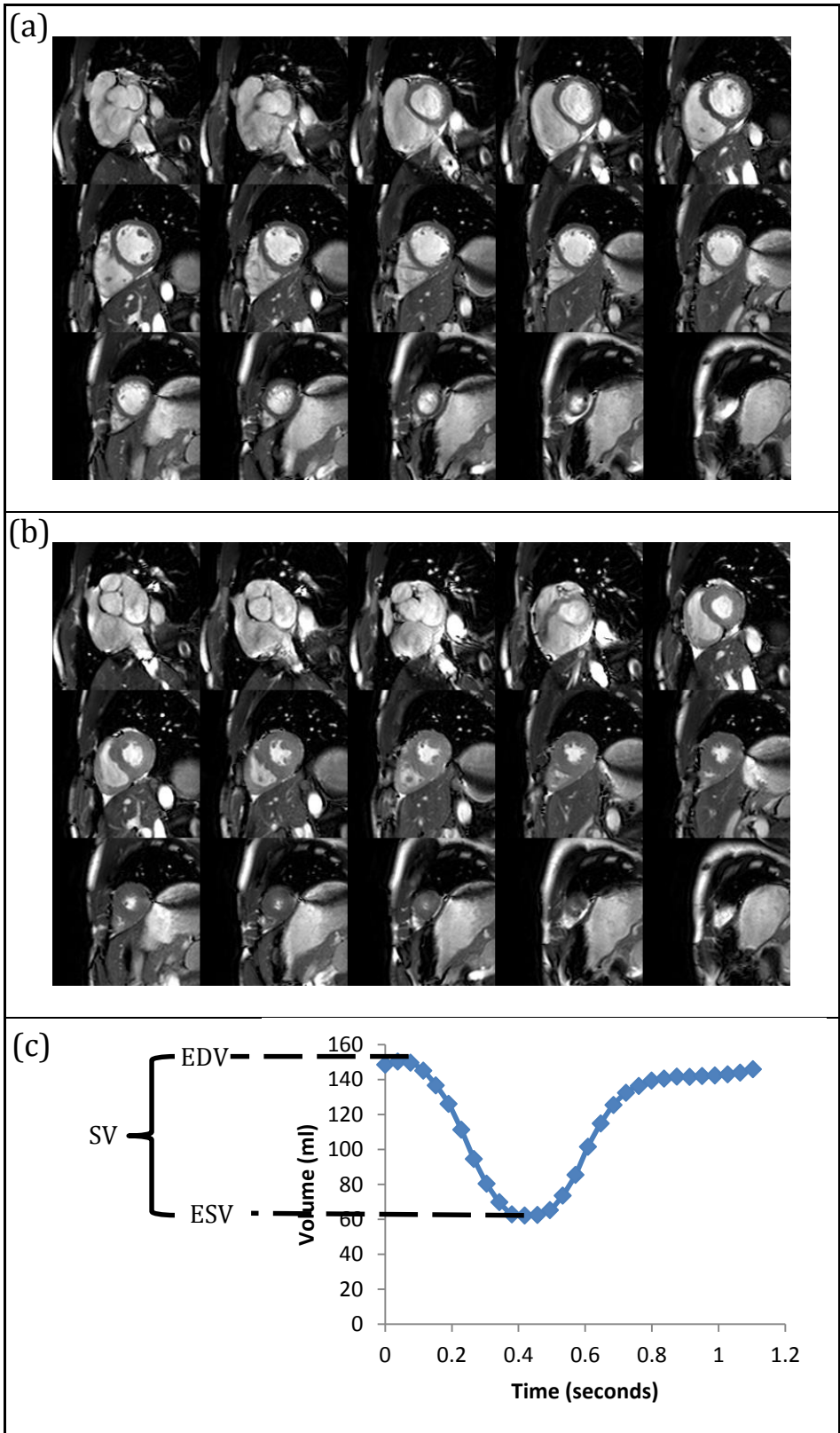


Figure 5.22: Clinical anatomical cardiac cine MR and volumetric quantitation
 Fifteen left ventricle short-axis slices (8 mm thickness) extending to the apex (a,b, right lower corner image) are shown, from a normal volunteer. The stroke volume can be calculated from segmentation of endocardial areas at end diastole (a) and end systole (b). Segmentation of ventricular volumes through multiple phases of cardiac cycle can be used to generate volume-time curves (c).

Estimated TLBF can then be normalised to systemic haemodynamics using measurement of CO assessed with cardiac cine MRI (figure 5.22). CO measured by cine MRI was 5891

ml/min (compared with aortic root flow of 5585 ml/min), so that estimated TLBF as a percentage of CO was 25.00% and estimated HA flow as a percentage of CO was 2.105%.

5.5.3.3 Cardiac cine MRI validation

Validation of PCMRI measurements of aortic root flow were undertaken using measurements of cardiac output derived from short-axis cardiac cine MRI volumetric analysis (figure 5.22) in normal volunteers ($n = 13$). Including baseline, post-prandial and reproducibility studies, thirty-five PCMRI aortic root flow measurements were validated using cardiac cine MRI (table 5.4). Paired t-tests demonstrated non-significant differences between PCMRI cardiac output and cardiac cine MRI cardiac output in fasted (mean difference 65.83 ± 52.18 ml/min; $p = 0.2197$) and post-prandial states (mean difference 16.99 ± 77.49 ml/min; $p = 0.8309$). The coefficient of variation was slightly lower for PCMRI cardiac output in both the fasted (17.55% vs 17.88%; PCMRI vs cardiac cine MRI) and post-prandial states (21.08% vs 24.25%; PCMRI vs cardiac cine MRI). Graphical analysis (figure 5.23b) showed significant and strong correlations between PCMRI and cardiac cine MRI derived cardiac output measurements ($r = 0.9567$; $p < 0.0001$).

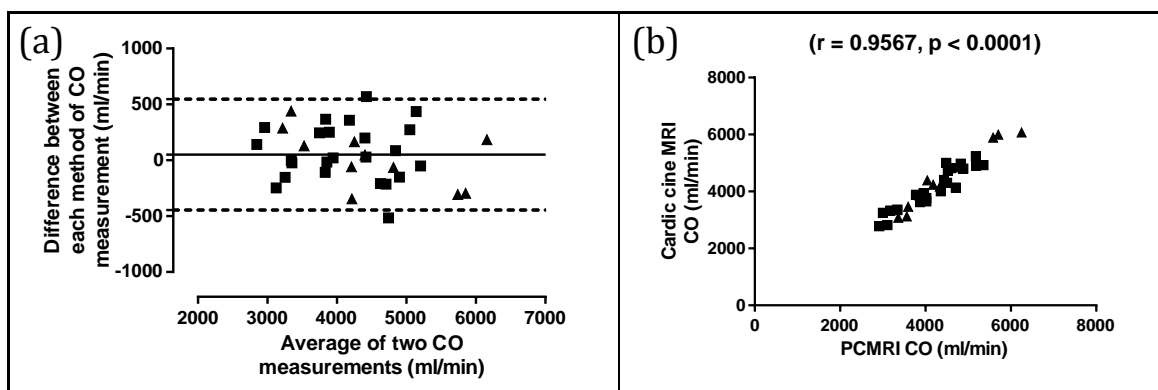


Figure 5.23: Validation of aortic root PCMRI using short axis cardiac cine MRI

Strong correlations and encouraging agreements between PCMRI and cardiac cine MRI derived cardiac output measurements were demonstrated in the fasted (■) and post-prandial (▲) state. The coefficient of repeatability between measurement methods for the entire dataset was 496.4 ml/min.

5.5.3.4 Caval subtraction PCMRI consistency

Consistency of caval subtraction PCMRI was assessed by comparison of (a) estimated TLBF with the sum of directly measured PV and HA flow, (b) estimated HA flow with directly measured HA flow and (c) estimated HA fraction with directly measured HA fraction. Agreement was assessed in normal volunteers ($n = 13$), at baseline, post-prandially and during reproducibility studies using thirty-seven measurements. Paired t-tests demonstrated a non-significant difference between estimated TLBF and directly measured TLBF in the fasted state (mean difference 1.330 ± 2.407 ml/min/100g; $p = 0.5859$). This difference was just non-significant in the post-prandial state (mean

difference 5.918 ± 3.082 ml/min/100g; $p = 0.0789$). The coefficient of variation was higher for caval subtraction PCMRI measurements in both fasted (23.01% vs 22.23%; estimated TLBF vs directly measured TLBF) and post-prandial states (14.24% vs 15.90%; estimated TLBF vs directly measured TLBF). Graphical analysis (figure 5.24b) showed significant and strong correlations between estimated and directly measured TLBF using PCMRI ($r = 0.9061$; $p < 0.0001$).

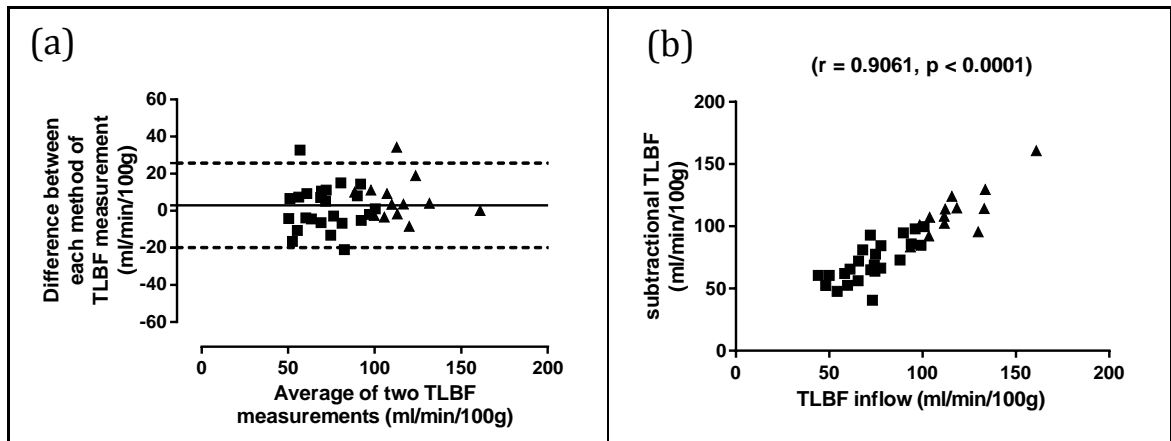


Figure 5.24: Agreement between estimated TLBF derived from caval subtraction PCMRI and inflow TLBF measured directly with PCMRI

Strong correlations and encouraging agreements between estimated TLBF and directly measured TLBF were demonstrated in the fasted (■) and post-prandial (▲) state. The coefficient of repeatability between measurement methods for the entire dataset was 22.77 ml/min/100g.

Because a fixed quantity (PCMRI PV flow) was subtracted from estimated and directly measured TLBF, paired t-tests for estimated and directly measured HA flow demonstrated the same mean differences and significance levels as previously. The coefficient of variation was considerably higher for estimated HA flow measurements in both fasted (123.2% vs 75.56%; estimated vs directly measured HA flow) and even greater in post-prandial states (331.6% vs 54.77%; estimated vs directly measured HA flow). Graphical analysis (figure 5.25b) showed significant correlations between estimated and directly measured HA flow using PCMRI ($r = 0.7065$; $p < 0.0001$).

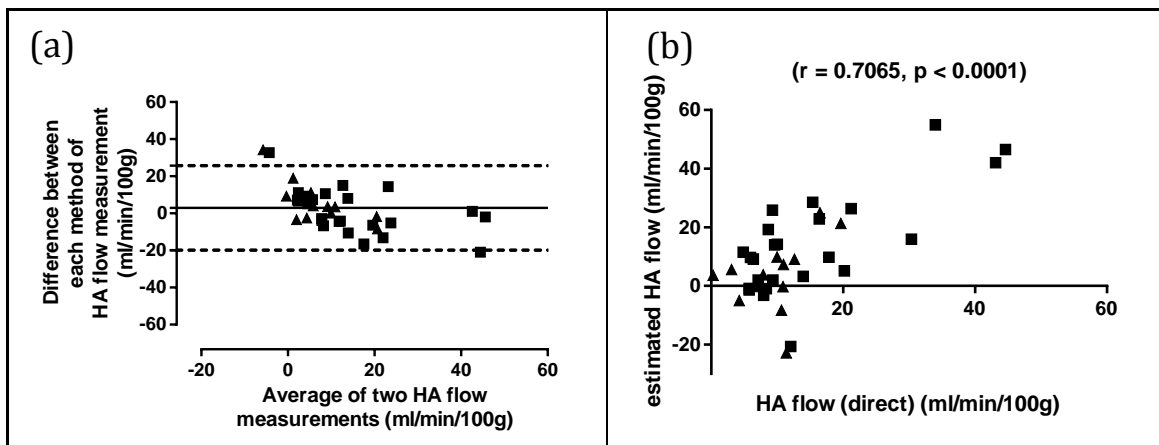


Figure 5.25: Agreement between estimated HA flow derived from caval subtraction PCMRI and HA flow measured directly with PCMRI

Although strong correlations were observed between estimated and directly measured HA flow in both the fasted (■) and post-prandial (▲) state, the coefficient of repeatability between measurement methods for the entire dataset was 22.77 ml/min/100g, which was large in view of physiological levels of absolute HA flow.

Paired t-tests demonstrated a non-significant difference between estimated and directly measured HA fraction in the fasted state (mean difference $3.615 \pm 3.545\%$; $p = 0.3185$). This difference was just non-significant in the post-prandial state (mean difference $5.461 \pm 2.815\%$; $p = 0.0762$). The coefficient of variation was considerably higher for caval subtraction PCMRI HA fraction measurements in both fasted (137.7% vs 57.71%; estimated vs directly measured HA fraction) and even greater in post-prandial states (426.42% vs 57.54%; estimated vs directly measured HA fraction). Graphical analysis (figure 5.26b) showed significant correlations between estimated and directly measured HA fraction using PCMRI ($r = 0.6849$; $p < 0.0001$).

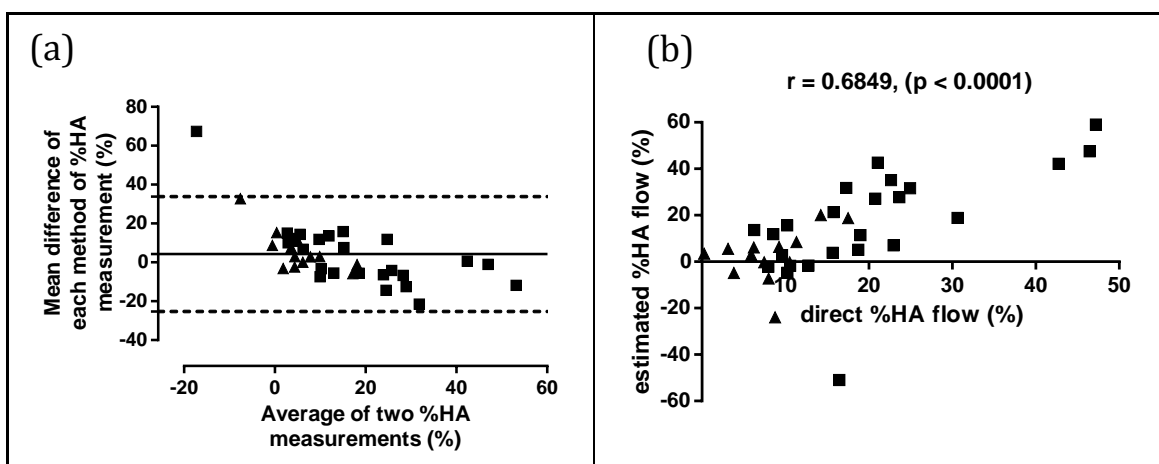


Figure 5.26: Agreement between estimated HA fraction derived from caval subtraction PCMRI and HA fraction measured directly with PCMRI

Although strong correlations were observed between estimated and directly measured HA fraction in both the fasted (■) and post-prandial (▲) state, the coefficient of repeatability between measurement methods for the entire dataset remained large (29.57%).

5.5.3.5 Reproducibility studies

Reproducibility was assessed using the same protocol with the same scanner in the same subjects exactly seven days after the initial study. Repeat measurements were obtained in normal volunteers ($n = 11$). No significant differences were demonstrated between repeated PV flow measurements (mean difference -1.234 ± 2.924 ml/min/100g; $p = 0.6819$). The coefficient of reproducibility was 19.01 ml/min/100g and graphical analysis (figure 5.27b) showed correlations between repeated PV flow measurements were significant ($r = 0.7152$; $p = 0.0132$).

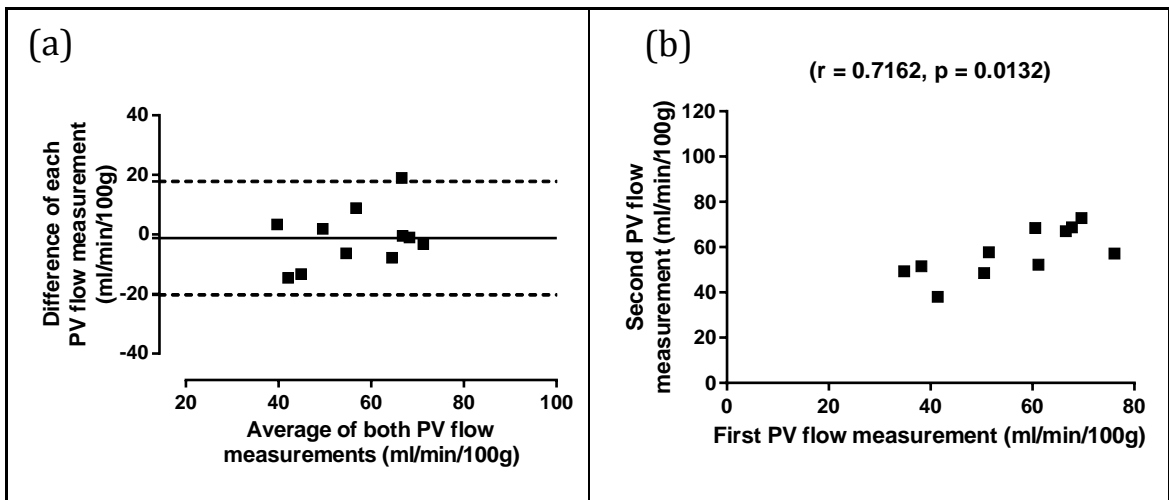


Figure 5.27: Seven day reproducibility of PCMRI PV flow measurements

Bland-Altman (a) and scatter plot of repeated measurements (b), demonstrated strong correlations and encouraging agreements between repeated PCMRI PV flow measurements were demonstrated. The coefficient of reproducibility was 19.01 ml/min/100g.

Reproducibility of estimated (caval subtraction) and directly measured TLBF were compared. No significant differences were demonstrated between repeated directly measured TLBFs (mean difference -2.345 ± 4.547 ml/min/100g; $p = 0.6172$) or estimated TLBFs (mean difference -8.460 ± 4.860 ml/min/100g; $p = 0.1124$). The coefficient of reproducibility was higher for estimated TLBFs (31.60 ml/min/100g) than in directly measured TLBFs (29.56 ml/min/100g). Graphical analysis (figure 5.28b, d) showed significant but moderate correlations between repeated direct TLBF measurements ($r = 0.6045$; $p = 0.0489$), but not for estimated TLBFs ($r = 0.4858$; $p = 0.1297$).

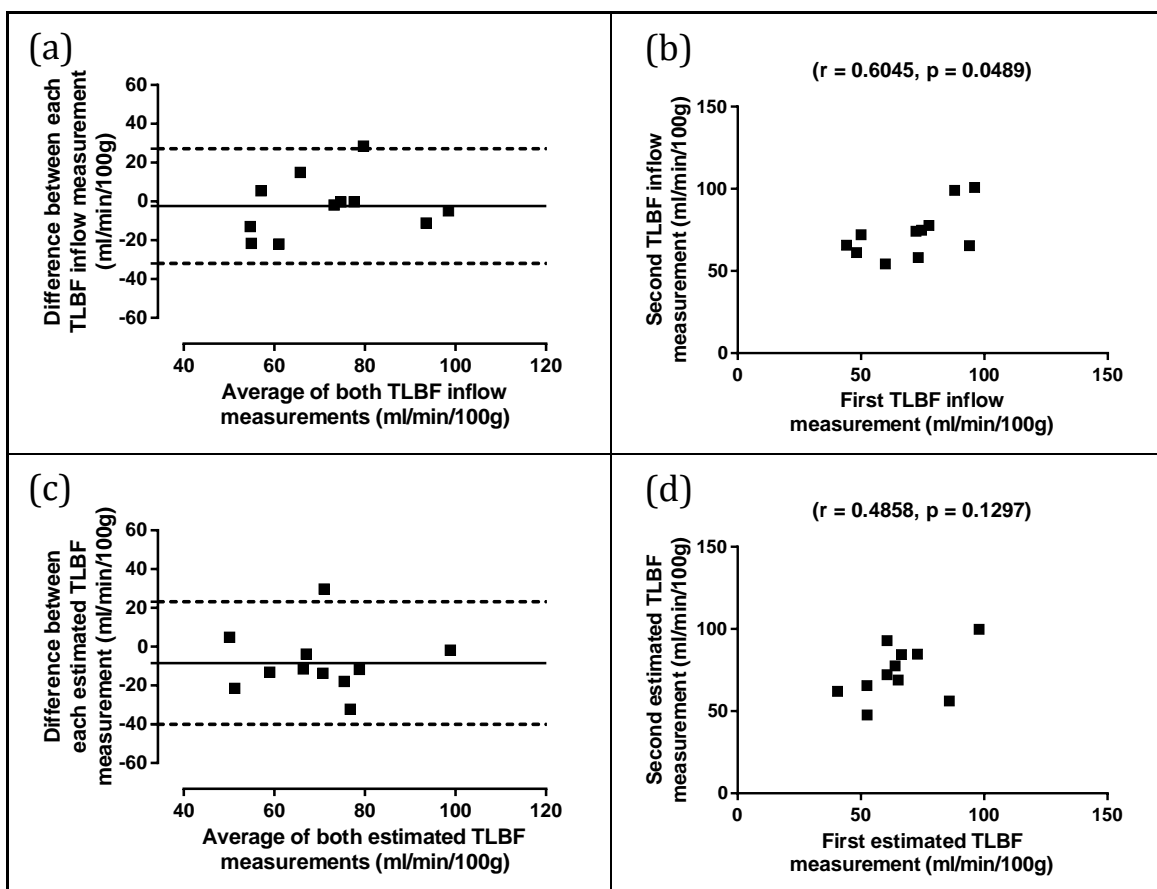


Figure 5.28: Seven day reproducibility of TLBF measurements

Bland-Altman and scatter plots of repeated measurements for reproducibility of directly measured TLBF (a), (b) and estimated (caval subtraction) TLBF (c),(d). Estimated TLBF demonstrated a slightly larger coefficient of reproducibility, and non-significant correlations between repeated measurements.

Reproducibility of estimated (caval subtraction) and directly measured HA flow were compared. No significant differences were demonstrated between repeated directly measured HA flows (mean difference 1.111 ± 3.005 ml/min/100g; $p = 0.7193$) or estimated HA flows (mean difference 7.226 ± 4.425 ml/min/100g; $p = 0.1335$). The coefficient of reproducibility was higher for estimated HA flows (28.77 ml/min/100g) than in directly measured HA flows (19.53 ml/min/100g). Graphical analysis (figure 5.29b, d) showed significant correlations between repeated direct HA flow measurements ($r = 0.6915$; $p = 0.0184$) and estimated HA flows ($r = 0.6511$; $p = 0.0300$).

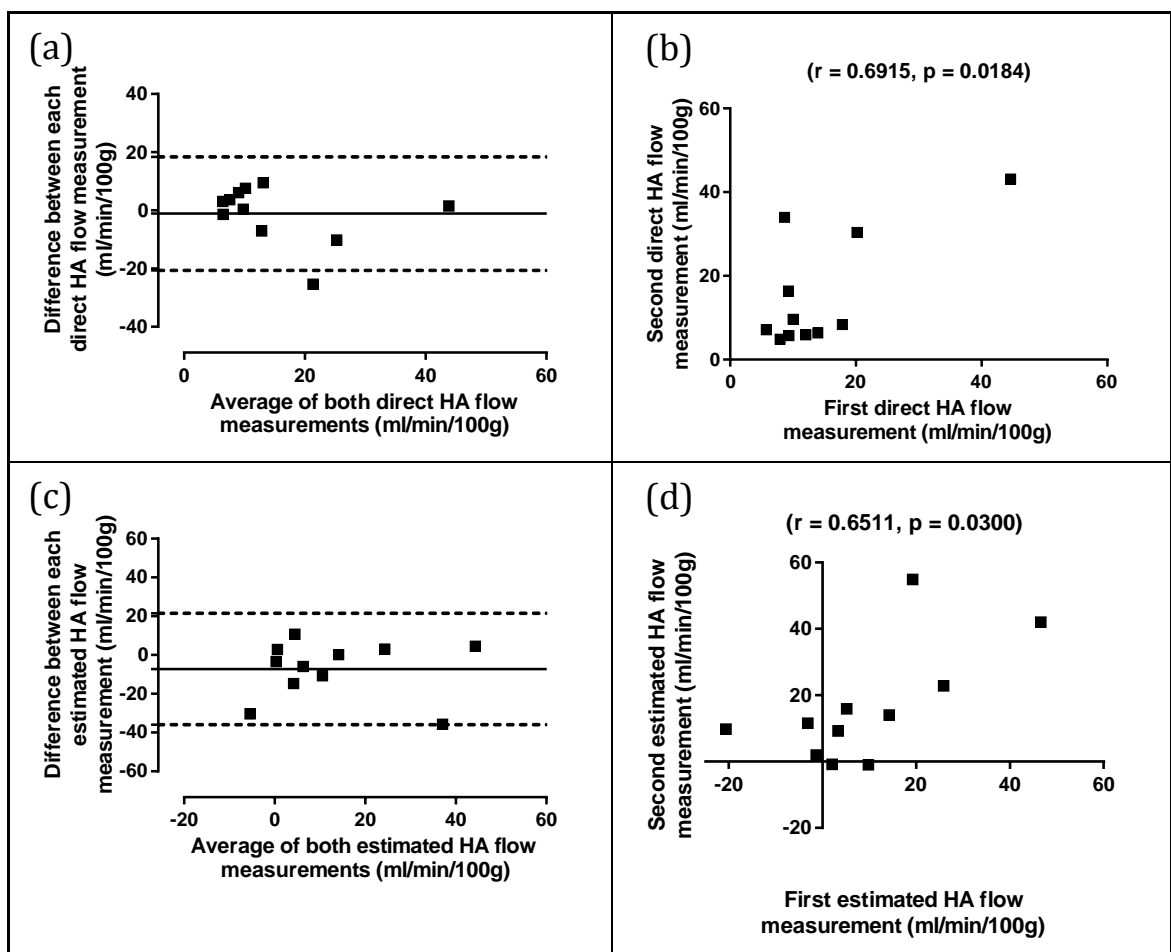


Figure 5.29: Seven day reproducibility of HA flow measurements

Bland-Altman and scatter plots of repeated measurements for reproducibility of directly measured HA flow (a), (b) and estimated (caval subtraction) HA flow (c),(d). Estimated HA flow demonstrated a larger coefficient of reproducibility, but significant correlations between repeated measurements.

Reproducibility of estimated (caval subtraction) and directly measured HA fraction were compared. No significant differences were demonstrated between repeated directly measured HA fraction (mean difference 0.2403 ± 3.348 %; $p = 0.9442$) or estimated HA fraction (mean difference 8.643 ± 6.943 %; $p = 0.1335$). The coefficient of reproducibility was considerably higher for estimated HA fraction (45.13%) than in directly measured HA fraction (21.76%). Graphical analysis (figure 5.30b, d) showed significant but moderate correlations between repeated direct HA fraction measurements ($r = 0.6397$; $p = 0.0341$). No significant correlation was demonstrated between repeated measurements of estimated HA fraction ($r = 0.5491$; $p = 0.0802$).

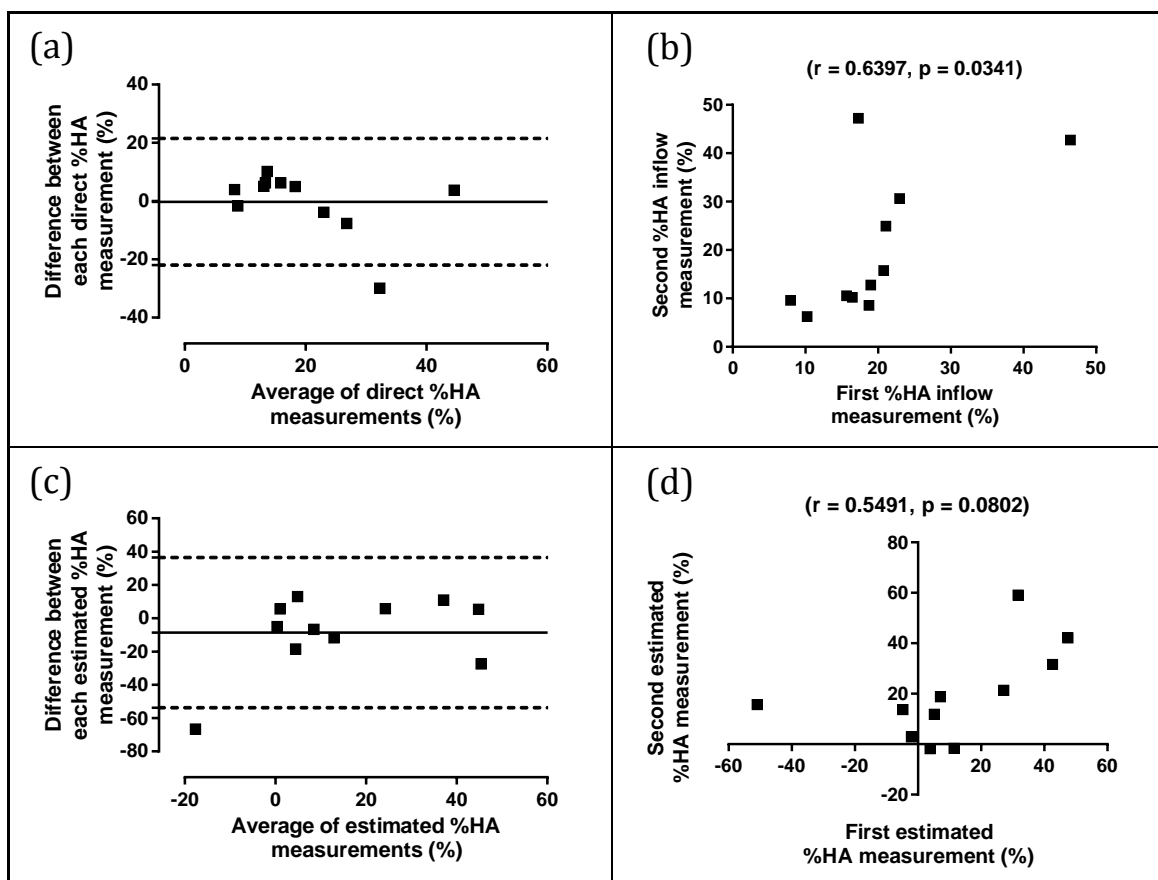


Figure 5.30: Seven day reproducibility of HA fraction measurements

Bland-Altman and scatter plots of repeated measurements for reproducibility of directly measured HA fraction (a), (b) and estimated (caval subtraction) HA fraction (c),(d). Estimated HA fraction demonstrated a much larger coefficient of reproducibility, and non-significant correlations between repeated measurements.

To assess the reproducibility of TLBF and HA fraction as a percentage of CO, reproducibility of PCMRI derived CO was compared initially. No significant differences were demonstrated between repeated aortic root flow measurements (mean difference 112.7 ± 215.8 ml/min; $p = 0.6119$). The coefficient of reproducibility was 1466 ml/min. Graphical analysis (figure 5.31b) showed no significant correlation between repeated aortic root flow measurements ($r = 0.5126$; $p = 0.0884$).

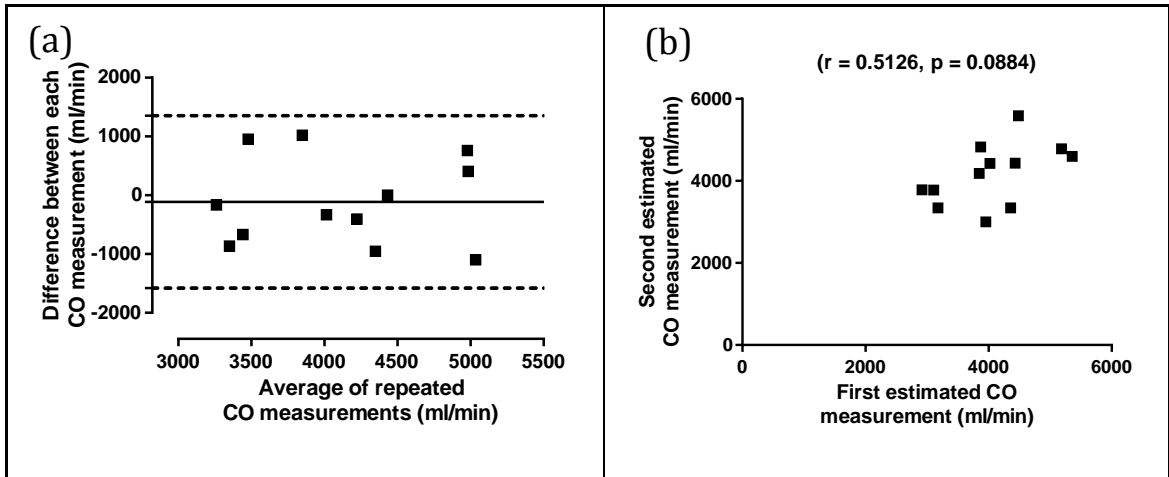


Figure 5.31: Seven day reproducibility of PCMRI aortic root flow measurements

Bland-Altman (a) and scatter plot of repeated measurements (b) demonstrated poor correlations and agreement between repeated PCMRI aortic root flow measurements.

Reproducibility of estimated and directly measured TLBF as a percentage of CO were compared. No significant differences were demonstrated between repeated directly measured TLBF as a percentage of CO (mean difference 0.4318 ± 1.380 %; $p = 0.7607$) or estimated TLBF as a percentage of CO (mean difference 1.251 ± 1.621 %; $p = 0.4582$). The coefficient of repeatability was higher for estimated TLBF as a percentage of CO (10.54%) than for directly measured TLBF as a percentage of CO (8.968%). Graphical analysis (figure 5.32b, d) showed significant correlations between repeated directly measured TLBF as a percentage of CO ($r = 0.7200$; $p = 0.0125$), but only a modest and just non-significant correlation was demonstrated between repeated measurements of estimated TLBF as a percentage of CO ($r = 0.5919$; $p = 0.0551$).

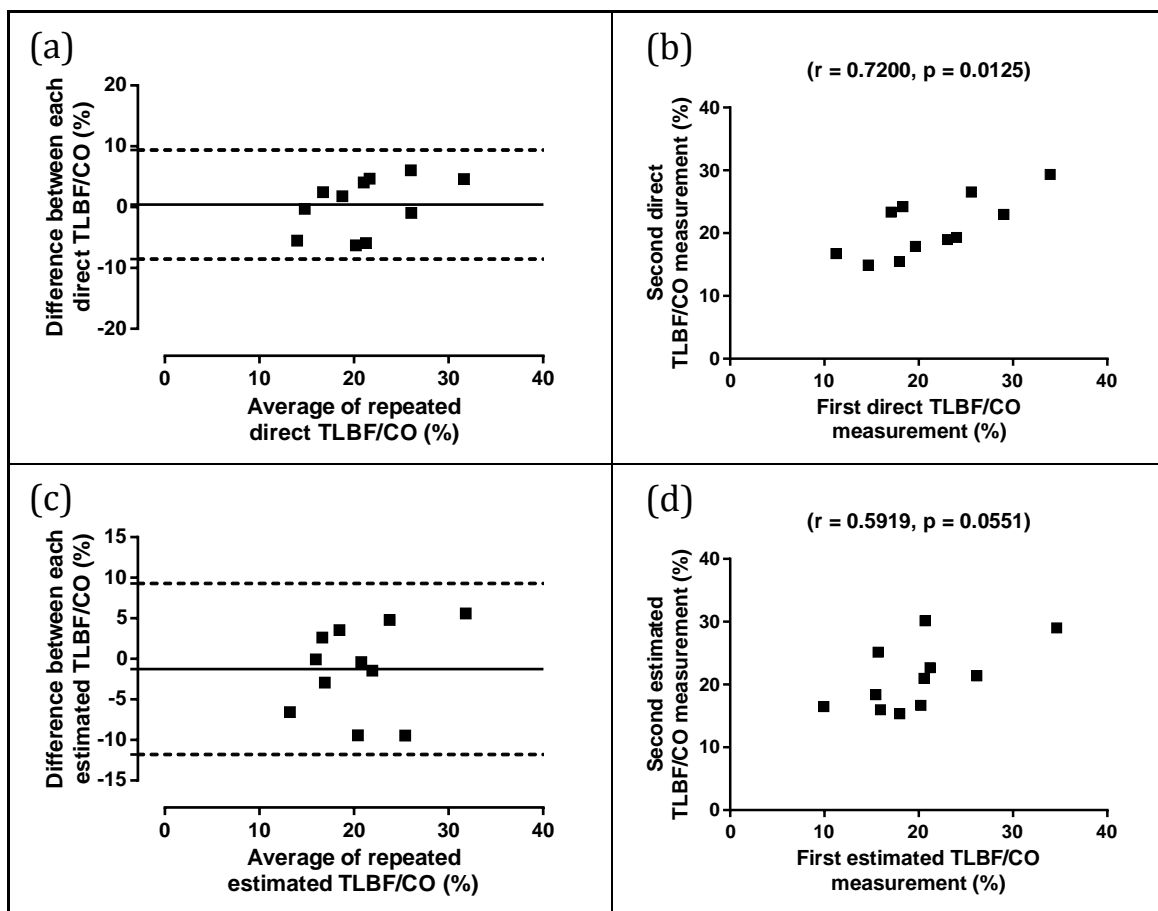


Figure 5.32: Seven day reproducibility of TLBF as a percentage of CO measurements

Bland-Altman and scatter plots of repeated measurements for reproducibility of directly measured TLBF fraction (a), (b) and estimated (caval subtraction) TLBF (c),(d) as a percentage of CO. Estimated TLBF as a percentage of CO demonstrated a larger coefficient of reproducibility, and non-significant correlations between repeated measurements.

Reproducibility of estimated and directly measured HA flow as a percentage of CO were compared. No significant differences were demonstrated between repeated directly measured HA flow as a percentage of CO (mean difference $0.09752 \pm 0.9260\%$; $p = 0.9182$) or estimated HA flow as a percentage of CO (mean difference $1.780 \pm 1.364\%$; $p = 0.2210$). The coefficient of repeatability was higher for estimated HA flow as a percentage of CO (8.866%) than for directly measured HA flow as a percentage of CO (6.020%). Graphical analysis (figure 5.33b, d) showed significant correlations between repeated directly measured HA flow as a percentage of CO ($r = 0.7045$; $p = 0.0155$) and between repeated measurements of estimated HA flow as a percentage of CO ($r = 0.6717$; $p = 0.0236$).

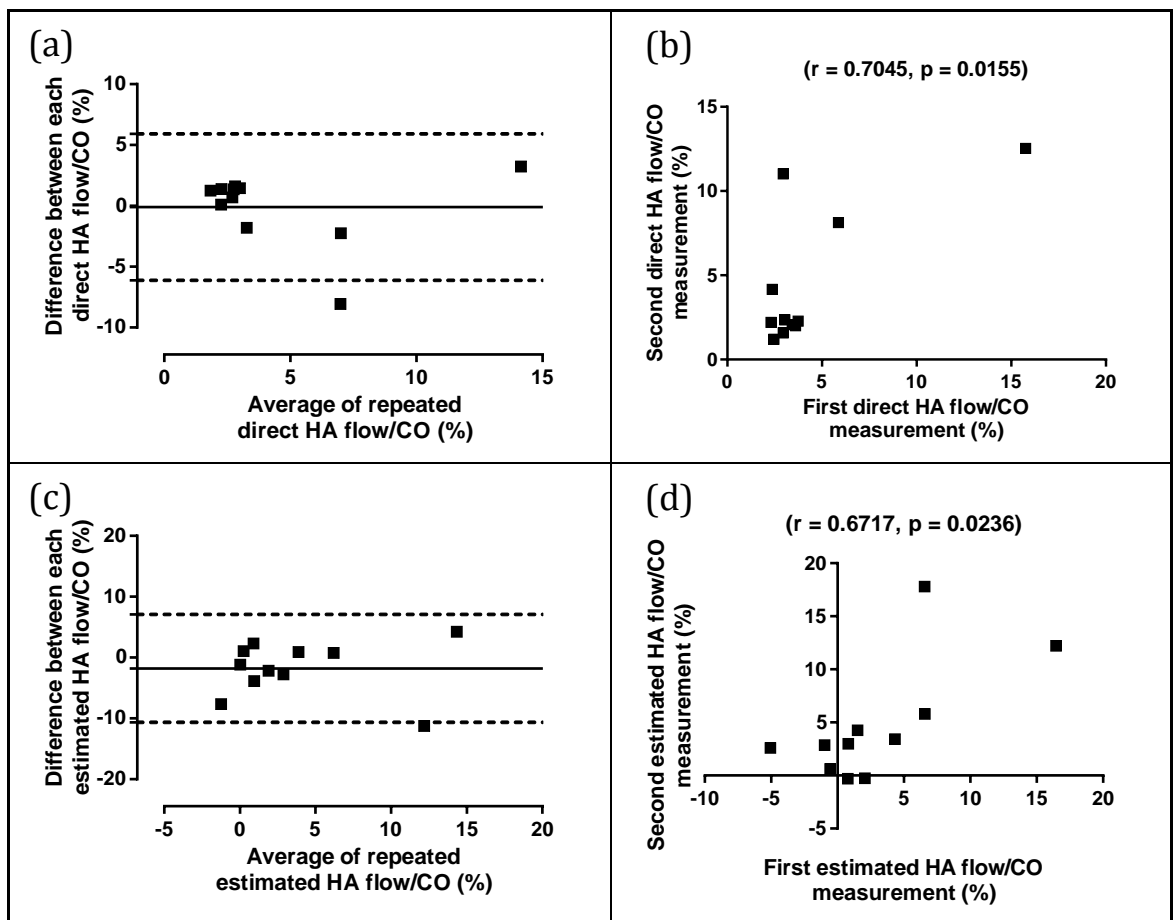


Figure 5.33: Seven day reproducibility of HA flow as a percentage of CO measurements

Bland-Altman and scatter plots of repeated measurements for reproducibility of directly measured HA flow (a), (b) and estimated (caval subtraction) HA flow (c),(d) as a percentage of CO. Estimated HA flow as a percentage of CO demonstrated a larger coefficient of reproducibility, and non-significant correlations between repeated measurements.

5.5.3.4 Physiological stress studies

The response to post-prandial stress was evaluated in normal volunteers ($n = 13$). PV flow measured with PCMRI was 56.86 ± 3.647 ml/min/100g at baseline and showed a significant rise post-prandially (mean difference 52.20 ± 4.371 ml/min/100g; $p < 0.0001$) (figure 5.34a). Fasted TLBF was 71.96 ± 4.840 ml/min/100g when measured directly and 68.95 ± 4.737 ml/min/100g when measured indirectly (using caval subtraction methods). Significant post-prandial rises in TLBF were recorded for direct (mean difference 45.47 ± 5.131 ml/min/100g; $p < 0.0001$) and for indirect measurement methods (mean difference 42.49 ± 4.649 ml/min/100g; $p < 0.0001$) (figure 5.34b and c). Fasted HA flow was 15.10 ± 2.803 ml/min/100g when measured directly and 11.99 ± 4.827 ml/min/100g when measured indirectly (using caval subtraction methods). Significant post-prandial reductions in HA flow were recorded for direct measurement methods (mean difference -5.841 ± 2.424 ml/min/100g; $p = 0.0431$) but the reduction was just above significance for indirect measurement methods (mean difference -8.221 ± 3.945 ml/min/100g; $p = 0.0592$) (figure 5.34d and e). Fasted HA fraction was $20.22 \pm 2.547\%$ when measured directly and $13.97 \pm 7.221\%$ when measured indirectly (using caval subtraction methods). Significant post-prandial reductions in HA fraction were recorded for direct measurement methods (mean difference $-12.04 \pm 2.393\%$; $p = 0.0003$) but the reduction was just above significance for indirect measurement methods (mean difference $-11.27 \pm 5.878\%$; $p = 0.0792$) (figure 5.34f and g).

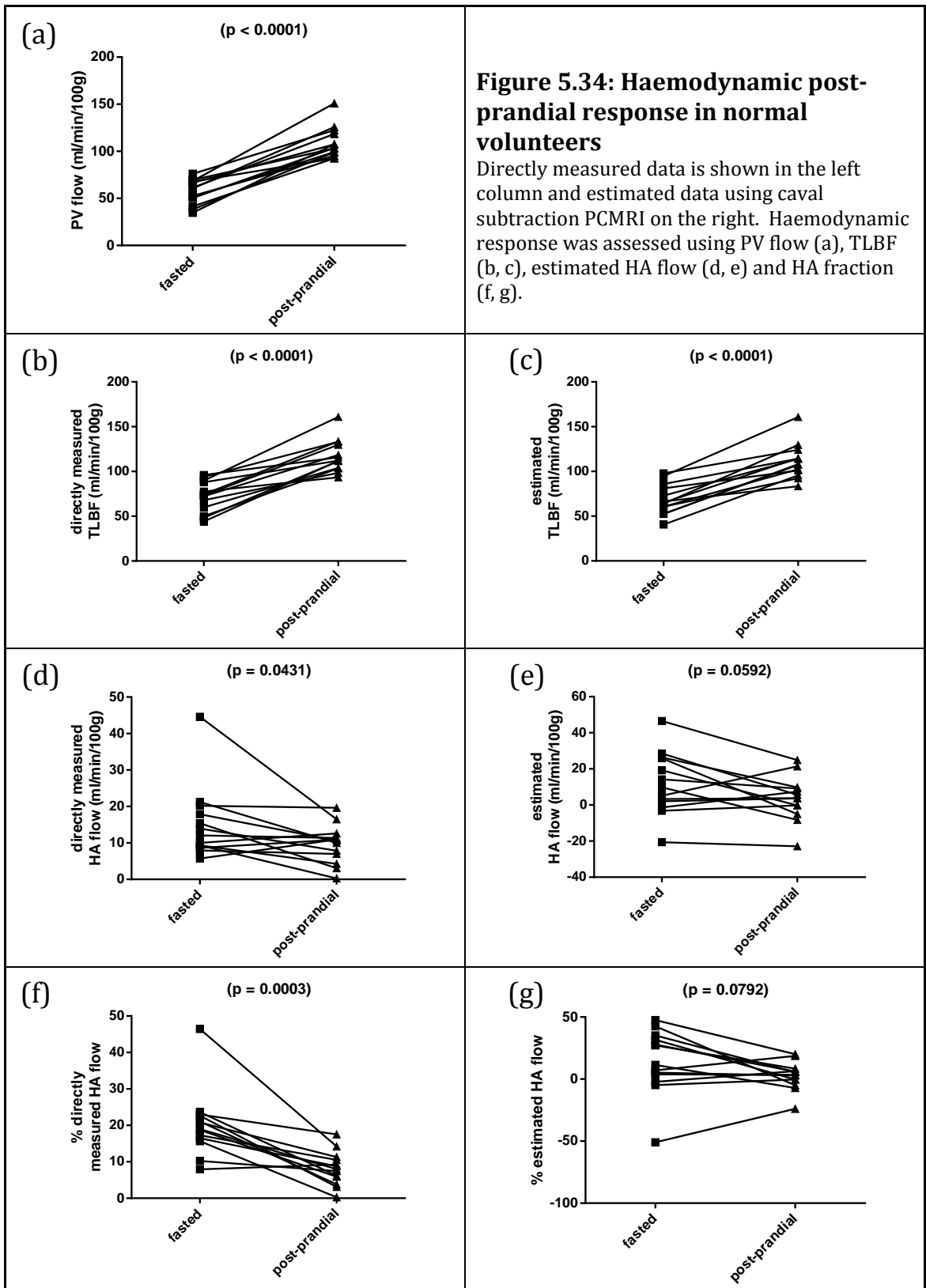


Figure 5.34: Haemodynamic post-prandial response in normal volunteers

Directly measured data is shown in the left column and estimated data using caval subtraction PCMRI on the right. Haemodynamic response was assessed using PV flow (a), TLBF (b, c), estimated HA flow (d, e) and HA fraction (f, g).

Cardiac output measured with PCMRI was 3999 ± 210.6 ml/min at baseline and showed a significant rise post-prandially (mean difference 529.9 ± 231.9 ml/min; $p = 0.0453$) (figure 5.35a). Fasted TLBF as a percentage of CO was $21.08 \pm 1.970\%$ when measured directly and $20.31 \pm 2.010\%$ when measured indirectly (using caval subtraction methods). Significant post-prandial increased in TLBF as a percentage of CO recorded for direct (mean difference $9.870 \pm 1.803\%$; $p = 0.0003$) and indirect measurement methods (mean difference $9.032 \pm 1.859\%$; $p = 0.0007$) (figure 5.35b and c). Fasted HA flow as a percentage of CO was $4.626 \pm 1.158\%$ when measured directly and $3.856 \pm 1.723\%$ when measured indirectly (using caval subtraction methods). No significant post-prandial reductions in HA flow as a percentage of CO were recorded for direct (mean difference $-1.988 \pm 1.049\%$; $p = 0.0875$) and indirect measurement methods (mean difference $-2.825 \pm 1.396\%$; $p = 0.0705$) (figure 5.35d and e). Findings are summarised in table 5.6.

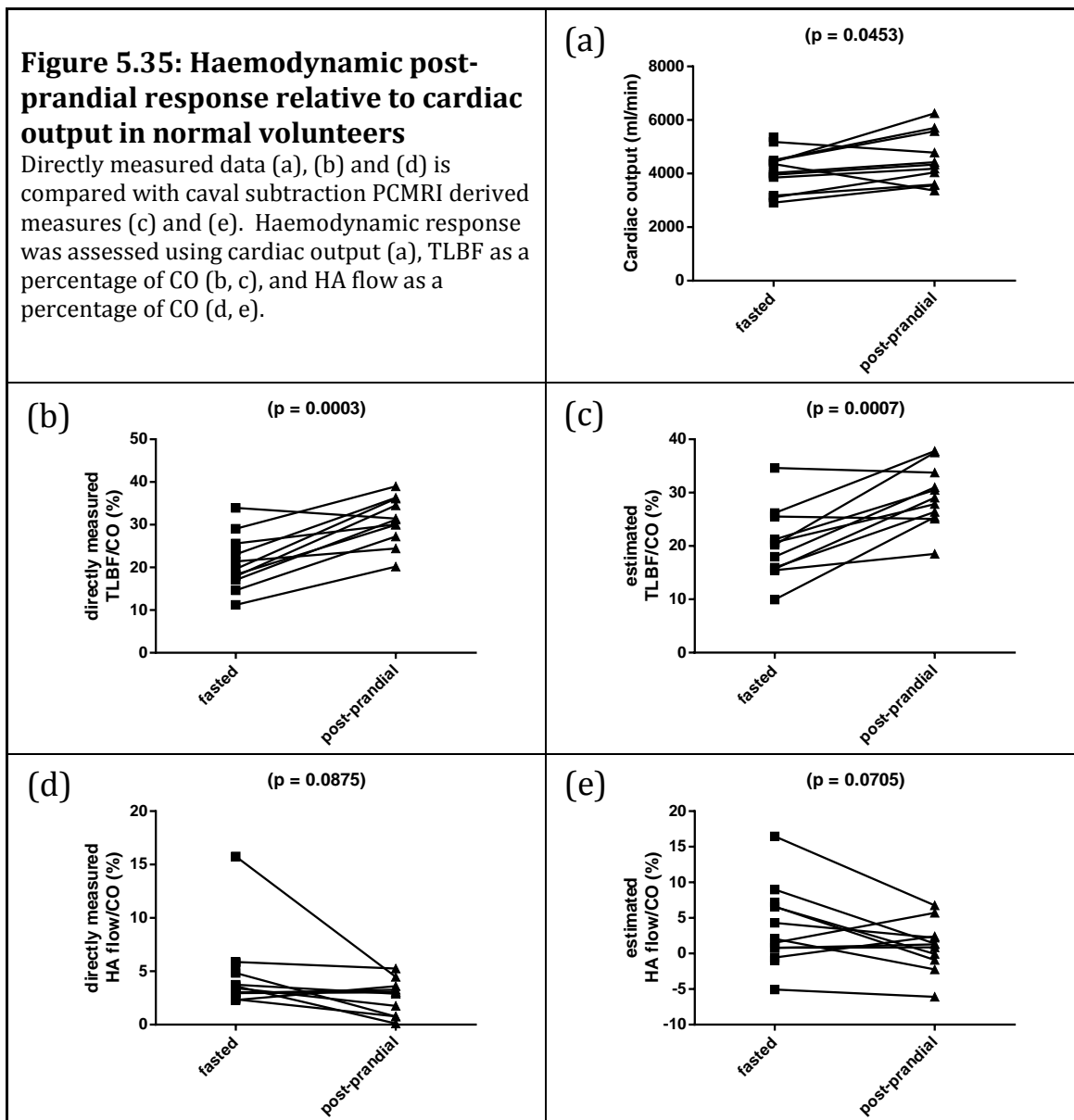


Table 5.6: Fasted and post-prandial haemodynamic changes using direct and indirect PCMRI measurements

	DIRECT PCMRI MEASUREMENT		INDIRECT (CAVAL SUBTRACTION) PCMRI MEASUREMENT	
	FASTED	POST-PRANDIAL CHANGE	FASTED	POST-PRANDIAL CHANGE
<i>PV flow</i> (ml/min/100g)	56.86±3.647	-52.20±4.371*		
<i>TLBF</i> (ml/min/100g)	71.96±4.840	+45.45±5.131*	68.95±4.737	+42.49±4.649*
<i>HA flow</i> (ml/min/100g)	15.10±2.803	-5.841±2.424*	11.99±4.821	-8.221±3.945
<i>HA fraction</i> (%)	20.22±2.547	-12.04±2.393*	13.97±7.221	-11.27±5.878
<i>Cardiac output</i> (ml/min)	3999±210.6	+529.9±231.9*		
<i>TLBF/CO</i> (%)	21.08±1.970	+9.870±1.803*	20.31±2.010	+9.032±1.859*
<i>HA flow/CO</i> (%)	4.626±1.158	-1.988±1.049	3.856±1.723	-2.825±1.396

(all parameters given as mean ± standard error of the mean; *p < 0.05)

5.5.4 DISCUSSION

We have successfully adapted standard clinical cine PCMRI protocols to measure bulk vessel flow in upper abdominal vessels in normal volunteers and translated our preclinical caval subtraction methods to estimate hepatic haemodynamic parameters in human subjects. Preclinical and clinical PCMRI face many similar challenges (discussed previously) and here we consider those specific to clinical PCMRI.

Much like preclinical estimations made using caval subtraction PCMRI, clinical estimations of TLBF, HA flow and subsequent derivatives suffer from error propagation. Errors in the measurement of proximal and distal IVC flows summate during estimation of TLBF. Estimated HA flow has additional error from the error associated with direct PV flow measurements. The exact error associated with caval subtraction PCMRI estimations is impossible to ascertain because no non-invasive reference-standard validation method exists that would be suitable for normal volunteers. It can be argued that transcutaneous Doppler US could have been used for validation, but as previously discussed – this is such a poor method of validation and not a genuine ‘gold-standard’. Defining validation as the assessment of agreement between two independent measurements, one of which is a recognised method for measuring PV and HA flow, we would argue that measuring consistency between direct inflow PCMRI measurements and caval subtraction PCMRI measurement does represent a means of validation. Analysis of agreement between these two independent methods demonstrated very good agreement in both fasted and post-prandial states. The coefficient of repeatability between each measurement method (22.77 ml/min/100g) would be acceptable for TLBF measurements and error associated with this measurement is very encouraging (table 5.7). Because HA flow was inferred from the subtraction of a fixed quantity (directly measured PV flow) from both direct and indirect measurements, the same absolute error resulted in a significant increase in relative error (table 5.7). The same coefficient of repeatability for measurement of much smaller absolute values does call into question whether estimated, caval subtraction HA flow can be made with sufficient accuracy. Where true HA flows are low, the risk of non-physiological negative flow estimates as a result of caval subtraction error propagation is also high, as was seen for a number of datasets. This was manifest on Bland-Altman plots for HA flow and HA fraction (figures 5.25a and 5.26a) as clustering of points in a generally negative trend (small averages of between method measurements, were likely to have positive differences between each method of measurement because of increased likelihood of negative caval subtraction flow measurements).

It is also worth noting that differences in the coefficient of variation in fasted and prandial states were noted across all estimated parameters. For estimated TLBF, the

coefficient of variation was lower in the post-prandial state, however for both estimated HA flow and fraction the coefficient of variation increased in the post-prandial state. Both the increases and decreases are likely to reflect similar absolute errors (and standard deviations) but higher mean TLBFs and lower mean HA flows/fractions observed in the post-prandial state.

As in section 5.4, cardiac cine MRI stroke volume measurements were used to validate aortic root PCMRI flow. Unlike in preclinical experiments, clinical systems optimise image quality by shifting the patient table to ensure the area being scanned is as close as possible to the centre of B_0 , where field inhomogeneities are less variable. Although this does mitigate some of the differences between hepatic and cardiac measurements introduced by scanner factors, subject specific factors still imply that the reliability of PCMRI IVC flow for example, cannot be inferred because of the accuracy of aortic root PCMRI. While we acknowledge once again that validation does not in any way enable validation of hepatic haemodynamic flow parameters, we would argue that this experiment does provide added confidence in the reliability of PCMRI quantification.

Table 5.7: Error estimation for PCMRI derived flow measurements in normal volunteers

	GLOBAL MEAN*	MEAN DIFFERENCE TO REFERENCE STANDARD	ESTIMATED PERCENTAGE ERROR
<i>Caval subtraction PCMRI estimated TLBF</i>	85.76±4.300 ml/min/100g	2.942±1.910 ml/min/100g [†]	3.431±2.227%
<i>Caval subtraction PCMRI estimated HA flow</i>	10.39±2.679 ml/min/100g	2.942±1.910 ml/min/100g [†]	28.32±18.38%
<i>Caval subtraction PCMRI HA fraction</i>	11.61±3.351%	4.264±2.482% [†]	36.73±21.38%
<i>PCMRI aortic root flow</i>	4264±137.2 ml/min	50.48±42.82 ml/min [‡]	1.184±1.004%

(*pooled mean across fasted and post-prandial measurements; [†]direct inflow PCMRI measurements reference standard; [‡]cardiac cine MRI derived CO reference standard)

In the absence of good, reference-standard validation data, perhaps an even more important parameter is reproducibility. If PCMRI derived bulk flow measurements are to inform patient care, these need to be reproducible in patients with stable disease (and normal volunteers). Even if validation data is poor, a stable reproducible parameter is arguably more clinically useful. Good reproducibility of PV flow measurements was demonstrated. The coefficient of reproducibility (19.01 ml/min/100g) is arguably high, but this is likely to indicate natural variation in vessel flow rates. Because simultaneous direct and indirect (caval subtraction) PCMRI flow measurements were made in all subjects, a comparative study of reproducibility was undertaken. For estimated TLBF, the

coefficient of reproducibility was only marginally greater than directly measured TLBF (31.60 vs 29.56 ml/min/100g). Correlations between repeat estimated TLBF measurements were however poor and disappointing ($r = 0.4858$, $p = 0.1297$). It is perhaps surprising then that the correlations for repeat measurements of estimated HA flow were so encouraging ($r = 0.6511$, $p = 0.0300$). Crucially, the coefficient of reproducibility of HA flow measurements was wide (28.77 ml/min/100g) and more worryingly, just over twice the mean value for the entire cohort (14.01 ± 3.524 ml/min/100g). A similar and equally concerning poor reproducibility of HA fraction was demonstrated (coefficient of reproducibility of 45.13%, mean HA fraction across cohort $16.47 \pm 4.629\%$). It is however worth noting that although coefficients of reproducibility were smaller for both directly measured HA flow (coefficient of reproducibility 19.77 ml/min/100g, mean direct HA flow across cohort 15.34 ± 2.366 ml/min/100g) and fraction (coefficient of reproducibility 21.76%, mean direct HA fraction across cohort $20.09 \pm 2.366\%$), these still remained large and questionably reproducible.

An important source of variation in haemodynamic parameters would be differences in overall haemodynamic state. It was therefore significant that reproducibility of cardiac output was also poor (coefficient of reproducibility 1466 ml/min). Assessment of TLBF and HA flow relative to CO was a viable way of removing the effects of changes in systemic factors as a source of variability in repeated measurements. Reproducibility of measurements of estimated TLBF as a percentage of CO were much more encouraging (coefficient of reproducibility 10.54%, mean cohort estimated TLBF as a percentage of CO $21.36 \pm 1.138\%$). Reproducibility of estimated HA flow as a percentage of CO was poorer than estimated TLBF (coefficient of reproducibility 8.866%, mean cohort estimated HA as a percentage of CO $4.194 \pm 1.106\%$), but still better than for estimated HA flow or HA fraction.

The measurement of post-prandial haemodynamic changes was an important method of demonstrating the sensitivity of PCMRI methods to PV flow modulation, but also demonstrating the potential of caval subtraction PCMRI to infer changes in estimated TLBF and HA flow. We have demonstrated expected post-prandial rises in PV flow and TLBF. But also reductions in directly measured HA flow and fraction. Estimated HA flow and fraction also showed post-prandial reductions, which for estimated HA flow approached significance ($p = 0.0592$). Our data is the first to our knowledge that uses PCMRI to demonstrate the negative hepatic arterial buffer response – reductions in HA flow in response to increases in PV flow. Interestingly, although significant rises in CO and TLBF as a percentage of CO were demonstrated post-prandially using both direct and indirect methods, no significant change in HA flow as a percentage of CO was

demonstrated with either direct or indirect (caval subtraction) methods. Over the years, there have been multiple studies demonstrating post-prandial PV/splanchnic flow changes in cirrhotic patients, predominantly using Doppler US. Post-prandial rises in PV flow have been well characterised, but changes in HA flow parameters have seldom been studied[381, 382, 385, 386]. Only a few studies have reported post-prandial reductions in HA resistive indices, a measure of differences in peak systolic and end diastolic velocity rather than absolute flow (section 1.3.2) [387, 388].

Reproducibility and physiological stress studies raise important questions about the use and value of estimated HA flow, HA fraction and HA flow as a percentage of CO. Preclinical studies demonstrated the feasibility of measuring all of these parameters and highlighted the use of HA flow as a percentage of CO in discriminating haemodynamic differences between healthy and cirrhotic animals at baseline. Clinical studies however, have demonstrated poor reproducibility of estimated HA flow, estimated HA fraction and estimated HA flow as a percentage of CO, with subsequent failure to demonstrate significant changes in any of these parameters post-prandially. Because the change in estimated HA flow approaches significance, this could represent a type II error perhaps as a result of an under powered study. Conversely it could be argued that because direct PCMRI HA flow measurements have demonstrated post-prandial changes in HA flow and HA fraction, one could ascribe the failure to show these changes to errors in estimated (caval subtraction) HA flow and HA fraction measurements.

The clinical use of estimated HA flow and fraction must however be considered alongside alternatives. Although we have demonstrated direct PCMRI HA flow measurements to be superior, complexities of planning preclude practical clinical implementation. Unfortunately simultaneous Doppler US HA flow was not measured, but the reproducibility of Doppler HA flow measurements has been previously shown to be inferior to direct PCMRI [199, 389]. In this context, we would argue that the estimation of HA flow and HA fraction using caval subtraction PCMRI does merit quantification. The true value of either of these parameters however, can only genuinely be considered after formal evaluation in patients with liver disease.

There are a number of methodological considerations which also require discussion. Firstly although baseline heart rate is lower in humans and consequently R-R interval is much longer, a major criticism of the study is the choice to only collect flow data for only six phases through the cardiac cycle. This was based on the desire to collect data within a single breath-hold using a protocol that would be suitable for patients with more elevated heart rates. Previous studies have quoted single PCMRI measurements

(excluding planning time) as requiring acquisition times of up to 2.5 minutes [197, 199]. In our study – with five triplicate vessel site measurements – this could take up an unwieldy 37.5 minutes of scanning time for PCMRI alone! Our rapid acquisition protocol also enabled triplicate measurements and averaging for quantification. This is a major strength as averaging would help reduce the effects of other errors inherent to PCMRI methods (background, Chapter 4).

Bulk vessel flow can also be quite variable, even in physiological states [390]. The use of triplicate measurement averaging helps to overcome some of this variability. In this study, a potential cause of vessel flow variability were inter-measurement changes in the length and quality of breath-hold. The use of expiration (rather than inspiration) breath-holds goes some way to address this issue, but there is little doubt that towards the end of the study (after at least 15 breath-holds for PCMRI), subjects would experience ‘breath-hold fatigue’. The effect of alterations in intra-thoracic (and intra-abdominal) pressure through the respiratory cycle is known to affect heart rate (sinus arrhythmia) but is also likely to affect low pressure vessels such as the IVC. Although changes in heart rate were factored into bulk flow quantitation, the changes in flow induced by differences in the quality and depth of breath-hold between studies in the proximal and distal IVC represent a potential source of error.

The importance of minimising acquisition time is of major significance in developing protocols that are suitable for routine clinical implementation. Depending on the institution, liver MRI protocols usually include a variety of anatomical and semi-quantitative techniques (multi-planar T2 and T1 weighted anatomical imaging, in- and out-of-phase imaging, T2* weighted imaging, diffusion-weighted imaging and DCE MRI protocols), all of which at our institution require approximately 45 minutes of scanning time. Implementation of a novel quantitative imaging method would therefore need to either be (a) rapidly acquired, thereby not significantly extending the time required for the overall scan or (b) be of sufficient value to justify replacement of certain less valuable semi-quantitative protocols.

Finally, the transferability of our PCMRI protocols to other scanners, at our and other institutions is important in the development of multi-centre clinical studies but also in ensuring feasible implementation into clinical protocols elsewhere. With this in mind, changes to the manufacturer-derived PCMRI sequence were minimised, with most changes limited to subject-specific factors. An important attraction of caval subtraction PCMRI in this context is the simplicity and greater reliability of bulk flow measurements in

large vessels such as the IVC (compared with direct HA flow measurements) using lower SNR on more widely clinically available lower field strength (1.5T) systems.

5.5.5 CONCLUSION

In this section, we have adapted and implemented standard clinical cine PCMRI protocols to measure bulk vessel flow in normal volunteers and translated our preclinical caval subtraction methods to estimate hepatic haemodynamic parameters in human subjects.

We have demonstrated good agreement with reference methods for measurement of cardiac output using aortic root and PCMRI and shown good consistency of estimated (caval subtraction) TLBF with directly measured PCMRI TLBF in the same subject. Estimated HA flow and fraction have been found to be less consistent when compared to their directly measured counterparts, likely secondary to error propagation.

Our results demonstrate good seven day reproducibility of PV flow and estimated TLBF, but were less encouraging for reproducibility of estimated HA flow, HA fraction and HA flow as a percentage of CO.

Finally, we have investigated the post-prandial response in normal volunteers using direct and caval subtraction PCMRI and demonstrated (a) expected rises in PV flow, (b) expected rises in TLBF and (c) a negative hepatic arterial buffer response to increased PV flow (using direct PCMRI).

These findings highlight the need for patient studies to determine the value of estimation of HA flow and fraction using caval subtraction PCMRI in clinical practice.

5.6 CLOSING COMMENTS

We have proposed at the start of this chapter a novel strategy to measure TLBF and HA flow, thereby overcoming challenges that arise from variable anatomy and small vessel size. We subsequently applied this method preclinically at high-field strength, demonstrating feasibility, repeatability of PV flow measurements and invasively validating our measurements in healthy and diseased animals. We used our new method to demonstrate intrinsic differences in hepatic haemodynamic parameters at baseline in animal models of disease and demonstrated the hepatic arterial buffer response and its failure in cirrhotic animals using terlipressin.

Finally, we translated these methods into the clinical setting, demonstrating feasibility, consistency and reproducibility of caval subtraction TLBF measurements in normal volunteer studies. Clinical translation highlighted difficulties in the estimation of HA flow and HA fraction and underlined the importance of patient studies in considering the application of this method to clinical practice.

Although the PCMRI methods developed in this chapter are exciting and have for the first time demonstrated hepatic haemodynamic phenomena non-invasively, the quantification of bulk flow with PCMRI fails to provide any anatomical information about regional changes in segmental and/or tissue perfusion. The latter would be particularly valuable to patients and clinicians in the context of surgical or endovascular treatment planning. In Chapters 2 and 3, we used DCE MRI on a preclinical system to demonstrate that such regional perfusion data could be measured, albeit with technical challenges that ultimately proved insurmountable. Moving forward, the use of DCE MRI on a clinical system could prove less challenging and perhaps provide useful regional perfusion data in a clinical setting.

CHAPTER 6

CLINICAL DCE MRI

“...Austere portion
or the whole
of myself,
grandfather
of the heart,
generator
of energy:
I sing to you
and I fear you
as though you were judge...”

- Ode to the liver [2].

6.1 INTRODUCTION

Early experience with DCE MRI at 9.4T (Chapters 2 and 3) though promising was ultimately limited by technical difficulties. Tissue signal changes throughout a DCE MRI study provide useful information related to perfusion, but accurately quantifying these signal intensity changes can be problematic at high field strength in particular. In this chapter we translate our earlier DCE MRI experience to a lower field strength system (3.0T) for clinical use and study its feasibility in normal volunteers.

The developmental focus of this chapter has been driven towards post-processing and modelling, which we have previously demonstrated to have a significant effect on quantification. In the first section of this chapter we demonstrate feasibility and study the effects of alternative approaches to dealing with differences in contrast agent (CA) bolus arrival times in vascular input and parenchymal regions of interest (ROIs) for dual input single compartment modelling. We then consider alternative approaches to DCE modelling, including the dual input dual compartment model and the hepatic perfusion index method.

The third section is based upon novel approaches for the integration of DCE and PCMRI for more robust quantification. The initial part involves using PCMRI measurements of aortic root flow to correct DCE arterial input functions and the final part uses subtraction PCMRI estimates of total liver blood flow to correct DCE perfusion estimates.

6.2 AUTHOR CONTRIBUTIONS

In fulfilment of the aims in this chapters, I: (a) developed and optimised clinical DCE MRI protocols; (b) conceptualised, developed and implemented novel methods for handling vascular input function (VIF) delays; (c) implemented alternative models for DCE MRI quantification; (d) implemented methods for arterial input function (AIF) correction using PCMRI measured cardiac output; (e) conceptualised, developed and implemented novel methods for correction of DCE MRI absolute perfusion parameters using PCMRI; (f) set up a DCE MRI post-processing 'pipeline' using Matlab, including pharmacokinetic modelling for final DCE MRI parametric quantification and generation of DCE MRI perfusion maps; (g) recruited normal volunteers into validation and reproducibility studies; (h) supervised the scanning of all normal volunteer scans; (i) collected and analysed all the data; and (j) prepared all the material contained within this chapter.

Development of clinical DCE MRI sequences was undertaken with the help of Alan Bainbridge, with additional input from David Atkinson. Gradient echo multi-flip angle T1 measurement with B_1 mapping was developed by Catherine Morgan. Post-processing Matlab code for T1 measurement was developed by Jonathon Delve and adapted by myself for the post-processing pipeline. Robust Data Decomposition Registration was developed by Valentin Hamy and adapted by myself for the post-processing pipeline. Normal volunteer recruitment took place using ethical approval originally sought by Margaret Hall-Craggs. All clinical scans were conducted by MRI radiographers.

6.3 CLINICAL DCE MRI FEASIBILITY AND APPROACHES TO HANDLING VASCULAR INPUT FUNCTION DELAYS

6.3.1 BACKGROUND

Clinical DCE MRI is well established and protocols in the literature can be implemented avoiding the complexities of sequence design required on preclinical systems. As with preclinical DCE MRI, quantification requires: (i) dynamic T1-weighted images for serial ROI signal intensity measurements, (ii) measurement of the intrinsic T1 of the tissue within each ROI and (iii) measurement of the contrast agent T1 relaxivity (r_1). The latter is readily available from the literature and fixed across all measurements for a given temperature, such that the accuracy of a clinical DCE MRI study is predominantly reliant on adequate DCE data (especially for vascular input functions) and measurements of blood and tissue T1. The development of DCE MRI protocols was therefore directed at optimising the accuracy of each of these.

6.3.1.1 Protocol justification – Dynamic imaging

Clinical acquisition protocols for DCE MRI vary depending on the anatomical site being studied, but common to all quantitative approaches is the need for high temporal resolution acquisitions, good signal-to-noise ratio (SNR) and minimisation of artefacts.

Temporal resolution is especially important for pharmacokinetic modelling and vascular input functions (VIFs) are particularly susceptible to sampling errors. Poor temporal resolution, particularly in the early CA ‘bolus mixing’ phase of a DCE MRI study can result in inadequate sampling of key first-pass VIF features, such as peak signal intensity. This can then have deleterious effects on quantification. Liver DCE MRI pharmacokinetic studies in the literature quote temporal resolutions of 1-5 seconds [82, 141, 391], which are broadly in accordance with DCE MRI studies performed elsewhere in the abdomen and with specific protocols to optimise VIF sampling [392-395]. Temporal resolution can be increased, but this is often at the expense of data quantity or quality. Based on existing clinical protocols, a matrix size of 256 x 256 with a spatial resolution of 1.87 mm², and 5 mm slice thickness was used. A volume of 60 slices was sampled repeatedly with a temporal resolution of 3.35 seconds. This spatial resolution and slice thickness afforded adequate SNR for VIF and parenchymal signal intensity measurements.

The need for accurate AIFs for clinical quantification has proven so troublesome that some researchers have opted to use population-derived ‘average’ AIFs [394, 396-398]. While this approach might be suited for quantification of regional perfusion changes

in tumours, it is likely to be flawed where absolute tissue perfusion is the parameter of interest. The AIF delay and AIF itself are likely to vary in health and disease, particularly in liver disease where patients (and animals, as demonstrated by our own data) are known to have hyperdynamic circulation and altered cardiac function. Moreover, the VIF tail for Gd-DTPA is ultimately determined by renal clearance of CA – a factor which is also likely to vary significantly in disease. The situation is also complicated by dual VIF sampling for dual input pharmacokinetic models for liver perfusion. For this reason, aortic and PV VIFs were sampled in each individual subject.

A recognised problem of working at higher field strengths is the loss of signal intensity at higher contrast agent concentrations when T2* effects predominate [399, 400]. This is still much less of an issue at 3.0T than at 9.4T, but nonetheless a source of error in measured VIFs. As demonstrated during earlier work at 9.4T, these effects can be minimised using more dilute and more slowly administered CA boluses. Our protocols were therefore based on a dilution of 10 mls Gd-DTPA with an equal volume of normal saline. After reviewing published protocols for hepatic DCE MRI at 3.0T [145, 147], a decision was made to use an injection rate of 4 ml/s followed by 20 mls of normal saline. Data presented in this chapter demonstrates that this protocol is capable of producing distinct aortic and PV VIFs, without obvious degradation in the measured VIF signal.

Finally, visceral motion through the respiratory cycle is a major challenge in any quantitative liver imaging, especially because of its subdiaphragmatic location. Whole organ motion and also tissue deformation can result in sampling errors in fixed ROIs. At best, this will result in differing areas of liver tissue sampled through a study; at worst, this will result in corruption of data through inclusion of signal from adjacent non-hepatic tissues. Respiratory motion artefact is a major obstacle to exploiting the higher anatomical resolution offered by MRI to generate parametric maps of perfusion. There are number of strategies that can be used to overcome these issues. Respiratory gating using navigator triggering has been proposed [197], but this has the potential to reduce temporal resolution and undersample crucial initial portions of the VIFs and parenchymal enhancement curves. More commonly, breath-holds can be used, with imaging usually in expiration (as expiratory phase diaphragmatic position is less variable than inspiratory phase position). There are several published protocols, but common approaches include (i) initial breath hold followed by shallow breathing for the duration of the study or then (ii) successive expiratory breath holds [391, 401-403]. The latter has been previously demonstrated to be more effective than shallow breathing for liver DCE MRI pharmacokinetic modelling [391]. Subjects participating in our study received an initial breath hold instruction and thereafter conducted sequential expiratory breath holds

independently for the duration of the study. To maximise patient compliance with the breath hold protocol, subjects were instructed before entering the scanner.

Each study involved the acquisition of ninety upper abdominal volumes in just over 5 minutes. Although most volumes were adequate for inclusion in quantitative post-processing, datasets with significant motion artefact were discarded. To account for excursions in liver position and tissue deformation, registration algorithms can also be applied. Several registration methods have been proposed [404, 405], but we have previously demonstrated robust data decomposition registration (RDDR) to be superior to alternative methods in several different abdominal tissue types including the liver (figure 6.1) [406]. To minimise the deleterious effects of motion artefact, each selected slice therefore underwent RDDR before ROI placement.

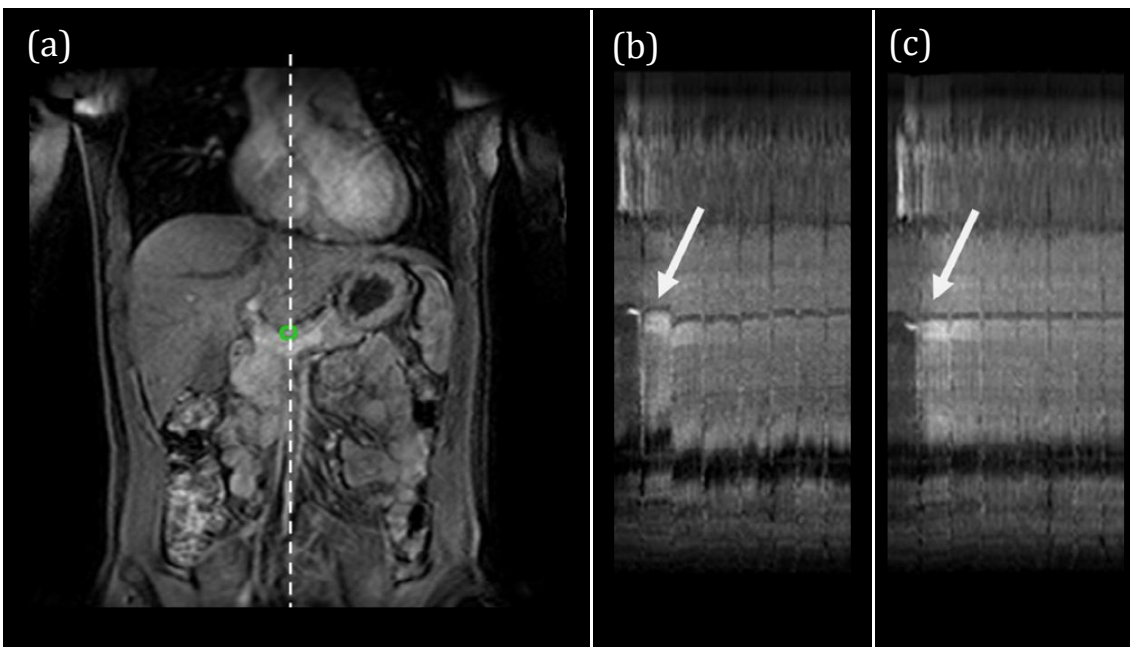


Figure 6.1: Robust data decomposition registration for liver DCE MRI

(a) Coronal image of the abdomen and lower thorax. The dashed white line through the midline intersects cardiac and hepatic parenchyma but also the portal vein and hepatic artery (green circle). The signal intensity of this line of data can then be tracked through a DCE experiment (b) and (c). Maximal PV enhancement is demonstrated by the white arrow. Data set (b) was obtained without any registration. Note the considerable potential for ROI misregistration through misalignment of sequential ROI signal intensity data. The data show in (c) was obtained from the same subject after RDDR. Note how alignment between successive data sets is only interrupted by gross motion artefact during inspiration/expiration between breath holds (diagram adapted from reference [406]).

6.3.1.2 Protocol justification – T1 measurement

There are several approaches to measuring T1 on clinical systems, but as demonstrated in section 3.3, the inversion recover (IR) method is widely regarded as the ‘gold standard’ [407]. While this method is accurate, it is time-consuming. For our protocol, T1 measurements would be required for a sixty slice volume, making the IR approach unfeasible. Data for T1 measurement using the gradient echo multi-flip angle method can be acquired much more quickly, but as demonstrated in section 3.3, this method can result in substantial errors because of inhomogeneities in B_1 . This phenomenon results in areas of imaged tissue experiencing flip angles other than the exact angle specified by the sequence. B_1 inhomogeneities can result in errors in the final estimated T1 measurements (relative to IR T1 measurements in the same subject on the same scanner) of as much as 63% at 3.0T. B_1 mapping has been proposed and demonstrated by several groups as a method for overcoming this issue [407-410]. By mapping B_1 field inhomogeneities, multi-flip angle data can be corrected before quantification thereby yielding more accurate T1 measurements. In this study, gradient echo data using five different flip angles was collected and then B_1 mapping was used to account for non-uniformity of the B_1 field. Pixel-wise T1 measurements were then made fitting corrected flip angle data in the same way as described in section 3.3.

6.3.1.3 Protocol justification – post-processing

Building on post-processing experience acquired from previous preclinical work (section 3.3), we begin by optimising use of the dual input single compartment model, through developing a robust method for dealing with VIF delays. Previously, we developed a novel approach to VIF delays, using pre-estimated delays with constrained free-modelling (figure 6.2).

In this section we demonstrate the feasibility of clinical DCE MRI and compare modelling approaches with the assumption of zero VIF delays, free modelling and constrained free modelling with pre-estimation of VIF delays for perfusion parameter estimation. Traditionally, the merits of a modelling method can be assessed using the goodness-of-fit (residual sum of squares) statistic. As previously demonstrated, improved model fitting can still result in physiologically inaccurate or even non-physiological estimates of perfusion parameters. We previously invasively validated preclinical PCMRI and demonstrated consistency of caval subtraction clinical PCMRI measurements using independent PCMRI measurements. As these measurements were obtained from the same subjects, this provides an opportunity to “validate” DCE MRI perfusion measurements with matched caval subtraction PCMRI flow measurements. In this chapter we have chosen to

assess differing approaches and refinements using (i) seven day reproducibility and (ii) validation of tissue perfusion estimates with volume normalised PCMRI flow measurements.

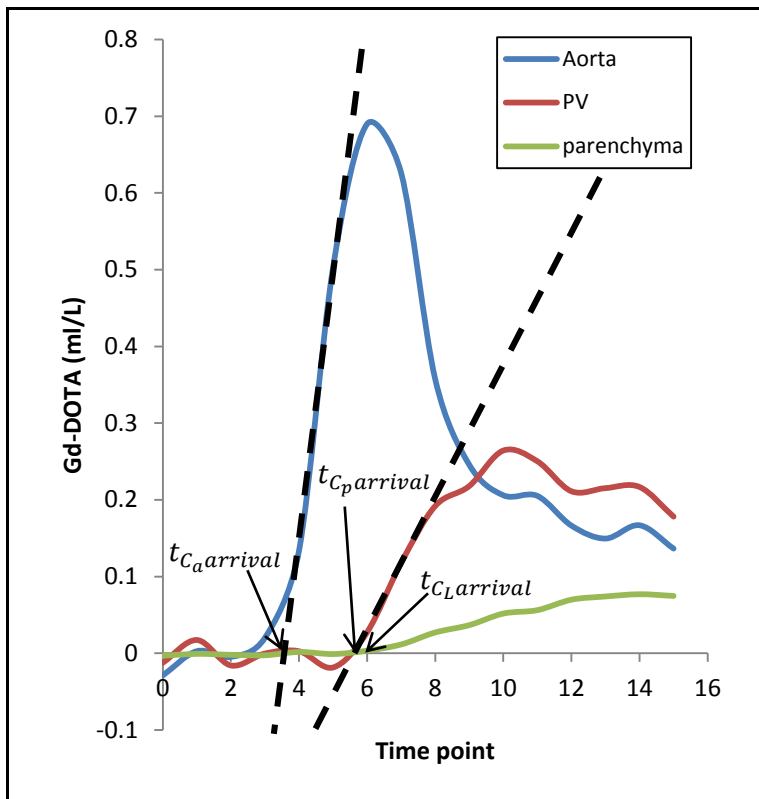


Figure 6.2: DCE enhancement curves for pre-estimation of aortic and PV CA bolus arrival times to constrain free modelling of delay parameters

The maximum gradient of the upstroke for each VIF was modelled using linear regression to estimate aortic ($t_{C_a arrival}$) and PV ($t_{C_p arrival}$) CA bolus arrival times. Parenchymal CA arrival time ($t_{C_L arrival}$) was determined using the 95% upper limit confidence interval of baseline data. This diagram was replicated from figure 3.16, using rat DCE data for illustrative purposes.

6.3.2 METHODS

6.3.2.1 Subjects and preparation

Local ethics committee approval was obtained and all participants provided informed written consent. Participant information sheets and consent form copies can be found in Appendix D. Healthy volunteers were recruited by means of advertisement. There were seven male (aged 26.5 ± 1.36 years) and six female (aged 31.2 ± 2.62 years) participants. Volunteers were excluded if (a) they had any contraindication to standard MR imaging, (b) if they were taking any long-term medication (excluding the oral contraceptive pill) and (c) if they had any documented history of previous liver or gastrointestinal disease. As subjects were to receive a dose of CA for DCE MRI, those with any prior history of renal disease were excluded. One subject was excluded because of claustrophobia. Participants were asked to remain fasted for six hours prior to imaging and were advised to consume water ad libitum, but asked to refrain from the consumption of caffeinated fluids. A 19G cannula was sited in a peripheral upper limb vein in preparation for administration of contrast. Subjects were then instructed on the breath hold protocol for the DCE MRI study before transferring to the scanner.

6.3.2.2 Clinical DCE MRI

Imaging was performed using a 3.0T scanner (Achieva, Philips Healthcare, Best, Netherlands) using a 16 channel body coil (SENSE XL-Torso, Philips Healthcare, Best, Netherlands). The coil was positioned over the lower thorax and upper abdomen and subjects were monitored using digital pulse oximetry and bellows.

Initial scouts were performed to ensure inclusion of the entire cardiac and liver volume within the field-of-view. Coronal images of the upper abdomen and lower thorax were obtained with successive expiratory breath-holds using a gradient echo sequence (table 6.1). Studies were planned with upper abdominal and lower thoracic volume coverage, ensuring inclusion of the liver, spleen, kidneys, retroperitoneal great vessels and the heart. Identical planning settings were used for T1 measurement and DCE MRI studies.

Data for T1 measurement was collected in expiratory breath hold using three-dimensional gradient echo imaging at five different flip angles (5, 7, 10, 15 and 20°). Finally, phase based B_1 mapping was performed during free breathing. Acquisition of T1 measurement data was normally completed within 5 minutes. T1 measurements, including B_1 non-uniformity correction were estimated using previously described

methods (section 3.3.2.5, [409]). Data was processed using in-house developed Matlab code (MathWorks, Natick, USA).

After T1 measurement, DCE imaging was performed using gradient echo imaging (table 6.1). Sixty coronal images were obtained in 3.35 seconds. After acquiring five initial volumes of data, 10 ml of Gd-DOTA (gadoterate dimeglumine, Dotarem®, Guerbet, Roissy, France) was diluted in 10 ml of normal saline, and injected via a peripheral cannula at 4 ml/s. This was followed by another bolus of 20 ml of normal saline at the same rate (Spectris®, Medrad Inc., USA). Sequential image volumes continued to be acquired during this time and until five minutes had elapsed. A total of ninety volumes were obtained per subject. For the DCE acquisition, subjects were given the first breath hold instruction and thereafter asked to continue self-directed breath holds in expiration for the duration of the study.

Table 6.1: Sequence parameters

	T1 MULTI-FLIP ANGLE	B1 MAP	DCE MRI
<i>TR/TE (seconds)</i>	4.0/2.0	100/1.0	2.0/1.0
<i>Flip angle (°)</i>	5, 7, 10, 15, 20	60	10
<i>Matrix size (pixels)</i>	240 x 240	100 x 100	240 x 240
<i>Field-of-view (mm)</i>	475 x 475	475 x 475	475 x 475
<i>Spatial resolution (mm²)</i>	1.98 x 1.98	4.75 x 4.75	1.98 x 1.98
<i>Bandwidth (Hz/pixel)</i>	389	1447	1411
<i>Slice thickness (mm)</i>	5	5	5
<i>Slice gap (mm)</i>	2.5	5	2.5
<i>Slices per volume</i>	60	30	60

6.3.2.3 Post-processing

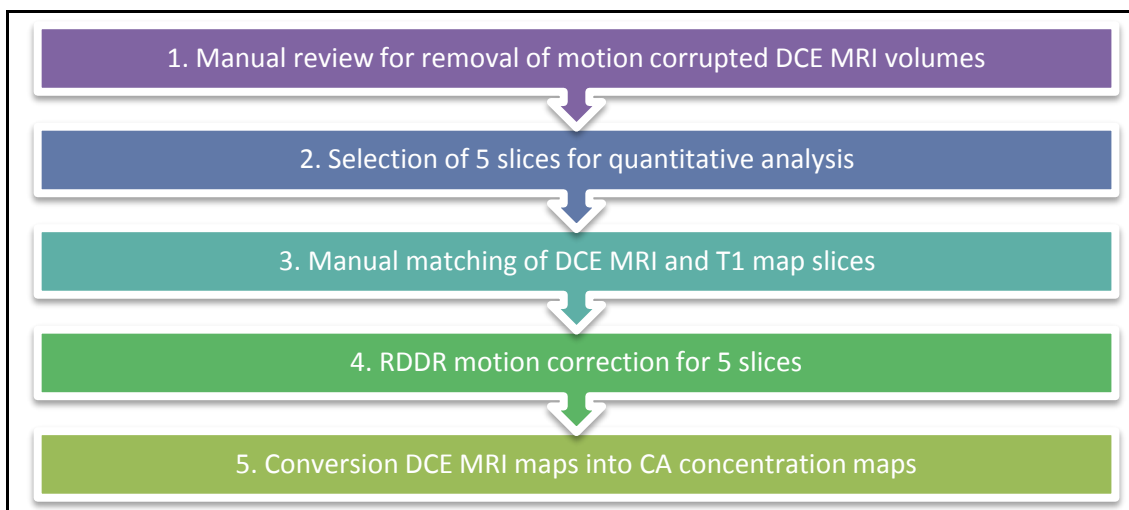


Figure 6.3: DCE MRI post-processing pipeline

To generate useful and accurate DCE MRI perfusion maps, a five step process was used after T1 maps had been calculated. Obviously motion artefacted data was discarded, slices were carefully selected, matched and then registered before generating CA concentration maps.

All post-processing was performed using in house developed Matlab code with a five-step processing pipeline (figure 6.3). DCE data was first reviewed manually and volumes corrupted by motion artefact noise were discarded. Five coronal slices, each 10 mm apart were selected for inclusion of large volume of liver parenchyma, PV and aorta. Each slice was then visually matched to corresponding data from the previously derived T1 maps (figure 6.4). DCE data was then registered using RDDR to correct for tissue displacement and deformation. Conversions of sequential post-contrast signal intensity into CA concentration were then undertaken using a previously published two-step method [145, 146]: (i) sequential post-contrast T1 ($T1_{(t)}$) was determined from repetition time (TR) and flip angle (θ) data using the following expression for post-contrast gradient echo signal intensity ($SI_{(t)}$):

$$SI_{(t)} = M_0 \sin \theta \left(\frac{1 - e^{-\frac{TR}{T1_{(t)}}}}{1 - \cos \theta e^{-\frac{TR}{T1_{(t)}}}} \right)$$

(Equation 6.1)

(ii) Using literature based values for CA R1 at 3.0T at 37°C [411], and baseline T1 measurements ($T1_{pre}$), sequential CA concentration ($[CA]_{(t)}$) was then estimated using the following expression:

$$[CA]_{(t)} = \frac{1}{R1} \left(\frac{1}{T1_{(t)}} - \frac{1}{T1_{pre}} \right)$$

(Equation 6.2)

Pixel wise conversion of signal intensity maps into sequential CA concentration maps was then performed for each of the five slices (figure 6.5).

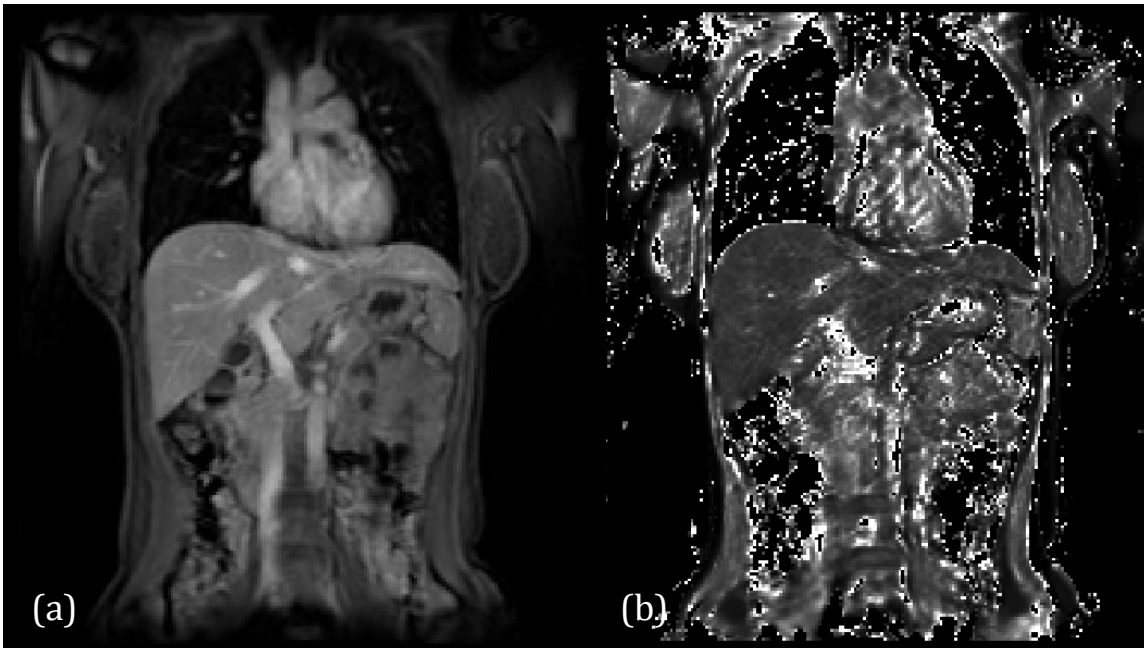


Figure 6.4: Example of selected DCE MRI slice and matching T1 map slice

Because acquisitions were performed separately, the corresponding T1 map (b) for each selected DCE MRI slice (a) was chosen carefully to minimise any quantification errors in parametric mapping. Note how care was taken to ensure all major hepatic vascular and parenchymal structures were matched.

Where there was poor matching of T1 maps and DCE data ($n = 2$ datasets), ROI based T1 measurements and DCE signal intensity were extracted before CA concentration was calculated. Every attempt was made to ensure that T1 and DCE ROIs were extracted from tissue at similar locations.

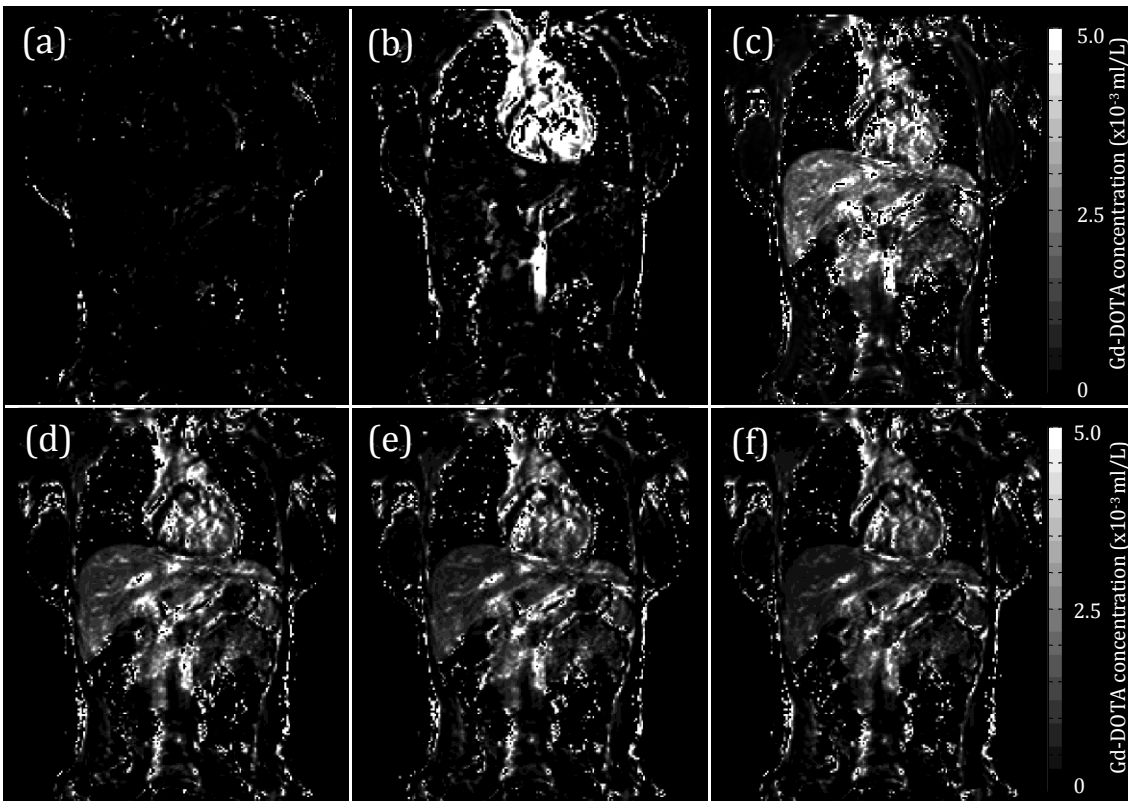


Figure 6.5: Selected Gd-DTPA concentration maps from a single DCE MRI study

Concentration agent concentration maps for a sample dataset are shown at (a) baseline, (b) 23.45 seconds, (c) 70.35 seconds, (d) 120.6 seconds, (e) 224.5 seconds and (f) 301.5 seconds. Signal intensity is linearly related to contrast agent concentration, based on the scale on the far right. Note the predominantly arterial phase enhancement (b), portal venous phase enhancement (c) and progressive parenchymal wash out through to (f).

Three parenchymal ROIs were positioned on each slice (total 15 ROIs), firstly in the right upper region (segments VII/VIII), left liver (segments II/III) and right lower region (segments V/VI). Care was taken to ensure parenchymal ROIs excluded any major inflow or outflow vessels (HA, PV and hepatic venous radicles). ROIs were then also positioned within the left ventricle and PV to derive each VIF (figure 6.6).

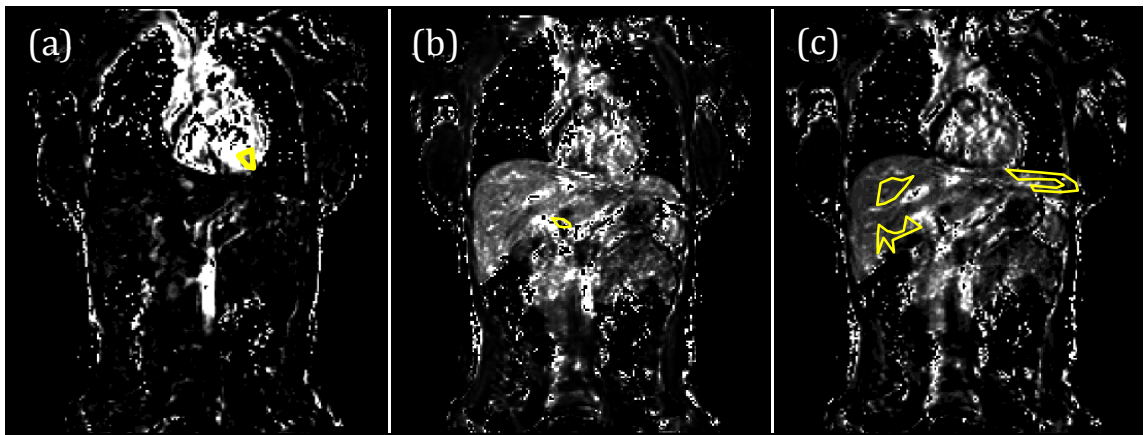


Figure 6.6: Example of ROI placement for DCE MRI quantification

Intra-ventricular ROI placement for AIF (a), PV ROI placement of PVIF (b) and parenchymal ROI placement (c) for segments II/III (far left), segments V/VI (right lower) and segments VII/VIII (right upper). Parenchymal ROIs were placed in each of the three locations on five slices.

As this study was conducted in normal volunteers, significant regional differences in perfusion parameters were not expected. For the purposes of evaluating and refining methodologies, perfusion parameters extracted from all fifteen ROIs (three ROIs on five slices) were therefore averaged for different post-processing method comparisons.

6.3.2.4 Dual input single compartment modelling and VIF delay studies

Dual input single compartment modelling was undertaken in the same way as described previously (section 3.5.1.1). Briefly, liver parenchymal enhancement as a function of time ($C_L(t)$) can be expressed as:

$$C_L(t) = \int_0^t [k_{1a}C_a(t' - \tau_a) + k_{1p}C_p(t' - \tau_p)]e^{-k_2(t-t')} dt' \quad \text{(Equation 6.3)}$$

where variables are defined as follows:

$C_a(t)$	arterial input CA concentration as a function of time
$C_p(t)$	PV input CA concentration as a function of time
k_{1a}	arterial inflow constant
k_{1p}	PV inflow constant
k_2	outflow constant
τ_a	delay between AIF and parenchymal CA arrival
τ_p	delay between PVIF and parenchymal CA arrival

In this study, three modelling approaches were evaluated: (i) Method 1 – assumption of zero-delays between the vascular input functions and parenchymal enhancement (τ_a and τ_p set to zero), (ii) Method 2 – free modelling of AIF and PVIF delays to optimise the fit quality by minimising residual sum of squares and (iii) Method 3 – pre-estimation of bolus arrival times with constrained free modelling as demonstrated by figure 6.2.

Coronally sampled VIFs were subject to additional cardiac motion artefact, which resulted in potentially noisier data. The slower upstroke demonstrated by PVIFs was also found to be more susceptible to undervaluation if the maximum slope was used to pre-estimate the CA arrival time (figure 6.2). To overcome this problem, pre-estimation was undertaken in all data sets using linear regression of the line between the first point above the 95% confidence interval of the baseline and the VIF maximum (figure 6.7).

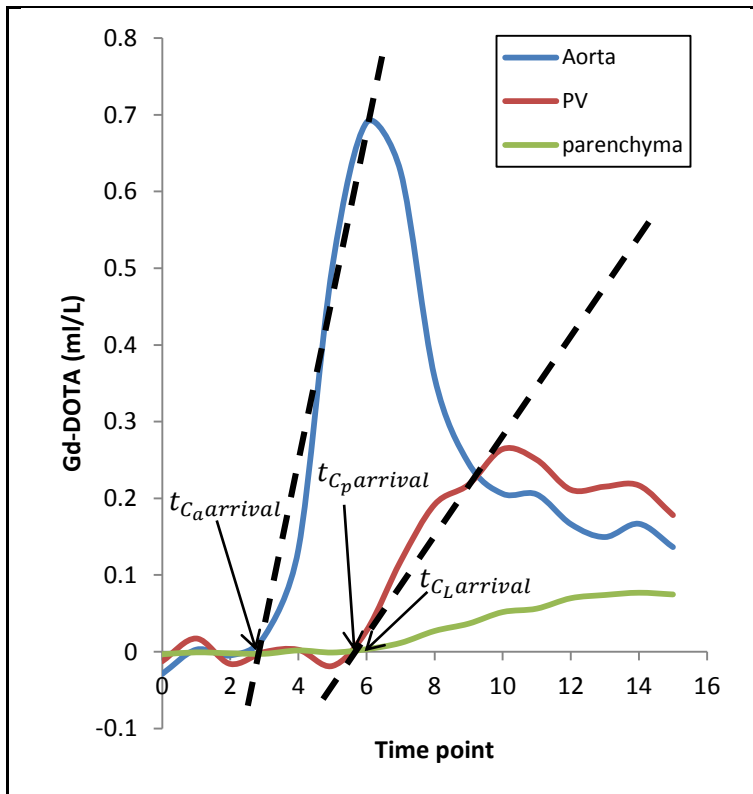


Figure 6.7: Corrected linear regression for pre-estimation of AIF and PVIF CA bolus arrival delays

Enhancement data between the first data point above the 95% confidence interval of the baseline and the VIF upstroke peak was modelled using linear regression (rather than the maximum gradient of the upstroke) to estimate aortic ($t_{C_a arrival}$) and PV ($t_{C_p arrival}$) CA bolus arrival times. Parenchymal CA arrival time ($t_{C_L arrival}$) was determined using the 95% upper limit confidence interval of baseline data. This diagram uses the same data as figure 6.2 for illustrative purposes.

Estimates of VIF CA arrival time ($t_{C_a arrival}$ and $t_{C_p arrival}$) were thus obtained. CA arrival in the parenchymal ROI ($t_{C_L arrival}$) was determined as the time of the last point before parenchymal CA concentration exceeded the upper limit of the 95% confidence interval of the baseline (pre-contrast) data (figure 6.2). Estimates for τ_a and τ_p were then determined as:

$$\tau_a' = t_{C_L arrival} - t_{C_a arrival}$$

$$\tau_p' = t_{C_L arrival} - t_{C_p arrival}$$

(Equations 6.4 and 6.5)

As τ_a' and τ_p' represented estimates of VIF delays, limited by temporal resolution (3.35 seconds), the pre-estimates were then used to constrain the range in which free modelling of τ_a and τ_p could occur, to one time point before and one time point after each estimate (i.e. within a 6.7 second window).

To enable comparison with clinical PCMRI perfusion parameters (section 5.5), PV perfusion was calculated from k_{1p} , total liver blood flow (TLBF) and HA fraction was calculated from k_1 , the sum of arterial (k_{1a}) and PV (k_{1p}) inflow constants and mean transit time (MTT) and distribution volume (DV) were calculated from k_2 as previously .

6.3.2.5 Reproducibility studies

To measure reproducibility, subjects were scanned using the same MRI protocol 7 days later. As with the initial study, subjects were asked to remain fasted for at least 6 hours prior to the study and were advised to consume water ad libitum, but refrain from the consumption of caffeinated fluids. Care was taken to ensure subjects were scanned at a comparable time of the day to the original study.

6.3.2.6 Validation studies

Validation was undertaken with PCMRI studies performed just prior to DCE MRI, in the same scanning session. PCMRI methodology is described in detail in section 5.5.2.2. PCMRI derived volume normalised PV flow (direct measurement), estimated TLBF (caval subtraction measurement) and estimated HA fraction (percentage estimated HA flow calculated from directly measured PV flow and estimated TLBF) were used to validate DCE MRI PV perfusion, TLBF and HA fraction measurements respectively.

6.3.2.7 Statistical analysis

Kolmogorov-Smirnov tests were used to confirm normality of variable distributions. Repeated measures one-way analysis of variance (ANOVA) with corrections for non-

sphericity were used to compare perfusion parameters from dual input single compartment modelling using each of the three approaches to VIF delay estimation. Post-hoc Tukey's test was then applied where significant differences were identified. Where variables were found not to be normally distributed, the Kruskal-Wallis test was used followed by post-hoc Dunn's test where significant differences were identified. Reproducibility and validation studies were assessed using paired t-tests/Wilcoxon matched pairs signed rank tests, Bland-Altman analysis of agreement with calculation of the coefficient of repeatability and assessment of correlation between repeated/validated measurements using Pearson's or Spearman's correlation coefficient for parametric/non-parametric data as appropriate. The threshold of statistical significance was defined to be $p < 0.05$.

6.3.3 RESULTS

6.3.3.1 Cohort features

Data was collected in twelve normal volunteers. Male subjects ($n = 6$) had a mean age of 26.7 ± 1.55 years and female subjects ($n = 6$) had a mean age of 30.2 ± 2.37 years. Seven day reproducibility data was available for nine subjects ($n = 4$ male, $n = 5$ female).

6.3.3.2 VIF delay studies

A sample data set was used to demonstrate the VIFs and parenchymal enhancement curves obtained with corresponding curve fits in figure 6.8, using each of the three approaches. Alternative delays resulted in effective shifts of the VIF as shown in the charts on the left in figure 6.8. The effects of these shifts on estimated parameters resulted in profound differences in estimated perfusion parameters for each method, as shown by the data overlaying the charts on the right (figure 6.8).

Data for each of the perfusion parameters is plotted for each method in figure 6.9 and tabulated in table 6.2. HA fraction, DV and PVIF delay parameters demonstrated non-normal distributions and therefore underwent non-parametric statistical testing. Significant differences were demonstrated between the three methods for PV perfusion ($F(1.248, 24.96) = 7.293$; $p = 0.0085$), HA fraction ($H = 23.94$; $p < 0.0001$), AIF delay (mean difference -3.670 ± 1.109 seconds; $p = 0.0035$), PVIF delay (median difference 1.117 seconds; $p = 0.0288$) and residual sum of squares ($F(1.346, 26.93) = 32.73$; $p < 0.0001$). Post-hoc tests demonstrated significant differences between Method 1 and Method 2 for PV perfusion, HA fraction and residual sum of squares, but significant differences between Method 1 and Method 3 were only demonstrated for HA fraction. Significant differences in residual sum of squares were demonstrated between Method 2 and Method 3 on post-hoc testing.

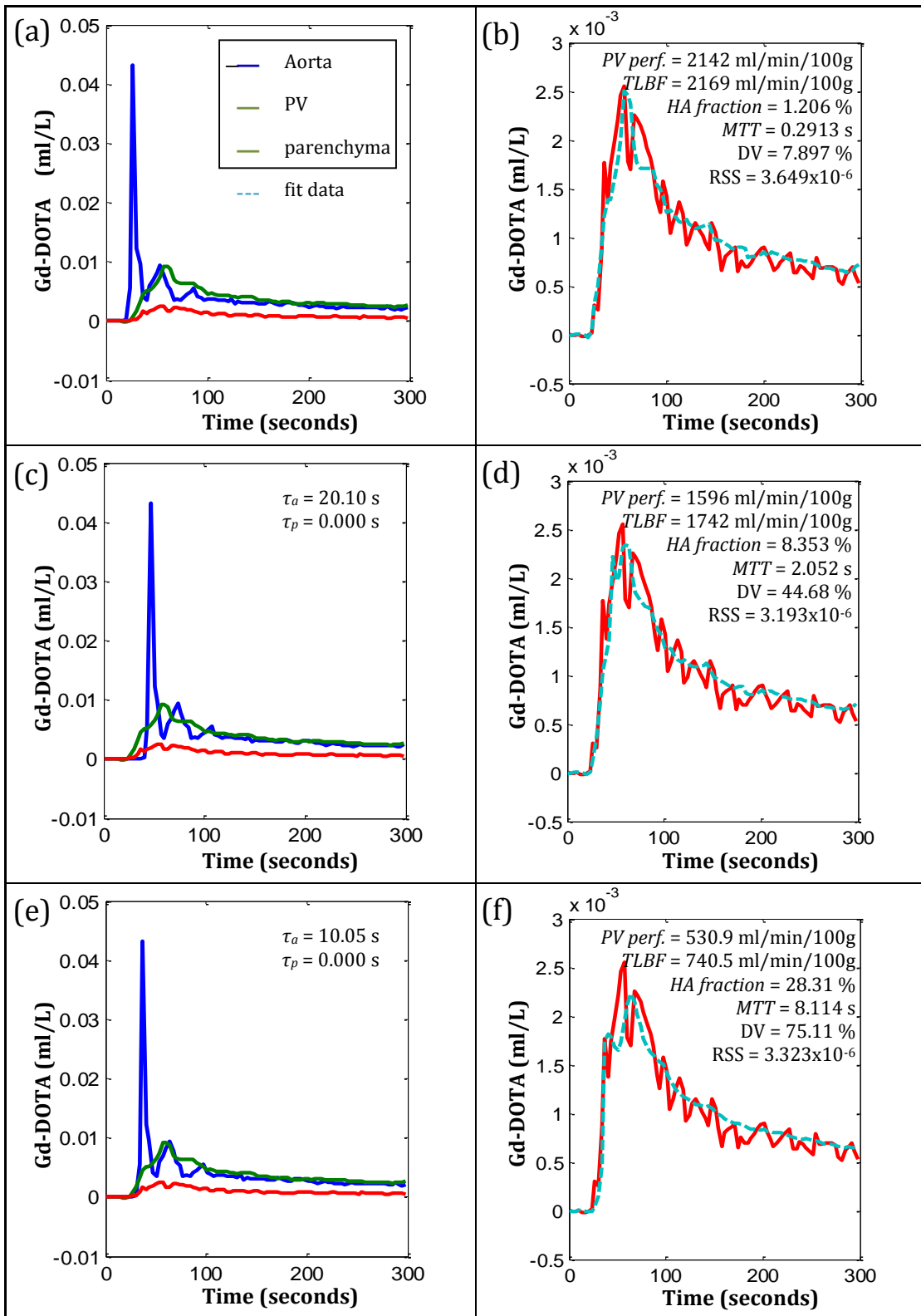


Figure 6.8: Dual input single compartment modelling VIFs and parenchymal enhancement curves with fitted parenchymal enhancement curves

Data assuming τ_a and τ_p are zero - (a) and (b), free modelling of τ_a and τ_p - (c) and (d), and finally pre-estimation of VIF delays with constrained free modelling of τ_a with τ_p - (e) and (f). Note considerable differences in estimated perfusion parameters using the same data with all three methods (for spacing reasons, 'PV perfusion' is abbreviated to 'PV perf.' And 'residual sum of squares' is abbreviated to 'RSS').

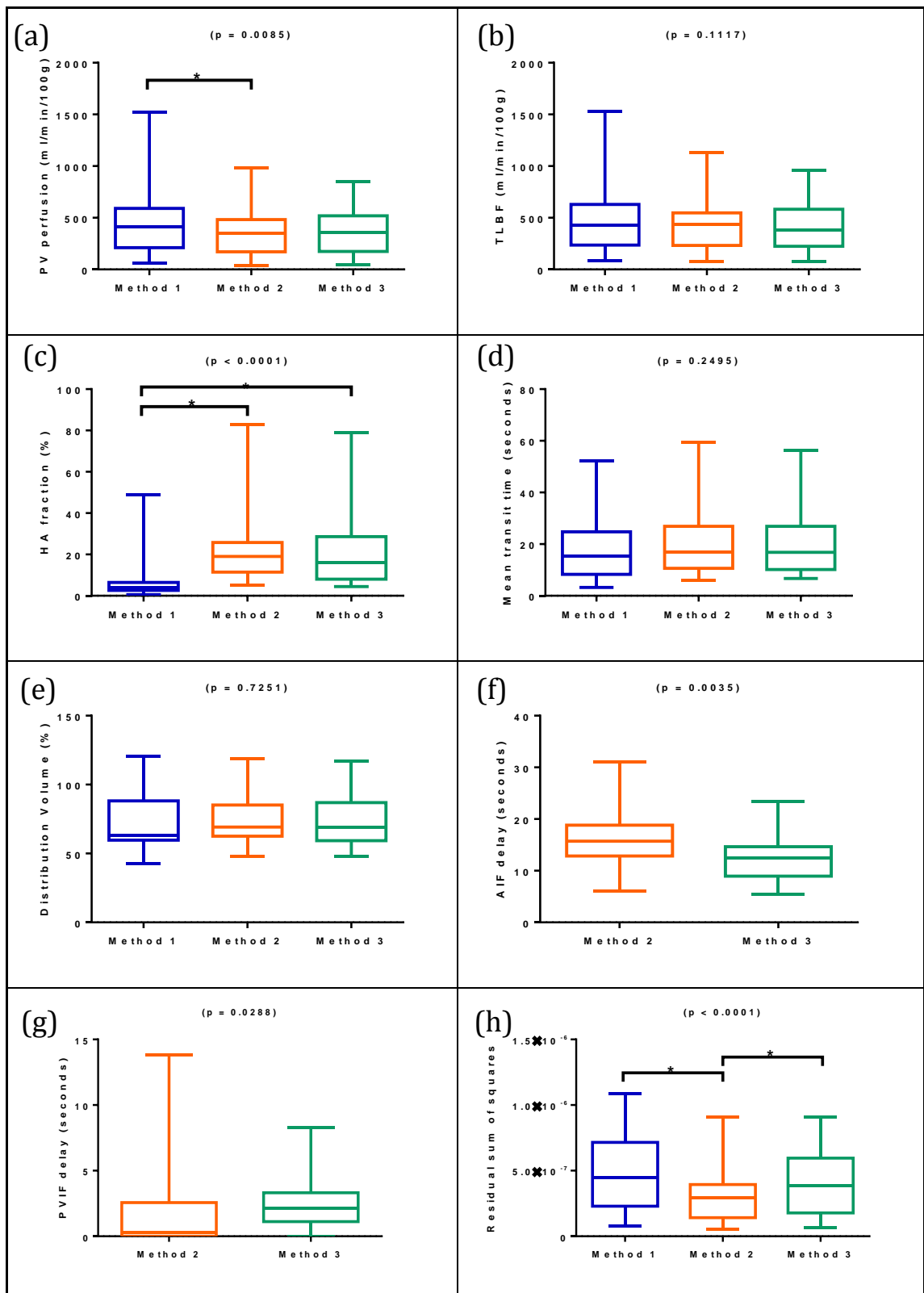


Figure 6.9: Perfusion parameters estimated using the dual input single compartment model, with each method of VIF delay estimation

p-values are quoted for one-way ANOVA/Kruskal-Wallis tests and paired t-tests/Wilcoxon matched-pairs signed rank tests where appropriate, with significant differences on post-hoc testing (*), for Method 1 (no delays), Method 2 (freely modelled delays) and Method 3 (pre-estimated delays with constrained free modelling). Comparisons of delay parameters were only undertaken when these were modelled ((f) and(g)).

Table 6.2: Perfusion parameters estimated using the dual input single compartment model, with each method of VIF delay estimation

	METHOD 1 (no delays)	METHOD 2 (freely modelled delays)	METHOD 3 (pre-estimated delays with constrained free modelling)
PV perfusion (ml/min/100g) *	469.3±73.51	350.3±49.83 [†]	365.7±51.13
TLBF (ml/min/100g)	489.7±72.85	428.0±54.96	436.7±55.55
HA fraction (%)*	7.377±2.340	21.73±3.620 [†]	20.72±3.695 [†]
Mean Transit Time (seconds)	18.62±2.666	20.01±2.676	19.92±2.644
Distribution Volume (%)*	71.24±4.328	74.07±3.847	73.45±3.951
Residuals ^{2*}	4.884x10 ⁻⁷ ±6.245x10 ⁻⁸	3.183x10 ⁻⁷ ±4.754x10 ^{-8†}	3.831x10 ⁻⁷ ±5.079x10 ^{-8††}
τ _a (seconds)*	-	16.14±1.338	12.48±1.054
τ _p (seconds)*	-	1.906±0.7174	2.626±0.4724

(*one-way ANOVA/Kruskal-Wallis/paired t-test/Wilcoxon p<0.05; [†] post-hoc Tukey test comparison with Method 1 p<0.05; [‡] post-hoc Tukey test comparison with Method 2 p < 0.05)

6.3.3.3 Reproducibility

Reproducibility was assessed using the same protocol with the same scanner in the same subjects exactly seven days after the initial study. Repeat measurements were obtained in normal volunteers ($n = 9$). All reproducibility analysis data are summarised and presented alongside seven day PCMRI reproducibility for comparison in table 6.3. No significant differences were demonstrated between repeated PV perfusion measurements using either of the three methods (figure 6.10, table 6.3). The smallest mean difference was demonstrated using Method 3 (-12.4 ± 114.8 ml/min/100g; $p = 0.9166$). This method also demonstrated the smallest coefficient of reproducibility (674.9 ml/min/100g). No correlations were identified between repeated measurements using any of the methods.

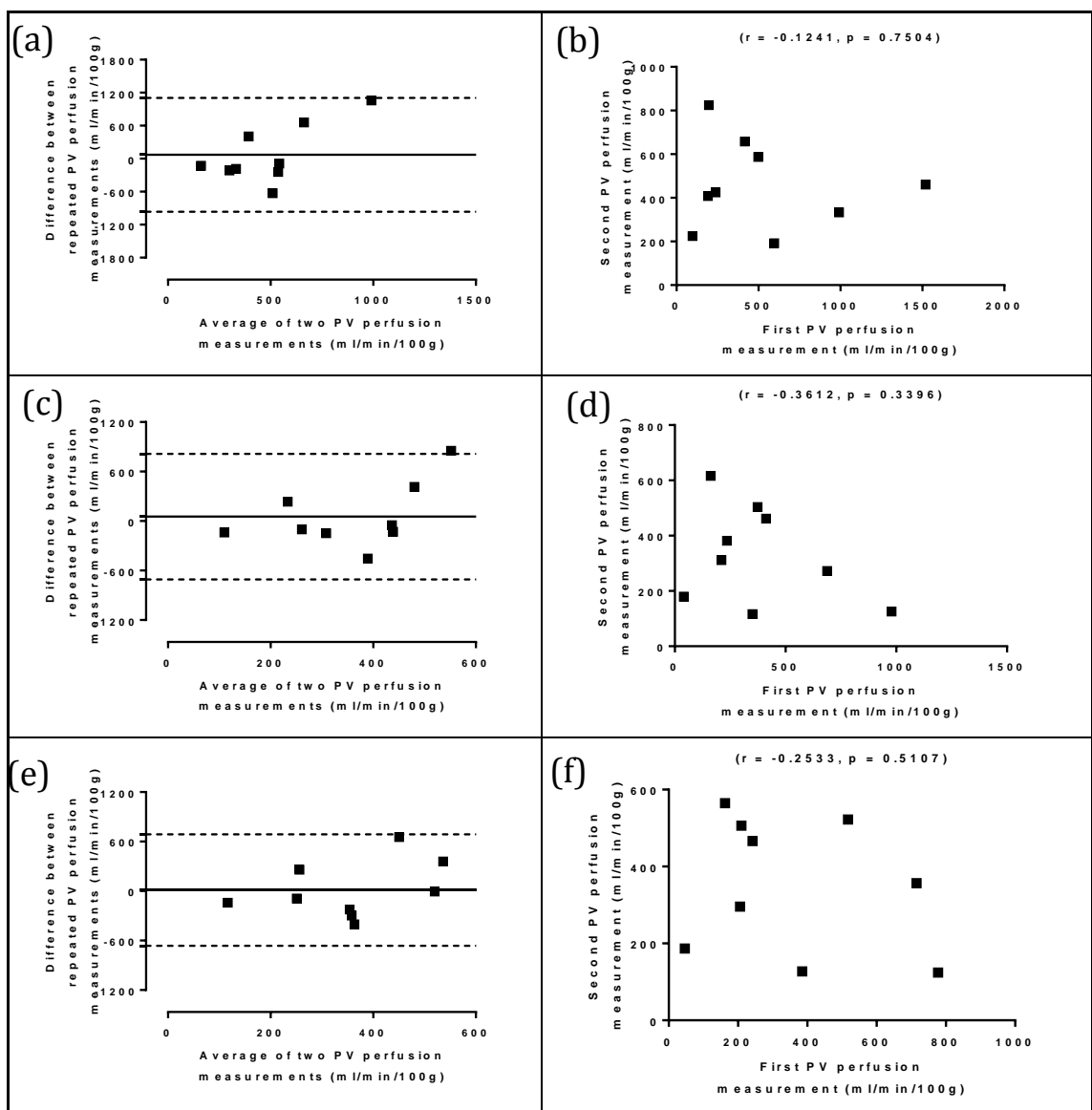


Figure 6.10: Analysis of agreement of repeated PV perfusion using alternative approaches to VIF delays with dual input single compartment modelling

Bland-Altman and regression analysis of (a, b) Method 1 – zero VIF delays, (c, d) Method 2 – free modelling of VIF delays, (e, f) Method 3 – constrained free modelling of pre-estimated VIF delays.

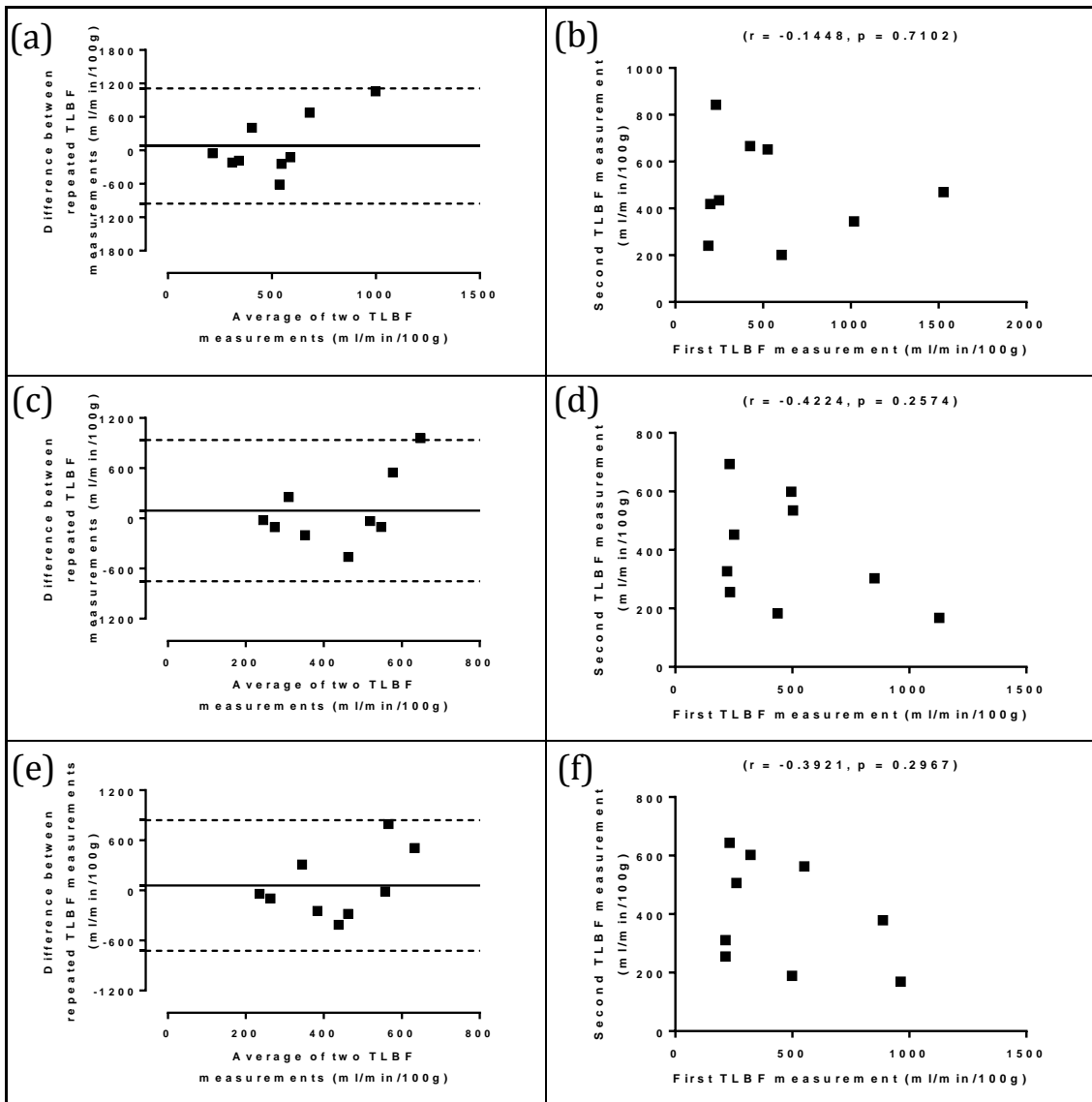


Figure 6.11: Analysis of agreement of repeated TLBF using alternative approaches to VIF delays with dual input single compartment modelling

Bland-Altman and regression analysis of (a, b) Method 1 – zero VIF delays, (c, d) Method 2 – free modelling of VIF delays, (e, f) Method 3 – constrained free modelling of pre-estimated VIF delays.

No significant differences were demonstrated between repeated TLBF measurements using either of the three methods (figure 6.11, table 6.3). The smallest mean difference was demonstrated using Method 3 (-58.33 ± 133.0 ml/min/100g; $p = 0.6726$). This method also demonstrated the smallest coefficient of reproducibility (782.3 ml/min/100g). No correlations were identified between repeated measurements using any of the methods.

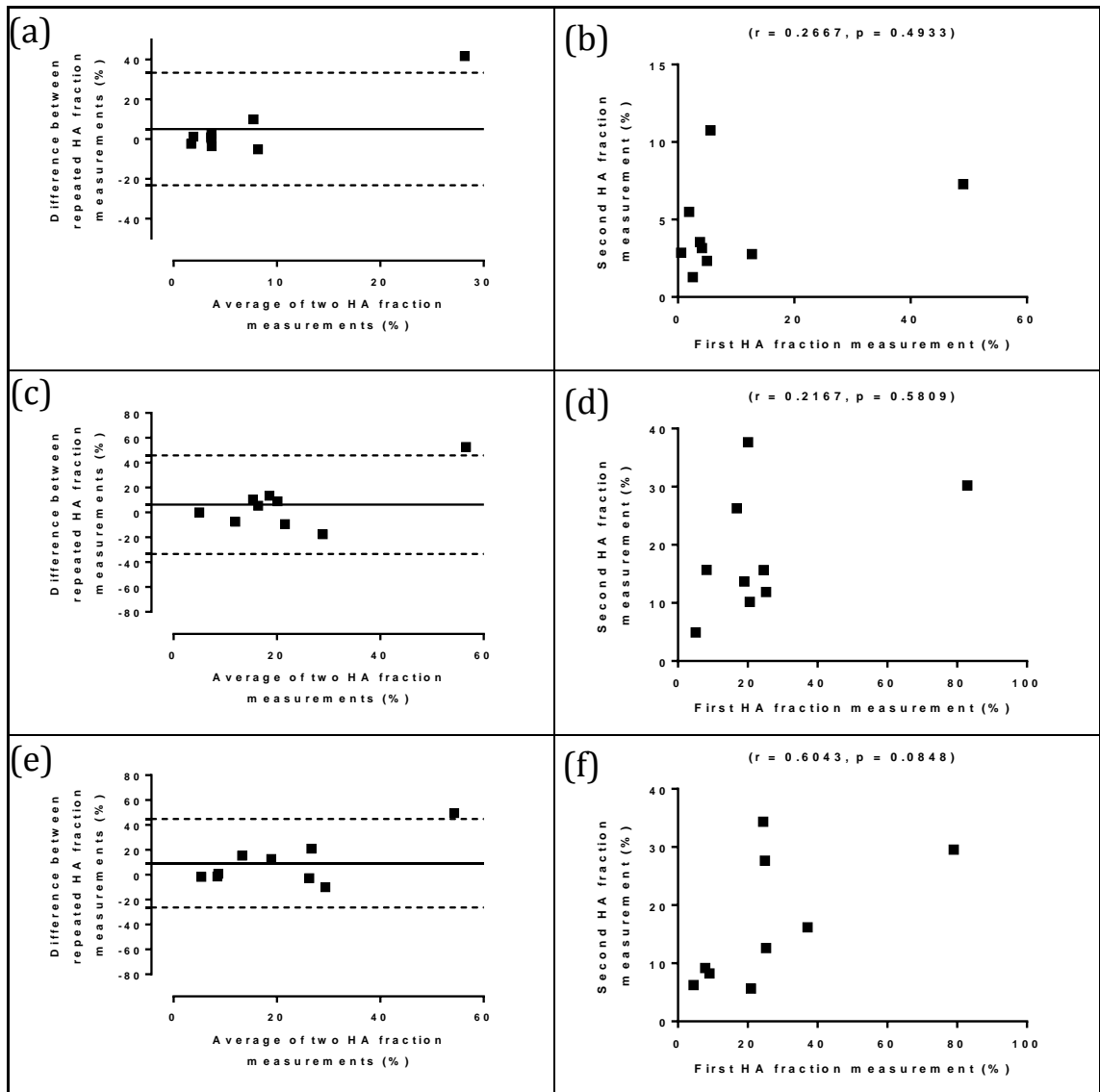


Figure 6.12: Analysis of agreement of repeated HA fraction using alternative approaches to VIF delays with dual input single compartment modelling

Bland-Altman and regression analysis of (a, b) Method 1 – zero VIF delays, (c, d) Method 2 – free modelling of VIF delays, (e, f) Method 3 – constrained free modelling of pre-estimated VIF delays.

No significant differences were demonstrated between repeated HA fraction measurements using either of the three methods (figure 6.12, table 6.3). Testing for variable normality demonstrated non-normal distributions for HA fraction using Methods 1 and 2 but not Method 3. The smallest mean difference was demonstrated using Method 1 (mean -0.9782%; $p = 0.5703$). This method also demonstrated the smallest coefficient of reproducibility (28.27%). The strongest correlation between repeated measurements was demonstrated with Method 3 ($r = 0.6043$; $p = 0.0848$). No other correlations were demonstrated.

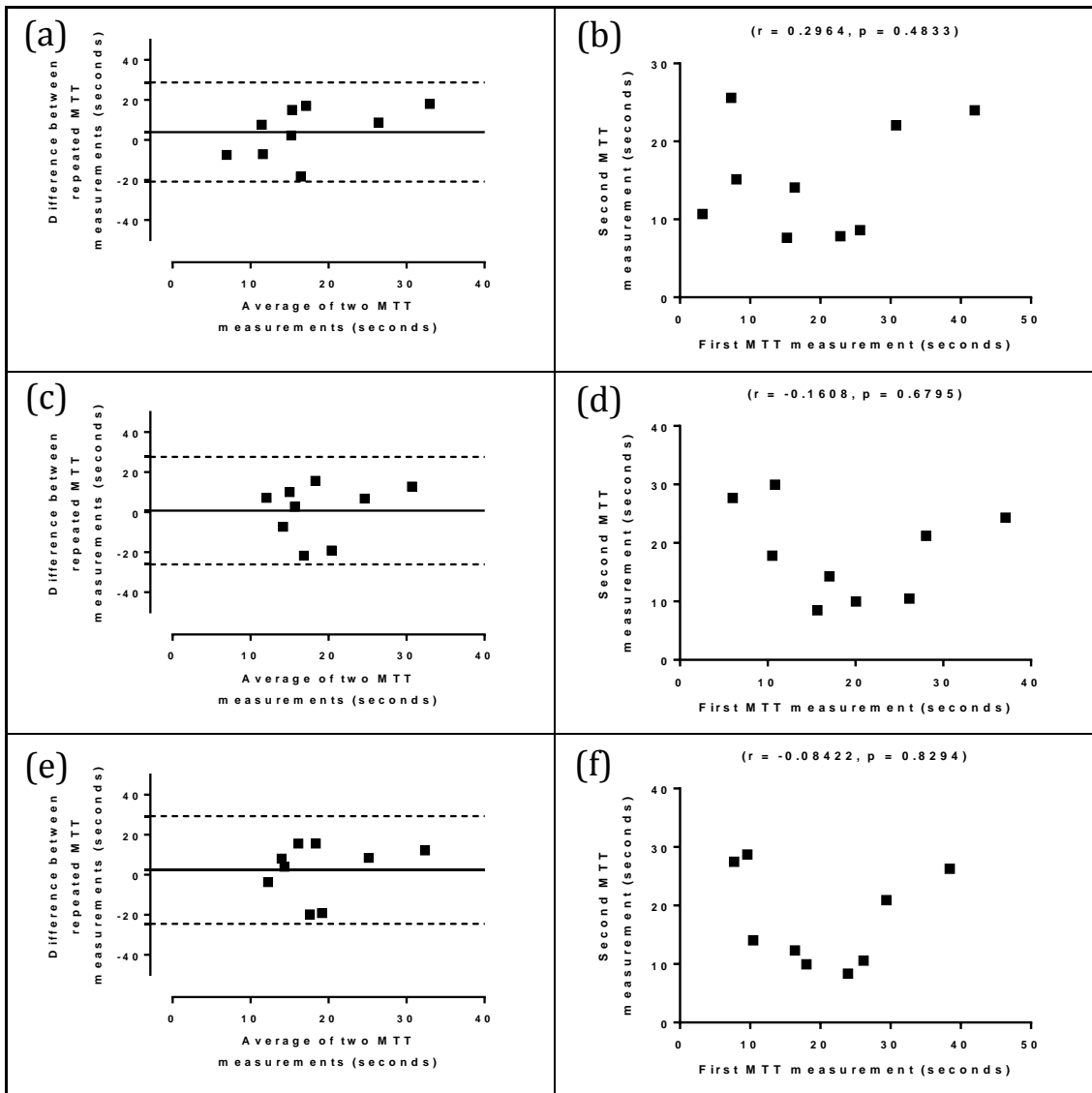


Figure 6.13: Analysis of agreement of repeated Mean Transit Time using alternative approaches to VIF delays with dual input single compartment modelling

Bland-Altman and regression analysis of (a, b) Method 1 – zero VIF delays, (c, d) Method 2 – free modelling of VIF delays, (e, f) Method 3 – constrained free modelling of pre-estimated VIF delays.

No significant differences were demonstrated between repeated MTT measurements using either of the three methods (figure 6.13, table 6.3). The smallest mean difference was demonstrated using Method 3 (-2.374 ± 4.573 seconds; $p = 0.6176$). Method 1 however demonstrated the smallest coefficient of reproducibility (24.76 seconds). No correlations were demonstrated between repeated measurements using any of the methods.

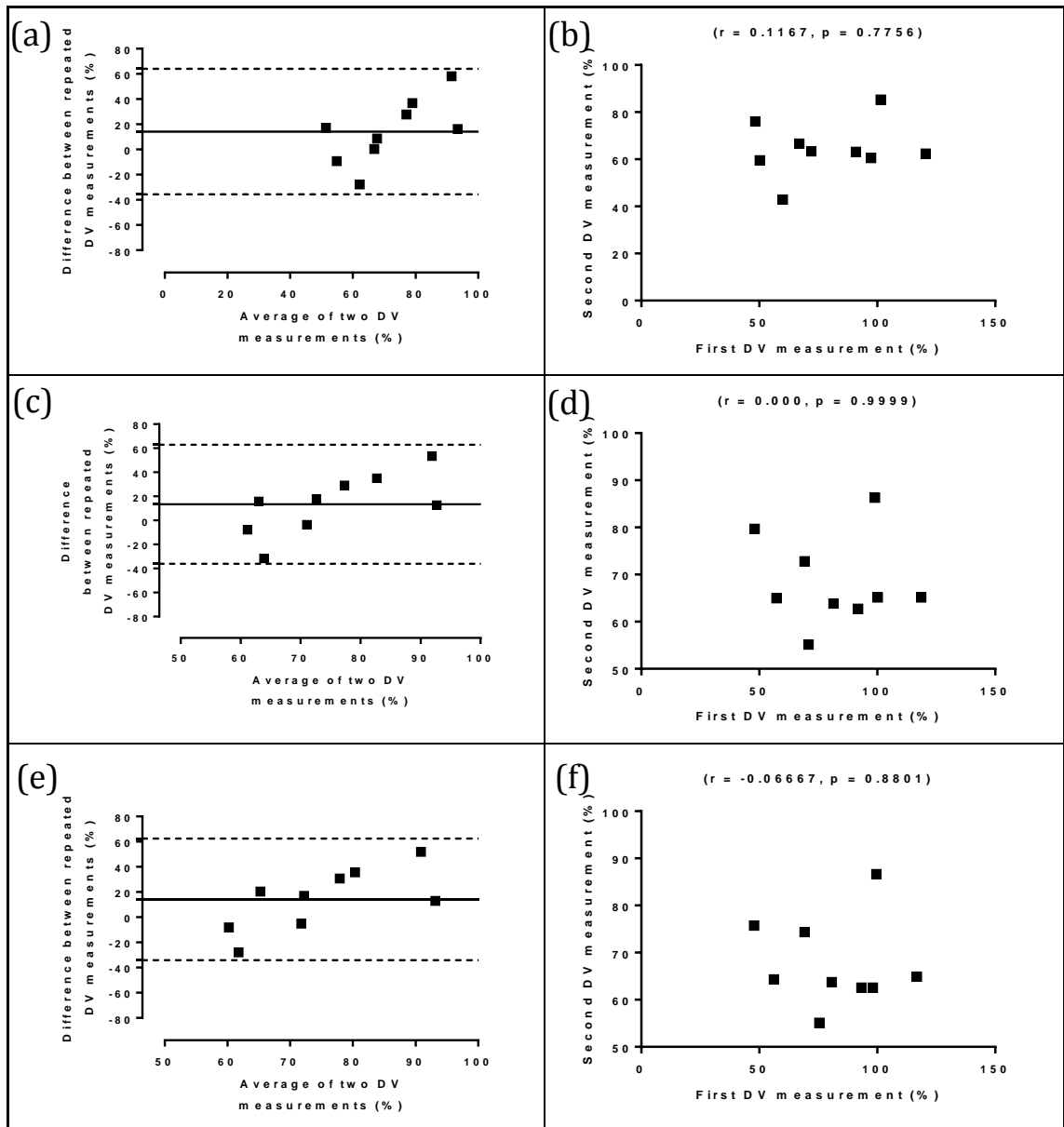


Figure 6.14: Analysis of agreement of repeated Distribution Volume using alternative approaches to VIF delays with dual input single compartment modelling

Bland-Altman and regression analysis of (a, b) Method 1 – zero VIF delays, (c, d) Method 2 – free modelling of VIF delays, (e, f) Method 3 – constrained free modelling of pre-estimated VIF delays.

Testing for variable normality demonstrated non-normal distributions for DV using all three methods. No significant differences were demonstrated between repeated DV measurements using either of the three methods (figure 6.14, table 6.3). The smallest median difference was demonstrated using Method 2 (median -15.74%; $p = 0.1641$). Method 3 however demonstrated the smallest coefficient of reproducibility (48.24%). No correlations were demonstrated between repeated measurements using any of the methods.

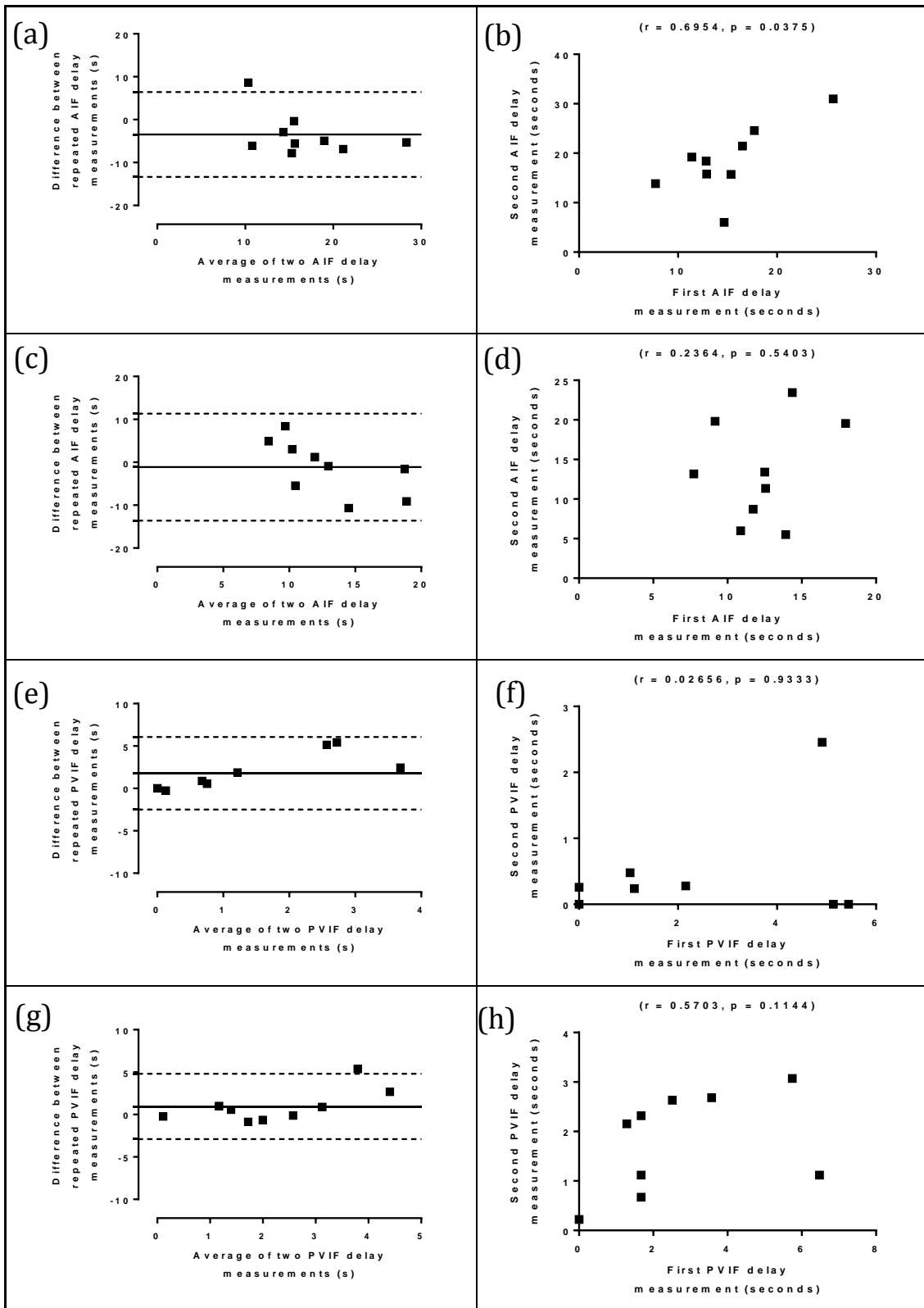


Figure 6.15: Analysis of agreement of repeated VIF delays using alternative approaches with dual input single compartment modelling

Bland-Altman and regression analysis of (a, b) Method 2 – free modelling of AIF delays, (c, d) Method 3 – constrained free modelling of pre-estimated AIF delays, (e, f) Method 2 – free modelling of PVIF delays and (g, h) Method 3 – constrained free modelling of pre-estimated PVIF delays..

No significant differences were demonstrated between repeated AIF delay parameters but freely modelled PVIF delays using Method 2 were significantly different (median difference -0.877 seconds; $p = 0.0313$) (figure 6.15, table 6.3). The smallest difference between repeated AIF delay parameters was demonstrated with Method 3 (mean difference 1.126 ± 2.119 seconds; $p = 0.6096$). Method 2 demonstrated a smaller coefficient of reproducibility (9.888 seconds) and also a significant correlation between repeated AIF delay parameters ($r = 0.6954$; $p = 0.0375$). The smallest difference between repeated PVIF delay parameters was demonstrated with Method 3 (median -0.5583 seconds; $p = 0.2500$). A positive correlation between repeated PVIF delay parameters was demonstrated using Method 3, but this was non-significant ($r = 0.5703$; $p = 0.1144$).

Table 6.3: Summary of reproducibility of perfusion parameters estimated using alternative approaches to VIF delays with dual input single compartment modelling alongside PCMRI reproducibility[§]

	METHOD 1 (no delays)	METHOD 2 (freely modelled delays)	METHOD 3 (pre-estimated delays with constrained free modelling)	PCMRI
PV perfusion (ml/min/100g)				
Mean difference	-70.48±176.1	-53.43±129.4	-12.4±114.8	-1.234±2.924
Coefficient of Reproducibility	1036	760.8	674.9	19.01
Correlation (r)	-0.1241	-0.3612	-0.2533	0.7152
TLBF (ml/min/100g)				
Mean difference	-78.17±175.5	-92.81±143.7	-58.33±133.0	-8.460±4.860
Coefficient of Reproducibility	1032	844.8	782.3	31.60
Correlation (r)	-0.1448	-0.4224	-0.3921	0.4858
HA fraction (%)				
Mean difference	-0.9782	-5.349	-9.26±6.036	8.643±6.943
Coefficient of Reproducibility	28.27	39.64	35.49	45.13
Correlation (r)	0.2667	0.2167	0.6043[†]	0.5491
Mean Transit Time (seconds)				
Mean difference	-3.975±4.21	-0.8009±4.564	-2.374±4.573	-
Coefficient of Reproducibility	24.76	26.84	26.89	-
Correlation (r)	0.2964	-0.1608	-0.08422	-
Distribution Volume (%)				
Mean difference	-16.16	-15.74	-16.98	-
Coefficient of Reproducibility	49.85	49.54	48.24	-
Correlation (r)	0.1167	0.000	-0.06667	-
τ_a (seconds)				
Mean difference	-	3.473±1.682	1.126±2.119	-
Coefficient of Reproducibility	-	9.888	12.47	-
Correlation (r)	-	0.6954^{**}	0.2364	-
τ_p (seconds)				
Mean difference	-	-0.8774*	-0.5583	-
Coefficient of Reproducibility	-	4.270	3.853	-
Correlation (r)	-	0.02656	0.5703	-

[§]Embodened values in the table highlight the best performing Method for each statistic;

*paired t-test/Wilcoxon $p < 0.05$;

**Pearson's correlation coefficient $p < 0.05$;

[†]Pearson's correlation coefficient $p = 0.0848$

6.3.3.4 Validation

Validation of DCE MRI measurements was undertaken using PCMRI measurements of PV perfusion, estimated (caval subtraction) TLBF and estimated HA fraction measured at the same time as DCE MRI studies. Baseline and seven day reproducibility scans were analysed for twelve subjects (21 datasets). DCE MRI measurements were compared for the three approaches to VIF delays using dual input single compartment modelling.

Simply eye-balling the data (table 6.4), it was clear that DCE MRI tended to grossly overestimate absolute perfusion measurements. This compromised the Bland-Altman analysis so that both the averages and differences of each pair of validated perfusion measurements were heavily weighted towards each DCE MRI measurement. Plots therefore appear to show a linear trend (figures 6.16 (a, c, e) and 6.17 (a, c, e)).

Table 6.4: DCE MRI perfusion parameters estimated using alternative approaches to VIF delays and PCMRI validation data

	METHOD 1 (no delays)	METHOD 2 (freely modelled delays)	METHOD 3 (pre-estimated delays with constrained free modelling)	PCMRI
PV perfusion (ml/min/100g)	469.3±73.51	350.3±56.65	365.7±51.13	56.65±2.698
TLBF (ml/min/100g)	489.7±72.85	428.0±54.96	436.7±55.55	71.72±3.318
HA fraction (%)	7.377±2.34	21.73±3.62	20.72±3.695	18.91±4.084

(data replicated from table 6.2 for review)

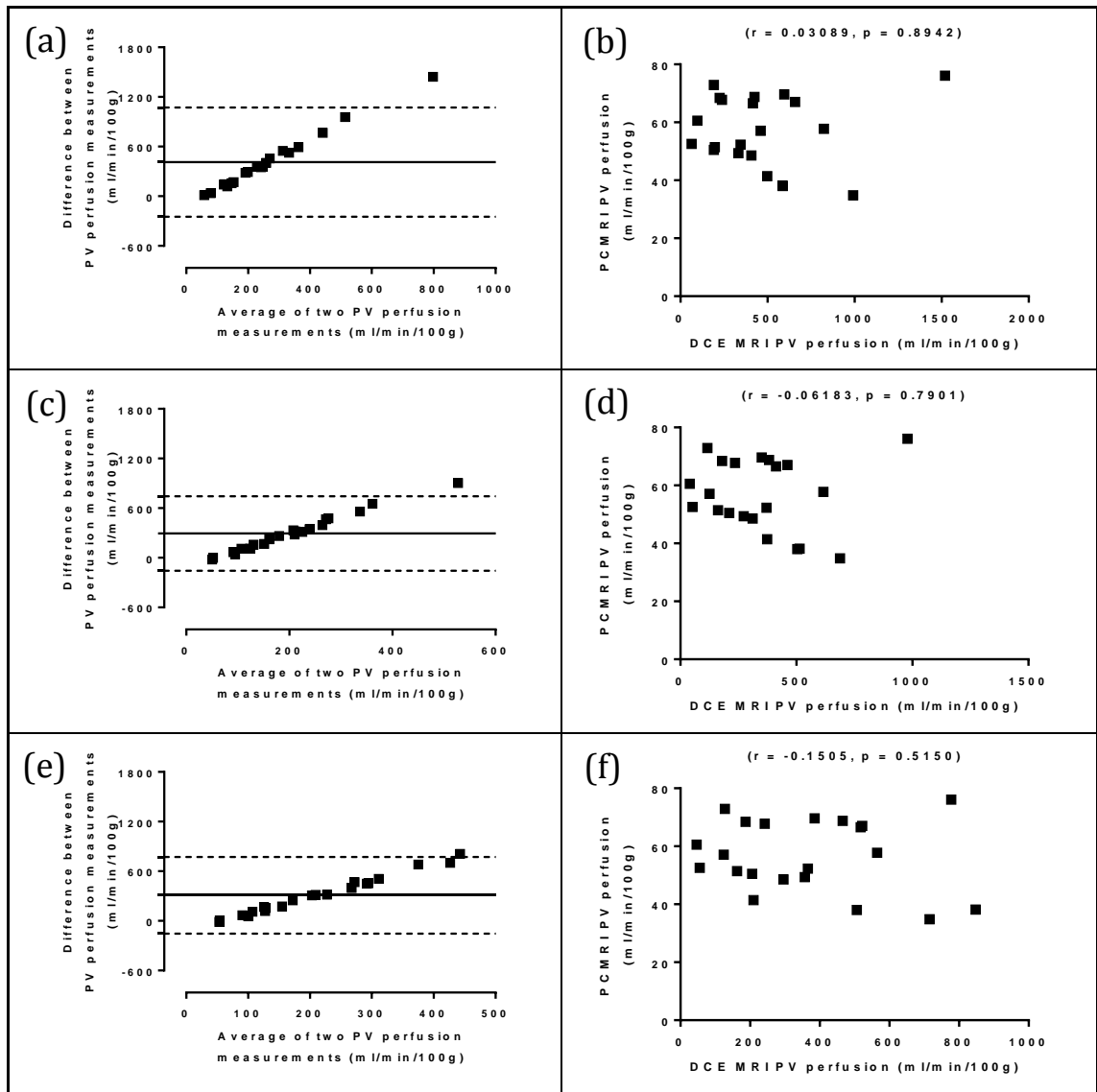


Figure 6.16: Analysis of agreement with PCMRI PV perfusion using alternative approaches to VIF delays with dual input single compartment modelling

Bland-Altman and regression analysis of (a, b) Method 1 – zero VIF delays, (c, d) Method 2 – free modelling of VIF delays, (e, f) Method 3 – constrained free modelling of pre-estimated VIF delays.

Expectably, significant differences were demonstrated between absolute perfusion parameters using all three methods and PCMRI absolute perfusion. The smallest mean difference in PV perfusion (-293.6 ± 50.07 ml/min/100g; $p < 0.0001$) and TLBF (-356.3 ± 54.58 ml/min/100g; $p < 0.0001$) was demonstrated by Method 2 in both cases. The smallest coefficient of variation for PV perfusion (64.07%) and TLBF (58.29%) was demonstrated by Method 3 in both cases. These were still considerably larger than those observed for PV perfusion (21.82%) and TLBF (21.20%) using PCMRI. No significant correlations were demonstrated between DCE MRI and PCMRI absolute perfusion measurements.

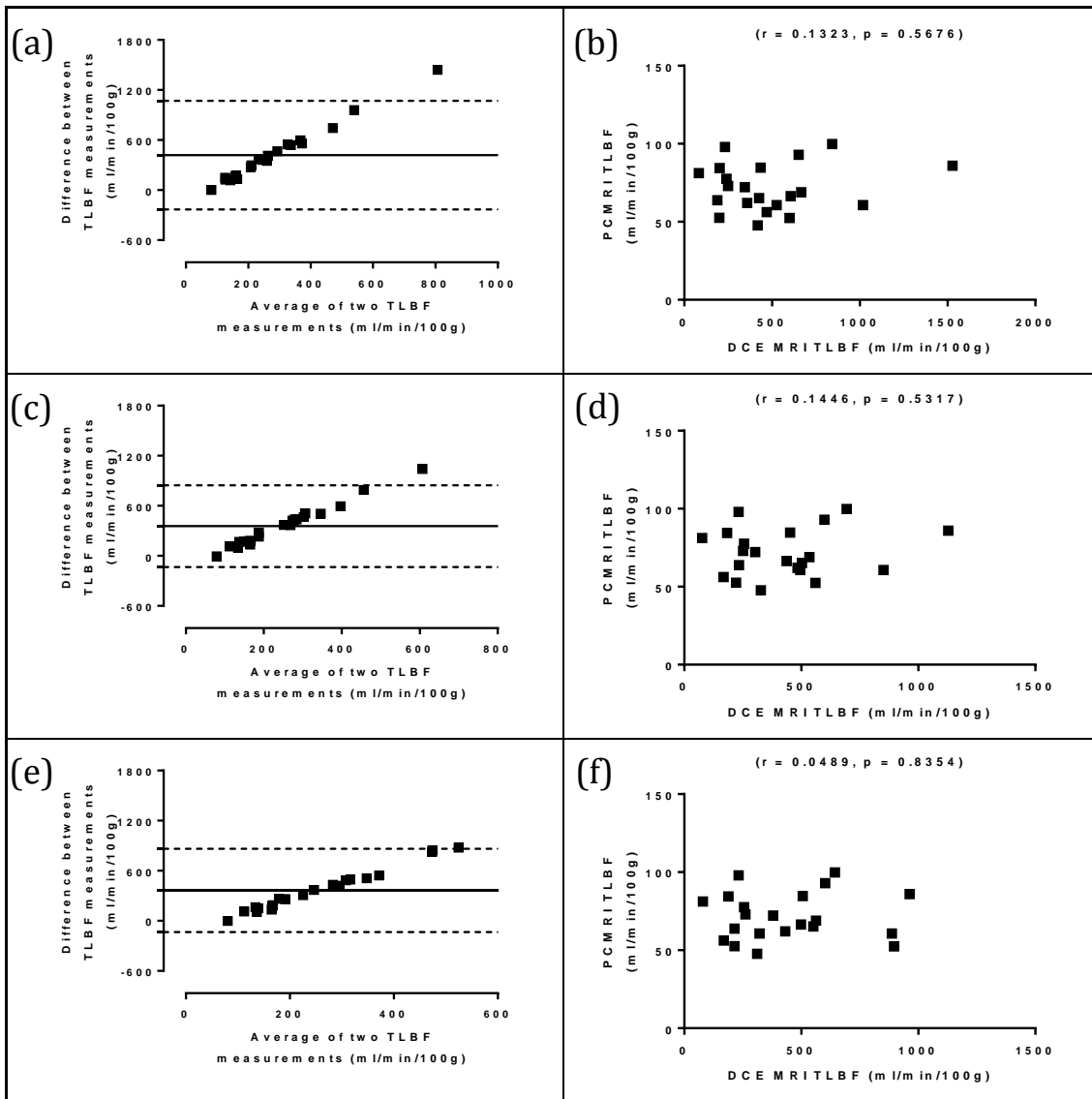


Figure 6.17: Analysis of agreement with PCMRI estimated TLBF using alternative approaches to VIF delays with dual input single compartment modelling

Bland-Altman and regression analysis of (a, b) Method 1 – zero VIF delays, (c, d) Method 2 – free modelling of VIF delays, (e, f) Method 3 – constrained free modelling of pre-estimated VIF delays.

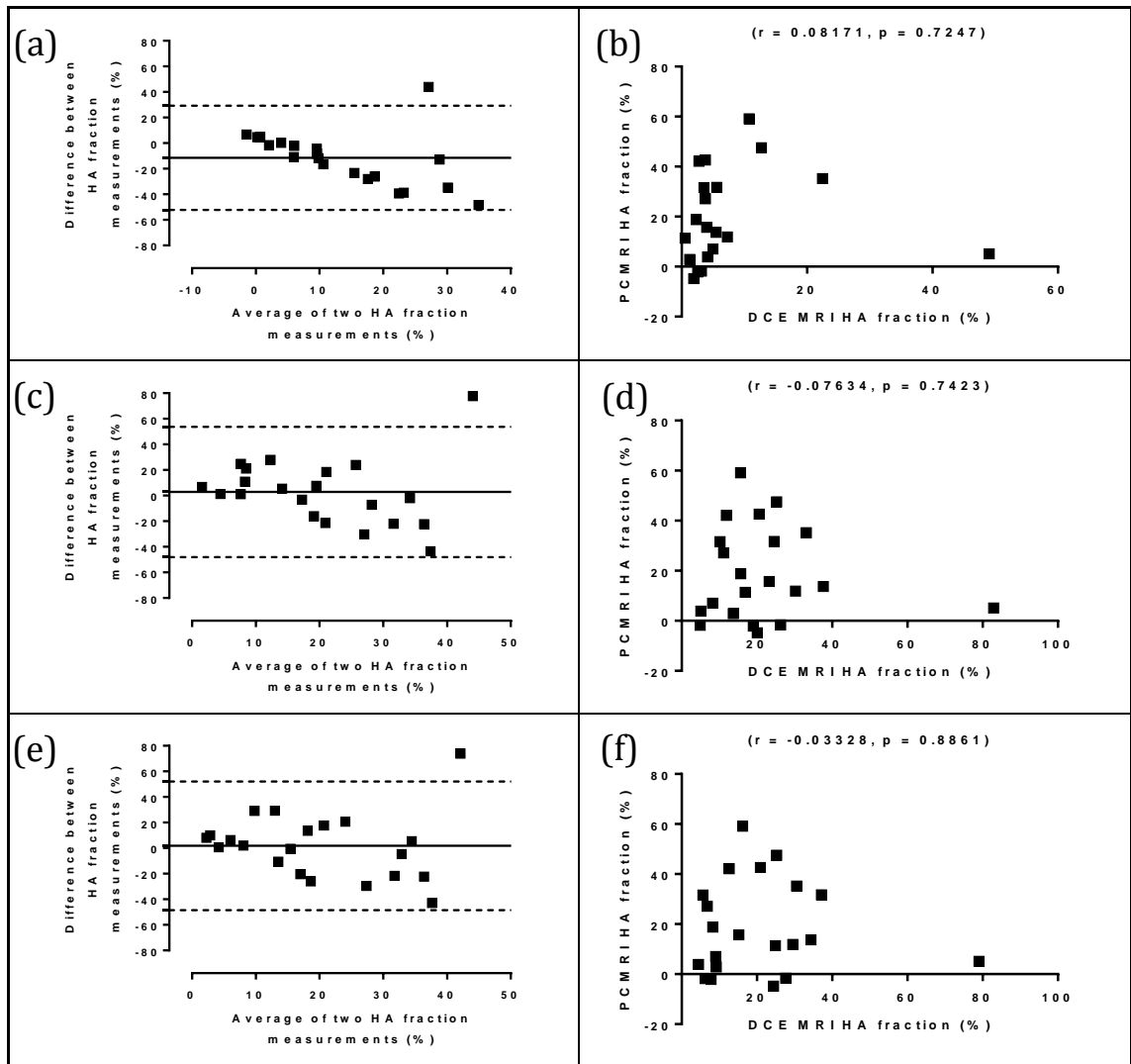


Figure 6.18: Analysis of agreement with PCMRI HA fraction using alternative approaches to VIF delays with dual input single compartment modelling

Bland-Altman and regression analysis of (a, b) Method 1 – zero VIF delays, (c, d) Method 2 – free modelling of VIF delays, (e, f) Method 3 – constrained free modelling of pre-estimated VIF delays.

A significant difference between PCMRI and DCE MRI HA fraction measured using Method 1 was demonstrated (median 10.86%; $p = 0.0142$). No significant differences were demonstrated using Methods 2 and 3. The smallest difference in HA fraction (median -1.223%; $p = 0.7335$) was demonstrated using Method 2. Once again, because of the smaller HA fractions estimated using Method 1 ($7.377 \pm 2.34\%$), both average and differences between data pairs are more heavily weighted towards the PCMRI measurement thereby demonstrating an apparent linear trend on the chart (figure 6.18a). The Bland-Altman charts for Methods 2 and 3 also demonstrate an expected ‘funnelling’ of smaller values. This phenomenon is expected for percent measurements as differences between methods are naturally smaller towards the lower end of the scale [412].

The smallest coefficient of variation for HA fraction was also demonstrated using Method 2 (76.34%) and was smaller than the coefficient of variation for estimated HA

fraction using PCMRI (98.97%). No significant correlations were demonstrated between HA fraction measured using DCE MRI and PCMRI.

Table 6.5: Summary of validation of perfusion parameters estimated using alternative approaches to VIF delays with dual input single compartment modelling using PCMRI[†]

	METHOD 1 <i>(no delays)</i>	METHOD 2 <i>(freely modelled delays)</i>	METHOD 3 <i>(pre-estimated delays with constrained free modelling)</i>
PV perfusion (ml/min/100g)			
Mean difference	-412.6±73.48*	-293.6±50.07*	-309.1±51.60*
Coefficient of Variation	71.78%	65.19%	64.07%
Correlation (<i>r</i>)	0.03089	-0.06183	-0.1505
TLBF (ml/min/100g)			
Mean difference	-417.9±72.48*	-356.3±54.58*	-365.0±55.49*
Coefficient of Variation	68.17%	58.85%	58.29%
Correlation (<i>r</i>)	0.1323	0.1446	0.04829
HA fraction (%)			
Mean difference	10.86*	-1.223	-1.815±5.598
Coefficient of Variation	145.4%	76.34%	81.72%
Correlation (<i>r</i>)	0.08171	-0.07634	-0.03328

([†]Emboldened values in the table highlight the best performing Method for each statistic;
*paired t-test/Wilcoxon matched pairs p<0.05)

6.3.4 DISCUSSION

We have demonstrated that clinical DCE MRI is feasible and applied several methodological refinements (multi-flip angle gradient echo T1 mapping with B_1 inhomogeneity correction, whole volume high temporal resolution DCE MRI acquired with successive expiratory breath holds and RDDR motion correction) to optimise the quality of DCE MRI data. We have then applied three different approaches to VIF delays using dual input single compartment pharmacokinetic modelling to determine hepatic perfusion parameters and the optimal modelling approach.

Our findings have supported some of the issues highlighted with preclinical DCE MRI. Absolute quantification using the dual input single compartment remains troublesome and prone to considerable overestimation. The magnitude of the overestimation was disappointing, but not necessarily unexpected. To assess this better, we have compared our perfusion parameters with published values for control cohorts in clinical and preclinical studies (table 6.6). Given that previously presented PCMRI data for the same cohort (section 5.5) demonstrated average PV perfusion of 56.65 ± 2.698 ml/min/100g, TLBF of 71.72 ± 3.318 ml/min/100g and HA fraction of $18.91 \pm 4.084\%$, the only published DCE MRI data that approaches these values is presented by Annet et al. [82] using dual input single compartment modelling and Koh et al. [151] using dual input dual compartment modelling. While a large number of studies have published DCE MRI TLBF in the region of 120-150 ml/min/100g [141, 144, 413, 414], notable outliers include Bultman et al. [147] (TLBF 213.20 ± 20 ml/min/100g) and Aronhime et al. [146] (TLBF 387.33 ± 290.43 ml/min/100g). Data from the latter, though similar on average to our own (method 3 TLBF 436.7 ± 55.55 ml/min/100g) demonstrated much greater variation. This may be secondary to intrinsic heterogeneity in the chronic hepatitis C cohort of patients studied by Aronhime et al. [146], but study-specific methodological issues would need to be considered.

Table 6.6: DCE MRI perfusion parameters compared with literature reported values for control cohorts

STUDY	SPECIES/COHORT	PV PERFUSION (ml/min/100g)	TLBF (ml/min/100g)	HA FRACTION (%)	MEAN TRANSIT TIME (seconds)	DISTRIBUTION VOLUME (%)
<i>Our study (n = 12)</i>						
METHOD 1 (<i>no delays</i>)	Human, healthy normal volunteers	469.3±73.51	489.7±72.85	7.377±2.340	18.62±2.666	71.24±4.328
METHOD 2 (<i>freely modelled delays</i>)		350.3±49.83	428.0±54.96	21.73±3.620	20.01±2.676	74.07±3.847
METHOD 3 (<i>pre-estimated delays with constrained free modelling</i>)		365.7±51.13	436.7±55.55	20.72±3.695	19.92±2.644	73.45±3.951
<i>Annet et al.[82] (n = 15)</i>	Humans, non-cirrhotic chronic liver disease	56.39±27.82	65.22±24.73	17.42±14.88	12.70±8.63	11.43±4.48
<i>Hagiwara et al.[141] (n = 10)</i>	Humans, non-fibrotic chronic liver disease	126.3±66.7	138.4±68.9	7.5±7.9	9.4±4.3	17.3±3.9
<i>Baxter et al.[413] (n = 35)</i>	Humans, non-cirrhotic, no liver disease	129.4±45.1	147.5±49.4	18.7±4.4	7.5±1.5	14.0±4.2
<i>Patel et al.[414] (n = 6)</i>	Humans, non-cirrhotic chronic liver disease	114.45±73.11	133.34±82.35	16.33±3.29	17.36±15.38	23.87±8.44
<i>Cao et al.[143] (n = 17)</i>	Humans, unresectable intrahepatic HCC	104.0±11.1	-	-	-	-
<i>Wang et al.[144] (n = 12)</i>	Humans, unresectable intrahepatic HCC	120.5±30.0	142.9±38.0	-	-	-
<i>Aronhime et al.[146] (n = 17)</i>	Humans, untreated chronic HCV	316.55±124.8	387.33±290.43	24.29±25.83	20.43±0.43	60.97±24.28
<i>Bultman et al.[147] (n = 12)</i>	Humans, healthy normal volunteers	-	213.20±20	14±8	12.3±0.9	30±4
<i>Koh et al.[151] (n = 3)*§</i>	Humans, liver metastases	23.6-39.3	53.2-66.1	45.9-56.1	-	-
<i>Materne et al.[140] (n = 9)</i>	Naïve rabbits	84±32	100±35	24±11	8.9±4.1	13.0±3.7
<i>Kim et al.[142] (n = 12)</i>	Naïve wistar rats	1021.62†	1362.16†	25	3.7	63
<i>Leporq et al. [415] (n = 5)</i>	Naïve pigs	101.3±26.1	135.4±34.2	25.9±8.2	5.2±1.4	-
<i>Hartono et al.[149] (n = 5)*</i>	Naïve C57BL/6 mice	-	496.2±83.63	-	-	-

*(Data from dual input dual compartment modelling);

§(data given for whole liver perfusion, upper and lower range values quoted given small sample size);

†(Unpublished values. These were calculated from published values of DV, MTT and portal fraction).

Faced with the magnitude of the overestimation, all protocols were scrutinised for any errors in data collection, post-processing and quantification. All calculations were checked and compared with published methods. Data was also reviewed at each step of the quantification process. T1 measurement could represent a potential source of error, hence absolute measurements and reproducibility of baseline AIF, PVIF and hepatic parenchymal T1 were reviewed.

Table 6.7: Summary of T1 measurement statistics and literature comparison

	MEASURED COHORT T1 (milliseconds)	LITERATURE DERIVED AVERAGED T1* (milliseconds)
AIF	1490±211.2	1645±106
PVIF	1205±200.0	1584±5 [§]
Hepatic Parenchyma	583.8±26.94 [†]	822.3±85

*(based on data from [328, 416-419])

[§](based on bovine venous blood at 3.0T [418])

[†](one-sample t-test against literature derived average value $p < 0.05$)

Table 6.8: Summary of T1 measurement reproducibility

	ARTERIAL INPUT FUNCTION	PV INPUT FUNCTION	HEPATIC PARENCHYMA
Mean difference	-241.6±320.3	-193.5±263.4	-14.97±13.83
Coefficient of Reproducibility	1775	1460	81.32
Correlation (r)	-0.2410	0.2193	0.9113*

*(Pearson's correlation coefficient $p < 0.05$)

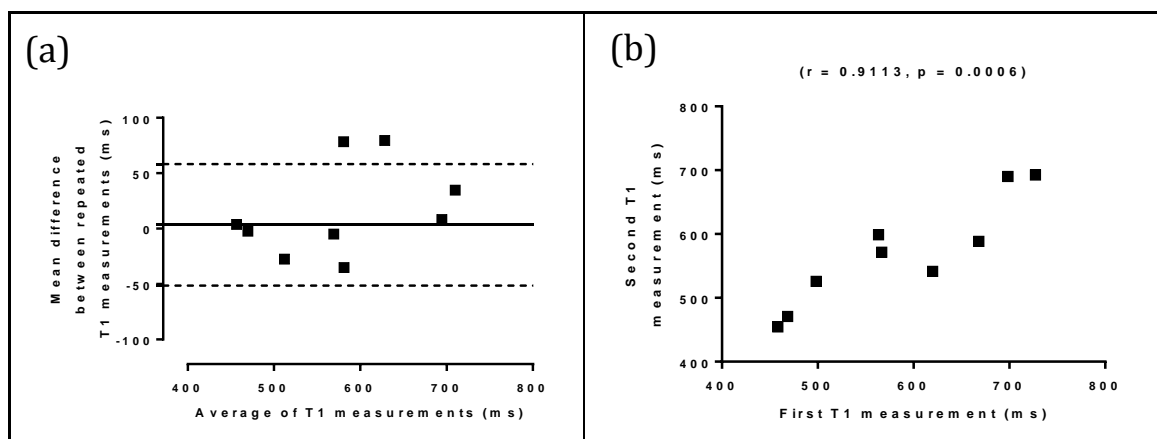


Figure 6.19: Analysis of agreement of repeated hepatic parenchymal T1 measurements

Bland-Altman (a) and regression analysis of (b) repeated hepatic parenchymal T1 measurements in normal volunteers after a seven day interval

Published literature was searched for data on blood and liver T1 measurements at 3.0T. All data was derived from in vivo human samples [328, 416, 417, 419], with the exception of one study which was based on bovine arterial and venous blood [418]. Our data demonstrated a tendency to underestimate baseline blood and parenchymal hepatic T1 (table 6.7), although one-sample t-tests only demonstrated significant differences between

measured and literature derived average hepatic parenchymal T1. Reproducibility of arterial and PV blood T1 was poor, with large differences demonstrated between subsequent measurements (though none of these were statistically significant on paired t-tests), and coefficients of reproducibility exceeding 1000 ms for both measurements. Correlation between repeated blood T1 measurements was also poor (table 6.8). Conversely, hepatic parenchymal T1 was measured much more reproducibly, with a small mean difference, and impressive coefficient of reproducibility of 81.32 ms. Significant correlations were detected between repeat measurements ($r = 0.9113$, $p = 0.0006$) (figure 6.19b).

As demonstrated by previous data in (section 3.3), and discussed briefly at the start of this chapter (section 6.3.1.2), gradient echo multi-flip angle measurements can have a tendency to underestimate T1. In this study we addressed issues with B_1 field inhomogeneities using B_1 mapping. The reproducibility of hepatic parenchymal measurements is however encouraging. The poor reproducibility and wide range of arterial and venous T1 is not necessarily surprising. Many authors of liver DCE MRI studies fail to provide an accurate description of the method of T1 quantification at publication (often just stating that this was undertaken) or then choosing to assume a fixed blood T1 across a DCE MRI study without sampling this individually for each subject [146]. We would argue that any assumptions in relation to T1 are perilous, and while some may result in more stable DCE MRI quantification, can also undermine the physiological value of the overall results.

Baseline T1 measurement is an essential step in the quantification of DCE MRI perfusion parameters. The method for T1 measurement used in this study was developed based on formal validation work with phantoms, empirical comparison with alternative T1 measurement strategies and repeatability studies undertaken independently by other researchers on our team [420]. Though formal simulations to evaluate the effect of changes in VIF or parenchymal T1 on dual input single compartment quantification were not undertaken as part of this study (nor are they available in the literature), these are likely to have a significant effect on final quantification and may represent a potential source of the discrepancy between our data and published values [311].

Throughout the quantification process, there are several independent parameters which can arbitrarily have a significant impact on the size of both VIF and parenchymal CA concentration enhancement curves. The generation of CA concentration data is reliant on $R1$, a measure of relaxivity of the CA at 3.0T at 37°C, assumed in this study to be 3.5 L/mmol s⁻¹ [411]. Published $R1$ values can however vary [421, 422], and the use of

different relaxivities for the same contrast agent, by authors of different studies will affect enhancement curves and subsequent DCE MRI quantification.

The incorporation of plasma haematocrit into the derivation of VIF curves but also small vessel haematocrit into the quantification of parenchymal perfusion is described in the original DCE MRI paper by Materne et al. [140], but seldom mentioned consistently in published DCE MRI studies. In this study, both VIF curves and final parenchymal perfusion measurements were corrected using an assumed plasma haematocrit of 0.45 (an approach taken by most authors), but also assuming a small vessel haematocrit of 0.25 as stipulated by Materne et al. [140]. Some studies mention the incorporation of plasma haematocrit into the generation of VIFs, but there is no mention of the incorporation of small vessel haematocrit into any published methods other than the original Materne et al. paper [140]. Interestingly, some published DCE MRI studies, make no mention of incorporation of haematocrit at any stage of quantification. Incorporation of plasma and small vessel haematocrit will have significant effects on the scaling of VIF curves and final absolute quantification, and may represent another potential source of discrepancy between our data and published values. There may also be merit in applying a population-derived AIF to determine if this was an important source of variation [423].

In this study, we have also chosen to sample AIFs using ROIs placed directly over the left ventricle, which differs from published DCE MRI studies where typically aortic ROIs were used. We would argue that left ventricular ROIs should theoretically generate identical AIFs to those seen in the aorta and be less prone to inflow effects, by the very nature of the motion of flow within the ventricle itself. Early experience demonstrated a tendency for aortic ROIs to be noisier, more prone to artefact and of smaller size than their ventricular counterparts and on this basis, we adopted this approach into our protocols. It is also worth noting that large anatomical coverage (60 slices) may have implications for SNR, thereby potentially adding to noise within both VIFs and parenchymal enhancement curves.

In summary, hepatic DCE MRI quantification is a complex multi-step process, with many methodological details that can vary from author to author and have significant effects on quantification. This is reflected in the heterogeneity of previously published DCE MRI perfusion parameters. Given the overestimation of DCE MRI perfusion parameters from our data, we have reviewed several aspects of our methods and offered potential explanations for the divergence between our values and published data. We have not conducted formal simulations to evaluate the exact impact of changing these parameters on quantification, but this would be an important focus of future work.

Although problems with absolute quantification could be driven by factors in the data acquisition process, we have demonstrated that post-processing pharmacokinetic modelling can have a substantial effect on absolute and more importantly relative quantification (i.e. HA fraction). We would argue that the latter is more important, especially as we have previously demonstrated that PCMRI can be used to successfully estimate absolute perfusion.

The use of zero VIF delays (Method 1), was both non-physiological but also prone to underestimation of HA fraction (figure 6.9, table 6.2). Although reproducibility of Method 1 HA fraction appears superior to methods 2 and 3, it is worth noting that HA perfusion was restricted in all dual input single compartment modelling to be greater than 1 ml/min/100g, to prevent errors arising should ' k_{1a} ' be best fitted as zero. This resulted in clustering of HA perfusion (and therefore HA fraction) around small values, failure to demonstrate a Gaussian distribution in HA fraction data, and a potentially spurious suggestion of a smaller coefficient of reproducibility than demonstrated by other methods.

Free modelling of VIF delays (Method 2) commonly resulted in non-physiological data (figure 6.8c). The residual sum of squares can often be minimised by shifting the AIF to arrive after the PVIF or indeed the parenchymal enhancement curve. More worryingly, this was not necessarily associated with non-physiological estimates of perfusion parameters (e.g. HA fraction greater than 50% or DV over 100%). Interestingly, although the mean difference between repeated Method 2 AIF delays was larger than with Method 3 (3.473 ± 1.682 vs 1.126 ± 2.119 seconds), the coefficient of reproducibility was smaller (9.888 vs 12.47 seconds) and a significant positive correlation was demonstrated between repeated Method 2 AIF delays ($r = 0.6954$; $p = 0.0375$). The propensity for small PVIF delays resulted in a non-normal distribution of these parameters, with a significant difference between repeated measurements using Method 2. Interestingly no instances were observed where the residual sum of squares was minimised by shifting the PVIF to arrive after the parenchymal enhancement curve.

Pre-estimation of VIF delays with constrained free modelling (Method 3) provided a viable method for estimation of physiological delays. Method 3 demonstrated smaller coefficients of reproducibility than methods 1 and 2 for all parameters except HA fraction, MTT and AIF delays. Given that Method 1 was non-physiological, Method 3 still demonstrated a smaller HA fraction coefficient of reproducibility than Method 2, and was the only method to deliver a positive correlation between repeated HA fraction measurements ($r = 0.6043$; $p = 0.0848$), albeit only approaching significance. Comparison with PCMRI estimated HA fraction (table 6.3) demonstrated smaller a coefficient of

reproducibility (35.49 vs 45.13%) and a marginally better correlation ($r = 0.6043$, $p = 0.0848$ vs $r = 0.5491$, $p = 0.0802$), but slightly larger mean difference (-9.260 ± 6.036 vs 8.643 ± 6.943) between repeated Method 3 HA fraction measurements.

It is also surprising that given that no non-physiological PVIF delays were identified using Method 2, that repeated PVIF delays using Method 3 demonstrated smaller mean differences (median -0.5583 vs -0.8774 seconds), coefficients of reproducibility (3.853 vs 4.270 seconds) and positive but non-significant correlations ($r = 0.5703$ vs $r = 0.02656$) compared with Method 2.

Even when disregarding absolute perfusion parameters, the coefficients of reproducibility for all three DCE MRI methods are still alarmingly large. A coefficient of reproducibility of 35.49% (Method 3) for an average HA fraction of $24.58 \pm 6.336\%$ is concerning. Other perfusion parameters including MTT and DV also demonstrated large and poor coefficients of reproducibility regardless of the modelling method.

Validation of DCE MRI measurements was also disappointing. We previously invasively validated preclinical PCMRI and demonstrated consistency of clinical caval subtraction PCMRI measurements using alternative independent PCMRI measurements. These clinical PCMRI measurements were subsequently used to validate DCE MRI PV perfusion, TLBF and HA fraction measurements. The gross overestimation of DCE MRI perfusion parameters complicated Bland-Altman plot analysis (figures 6.16 and 6.17) and underscored the value of DCE MRI in measurements of relative (HA fraction) rather than absolute perfusion. Importantly, although Method 2 demonstrated a smaller average difference to paired PCMRI HA fraction measurements (-1.223 vs $-1.815 \pm 5.598\%$) and coefficient of variation (76.34 vs 81.72%), both methods yielded no significant differences between DCE MRI HA fraction and PCMRI estimated HA fraction (unlike Method 1). Crucially, the coefficient of variation for both Methods 2 and 3 was also still less than that observed with PCMRI estimated HA fraction (98.97%).

Both MTT and DV represent interesting physiological parameters but present a significant challenge both to pharmacokinetic modelling and validation. Our data highlighted poor reproducibility for both of these parameters and challenges in deriving physiologically valid data (i.e. DV values over 100% or unusually large MTT values). Validation of DV could for example be undertaken using histopathological quantification, but this would not be without controversy, if not unfeasible in normal volunteers.

An important criticism is the lack of data demonstrating the ability of DCE MRI to detect an expected alteration in hepatic perfusion parameters in response to a controlled

insult (as demonstrated by post-prandial stress studies with clinical PCMRI in section 5.5). Repeated CA dosing in a short time frame would be difficult to justify ethically in a cohort of healthy volunteers and was therefore not undertaken.

Finally, we have demonstrated that small changes in VIF delays can have a significant impact on absolute and relative hepatic perfusion quantification. Both Methods 2 and 3 are however restricted by the temporal resolution so that VIFs can only be shifted by units determined by the temporal resolution (i.e. 3.35 seconds). For pre-estimation with constrained free modelling, this restricts the VIF shift to within ± 3.35 seconds of the time point nearest to the pre-estimated VIF CA bolus arrival time. While a window of 6.7 seconds might be acceptable, because the VIF delay can only adopt one of three delays in this range, errors in CA bolus arrival time are inevitably introduced. These could then precipitate further errors in estimated hepatic perfusion parameters.

In summary our data is the first demonstration of pre-estimation of VIF delays with constrained free modelling (Method 3) and its superiority over alternative approaches to VIF delays in clinical dual input single compartment modelling, specifically the assumption of zero (Method 1) or free modelling (Method 2) of VIF delays. All methods demonstrate poor reproducibility, but Method 3 remains the most physiologically valid and reproducible approach, with reproducibility of relative perfusion superior to that of PCMRI estimated HA fraction. We have demonstrated the tendency of DCE MRI to overestimate absolute perfusion parameters and shown that HA fraction is a meaningful DCE MRI perfusion parameter, with a smaller coefficient of variation than PCMRI estimated HA fraction using Methods 2 and 3. Taking into account the validation data, we would still argue that Method 3 is superior to Method 2 because of improved physiological validity.

6.3.5 CONCLUSION

We have demonstrated that our clinical DCE MRI protocols are feasible and compared the reproducibility and PCMRI validation of dual input single compartment modelling with different approaches to VIF delays. Our data supports the use of pre-estimation with constrained free modelling of VIF delays as the most physiological and reproducible method for incorporating VIF CA bolus arrival delays into dual input single compartment modelling. We have also shown greater value of DCE MRI with dual input single compartment modelling in relative but not absolute quantification of hepatic perfusion parameters.

6.4 ALTERNATIVE APPROACHES TO DCE MODELLING

6.4.1 BACKGROUND

Previous preclinical work (section 3.5) has highlighted differences in hepatic perfusion parameters when using alternative modelling/quantification methods. Given that absolute perfusion was so poor with dual input single compartment modelling, this issue could be addressed with alternative approaches.

6.4.1.1 Dual input dual compartment modelling

Dual input dual compartment modelling was undertaken in the same way as described previously (section 3.5.1.2). Briefly, the dual input single compartment model can be expressed using the following system of equations:

$$v_1 \frac{d}{dt} C_{L1}(t) = F\rho(C_{in}(t) - C_{L1}(t)) - PS\rho(C_{L1}(t) - C_{L2}(t)) \quad (\text{Equation 6.6})$$

$$v_2 \frac{d}{dt} C_{L2}(t) = PS\rho(C_{L1}(t) - C_{L2}(t)) \quad (\text{Equation 6.7})$$

$$C_{in}(t) = \alpha C_a(t) + (1 - \alpha)C_p(t) \quad (\text{Equation 6.8})$$

$$C_L(t) = FC_{in}(t) \otimes [Ae^{s_1 t} + (1 - A)e^{s_2 t}] \quad (\text{Equation 6.9})$$

where,

v_1	Fractional vascular volume (%)
v_2	Fractional interstitial volume (%)
$C_{L1}(t)$	CA concentration in the vascular compartment (mmol/L)
$C_{L2}(t)$	CA concentration in the interstitial compartment (mmol/L)
$C_{in}(t)$	CA input function (mmol/L) – this term is represented by equation 6.8
F	Total blood inflow/tissue perfusion (ml/min/100g)
ρ	Tissue density (assumed to be 1 g/ml)[149]
PS	Permeability surface-area product (measure of endothelial permeability; ml/min/100g)
$C_a(t)$	Arterial input function
$C_p(t)$	PV input function
α	HA fraction

and s_1 and s_2 are solutions for s in the following quadratic equation:

$$s^2 + \left(\frac{PS\rho}{v_1} + \frac{PS\rho}{v_2} + \frac{F\rho}{v_1} \right) s + \left(\frac{PS\rho F\rho}{v_2 v_1} \right) = 0 \quad (\text{Equation 6.10})$$

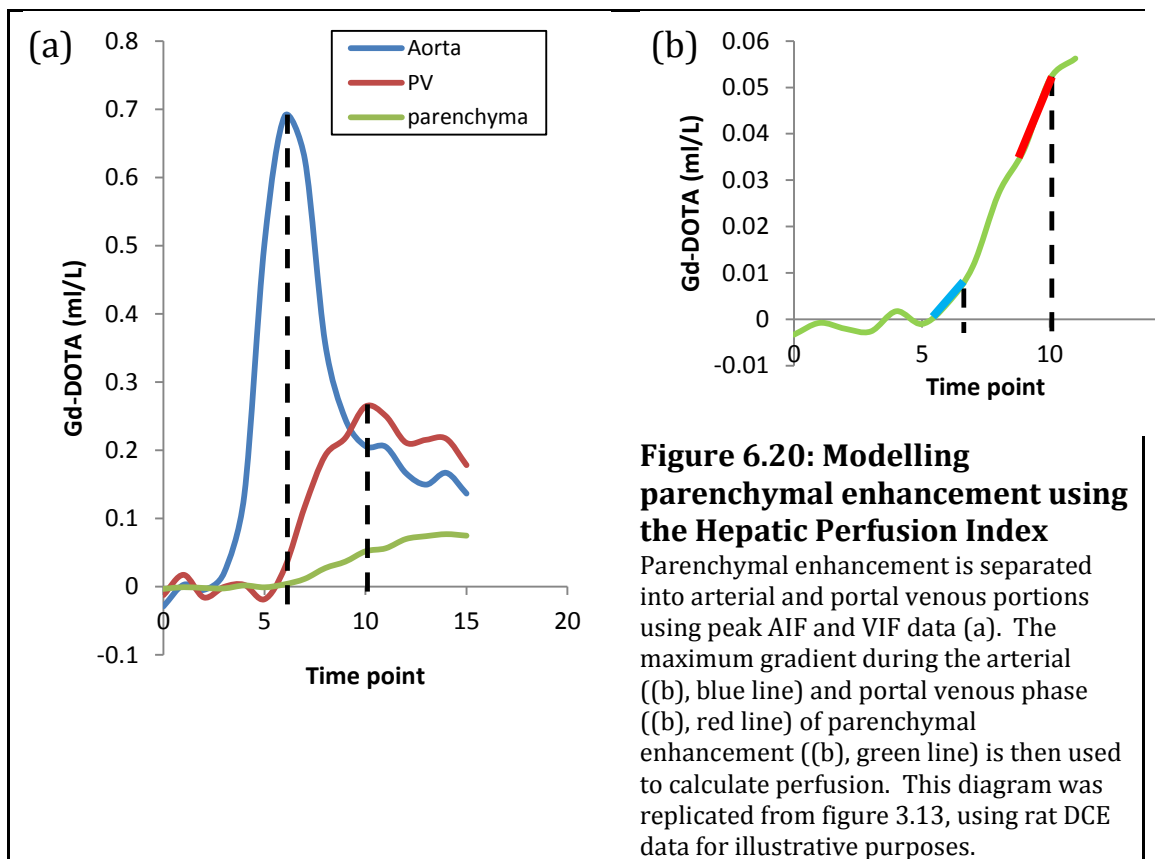
and:

$$A = \frac{\left(s_1 + \frac{PS\rho}{v_1} + \frac{PS\rho}{v_2}\right)}{s_1 - s_2} \quad (\text{Equation 6.11})$$

TLBF (F), HA fraction (α) derived directly from the model enabled the calculation of PV perfusion. Other parameters such as fractional vascular volume (v_1), fractional interstitial volume (v_2) and permeability surface-area product (PS) were also recorded.

6.4.1.2 Hepatic perfusion index modelling

Much simpler than its dual input single and dual compartment counterparts, the hepatic perfusion index was calculated as previously using slope-based methods [107]. Briefly, the parenchymal enhancement curve ($C_L(t)$) can be separated into predominantly arterial ($C_{La}(t)$) and portal venous ($C_{Lp}(t)$) portions using the timings for the peak aortic and portal venous enhancement curves respectively (figure 6.20a).



The peak gradient during the arterial ($\Delta C_{La}(t)'$) and portal venous phase ($\Delta C_{Lp}(t)'$) is then used to estimate perfusion using the maximum AIF CA concentration ($C_a(t)'$)[138, 139]:

$$F_{\text{Arterial perfusion}}(\text{ml/s/g}) = \frac{\Delta C_{La}(t)'}{C_a(t)'}$$

and:

$$F_{\text{PV perfusion}}(\text{ml/s/g}) = \frac{\Delta C_{Lp}(t)'}{C_a(t)'} \quad (\text{Equations 6.12 and 6.13})$$

Data for PV perfusion, TLBF and HA fraction was recorded for comparison with other quantification methods.

In this section we consider DCE MRI quantification using the dual input dual compartment model and the hepatic perfusion index method alongside the dual input single compartment modelling methods developed in section 6.3. We compare each quantification method using (i) seven day reproducibility and (ii) validation of tissue perfusion estimates with volume normalised PCMRI flow measurements.

6.4.2 METHODS

6.4.2.1 Subjects and preparation

As described in section 6.3.2.1.

6.4.2.2 Clinical DCE MRI

As described in section 6.3.2.2.

6.4.2.3 Post-processing

As described in section 6.3.2. Data for AIF, PVIF and parenchymal ROI CA concentration was then modelled using (i) the dual input single compartment model, (ii) the dual input dual compartment model and (iii) the hepatic perfusion index method as described in section 6.4.1.2. Based on section 6.3, pre-estimation of delays with constrained free modelling of VIF delays was used for dual input single and dual compartment methods.

6.4.2.4 Reproducibility studies

As described in section 6.3.2.5.

6.4.2.5 Validation studies

As described in section 6.3.2.6.

6.4.2.6 Statistical analysis

Kolmogorov-Smirnov tests were used to confirm normality of variable distributions. Repeated measures one-way analysis of variance (ANOVA) with corrections for non-sphericity were used to compare perfusion parameters from each of the quantification

methods. Post-hoc Tukey's test was then applied where significant differences were identified. Where variables were found not to be normally distributed, the Kruskal-Wallis test was used followed by post-hoc Dunn's test where significant differences were identified. Reproducibility and validation studies were assessed using paired t-tests/Wilcoxon matched pairs signed rank tests, Bland-Altman analysis of agreement with calculation of the coefficient of repeatability and assessment of correlation between repeated/validated measurements using Pearson's or Spearman's correlation coefficient for parametric/non-parametric data as appropriate. The threshold of statistical significance was defined to be $p < 0.05$.

6.4.3 RESULTS

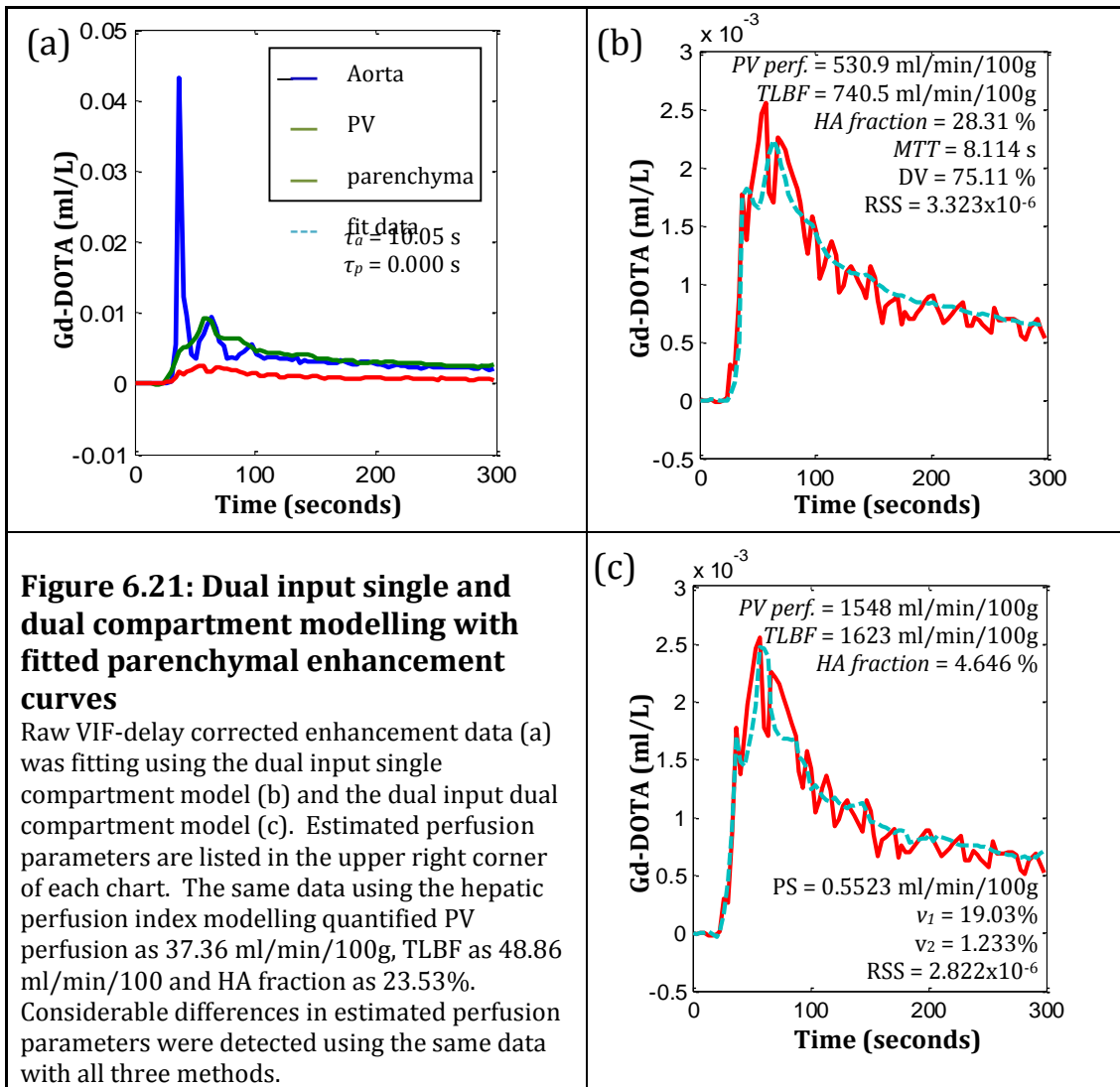
6.4.3.1 Cohort features

Data was collected in twelve normal volunteers. Male subjects ($n = 6$) had a mean age of 26.7 ± 1.55 years and female subjects ($n = 6$) had a mean age of 30.2 ± 2.37 years. Seven day reproducibility data was available for nine subjects ($n = 4$ male, $n = 5$ female).

6.4.3.2 Alternative quantification methods

A sample data set was used to demonstrate the parenchymal enhancement curves obtained with corresponding curve fits in figure 6.21, using dual input single and dual compartment modelling methods. Alternative quantification methods resulted in profound differences in estimated perfusion parameters, as shown by the data overlaying the charts on the right (figure 6.21). Hepatic perfusion index data for the same data set is given in the legend.

Data for each of the perfusion parameters is plotted for each method in figure 6.22 and tabulated in table 6.9. TLBF, HA fraction and residual sum of squares demonstrated non-normal distributions and therefore underwent non-parametric statistical testing. Significant differences were demonstrated between the three quantification methods for PV perfusion ($F(1.553,31.05) = 190.9$; $p < 0.0001$), TLBF ($H = 54.02$; $p < 0.0001$) and HA fraction ($H = 33.52$; $p < 0.0001$). Post-hoc tests demonstrated significant differences between all three quantification methods for all three common parameters, except HA fraction where no significant difference was identified between dual input single compartment and hepatic perfusion index modelling. The residual sum of squares was also significantly smaller with single compartment modelling ($3.831 \times 10^{-7} \pm 5.079 \times 10^{-8}$ vs $3.621 \times 10^{-6} \pm 8.162 \times 10^{-7}$; median difference 1.508×10^{-6} ; $p < 0.0001$).



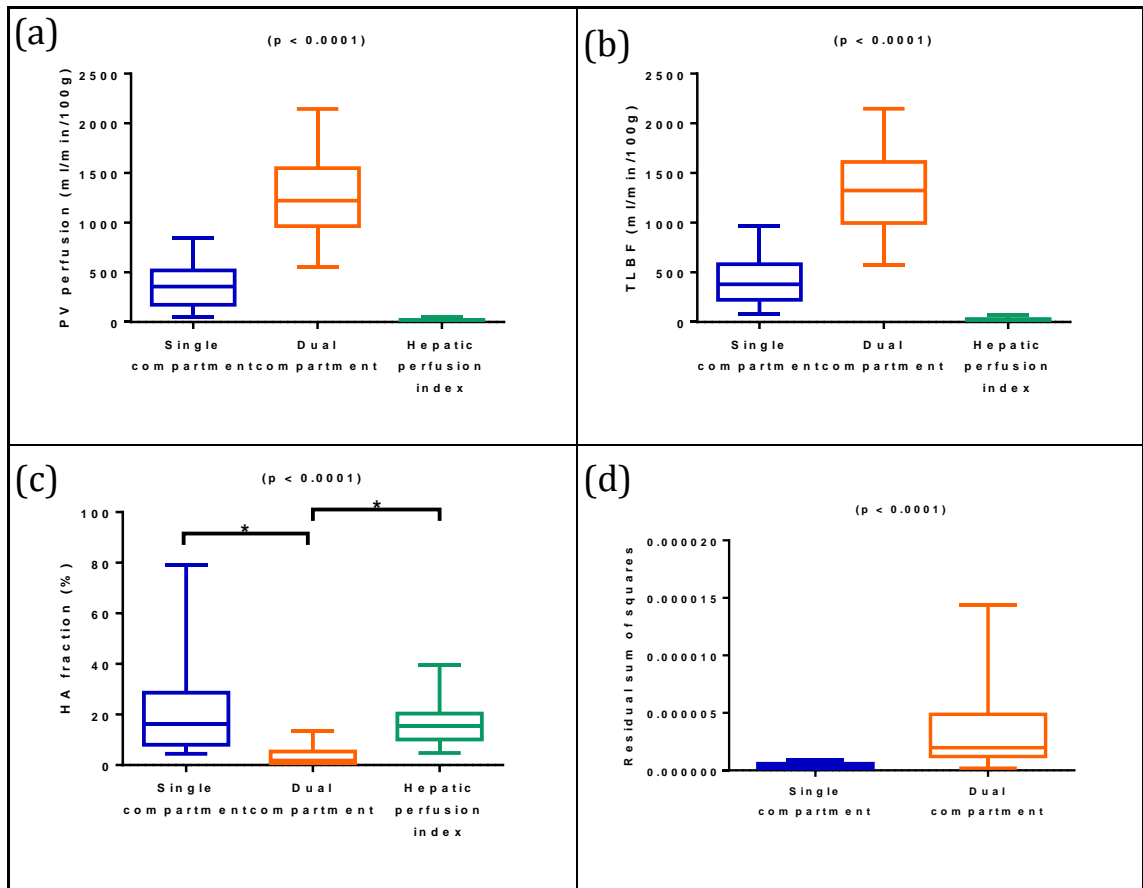


Figure 6.22: Perfusion parameters estimated using each of the modelling methods

p-values are quoted for one-way ANOVA/Kruskal-Wallis tests and paired t-tests/Wilcoxon matched-pairs signed rank tests where appropriate. Significant differences were demonstrated on post-hoc testing between all paired comparisons for PV perfusion and TLBF and ‘*’ comparisons for HA fraction. As the hepatic perfusion index method does not involve data-fitting, residual sum of squares is only compared between the compartment methods (d).

Table 6.9: Perfusion parameters estimated using each of the modelling methods

	DUAL INPUT SINGLE COMPARTMENT	DUAL INPUT DUAL COMPARTMENT	HEPATIC PERFUSION INDEX
PV perfusion (ml/min/100g) *	365.7±51.13 ^{‡§}	1285±82.88 ^{†§}	17.09±2.647 ^{†‡}
TLBF (ml/min/100g)*	436.7±55.55 [‡]	1329±85.62 ^{†§}	21.47±3.620 [‡]
HA fraction (%)*	20.72±3.695 ^{‡§}	3.375±0.7837 ^{†§}	16.90±1.899 ^{†‡}
Mean Transit Time (seconds)	19.92±2.644	-	-
Distribution Volume (%)	73.45±3.951	-	-
Vascular volume (%)	-	13.41±1.014	-
Interstitial volume (%)	-	15.01±2.556	-
Permeability surface area (ml/min/100g)	-	1.399±0.2290	-
Residuals ² *	3.831x10 ⁻⁷ ±5.079x10 ⁻⁸	3.621x10 ⁻⁶ ±8.162x10 ⁻⁷ *	-

(*one-way ANOVA/Kruskal-Wallis/paired t-test p<0.05;

[†]post-hoc Tukey/Dunn’s test comparison with single compartment modelling p<0.05;

[‡]post-hoc Tukey/Dunn’s test comparison with dual compartment modelling p < 0.05;

[§]post-hoc Tukey/Dunn’s test comparison with hepatic perfusion index modelling p < 0.05)

6.4.3.3 Reproducibility

Reproducibility was assessed using the same protocol with the same scanner in the same subjects exactly seven days after the initial study. Repeat measurements were obtained in normal volunteers ($n = 9$). All reproducibility analysis data are summarised and presented alongside seven day PCMRI reproducibility for comparison in table 6.10. No significant differences were demonstrated between repeated PV perfusion measurements using either of the three quantification methods (figure 6.23, table 6.10). The smallest mean difference was demonstrated using the hepatic perfusion index (-8.187 ± 6.052 ml/min/100g; $p = 0.2131$). This method also demonstrated the smallest coefficient of reproducibility (35.583 ml/min/100g). No correlations were identified between repeated measurements using any of the methods.

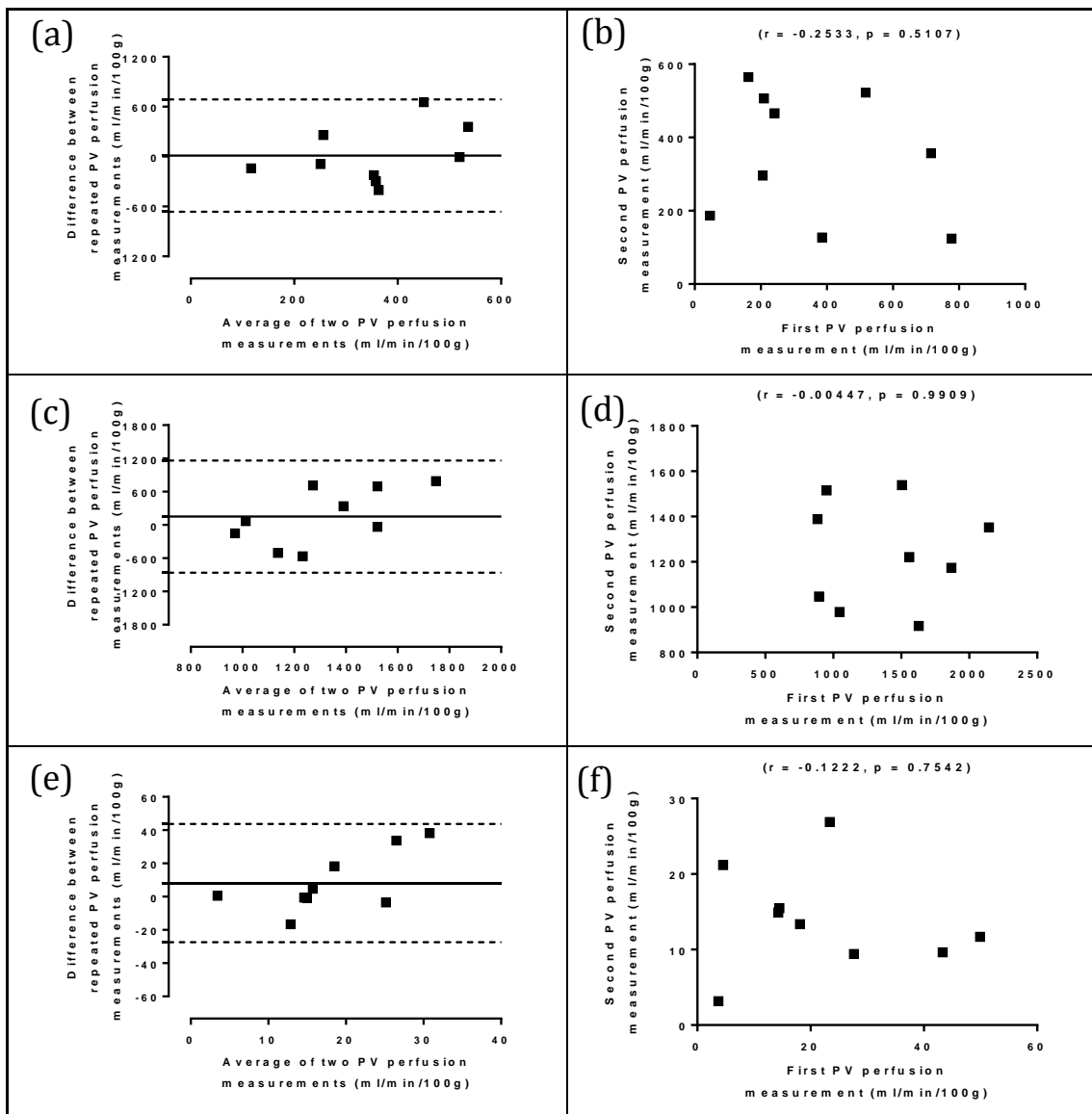


Figure 6.23: Analysis of agreement of repeated PV perfusion measurements using alternative quantification methods

Bland-Altman and regression analysis of (a, b) dual input single compartment modelling, (c, d) dual input dual compartment modelling, (e, f) hepatic perfusion index modelling.

No significant differences were demonstrated between repeated TLBF measurements using either of the three quantification methods (figure 6.24, table 6.10). The smallest mean difference was demonstrated using the hepatic perfusion index (-12.31 ± 8.110 ml/min/100g; $p = 0.1674$). This method also demonstrated the smallest coefficient of reproducibility (47.69 ml/min/100g). No correlations were identified between repeated measurements using any of the methods.

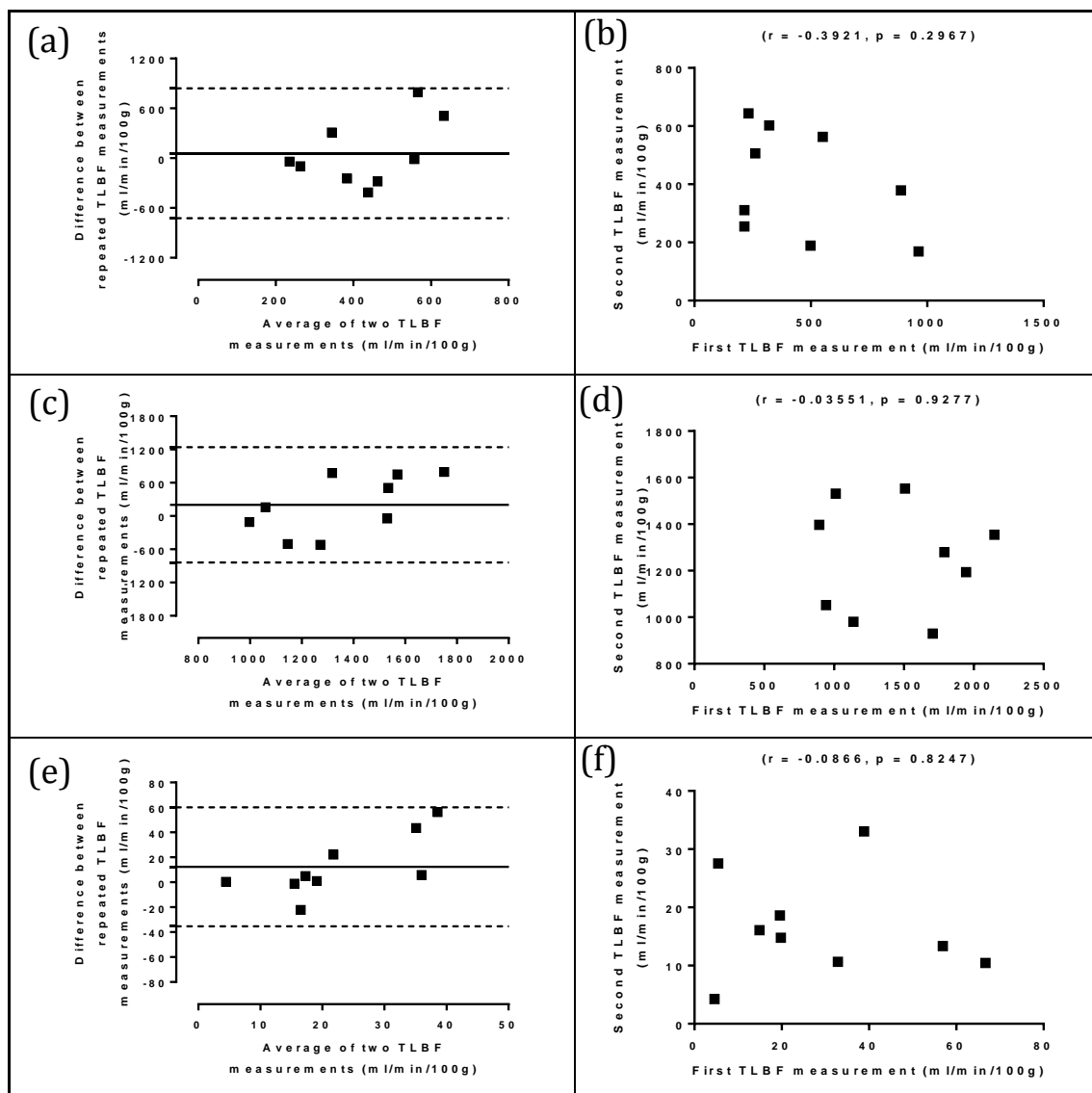


Figure 6.24: Analysis of agreement of repeated TLBF measurements using alternative quantification methods

Bland-Altman and regression analysis of (a, b) dual input single compartment modelling, (c, d) dual input dual compartment modelling, (e, f) hepatic perfusion index modelling.

No significant differences were demonstrated between repeated HA fraction measurements using dual input single compartment and hepatic perfusion index modelling (figure 6.25, table 6.10). The smallest mean difference was demonstrated using dual input dual compartment modelling ($-3.643 \pm 1.128\%$; $p = 0.0121$), but this difference was statistically significant. Dual input dual compartment modelling also demonstrated the smallest coefficient of reproducibility (6.637%) and a significant positive correlation between repeated measurements ($r = 0.7537$; $p = 0.0190$). As demonstrated previously, a positive correlation between repeat HA fraction measurements was also seen with dual input single compartment modelling ($r = 0.6043$; $p = 0.0848$), but this correlation was just non-significant.

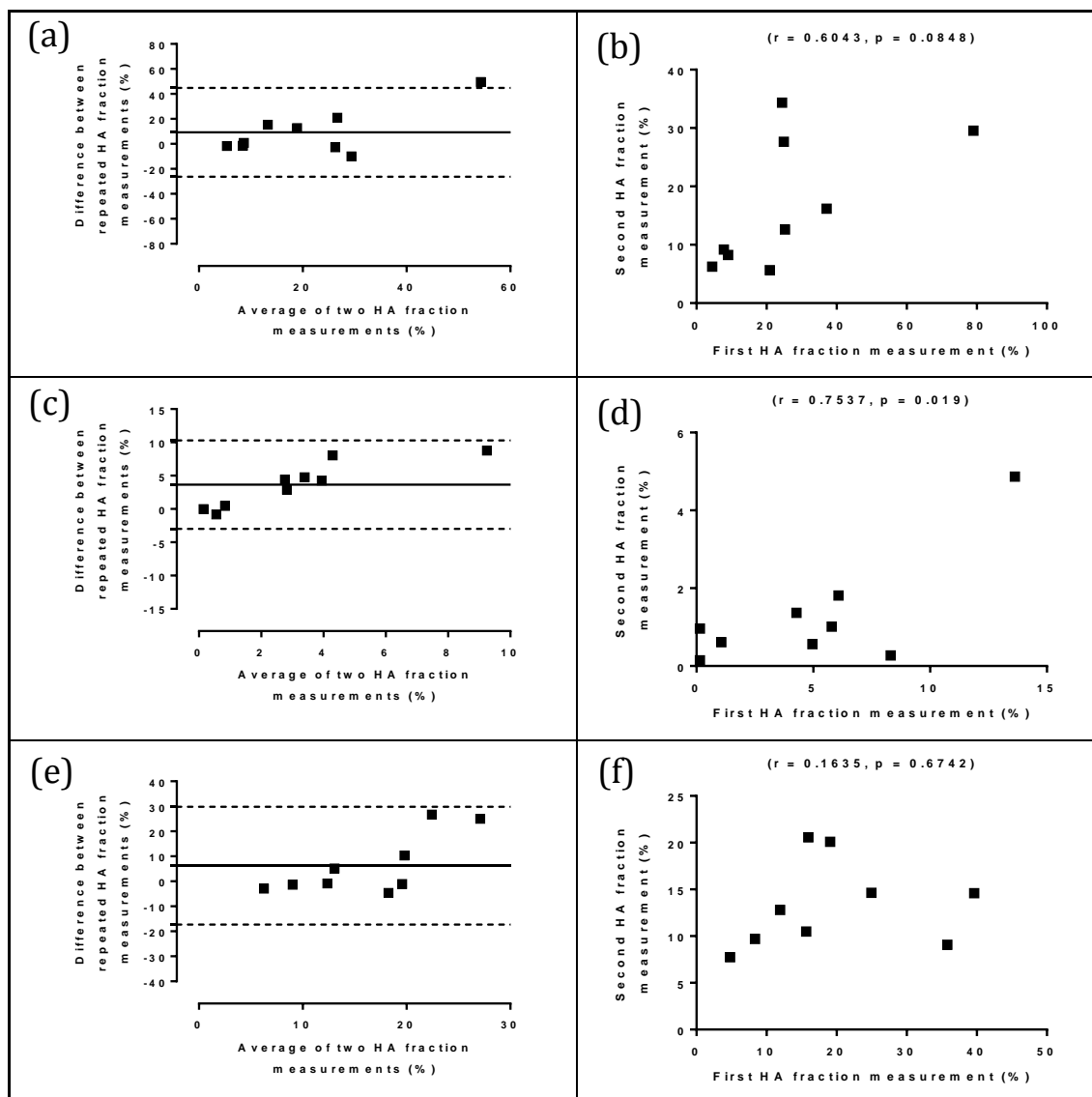


Figure 6.25: Analysis of agreement of repeated HA fraction measurements using alternative quantification methods

Bland-Altman and regression analysis of (a, b) dual input single compartment modelling, (c, d) dual input dual compartment modelling, (e, f) hepatic perfusion index modelling.

Data for reproducibility of MTT and DV using dual input single compartment modelling with pre-estimation of VIF delays and constrained free modelling was presented in section 6.3 (figures 6.13, 6.14 and table 6.3).

No significant differences were demonstrated between repeated vascular volume ($-0.5916 \pm 2.114\%$; $p = 0.7867$), interstitial volume ($1.385 \pm 6.553\%$; $p = 0.8379$) and permeability surface area (median 0.04400 ml/min/100g; $p = 0.8203$) (figure 6.26, table 6.10). No correlations were demonstrated between repeated measurements for any of these parameters.

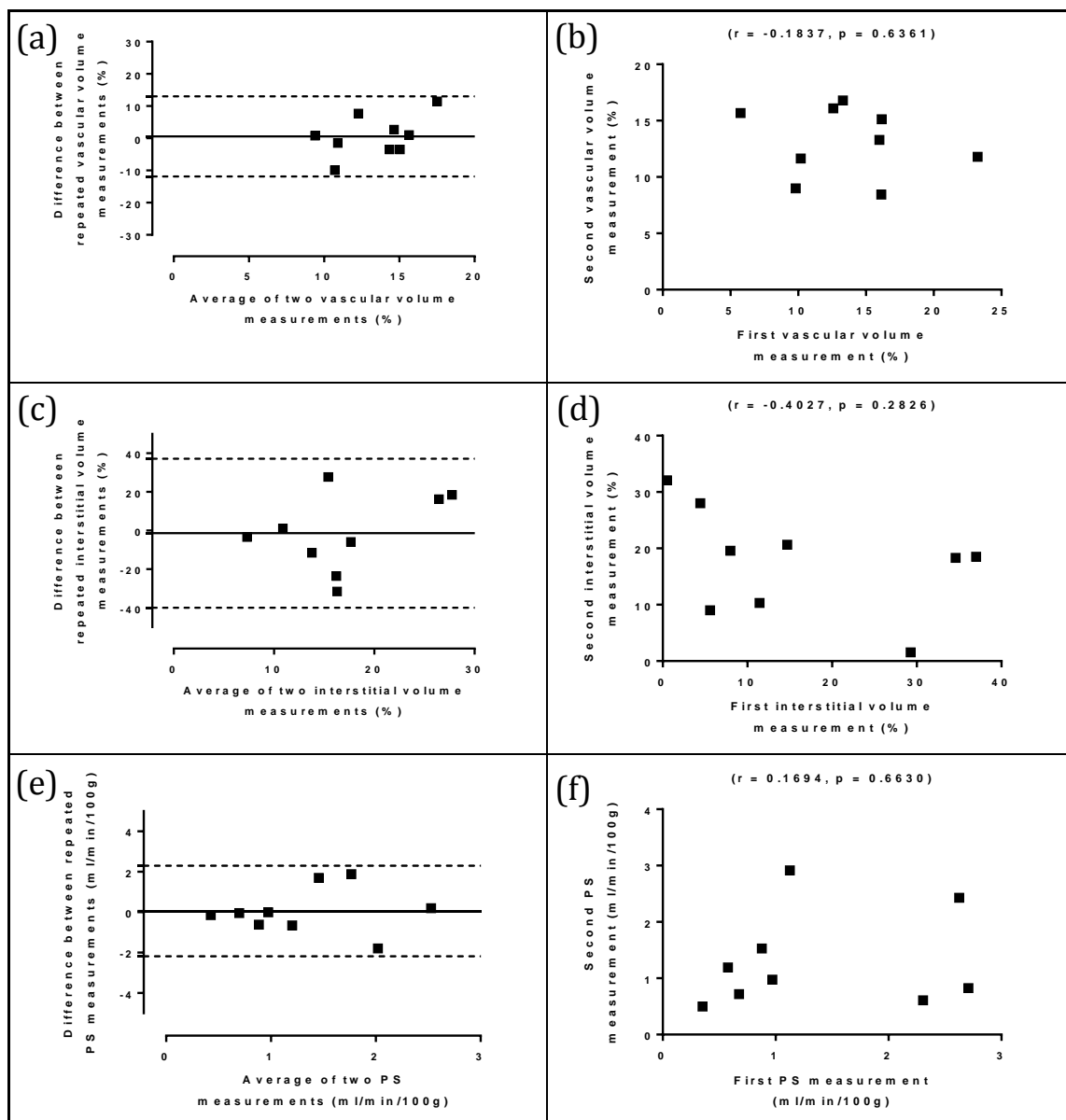


Figure 6.26: Analysis of agreement of repeated dual input dual compartment additional perfusion parameter measurements

Bland-Altman and regression analysis of (a, b) fractional vascular volume, (c, d) fractional interstitial volume, (e, f) permeability surface area.

Table 6.10: Summary of reproducibility of perfusion parameters estimated using alternative DCE MRI quantification methods alongside PCMRI reproducibility[§]

	DUAL INPUT SINGLE COMPARTMENT	DUAL INPUT DUAL COMPARTMENT	HEPATIC PERFUSION INDEX	PCMRI
PV perfusion (ml/min/100g)				
Mean difference	-12.4±114.8	-150.2±172.0	-8.187±6.052	-1.234±2.924
Coefficient of Reproducibility	674.9	1011.8	35.583	19.01
Correlation (r)	-0.2533	-0.00447	-0.1222	0.7152
TLBF (ml/min/100g)				
Mean difference	-58.33±133.0	-201.0±177.0	-12.31±8.110	-8.460±4.860
Coefficient of Reproducibility	782.3	1041	47.69	31.60
Correlation (r)	-0.3921	-0.03551	-0.08660	0.4858
HA fraction (%)				
Mean difference	-9.26±6.036	-3.643±1.128*	-6.269±4.005	8.643±6.943
Coefficient of Reproducibility	35.49	6.637	23.551	45.13
Correlation (r)	0.6043 [†]	0.7537**	0.1635	0.5491
Mean Transit Time (seconds)				
Mean difference	-2.374±4.573	-	-	-
Coefficient of Reproducibility	26.89	-	-	-
Correlation (r)	-0.08422	-	-	-
Distribution Volume (%)				
Mean difference	-16.98	-	-	-
Coefficient of Reproducibility	48.24	-	-	-
Correlation (r)	-0.06667	-	-	-
Vascular volume (%)				
Mean difference	-	-0.5916±2.114	-	-
Coefficient of Reproducibility	-	12.43	-	-
Correlation (r)	-	-0.1837	-	-
Interstitial volume (%)				
Mean difference	-	1.385±6.553	-	-
Coefficient of Reproducibility	-	38.54	-	-
Correlation (r)	-	-0.4027	-	-
Permeability surface area (ml/min/100g)				
Mean difference	-	0.04400	-	-
Coefficient of Reproducibility	-	2.241	-	-
Correlation (r)	-	0.1694	-	-

(§Embodened values in the table highlight the best performing Method for each statistic;

*paired t-test/Wilcoxon p<0.05;

**Pearson's correlation coefficient p < 0.05;

†Pearson's correlation coefficient p = 0.0848)

6.4.3.4 Validation

Validation of DCE MRI measurements was undertaken using PCMRI measurements of PV perfusion, estimated (subtraction) TLBF and estimated HA fraction measured in the same session as DCE MRI studies. Baseline and seven day reproducibility scans were analysed for twelve subjects (21 datasets). DCE MRI measurements were compared for the three quantification methods.

Simply eye-balling the data (table 6.11), it was clear that dual input single and dual compartment quantification methods both tended to grossly overestimate absolute perfusion measurements. This compromised the Bland-Altman analysis so that both the averages and differences of each pair of validated perfusion measurements were heavily weighted towards each DCE MRI measurement. Plots therefore appear to show a linear trend (figures 6.27 (a, c) and 6.28 (a, c)).

Table 6.11: DCE MRI perfusion parameters estimated using alternative quantification methods

	DUAL INPUT SINGLE COMPARTMENT	DUAL INPUT DUAL COMPARTMENT	HEPATIC PERFUSION INDEX	PCMRI
PV perfusion (ml/min/100g)	365.7±51.13*	1285±82.88*	17.09±2.647*	56.65±2.698
TLBF (ml/min/100g)	436.7±55.55*	1329±85.62*	21.47±3.620*	71.72±3.318
HA fraction (%)	20.72±3.695	3.375±0.7837*	16.90±1.899	18.91±4.084

(*paired t-test/Wilcoxon p<0.05 relative to PCMRI measurement; data replicated from table 6.9 for review)

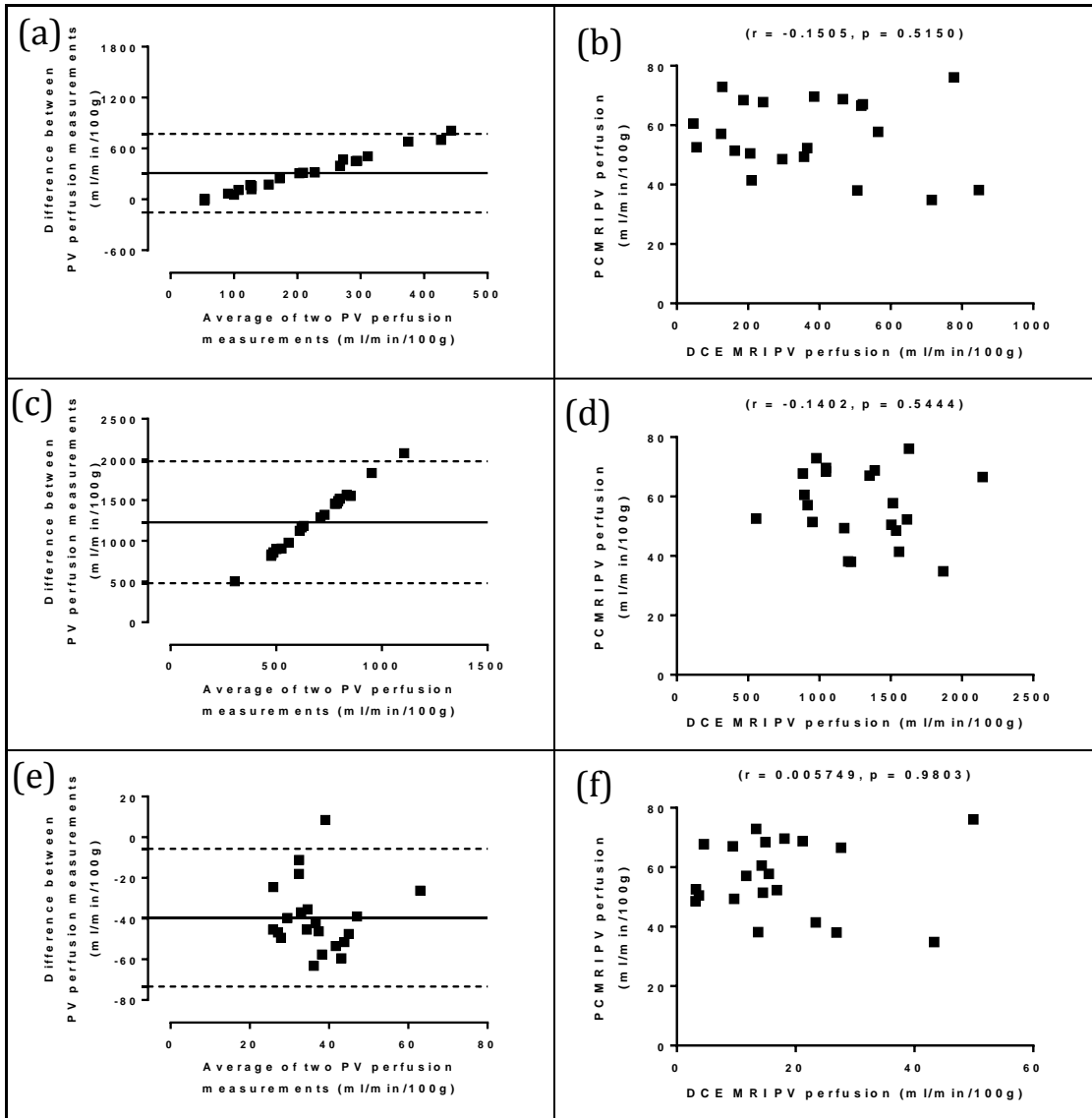


Figure 6.27: Analysis of agreement with PCMRI PV perfusion measurements using alternative DCE MRI quantification methods

Bland-Altman and regression analysis of (a, b) dual input single compartment modelling, (c, d) dual input dual compartment modelling, (e, f) hepatic perfusion index modelling.

Despite the smaller values of absolute perfusion parameters obtained using hepatic perfusion index modelling, significant differences were demonstrated between absolute perfusion parameters using all three quantification methods and PCMRI absolute perfusion. The smallest mean difference in PV perfusion (39.56 ± 3.769 ml/min/100g; $p < 0.0001$) and TLBF (median 48.97 ml/min/100g; $p < 0.0001$) was demonstrated using the hepatic perfusion index method in both cases. The smallest coefficient of variation for PV perfusion (29.55%) and TLBF (29.52%) was demonstrated by dual input dual compartment modelling in both cases. There were still larger than those observed for PV perfusion (21.82%) and TLBF (21.20%) using PCMRI. No significant correlations were demonstrated between any DCE MRI quantification method and PCMRI absolute perfusion measurements.

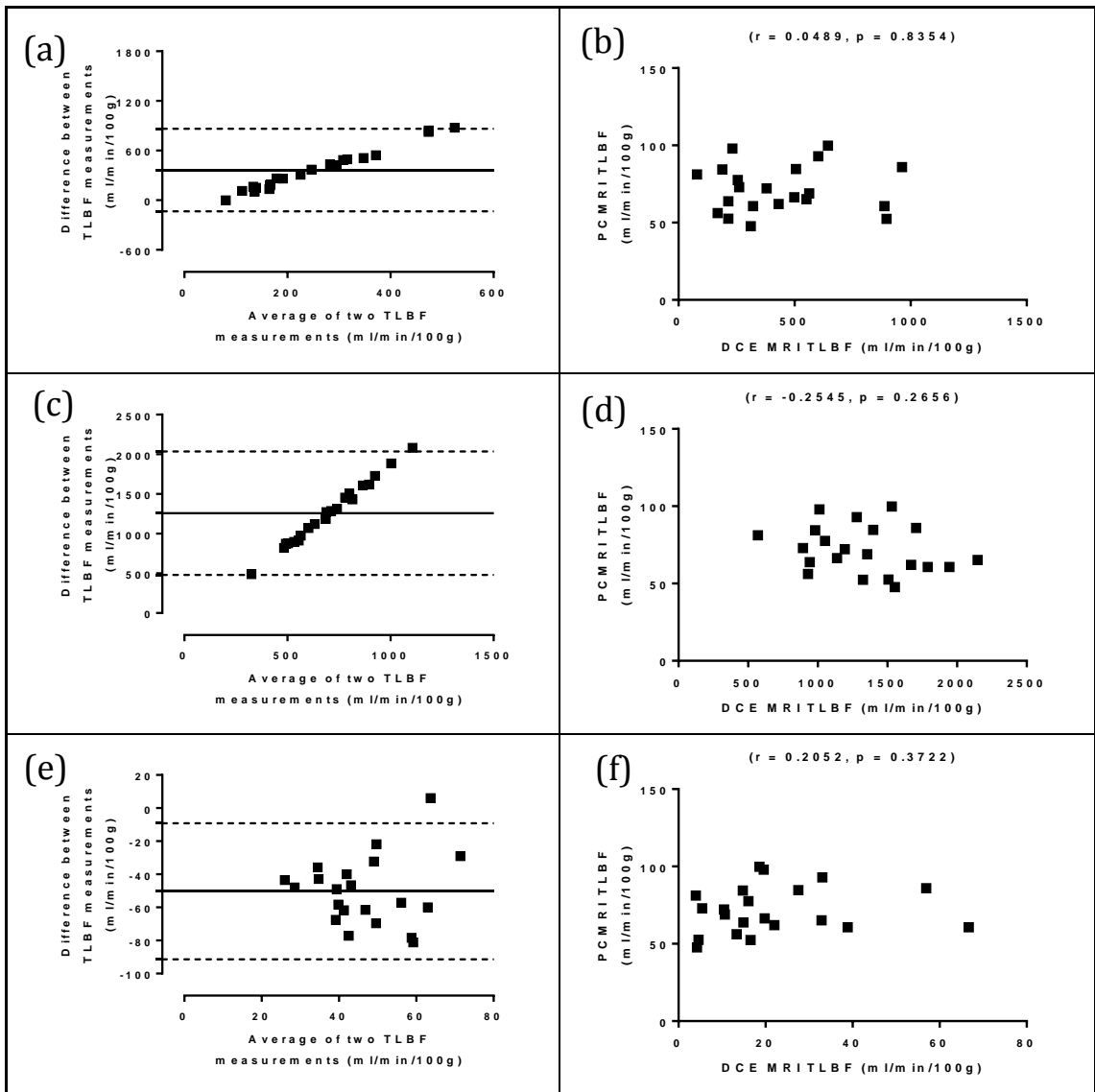


Figure 6.28: Analysis of agreement with PCMRI TLBF measurements using alternative DCE MRI quantification methods

Bland-Altman and regression analysis of (a, b) dual input single compartment modelling, (c, d) dual input dual compartment modelling, (e, f) hepatic perfusion index modelling.

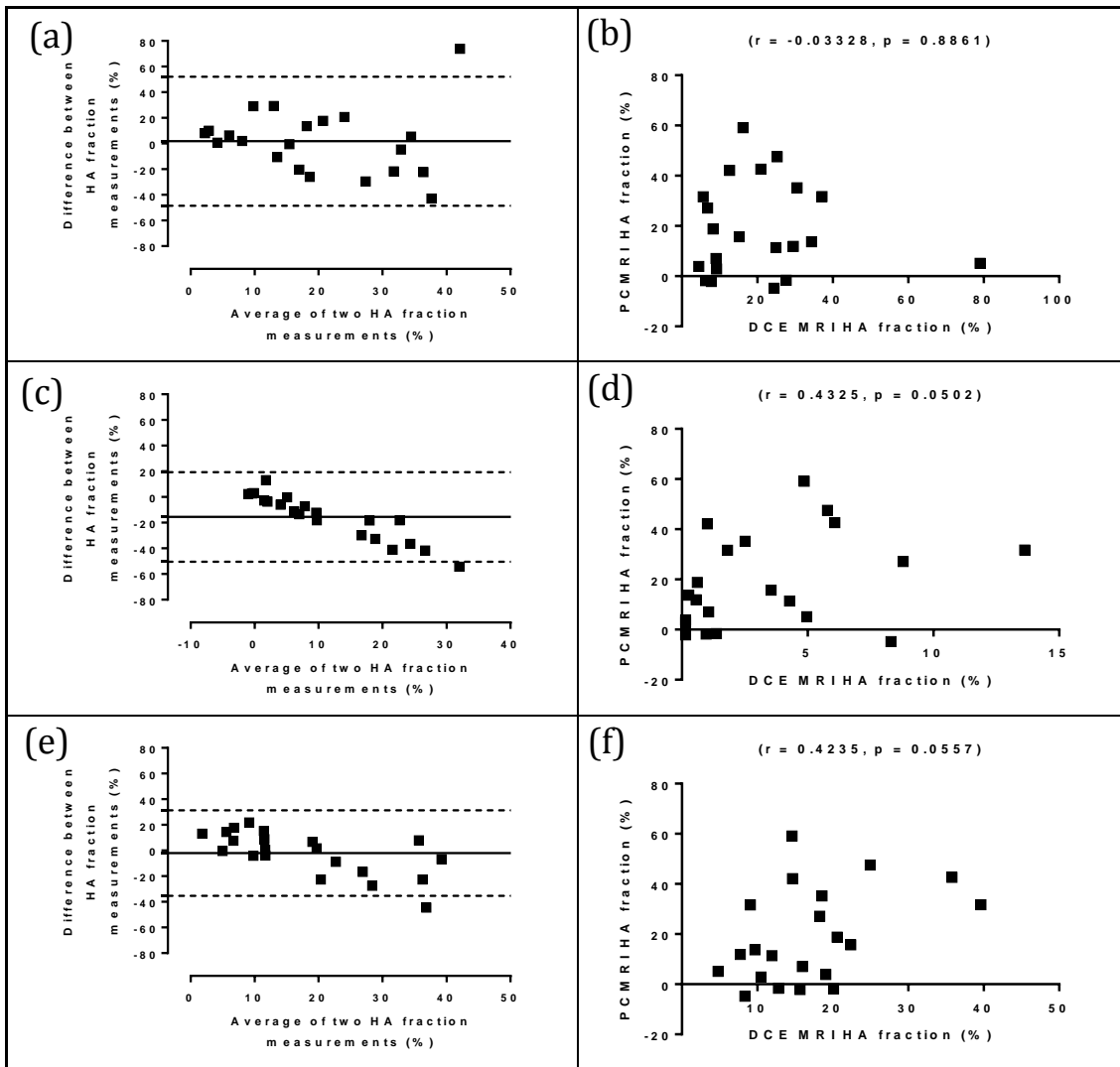


Figure 6.29: Analysis of agreement with PCMRI HA fraction measurements using alternative DCE MRI quantification methods

Bland-Altman and regression analysis of (a, b) dual input single compartment modelling, (c, d) dual input dual compartment modelling, (e, f) hepatic perfusion index modelling.

A significant difference between PCMRI and DCE MRI HA fraction measured using dual input dual compartment modelling was demonstrated (median 12.15%; $p = 0.0005$). The small HA fractions derived from dual compartment modelling resulted in averages and differences between validation data pairs being more heavily weighted towards the PCMRI measurement, therefore demonstrating an apparent linear trend on the Bland-Altman chart (figure 6.29c). No significant differences were demonstrated using single compartment modelling and the hepatic perfusion index method. The smallest difference in HA fraction ($-1.815 \pm 5.598\%$; $p = 0.7491$) was demonstrated using dual input single compartment modelling. The Bland-Altman charts for dual input single compartment and hepatic perfusion index HA fraction validation once again demonstrate an expected 'funnelling' of smaller values. This phenomenon is expected for percent measurements as differences between methods are naturally smaller towards the lower end of the scale [412].

The smallest coefficient of variation for HA fraction was demonstrated with hepatic perfusion index modelling (51.49%) and was smaller than the coefficient of variation for estimated HA fraction using PCMRI (98.97%). Underwhelming (though almost significant) correlations with PCMRI HA fraction were demonstrated with HA fraction measured using the dual input dual compartment ($r = 0.4325$; $p = 0.0502$) and hepatic perfusion index methods ($r = 0.4235$; $p = 0.0557$).

Table 6.12: Summary of validation of perfusion parameters estimated using alternative DCE MRI quantification methods using PCMRI[†]

	DUAL INPUT SINGLE COMPARTMENT	DUAL INPUT DUAL COMPARTMENT	HEPATIC PERFUSION INDEX
PV perfusion (ml/min/100g)			
Mean difference	-309.1±51.60*	-1229±83.81*	39.56±3.769*
Coefficient of Variation	64.07%	29.55%	70.98%
Correlation (<i>r</i>)	-0.1505	-0.1402	0.005749
TLBF (ml/min/100g)			
Mean difference	-365.0±55.49*	-1258±86.52*	48.97*
Coefficient of Variation	58.29%	29.52%	77.27%
Correlation (<i>r</i>)	0.04829	-0.2545	0.2052
HA fraction (%)			
Mean difference	-1.815±5.598	12.15*	2.003±3.703
Coefficient of Variation	81.72%	106.4%	51.49%
Correlation (<i>r</i>)	-0.03328	0.4325	0.4235

([†]Emboldened values in the table highlight the best performing Method for each statistic;
*paired t-test/Wilcoxon matched pairs $p < 0.05$)

6.4.4 DISCUSSION

We have demonstrated that data obtained with our clinical DCE MRI protocols is amenable to quantification using alternative modelling methods, specifically the dual input dual compartment and hepatic perfusion index models. The rationale for using different quantification methods was based around identifying alternatives that may improve the reproducibility and accuracy (through corroboration with PCMRI measurements) of estimated hepatic perfusion parameters. Our data demonstrated that this was not necessarily the case.

6.4.4.1 Dual input dual compartment modelling

Previous preclinical use of the dual input dual compartment model resulted in erroneous impulse residue functions (section 3.5.3.2), that were only corrected with restriction of modelling parameters. This was not an issue with clinical data and free modelling of all the parameters (fractional parameters were modelled between at 0-100% range) consistently produced physiological impulse residue functions. In spite of this, gross overestimation of absolute perfusion parameters remained an even bigger issue than with single compartment modelling.

Data for HA fraction demonstrated a normal distribution, but there was a tendency to underestimate HA perfusion and fraction. This is best appreciated on the validation Bland-Altman chart where weighting of the average and differences towards larger PCMRI estimates of HA fraction resulted in an apparent linear trend (figure 6.23c). Although a small HA fraction coefficient of reproducibility was recorded (6.637 vs 35.49 dual input single compartment; vs 23.551 hepatic perfusion index) and significant positive correlation was identified between repeated measurements ($r = 0.7537$; $p = 0.0095$), a significant mean difference between repeated measurements was detected (mean difference $-3.643 \pm 1.128\%$; $p = 0.0121$), suggestive of poor reproducibility. Validation of HA fraction measurements with PCMRI demonstrated mild positive correlations that were just approaching significance ($r = 0.4325$; $p = 0.0502$), but once again a significant difference was detected between DCE MRI and PCMRI paired validation data (median difference 12.15% ; $p = 0.0005$). No significant differences were detected using alternative quantification methods and the coefficient of variation was still larger for this method (106.4%), compared to other modelling approaches.

The dual input dual compartment model is especially interesting because it purports to measure vascular volume fraction, interstitial volume fraction and

permeability surface area, all of which in theory are likely to vary in liver disease. Vascular volume and interstitial volume fraction are likely to change as a result of gross morphological changes in tissue architecture secondary to fibrosis and revascularisation. Permeability surface area, a measure broadly linked to capillary permeability should in theory be altered in the inflammatory states that characterise liver disease. Measurements of v_1 , v_2 , and PS demonstrate reasonable reproducibility, although the absolute values of interstitial volume fraction are lower than quoted in the literature when measured by other methods [424, 425]. Validation of this data, as with MTT and DV in single compartment modelling would be methodologically challenging if not unfeasible in a normal volunteer study. In the absence of larger scale studies including patients with disease, it remains difficult to ascertain if the coefficients of reproducibility for these parameters are indeed adequate or too large.

Finally, the quality of the dual input dual compartment data fitting was much poorer than dual input single compartment modelling as demonstrated by comparison of the residual sum of squares (figure 6.22d). This finding is in itself surprising as a model with more variables should theoretically accommodate better fits. Additional variables absorb differences between modelled and observed data, thereby minimising the residual sum of squares. It is possible that these poorer fits will have arisen as a result of restricting v_1 and v_2 to a positive value less than 100%. Nonetheless, the combination of poor fits, poor reproducibility and poor validation of HA fraction data all favour use of alternative methods over dual input dual compartment modelling for quantification of HA fraction.

6.4.4.2 Hepatic perfusion index modelling

Occasionally termed ‘model-free’ quantification as this method does not involve fitting raw data, the hepatic perfusion index is a much simpler than its dual input single and dual compartment counterparts. Our data demonstrated a tendency to underestimate absolute perfusion parameters, although coefficients of reproducibility of absolute perfusion parameters were still smaller than those measured for alternative quantification methods.

More importantly, the mean difference and coefficient of reproducibility for repeated HA fraction measurements were both smaller than when measured with PCMRI and dual input single compartment methods. Additionally, no significant differences were demonstrated between DCE MRI HA fraction and PCMRI. Crucially, the coefficient of variation for HA fraction measured with the hepatic perfusion index method (51.49%) was still considerably less than for PCMRI (98.97%). This, combined with the mild, just non-significant correlation with PCMRI HA fraction ($r = 0.4235$; $p = 0.0557$), all tentatively

support the use of the hepatic perfusion index as an alternative method to dual input single compartment modelling for quantifying HA fraction.

6.4.5 CONCLUSION

We have demonstrated that clinical DCE MRI data is amenable to dual input dual compartment and hepatic perfusion index modelling. Both of these quantification methods fail to provide accurate absolute perfusion quantification but relative perfusion (i.e. HA fraction) can be measured with greater confidence. Although seven day reproducibility and PCMRI validation data is disappointing, HA fraction can potentially be measured with dual input single compartment or hepatic perfusion index methods.

6.5 COMBINED DCE AND PCMRI – PART I – ARTERIAL INPUT FUNCTION CORRECTION

6.5.1 BACKGROUND

Despite methodological and post-processing refinements, we have demonstrated that in a cohort of normal volunteers, reproducibility and accuracy of DCE MRI measurements is poor. The superior reproducibility of PCMRI measurements suggests that measurement error, rather than inherent physiological variability are to blame. From our earlier preclinical work, we have demonstrated that an important source of error in DCE MRI quantification is AIF sampling. The size and shape of the AIF are determined by a number of subject specific factors, an important determinant being bulk flow. AIFs sampled in the left ventricle would therefore be dependent on cardiac output – a variable we have measured using PCMRI and cardiac cine MRI in all subjects undergoing DCE MRI. The use of aortic root PCMRI cardiac output measurements to correct AIFs has been proposed previously [426], and used to demonstrate improved repeatability of renal perfusion measurements using the single input dual compartment Tofts model [131].

6.5.1.1 AIF correction using independently quantified cardiac output

In a simple non-recirculating system, bulk flow (Q) can be expressed as the mass of injected extracellular CA (D) divided by the area under the curve of the concentration of CA as a function of time ($C_a(t)$):

$$Q = \frac{D}{\int C_a(t) dt} \quad (\text{Equation 6.14})$$

This so-called indicator-dilution principle, based on the work of Stewart [427] and later Hamilton [428], lies at the heart of many methods for flow measurement. Based on the principle of conservation of mass, it has the advantage of being independent of the site, rate and method of injection, but is reliant on there being no CA recirculation. The latter can only be achieved if the CA becomes permanently lodged in the capillary beds on first pass, which is not true of Gd-DTPA or indeed many of the agents which use this principle for quantification (figure 6.30).

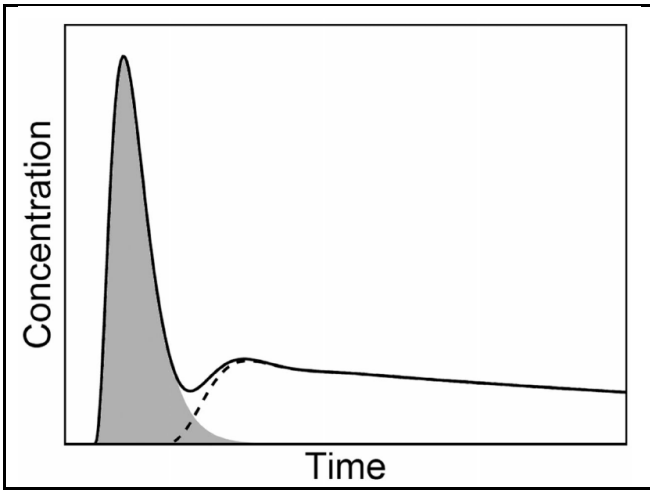


Figure 6.30: Measured AIF and first pass enhancement

AIFs (solid line) as previously demonstrated by our own data classically have an initial sharp peak, followed by a smaller peak and tail as a result of recirculation (dashed line). The first pass of the CA is however represented by the shaded area. (obtained from reference [426]).

A method for overcoming this issue is to correct $C_a(t)$ so that the enhancement curve represents first-pass enhancement only [429]. In order to do this, standard $C_a(t)$ curves are converted back into their raw SI curves ($S_a(t)$). The main peak of the raw SI AIF can then be extrapolated and fitted with the gamma variate function to derive an expression for first pass SI ($S_{fp}(t)$):

$$S_{fp}(t) = S_0 + A(t - \tau_a)^\alpha e^{-(t-\tau_a)/\beta} \quad (\text{Equation 6.15})$$

Where, ' S_0 ' represents baseline SI, ' τ_a ' is the AIF delay and ' A ', ' α ' and ' β ' are fitted parameters. The first pass SI curve ($S_{fp}(t)$) can then be converted using previous methods into a first pass AIF CA curve ($C_{fp}(t)$). From equation 6.12:

$$\int C_{fp}(t) dt = \frac{D}{Q} \quad (\text{Equation 6.16})$$

As ' D ' is known and ' Q ' was measured independently using PCMRI aortic root flow, ' $C_{fp}(t)$ ' could be adjusted to represent the expected first pass CA concentration curve based on known cardiac output. This adjusted first pass CA concentration curve could then be converted back into corrected raw first pass SI data. Based on Zhang et al. [426], the converted SI curves could then be used to derive a new estimate for baseline signal intensity (S_0').

In the final steps, the raw SI curves for the entire AIF (including the recirculated portion) are shifted a new baseline (S_0'). The new corrected raw SI AIF is then converted back to a corrected AIF CA concentration curve ($C_a'(t)$), ready for use in pharmacokinetic modelling.

Correction of AIFs using cardiac output data for improved pharmacokinetic modelling of hepatic DCE MRI data has not been attempted previously. In this section we

demonstrate the feasibility of the method proposed by Zhang et al. [426] for correction of previously measured AIFs using PCMRI aortic root flow data. We then assess the effects of AIF correction on (i) seven day reproducibility and (ii) validation of tissue perfusion estimates with volume normalised PCMRI flow measurements.

6.5.2 METHODS

6.5.2.1 Subjects and preparation

As described in section 6.3.2.1.

6.5.2.2 Clinical PCMRI

As described in section 5.5.2. PCMRI studies were planned orthogonal to the aortic root. Studies were performed in expiratory breath-hold and cardiac gated using peripheral pulse oximetry. The following settings were used: TR/TE 8.70/5.22 seconds, flip angle = 10° , matrix size 336x336, field of view 271x210 mm, bandwidth 210 Hz/pixel, slice thickness 5 mm, 7 cardiac cycle phases and velocity encoding settings of 120 cm/s. Each measurement was repeated three times in succession. Quantification was performed using the freely available software package, Segment (Medviso, Lund, Sweden).

6.5.2.3 Clinical DCE MRI

As described in section 6.3.2.2.

6.5.2.4 Post-processing

AIFs were corrected using PCMRI aortic root flow measurements, using the previously described method [426]. Data was then modelled using (i) the dual input single compartment method with pre-estimation and constrained free modelling of VIF delays and (ii) the hepatic perfusion index method, as described in section 6.4.1.2. Hepatic perfusion parameters estimated from both methods were compared with parameters obtained using uncorrected AIF data in section 6.4.

6.5.2.5 Reproducibility studies

As described in section 6.3.2.5.

6.5.2.6 Validation studies

As described in section 6.3.2.6.

6.5.2.7 Statistical analysis

Kolmogorov-Smirnov tests were used to confirm normality of variable distributions. Paired t-tests/Wilcoxon matched pairs signed rank tests were used to compare perfusion parameters derived from corrected and uncorrected AIF data. Reproducibility and validation studies were also assessed using paired t-tests/Wilcoxon matched pairs signed rank tests, Bland-Altman analysis of agreement with calculation of the coefficient of repeatability and assessment of correlation between repeated/validated measurements using Pearson's or Spearman's correlation coefficient for parametric/non-parametric data as appropriate. The threshold of statistical significance was defined to be $p < 0.05$.

6.5.3 RESULTS

6.5.3.1 Cohort features

Data was collected in twelve normal volunteers. Male subjects ($n = 6$) had a mean age of 26.7 ± 1.55 years and female subjects ($n = 6$) had a mean age of 30.2 ± 2.37 years. Seven day reproducibility data was available for nine subjects ($n = 4$ male, $n = 5$ female).

6.5.3.2 AIF correction

A sample data set was used to demonstrate the uncorrected AIF, uncorrected and first pass AIF SI curve with gamma variate fit, corrected first pass CA concentration curve and corrected AIF (figure 6.31).

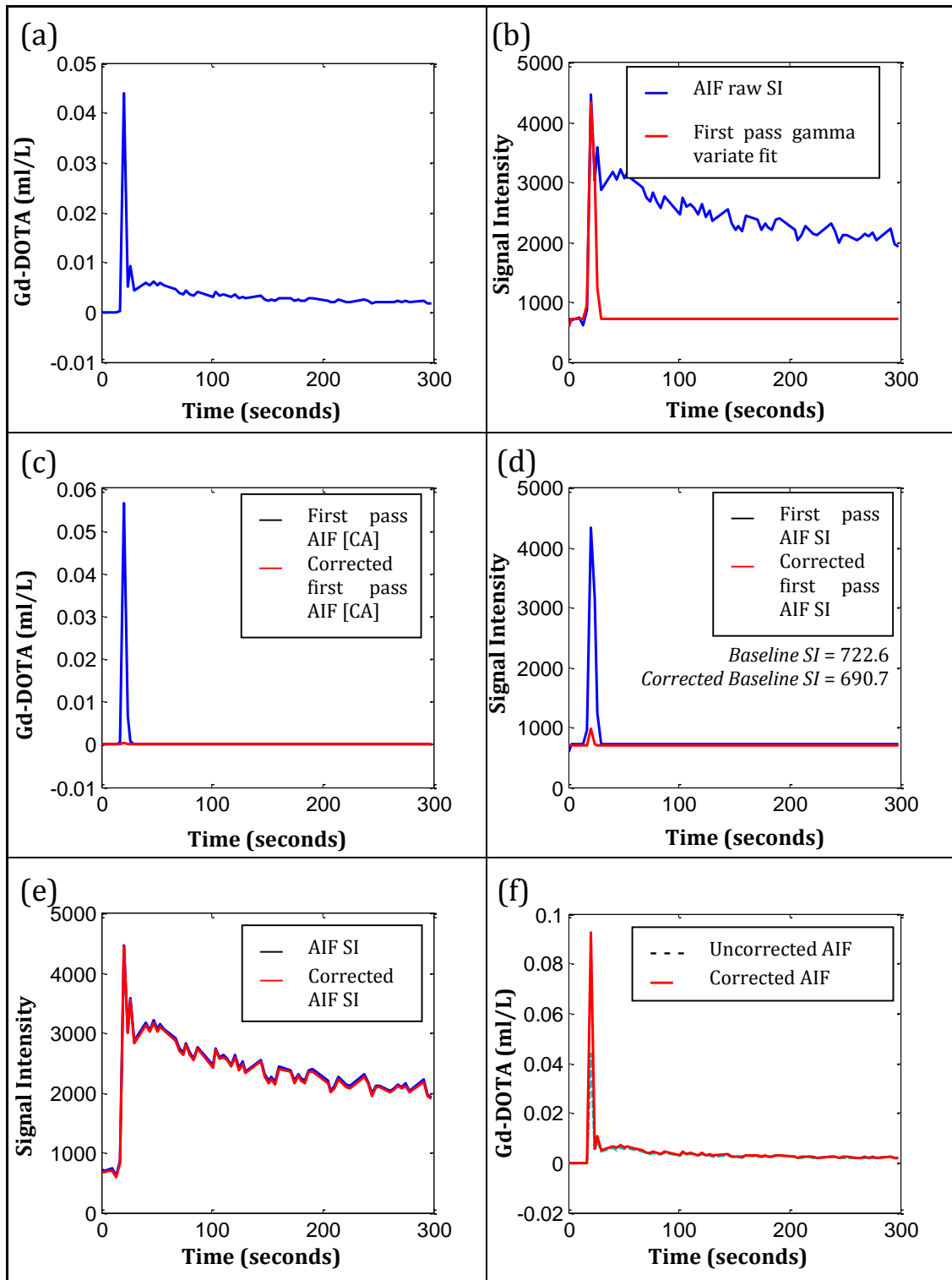


Figure 6.31: Sample data demonstrating sequential steps for AIF correction

The uncorrected AIF (a), is converted back into raw signal intensity (b, blue curve). The first pass portion of the SI curve is modelled using the gamma variate function (b, red curve). The SI gamma variate function is then converted back to derive a first pass CA concentration curve (c, blue curve) and adjusted using cardiac output data (c, red curve). This is then converted back into raw SI data (d). The corrected first-pass curve will provide an alternate estimate for baseline SI. The original AIF raw SI curve is then adjusted to the new baseline (e). The new adjusted curve is used to derive a corrected AIF CA concentration curve (f, red curve).

The effects of AIF correction were variable. For most data sets, the corrected AIF was larger, but for some, the corrected AIF was the same or smaller (figure 6.32).

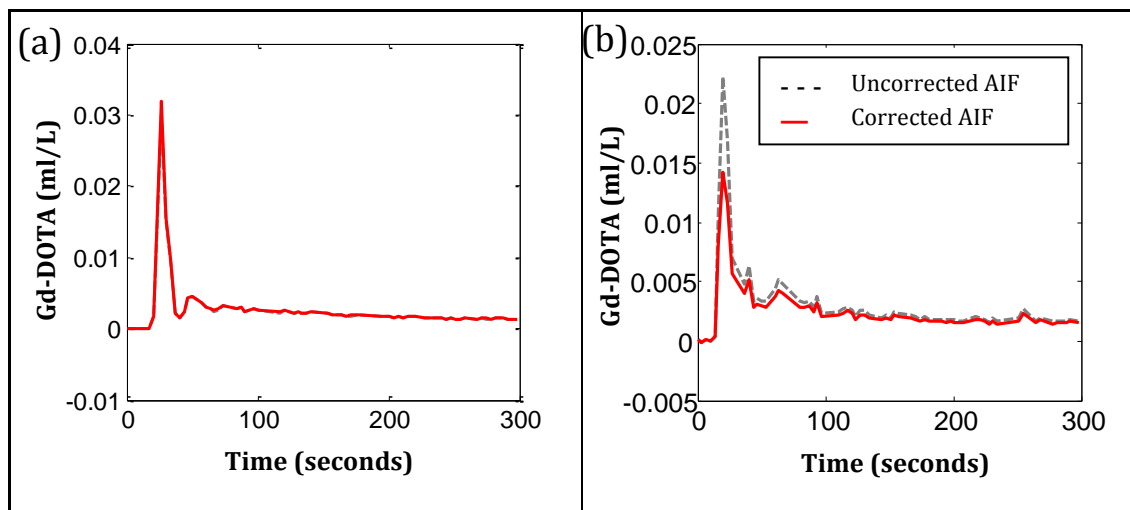


Figure 6.32: Effects of correction process on AIF size

On both diagrams, the corrected AIF is shown in red and the uncorrected AIF is shown in dashed green. In some instances, correction resulted in little or no change to the AIF itself, as shown by the dataset in (a), in a few cases, a reduction in AIF size was noted, as shown by the dataset in (b). An increase in the size of the AIF was noted in most cases (figure 6.30f).

Data for each of the perfusion parameters is plotted for uncorrected and corrected AIF modelling in figures 6.33 and 6.34, and tabulated in table 6.13. DV, PVIF delay and residual sum of squares demonstrated non-normal distributions and therefore underwent non-parametric statistical testing. Comparison of PV perfusion before and after AIF correction approached significance (mean difference 23.05 ± 11.88 ml/min/100g; $p = 0.0666$), but no significant differences were demonstrated between uncorrected and corrected AIF perfusion parameters. The standard deviation increased after AIF correction for all parameters except HA fraction, MTT and AIF delay.

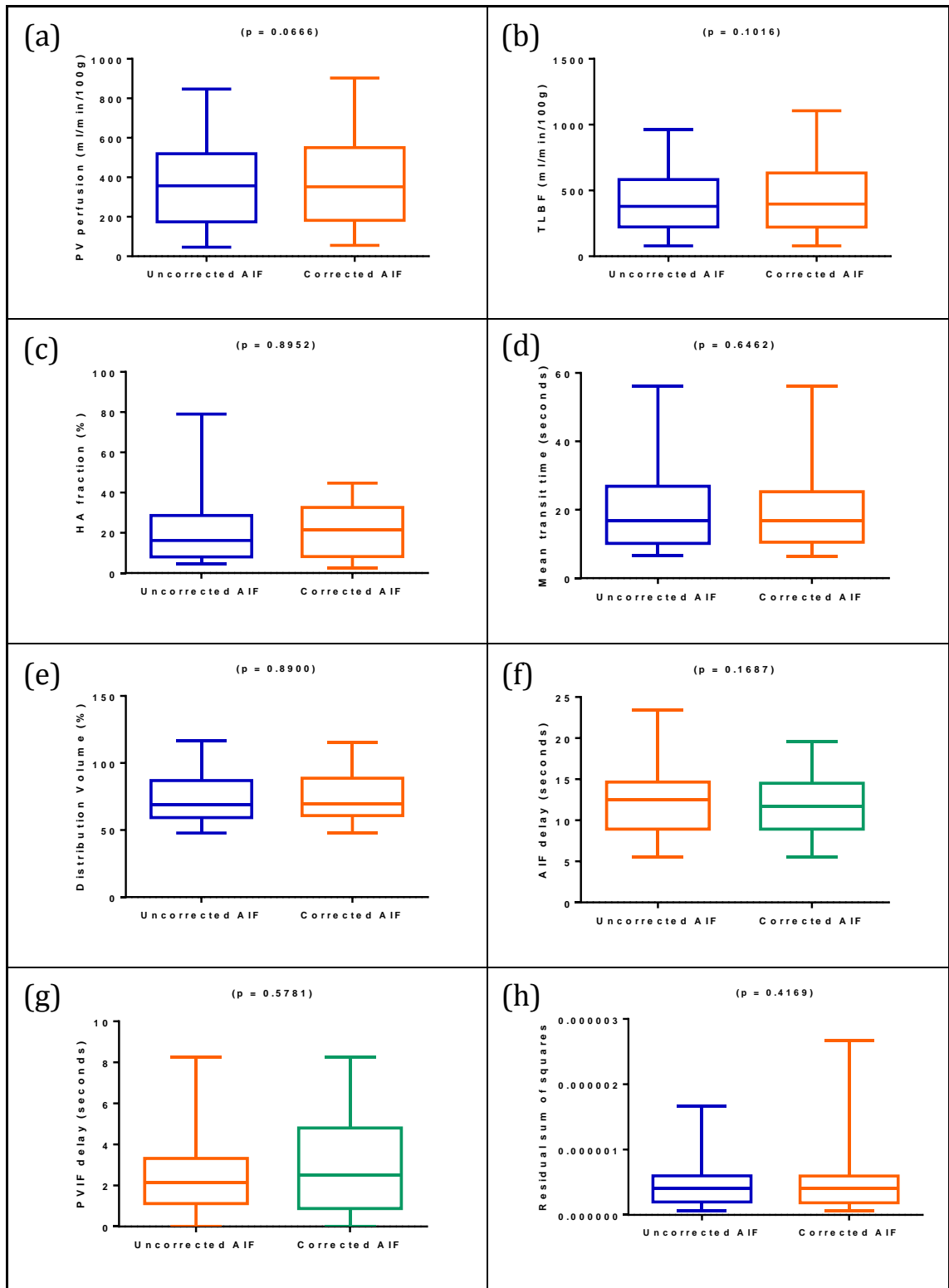


Figure 6.32: Effects of AIF correction on dual input single compartment hepatic perfusion parameters

Box and whisker plots for each of the perfusion parameters demonstrate the distribution of perfusion parameter data from uncorrected AIF data on the left and corrected AIF data on the right.

PV perfusion and TLBF measured using the hepatic perfusion index method demonstrated non-normal distributions and therefore underwent non-parametric statistical testing. No significant differences were demonstrated between corrected and uncorrected AIF perfusion parameters, with increased in the standard deviation for all three parameters.

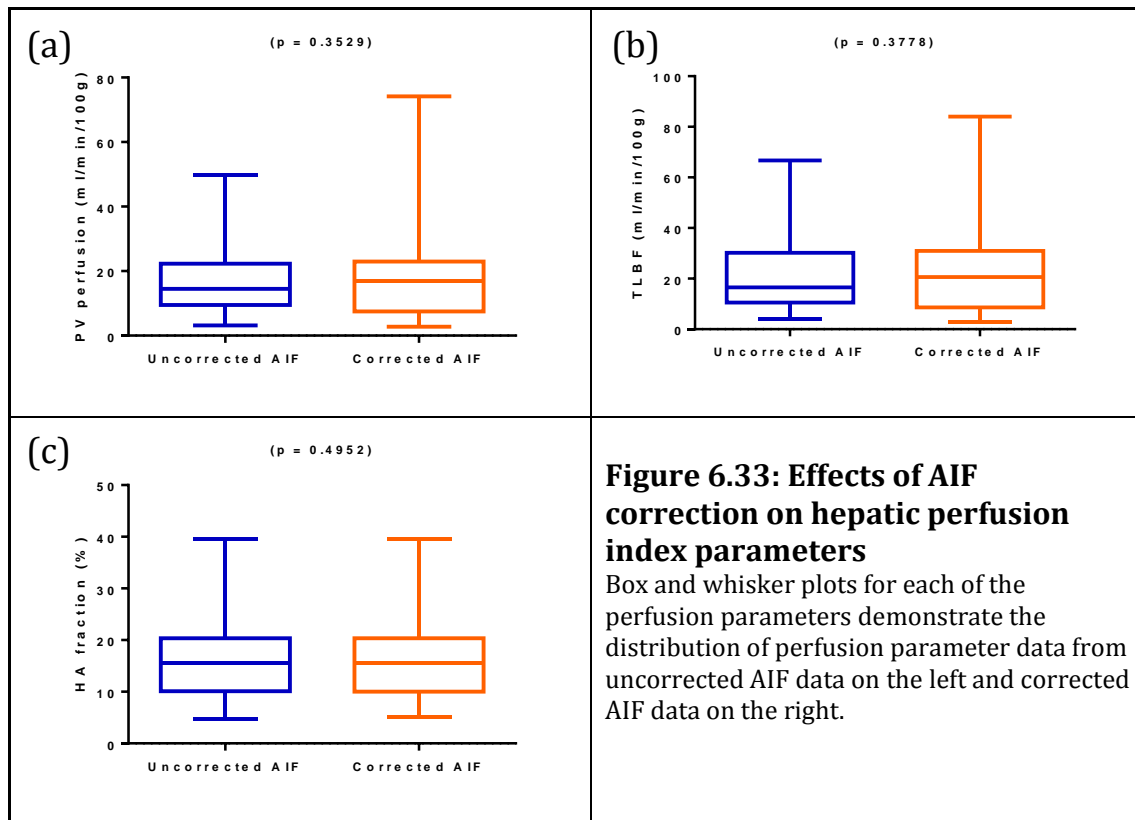


Table 6.13: Perfusion parameters for uncorrected and corrected AIFs using dual input single compartment and hepatic perfusion index methods

	UNCORRECTED AIF DUAL INPUT SINGLE COMPARTMENT	CORRECTED AIF DUAL INPUT SINGLE COMPARTMENT	UNCORRECTED AIF HEPATIC PERFUSION INDEX	CORRECTED AIF HEPATIC PERFUSION INDEX
PV perfusion (ml/min/100g)	365.7±51.13	388.8±55.23	17.09±2.647	20.00±3.761
TLBF (ml/min/100g)	436.7±55.55	462.2±61.37	21.47±3.620	24.83±4.666
HA fraction (%)	20.72±3.695	20.45±2.739	16.90±1.899	16.82±1.922
Mean Transit Time (s)	19.92±2.644	19.74±2.669	-	-
Distribution Volume (%)	73.45±3.951	73.68±3.847	-	-
Residuals ²	4.651x10 ⁻⁷ 7±7.815x10 ⁻⁸	5.245x10 ⁻⁷ 7±1.238x10 ⁻⁷	-	-

(no significant differences between uncorrected and corrected AIF parameters were demonstrated)

6.5.3.3 Reproducibility

Reproducibility was assessed using the same protocol with the same scanner in the same subjects exactly seven days after the initial study. Repeat measurements were obtained in normal volunteers ($n = 9$). All reproducibility analysis data are summarised and presented alongside seven day PCMRI reproducibility for comparison in table 6.11. Figures in this section have been arranged so that uncorrected and corrected AIF Bland-Altman diagrams are alongside each other to facilitate inspection of the limits of agreement.

6.5.3.3.1 Dual input single compartment modelling

No significant differences were demonstrated between repeated PV perfusion (figure 6.34) and TLBF (figure 6.35) measured with uncorrected and corrected AIFs using dual input single compartment modelling. AIF correction resulted in a rise in the coefficient of reproducibility for both absolute perfusion parameters. There was however a reduction in the mean difference for both PV perfusion (-12.40 ± 114.8 ml/min/100g uncorrected vs -1.229 ± 127.6 ml/min/100g corrected) and TLBF (-58.33 ± 133.0 ml/min/100g uncorrected vs -17.76 ± 150.0 ml/min/100g corrected). No correlations were demonstrated between repeated absolute perfusion measurements using uncorrected and corrected AIF data.

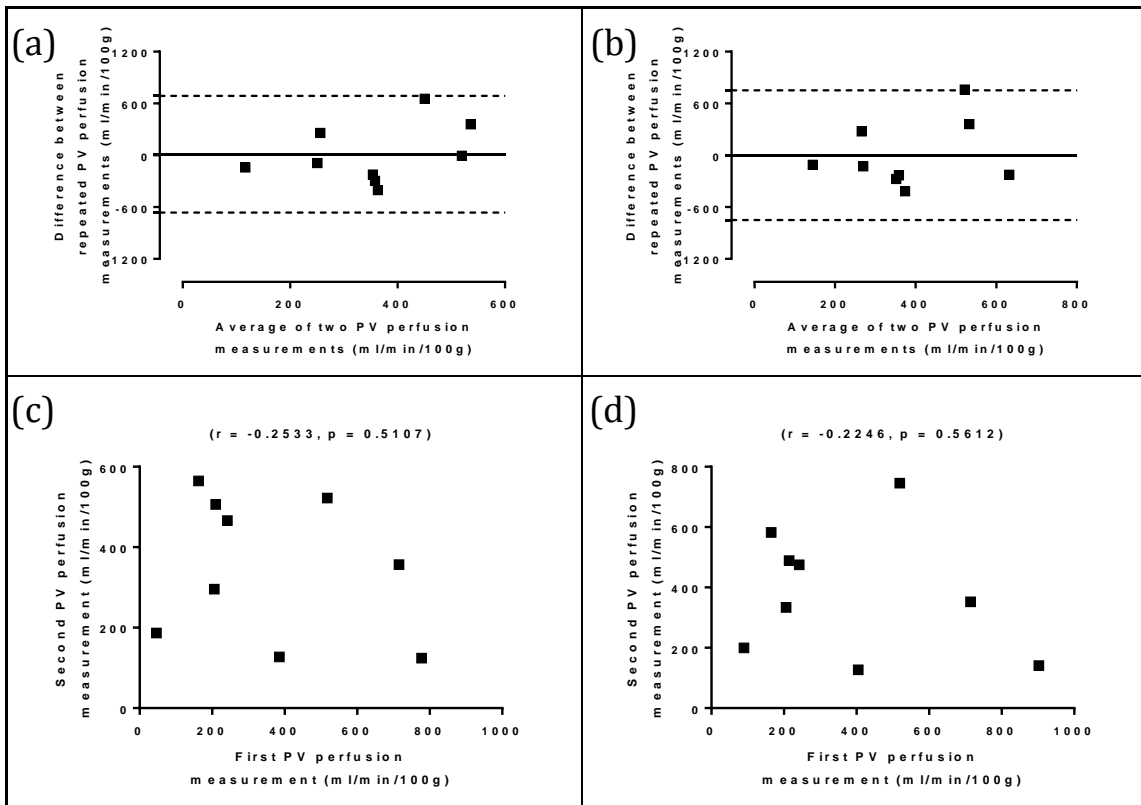


Figure 6.34: Analysis of agreement of repeated PV perfusion measurements using uncorrected and corrected AIF dual input single compartment modelling

Bland-Altman and regression analysis of (a, c) uncorrected AIF and (b, d) corrected AIF dual input single compartment modelling.

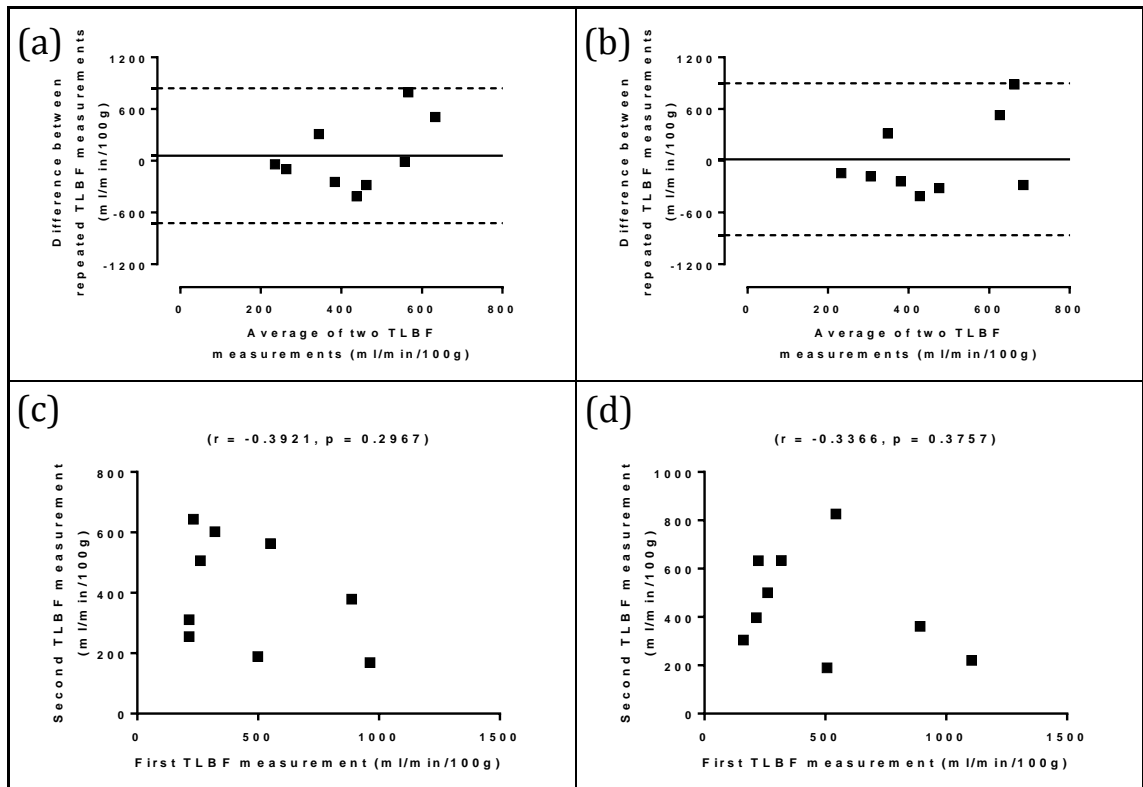


Figure 6.35: Analysis of agreement of repeated TLBF measurements using uncorrected and corrected AIF dual input single compartment modelling

Bland-Altman and regression analysis of (a, c) uncorrected AIF and (b, d) corrected AIF dual input single compartment modelling.

No significant differences were demonstrated between repeated HA fraction measurements using uncorrected and corrected AIFs with dual input single compartment modelling (figure 6.36). AIF correction did however result in a reduction in the coefficient of reproducibility (35.49% uncorrected vs 27.85% corrected) and mean difference (9.26% uncorrected vs 0.3204% corrected) between repeated measurements. No correlations were demonstrated between repeated HA fraction measurements using uncorrected and corrected AIF data (table 6.14).

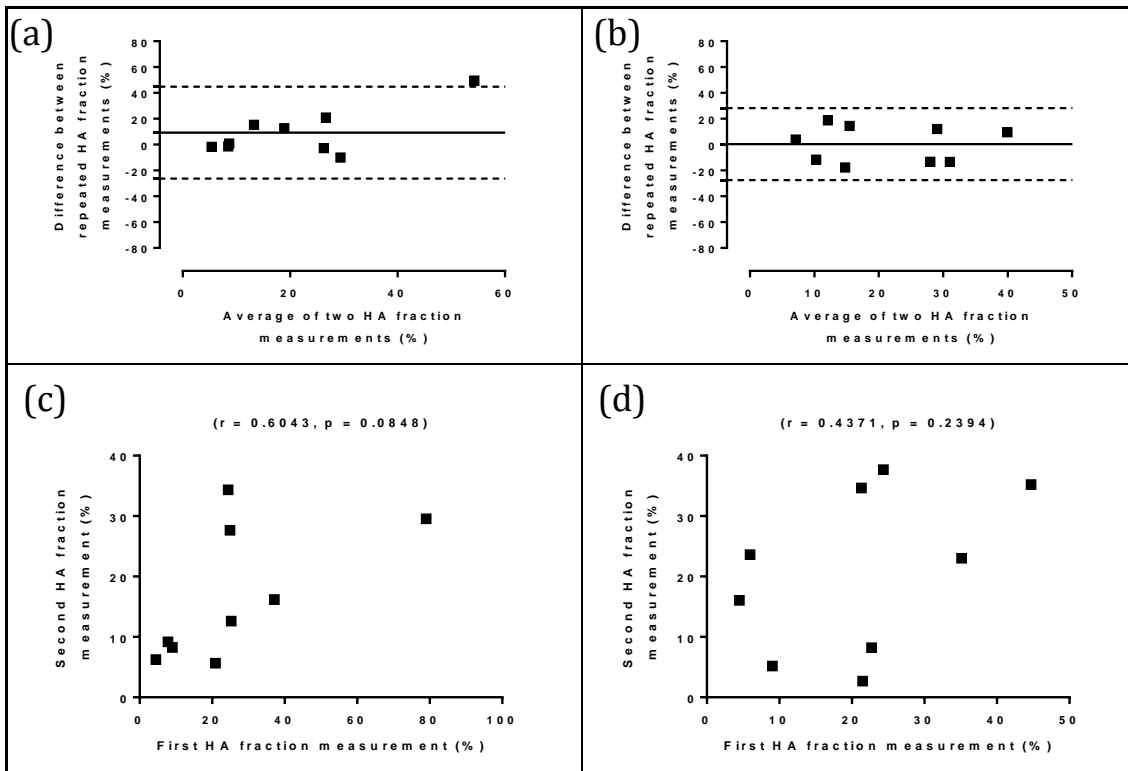


Figure 6.36: Analysis of agreement of repeated HA fraction measurements using uncorrected and corrected AIF dual input single compartment modelling

Bland-Altman and regression analysis of (a, c) uncorrected AIF and (b, d) corrected AIF dual input single compartment modelling.

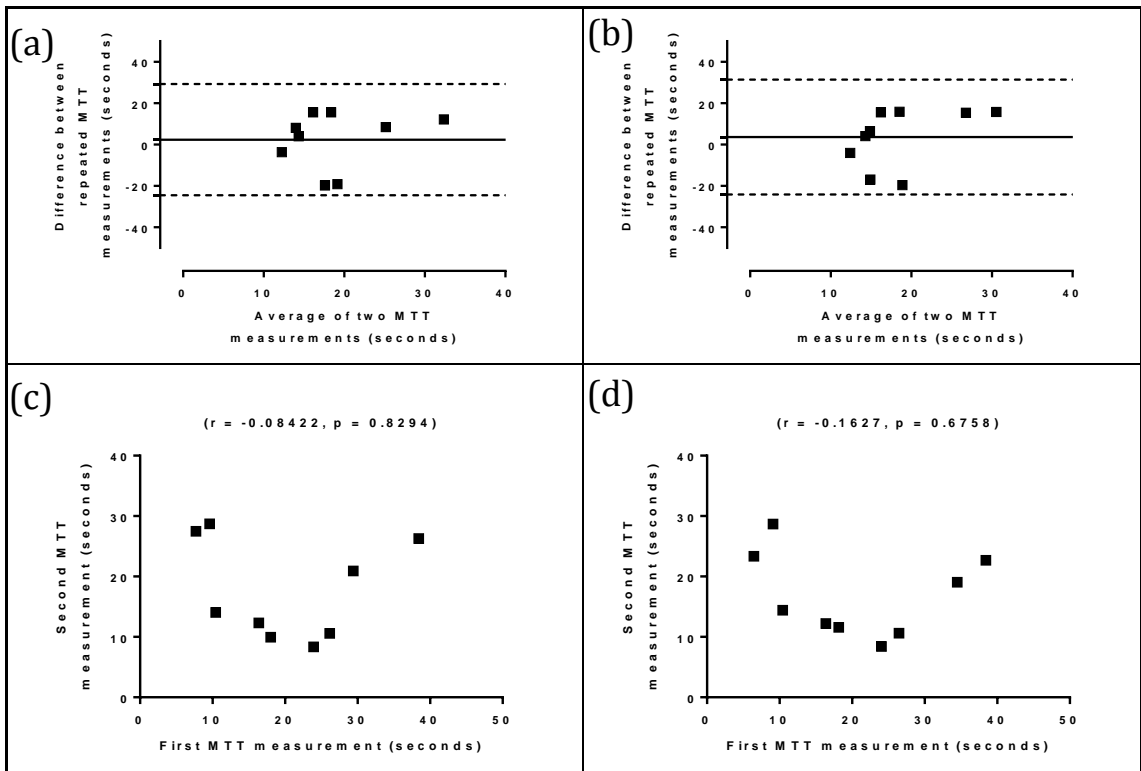


Figure 6.37: Analysis of agreement of repeated mean transit time measurements using uncorrected and corrected AIF dual input single compartment modelling

Bland-Altman and regression analysis of (a, c) uncorrected AIF and (b, d) corrected AIF dual input single compartment modelling.

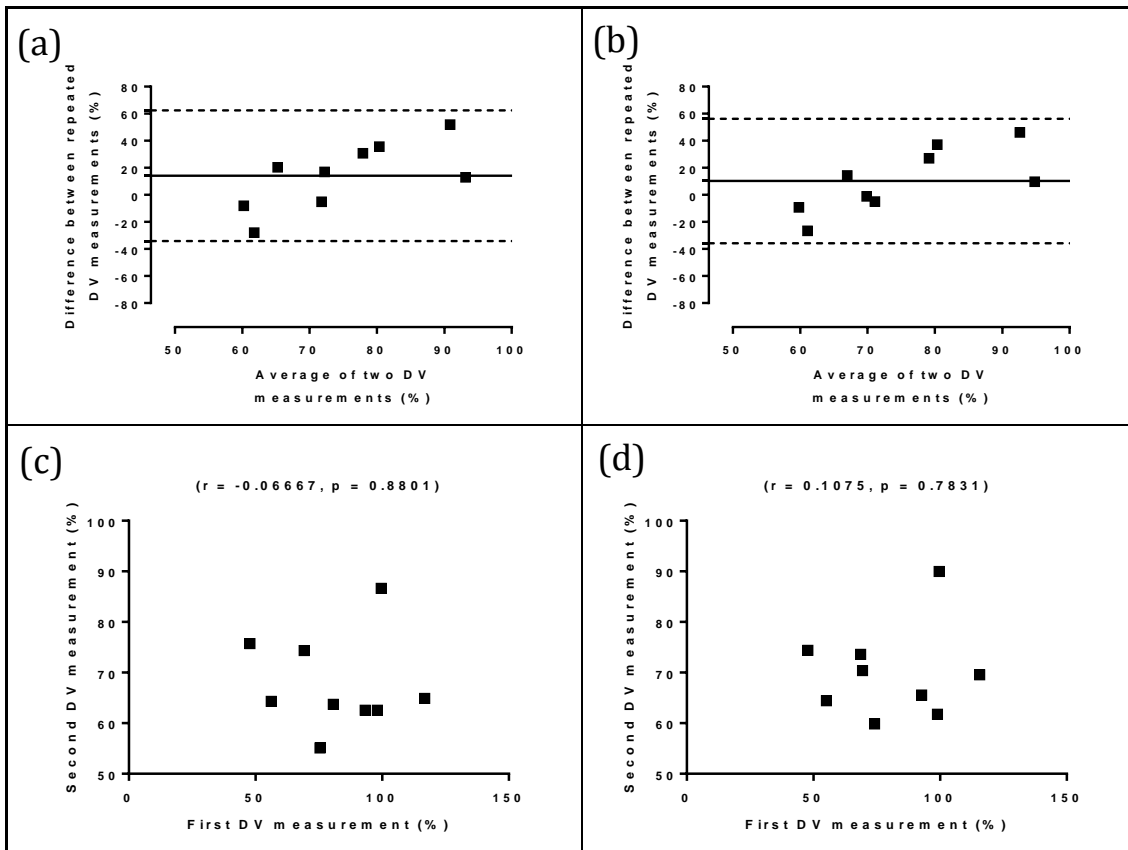


Figure 6.38: Analysis of agreement of repeated distribution volume measurements using uncorrected and corrected AIF dual input single compartment modelling

Bland-Altman and regression analysis of (a, c) uncorrected AIF and (b, d) corrected AIF dual input single compartment modelling.

No significant differences were demonstrated between repeated MTT (figure 6.37) and DV (figure 6.38) measured with uncorrected and corrected AIFs using dual input single compartment modelling. AIF correction resulted in an increase in the coefficient of reproducibility (26.89 seconds uncorrected vs 27.79 seconds corrected) and mean difference of MTT (2.374 seconds uncorrected vs 3.659 seconds corrected) but also produced a small reduction in the coefficient of reproducibility (48.24% uncorrected vs 46.02% corrected) and mean difference (16.98% uncorrected vs 10.26% corrected) between repeated DV measurements. No correlations were demonstrated between repeated MTT and DV measurements using uncorrected and corrected AIF data (table 6.14).

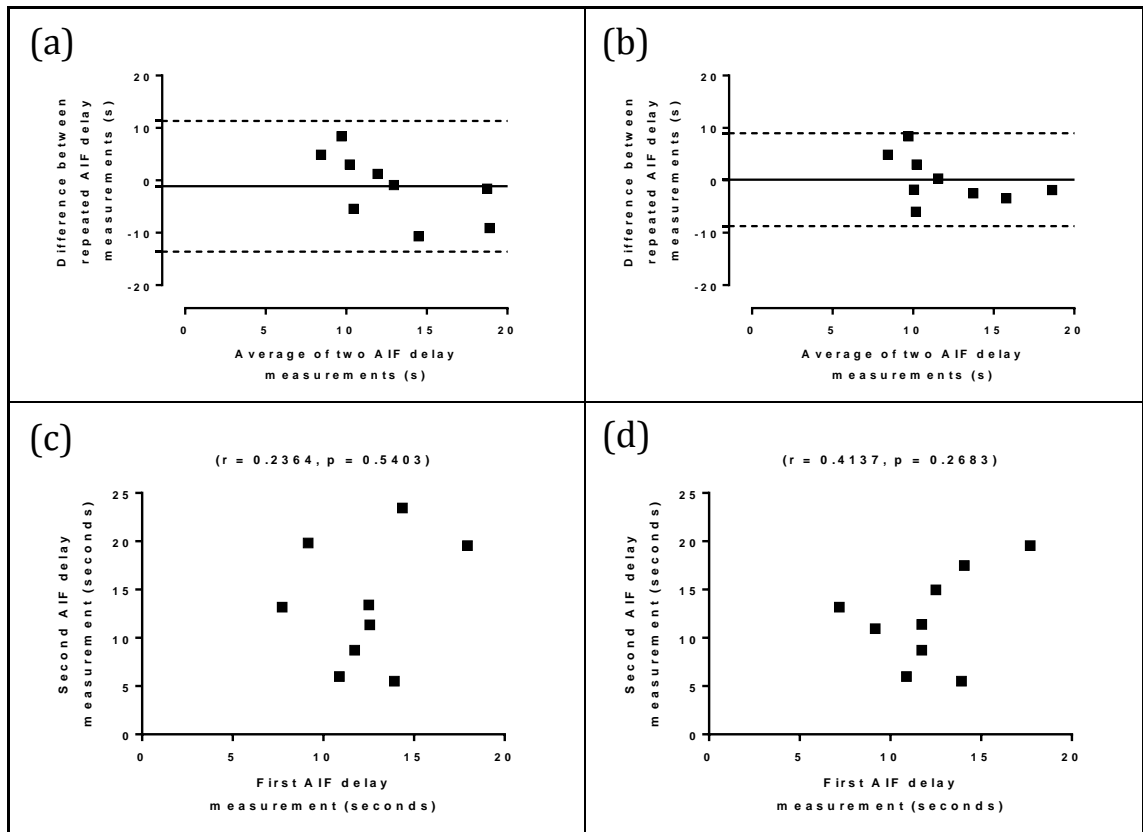


Figure 6.39: Analysis of agreement of repeated AIF delay measurements using uncorrected and corrected AIF dual input single compartment modelling

Bland-Altman and regression analysis of (a, c) uncorrected AIF and (b, d) corrected AIF dual input single compartment modelling.

No significant differences were demonstrated between repeated AIF and PVIF delay measurements using uncorrected and corrected AIFs with dual input single compartment modelling and constrained free modelling of pre-estimated delays (figures 6.39 and 6.40). AIF correction reduced the coefficient of reproducibility for both AIF (12.47 seconds uncorrected vs 8.878 seconds corrected) and PVIF (3.853 seconds uncorrected vs 3.181 seconds corrected) delays. AIF correction also reduced the mean difference between repeated AIF delays (1.126 seconds uncorrected vs 0.1296 seconds corrected) and PVIF delays (0.5583 seconds uncorrected vs 0.1307 seconds corrected). No correlations were demonstrated between repeated AIF delays, but a rise and statistically significant positive correlation coefficient between repeated PVIF delays was demonstrated ($r = 0.7045$; $p = 0.0341$) (figure 6.40, table 6.14).

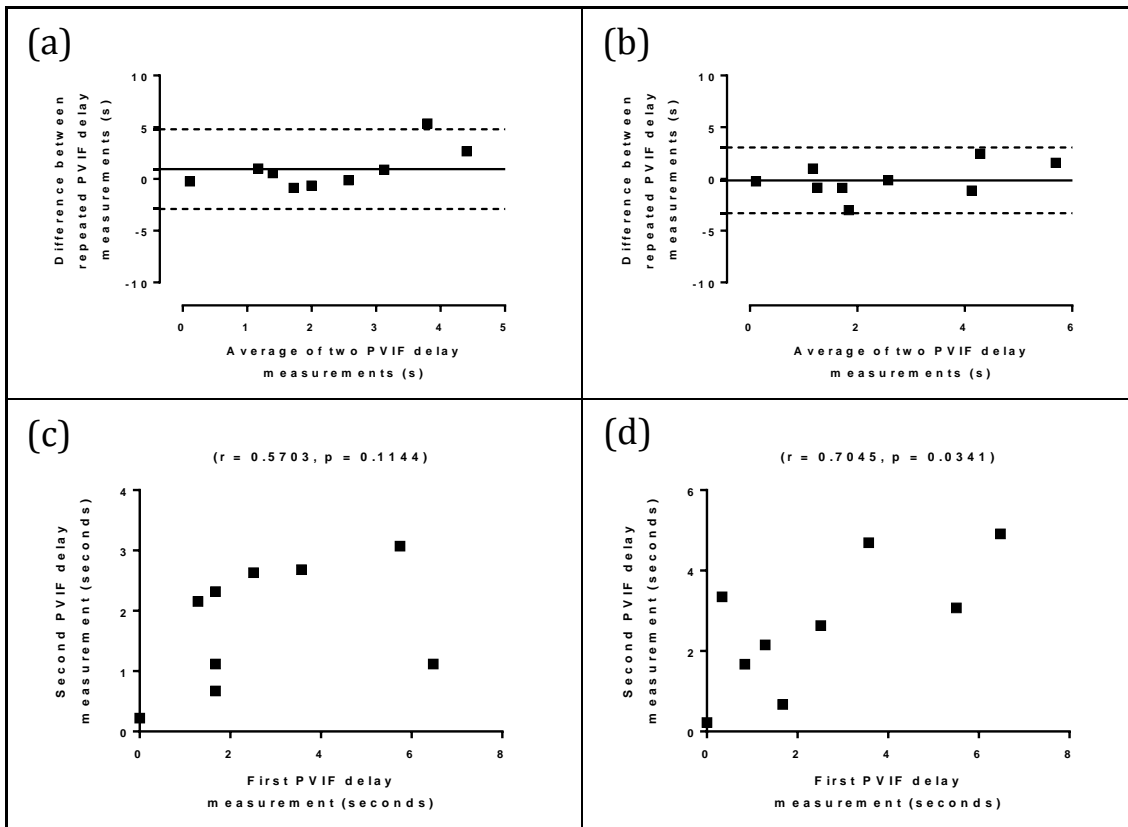


Figure 6.40: Analysis of agreement of repeated PVIF delay measurements using uncorrected and corrected AIF dual input single compartment modelling

Bland-Altman and regression analysis of (a, c) uncorrected AIF and (b, d) corrected AIF dual input single compartment modelling.

6.5.3.3.2 Hepatic perfusion index modelling

No significant differences were demonstrated between repeated PV perfusion (figure 6.41) and TLBF (figure 6.42) measured with uncorrected and corrected AIFs using the hepatic perfusion index method. AIF corrected resulted in a rise in the coefficient of reproducibility for both absolute perfusion parameters. No correlations were demonstrated between repeated absolute perfusion measurements using uncorrected and corrected AIF data (table 6.14).

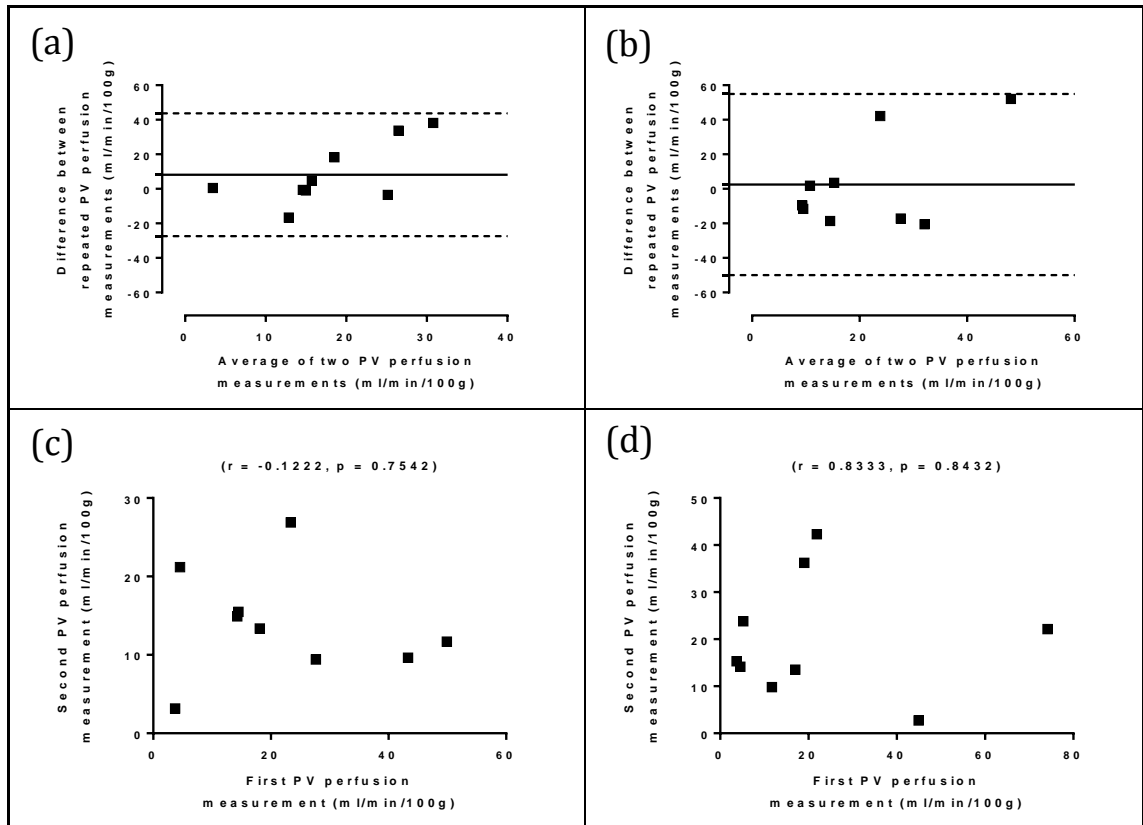


Figure 6.41: Analysis of agreement of repeated PV perfusion measurements using uncorrected and corrected AIF hepatic perfusion index modelling

Bland-Altman and regression analysis of (a, c) uncorrected AIF and (b, d) corrected AIF hepatic perfusion index modelling.

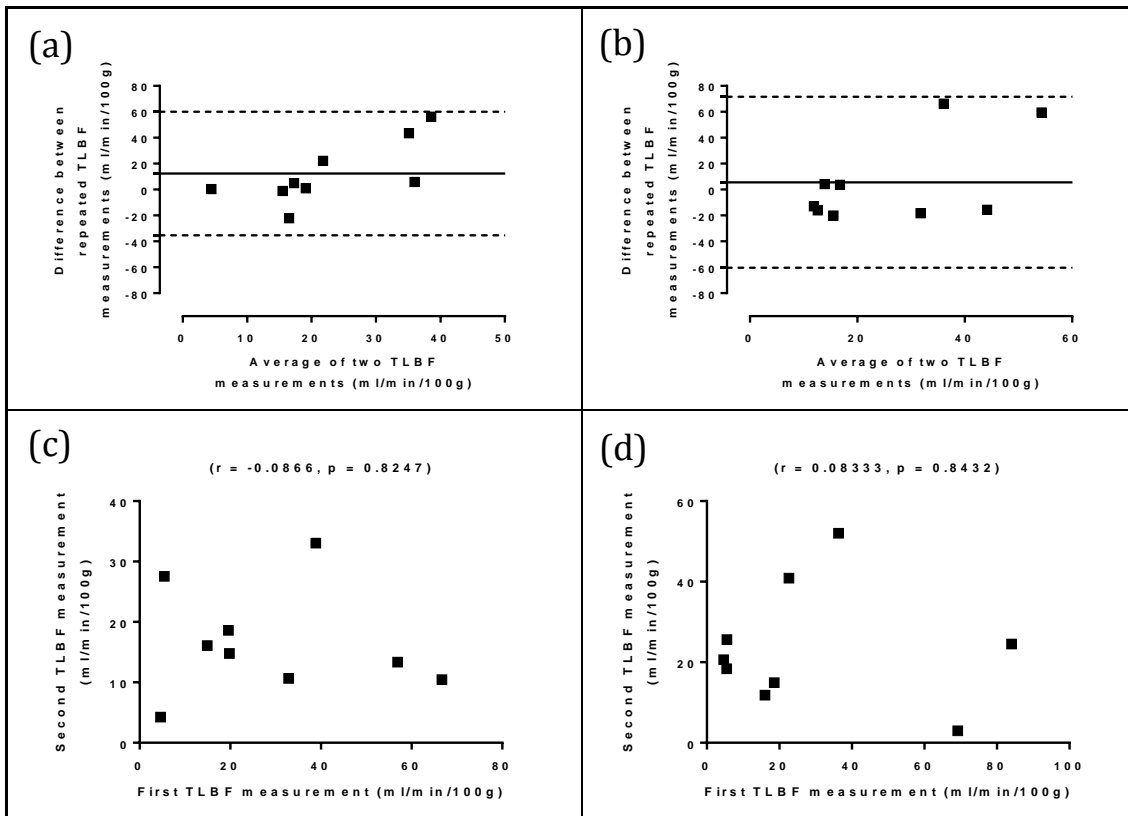


Figure 6.42: Analysis of agreement of repeated TLBF measurements using uncorrected and corrected AIF hepatic perfusion index modelling

Bland-Altman and regression analysis of (a, c) uncorrected AIF and (b, d) corrected AIF hepatic perfusion index modelling.

No significant differences were demonstrated between repeated HA fraction measurements using uncorrected and corrected AIFs using the hepatic perfusion index method (figure 6.43). AIF correction did however result in a minimal reduction in the coefficient of reproducibility (23.55% uncorrected vs 23.34% corrected), but not mean difference (6.269% uncorrected vs 6.594% corrected) between repeated measurements. No correlations were demonstrated between repeated HA fraction measurements using uncorrected and corrected AIF data (table 6.14).

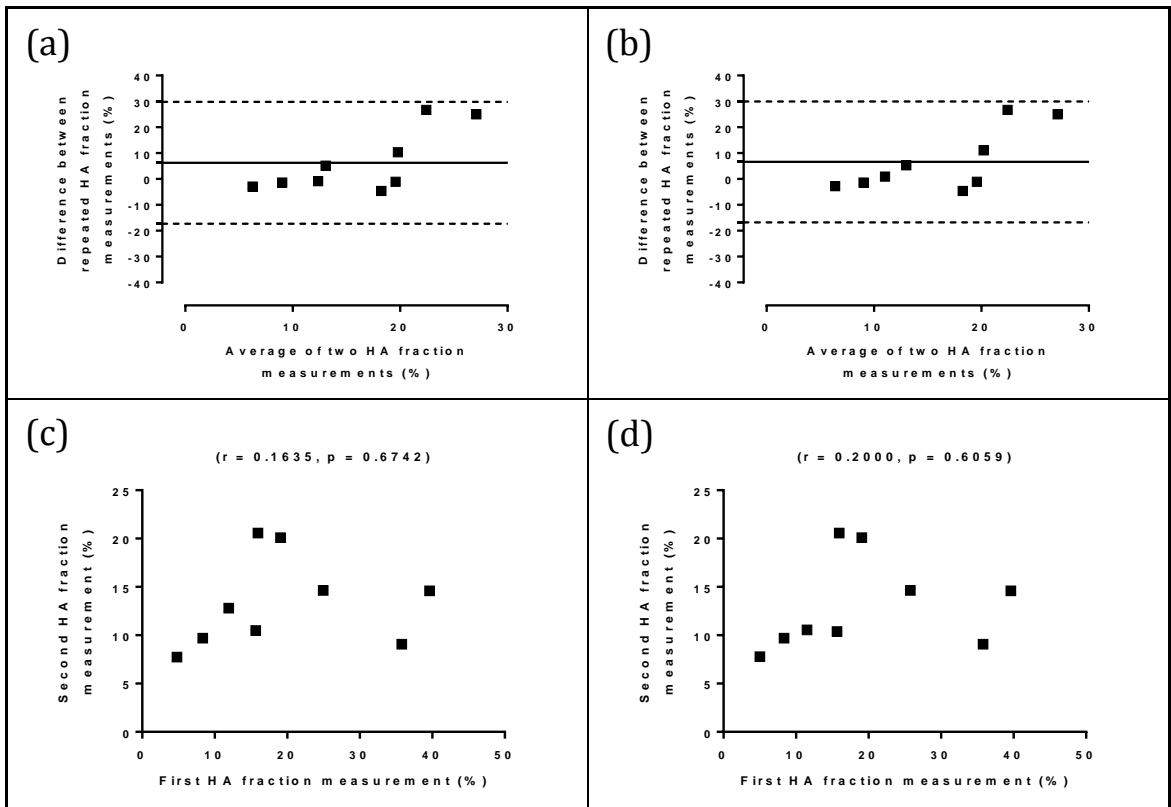


Figure 6.43: Analysis of agreement of repeated HA fraction measurements using uncorrected and corrected AIF hepatic perfusion index modelling
 Bland-Altman and regression analysis of (c, b) uncorrected AIF and (b, d) corrected AIF hepatic perfusion index modelling.

Table 6.14: Summary of reproducibility of perfusion parameters estimated using uncorrected and corrected AIFs alongside PCMRI reproducibility[§]

	UNCORRECTED AIF DUAL INPUT SINGLE COMPARTMENT	CORRECTED AIF DUAL INPUT SINGLE COMPARTMENT	UNCORRECTED AIF HEPATIC PERFUSION INDEX	CORRECTED AIF HEPATIC PERFUSION INDEX	PCMRI
PV perfusion (ml/min/100g)					
Mean difference	-12.4±114.8	-1.229±127.6	-8.187±6.052	9.585	-1.234±2.924
Coefficient of Reproducibility	674.9	750.4	35.583	52.471	19.01
Correlation (<i>r</i>)	-0.2533	-0.2246	-0.1222	0.08333	0.7152
TLBF (ml/min/100g)					
Mean difference	-58.33±133.0	-17.76±150.0	-12.31±8.110	12.95	-8.460±4.860
Coefficient of Reproducibility	782.3	882.0	47.69	66.048	31.60
Correlation (<i>r</i>)	-0.3921	-0.3366	-0.08660	0.08333	0.4858
HA fraction (%)					
Mean difference	-9.26±6.036	-0.3204±4.736	-6.269±4.005	-6.594±3.969	8.643±6.943
Coefficient of Reproducibility	35.49	27.85	23.551	23.336	45.13
Correlation (<i>r</i>)	0.6043	0.4371	0.1635	0.2000	0.5491
Mean Transit Time (seconds)					
Mean difference	-2.374±4.573	-3.659±4.726	-	-	-
Coefficient of Reproducibility	26.89	27.791	-	-	-
Correlation (<i>r</i>)	-0.08422	-0.1627	-	-	-
Distribution Volume (%)					
Mean difference	-16.98	-10.26±7.827	-	-	-
Coefficient of Reproducibility	48.24	46.02	-	-	-
Correlation (<i>r</i>)	-0.06667	0.1075	-	-	-
τ_a (seconds)					
Mean difference	1.126±2.119	-0.1296±1.510	-	-	-
Coefficient of Reproducibility	12.47	8.878	-	-	-
Correlation (<i>r</i>)	0.2364	0.4317	-	-	-
τ_p (seconds)					
Mean difference	-0.5583	0.1307±0.541	-	-	-
Coefficient of Reproducibility	3.853	3.181	-	-	-
Correlation (<i>r</i>)	0.5703	0.7045*	-	-	-

([§]Embodened values in the table highlight the best performing Method for each statistic;

*Pearson's correlation coefficient $p < 0.05$)

6.5.3.4 Validation

Validation of uncorrected and corrected DCE MRI measurements was undertaken using PCMRI measurements of PV perfusion, estimated (subtraction) TLBF and estimated HA fraction measured in the same session as DCE MRI studies. Baseline and seven day reproducibility scans were analysed for twelve subjects (21 datasets). DCE MRI measurements were compared for uncorrected and corrected AIF data.

Table 6.15: DCE MRI perfusion parameters estimated using uncorrected and corrected AIFs and PCMRI validation data

	UNCORRECTED AIF DUAL INPUT SINGLE COMPARTMENT	CORRECTED AIF DUAL INPUT SINGLE COMPARTMENT	UNCORRECTED AIF HEPATIC PERFUSION INDEX	CORRECTED AIF HEPATIC PERFUSION INDEX	PCMRI
PV perfusion (ml/min/100g)	365.7±51.13	388.8±55.23	17.09±2.647	20.00±3.761	56.65±2.698
TLBF (ml/min/100g)	436.7±55.55	462.2±61.37	21.47±3.620	24.83±4.666	71.72±3.318
HA fraction (%)	20.72±3.695	20.45±2.739	16.90±1.899	16.82±1.922	18.91±4.084

(data replicated from table 6.10 for review)

6.5.3.4.1 Dual input single compartment modelling

As previously, dual input single compartment modelling tended to grossly overestimate absolute perfusion measurements (table 6.15). This compromised Bland-Altman analysis so that both the averages and differences of each of validated perfusion measurements were heavily weighted towards each DCE MRI measurement. Plots for absolute perfusion parameters therefore appear to show a linear trend (figures 6.44 (a, b) and 6.45 (a, b)). The smallest mean difference in between DCE MRI and PCMRI PV perfusion (-309.1 ± 51.60 ml/min/100g; $p < 0.0001$) and TLBF (-365.0 ± 55.49 ml/min/100g; $p < 0.0001$) were both demonstrated using uncorrected AIF data. The smallest coefficient of variation for PV perfusion (64.07%) and TLBF (58.29%) was demonstrated in both cases using uncorrected AIF data. These were still larger than those observed for PV perfusion (21.82%) and TLBF (21.20%) using PCMRI. No significant correlations were demonstrated between uncorrected/corrected AIF quantification and PCMRI absolute perfusion measurements (figures 6.44 (c, d) and 6.45 (c, d)).

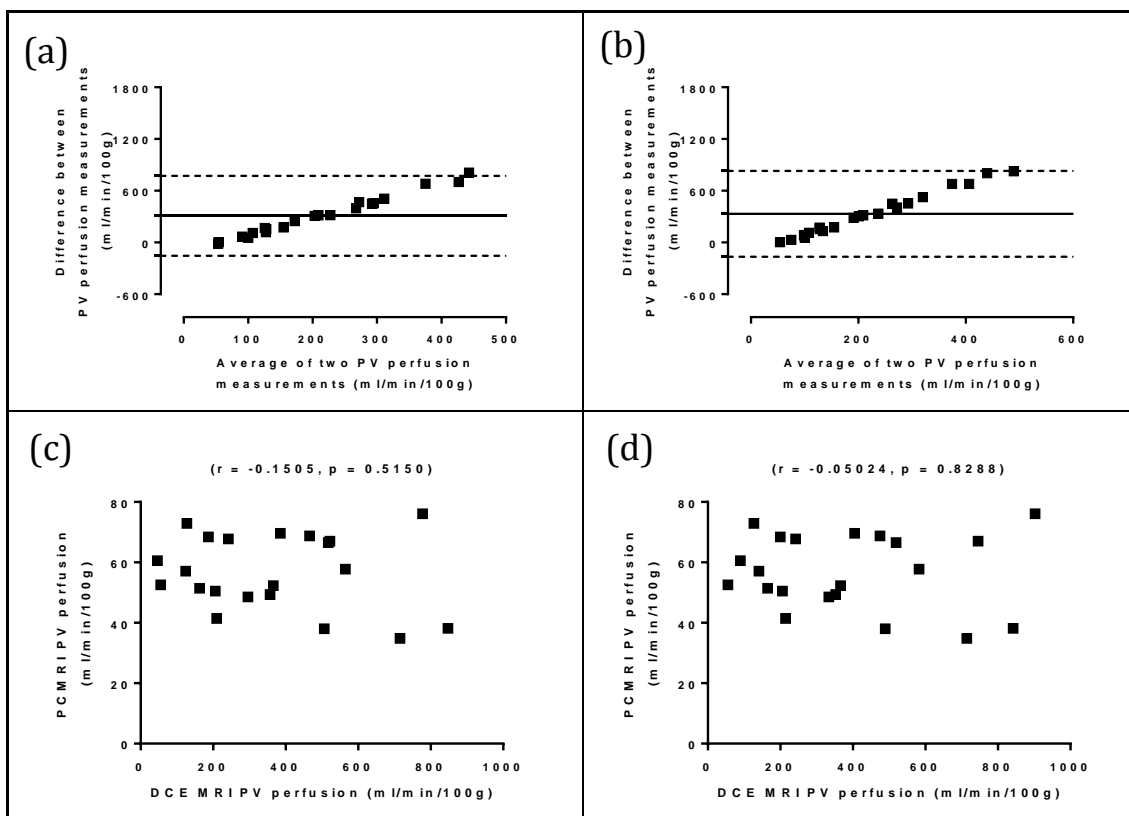


Figure 6.44: Analysis of agreement with PCMRI PV perfusion measurements using uncorrected and corrected AIF dual input single compartment modelling

Bland-Altman and regression analysis of (a, c) uncorrected AIF and (b, d) corrected AIF dual input single compartment modelling.

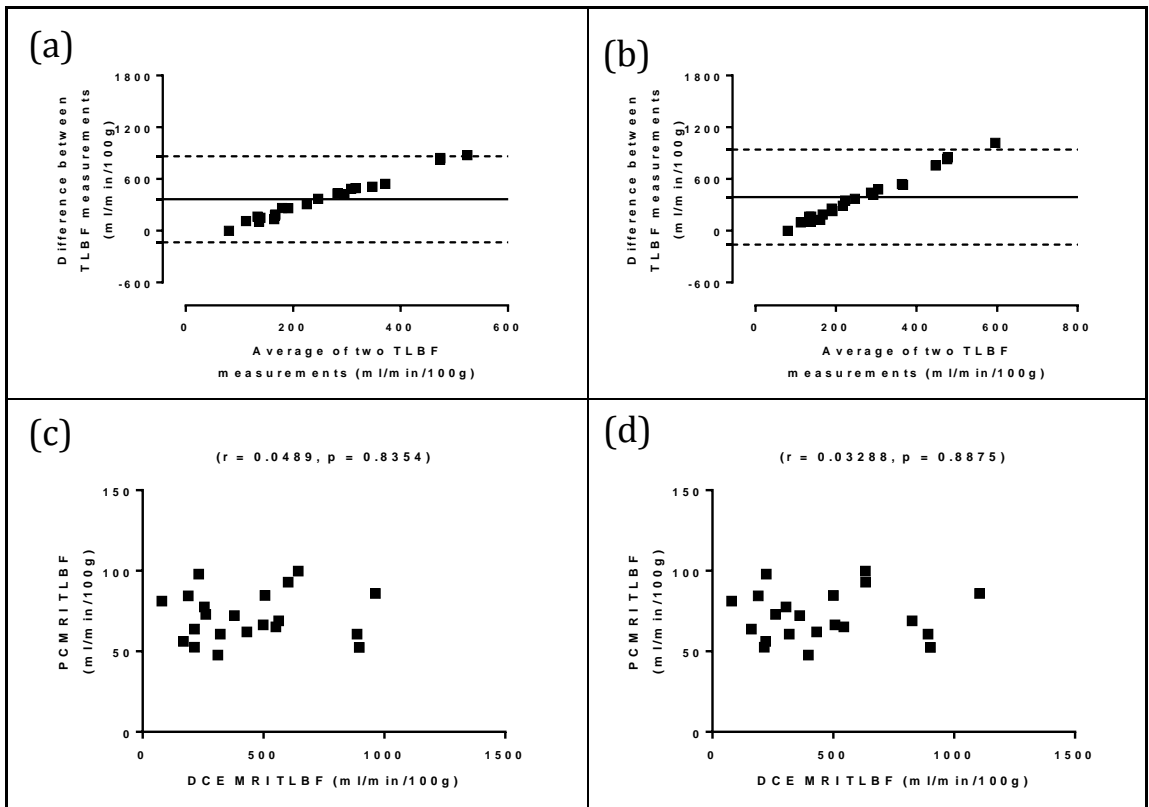


Figure 6.45: Analysis of agreement with PCMRI TLBF measurements using uncorrected and corrected AIF dual input single compartment modelling
 Bland-Altman and regression analysis of (a, c) uncorrected AIF and (b, d) corrected AIF dual input single compartment modelling.

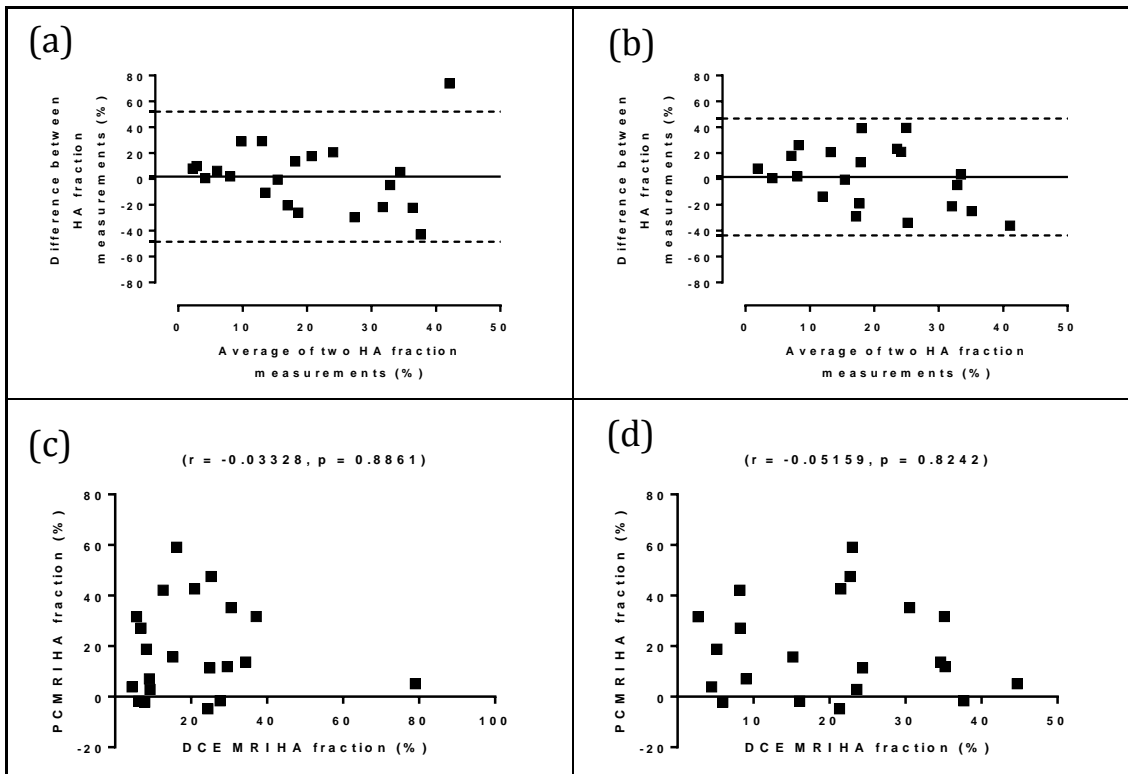


Figure 6.46: Analysis of agreement with PCMRI HA fraction measurements using uncorrected and corrected AIF dual input single compartment modelling

Bland-Altman and regression analysis of (a, c) uncorrected AIF and (b, d) corrected AIF dual input single compartment modelling.

The Bland-Altman charts for uncorrected/corrected AIF dual input single compartment HA fraction as previously demonstrate an expected ‘funneling’ of smaller values (figure 6.46 (a, b)) [412]. No significant differences between uncorrected/corrected AIF DCE MRI and PCMRI HA fraction measurements were demonstrated. The smallest difference in HA fraction ($-1.544 \pm 5.033\%$; $p = 0.7621$) was demonstrated using corrected AIF dual input single compartment modelling. The smallest coefficient of variation (61.34%) was demonstrated using corrected AIF data and this was still smaller than the PCMRI HA fraction coefficient of variation (98.97%). No significant correlations were demonstrated between uncorrected/corrected AIF DCE MRI and PCMRI HA fraction measurements (figure 6.46 (c, d)).

6.5.3.4.2 Hepatic perfusion index modelling

Bland-Altman charts for absolute perfusion parameters are shown in figures 6.47 (a, b) and 6.48 (c, d). Despite the smaller values of absolute perfusion parameters obtained using hepatic perfusion index modelling, significant differences were demonstrated between absolute perfusion parameters using corrected AIF DCE MRI modelling and PCMRI absolute perfusion. The smallest mean difference in PV perfusion (39.56 ml/min/100g; $p < 0.0001$) was demonstrated using uncorrected AIF hepatic perfusion index modelling, while the smallest average difference in TLBF (median 47.86 ml/min/100g; $p < 0.0001$) was demonstrated using corrected AIF hepatic perfusion index modelling.

The smallest coefficient of variation for PV perfusion (70.98%) and TLBF (77.27%) was demonstrated in both cases using uncorrected AIF data. These were still larger than those observed for PV perfusion (21.82%) and TLBF (21.20%) using PCMRI. No significant correlations were demonstrated between uncorrected/corrected AIF quantification and PCMRI absolute perfusion measurements (figures 6.47 (c, d) and 6.48 (c, d)).

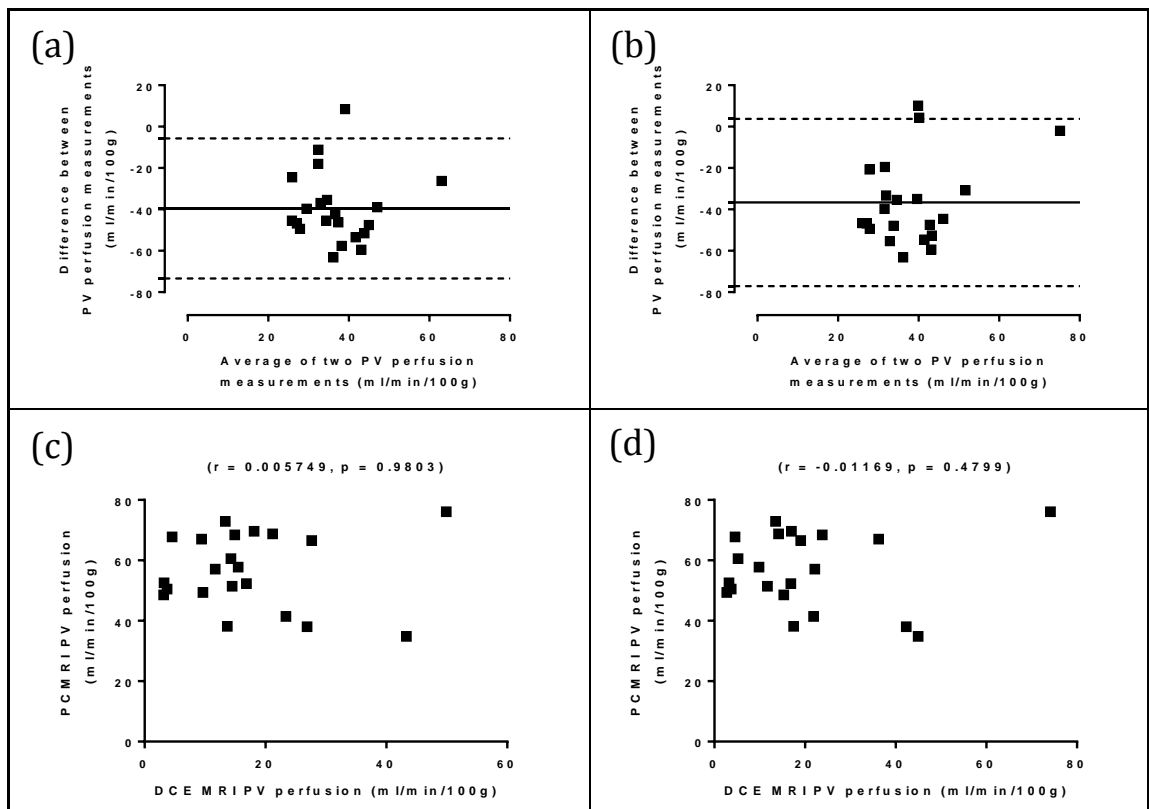


Figure 6.47: Analysis of agreement with PCMRI PV perfusion measurements using uncorrected and corrected AIF hepatic perfusion index modelling

Bland-Altman and regression analysis of (a, c) uncorrected AIF and (b, d) corrected AIF hepatic perfusion index modelling.

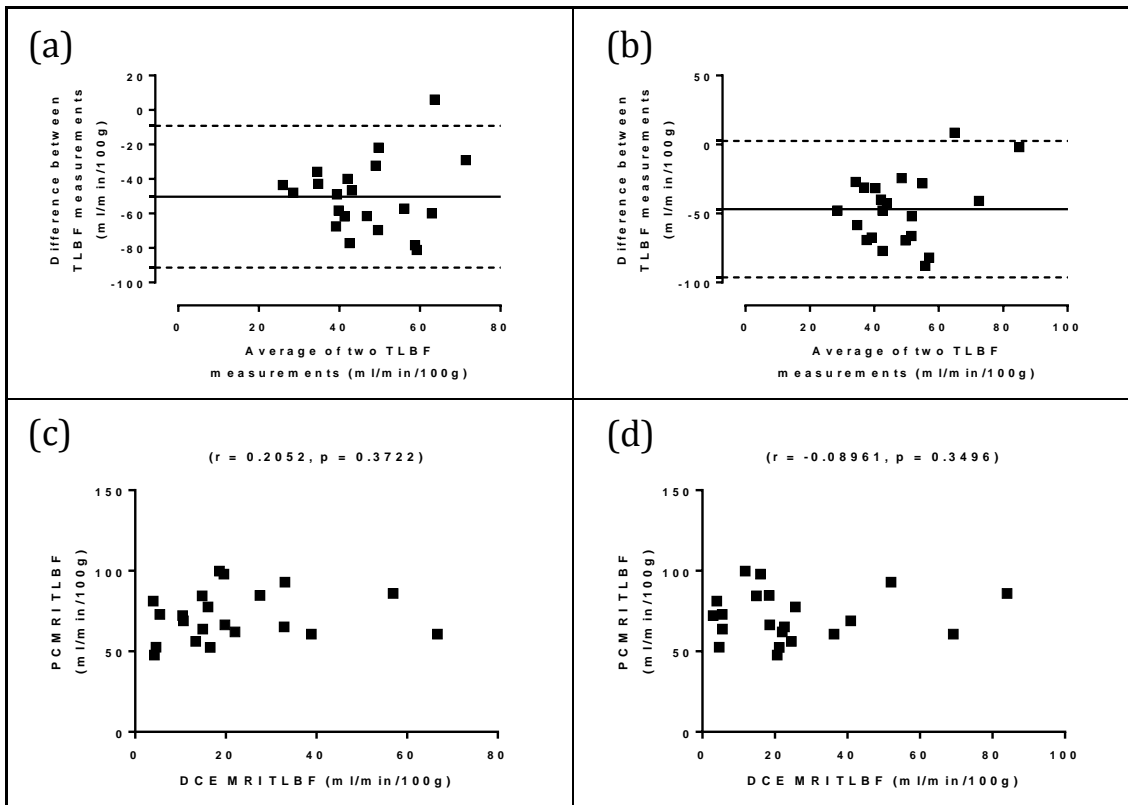


Figure 6.48: Analysis of agreement with PCMRI TLBF measurements using uncorrected and corrected AIF hepatic perfusion index modelling

Bland-Altman and regression analysis of (a, c) uncorrected AIF and (b, d) corrected AIF hepatic perfusion index modelling.

The Bland-Altman charts for uncorrected/corrected AIF hepatic perfusion index HA fraction once again demonstrate an expected ‘funneling’ of smaller values (figure 6.49 (a, b)) [412]. No significant differences between uncorrected/corrected AIF DCE MRI and PCMRI HA fraction measurements were demonstrated. The smallest difference in HA fraction $2.003 \pm 3.703\%$; $p = 0.5945$) and coefficient of variation (51.49%) was demonstrated using uncorrected AIF hepatic perfusion index modelling. The coefficient of variation was also smaller than the coefficient of variation for estimated HA fraction using PCMRI (98.97%). A significant but weak positive correlation ($r = 0.4400$; $p = 0.02300$) was demonstrated between HA fraction measured using corrected AIF hepatic perfusion index modelling and PCMRI (figure 6.49d).

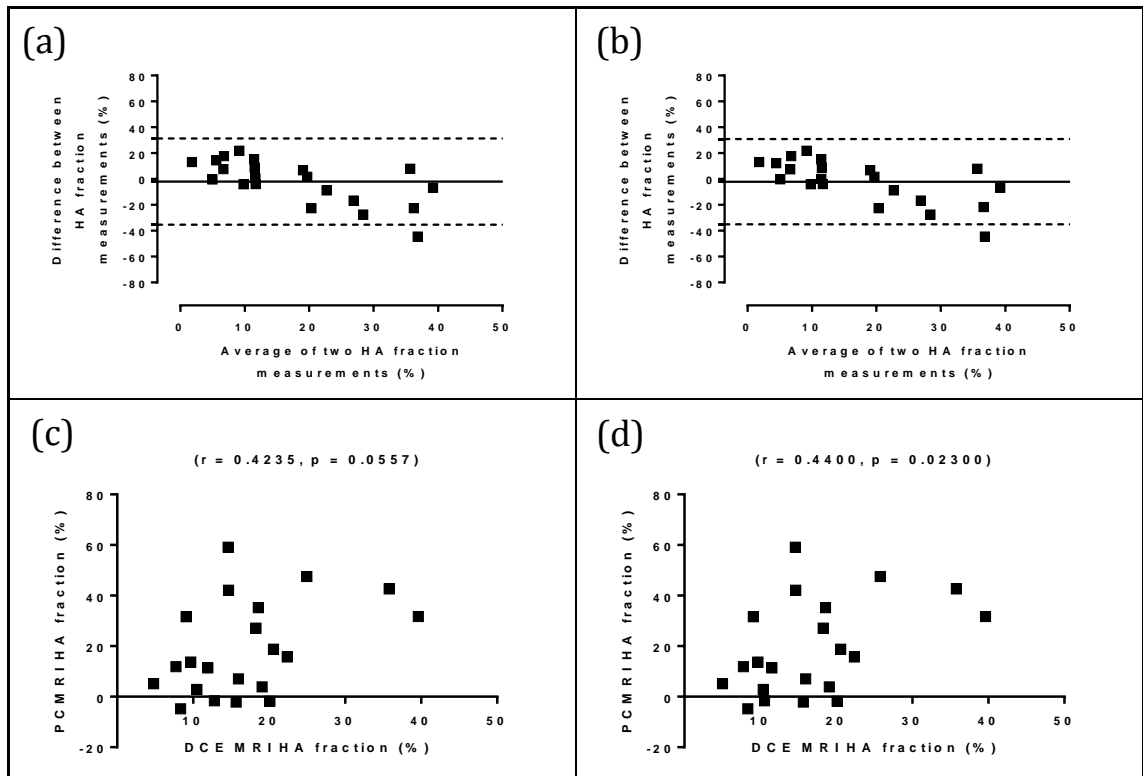


Figure 6.49: Analysis of agreement with PCMRI HA fraction measurements using uncorrected and corrected AIF hepatic perfusion index modelling
 Bland-Altman and regression analysis of (a, c) uncorrected AIF and (b, d) corrected AIF hepatic perfusion index modelling.

Table 6.16: Summary of validation of perfusion parameters estimated using uncorrected and corrected AIF DCE MRI modelling using PCMRI†

	UNCORRECTED AIF DUAL INPUT SINGLE COMPARTMENT	CORRECTED AIF DUAL INPUT SINGLE COMPARTMENT	UNCORRECTED AIF HEPATIC PERFUSION INDEX	CORRECTED AIF HEPATIC PERFUSION INDEX
PV perfusion (ml/min/100g)				
Mean difference	-309.1±51.60*	-332.1±55.43*	39.56±3.769*	44.61*
Coefficient of Variation	64.07%	65.10%	70.98%	86.17%
Correlation (r)	-0.1505	-0.05024	0.005749	-0.01169
TLBF (ml/min/100g)				
Mean difference	-365.0±55.49*	-390.5±61.35*	48.97*	47.86*
Coefficient of Variation	58.29%	60.85%	77.27%	86.12%
Correlation (r)	0.04829	0.03288	0.2052	-0.08961
HA fraction (%)				
Mean difference	-1.815±5.598	-1.544±5.033	2.003±3.703	2.085±3.669
Coefficient of Variation	81.72%	61.34%	51.49%	52.35%
Correlation (r)	-0.03328	-0.05159	0.4235	0.4400*

(†Emboldened values in the table highlight the best performing Method for each statistic;
 *paired t-test/Wilcoxon matched pairs/Pearson's/Spearman's rank correlation coefficient p<0.05)

6.5.4 DISCUSSION

We have demonstrated that AIF correction using PCMRI aortic root flow data is feasible and shown that corrected AIFs can be used for dual input single compartment and hepatic perfusion index modelling. We have previously demonstrated encouraging validation data and reasonable seven day reproducibility of PCMRI aortic root flow measurements section 5.5.3.5. We have also previously shown that measuring AIFs directly can be troublesome and on this basis, the rationale for correcting AIFs using PCMRI aortic root flow measurements was to improve seven day reproducibility and accuracy of estimated perfusion parameters. Our data demonstrated that this was not necessarily the case.

6.5.4.1 Dual input single compartment modelling

The effects of AIF correction on estimated hepatic perfusion parameters were subtle. Gross overestimation of absolute perfusion parameters remained a problem using dual input single compartment modelling. More concerningly, AIF correction increased the spread of data, with a reduced standard deviation only detected for HA fraction, MTT and AIF delays. AIF correction did however have a positive effect on reproducibility, reducing the mean difference after seven days of all perfusion parameters, with the exception of MTT. Improvements in the coefficient of reproducibility were only demonstrated for HA fraction, DV and VIF delays. Contrastingly, the modest positive correlation between repeated HA fraction measurements using uncorrected AIF data declined after AIF correction (uncorrected AIF $r = 0.6043$; $p = 0.0848$ vs corrected AIF $r = 0.4371$; $p = 0.2394$). Validation with volume normalised PCMRI bulk flow highlighted gross over estimation of absolute perfusion parameters. HA fraction measurements with PCMRI however, demonstrated a reduction in mean difference and coefficient of variation after AIF correction.

6.5.4.2 Hepatic perfusion index modelling

The effects of AIF correction were largely negative using the hepatic perfusion index method. AIF correction resulted in an increase in the spread of all perfusion parameters, although only a negligible increase in standard deviation was detected for HA fraction (8.702% uncorrected AIF vs 8.808% corrected AIF). Reproducibility was unaffected by AIF correction, with a minor reduction demonstrated for the HA fraction coefficient of reproducibility (23.551% uncorrected AIF vs 23.336% corrected AIF). Validation with volume normalised PCMRI bulk flow demonstrated a small reduction in the mean difference between TLBF measurements after AIF correction (48.97 ml/min/100g uncorrected AIF vs 47.86 ml/min/100g corrected AIF).

There are several reasons which may explain the lacklustre effects of AIF correction. The method itself is reliant on several important assumptions which though theoretically sound may have practical flaws. The first of these is the derivation of a first pass curve using a gamma variate function. This is an established technique in nuclear medicine but one that has not been applied extensively to MRI AIFs. The raw SI AIFs have variable positive baseline values (S_0) mainly dependent on the blood pool T1 and inflow effects. It is the adjustment of the raw SI curve to a new estimated baseline SI (S_0'), which drives the modification of the CA concentration AIF. Because of the way SI is converted to CA concentration, the effects of changing the baseline SI affect the entire AIF curve, including the peak AIF SI. In doing so, it inherently corrects errors in baseline SI estimation, but does not address the issue of potential signal loss resulting from T2* effects at the VIF peak. It is worth noting that this method was described at 1.5T, where such effects are less significant than at the higher field strength used in this study.

Finally, both modelling approaches are reliant on a PVIF as well as the AIF. Correction of one without correction of the other could in principle account for the limited impact on overall estimated perfusion parameters. Unlike AIF curves, PVIF curves have a slow rise compatible with low pressure and relatively non-pulsatile splanchnic flow. Derivation of a first pass curve using the methods employed would therefore be unfeasible. Correction of the PVIF curve by simply assuming the new estimated baseline SI (S_0'), would only be acceptable if raw baseline SI at the site of AIF and VIF sampling were identical – a phenomenon which is not supported by theory or the data collected in this study. Of note, PVIF curves are less prone to VIF sampling errors, because of their slower flow and lower peak CA concentration compared to their AIF counterparts and therefore (in theory) less likely to benefit from correction than AIFs.

6.5.5 CONCLUSION

We have demonstrated that clinical DCE MRI AIFs are amenable to correction using PCMRI aortic flow measurements, but that these have subtle and mixed effects on estimated perfusion parameters using the dual input single compartment model and largely deleterious effects on the hepatic perfusion index model. Importantly, AIF correction improves dual input single compartment HA fraction seven-day reproducibility and PCMRI validation data. AIF correction is therefore potentially valuable in improving the reproducibility and accuracy of DCE MRI relative perfusion measurements.

6.6 COMBINED DCE AND PCMRI – PART II – TISSUE PERFUSION CORRECTION

6.6.1 BACKGROUND

In previous sections of this Chapter, we implemented progressive refinements to improve the reproducibility and accuracy of DCE MRI measurements. DCE MRI provides a feasible strategy for relative quantification (HA fraction), but absolute quantification remains disappointing. We have previously demonstrated in both animal models and normal volunteers that absolute quantification with PCMRI is both accurate and reproducible. Unlike DCE MRI however, PCMRI fails to deliver any information about regional perfusion. In this section, we propose a novel method for correcting DCE MRI absolute perfusion measurements using PCMRI estimated TLBF. It would be anticipated that such a method would deliver (a) physiological feasible and accurate DCE MRI absolute quantification, (b) improved reproducibility of DCE MRI absolute quantification and (c) reliable evaluation and investigation of regional differences in absolute perfusion across the liver.

6.6.1.1 Conceptual development

For a given ROI or pixel, dual input single compartment modelling can be used to estimate ' k_{1a} ' and ' k_{1p} ', inflow constants weighted towards arterial and portal venous perfusion respectively. Traditionally, where ' F ' represents perfusion, ' E ' represents extraction fraction and ' Hct_{SV} ' represents small vessel haematocrit, we can calculate perfusion using the following expressions:

$$F_{\text{Arterial perfusion}} (\text{ml/s/g}) = \frac{k_{1a}}{E(1 - Hct_{SV})}$$

and:

$$F_{\text{PV perfusion}} (\text{ml/s/g}) = \frac{k_{1p}}{E(1 - Hct_{SV})} \quad (\text{Equations 6.17 and 6.18})$$

Quantification is therefore based on the assumption that the extraction fraction (E) is equal to 1.0, (as theoretically contrast agent can pass freely through the vascular endothelium to the interstitium and space of Disse) and the small vessel haematocrit (Hct_{SV}) is constant at 0.25.

The sum of the arterial and portal venous inflow constants (k_1) is weighted towards total perfusion in a given pixel/ROI, and can be expressed as:

$$k_1 = k_{1a} + k_{1p} \quad (\text{Equation 6.19})$$

Previously, we analysed DCE MRI data on five 5 mm slices, each separated by 10 mm. It would be reasonable to assume that average ' k_1 ' across n pixels of hepatic parenchyma from these five slices ($\overline{k_1}$), should in theory be directly proportional to PCMRI estimated (caval subtraction) bulk flow (Q_{TLBF}) normalised to total liver volume (V_{liver}):

$$\overline{k_1} = \frac{\sum(k_{1(1)} + \dots + k_{1(n)})}{n} \quad (\text{Equation 6.20})$$

and:

$$\overline{k_1} \propto \frac{Q_{TLBF}}{V_{\text{liver}}} \quad (\text{Equation 6.21})$$

The estimated ' k_1 ', for a given pixel can then be corrected by normalising to ' $\overline{k_1}$ ' and an adjusted estimate of total perfusion for that pixel (F') can be obtained by multiplying through by PCMRI estimated TLBF normalised to liver volume:

$$F' = \left(\frac{k_1}{\overline{k_1}} \right) \left(\frac{Q_{TLBF}}{V_{\text{liver}}} \right) \quad (\text{Equation 6.22})$$

Using HA fraction measured in the usual way from uncorrected ' k_{1a} ' and ' k_{1p} ' data, pixel wise PV and HA perfusion data can be obtained and physiologically feasible and accurate pixel wise estimates of PV and HA perfusion can be made.

The ability to correct parametric maps is of course based on the presence of DCE MRI maps inclusive of purely hepatic parenchyma and no other tissue. Such data could be obtained by careful manual segmentation, but this would be error prone and subject to inter-observer variation. An alternative method would be to threshold parametric maps in such a way as to exclude vessels or corrupt data. Enhancement curves for pixels overlying arterial, portal venous and hepatic venous vessels demonstrate fundamentally different enhancement curves which are less successfully modelled by the dual input single compartment model (figure 6.50).

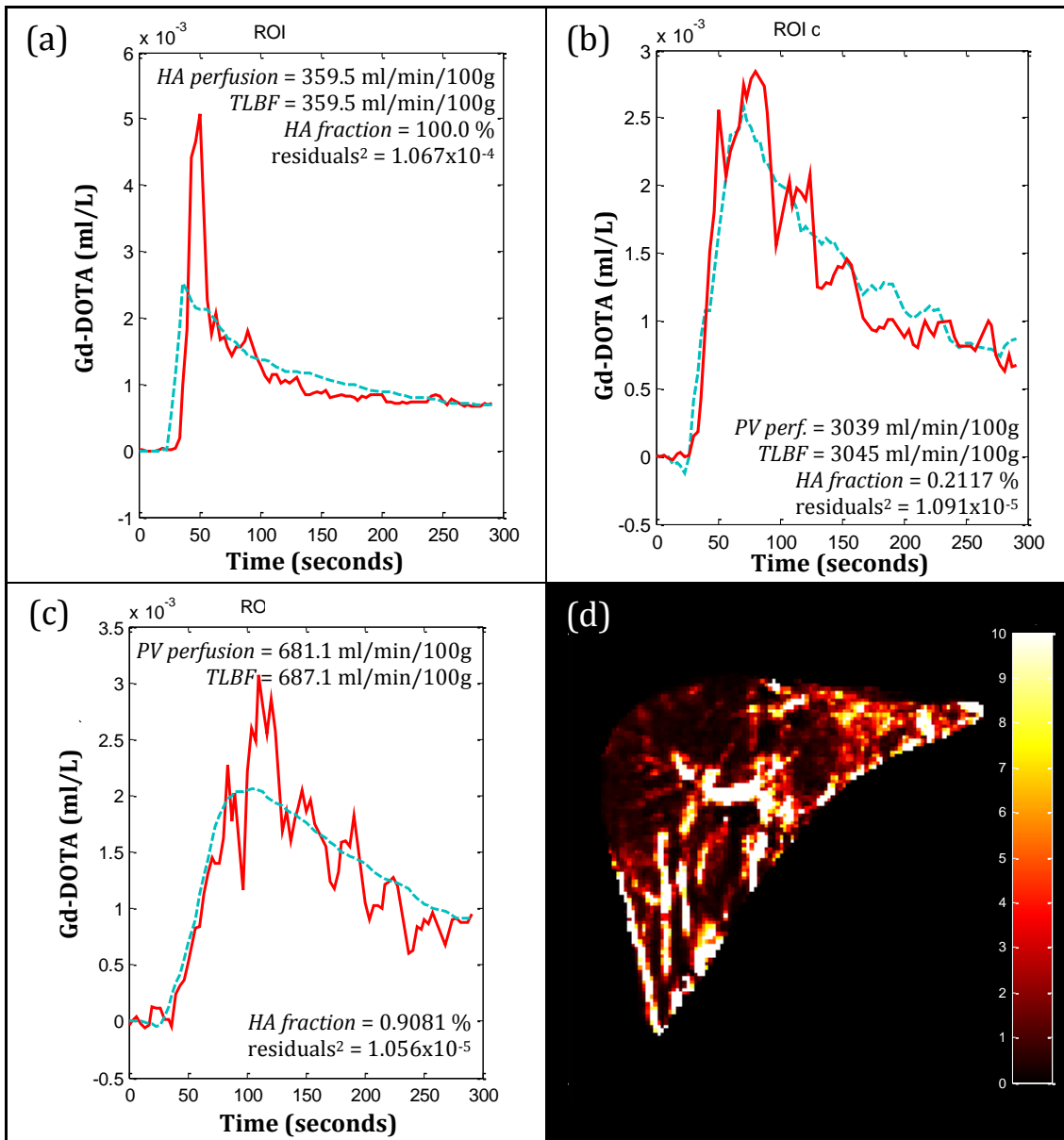


Figure 6.50: Hepatic parenchymal thresholding using residual sum of squares

Enhancement curves and curve fits for ROIs placed over parenchymal (a) arterial vessel, (b) portal venous vessel and (c) hepatic venous vessel, demonstrating elevated fit residual sum of squares, at least one order of magnitude over the parenchymal enhancement curve fits.

Parametric pixel-wise mapping of the residual sum of squares for a single slice (d), using a scale of $0-10.0 \times 10^{-6}$ (far right) visually highlights the poorer curve fits recorded over vascular tissues (vessels predominantly shown as white).

Thresholding based on the residual sum of squares could then be used to automate exclusion of this data and create a map of purely hepatic parenchymal enhancement data.

In this section, we apply our novel method for correction of DCE MRI absolute perfusion measurements to study regional differences in absolute perfusion. We compare our corrected measurements with regional DCE MRI perfusion parameters using previously developed refinements and assess the effects of our novel method on (i) seven day

reproducibility and (ii) comparison of regional tissue perfusion estimates with volume normalised PCMRI flow measurements.

6.6.2 METHODS

6.6.2.1 Subjects and preparation

As described in section 6.3.2.1.

6.6.2.2 Clinical PCMRI

As described in section 5.5.2. PCMRI studies were planned orthogonal to the IVC in at a (i) supra-renal but infra-hepatic position (proximal IVC) and a (ii) supra-hepatic but infra-cardiac position (distal IVC). Studies were performed in expiratory breath-hold and cardiac gated using peripheral pulse oximetry. The following settings were used: TR/TE 8.70/5.22 seconds, flip angle = 10°, matrix size 336x336, field of view 271x210 mm, bandwidth 210 Hz/pixel, slice thickness 5 mm, 7 cardiac cycle phases and velocity encoding settings of 60 and 80 cm/s for proximal and distal IVC studies respectively. Each measurement was repeated three times in succession. Quantification was performed using the freely available software package, Segment (Medviso, Lund, Sweden) and TLBF was estimated by subtracting proximal IVC from distal IVC bulk flow.

6.6.2.3 Volumetric assessment and bulk flow normalisation

PCMRI bulk flow measurements were normalised to liver volume as described in section 5.5.2.4. Liver volume was measured using 5 mm slice thickness gradient echo coronal anatomical images. Segmentation was performed manually using Amira (FEI Visualisation Sciences Group, Burlington, USA). A tissue density of 1.0 g/ml was assumed based on [193].

6.6.2.4 Clinical DCE MRI

As described in section 6.3.2.2.

6.6.2.5 Post-processing

To enable accurate comparison with previous data, the same ROIs were used as previously. Three parenchymal ROIs were positioned on each slice (total 15 ROIs), firstly in the right upper region (segments VII/VIII), left liver (segments II/III) and right lower region (segments V/VI). Regional analysis for each of segments II/III, V/VI and VII/VIII was based on averages from ROIs across five slices. Absolute perfusion data was then subjected to (a) dual input single compartment modelling with pre-estimation and constrained free modelling of VIF delays and cardiac output AIF correction and (b) the

latter with additional correction using volume normalised PCMRI estimated TLBF measurements. PCMRI correction was applied to absolute perfusion measurements, but relative perfusion measurements (HA fraction, MTT and DV) were constant for both corrected and uncorrected data sets.

6.6.2.6 Reproducibility studies

As described in section 6.3.2.5.

6.6.2.7 Validation studies

As described in section 6.3.2.6.

6.6.2.8 Statistical analysis

Kolmogorov-Smirnov tests were used to confirm normality of variable distributions. Repeated measures one-way analysis of variance (ANOVA) with corrections for non-sphericity were used to compare perfusion parameters measured across different regions. Post-hoc Tukey's test was then applied where significant regional differences were identified. Regional uncorrected absolute and relative DCE MRI perfusion parameters were analysed in addition to regional PCMRI corrected absolute perfusion measurements. Paired t-tests/Wilcoxon matched pairs signed rank tests were used to compare absolute regional uncorrected and corrected DCE MRI perfusion parameters. Reproducibility and comparative studies were also assessed using paired t-tests/Wilcoxon matched pairs signed rank tests, Bland-Altman analysis of agreement with calculation of the coefficient of repeatability and assessment of correlation between repeated/validated measurements using Pearson's or Spearman's correlation coefficient for parametric/non-parametric data as appropriate. Assessment of reproducibility and comparison of uncorrected and corrected DCE MRI perfusion parameters was undertaken for each of the three regions. The threshold of statistical significance was defined to be $p < 0.05$.

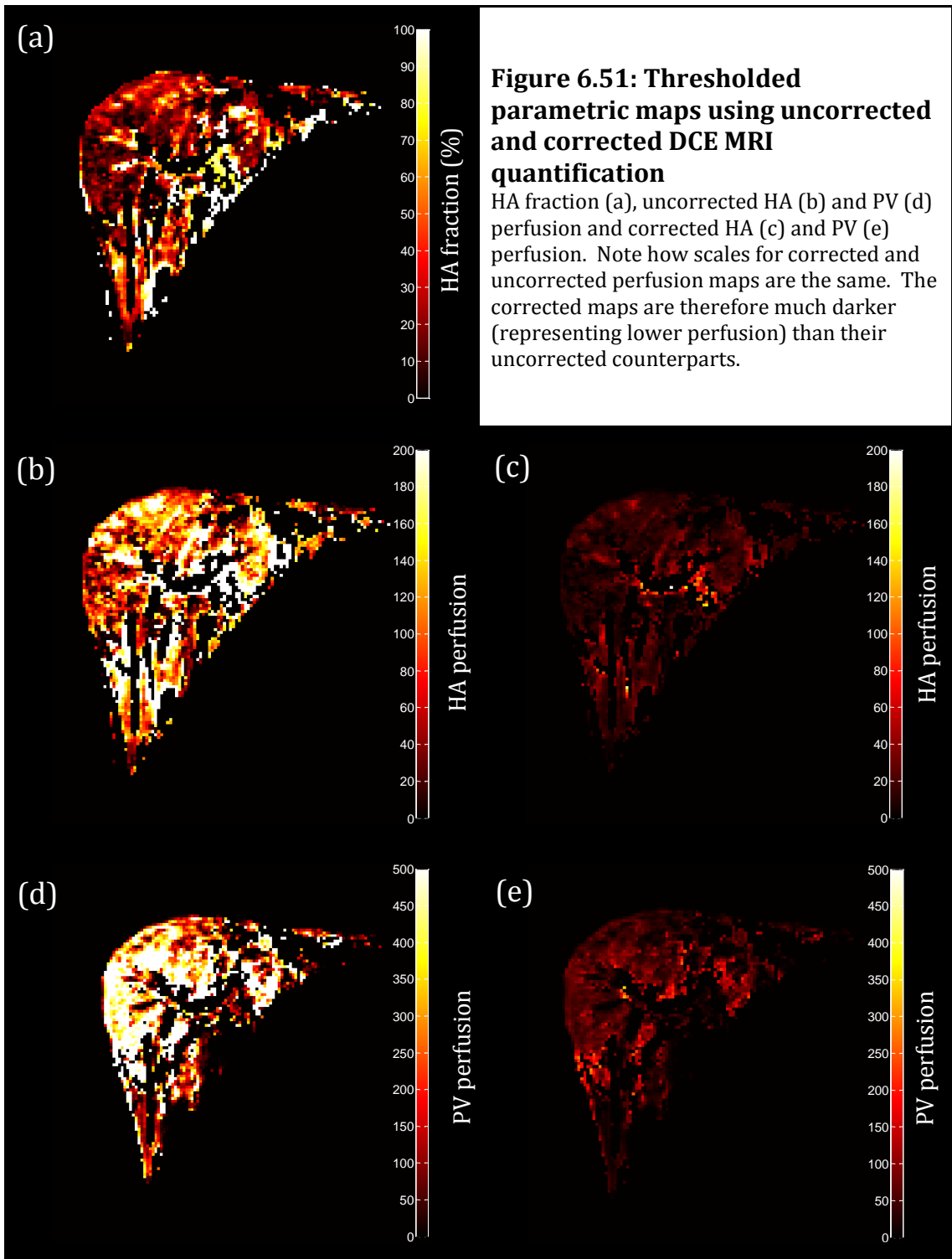
6.6.3 RESULTS

6.6.3.1 Cohort features

Data was collected in twelve normal volunteers. Male subjects ($n = 6$) had a mean age of 26.7 ± 1.55 years and female subjects ($n = 6$) had a mean age of 30.2 ± 2.37 years. One subject was excluded because of significant artefact degrading data from segments II/III. Seven day reproducibility data was therefore available for eight subjects ($n = 4$ male, $n = 4$ female).

6.6.3.2 Parametric mapping

A sample data set was used to demonstrate dual input single compartment modelling residual sum of squares thresholding for parametric mapping of hepatic parenchyma. ROIs placed over thresholded parenchyma were subjected to uncorrected and corrected DCE MRI quantification (figure 6.51, table 6.17).



6.6.3.3 Regional perfusion studies

Data for each of the perfusion parameters for each segment is plotted for uncorrected and PCMRI corrected data in figure 6.52 and tabulated in table 6.17. No significant differences were demonstrated between absolute and relative perfusion parameters for any of the three regions. Regional differences between TLBF approached significance ($F(2,52) = 1.628$; $p = 0.05030$), but there were no significant differences between regions demonstrated on post-hoc testing. Significant differences were demonstrated between regional residual sum of squares ($F(2,52) = 6.333$; $p = 0.0027$), with significant differences demonstrated on post-hoc testing between segments II/III and the other two regions, but not between segments V/VI and VII/VIII.

Significant differences were demonstrated between uncorrected and PCMRI corrected absolute perfusion parameters in segments II/III PV perfusion (mean difference -400.5 ± 74.54 ml/min/100g; $p < 0.0001$) and TLBF (mean difference -462.2 ± 79.71 ml/min/100g; $p < 0.0001$); segments V/VI PV perfusion (mean difference -337.8 ± 50.95 ml/min/100g; $p < 0.0001$) and TLBF (mean difference -410.5 ± 62.72 ml/min/100g; $p < 0.0001$); and finally segments VII/VIII PV perfusion (mean difference -400.3 ± 62.62 ml/min/100g; $p < 0.0001$) and TLBF (mean difference -453.8 ± 67.61 ml/min/100g; $p < 0.0001$).

Table 6.17: Regional DCE MRI perfusion parameters for uncorrected and PCMRI corrected dual input single compartment modelling

	SEGMENTS II/III		SEGMENTS V/VI		SEGMENTS VII/VIII	
	UNCORRECTED	PCMRI CORRECTED	UNCORRECTED	PCMRI CORRECTED	UNCORRECTED	PCMRI CORRECTED
PV perfusion (ml/min/100g)	460.8±77.55	60.27±5.171*	395.2±52.51	57.43±4.756*	463.2±62.79	62.90±2.886*
TLBF (ml/min/100g)	535.5±81.83	73.31±6.028*	481.5±64.24	71.00±5.600*	526.2±67.22	72.40±3.581*
HA fraction (%)		17.85±2.847		18.51±3.136		12.39±2.608
Mean Transit Time (s)		17.42±2.334		18.04±2.560		14.06±1.952
Distribution Volume (%)		76.87±7.136		76.16±4.505		69.18±4.809
Residuals ²		6.525x10 ⁻⁷ ±1.305x10 ⁻⁷		2.829x10 ⁻⁷ ±4.335x10 ⁻⁸ †		2.702x10 ⁻⁷ ±3.932x10 ⁻⁸ †

(*paired t-test p < 0.0001, †post-hoc Tukey test p < 0.05 relative to segments II/III)

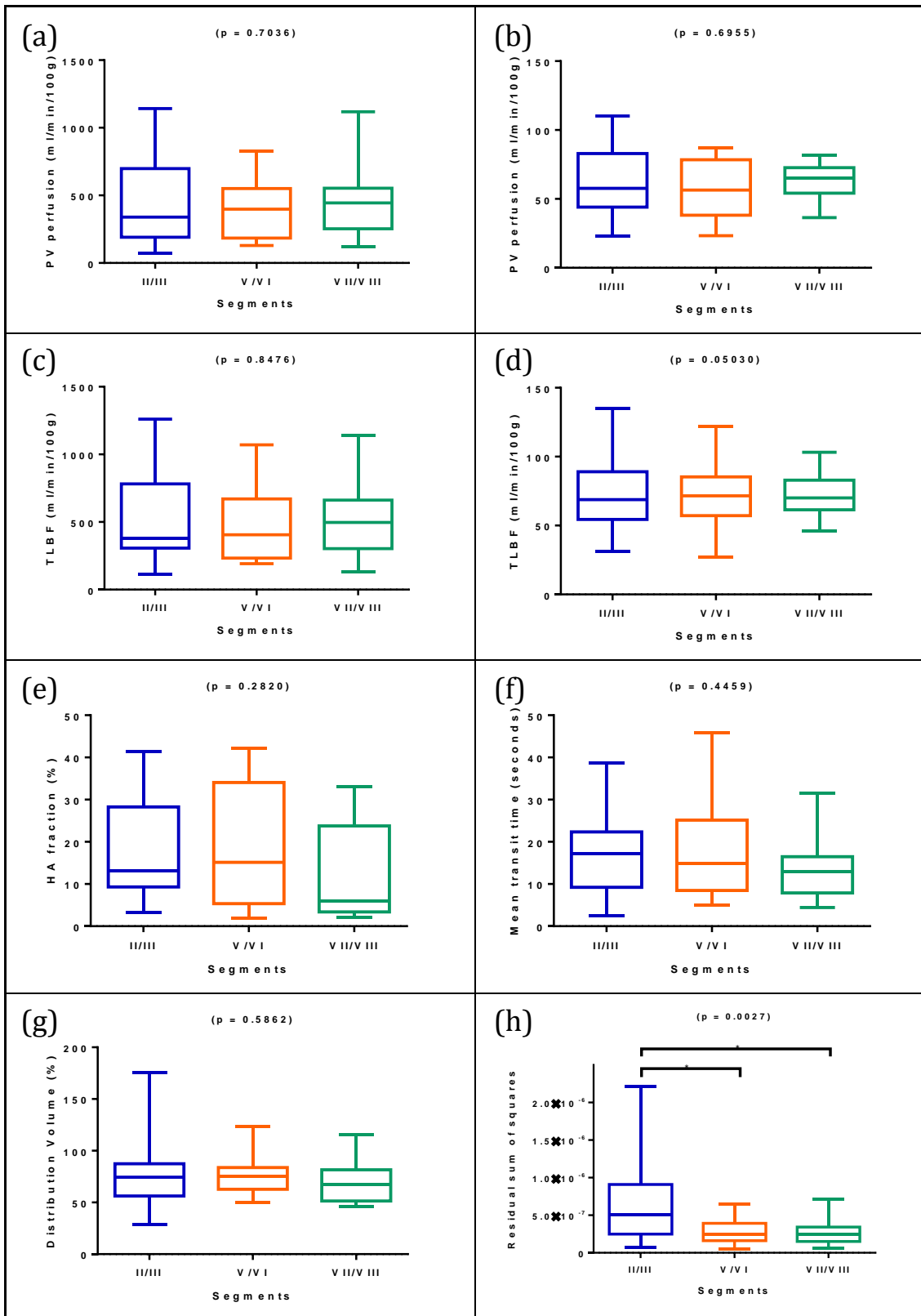


Figure 6.52: Regional uncorrected and PCMRI corrected DCE MRI hepatic perfusion parameters

Box and whisker plots for each of the perfusion parameters demonstrate regional differences in perfusion parameters for uncorrected ((a) and (c)) and corrected ((b) and (d)) absolute perfusion parameters and relative perfusion parameters ((e), (f) and (g)). p-values are quoted for one-way ANOVA tests, with significant differences on post-hoc testing (*).

6.6.3.4 Reproducibility

Reproducibility was assessed using the same protocol with the same scanner in the same subjects exactly seven days after the initial study. Repeat measurements were obtained in normal volunteers ($n = 8$). All reproducibility analysis data are summarised and presented alongside seven day PCMRI reproducibility for comparison in table 6.18. Figures in this section have been arranged so that uncorrected and PCMRI corrected Bland-Altman diagrams are alongside each other to facilitate inspection of the limits of agreement.

No significant differences were demonstrated between repeated PV perfusion (figure 6.53) and TLBF (figure 6.54) measured with uncorrected and PCMRI corrected dual input single compartment modelling in segments II/III. PCMRI correction resulted in a substantial reduction in the coefficient of reproducibility for both absolute perfusion parameters. There was a reduction in the mean difference for PV perfusion (-24.15 ± 212.7 ml/min/100g uncorrected vs -9.308 ± 13.44 ml/min/100g corrected) but not TLBF (-1.233 ± 226.2 ml/min/100g uncorrected vs -6.041 ± 11.66 ml/min/100g corrected) as a result of PCMRI correction. The standard error for both absolute perfusion parameters was reduced by PCMRI correction. No correlations were demonstrated between repeated absolute perfusion measurements using uncorrected and PCMRI corrected modelling (table 6.18).

No significant differences were demonstrated between repeated HA fraction, MTT and DV measurements in segments II/III (figure 6.55). The mean differences between repeated MTT (mean difference 5.843 ± 6.354 seconds) and DV (mean difference $26.38 \pm 15.08\%$) measurements were larger than for the other regions. No correlations were demonstrated between repeated HA fraction, MTT or DV measurements in segments II/III (figure 6.54; table 6.18).

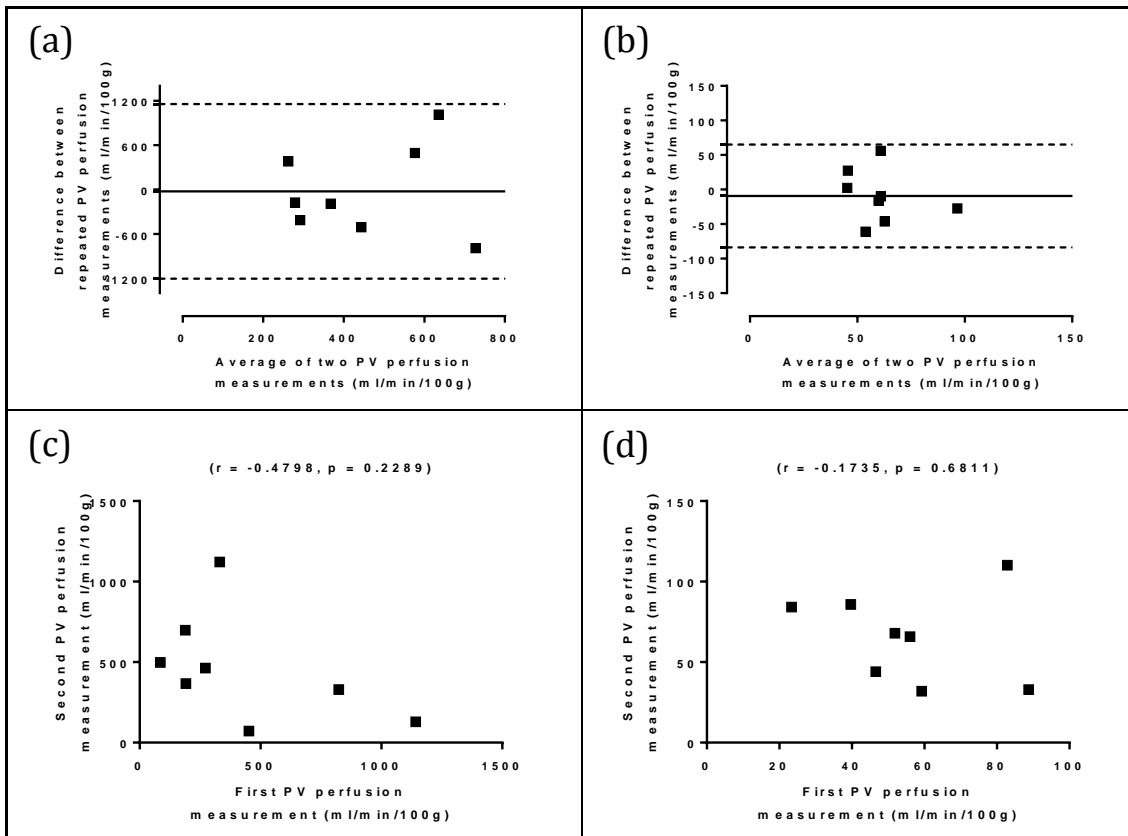


Figure 6.53: Analysis of agreement of segment II/III PV perfusion reproducibility using uncorrected and PCMRI corrected DCE MRI dual input single compartment modelling

Bland-Altman and regression analysis of (a, c) uncorrected and (b, d) PCMRI corrected dual input single compartment modelling.

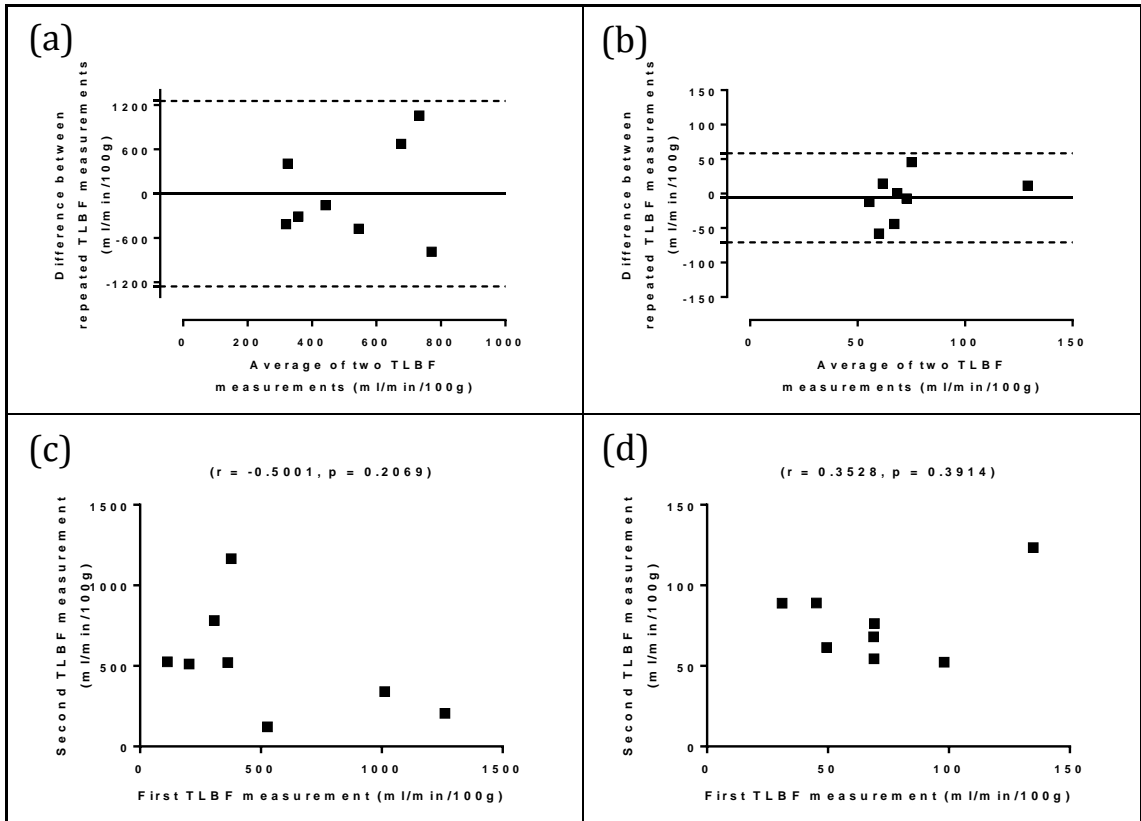


Figure 6.54: Analysis of agreement of segment II/III TLBF reproducibility using uncorrected and PCMRI corrected DCE MRI dual input single compartment modelling

Bland-Altman and regression analysis of (a, c) uncorrected and (b, d) PCMRI corrected dual input single compartment modelling.

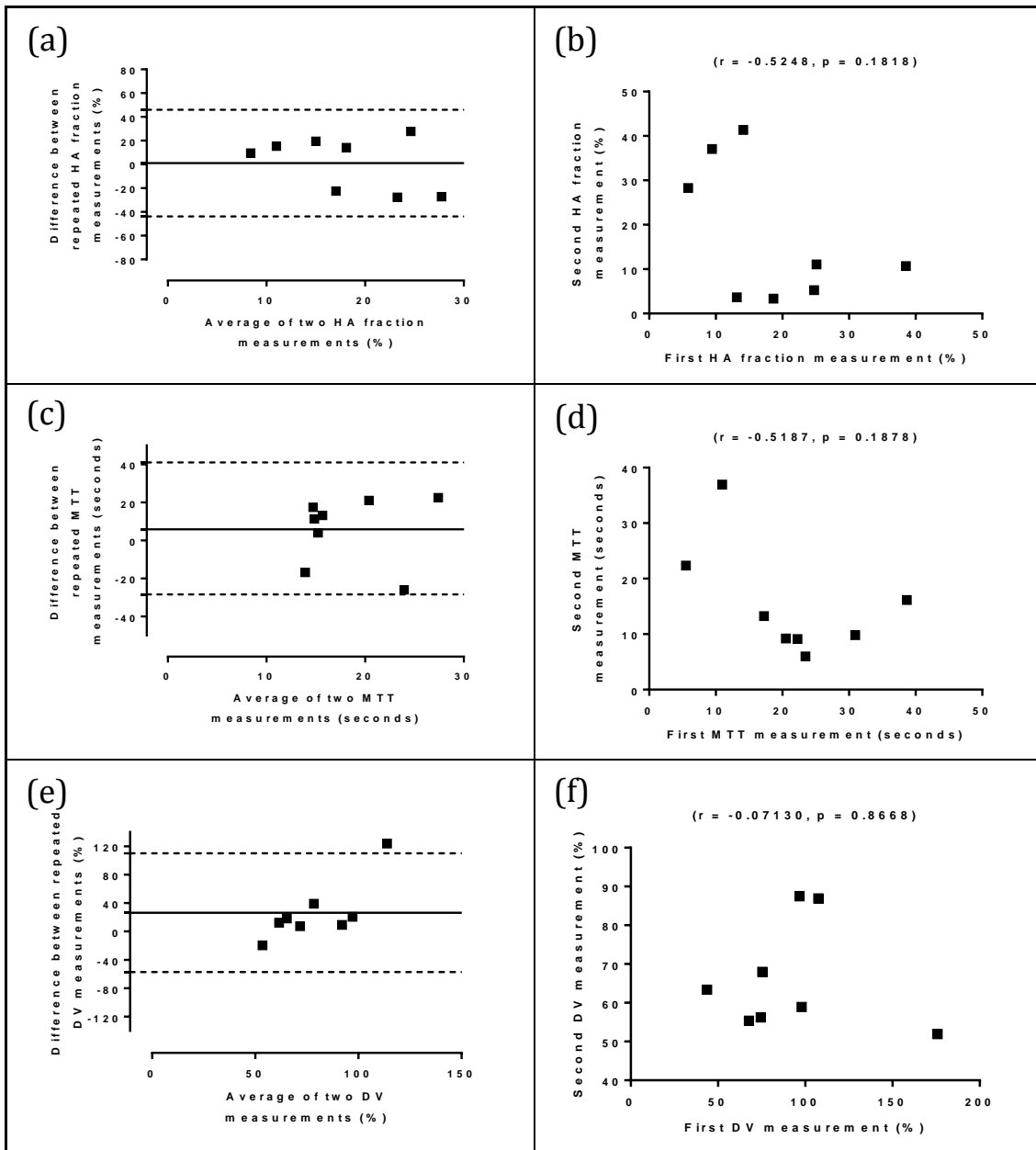


Figure 6.55: Analysis of agreement of segment II/III relative perfusion parameter reproducibility using DCE MRI dual input single compartment modelling

Bland-Altman and regression analysis of (a, b) HA fraction, (c, d) mean transit time and (e, f) distribution volume.

No significant differences were demonstrated between repeated PV perfusion (figure 6.55) and TLBF (figure 6.56) measured with uncorrected and PCMRI corrected dual input single compartment modelling in segments V/VI. PCMRI correction resulted in a substantial improvement in the coefficient of reproducibility for both absolute perfusion parameters. There was a reduction in the mean difference for PV perfusion (51.49 ± 128.6 ml/min/100g uncorrected vs -0.1307 ± 8.435 ml/min/100g corrected) and TLBF (82.35 ± 169.9 ml/min/100g uncorrected vs -0.7303 ± 10.84 ml/min/100g corrected) as a result of PCMRI correction. The standard error for both absolute perfusion parameters was also reduced by PCMRI correction. No correlations were demonstrated between

repeated absolute perfusion measurements using uncorrected and PCMRI corrected modelling (table 6.18).

No significant differences were demonstrated between repeated HA fraction, MTT and DV measurements in segments V/VI (figure 6.58). The mean differences between repeated HA fraction (mean difference $0.7868 \pm 4.108\%$) and MTT measurements (mean difference 0.1551 ± 5.307 seconds) were smaller than for the other regions. A positive correlation was demonstrated between repeated HA fraction measurements, but this was just above significance ($r = 0.6688$; $p = 0.0697$). No correlations were demonstrated between repeated MTT and DV measurements in segments V/VI (figure 6.58; table 6.18).

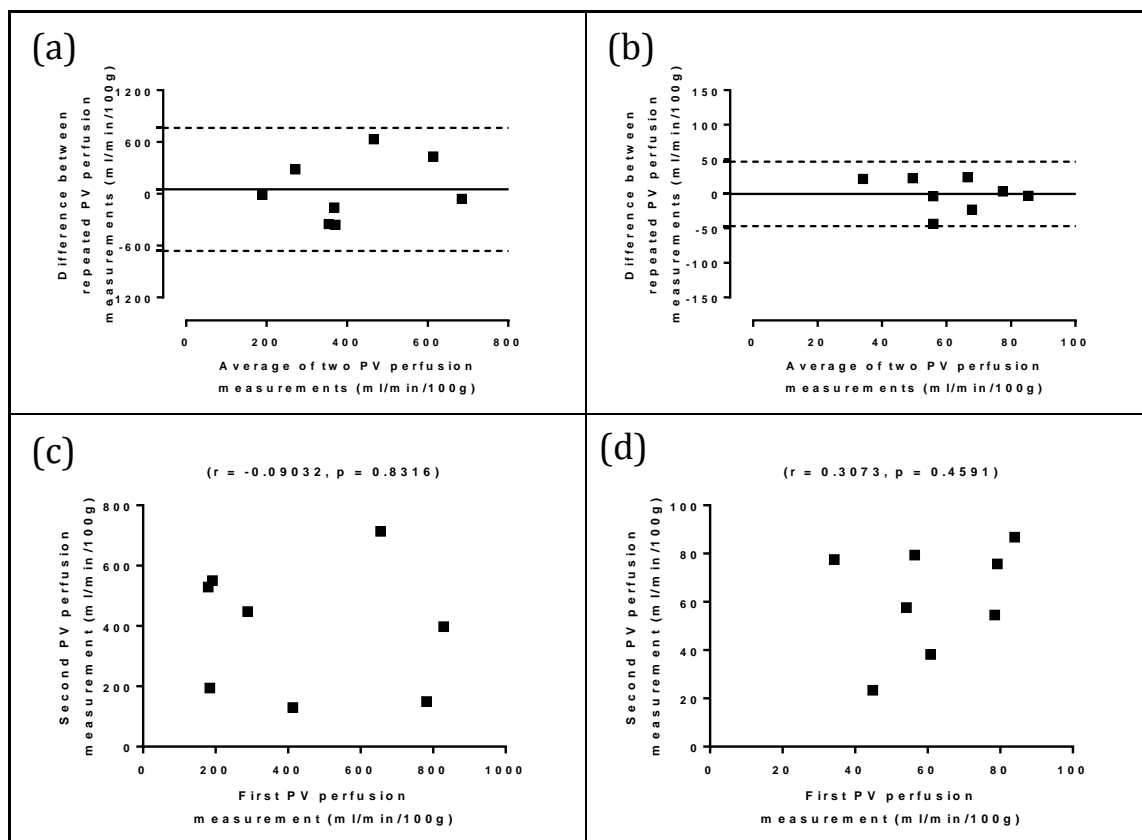


Figure 6.56: Analysis of agreement of segment V/VI PV perfusion reproducibility using uncorrected and PCMRI corrected DCE MRI dual input single compartment modelling

Bland-Altman and regression analysis of (a, c) uncorrected and (b, d) PCMRI corrected dual input single compartment modelling.

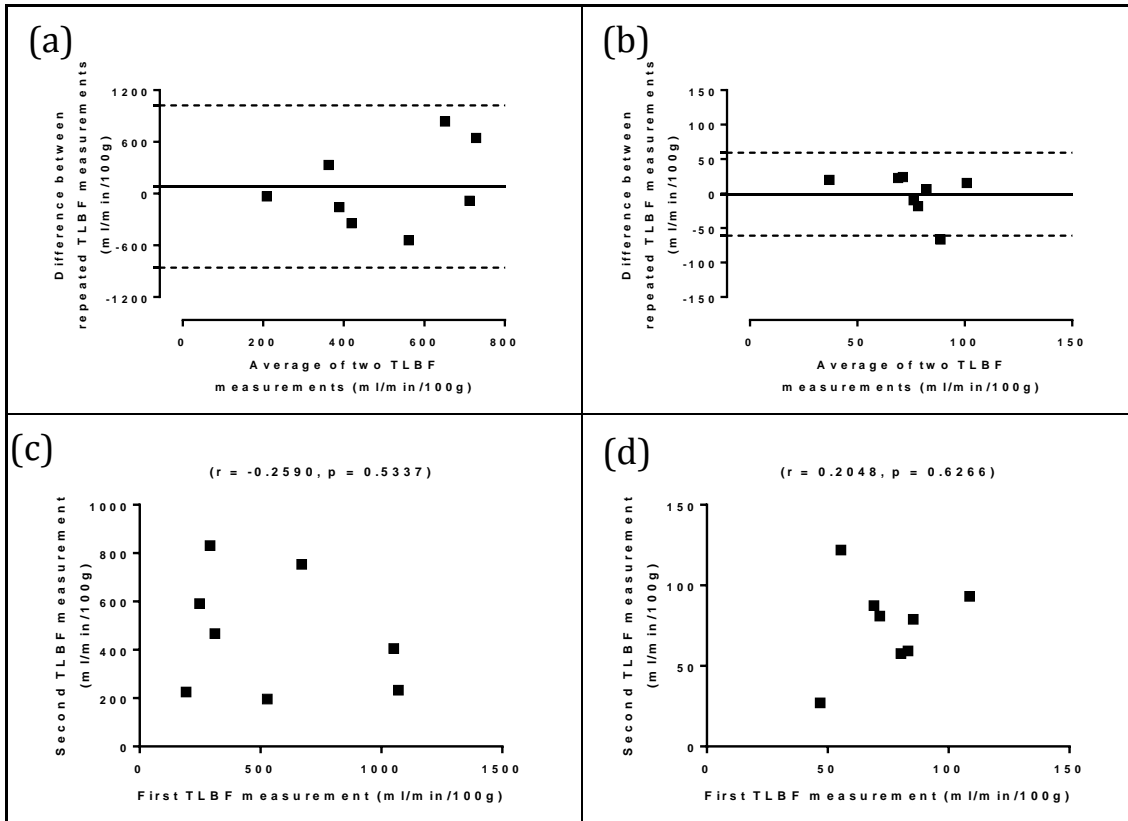


Figure 6.57: Analysis of agreement of segment V/VI TLBF reproducibility using uncorrected and PCMRI corrected DCE MRI dual input single compartment modelling

Bland-Altman and regression analysis of (a, c) uncorrected and (b, d) PCMRI corrected dual input single compartment modelling.

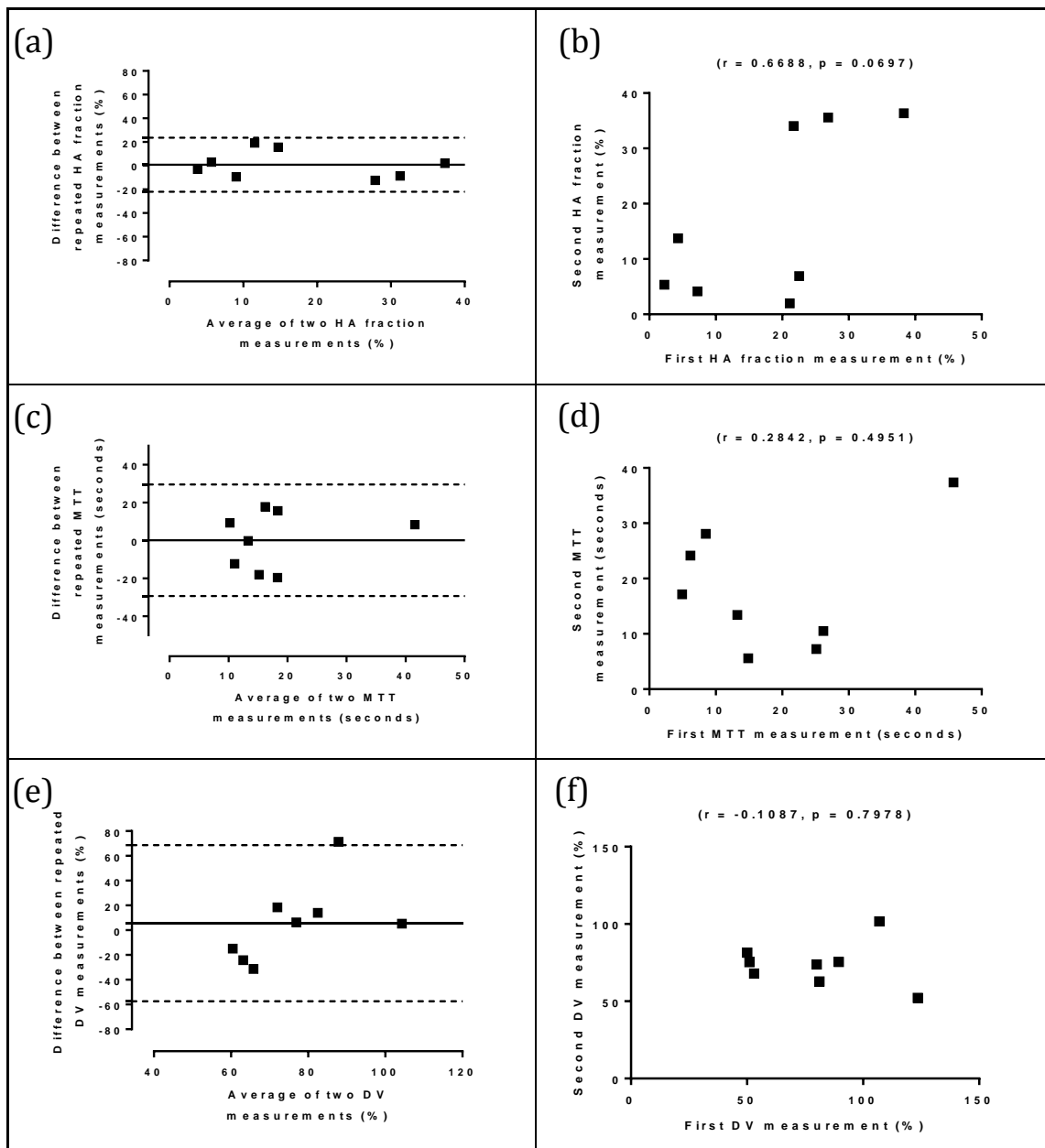


Figure 6.58: Analysis of agreement of segment V/VI relative perfusion parameter reproducibility using DCE MRI dual input single compartment modelling

Bland-Altman and regression analysis of (a, b) HA fraction, (c, d) mean transit time and (e, f) distribution volume.

No significant differences were demonstrated between repeated PV perfusion (figure 6.59) and TLBF (figure 6.60) measured with uncorrected and PCMRI corrected dual input single compartment modelling in segments VII/VIII. PCMRI correction resulted in a substantial reduction in the coefficient of reproducibility for both absolute perfusion parameters. There was a reduction in the mean difference for PV perfusion (-116.6 ± 104.1 ml/min/100g uncorrected vs -13.95 ± 6.303 ml/min/100g corrected) and TLBF (-96.56 ± 126.4 ml/min/100g uncorrected vs -15.03 ± 7.181 ml/min/100g corrected) as a result of PCMRI correction. The standard error for both absolute perfusion parameters was also reduced by PCMRI correction. No correlations were demonstrated between

repeated absolute perfusion measurements using uncorrected and PCMRI corrected modelling (table 6.18).

No significant differences were demonstrated between repeated HA fraction, MTT and DV measurements in segments VII/VIII (figure 6.61). The mean difference between repeated HA fraction (mean difference $2.905 \pm 3.322\%$) was larger than for the other regions. Conversely, the mean difference between repeated MTT measurements (mean difference -0.2980 ± 15.11 seconds) was smaller than for the other regions. A positive correlation was demonstrated between repeated HA fraction measurements, but this was not significant ($r = 0.6359$; $p = 0.1747$). No correlations were demonstrated between repeated MTT and DV measurements in segments VII/VIII (figure 6.61; table 6.18).

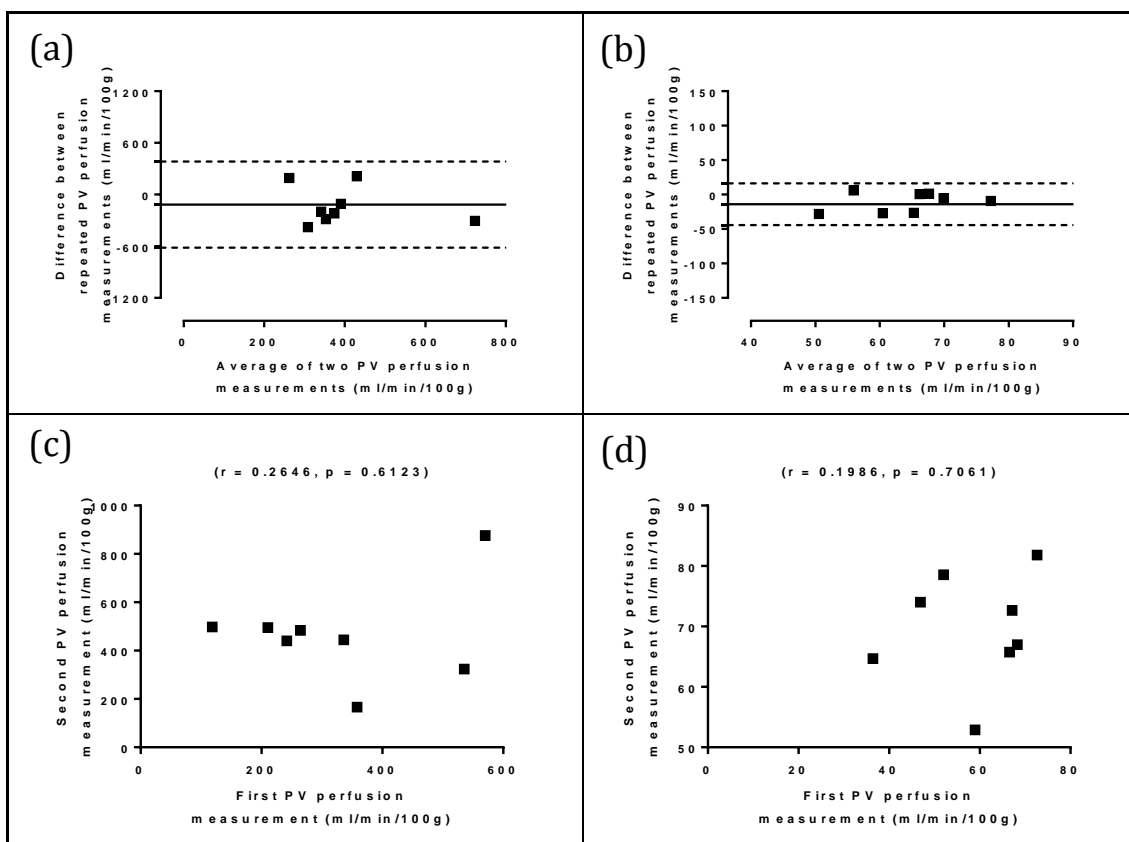


Figure 6.59: Analysis of agreement of segment VII/VIII PV perfusion reproducibility using uncorrected and PCMRI corrected DCE MRI dual input single compartment modelling

Bland-Altman and regression analysis of (a, c) uncorrected and (b, d) PCMRI corrected dual input single compartment modelling.

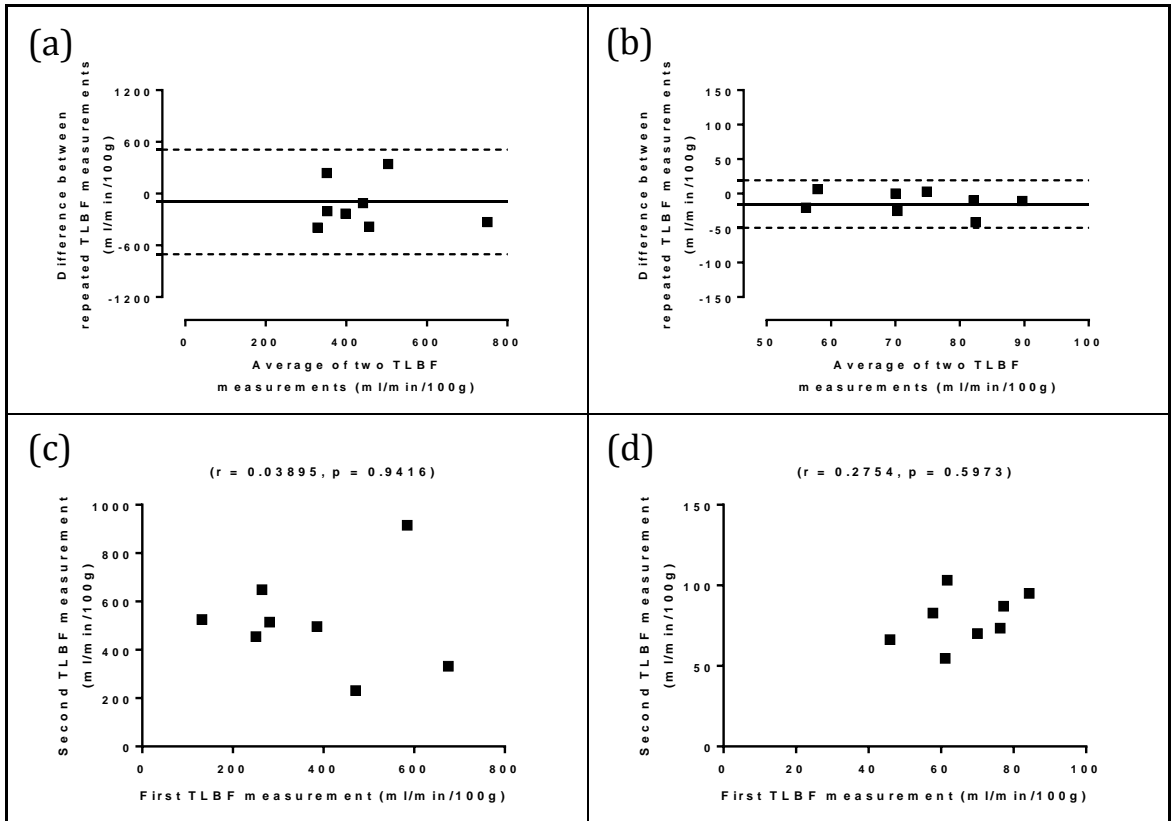


Figure 6.60: Analysis of agreement of segment VII/VIII TLBF reproducibility using uncorrected and PCMRI corrected DCE MRI dual input single compartment modelling

Bland-Altman and regression analysis of (a, c) uncorrected and (b, d) PCMRI corrected dual input single compartment modelling.

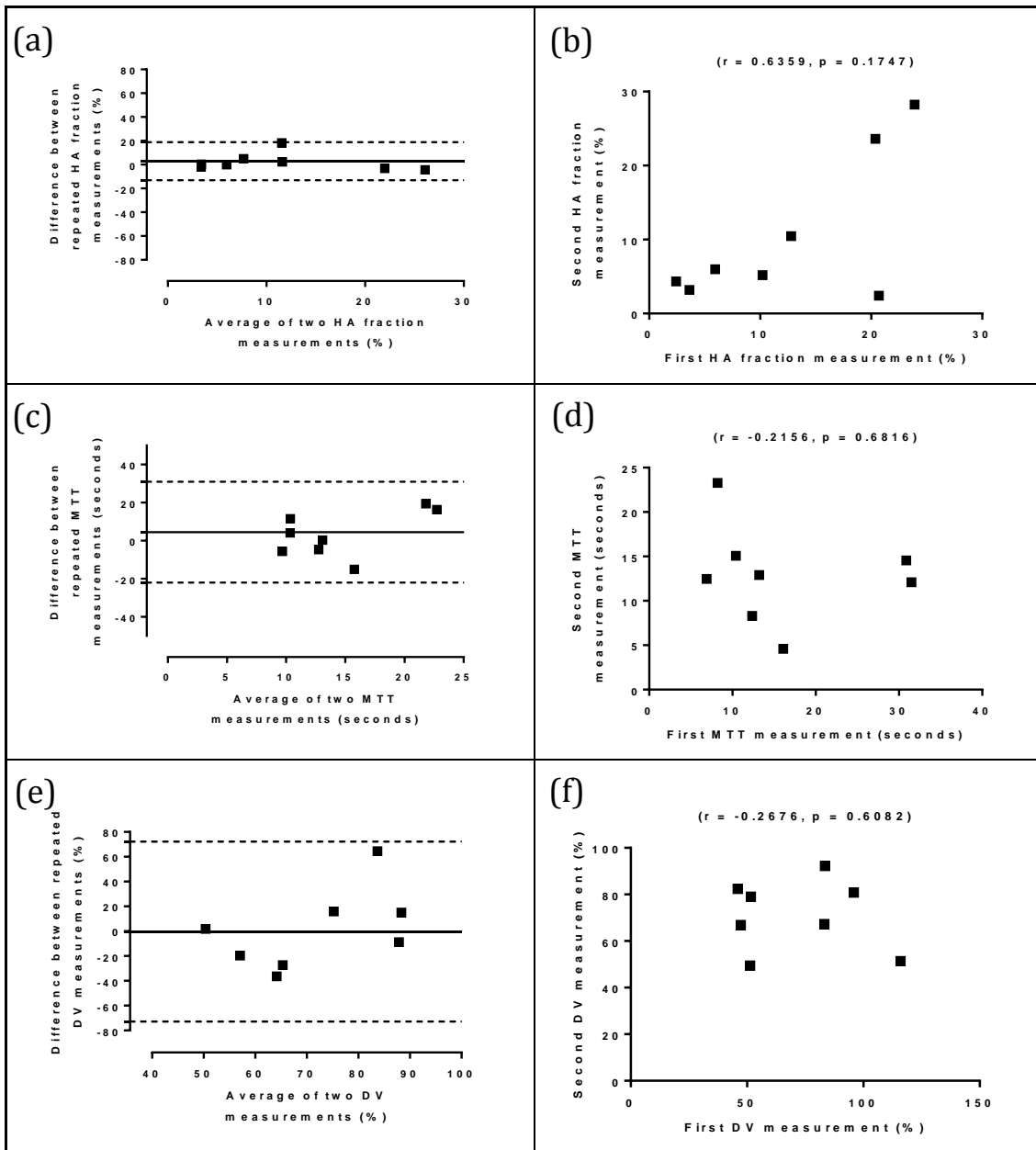


Figure 6.61: Analysis of agreement of segment VII/VIII relative perfusion parameter reproducibility using DCE MRI dual input single compartment modelling

Bland-Altman and regression analysis of (a, b) HA fraction, (c, d) mean transit time and (e, f) distribution volume.

Table 6.18: Regional DCE MRI perfusion parameter reproducibility for uncorrected and PCMRI corrected dual input single compartment modellings[§]

	SEGMENTS II/III		SEGMENTS V/VI		SEGMENTS VII/VIII		PCMRI
	UNCORRECTED	PCMRI CORRECTED	UNCORRECTED	PCMRI CORRECTED	UNCORRECTED	PCMRI CORRECTED	
PV perfusion (ml/min/100g)							
Mean difference	-24.15±212.7	-9.308±13.44	51.49±128.6	-0.1307±8.435	-116.6±104.1	-13.95±6.303	-1.234±2.924
Coefficient of Reproducibility	1179	74.49	712.6	46.76	499.8	30.26	19.01
Correlation (r)	-0.4798	-0.1735	0.2646	0.3073	0.2646	0.1986	0.7152
TLBF (ml/min/100g)							
Mean difference	-1.233±226.2	-6.041±11.66	82.35±169.9	-0.7303±10.84	-96.56±126.4	-15.03±7.181	-8.460±4.860
Coefficient of Reproducibility	1254	64.62	941.65	60.12	607.1	34.47	31.60
Correlation (r)	0.2069	0.3528	-0.2570	0.2048	0.03895	0.2754	0.4858
HA fraction (%)							
Mean difference	1.117±8.103		0.7868±4.108		2.905±3.322		8.643±6.943
Coefficient of Reproducibility	44.92		22.77		15.60		45.13
Correlation (r)	-0.5248		0.6688		0.6359		0.5491
Mean Transit Time (s)							
Mean difference	5.843±6.354		0.1551±5.307		4.485±5.517		-
Coefficient of Reproducibility	35.23		29.42		26.49		-
Correlation (r)	-0.5187		0.2842		-0.2156		-
Distribution Volume (%)							
Mean difference	26.38±15.08		5.617±11.36		-0.2980±15.11		-
Coefficient of Reproducibility	83.62		62.99		72.57		-
Correlation (r)	-0.07130		-0.1087		-0.2676		-

([§]Embodened values in the table highlight the best performing method/region for each statistic;
*paired t-test p < 0.0001)

6.6.3.5 Comparative studies

Comparison of uncorrected and PCMRI corrected DCE MRI measurements was undertaken for each region using whole liver volume normalised PCMRI measurements of PV perfusion, estimated (subtraction) TLBF and estimated HA fraction measured in the same session as DCE MRI studies. Baseline and seven day reproducibility scans were analysed for twelve subjects (21 datasets).

Regional absolute and relative perfusion DCE MRI validation data is summarised in table 6.19. For all regions, uncorrected dual input single compartment modelling tended to grossly overestimate absolute perfusion measurements. As with previous validation analysis, this compromised Bland-Altman analysis so that both the averages and differences of each validated perfusion measurement were heavily weighted towards the uncorrected DCE MRI parameter. Plots for uncorrected absolute perfusion parameters therefore appear to show a linear trend (figures 6.62(a), 6.63(a), 6.65(a), 6.66(a), 6.68(a) and 6.69(a)).

Table 6.19: Regional DCE MRI perfusion parameter validation for uncorrected and PCMRI corrected dual input single compartment modelling

	SEGMENTS II/III		SEGMENTS V/VI		SEGMENTS VII/VIII		PCMRI
	UNCORRECTED	PCMRI CORRECTED	UNCORRECTED	PCMRI CORRECTED	UNCORRECTED	PCMRI CORRECTED	
PV perfusion (ml/min/100g)	460.8±77.55	60.27±5.171	395.2±52.51	57.43±4.756	463.2±62.79	62.90±2.886	56.65±2.698
TLBF (ml/min/100g)	535.5±81.83	73.31±6.028	481.5±64.24	71.00±5.600	526.2±67.22	72.40±3.581	71.72±3.318
HA fraction (%)	17.85±2.847		18.51±3.136		12.39±2.608		18.91±4.084

(data replicated from table 6.17 for review)

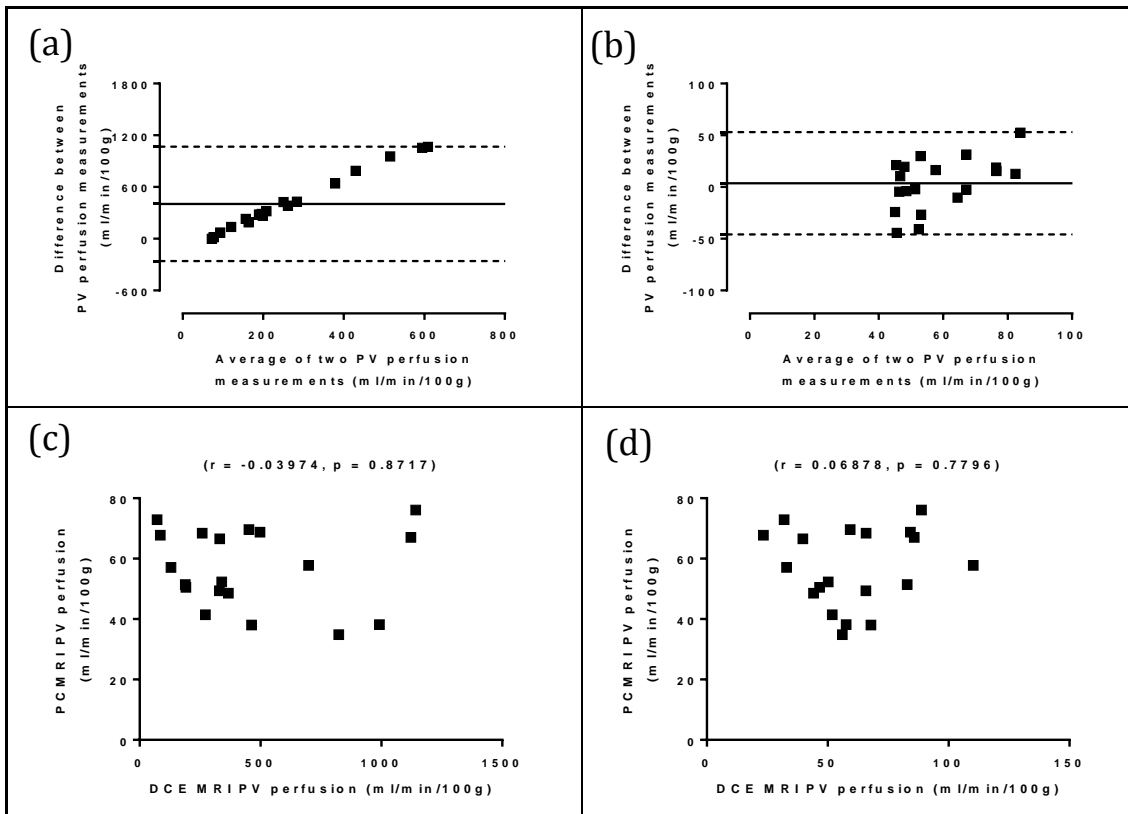


Figure 6.62: Analysis of agreement of segment II/III PV perfusion using uncorrected/PCMRI corrected DCE MRI dual input single compartment modelling with PCMRI PV perfusion measurements

Bland-Altman and regression analysis of (a, c) uncorrected and (b, d) PCMRI corrected dual input single compartment modelling.

For segments II/III, the smallest mean difference between DCE MRI and PCMRI PV perfusion (3.606 ± 5.785 ml/min/100g; $p = 0.5409$) and TLBF (1.672 ± 4.386 ml/min/100g; $p = 0.7074$) were both demonstrated using PCMRI corrected data. The smallest coefficient of variation for PV perfusion (37.40%) and TLBF (35.84%) was demonstrated in both cases using PCMRI corrected data. These were still larger than those observed for PV perfusion (21.82%) and TLBF (21.20%) using PCMRI. A significant correlation was demonstrated between corrected DCE MRI TLBF and PCMRI estimated TLBF ($r = 0.6922$; $p = 0.0010$) (figure 6.63(d)), but not for corrected PV perfusion or any uncorrected DCE MRI absolute perfusion parameters.

The Bland-Altman charts for DCE MRI segments II/III HA fraction as previously demonstrate an expected ‘funnelling’ of smaller values (figure 6.64(a)). No significant differences between DCE MRI and PCMRI HA fraction measurements were demonstrated (mean difference $-0.9229 \pm 5.334\%$; $p = 0.8645$). The DCE MRI HA fraction coefficient of variation (69.53%) was smaller than the PCMRI HA fraction coefficient of variation (98.97%). No significant correlations were demonstrated between segments II/III DCE MRI and PCMRI HA fraction measurements (figure 6.64(b)).

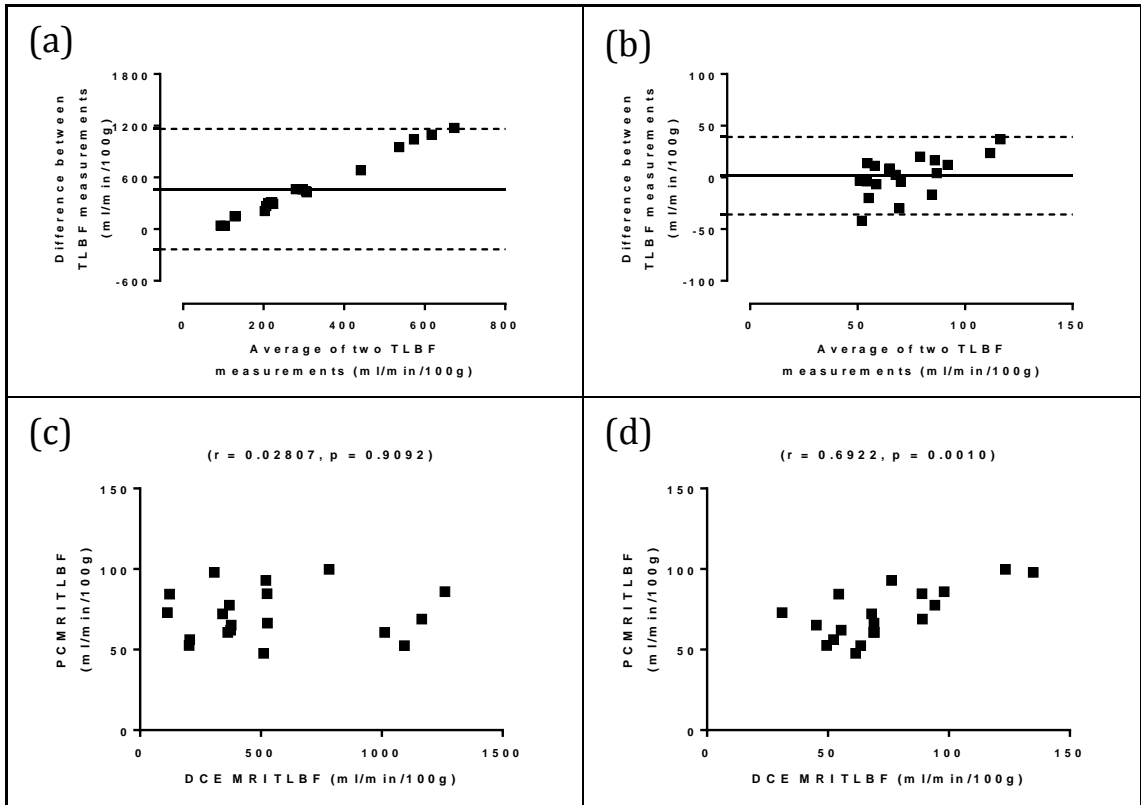


Figure 6.63: Analysis of agreement of segment II/III TLBF using uncorrected/PCMRI corrected DCE MRI dual input single compartment modelling with PCMRI estimated TLBF measurements

Bland-Altman and regression analysis of (a, c) uncorrected and (b, d) PCMRI corrected dual input single compartment modelling.

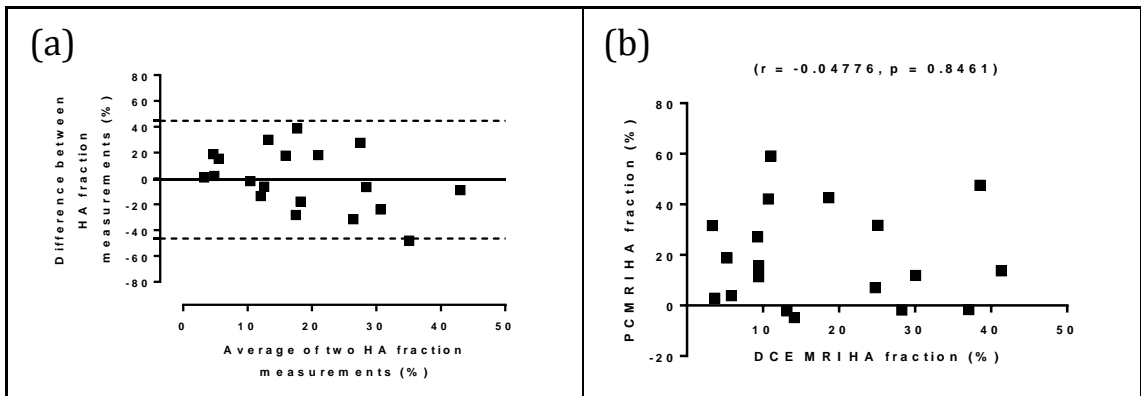


Figure 6.64: Analysis of agreement of segment II/III HA fraction using DCE MRI dual input single compartment modelling with PCMRI estimated HA fraction measurements

DCE MRI dual input single compartment HA fraction with PCMRI validation (a) Bland-Altman and (b) regression analysis.

For segments V/VI, the smallest mean difference between DCE MRI and PCMRI PV perfusion (0.7711 ± 4.995 ml/min/100g; $p = 0.8790$) and TLBF (-0.6410 ± 3.108 ml/min/100g; $p = 0.8389$) were both demonstrated using PCMRI corrected data. The smallest coefficient of variation for PV perfusion (36.09%) and TLBF (34.83%) was demonstrated in both cases using PCMRI corrected data. These were still larger than those observed for PV perfusion (21.82%) and TLBF (21.20%) using PCMRI. A significant correlation was demonstrated between corrected DCE MRI TLBF and PCMRI estimated TLBF ($r = 0.8586$; $p < 0.0001$) (figure 6.66(d)), but not for corrected PV perfusion or any uncorrected DCE MRI absolute perfusion parameters.

The Bland-Altman charts for DCE MRI segments V/VI HA fraction as previously demonstrate an expected ‘funnelling’ of smaller values (figure 6.67(a)). No significant differences between DCE MRI and PCMRI HA fraction measurements were demonstrated (mean difference $-0.26660 \pm 4.878\%$; $p = 0.9571$). The DCE MRI HA fraction coefficient of variation (73.86%) was smaller than the PCMRI HA fraction coefficient of variation (98.97%). No significant correlations were demonstrated between segments V/VI DCE MRI and PCMRI HA fraction measurements (figure 6.67(b)).

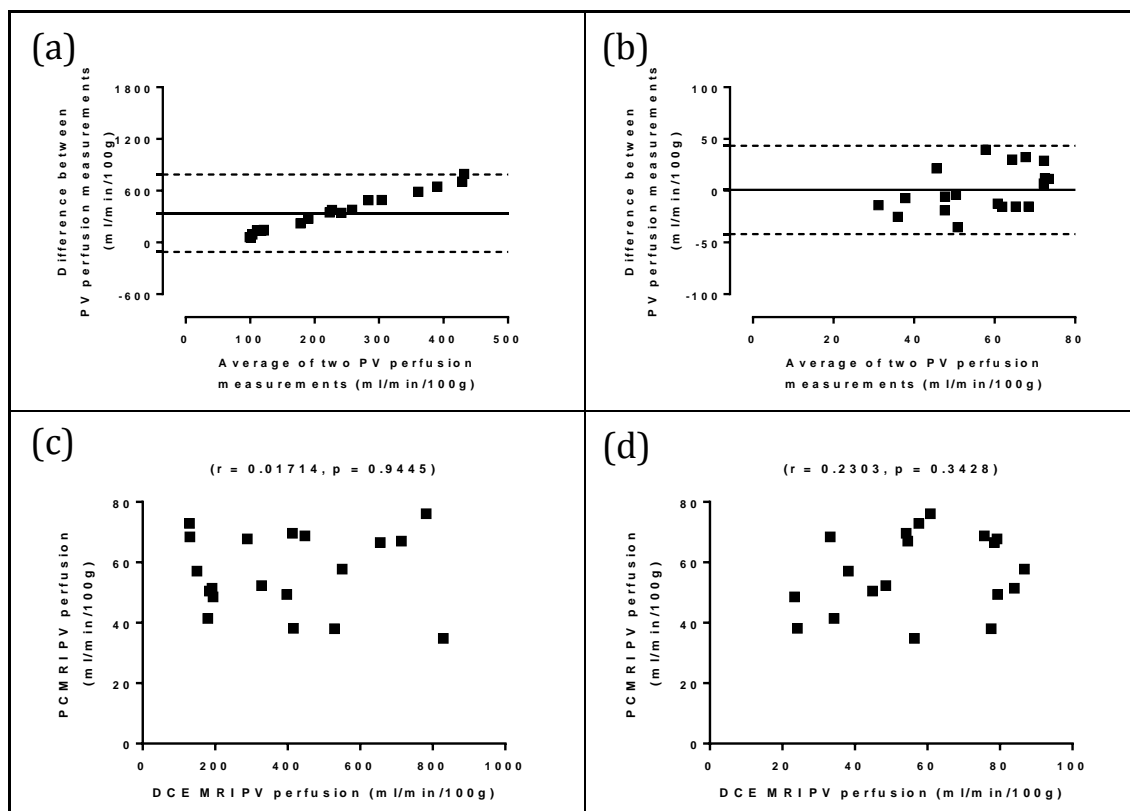


Figure 6.65: Analysis of agreement of segment V/VI PV perfusion using uncorrected/PCMRI corrected DCE MRI dual input single compartment modelling with PCMRI PV perfusion measurements

Bland-Altman and regression analysis of (a, c) uncorrected and (b, d) PCMRI corrected dual input single compartment modelling.

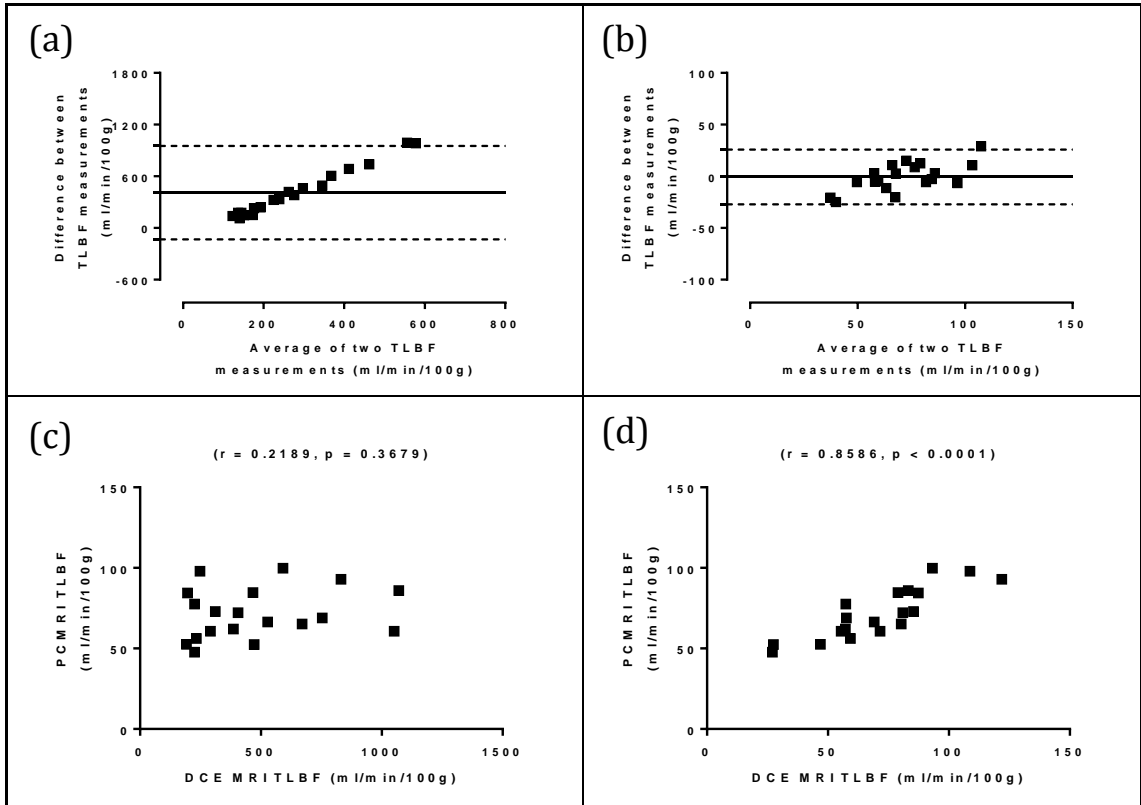


Figure 6.66: Analysis of agreement of segment V/VI TLBF using uncorrected/PCMRI corrected DCE MRI dual input single compartment modelling with PCMRI estimated TLBF measurements

Bland-Altman and regression analysis of (a, c) uncorrected and (b, d) PCMRI corrected dual input single compartment modelling.

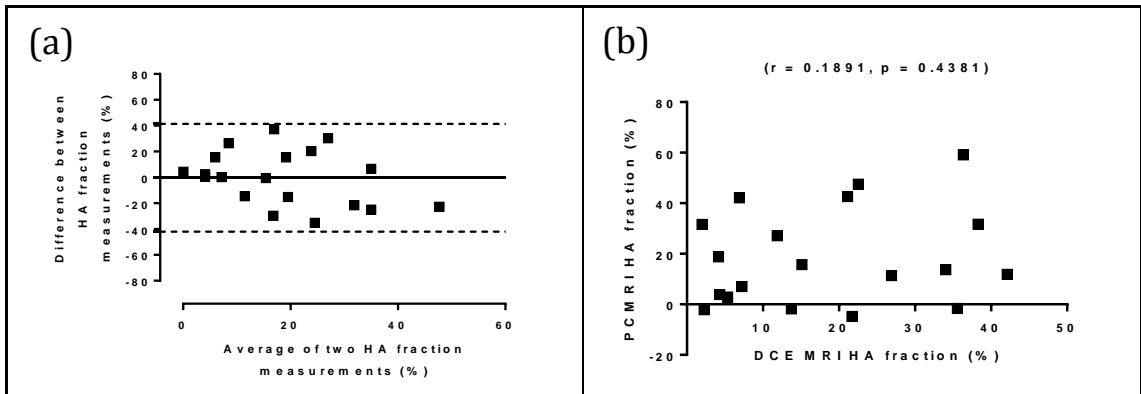


Figure 6.67: Analysis of agreement of segment V/VI HA fraction using DCE MRI dual input single compartment modelling with PCMRI estimated HA fraction measurements

DCE MRI dual input single compartment HA fraction with PCMRI validation (a) Bland-Altman and (b) regression analysis.

For segments VII/VIII, the smallest mean difference between DCE MRI and PCMRI PV perfusion (5.370 ± 3.659 ml/min/100g; $p = 0.1615$) and TLBF (-0.7991 ± 3.410 ml/min/100g; $p = 0.8177$) were both demonstrated using PCMRI corrected data. The smallest coefficient of variation for PV perfusion (18.92%) and TLBF (20.39%) was demonstrated in both cases using PCMRI corrected data. These were just less than those observed for PV perfusion (21.82%) and TLBF (21.20%) using PCMRI. A significant correlation was demonstrated between corrected DCE MRI TLBF and PCMRI estimated TLBF ($r = 0.5833$; $p = 0.0140$) (figure 6.69(d)), but not for corrected PV perfusion or any uncorrected DCE MRI absolute perfusion parameters.

The Bland-Altman charts for DCE MRI segments VII/VIII HA fraction as previously demonstrate an expected ‘funnelling’ of smaller values (figure 6.70(a)). No significant differences between DCE MRI and PCMRI HA fraction measurements were demonstrated (mean difference $-6.829 \pm 5.112\%$; $p = 0.2003$). The DCE MRI HA fraction coefficient of variation (86.81%) was smaller than the PCMRI HA fraction coefficient of variation (98.97%). No significant correlations were demonstrated between segments VII/VIII DCE MRI and PCMRI HA fraction measurements (figure 6.70(b)).

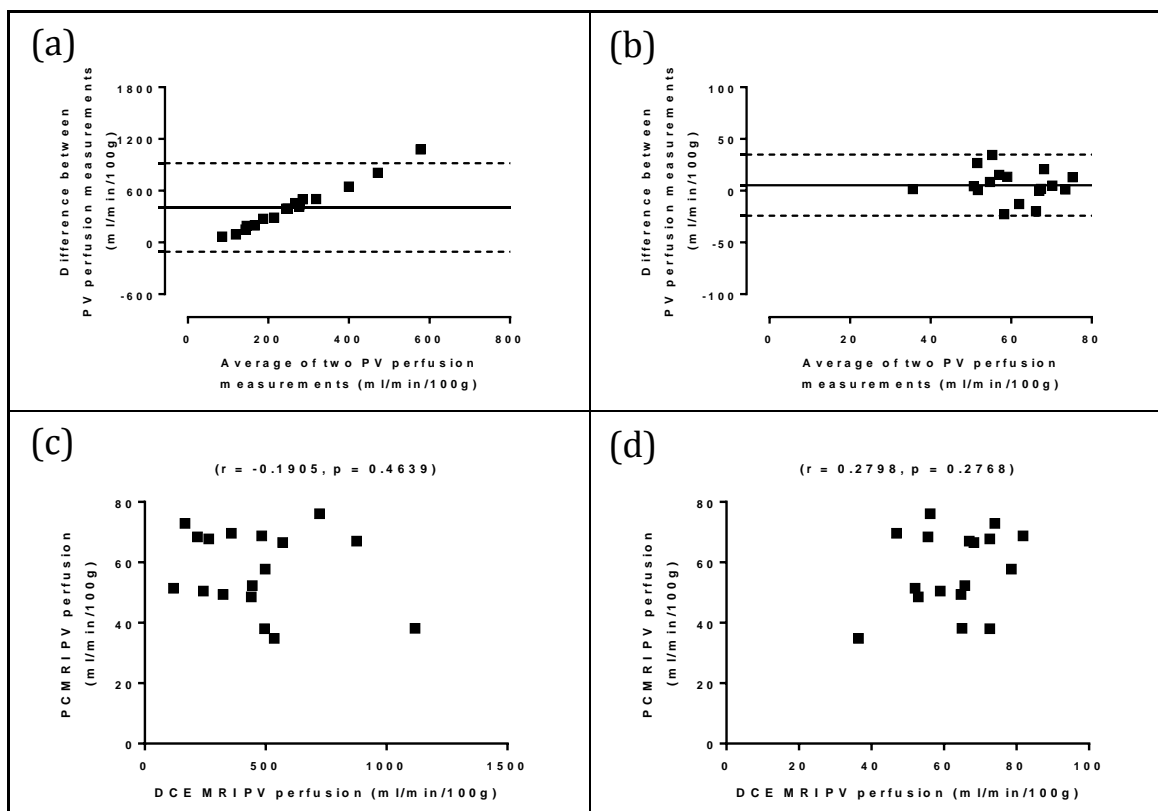


Figure 6.68: Analysis of agreement of segment VII/VIII PV perfusion using uncorrected/PCMRI corrected DCE MRI dual input single compartment modelling with PCMRI PV perfusion measurements

Bland-Altman and regression analysis of (a, c) uncorrected and (b, d) PCMRI corrected dual input single compartment modelling.

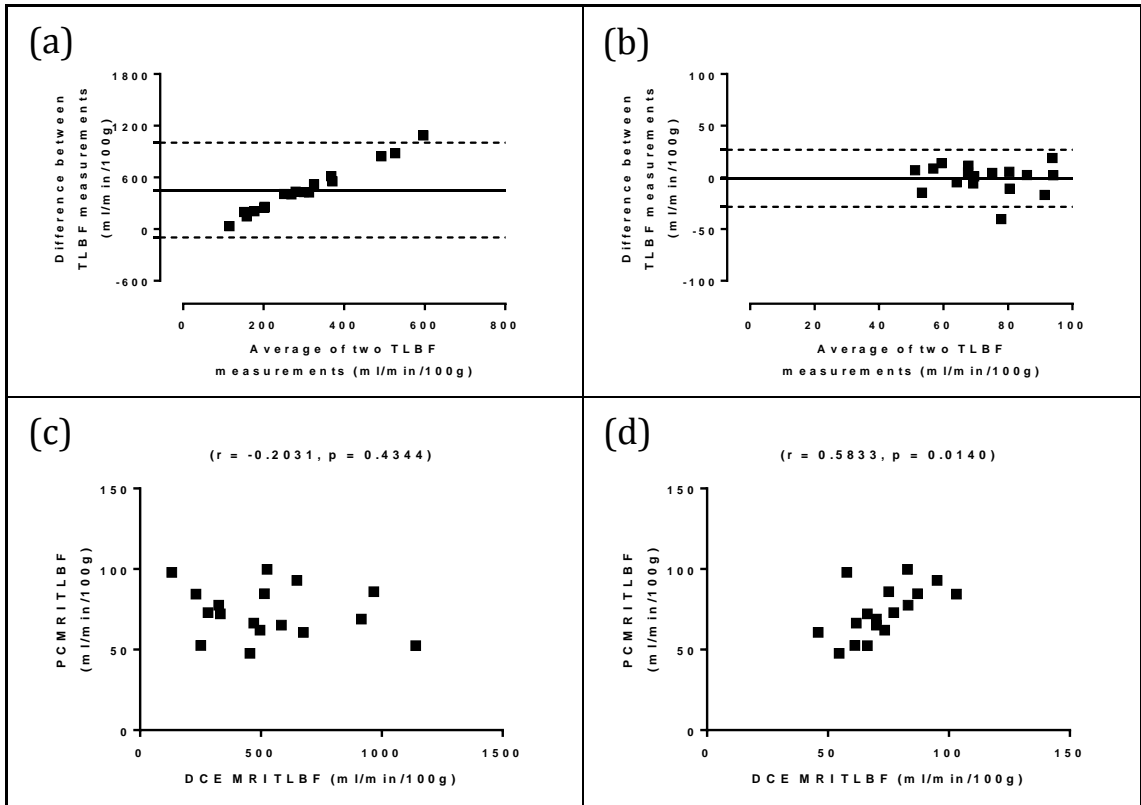


Figure 6.69: Analysis of agreement of segment VII/VIII TLBF using uncorrected/PCMRI corrected DCE MRI dual input single compartment modelling with PCMRI estimated TLBF measurements

Bland-Altman and regression analysis of (a, c) uncorrected and (b, d) PCMRI corrected dual input single compartment modelling.

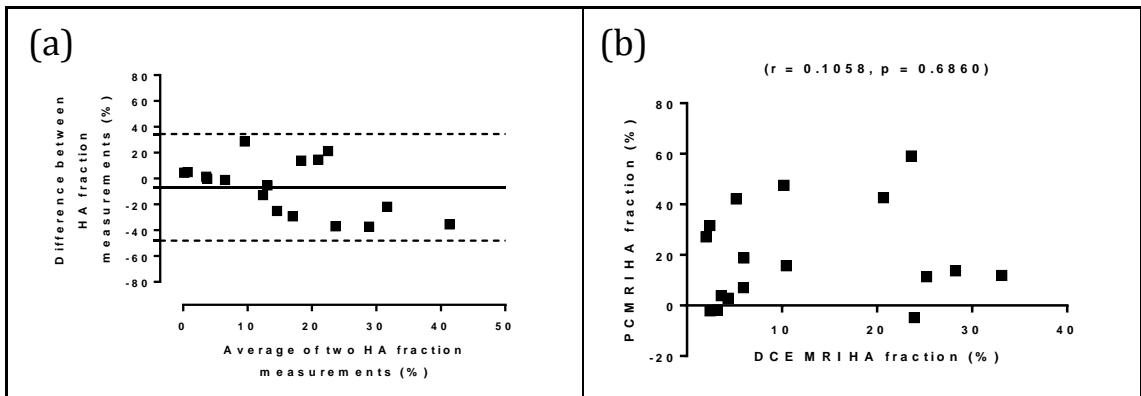


Figure 6.70: Analysis of agreement of segment VII/VIII HA fraction using DCE MRI dual input single compartment modelling with PCMRI estimated HA fraction measurements

DCE MRI dual input single compartment HA fraction with PCMRI validation (a) Bland-Altman and (b) regression analysis.

Table 6.20: Summary of PCMRI validation of regional DCE MRI perfusion parameters for uncorrected and PCMRI corrected dual input single compartment modelling†

	SEGMENTS II/III		SEGMENTS V/VI		SEGMENTS VII/VIII	
	UNCORRECTED	PCMRI CORRECTED	UNCORRECTED	PCMRI CORRECTED	UNCORRECTED	PCMRI CORRECTED
PV perfusion (ml/min/100g)						
Mean difference	404.1±77.72	3.606±5.785	338.6±52.54	0.7711±4.995	405.7±63.48	5.370±3.659
Coefficient of Variation	73.36%	37.40%	57.91%	36.09%	55.89%	18.92%
Correlation (<i>r</i>)	-0.03974	0.06878	0.01714	0.2303	-0.1905	0.2798
TLBF (ml/min/100g)						
Mean difference	463.9±81.81	1.672±4.386	409.8±63.54	-0.6410±3.108	453.0±68.11	-0.7991±3.410
Coefficient of Variation	66.60%	35.84%	58.16%	34.83%	52.67%	20.39%
Correlation (<i>r</i>)	0.02807	0.6922*	0.2189	0.8586*	-0.2031	0.5833*
HA fraction (%)						
Mean difference	-0.9229±5.334		-0.2660±4.878		-6.829±5.112	
Coefficient of Variation	69.53%		73.86%		86.81%	
Correlation (<i>r</i>)	-0.04776		0.1891		0.1058	

(†Emboldened values in the table highlight the best performing Method for each statistic;

*Pearson's correlation coefficient $p < 0.05$)

6.6.4 DISCUSSION

We have demonstrated that correction of DCE MRI absolute perfusion measurements using PCMRI volume normalised estimated (subtraction) TLBF is (i) feasible, (ii) can be used to study regional differences in absolute perfusion and deliver improvements in (iii) seven day reproducibility and (iv) comparative agreement of DCE MRI regional tissue perfusion estimates. We have previously demonstrated encouraging invasive and non-invasive validation data and seven day reproducibility of estimated TLBF PCMRI measurements (sections 5.4 and 5.5). In this section we have shown that PCMRI correction allows DCE MRI absolute perfusion measurements to exploit the consistency of PCMRI data, while simultaneously profiting from the ability of DCE MRI to discriminate between regional differences in absolute and relative perfusion.

Parametric mapping after residual sum of squares thresholding was shown to be a potentially feasible method for excluding large vessels from before applying PCMRI correction. This method also has the advantage of also excluding poorly modelled parenchymal data (as a result of noise, motion corruption and other MR artefacts), which would otherwise compromise averaging and overall quantification. There are of course many more complex methods of thresholding which are beyond the remit of this thesis, which could improve this process. It is worth noting that in the context of focal liver lesions (particularly neovascularised malignant lesions), the proposed method of thresholding would have the disadvantage of potentially excluding these pixels and therefore excluding the potentially useful quantification of the hypervascularity shown in these lesions from the analysis.

As the study was performed in a cohort of normal volunteers, our data reassuringly demonstrated no significant regional differences in absolute and relative DCE MRI perfusion parameters both before and after correction. PCMRI correction delivered regional absolute perfusion estimates within physiological range and reduced absolute and relative dispersion of both PV perfusion and TLBF DCE MRI measurements in all three regions. This was demonstrated by consistent reductions across all three regions in the absolute perfusion coefficients of variation (segments II/III uncorrected PV perfusion 73.36% and TLBF 66.60% vs corrected PV perfusion 37.40% and TLBF 35.84%; segments V/VI uncorrected PV perfusion 57.91% and TLBF 58.16% vs corrected PV perfusion 36.09% and TLBF 34.83%; segments VII/VIII uncorrected PV perfusion 55.89% and TLBF 52.67% vs corrected PV perfusion 18.92% and TLBF 20.39%). Comparison of regional residual sum of squares demonstrated poorer fits in segments II/III (mean $6.525 \times 10^{-7} \pm 1.304 \times 10^{-7}$; compared with segments V/VI $2.829 \times 10^{-7} \pm 4.335 \times 10^{-8}$ and

segments VII/VIII $2.702 \times 10^{-7} \pm 3.932 \times 10^{-8}$; $p = 0.0027$). Relative to the other regions, segments II/III are not only most affected by cardiac motion but are also potentially subject to artefact from the adjacent rapidly changing post-contrast intra-ventricular signal. This could therefore account for the poorer fits, but also increased dispersion of absolute perfusion parameters.

Reproducibility studies demonstrate striking improvements in mean differences and coefficient of reproducibility as a result of PCMRI correction (table 6.15). Regional differences in reproducibility also bear witness to the poorer model fits recorded in segments II/III. The coefficient of reproducibility for all perfusion parameters in segments II/III is consistently larger for both corrected and uncorrected data. Although no correlation was recorded between repeated HA fraction measurements for segments II/III, positive correlations emerging between measurements for segments V/VI ($r = 0.6688$; $p = 0.0697$) and segments VII/VIII ($r = 0.6359$; $p = 0.1747$) though modest and non-significant are encouraging.

PCMRI correction delivers improvements in the coefficient of variance in absolute perfusion parameters for all three regions (table 6.17). TLBF validation was undertaken using the same data as used for PCMRI correction and therefore it is unsurprising that regional TLBF validation data following PCMRI correction should be strong. This is borne out in significant positive correlations with PCMRI data for all three regions (segments II/III $r = 0.6922$, $p = 0.0010$; segments V/VI $r = 0.8586$, $p < 0.0001$; segments VII/VIII $r = 0.5833$; $p = 0.0140$). PCMRI PV perfusion measurements, independent of PCMRI TLBF demonstrate much poorer correlations across all three regions, and even after PCMRI correction, the coefficient of variation of both PV perfusion and TLBF is only marginally improved by DCE MRI in segments VII/VIII (corrected DCE MRI PV perfusion 18.92% and TLBF 20.39% vs PCMRI PV perfusion 21.82% and TLBF 21.20%). Importantly, the coefficient of variation of HA fraction measurements across all three regions was better with DCE MRI (segments II/III 69.53%, segments V/VI 73.86%, segments VII/VIII 86.81% vs PCMRI 98.97%), highlighting the value of DCE MRI in the assessment of relative perfusion. It is also worth noting that while validation in this study has been undertaken using simultaneous PCMRI measurements, true validation of regional perfusion measurements would require invasive (experimental) methods such as laser Doppler flowmetry or near-infrared spectroscopy, less feasible in clinical contexts.

In this section, we have applied the correction to dual input single compartment modelling with progressive refinements we introduced earlier in the chapter – (i) pre-estimated VIF delays with constrained free modelling and (ii) cardiac output AIF

correction. An important and interesting feature of PCMRI correction is the applicability to any method of perfusion modelling in the liver. The same DCE MRI data, processed using dual input dual compartment or the hepatic perfusion index model could be corrected using the same method. Indeed, once volume normalised PCMRI estimated (caval subtraction) TLBF measurements have been obtained, these could be used to correct perfusion quantification across any modality. The accuracy would of course be dependent on quality and quantity of hepatic parenchymal perfusion data – the more slices, better segmented and less artefacted the perfusion data, the more accurate the results.

In this section, we have applied PCMRI correction to ' k_1 ', but it is worth mentioning the outflow constant ' k_2 '. Although MTT is reliant on ' k_2 ' alone, DV is based on both inflow and outflow constants. It would seem that perhaps the corrected ' k_1 ' could provide an opportunity to correct MTT, or perhaps even ' k_2 ' and DV estimates. The method of correcting DCE MRI absolute perfusion however, exploits relative inter-pixel enhancement rather than providing a *true* correction of ' k_1 '. Because of these, we would argue that any attempt to use corrected ' k_1 ' to adjust DV or indeed ' k_2 ' would be theoretically flawed.

An interesting consequence of correcting pixel wise absolute perfusion can also be obtained from the original derivation of the dual input single compartment model, which is based upon the following expression, where ' F ' represents total perfusion and ' E ' represents extraction fraction:

$$k_{1a} + k_{1p} = F \cdot E(1 - Hct_{SV}) \quad (\text{Equation 6.23})$$

The potential is then to use uncorrected k_1 and the adjusted perfusion (F') for a given pixel to measure ' E ', or extraction fraction (where small vessel haematocrit ' Hct_{SV} ' is constant at 0.25):

$$E = \frac{k_1}{F'(1 - Hct_{SV})} \quad (\text{Equation 6.24})$$

The assumption that contrast agent can pass freely through the vascular endothelium to the interstitium and space of Disse seems reasonable in healthy individuals. Microarchitectural changes in the hepatic parenchyma seen in fibrosis and chronic liver disease however, have the theoretical potential to reduce extraction fraction thereby yielding another alternative potentially clinically valuable perfusion parameter in ' E '. While this may seem theoretically acceptable, the use of uncorrected ' k_1 ' would result in

very large non-physiological estimates of ' E ' (given prior gross overestimation of absolute perfusion ' F '). The use of corrected ' k_1 ' would result in measurement of 'relative extraction fraction', perhaps of value in the evaluation of focal liver lesions but of no obvious use in comparisons between subjects with and without disease.

Another interesting opportunity that PCMRI correction could afford is the ability to simplify or forgo some of the steps in DCE MRI post-processing. As the correction could apply to any method of DCE quantification, there is a potential role in the quantification of raw time-intensity curves for example. The correction of DCE MRI data is however reliant on a linear relationship between the SI and CA concentration and specifically in the context of regional quantification, a linear relationship between adjacent and distant pixels of imaged liver. In order to convert the raw SI data into this state, blood and tissue T1 quantification is essential. The latter would be especially important in the context of liver disease or evaluation of focal liver lesions, where heterogeneous involvement of the liver parenchyma and disease-based inter-subject variation would have significant effects quantification. We would therefore argue that PCMRI correction without T1 quantification and SI correction would be erroneous.

The clinical implications of improved regional DCE MRI quantification are wide ranging. While volume-normalised PCMRI subtraction TLBF offers a single numerical value, which may have potential as biomarker of liver disease, the anatomical data offered by regional DCE MRI quantification has real value in the planning and assessment of surgical treatments in the liver. Regional DCE MRI quantification has failed to find favour in clinical practice because of poor perfusion parameter reproducibility and validation, both of which can be overcome using PCMRI correction. Accurate regional perfusion assessment can then be used to guide resection volumes, determine segmental viability, assess changes in vascularisation pre and post treatment and determine subclinical perfusion changes which may precede macroscopic disease. Accurate quantification could also be used to simplify and improve lesion characterisation, moreover accurate perfusion quantification in malignant lesions may be used to inform treatment planning and response.

Finally it is worth briefly mentioning that difficulties with DCE MRI absolute perfusion parameter reproducibility and validation are not exclusive to the liver. Correction of DCE MRI regional perfusion with whole organ blood flow data (obtained using PCMRI or other methods) could be undertaken in a similar way elsewhere (e.g. the kidneys), where DCE MRI data is available for reasonable volumes of organ parenchyma.

6.6.5 CONCLUSION

We have demonstrated that DCE and PCMRI data can be combined to correct regional DCE MRI absolute perfusion quantification. We have shown that PCMRI subtraction TLBF can be used to deliver physiologically feasible DCE MRI quantification. We have used our method to investigate regional differences in absolute perfusion across the liver and demonstrated that measurements in segments II/III are more prone to artefact than in the right liver, and therefore more variable and less reproducible. PCMRI correction not only improves seven-day reproducibility, but also the comparative agreement of DCE MRI absolute perfusion parameters. PCMRI correction is therefore an essential step in deriving physiologically feasible, reproducible and accurate DCE MRI quantification.

6.7 CLOSING COMMENTS

Building on our unsuccessful experience of preclinical DCE MRI, we developed clinical protocols on a 3.0T system that addressed many of the challenges highlighted from working at higher field strengths. We demonstrated our protocol feasibility and then went on to introduce progressive refinements to the post-processing and modelling to optimise DCE MRI quantification. We proposed 'pre-estimation with constrained free modelling' as a novel method to deal with VIF arrival delays and demonstrated its feasibility and improved reproducibility relative to other methods. We also demonstrated dual input single compartment modelling as a reasonable approach to DCE MRI relative perfusion quantification. We then used PCMRI aortic root flow to correct AIF measurements and implemented this for the first time in the liver, to demonstrate improved reproducibility and validation. Finally we used our novel PCMRI subtraction method for quantifying TLBF (proposed and validated preclinically and clinically in sections 5.4 and 5.5) to successfully correct DCE MRI absolute perfusion measurements. With the introduction of PCMRI correction, we have demonstrated for the first time a method of obtaining regional DCE MRI data that can consistently deliver physiological, reproducible and accurate measurements of absolute perfusion.

The method development in this chapter was based on normal, healthy volunteers. Armed with the right tools for measurement of both bulk flow and tissue perfusion, we can now move forward and investigate haemodynamic changes in liver disease both in the preclinical (Chapter 7) and clinical setting (Chapter 8).

CHAPTER 7

BLOOD FLOW STUDIES IN CHRONIC LIVER DISEASE – PRECLINICAL STUDIES

“...let one tiny cell
be in error
or one fiber be worn
in your labour
and the pilot flies into the wrong sky,
the tenor collapses in a wheeze,
the astronomer loses a planet...”

- Ode to the liver [2].

7.1 INTRODUCTION

In chapter 5, we introduced a novel, validated and repeatable preclinical method for measuring total liver blood flow (TLBF) and hepatic arterial (HA) flow using phase contrast MRI (PCMRI). Our data established intrinsic differences in hepatic haemodynamic parameters at baseline, demonstrating the hepatic arterial buffer response and its failure in cirrhotic animals using terlipressin. Because of difficulties with dynamic contrast enhanced (DCE) MRI at 9.4T (Chapters 2 and 3), haemodynamic assessment was confined to measurement of bulk flow, with tissue perfusion only estimated through normalisation of bulk flow with explanted liver mass.

In this chapter we attempt to overcome this limitation in the preclinical setting through the introduction of arterial spin labelling (ASL), a non-contrast agent based method for measurement of tissue perfusion that to date has enjoyed very limited application in the liver. Although the development of this method does not form part of this thesis, in the first section we outline the methodology and use bulk flow PCMRI measurements normalised to explanted liver mass to validate ASL tissue perfusion measurements. We then assess the repeatability of hepatic parenchymal T1 measurements, measured as part of the ASL protocol and build on previous T1 measurement work presented in section 3.3 to explore differences in hepatic parenchymal T1 in health and disease.

In the final section, using PCMRI, ASL and cardiac cine MRI, we then study hepatic haemodynamic phenomena in chronic liver disease during stress, evaluating differences in health and disease at baseline, the response to intravenous hydration and finally inflammatory stress (acute endotoxaemia) as a means of simulating 'acute-on-chronic' liver failure (ACLF).

7.2 AUTHOR CONTRIBUTIONS

In fulfilment of the aims in this chapters, I: (a) implemented preclinical PCMRI protocols developed previously (Chapter 5); (b) implemented preclinical cardiac cine MRI and ASL protocols developed at our institution; (c) prepared and conducted all animal scanning experiments; (d) developed Matlab code for region-of-interest ASL quantification; (e) collected and analysed all the data; and (f) prepared all the material contained within this chapter.

Hepatic PCMRI protocols were developed by Alan Bainbridge with input from Tom Roberts for cine modification and Raj Ramasawmy for quantification. Cardiac cine MRI sequences were originally developed by Anthony Price and adapted by Alan Bainbridge. Hepatic ASL protocols were developed by Raj Ramasawmy, based on original cardiac ASL protocols developed by Adrienne Campbell-Washburn.

For establishment of small animal intravenous access, I received help from Val Taylor and Asif Machada. Sham-operated and bile-duct ligated rats were prepared by Abe Habtieson. Protocols for acute endotoxaemia were developed in consultation with Nathan Davies. Statistical power calculations were undertaken by Paul Bassett.

7.3 ARTERIAL SPIN LABELLING – METHODOLOGY, VALIDATION AND T1 STUDIES

7.3.1 BACKGROUND

As briefly discussed in section 1.3.8, ASL is a promising non-contrast agent based method that to date has had limited application in the liver [225-227]. ASL uses endogenous blood water as a tracer: the blood is labelled by inversion and subsequent exchange of inverted blood with the tissue magnetisation can be used to generate perfusion-sensitised images. Two images are acquired – a ‘labelled’ or perfusion-weighted image, in which the signal reflects static tissue combined with magnetised inflowing blood and a ‘control’ image containing static tissue alone. The signal difference between these two images can be used to generate an image of the labelled blood, which in turn reflects tissue perfusion [222, 224].

There are several approaches to labelling and in this study, a pulsed ASL scheme was used. Classically, during a pulsed ASL experiment, a slab of arterial blood is labelled close to the imaging slice at a single instance in time, which is subsequently imaged at a fixed time interval to allow labelled blood to flow into the imaged slice and exchange with tissue [223, 224]. In this study, a flow-sensitive alternating inversion recovery (FAIR) preparation was used with a gradient echo Look-Locker read out [430]. The FAIR technique is based on generating two T1 measurements for a given slice. The slice-selective inversion is flow-sensitised because it contains non-inverted spins from blood perfusing the slice, entering from areas on either side of the selected slice. The global inversion slab includes the slice of interest and tissue on either side of it to ensure that the slice of interest contains only inverted, static tissue (figure 7.1a). The presence of additional non-inverted (perfusing) spins in the slice-selective inversion would be expected to cause T1 shortening. The differences in T1 between general and slice-selective (flow-sensitised) data would then allow estimation of perfusion based on measured blood T1 (figure 7.1b) [431, 432].

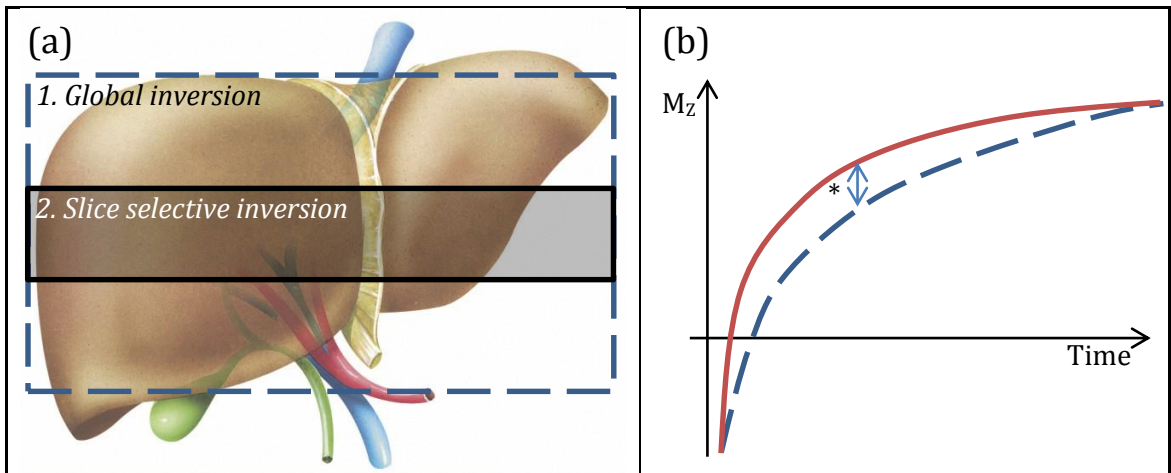


Figure 7.1: FAIR ASL labelling scheme and T1 based perfusion quantification
 Schematic diagram (a), demonstrating arrangement and orientation of consecutive global and slice selective inversions. Note slab sizes are not drawn to scale. The T1 recovery curves of the slice selective (b, red curve) and global (b, blue dashed curve) are shown in (b). The measured difference in T1 (*, blue arrow) is dependent on perfusion and can be quantified with knowledge of blood T1 and the blood-tissue partition coefficient (λ). (Adapted from reference [433]).

Based on this method, accurate T1 measurement is therefore an essential aspect of successful and reliable quantification. From our earlier work, this could be achieved using IR recovery methods, but at considerable time expense. To enable more rapid quantification, a segmented Look-Locker technique was used as an alternative method of T1 quantification. In a classic IR experiment, a 180° inversion pulse is followed by a 90° pulse separated by varying delays/inversion times. The Look-Locker sequence applies an inversion pulse, followed by many consecutive smaller excitation pulses with continuous sampling of the recovery (figure 7.2) [434]. This allows faster measurement of T1 and is useful in the context of small animals where ECG and respiratory gated measurements must be obtained in very small temporal sampling windows [430]. In this study, respiratory gated Look-Locker acquisitions were used with segmented k -space sampling.

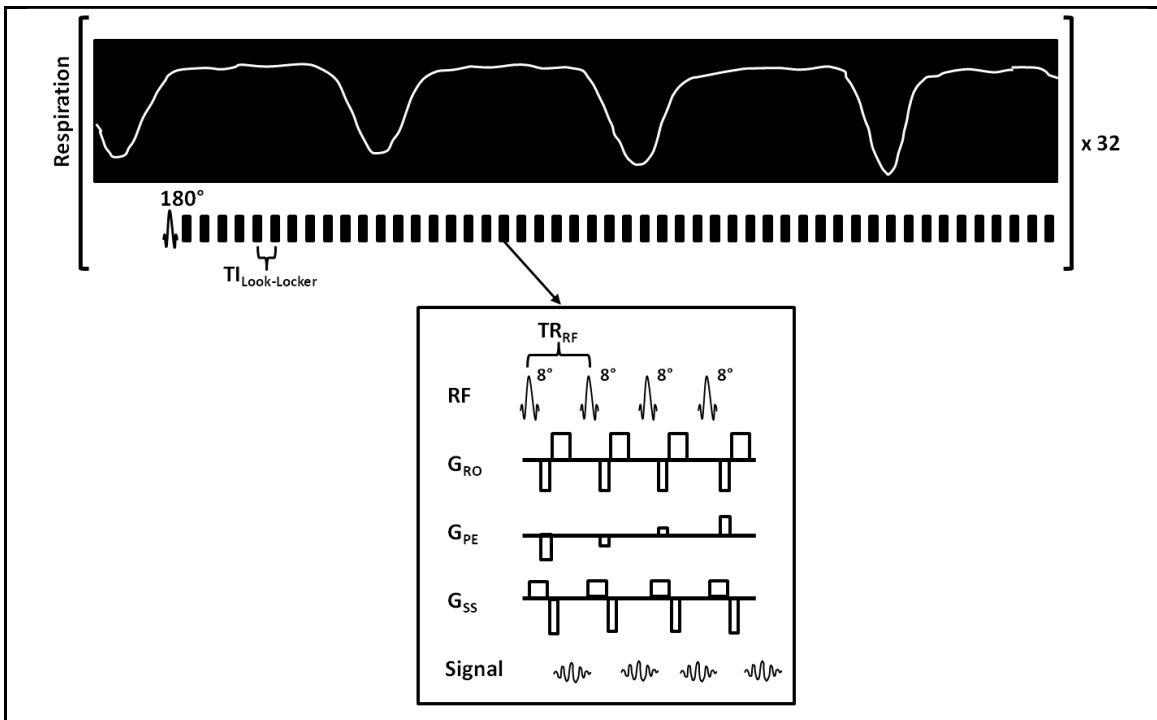


Figure 7.2: Look-Locker T1 quantification using segmented k -space sampling

Schematic diagram of the respiratory triggered, Look-Locker T1 mapping sequence used in this study. The inversion pulse is end-expiration triggered, followed by a free-breathing, a segmented Look-Locker sampling train. Each segmented block is separated by an inversion time ($T_{I\text{Look-Locker}}$) of 110 ms, with each block containing four sampling pulses separated by TR_{RF} (2.3 ms). Four lines of k -space are sampled per inversion. The full acquisition is performed twice in line with the FAIR ASL protocol. (Taken from reference [435]).

Unlike DCE MRI experiments where quantification is based on post-CA bolus tracking through sequential images, ASL is based upon measuring the difference in signal that arises as a result of labelled spins exchanging with protons in the tissue of interest [221]. Quantification based on comparison of the flow sensitised and control T1 maps of the same slice, was undertaken using the method proposed by Belle et al. [436, 437]. Using this model, pixel-wise perfusion (P) can be calculated from the two T1 measurements using the following expression:

$$P = \frac{\lambda}{T1_{blood}} \left(\frac{T1_{global}}{T1_{slice\ selective}} - 1 \right) \quad (\text{Equation 7.1})$$

Where ' λ ' is the blood-tissue partition coefficient - the ratio of water content in the parenchyma to the water content in the blood perfusing the tissue. We assumed this in this study ' λ ' to be 0.95 ml/g, based on ^{85}Kr gas clearance measurements in the liver [438]. Blood T1 was also assumed to be 1900 ms, based on murine left ventricular blood pool T1 quantification, measured as part of another study on the same imaging system [430].

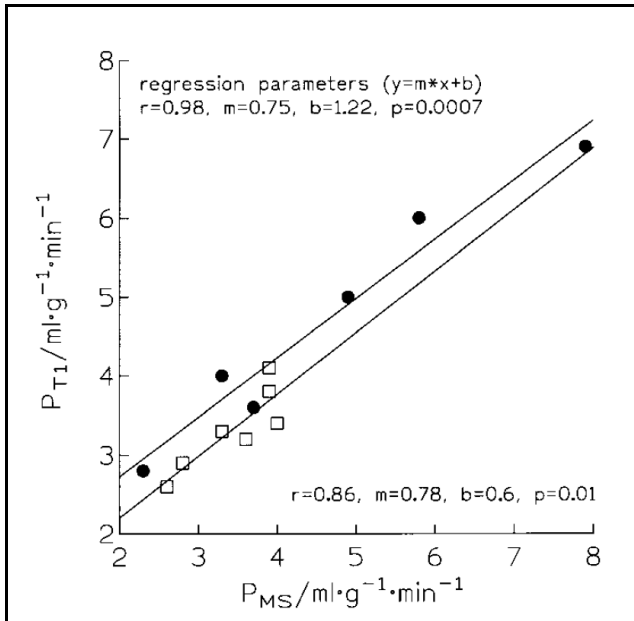


Figure 7.3: Myocardial FAIR ASL quantification and invasive validation

Paired ASL perfusion measurement (y-axis, P_{T1} , ml/g/min), plotted against microsphere perfusion measurements (P_{MS} , ml/g/min) from the same rat heart. Data at rest (□) and post adenosine (●) are shown, demonstrating encouraging positive correlation. Unfortunately, Bland-Altman analysis of agreement was not performed. (Taken from reference [439]).

The Belle et al. [437] method of quantification was applied to small animal cardiac perfusion measurements and subsequently invasively validated using microspheres (figure 7.3) [439, 440]. Though encouraging, this validation was undertaken in a different organ to the liver and on a different imaging system.

We presented in Chapter 5 a novel method for estimation of total liver blood flow using subtraction of caval flows, which when normalised to liver mass also provides an estimate of tissue perfusion. We have also validated PCMRI flow measurements using (a) TTUS for validation of PV PCMRI and (b) fluorescent microspheres for validation of caval subtraction PCMRI estimated HA fraction. Good agreement with invasive methods was demonstrated for PV flow PCMRI and encouraging correlations were demonstrated with microspheres (section 5.4). The measurement of HA fraction is reliant on caval subtraction PCMRI estimated TLBF and though validated indirectly, we would argue provides a means of assessing the accuracy of ASL perfusion when measured in the same subject and same scanning session.

Finally, there is a growing interest in the evaluation of intrinsic tissue T1 in the context of hepatic fibrosis [322-324]. Accurate tissue T1 measurements underpin ASL quantification and therefore can also be extracted to study differences between normal and diseased liver. Studies pre and post haemodynamic stress provide the opportunity to confirm the repeatability of baseline hepatic parenchymal T1 measurements, as these should remain stable regardless of changes in perfusion.

With this in mind, in this section we aim to (a) demonstrate the feasibility of using segmented FAIR Look-Locker ASL to measure hepatic parenchymal perfusion, (b) assess

the agreement between FAIR Look-Locker ASL and indirectly validated PCMRI measurements of estimated TLBF, (c) assess the repeatability of hepatic T1 parenchymal measurements and finally, (d) investigate any differences in hepatic parenchymal T1 in normal and diseased rats.

7.3.2 METHODS

7.3.2.1 Experimental subjects

All experiments were conducted according to the Home Office guidelines under the UK Animals in Scientific Procedures Act 1986. Animals were maintained as per guidelines and approval of the ethical committee for animal care of University College London. Experiments were performed on healthy male Sprague-Dawley rats (Charles River UK, Margate, UK) with normal liver function. Animals were housed in cages at 22-23°C, ~50% humidity and with 12 hours of light and ad libitum access to water and rat feed.

For studies in models of liver disease, subjects weighing 250-300g were randomised to bile-duct ligation (BDL) procedure ($n = 10$) or sham laparotomy ($n = 11$). BDL and sham surgery was conducted as described previously by researchers at our institution [350]. Briefly, a midline abdominal incision was made under 2% isoflurane and intraperitoneal levobupivacaine. For animals undergoing BDL procedure, the common bile duct was isolated, triply ligated with 3-0 silk and sectioned between the ligatures. After closure and recovery, animals were maintained for 5 weeks to allow the development of portal hypertension and features of chronic liver disease.

For each experiment/cohort, subjects were randomly selected at the time of removal from the cage. Any adverse events and subsequent protocol modifications were recorded and reported in the results.

7.3.2.2 Sample size

Data presented in this section was collected simultaneously with the data presented later in this chapter. Sample sizes therefore are based on more complex experiments presented in section 7.4.

7.3.2.3 Animal preparation

After induction with isoflurane, a 0.58 mm internal diameter fine bore polyethylene line (Portex, Smiths Medical, Kent, England) was sited in the jugular vein. The anaesthetised animal was then transferred to a 9.4T Agilent scanner (Oxford, UK) with a rectal probe for temperature monitoring. Core body temperature was maintained between 36 and 38°C

using circulating warm water pipes and warm air. Cardiac monitoring was undertaken using a triple electrode single lead system (SA instruments, New York, USA).

7.3.2.4 ASL and T1 measurement

Once positioned in the scanner, respiratory gated axial anatomical images were obtained to identify an imaging slice that enabled good visualisation of a large volume of hepatic parenchyma. Perfusion measurements were obtained using a respiratory gated inversion, segmented FAIR Look-Locker ASL sequence with a spoiled gradient-echo readout. Data was acquired using a FOV of 60 x 60 mm², 128 x 128 matrix size, 2 mm slice thickness, with echo-time (TE) of 1.18 ms, TI_{Look-Locker} of 110 ms, repetition time (TR_{RF}) of 2.3 ms, Look-Locker flip angle (α_{LL}) of 8°, and TR (inversion) of 13 seconds. A total of 50 inversion recovery readouts were used for each T1 measurement. A 6 mm slice selective and 200 mm global inversion slab was used, centred on the 2 mm slice of interest. Inversions were triggered at the end of the expiration, with four lines of *k*-space obtained per segmented acquisition. Total acquisition time was approximately 15 minutes.

Data was analysed using in-house developed Matlab code (MathWorks, Natick, USA). Images were retrospectively gated using an algorithm that used ghosting artefacts to discard motion corrupted images. Because 50 TIs, were acquired at Look-Locker readout, images could be discarded without affecting the accuracy of T1 fitting. The selected images were then smoothed using a Gaussian window ($\sigma = 1.6$ pixels, final resolution = 753 μm full width at half-maximum) before pixel-wise non-linear least-squares fitting to the Look-Locker recovery curve (equation 7.2). Estimates were then made of ' M_0 ' – the signal intensity at equilibrium magnetisation, ' α ' – the inversion efficiency (ranging from zero to two, with $\alpha = 2$ representing a perfect inversion) and ' $T1^*$ ', the apparent T1 (as a result of Look-Locker acceleration of magnetisation recovery).

$$M_z = M_0 \left(1 - \alpha \cdot e^{-\frac{TI}{T1^*}} \right) \quad \text{(Equation 7.2)}$$

Actual T1 was then estimated using from the apparent T1 ($T1^*$), using the Look-Locker correction factor in the small angle approximation and assuming a perfect inversion [441]:

$$T1 = T1^* \cdot (\alpha - 1) \quad \text{(Equation 7.3)}$$

Perfusion maps were then generated from global and slice selective T1 maps using equation 7.1. Final post-processing involved the placement of three identically sized circular ROIs on the right, middle and left hepatic parenchyma (figure 7.4). ROIs were carefully positioned to avoid major vascular structures and extra-hepatic tissues using T1

maps. Placement of ROIs was performed through joint consensus between a Radiologist with 5 years experience in abdominal imaging (Manil Chouhan) and an Imaging Scientist with 4 years experience in the development of preclinical hepatic ASL (Raj Ramasawmy). Both researchers were blinded to the presence of disease or haemodynamic stress in the dataset being processed. For each subject, ROIs of identical position were used for baseline and post-inflammatory stress measurements. Overall estimates of perfusion and parenchymal T1 were based on averages obtained from the three ROIs. Parenchymal T1 measurements were derived from control, non-flow sensitised acquisitions.

7.3.2.5 Two-dimensional cine PCMRI

Two-dimensional cine PCMRI was undertaken as previously described in section 5.4.2.3. Axial anatomical images were used to identify the vessel of interest. Three markers were placed in the vessel lumen, for automated planning of scanning slices through the vessel in the coronal plane (VnmrJ 3.2, Agilent, Oxford, UK). The vessel was then identified on angled coronal slices and studies were planned to ensure orthogonality to the vessel. Cardiac gated images were used for planning of studies on the distal IVC (figure 5.5) and aortic root. Proximal IVC flow measurements were obtained from the same slice used to measure PV flow (figure 4.7).

PCMRI planning provided time for the animal to settle before evaluating subject heart rate. Based on the heart rate (R-R interval) and sequence repetition time, the number of frames acquired through the cardiac cycle was set as two less than the maximum number of frames possible, to avoid cycle overlap should heart rate increase. Heart rate was recorded so that the extended interval between the final frame and end of the cycle could be accounted for in flow calculations. All datasets included at least 10 frames through the cardiac cycle.

Cardiac and respiratory-gated 2D cine PCMRI was then undertaken using 2 mm slice thickness, a 10° flip angle and a 192 x 192 (frequency encoding x phase encoding) acquisition matrix. Based on previous work (section 5.4.2.3), data was acquired using V_{enc} settings of 33 cm/s for PV and proximal IVC flows, 66 cm/s for distal IVC flows and 133 cm/s for aortic root flows. ROIs were manually positioned on each vessel for each frame of the cardiac cycle and quantitative analysis was undertaken as previously. All PV flow, estimated TLBF and HA flow measurements were normalised to explanted liver weight. Data was analysed using in-house developed Matlab code (MathWorks, Natick, USA).

7.3.2.6 Experimental in vivo protocol

All animals received continuous intravenous fluid resuscitation with normal saline at a rate of 8 ml/kg/hour once transferred to the MRI scanner. Baseline ASL and PCMRI measurements were performed before a 60 minute infusion of 0.3 mg/kg lipopolysaccharide (*E coli* LPS, Sigma Aldrich, UK), for inflammatory stress. The normal saline infusion was then resumed at the same initial rate and continued for the duration of the scanning protocol. Ten minutes post-LPS, repeat PCMRI and ASL measurements were performed. LPS doses and baseline normal saline infusion rates were based on prior experience within the research group [442].

7.3.2.7 Statistical analysis

Kolmogorov-Smirnov tests were used to confirm normality of variable distributions. Validation and repeatability studies were assessed using paired t-tests, Bland-Altman analysis of agreement with calculation of the coefficient of repeatability and assessment of correlation between validated/repeated measurements using Pearson's correlation coefficient. Comparisons between sham and BDL cohorts were undertaken using unpaired t-tests. The threshold of statistical significance was defined to be $p < 0.05$.

7.3.3 RESULTS

7.3.3.1 Cohort features

Experiments were performed in sham operated ($n = 11$) and BDL ($n = 11$) rats. Four weeks post-surgery, mean BDL body weight (403.4 ± 14.27 g) was lower than mean sham body weight (463.2 ± 6.606 g; $p = 0.0009$). Conversely, mean BDL wet liver mass (30.02 ± 1.949 g) was higher than mean sham wet liver mass (13.97 ± 0.6417 g; $p < 0.0001$). Unfortunately, two BDL subjects had problems with jugular venous cannulation such that it was impossible to determine if the correct doses of fluid resuscitation or LPS had been given. Problems with gating resulted in artefacted ASL data for two BDL and one sham operated subject. Final analysis was performed using data from ten sham operated and seven BDL rats. A detailed summary of subject participation can be found in Appendix E.

7.3.3.2 ASL feasibility

A sample ASL dataset is shown in figure 7.4. Anatomical imaging was used to select a slice for ASL quantification. Slice selective and global inversion T1 maps were generated and pixel wise perfusion maps were then created based on comparison of both slice selective and global inversion recovery curves. Parenchymal ROIs were then used to extract perfusion data from different sites across the liver and averaged to given an overall estimation of hepatic perfusion.

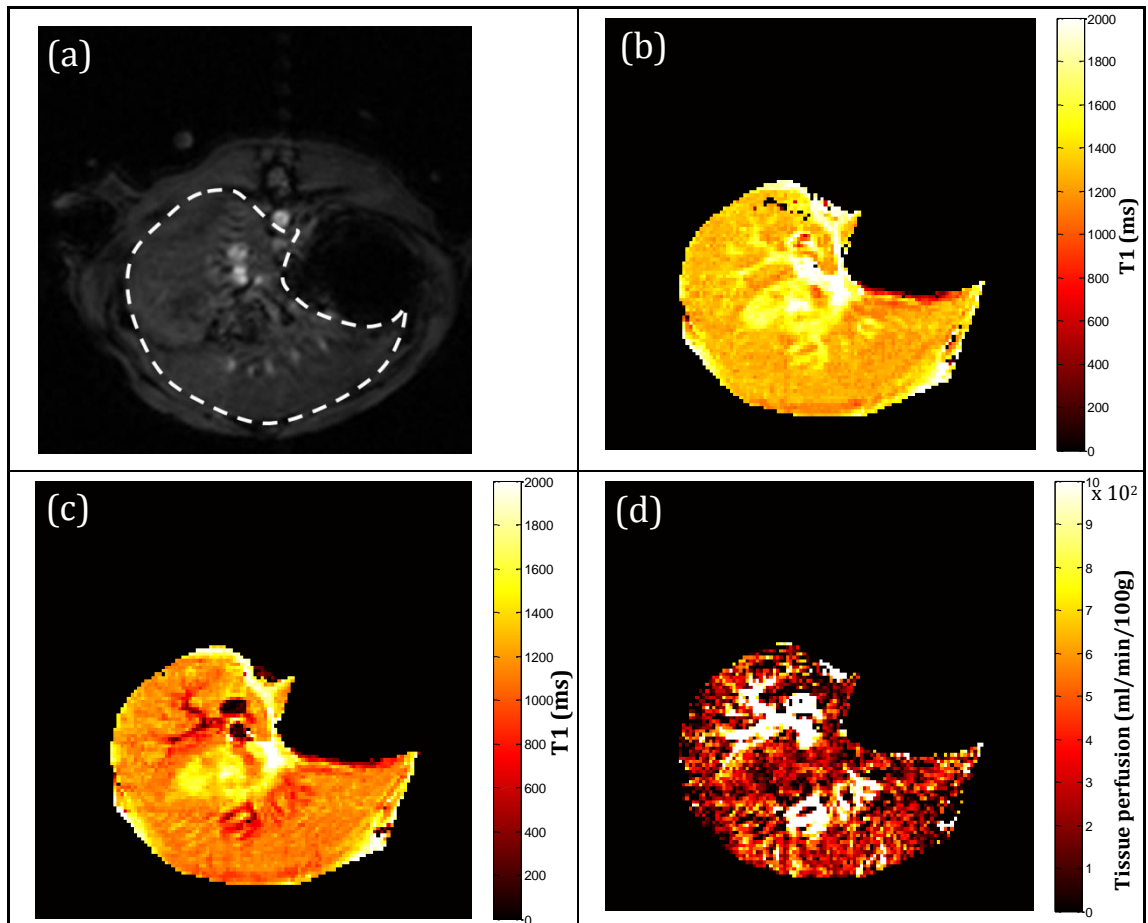


Figure 7.4: Example of FAIR ASL acquisition

Anatomical images (a) were used to select a slice for quantification. The segmented area for quantitative analysis is demonstrated by the dashed white line. Global (b) and slice selective (c) inversion T1 maps were generated. Note the reduction in parenchymal and vessel T1 on (c) in keeping with perfusion related T1 shortening. Finally, pixel wise perfusion maps were generated shown in (d).

7.3.3.3 Assessment of agreement of ASL with PCMRI

ASL measurements of parenchymal perfusion were compared with PCMRI measurements of estimated TLBF normalised to liver mass. Successive measurements using each method obtained at baseline and subsequently post-LPS were compared in both sham ($n = 10$) and BDL ($n = 7$) animals. Paired t-tests however demonstrated significant differences between ASL and PCMRI measurements of parenchymal perfusion (mean difference pooled across cohorts 52.36 ± 23.31 ml/min/100g; $p = 0.0320$). Significant differences between both measurements were demonstrated across all sub-cohorts (sham baseline mean difference -144.4 ± 25.39 ml/min/100g, $p = 0.0003$; sham post-LPS mean difference -106.4 ± 31.77 ml/min/100g, $p = 0.0086$; BDL baseline mean difference 89.90 ± 30.98 ml/min/100g, $p = 0.0273$) except for BDL animals post-LPS (mean difference 40.65 ± 50.51 ml/min/100g; $p = 0.4661$). The coefficient of variation was higher for PCMRI perfusion across all cohorts (50.71% vs 30.03%; PCMRI vs ASL) and for all sub-cohorts (25.04% vs 23.82%, sham baseline PCMRI vs ASL; 45.58% vs 19.49%, BDL baseline PCMRI vs ASL; 43.51% vs 25.36%, BDL post-LPS PCMRI vs ASL), with the exception of sham animals post-LPS (15.60% vs 26.52%; PCMRI vs ASL). Graphical analysis (figure 7.5b) showed correlations between PCMRI and ASL parenchymal perfusion were significant ($r = 0.6020$; $p = 0.0003$).

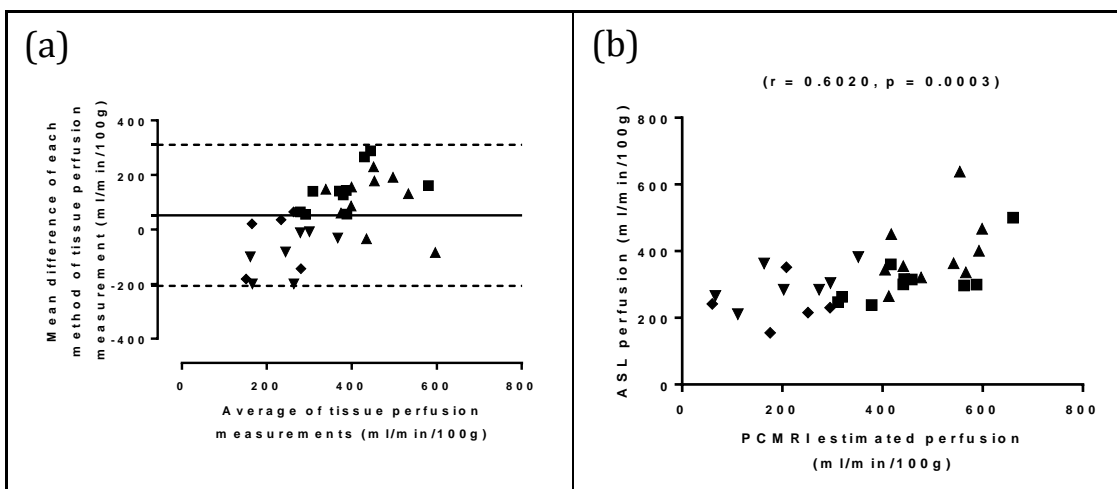


Figure 7.5: Agreement of hepatic perfusion measured with ASL and PCMRI estimated TLBF

Data from sham rats at baseline (■), sham rats post-LPS (▲), BDL rats at baseline (▼) and BDL rats post-LPS (◆). The coefficient of repeatability was 258.4 ml/min/100g across all cohorts, but smaller for sub cohorts (sham baseline 157.4 ml/min/100g; sham post-LPS 196.9 ml/min/100g; BDL baseline 160.67 ml/min/100g and BDL post-LPS 221.35 ml/min/100g). Despite these differences, an encouraging overall correlation was demonstrated between the two methods.

7.3.3.4 T1 measurement repeatability

Repeatability of ASL hepatic parenchymal T1 measurements was assessed in sham ($n = 10$) and BDL ($n = 7$) animals. Average time between repeat measurements across the entire cohort was 124.0 ± 4.100 minutes. No significant differences were demonstrated between repeated hepatic parenchymal T1 measurements in sham (mean difference 4.103 ± 3.305 ms; $p = 0.2093$) and BDL animals (mean difference -14.14 ± 15.66 ms; $p = 0.4013$). The coefficient of repeatability was smaller for sham (18.813 ms) compared with BDL (81.22 ms) animals. Graphical analysis (figure 7.6b) showed strong and significant positive correlations between repeated hepatic parenchymal T1 measurements ($r = 0.9845$; $p < 0.0001$).

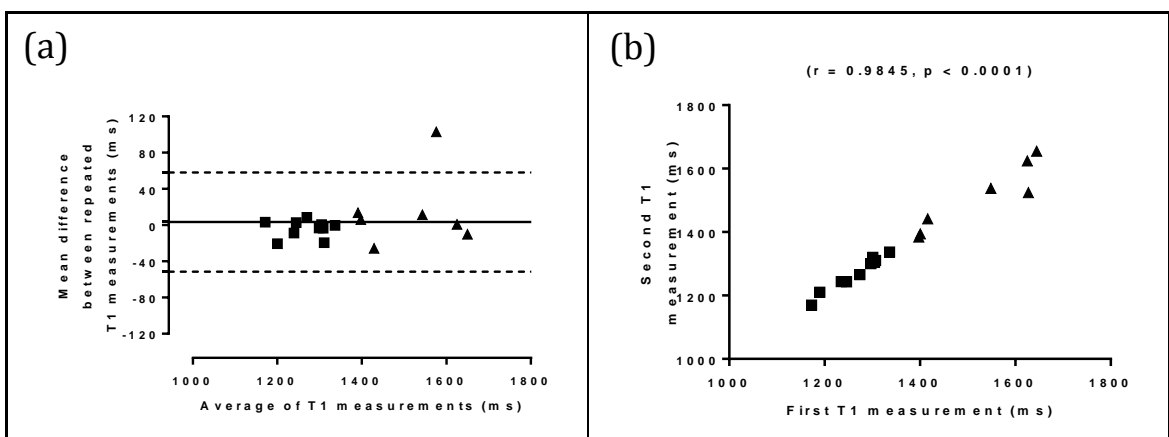


Figure 7.6: Repeatability of ASL hepatic parenchymal T1 measurements

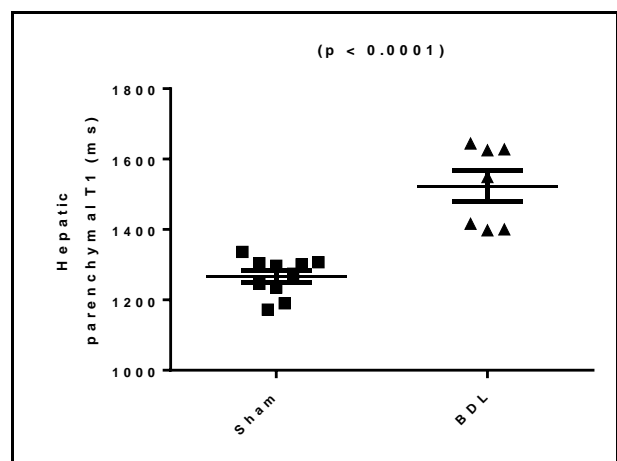
Data from sham (■) and BDL (▲) rats. Repeated measurements were obtained on average 124 ± 4.100 minutes apart. The overall cohort coefficient of repeatability was 54.79 ms. A strong and significant correlation between repeated measurements was demonstrated.

7.3.3.5 T1 measurement studies

Baseline T1 measurements were compared in sham ($n = 10$) and BDL ($n = 7$) rats. Baseline mean hepatic parenchymal T1 in sham operated animals (1266 ± 17.07 ms) was significantly lower than in BDL animals (1523 ± 43.36 ms) (figure 7.7).

Figure 7.7: Hepatic parenchymal T1 at baseline in sham and BDL rats

Baseline hepatic parenchymal T1 was found to be significantly higher in BDL rats.



7.3.4 DISCUSSION

We have demonstrated successful implementation of segmented FAIR Look-Locker ASL in rats at 9.4T. Quantification of hepatic parenchymal perfusion using this method can be used to yield physiologically feasible measurements.

We have used contemporaneous normalised PCMRI measurements of estimated TLBF to assess agreement between these independent quantification methods across healthy and diseased animals at baseline and after haemodynamic stress. Previous indirect invasive validation of PCMRI estimated TLBF (using fluorescent microsphere measurements of HA fraction and TTUS measurements of PV flow – section 5.4), supported the use of PCMRI estimated TLBF, and therefore our demonstration of a significant positive correlation between ASL and PCMRI is encouraging. The coefficient of repeatability between methods was however high (258.4 ml/min/100g), especially considering mean ASL perfusion across the cohort was 318.0 ml/min/100g. Bland-Altman analysis revealed a bias of 52.36 ml/min/100g, which in combination with the significant correlation could imply systematic underestimation of hepatic perfusion using ASL. Significant differences between mean ASL perfusion and PCMRI estimated TLBF were demonstrated across almost all cohorts, which could also be a reflection of a systematic error. Importantly, the coefficient of variation of ASL was lower than PCMRI across almost all the cohorts, which would suggest that while ASL measurements may be subject to error, but that these are still inherently more stable than their PCMRI counterparts.

We have also demonstrated that parenchymal T1 measurements underpinning ASL demonstrate excellent repeatability. This is an important result especially in the context of comparing baseline and post-LPS ASL data, as any measured changes in perfusion are therefore likely to reflect genuine changes in perfusion rather than any changes in the tissue T1 as a result of inflammatory stress. As with previous data (section 5.4), BDL rats demonstrated expectably greater hepatic parenchymal T1 variability and poorer repeatability than their sham counterparts.

Finally, we demonstrated significant differences between sham and BDL animal hepatic parenchymal T1 at baseline. BDL animals demonstrated significantly greater hepatic T1, corroborated by published clinical data on T1 mapping and hepatic fibrosis stage [416].

The introduction of ASL in this section was driven by the need to develop a tissue based method of directly measuring perfusion rather than estimation through measurement of PCMRI bulk flow. Our experience served to highlight several difficulties, specific to this

study and ASL in general which though discussed in this section are pertinent to all subsequently presented ASL data.

One of the major challenges with ASL rests with obtaining sufficient SNR for accurate quantification. Because the difference in magnetisation between flow sensitised and generalised inversion T1 maps is small, multiple averages are required for quantification. Working at higher field strength helped overcome this problem, but even a single non-averaged measurement (as was used in this study) required an acquisition time of approximately 15 minutes. In a preclinical context, acquisition times of that length may be acceptable, but it is worth noting that data for only a single 2 mm slice of tissue was acquired. A three slice acquisition has subsequently been developed with similar acquisition time [227], but whole liver coverage with ASL is not yet a reality.

FAIR ASL quantification is also only as good as the quality of the T1 measurement underpinning the acquisition. The Look-Locker method is a well-established method that is a variation of the “gold-standard” inversion recovery T1 measurement (section 3.3). It is however, not without its weaknesses, including a reliance on smaller flip angles and therefore vulnerability to inhomogeneities in B_1 , especially at higher field strength. A major advantage to comparing both T1 maps for quantification is that it can be argued that flip angle errors can be eliminated [443].

There are several important criticisms of the quantification process used in this study. Firstly the blood-tissue partition coefficient (λ) – the ratio of parenchymal water to perfusing blood water – was assumed to be constant across all sub-cohorts. Changes in the partition coefficient are however likely to occur both in states of disease and during inflammatory stress. In chronic liver disease for example, fibrotic collagen deposition is likely to reduce the volume (and therefore content) of parenchymal water. Similarly, derangements in intra- and extravascular fluid volume are a well-established feature of acute inflammatory septic states. The measurement of blood-tissue partition coefficient is however not easily undertaken, and in early studies has been shown to fluctuate by as much as 0.57 in the same animal as result of changes in tissue composition post-partial hepatectomy [444].

Secondly, blood T1 was assumed to be 1900 ms across all four sub-cohorts. Time constraints prevented measurement of blood pool T1 for each subject, which in reality would have varied both between subjects but also potentially as a result of inflammatory stress. Blood T1 is reliant predominantly on temperature and haematocrit [326, 329], both of which had the potential to change post-LPS as a result of (a) pyrogenic effects (although temperature was maintained for all subjects between 36 and 38°C) and as a

result of (b) interstitial and third space fluid losses (although fluid resuscitation was administered before and after LPS infusion).

Thirdly, we applied FAIR ASL in this study to obtain a singular measurement of tissue perfusion using the Belle model [437]. The latter was initially developed for myocardial perfusion measurements and incorporates assumptions that may not be valid in the liver. Inadequacies of the model account for systematic underestimation of ASL perfusion (when compared with PCMRI estimated TLBF).

Lastly, it is worth noting that FAIR ASL provides a measure of total tissue perfusion, without any separation of arterial and portal venous contributions or measurement of distribution volume or mean transit time. The latter, classically obtained from DCE MRI acquisitions can be obtained using ASL with several strategies proposed in the literature. Under the assumption that all labelled spins have perfused and exchanged with protons in the imaged slice, a general kinetic model can be used to estimate changes in magnetisation over time produced by inflowing labelled spins. Using the same principles underpinning DCE MRI, this can then be used to obtain additional haemodynamic parameters [221]. As data was obtained from multiple TI slice selective Look-Locker acquisitions, this could then be used to directly measure the changes in magnetisation over time and construct a 'dynamic' ASL data set [224]. Development of this quantification using a generalised kinetic model remains the subject of future work.

The ability to separately quantify arterial and portal venous contributions is an essential cornerstone of hepatic haemodynamic assessment which ultimately future hepatic ASL development should be aimed towards. Alternative ASL methods, specifically pseudo-continuous (PCASL) labelling strategies may provide a new means of separating these two contributions [222, 224]. Finally any preclinical developments should provide a platform for clinical translation. Application of ASL methods at lower clinical field strengths bring greater SNR challenges, concern over high specific absorption rate (SAR) doses to patients and logistical challenges regarding the length of the acquisition and strategies to overcome motion artefact.

In summary, we have demonstrated the successful implementation of ASL for hepatic parenchymal perfusion. In spite of poor agreement, the encouraging correlation with independent PCMRI estimated TLBF, excellent repeatability of underlying hepatic parenchymal T1 values and intrinsic differences in parenchymal T1 in both health and disease, set a precedent for the use of ASL in preclinical hepatic haemodynamic assessment in disease and post inflammatory stress.

7.3.5 CONCLUSION

In this section, we have implemented FAIR ASL, an alternative method for quantification of hepatic parenchymal perfusion in rats. We have demonstrated the feasibility of this technique and shown encouraging correlation with indirectly validated PCMRI estimated TLBF, but poor agreement. Our data suggested a tendency of FAIR ASL to underestimate hepatic parenchymal perfusion and we have offered technical reasons that may account for this difference.

Finally, we have demonstrated excellent repeatability of hepatic parenchymal Look-Locker T1 measurements underpinning ASL measurements. We have then applied these to demonstrate intrinsically higher parenchymal T1 values in BDL rats, in line with published clinical studies of hepatic fibrosis.

7.4 HAEMODYNAMIC STRESS IN CHRONIC LIVER DISEASE

7.4.1 BACKGROUND

In section 4.5, we studied differences in PCMRI PV flow between sham operated and BDL animals at baseline and using pharmacological agents (L-NAME and terlipressin) for the modulation of PV flow. In section 5.4 we built on our previous experience with terlipressin and used it to study the hepatic arterial buffer response using novel methods for HA flow quantification. In this section, we use the validated techniques presented in section 5.4 alongside ASL to study the effects of pathological haemodynamic stress.

Acute-on-chronic liver failure, is a recently described clinical entity in which patients with established but compensated liver cirrhosis develop an acute deterioration in liver function, decompensation and subsequent failure of one or more organs [445-447]. The condition is associated with elevated mortality, and while the clinical features are well recognised, the pathophysiology remains poorly understood. The rapid deterioration in liver function is associated with rises in portal pressure and the concurrent systemic inflammatory response and progression to sepsis ultimately result in multiorgan hypoperfusion before failure [30, 448]. While it is clear that hepatic haemodynamic phenomena play an essential role in the pathogenesis of ACLF, haemodynamic characterisation has been limited by the invasive nature of gold-standard measurement methods [449, 450]. We have demonstrated that PCMRI and ASL can be used for hepatic haemodynamic characterisation of bulk flow and parenchymal perfusion respectively. We have also previously used cardiac cine MRI to assess cardiac systolic function non-invasively. As inflammation and/or infection are the most common precipitants of ACLF, we have chosen in this study to emulate this condition using LPS in a BDL model of chronic liver disease [442]. Acute endotoxaemia is associated with profound haemodynamic instability, so unlike previous pharmacological studies, animals were given fluid resuscitation for the duration of the experiment, before, during and after LPS administration. Effects of fluid resuscitation also afford an interesting insight into haemodynamic differences in chronic liver disease, especially when compared with previous data obtained from animals not receiving intravenous fluid.

With this in mind, in this section we aim to (a) evaluate differences at baseline between normal and diseased rats receiving fluid resuscitation, (b) study haemodynamic differences in non-hydrated and hydrated normal and diseased rats and finally (c) investigate the haemodynamic response to LPS in normal and diseased rats using PCMRI,

ASL and cardiac cine MRI thereby gaining insight into the vascular pathophysiology of ACLF.

7.4.2 METHODS

Methods for experimental subjects, animal preparation, two-dimensional cine PCMRI and Look-Locker FAIR ASL were as described in section 7.3.2.

7.4.2.1 Sample size

Investigation of the haemodynamic response to LPS was prioritised for calculation of sample size. Experiments were planned based on two-way ANOVA, with the two factors being group (sham or BDL) and treatment (saline or LPS). Difference in TLBF after LPS in sham and BDL rats was used as the endpoint variable. Power calculations were undertaken for a statistical power of 90% and a 5% significance level. Assuming a post-saline change in TLBF of 20% (standard deviation approximately 10%) and post-LPS change in TLBF of 35% (based on prior experience within the research team), with a view to detecting a difference in change in TLBF of 20% between sham and BDL rats, a sample of $n = 24$ subjects (half of which would have liver disease) was advised. Projecting a 15% attrition rate, the final sample size would be $n = 28$.

7.4.2.2 Cardiac cine MRI

Cardiac cine MRI was performed as described previously in section 5.4.2.5. Cardiac and respiratory gated coronal images through the thorax were obtained for planning. Long-axis images were then acquired to ensure accurate short-axis view planning.

Because of the proximity of the mitral valve orifice to the aortic vestibule and obliquity of the cardiac axis in the rat, cardiac cine MRI was usually undertaken before aortic root PCMRI measurements so that the short axis slice orientation of slices adjacent to the aortic root could be used to plan aortic root flow PCMRI studies.

Planning provided time for the animal to settle before evaluating subject heart rate. As with cine PCMRI, the heart rate and repetition time were used to determine the maximum number of frames possible through the cardiac cycle. Acquisitions were for two frames less than this number, to avoid cycle overlap should heart rate increase. All datasets included at least 20 frames through the cardiac cycle. Spoiled gradient echo images were obtained with an echo time of 1.2 milliseconds, repetition time of 7.5 milliseconds, 15° flip angle, slice thickness of 1 mm, no slice separation, field of view of 40 x 40 mm² and 128 x 64 (frequency encoding x phase encoding) acquisition matrix. Data was analysed using the freely available software package Segment (Medviso, Lund,

Sweden). Automatic segmentation tools were used to identify the endocardial surface, with frame by frame manual review and segmentation correction where appropriate. For evaluation of cardiac systolic function, heart rate, stroke volume, cardiac output, left ventricular ejection fraction and cardiac index were recorded. Cardiac index (CI, ml/min/kg) was calculated by dividing cardiac output by body weight (kg).

7.4.2.3 Experimental *in vivo* protocol

All animals received continuous intravenous fluid resuscitation with normal saline at a rate of 8 ml/kg/hour once transferred to the MRI scanner. Baseline cardiac cine MRI, ASL and PCMRI measurements were performed before a 60 minute infusion of 0.3 mg/kg lipopolysaccharide (*E coli* LPS, Sigma Aldrich, UK), for inflammatory stress. The normal saline infusion was then resumed at the same initial rate and continued for the duration of the scanning protocol. Ten minutes post-LPS, repeat PCMRI, ASL and finally cardiac cine MRI measurements were performed (figure 7.8). LPS doses and baseline normal saline infusion rates were based on prior experience within the research group [442]. Because of the expectation of high attrition rates post-LPS in BDL subjects, the LPS protocol was prioritised and control, post-saline data was not collected. The response to fluid resuscitation was evaluated through comparison with previously acquired PCMRI and cardiac cine MRI data at baseline in non-hydrated sham operated and BDL rats in section 5.4. Planned statistical analyses were amended accordingly (section 7.4.2.4).

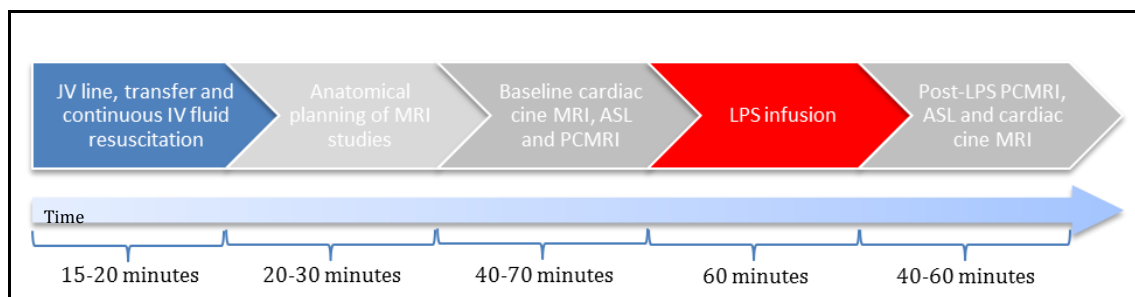


Figure 7.8: Experimental protocol

Continuous IV fluid resuscitation was commenced once the animal was transferred to the scanner. Approximate timings of each phase of the protocol are listed below on a non-linear scale. Timing ranges varied with physiological differences (heart rate, etc) and technical challenges that may have arisen during a given session.

7.4.2.4 Statistical analysis

Kolmogorov-Smirnov tests were used to confirm normality of variable distributions. Baseline differences between fluid resuscitated sham operated and BDL rats were assessed using unpaired t-tests. Comparisons between dry and fluid resuscitated animals were also made using unpaired t-tests in sham and BDL cohorts. The response to LPS was evaluated in normal and diseased animals using paired t-tests. Where data was found to non-normally distributed, Mann-Whitney U tests were used for unpaired comparisons and

Wilcoxon matched-pairs signed rank tests were used for paired comparisons. The threshold of statistical significance was defined as $p < 0.05$.

7.4.3 RESULTS

7.4.3.1 Cohort features

Experiments were performed in sham operated ($n = 11$) and BDL ($n = 11$) rats. Cohort features were as given for section 7.3.3.1. Cohort sizes varied for some parts of the study, primarily as a result of premature demise of BDL subjects before post-LPS data acquisition was complete, but also because of artefacted data.

Cohort features and sizes for non-hydrated “dry” animals were as given in section 5.4.3.1, briefly, studies were performed in sham operated ($n = 13$) and BDL ($n = 12$) rats. Four weeks post-surgery, mean BDL body weight (422.3 ± 11.10 g) was lower than mean sham body weight (484.0 ± 5.565 g; $p < 0.0001$) and conversely mean BDL wet liver mass (32.38 ± 1.941 g) was higher than mean sham wet liver mass (16.09 ± 0.6558 g; $p < 0.0001$).

Numbers of animals included in final analyses are summarised in table 7.1, but a detailed summary of subject participation in each stage of the protocol shown can be found in Appendix E.

Table 7.1: Cohort numbers for haemodynamic stress studies

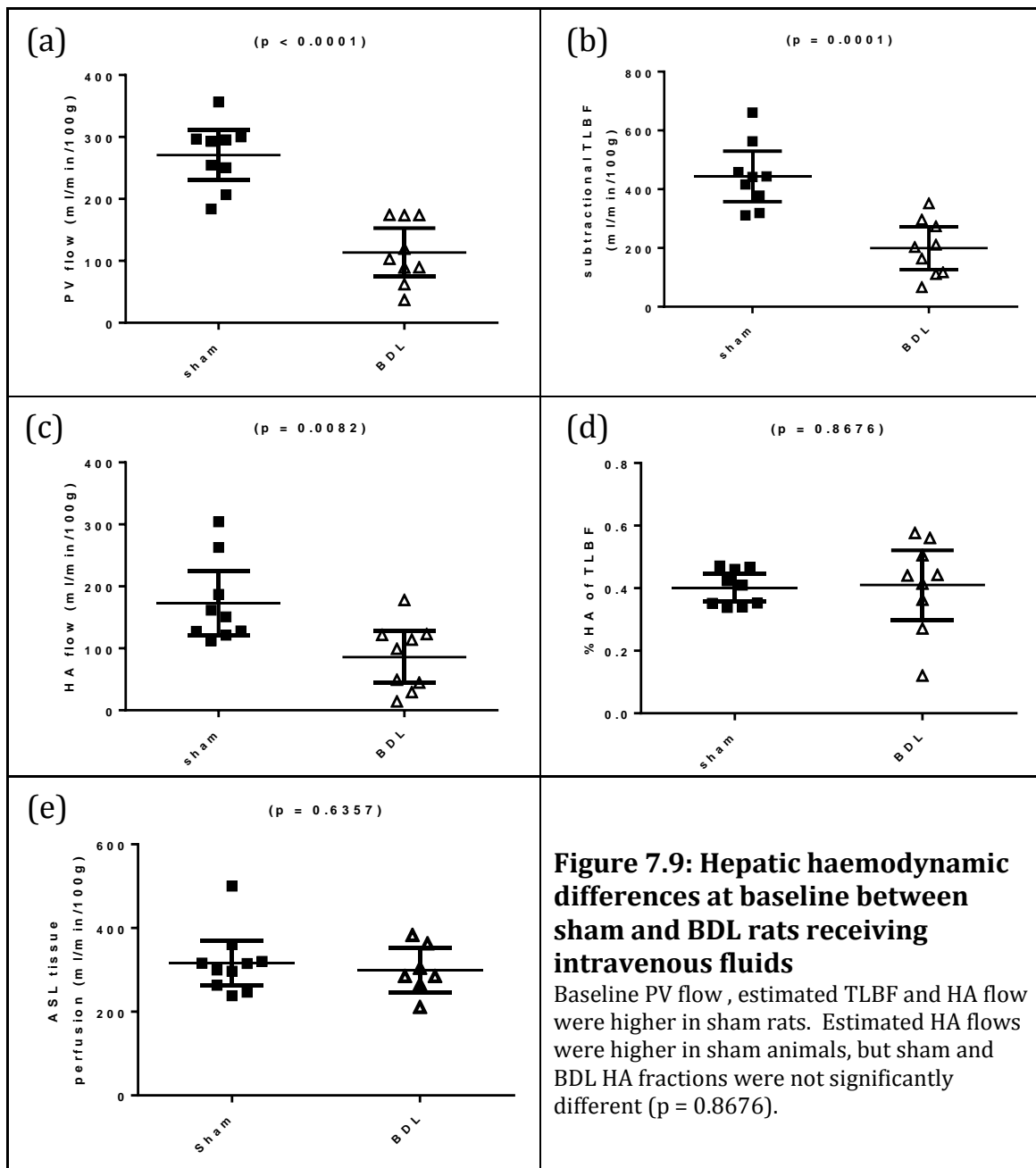
	HYDRATED		NON-HYDRATED*	
	SHAM ($n = 11$)	BDL ($n = 9$)	SHAM ($n = 13$)	BDL ($n = 12$)
<i>Baseline PCMRI</i>	9	9	7	9
<i>Baseline ASL</i>	10	7	-	-
<i>Baseline cardiac cine MRI</i>	11	9	13	12
<i>Post-LPS PCMRI</i>	9	6		
<i>Post-LPS ASL</i>	10	7		
<i>Post-LPS cardiac cine MRI</i>	10	5		

*(data from these subjects is presented in section 5.4).

7.4.3.2 Baseline haemodynamic studies in hydrated animals

Baseline hepatic haemodynamics were compared in sham ($n = 9$) and BDL ($n = 9$) rats. Baseline mean PV flow in sham operated animals (270.8 ± 17.61 ml/min/100g) was higher than in BDL animals (113.6 ± 16.96 ml/min/100g; $p < 0.0001$) (figure 7.9a). Estimated TLBF measured using caval subtraction PCMRI was on average higher in sham rats (443.7 ± 37.20 ml/min/100g) compared with BDL rats (199.3 ± 31.56 ml/min/100g; $p = 0.0001$) (figure 7.9b). Estimated HA flow was also on average higher in sham operated rats (172.8 ± 22.54 ml/min/100g) compared with their BDL counterparts (85.77 ± 18.05 ml/min/100g; $p = 0.0082$) (figure 7.9c). Estimated HA fraction (figure 7.9d) was however

not significantly different in sham operated ($40.16 \pm 1.894\%$) compared with BDL rats ($41.03 \pm 4.813\%$; $p = 0.8676$). Baseline hepatic perfusion was compared using ASL in sham ($n = 10$) and BDL ($n = 7$) rats. Mean ASL tissue perfusion in sham operated animals (315.6 ± 23.59 ml/min/100g) was higher than in BDL animals (299.3 ± 22.05 ml/min/100g), but this difference was not significant ($p = 0.6357$) (figure 7.9e). Examples of perfusion maps obtained at baseline are shown in figure 7.15a and b.



Cardiac output measurements were used to contextualise absolute hepatic haemodynamic parameters to systemic circulatory factors. BDL subjects had slightly lower HA flow relative to cardiac output ($13.97\pm 2.645\%$) when compared to their sham counterparts ($18.29\pm 1.993\%$) (figure 7.10a), but this difference was non-significant ($p = 0.2108$). Mean estimated TLBF relative to cardiac output was however significantly higher in sham ($47.20\pm 3.008\%$) when compared to BDL rats ($32.85\pm 4.807\%$; $p = 0.0223$) (figure 7.10b).

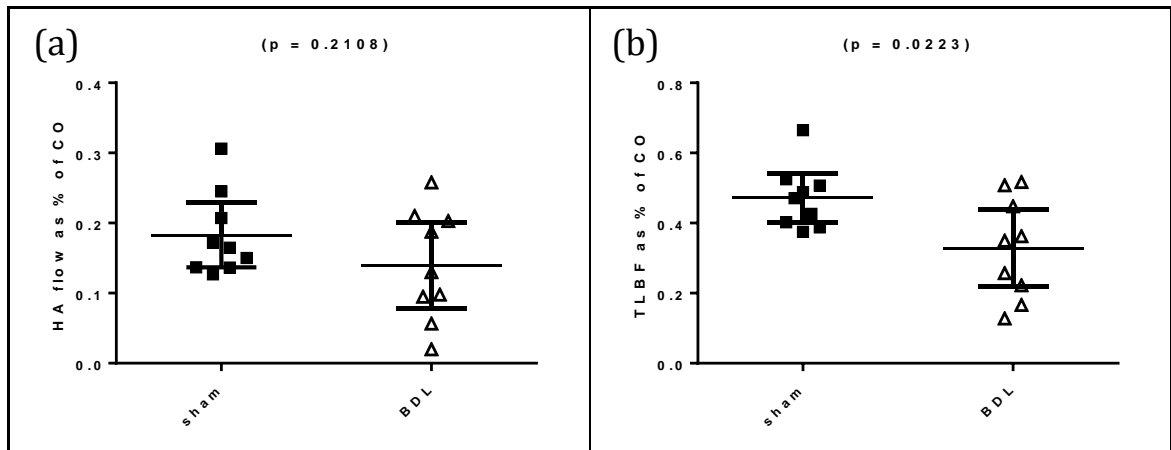
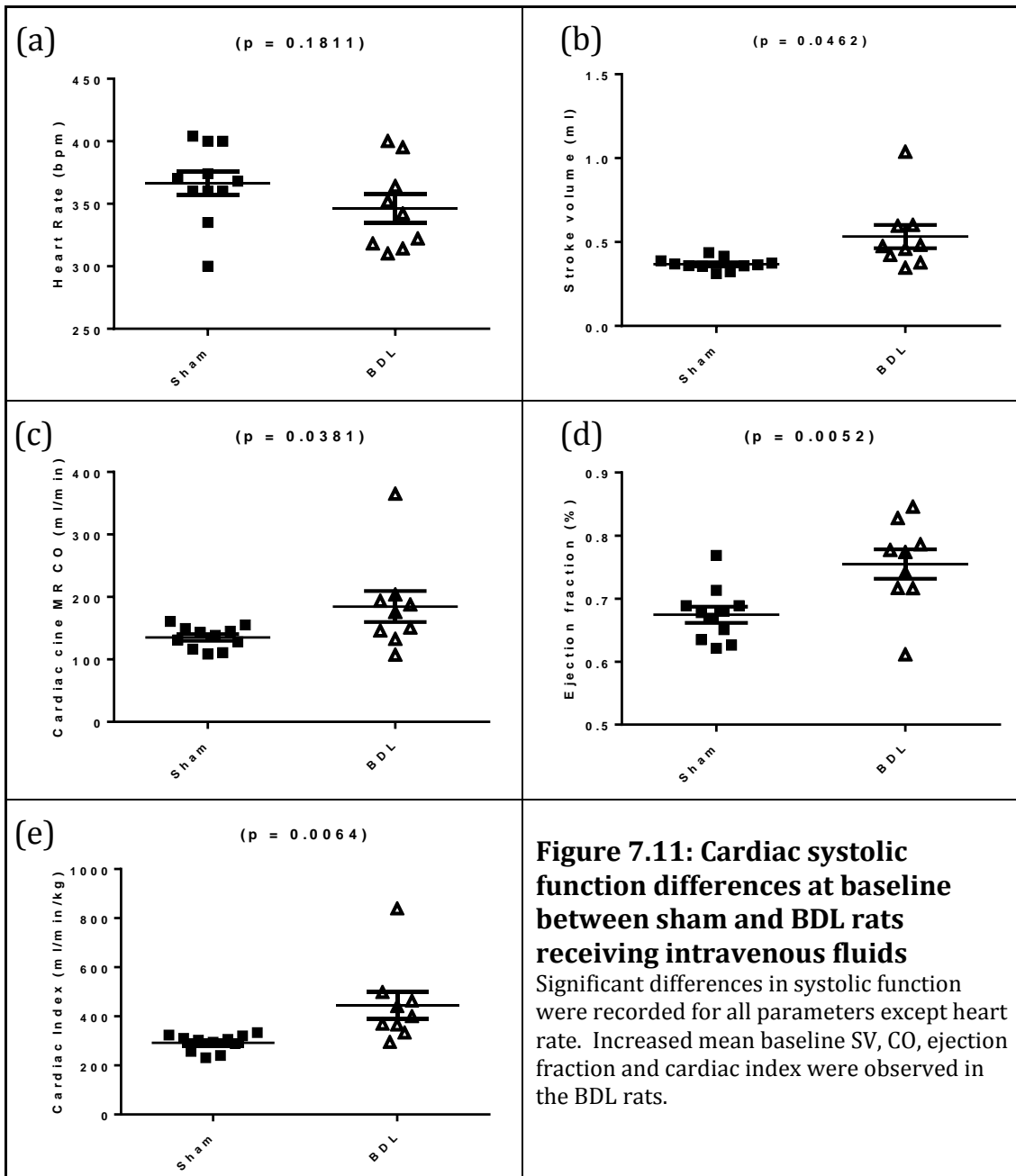


Figure 7.10: Haemodynamic differences relative to cardiac output at baseline between sham and BDL rats receiving intravenous fluids

HA flow (a) and TLBF (b) as a percentage of CO. Significant differences between cohorts were shown for TLBF relative to CO, but not HA flow.

Baseline cardiac systolic function was compared in sham ($n = 11$) and BDL ($n = 9$) rats. At baseline, no significant difference in heart rate was demonstrated between sham operated (366.5 ± 9.176 bpm) and BDL rats (346.3 ± 11.41 bpm; $p = 0.1811$) (figure 7.11a). Mean baseline stroke volume and CO was significantly larger in BDL animals (0.5326 ± 0.06925 mls and 184.6 ± 24.82 ml/min) than their sham counterparts (0.3687 ± 0.01084 mls and 135.2 ± 5.360 ml/min) (stroke volume $p = 0.0462$; cardiac output $U = 13.00$, $p = 0.0381$) (figures 7.11b and 7.11c). Left ventricular ejection fraction was also greater in BDL animals ($75.50\pm 2.330\%$) than their sham counterparts ($67.44\pm 1.284\%$; $p = 0.0052$) (figure 7.11d). Given the greater cardiac output and lower body weight of BDL rats, cardiac index was expectably larger in BDL (444.7 ± 53.56 ml/min/kg) compared with sham operated rats (291.8 ± 10.37 ml/min/kg; $p = 0.0064$) (figure 7.11e).



7.4.3.3 Haemodynamic response to intravenous fluid resuscitation

Hepatic haemodynamic response to fluid resuscitation was compared in sham (non-hydrated $n = 7$; hydrated $n = 9$) and BDL (non-hydrated $n = 9$; hydrated $n = 9$) rats. For sham and BDL animals, baseline mean PV flow in non-hydrated animals (sham 178.6 ± 11.65 ml/min/100g, BDL 69.48 ± 10.09 ml/min/100g) was lower than in hydrated animals (sham 270.8 ± 17.61 ml/min/100g, BDL 113.6 ± 16.96 ml/min/100g; sham $p = 0.0011$, BDL $p = 0.0401$) (figure 7.12a and 7.12b). Average estimated TLBF measured using caval subtraction PCMRI in non-hydrated sham operated rats (214.3 ± 16.68 ml/min/100g) was also lower than in hydrated animals (443.7 ± 37.20 ml/min/100g; $p = 0.0002$) (figure 7.12c). This was not observed in BDL rats, where non-hydrated TLBF (152.3 ± 18.68 ml/min/100g), though on average lower than in hydrated animals (199.3 ± 31.56 ml/min/100g) was not significantly different ($p = 0.2175$) (figure 7.12d). Baseline mean estimated HA flow in non-hydrated sham rats (35.78 ± 10.79 ml/min/100g) was also significantly higher in hydrated sham rats (172.8 ± 22.54 ml/min/100g; $p = 0.0002$) (figure 7.12e). Contrastingly, mean estimated HA flow in non-hydrated BDL rats (82.80 ± 19.28 ml/min/100g), was almost identical in hydrated BDL rats (85.77 ± 18.05 ml/min/100g; $p = 0.9121$) (figure 7.12f). Mean estimated HA fraction in non-hydrated sham rats ($15.69 \pm 4.222\%$) was also significantly higher in hydrated sham rats ($40.16 \pm 1.894\%$; $p < 0.0001$) (figure 7.12g). Contrastingly, mean estimated HA fraction in non-hydrated BDL rats ($50.72 \pm 6.832\%$) was lower than in hydrated BDL rats ($41.03 \pm 4.813\%$), but this difference was not significant ($p = 0.2636$) (figure 7.12h). Non-hydrated ASL tissue perfusion data was not available for comparison in either sham or BDL cohorts.

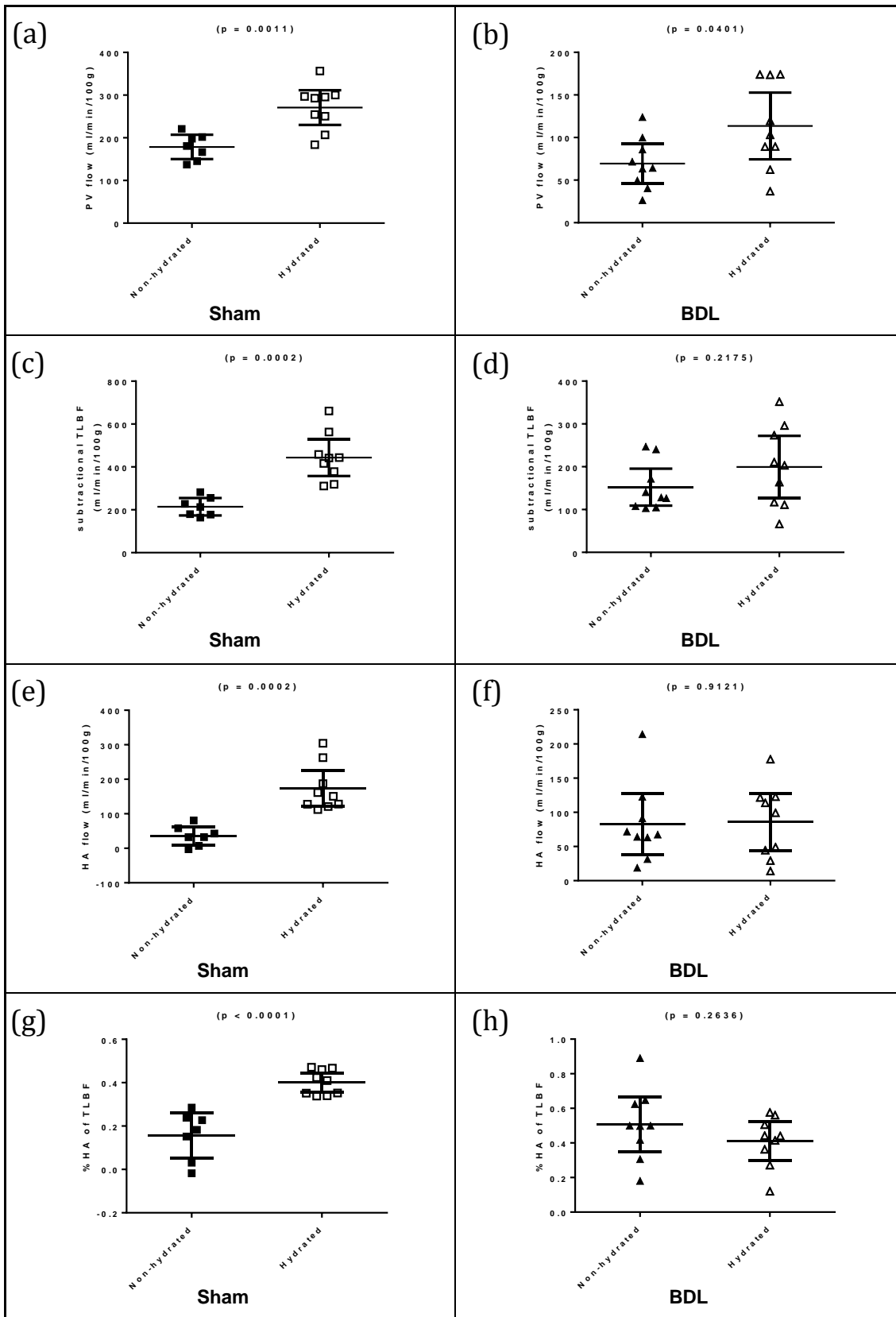


Figure 7.12: Hepatic haemodynamic differences in non-hydrated and hydrated sham and BDL rats

Data from sham operated (left column) non-hydrated (■) and hydrated (□) and BDL (right column) non-hydrated (▲) and hydrated (△) rats demonstrate profound differences in response to intravenous fluids.

Cardiac output measurements were used to contextualise absolute hepatic haemodynamic parameters to systemic circulatory factors. Non-hydrated sham operated rats mean HA flow relative to cardiac output ($3.796 \pm 1.070\%$) was lower than in hydrated sham rats ($18.29 \pm 1.993\%$; $p < 0.0001$) (figure 7.13a). Contrastingly non-hydrated BDL mean HA flow relative to cardiac output ($13.74 \pm 2.410\%$) was almost identical in hydrated BDL rats ($13.97 \pm 2.645\%$; $p = 0.9495$) (figure 7.13b). Mean estimated TLBF relative to cardiac output in non-hydrated sham operated rats ($24.49 \pm 1.615\%$) was also lower than in hydrated rats ($47.20 \pm 3.008\%$; $p < 0.0001$) (figure 7.13c). In non-hydrated BDL animals, mean estimated TLBF relative to cardiac output ($25.66 \pm 2.455\%$) was also lower than in hydrated BDL rats ($32.85 \pm 4.807\%$), but this difference was not significant ($p = 0.2015$) (figure 7.13d).

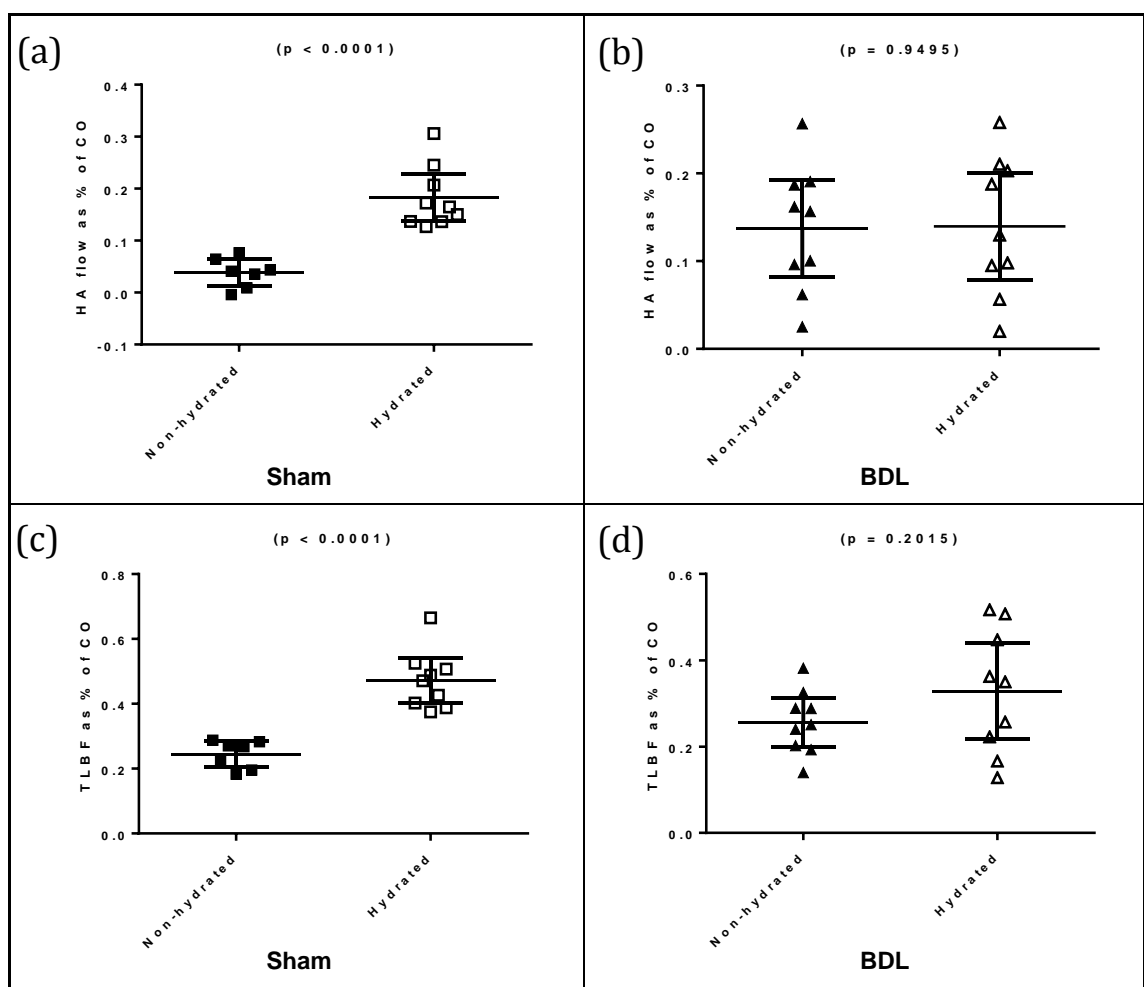


Figure 7.13: Hepatic haemodynamic differences relative to cardiac output in non-hydrated and hydrated sham and BDL rats

Data from sham operated (left column) non-hydrated (■) and hydrated (□) and BDL (right column) non-hydrated (▲) and hydrated (△) rats demonstrate profound differences in response to intravenous fluids.

Cardiac systolic function was compared in sham (non-hydrated $n = 13$; hydrated $n = 11$) and BDL (non-hydrated $n = 12$; hydrated $n = 9$) rats. Mean heart rate in non-hydrated

sham operated animals (325.3 ± 6.803 bpm) was lower than in their hydrated counterparts (366.5 ± 9.176 bpm; $p = 0.0013$) (figure 7.14a). Mean heart rate in non-hydrated BDL rats (333.6 ± 8.497 bpm) was also lower than in hydrated BDL rats (346.3 ± 11.41 bpm), but this difference was not significant ($p = 0.3708$) (figure 7.14b). Mean stroke volume in non-hydrated sham operated rats (0.4664 ± 0.01921 mls) was larger than in hydrated sham animals (0.3687 ± 0.01084 mls; $p = 0.0004$), but overall cardiac output in non-hydrated sham rats (151.4 ± 6.518 ml/min), though larger than in hydrated rats (135.2 ± 5.360 ml/min) was only just above significance ($p = 0.0740$) (figures 7.14c and 7.14e). Mean stroke volume and cardiac output in non-hydrated BDL rats (0.5929 ± 0.03390 mls and 197.6 ± 12.06 ml/min) were both greater than in hydrated BDL rats (0.5326 ± 0.06925 mls and 184.6 ± 24.82 ml/min) but these differences were both not significant (SV $p = 0.4077$; CO $U = 35.00$, $p = 0.1892$) (figures 7.14d and 7.14f). Left ventricular ejection fraction in non-hydrated sham ($67.95 \pm 2.567\%$) and non-hydrated BDL ($76.57 \pm 2.742\%$) rats were not significantly different to hydrated sham ($67.44 \pm 1.284\%$; $p = 0.8695$) or hydrated BDL ($75.50 \pm 2.330\%$; $p = 0.7791$) animals (figures 7.14g and 7.14h). Similarly, cardiac index in non-hydrated sham (313.0 ± 13.94 ml/min/kg) and non-hydrated BDL (469.0 ± 26.68 ml/min/kg) rats were not significantly different to hydrated sham (291.8 ± 10.37 ml/min/kg; $p = 0.2490$) or hydrated BDL (444.7 ± 53.65 ml/min/kg; $p = 0.6662$) rats (figures 7.14i and 7.14j).

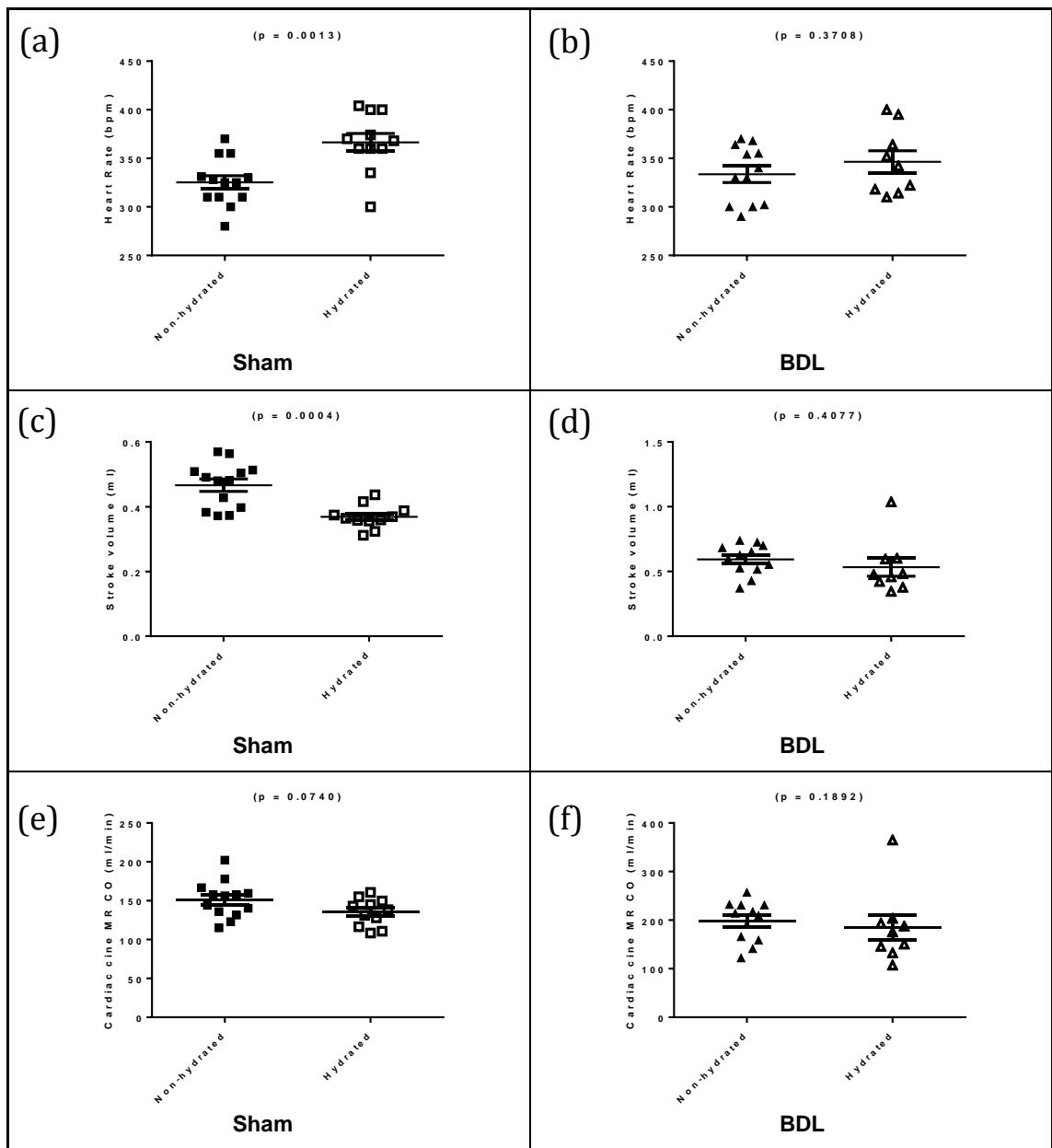


Figure 7.14: Cardiac systolic function differences between non-hydrated and hydrated sham and BDL rats

Data from sham operated (left column) non-hydrated (■) and hydrated (□) and BDL (right column) non-hydrated (▲) and hydrated (△) rats demonstrate differences in systolic function only for sham operated animals. Diagram continued on next page.

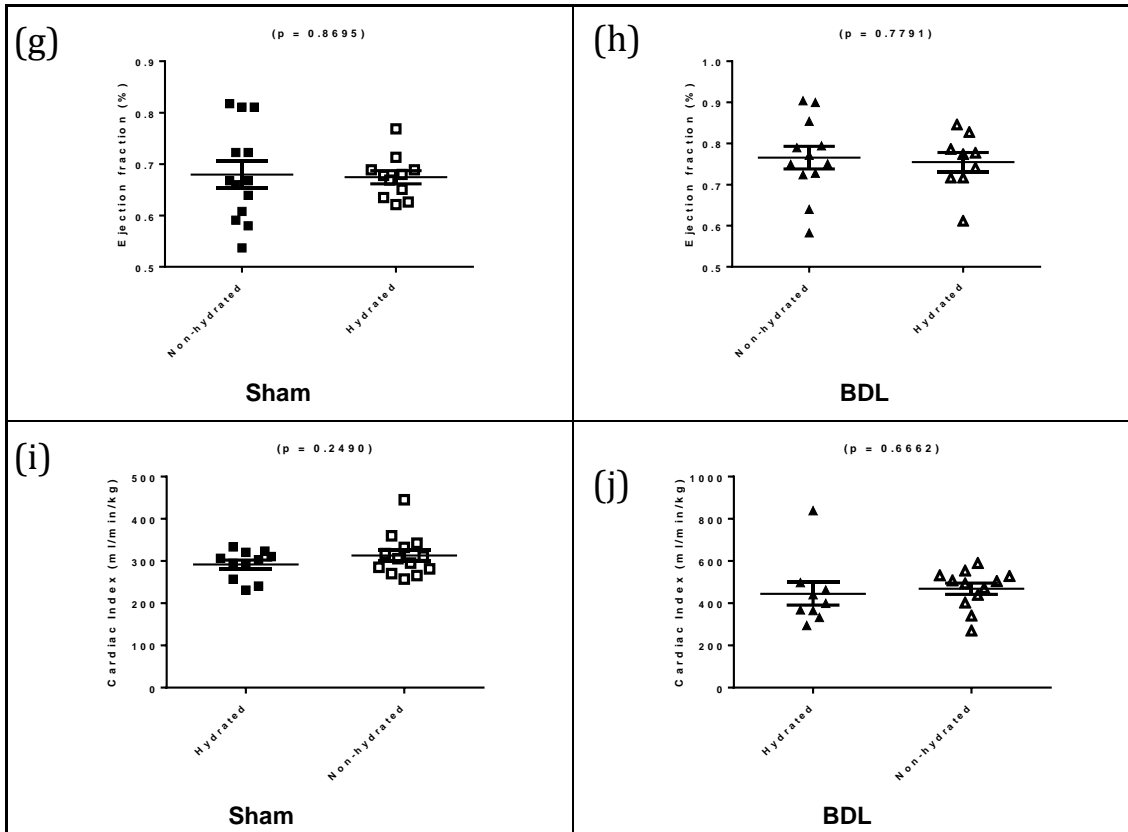


Figure 7.14 (continued): Cardiac systolic function differences between non-hydrated and hydrated sham and BDL rats

Data from sham operated (left column) non-hydrated (■) and hydrated (□) and BDL (right column) non-hydrated (▲) and hydrated (△) rats demonstrate differences in systolic function only for sham operated animals.

7.4.3.4 Haemodynamic response to LPS

The hepatic haemodynamic response to LPS was evaluated in sham ($n = 9$) and BDL ($n = 6$) rats. Post-LPS PCMRI flow measurements were acquired on average 88.55 ± 2.451 minutes after the baseline measurement. Paired t-tests demonstrated non-significant changes in baseline PV flow for sham (mean difference 15.76 ± 25.80 ml/min/100g; $p = 0.5564$) and BDL rats (mean difference -2.489 ± 12.60 ml/min/100g; $p = 0.8483$) (figures 7.15a and 7.15b). Estimated TLBF was greater post-LPS in sham operated animals (mean difference 67.87 ± 33.66 ml/min/100g) but this difference was just above significance ($p = 0.0787$) (figure 7.15c). A decline in estimated TLBF was observed post-LPS in BDL rats (mean difference -58.55 ± 19.72 ml/min/100g; $p = 0.0312$) (figure 7.15d). A non-significant rise in estimated HA flow was observed post-LPS in sham operated rats (mean difference 38.75 ± 41.30 ml/min/100g; $p = 0.3756$) (figure 7.15e). Contrastingly, a decline in estimated HA flow was observed post-LPS in BDL rats (mean difference -64.99 ml/min/100g; $p = 0.0339$) (figure 7.15f). Comparison of pre and post-LPS HA fraction demonstrated a non-significant rise in HA fraction in sham operated rats (mean difference $2.858 \pm 5.640\%$; $p = 0.6260$), but a just non-significant decline in HA fraction in BDL

animals (mean difference $-20.86 \pm 8.470\%$; $p = 0.0570$) (figures 7.15g and 7.15h). Hepatic perfusion was compared using ASL in sham ($n = 10$) and BDL ($n = 7$) rats. A rise in ASL tissue perfusion was observed in sham operated animals (mean difference 79.79 ± 33.27 ml/min/100g; $p = 0.0400$), while a non-significant decline in ASL tissue perfusion was observed in BDL rats (mean difference -65.58 ± 34.39 ml/min/100g; $p = 0.1052$) (figures 7.15i and 7.15j). Examples of perfusion maps obtained in sham and BDL rats at baseline and post-LPS are shown in figure 7.15.

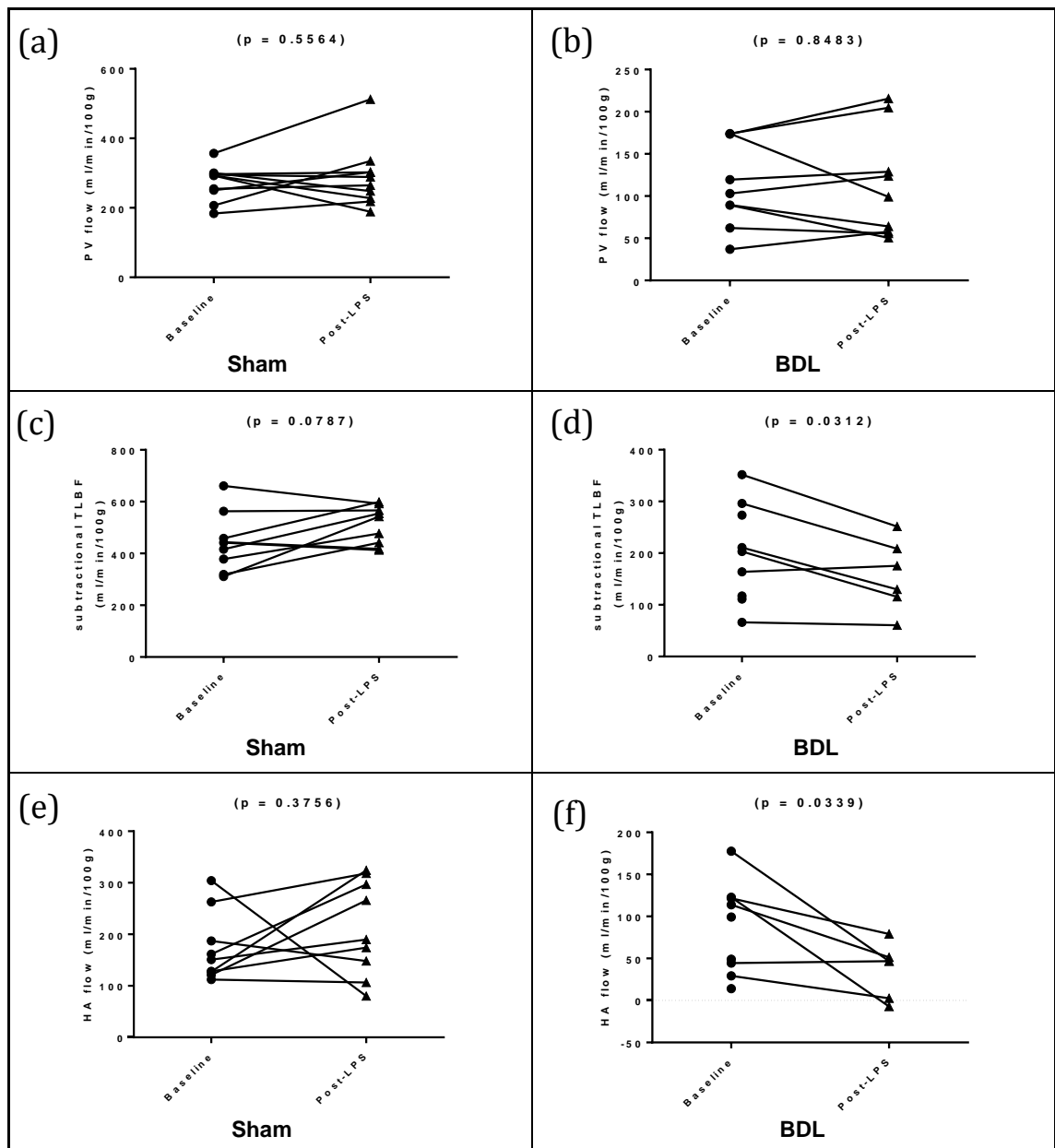


Figure 7.15: Hepatic haemodynamic response to LPS in sham and BDL rats
 Data from sham operated (left column) and BDL rats (right column). Baseline (●) and post-LPS (▲) data demonstrate differences in the hepatic haemodynamic response between cohorts.
 Diagram continued on next page.

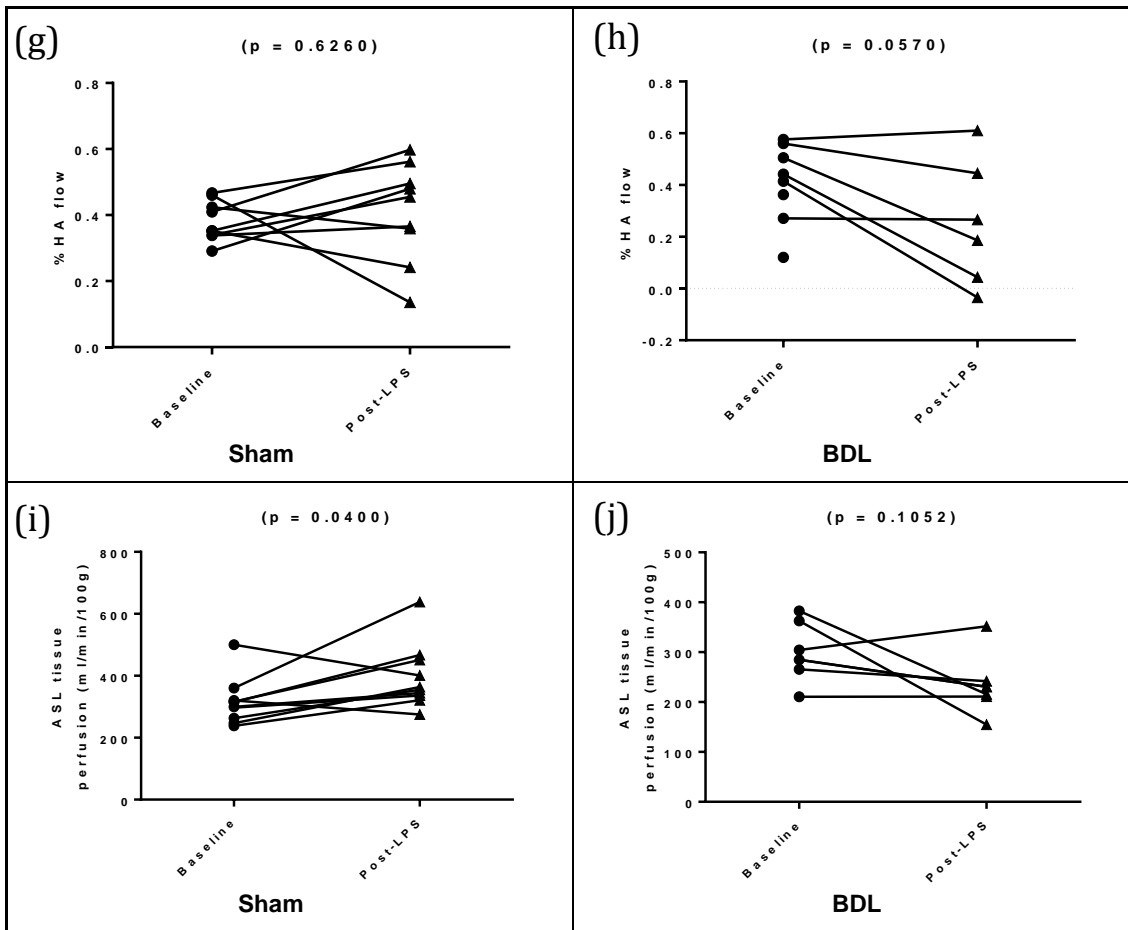


Figure 7.15 (continued): Hepatic haemodynamic response to LPS in sham and BDL rats

Data from sham operated (left column) and BDL rats (right column). Baseline (●) and post-LPS (▲) data demonstrate differences in the hepatic haemodynamic response between cohorts.

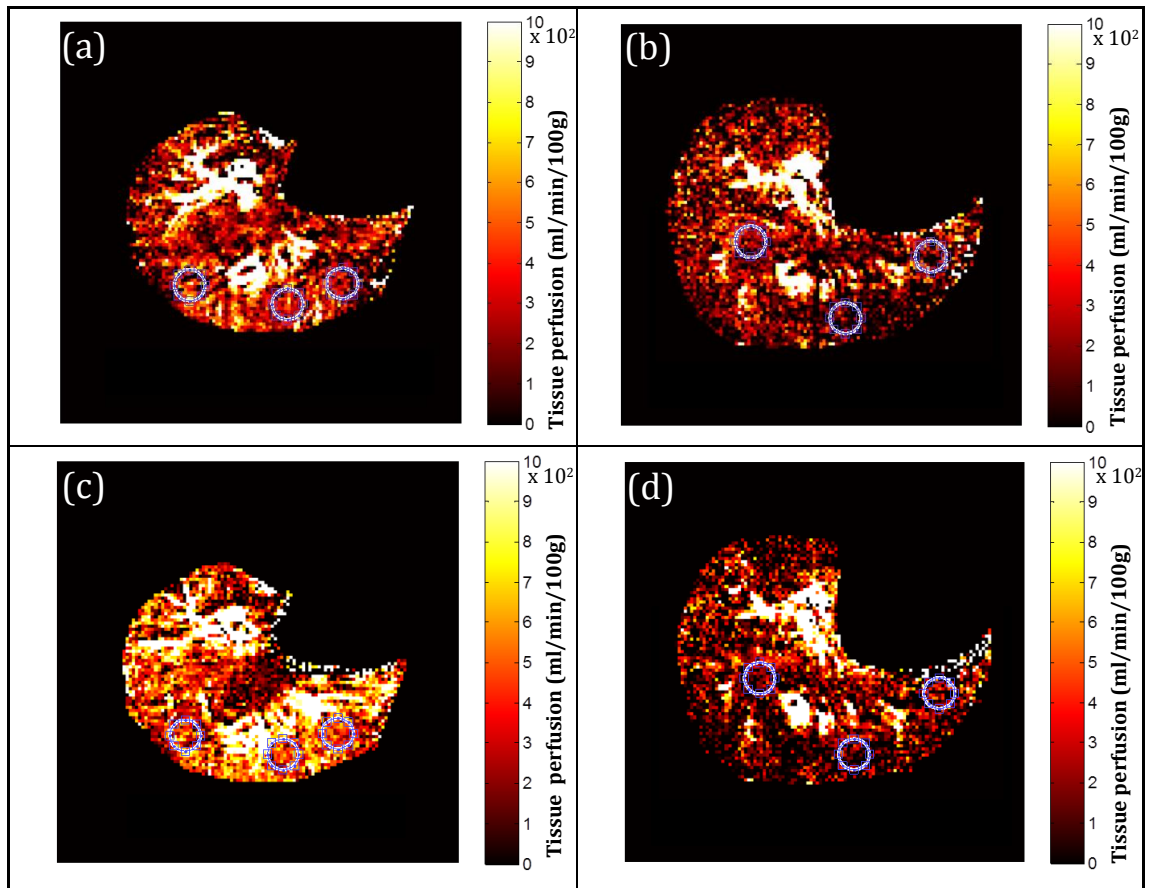


Figure 7.16: Sample ASL tissue perfusion maps at baseline and in response to LPS in sham and BDL rats

Data from sham operated (left column) and BDL rats (right column). Baseline (a, b) and post-LPS (c, d) perfusion maps with circular ROIs used for averaged parenchymal perfusion measurement. Tissue perfusion is given by the scale on the right of each map ($\times 10^2$, ml/min/100g). Recorded averages using these maps for sham baseline (296.3 ml/min/100g), sham post-LPS (442.6 ml/min/100g), BDL baseline (146.8 ml/min/100g) and BDL post-LPS (106.1 ml/min/100g) were included in final analyses. Data exemplify the post-LPS haemodynamic trend demonstrated between cohorts, with increased sham tissue perfusion post-LPS. Note how axial BDL liver is of greater size, in keeping with disease related hepatomegaly.

Cardiac output measurements were used to contextualise absolute hepatic haemodynamic parameters to systemic circulatory factors. Paired t-tests in sham rats demonstrated post-LPS rises in estimated HA flow relative to cardiac output (mean difference $6.201 \pm 5.037\%$) and estimated TLBF relative to cardiac output (mean difference $11.43 \pm 5.459\%$) but these differences were both non-significant ($p = 0.2532$ and $p = 0.0696$, respectively) (figure 7.17a and 7.17c). Unfortunately, post-LPS cardiac cine MRI protocols were only completed in three BDL rats, with premature demise of the remainder of the cohort. Wilcoxon matched-pairs signed rank tests demonstrated changes in post-LPS estimated HA flow relative to cardiac output (median difference -10.26% ; $W = -6.000$, $p = 0.2500$) and estimated TLBF relative to cardiac output (median difference 2.645% ; $W = 2.000$, $p = 0.7500$) which were both non-significant (figure 7.17b and 7.17d).

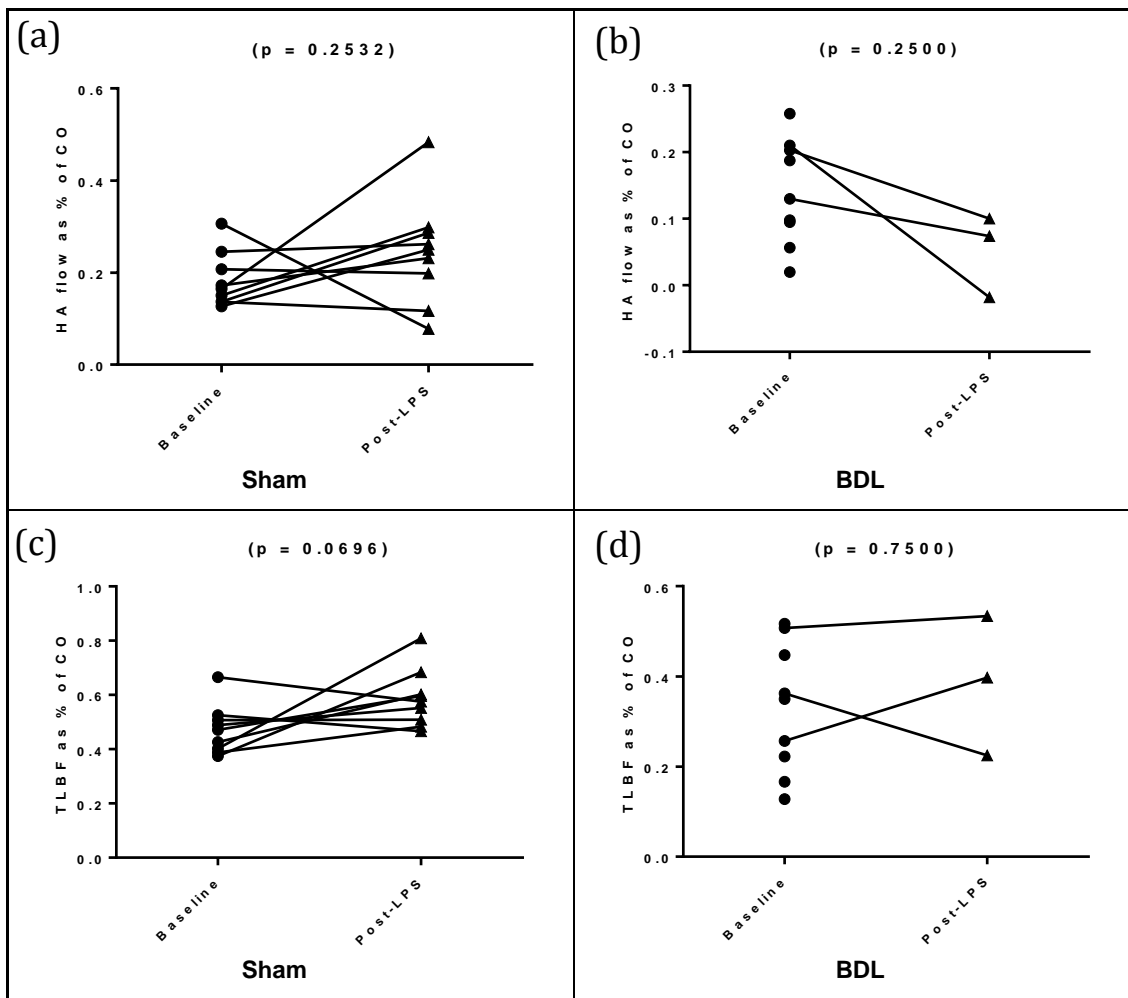


Figure 7.17: Response to LPS demonstrated by hepatic haemodynamic parameters relative to cardiac output in sham and BDL rats

Data from sham operated (left column) and BDL rats (right column) for baseline (●) and post-LPS (▲) data. The small number of BDL post-LPS datasets ($n = 3$) represent premature demise of subjects before cardiac cine MRI acquisitions were complete.

Cardiac systolic function was compared in sham ($n = 10$) and BDL ($n = 5$) rats. Paired t-tests demonstrated rises in post-LPS heart rate that were not significant in sham rats (mean difference 11.00 ± 9.025 bpm; $p = 0.2539$), but significant in BDL animals (mean difference 71.80 ± 24.70 bpm; $p = 0.0438$) (figure 7.18a and 7.18b). Non-significant reductions in post-LPS stroke volume were observed in both sham operated (mean difference -0.01858 ± 0.01966 mls; $p = 0.3693$) and BDL rats (mean difference -0.1966 ± 0.1110 mls; $p = 0.1466$) (figure 7.18c and 7.18d). Non-significant reductions in post-LPS cardiac output were also observed in both sham operated (mean difference -3.518 ± 6.241 ml/min; $p = 0.5868$) and BDL rats (mean difference -45.62 ± 37.34 ml/min; $W = -9.000$, $p = 0.3125$) (figure 7.18e and 7.18f). A rise in left ventricular ejection fraction was observed in sham operated (mean difference $6.011 \pm 2.100\%$; $p = 0.0187$) (figure 7.18g). A rise in left ventricular ejection fraction was also observed in BDL rats (mean difference $8.138 \pm 5.017\%$) but this was not significant ($p = 0.1801$) (figure 7.18h). Finally, a decline in cardiac index was observed in both sham operated (mean difference $-$

7.470±13.78 ml/min/100g; $p = 0.6009$) and BDL rats (mean difference -107.4±86.79 ml/min/100g; $p = 0.2837$) (figure 7.18i and 7.18j).

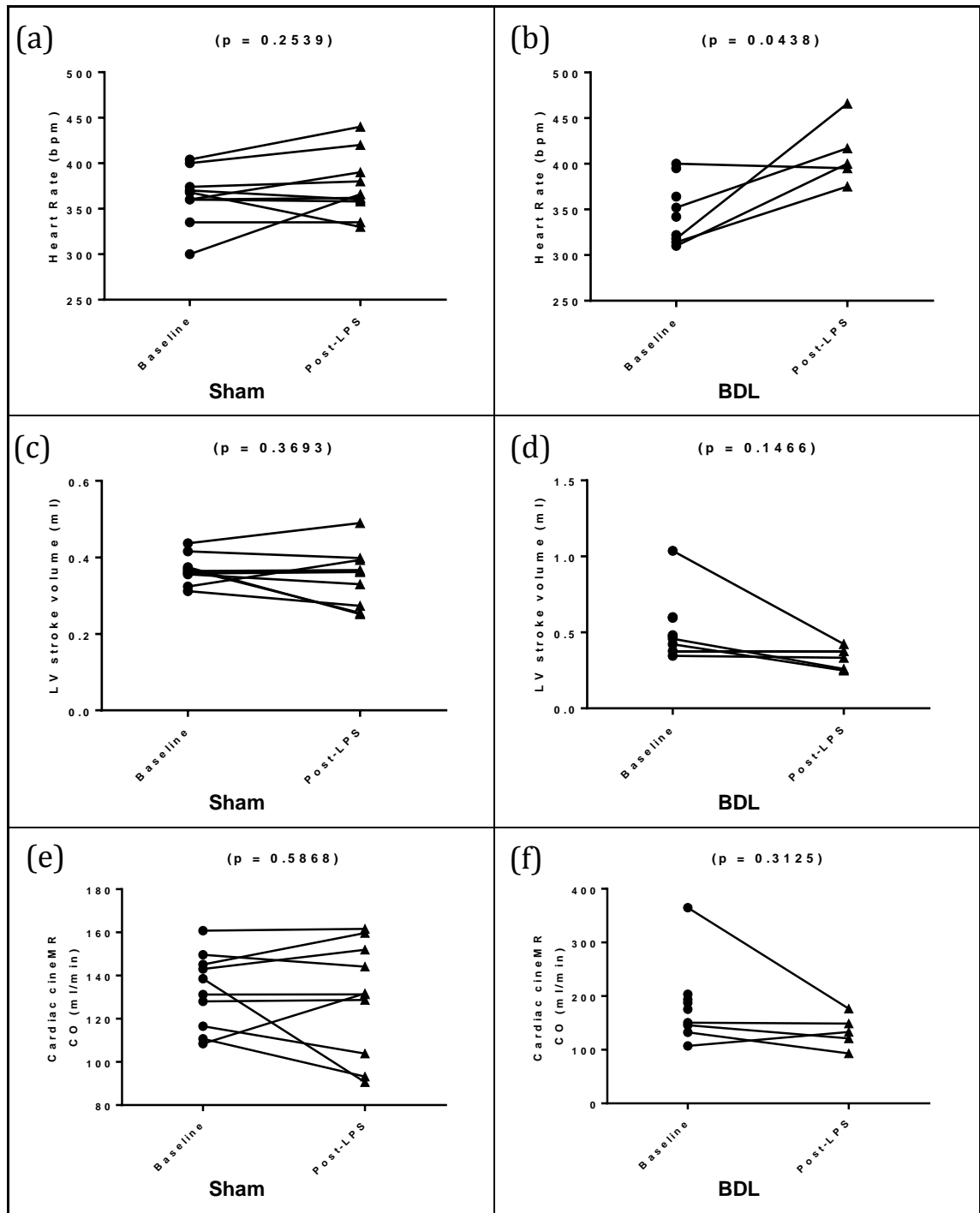


Figure 7.18: Cardiac systolic function response to LPS in sham and BDL rats
 Data from sham operated (left column) and BDL rats (right column). Baseline (●) and post-LPS (▲) data demonstrate a rise in heart rate in BDL rats but no significant differences post-LPS in stroke volume or cardiac output in sham and BDL rats. Diagram continued on next page.

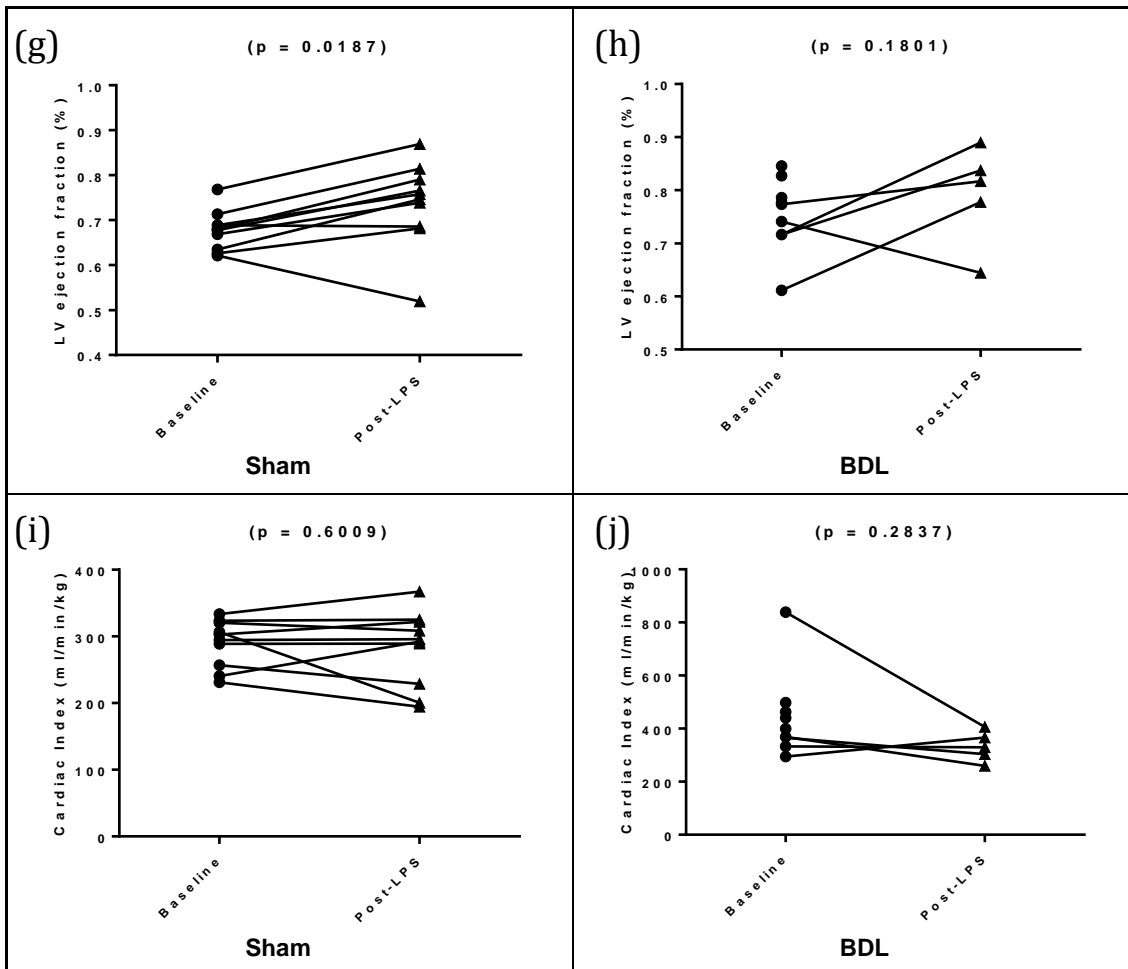


Figure 7.18 (continued): Cardiac systolic function response to LPS in sham and BDL rats

Data from sham operated (left column) and BDL rats (right column). Baseline (●) and post-LPS (▲) data demonstrate a significant rise in left ventricular ejection fraction in sham operated but not BDL rats.

7.4.4 DISCUSSION

For the first time to our knowledge, we have demonstrated fully non-invasive, comprehensive assessment of hepatic haemodynamics in the context of liver disease and in a model of ACLF. Data presented in this chapter corroborate the earlier finding of profound hepatic haemodynamic differences at baseline between sham and BDL cohorts, and when compared with earlier data demonstrate differences in perfusion parameters as a result of intravenous fluid resuscitation. Finally, changes in haemodynamic parameters post-LPS have provided insight into vascular phenomena underpinning ACLF.

At baseline, fluid resuscitated BDL rats have persistently lowered PV flow, and much more profound reductions in TLBF relative to their sham counterparts. HA flow is also significantly reduced, but HA fraction is comparable to their sham counterparts. This contrasts with baseline differences in non-hydrated animals presented in section 5.4, where BDL rats demonstrated higher HA flow, albeit just above the significance level (83.75 ± 19.12 ml/min/100g) compared with the non-hydrated sham cohort (32.98 ± 11.29 ml/min/100g; $p = 0.0526$), but HA fraction in BDL rats ($51.51 \pm 6.758\%$) was significantly higher than in their non-hydrated sham counterparts ($14.37 \pm 4.446\%$; $p = 0.0007$). Interestingly, ASL perfusion data failed to demonstrate any difference between sham and BDL rats. In the presence of a potential systematic error in quantification (section 7.3) affecting both cohorts, it was hoped that a difference would still be detected. Differences between the true sham and BDL blood-tissue partition coefficient (λ), may well account for the failure to record any difference at baseline between these two cohorts [444].

Hydrated BDL rats also direct a smaller portion of their cardiac output to the liver, although this occurs as a result of reduced proportion of portal venous rather than hepatic arterial flow. This also contrasts to non-hydrated BDL rats (figure 5.11), which direct a comparable portion of their cardiac output to the liver relative to their sham counterparts, driven contrastingly by increased proportion of HA flow.

Comparison of cardiac systolic function in hydrated sham and BDL rats confirm differences observed between cohorts in non-hydrated animals (figure 5.17), with increased stroke volume, cardiac output, left ventricular ejection fraction and cardiac index in BDL rats. These differences are supported by previously published findings in BDL rats, which in combination are consistent with hyperdynamic circulation and features of cirrhotic cardiomyopathy [353, 370, 451, 452].

Baseline differences between non-hydrated and hydrated hepatic haemodynamic parameters beg important questions about the physiological response to fluid resuscitation. With this in mind the haemodynamic response to intravenous fluid

resuscitation was compared in two separate cohorts. We demonstrated that PV flow in hydrated animals is greater in both sham and BDL rats, but HA flow and more importantly TLBF is only greater in hydrated sham and not BDL rats. Reflecting this, HA fraction and the proportion of cardiac output directed toward HA flow and TLBF are also only greater in hydrated sham but not BDL animals. These changes suggest relative passivity of PV flow in both cohorts as a result of increased plasma volume, but impaired regulation of HA flow in BDL rats perhaps either as result of intrinsic dysfunction of HA flow regulation at the level of the hepatic capillary bed or then as a result of abnormally prioritised shunting of blood to other capillary beds in BDL rats. An alternative explanation may be relate to chronic peripheral vasodilatation in BDL rats [452, 453]. It could be argued that because of this, the maintenance fluid requirements for euvolaemia are greater than in healthy subjects and therefore given a suitable dose of maintenance fluid, a rise in HA flow and TLBF would be observed.

Assessment of cardiac systolic function also revealed differences between non-hydrated and hydrated animals, some of which were unexpected, particularly in the sham cohort. Hydrated sham animals demonstrated increased heart rate, reduced stroke volume and comparable (albeit just non-significant) cardiac output in relation to their non-hydrated counterparts. These findings may reflect the tendency to maintain cardiac output in the face of systemic volaemic increase, but generally one would expect a higher baseline heart rate in non-hydrated animals, with a rise in cardiac output reflecting the replaced, and/or increased systemic plasma volume as a result of intravenous fluid resuscitation. Contrastingly, systolic function in BDL rats was unchanged in the hydrated cohort, supporting the presence of cardiomyopathy with an overall blunted response to physiological stress. At baseline, BDL rats are known to have lower mean arterial pressure and reduced systemic vascular resistance, consistent with a state of peripheral vasodilatation [370, 452]. It is therefore possible that the added fluid resuscitation could be absorbed within peripherally dilated capillary beds, and therefore have little effect on cardiac pre- or after-load, or subsequent systolic function.

It is worth noting that non-hydrated sham ($484.0 \pm 5.565\text{g}$) and BDL rats ($422.3 \pm 11.10\text{g}$) were larger than their hydrated counterparts (sham $463.2 \pm 6.606\text{g}$; BDL $403.4 \pm 14.27\text{g}$) even though these differences were non-significant. It is also important to bear in mind that in the absence of systemic pressure monitoring and inferred measurements of peripheral resistance, rats in the 'non-hydrated' cohort had the potential to be in either a state of dehydration (given prior instrumentation and laparotomy) or euvolaemia. Likewise animals in the 'hydrated' cohort were given maintenance fluid doses and therefore had the potential to be in a state of either euvolaemia or

hypervolaemia. While our data does demonstrate intrinsic differences between sham and BDL animals, a genuine weakness of interpretation of this comparison is the inability to discriminate between these fluid states. In the absence of paired data (before and after fluid resuscitation haemodynamic parameters) in the same animal, it is therefore difficult to be conclusive about the physiological significance of any specific differences other than that BDL rats respond differently, display a blunted cardiac systolic response and demonstrate impaired regulation of HA flow as a result of physiological haemodynamic stress.

The haemodynamic response to LPS also demonstrated profound differences between sham and BDL rats. Endotoxaemia was not associated with a change in PV flow in either sham or BDL cohorts, but a fall in TLBF was observed in BDL rats experiencing ACLF. In support of these findings, previously acquired clinical data at our institution has shown profound reductions in indocyanine green (ICG) determined TLBF in patients with ACLF relative to those with stable cirrhosis [450].

A rise in TLBF in septic sham rats was observed but this was above the significance level. A fall in HA flow was observed in BDL rats experiencing ACLF, but not in healthy septic animals. Taking the changes in TLBF and HA flow together, the post-LPS drop in HA fraction in BDL rats was just above the significance level ($p = 0.0570$). Interestingly, post-LPS ASL tissue perfusion demonstrated a rise in hepatic perfusion in sham animals, but no significant change in hepatic perfusion in BDL rats. Once again the difference between ASL and PCMRI findings could be ascribed to changes in post-LPS blood-tissue partition coefficient rather than systematic bias [444].

Findings remain inconclusive in the BDL cohort for post-LPS BDL hepatic flow parameters relative to cardiac output ($n = 3$), given the small sample size. Data from sham rats however suggest that healthy animals can sustain HA flow and TLBF despite acute endotoxaemia. It is worth noting that the rise in the proportion of a cardiac output directed towards the liver recorded in septic sham rats was just above significance ($p = 0.0696$).

Finally, assessment of cardiac systolic function demonstrated a rise in heart rate in septic BDL rats, and surviving animals were able to sustain stroke volume, cardiac output, left ventricular ejection fraction and cardiac index. Importantly however, sham rats demonstrated a positive response to the septic insult, increasing left ventricular ejection fraction and demonstrating the capacity to maintain heart rate. These phenomena were not observed in BDL rats experiencing ACLF suggesting that the absence of reserve

systolic function, may be an important factor contributing to their premature sepsis-induced demise.

This finding highlights an important pitfall in evaluating BDL rat post-LPS data. It is well recognised that even lower doses of LPS administered using routes with lower bioavailability (intraperitoneal injection) will trigger progressive demise of BDL rats [454]. Although measurements were made after a fixed 60 minute infusion of a weight-dependent dose of endotoxin, from a total of 9 subjects, $n = 4$ failed to complete the entire imaging protocol due to premature demise, with $n = 2$ expiring before the PCMRI protocol (the first part of the post-LPS acquisition) was complete. This therefore implies a selection bias in that measurements from the surviving subjects may not be representative of BDL population, but rather reflective of those with the capacity to survive (possibly as a result of BDL heterogeneity and added haemodynamic, hepatic or cardiac reserve).

This also highlights an important logistical challenge for the use of non-invasive assessment using MRI. Post-LPS data was obtained approximately 69.48 ± 1.806 minutes after starting the LPS infusion, but lasted for 40-60 minutes (figure 7.8). There is little doubt that in the context of acute sepsis and particularly BDL animals entering a peri-arrest state, hepatic and cardiac variables are likely to have experienced considerable fluctuation during this time. While each individual measurement might have only taken minutes to acquire, it is very possible that recorded TLBF for example, could have changed by the time cardiac output was being measured. An important method of monitoring the overall haemodynamic status of the animal through the experiment (and perhaps controlling for changes during sepsis and peri-arrest) would have been using continuous mean arterial pressure measurement. This unfortunately, was not feasible at the time of scanning.

It is also worth noting that in view of time and resource constraints, an experiment to control for the effects of anaesthesia, scanning and intravenous infusion, in which both sham and BDL rats were given a continuous saline 'vehicle' infusion instead of LPS, was not performed. This was planned, but given the small number of BDL rats completing the protocol, the decision was made to prioritise post-LPS data. Conducting these experiments remains the subject of future work.

Lastly, cardiac cine MRI was used in this study to characterise cardiac systolic function. Cardiac diastolic dysfunction however, is itself a subject of growing interest in the context of chronic liver disease [453, 455]. Diastolic function can be quantified using cardiac PCMRI planned across the mitral valve [456]. Experiments to characterise

changes in diastolic function, both as a result of disease and as a result of inflammatory stress would be important in future work.

The findings presented in this section have important implications for our clinical understanding of hepatic haemodynamics in chronic liver disease and in ACLF. We have shown profound differences between normal and diseased rats, with reduced PV flow and impaired hepatic arterial buffer response at baseline in hydrated BDL rats. We have shown that despite hyperdynamic circulation and fluid resuscitation, BDL livers fail to place a comparable demand on systemic circulation in view of their increased organ:body mass ratio. These findings corroborate earlier differences between non-hydrated healthy and diseased animals at baseline. Our data also confirm the presence of cirrhotic cardiomyopathy, with elevated systolic function at rest and poor reserve under stress.

We have evaluated the effects of hydration by comparison with previously acquired data in non-hydrated animals to show that hydrated BDL rats demonstrate a passive splanchnic response, with increased PV flow. Contrastingly, hydrated BDL rats fail to exploit the added fluid resuscitation, demonstrating persistent global and arterial hypoperfusion. We have also shown a blunted cardiac response, with no difference in systolic function in hydrated BDL rats.

Finally, we have studied the vascular pathophysiology of ACLF non-invasively to demonstrate an exacerbation of global hepatic and arterial hypoperfusion in diseased rats. The significance of this finding is underscored by the observed increase in TLBF and tissue perfusion observed in septic sham animals. We have also shown an impaired cardiac systolic response in ACLF, with failure to respond to endotoxaemia with rises in ejection fraction, as seen with sham rats.

The observation of these phenomena raises important questions about the causes and effects of decline in chronic liver disease and ACLF. It is still unclear for example whether hepatic hypoperfusion is a cause or sequelae of ACLF. Future work should be directed towards investigating the relationship between hepatic perfusion, cardiac reserve and survival in BDL rats post-LPS. Taking advantage of the non-invasive nature of MR assessment, sequential haemodynamic characterisation studies in the same animal as biliary cirrhosis evolves over a 4-5 week period would also provide invaluable insight into the development of chronic liver disease. This could be achieved using fewer experimental subjects in line with the concept of 'reduction' as part of the 3Rs of animal research [457]. Such studies could also easily be performed to study vascular phenomena in alternative acute and chronic models of liver injury (e.g. carbon tetrachloride, thioacetamide). The non-invasive methods proposed also set a novel precedent for the

development and assessment of new therapies in the context of hepatic haemodynamic parameters. New treatments for ACLF could be developed preclinically, aimed at improving TLBF as measured non-invasively using our methods.

7.4.5 CONCLUSION

In this section, we have used preclinical PCMRI, cardiac cine MRI and ASL to characterise hepatic haemodynamics non-invasively in a model of chronic liver disease and in ACLF. Our data demonstrate hepatic hypoperfusion in hydrated animal models of liver disease, with reduced PV flow and impaired hepatic arterial buffer response. Despite hyperdynamic circulation, fluid resuscitation and increased organ:body mass ratio, diseased livers fail to place a comparable demand on systemic circulation. We have confirmed the presence of cirrhotic cardiomyopathy, with elevated systolic function at rest and poor reserve under stress. We have demonstrated relative passivity to changes in PV flow, with impaired HA flow response following hydration in disease. Finally, we have demonstrated that ACLF is characterised by exacerbation of global hepatic and arterial hypoperfusion, absence of normal sepsis-induced hepatic hyperaemia and a blunted cardiac systolic response to sepsis.

7.5 CLOSING COMMENTS

This chapter represents the culmination of previous preclinical work presented in Chapters 2, 3, 4 and 5. Building on the methods developed in these chapters, we addressed an important limitation through the implementation of FAIR ASL – a novel method for quantification and quantitative anatomical assessment of hepatic tissue perfusion. We evaluated the agreement of this method with previously invasively validated PCMRI techniques and demonstrated that the T1 measurements underpinning quantification are repeatable and capable of demonstrating differences between sham and BDL rats.

We subsequently applied PCMRI, cardiac cine MRI and ASL to study haemodynamic differences non-invasively in healthy and diseased animals at baseline, during hydration and post-inflammatory stress. Our findings have demonstrated profound hepatic haemodynamic differences between healthy and diseased rats and provided novel insights in the vascular pathophysiology of ACLF.

While these changes have valuable implications for developing both our understanding and novel therapeutic strategies in managing chronic liver disease and ACLF, the preclinical imaging methods developed in this thesis are especially interesting because of their potential for translation onto clinical imaging systems. We have previously implemented, validated and studied the reproducibility of clinical PCMRI for hepatic haemodynamic assessment in normal volunteers (section 5.5). Using these tools, we can now finally translate this work into the clinical environment, using non-invasive MR haemodynamic assessment to further our understanding of vascular pathophysiology and investigate haemodynamic effects of treatments for portal hypertension in patients with chronic liver disease.

CHAPTER 8

BLOOD FLOW STUDIES IN CHRONIC LIVER DISEASE – CLINICAL STUDIES

“...and down below,
the filter and the balance,
the delicate chemistry
of the liver,
the storehouse
of the subtle changes:
no one
sees or celebrates it,
but, when it ages
or its mortar wastes away,
the eyes of the rose are gone...”

- Ode to the liver [2].

8.1 INTRODUCTION

In section 5.5, we translated preclinical PCMRI methods onto a clinical system and demonstrated feasibility, consistency and reproducibility of PCMRI measurements in normal volunteer studies. Clinical translation however brings practical challenges as well as opportunities. Unlike normal volunteers, patients can struggle with lengthy scanning protocols particularly when these require multiple and extended breath holds. Contrastingly, patients with chronic liver disease undergoing invasive haemodynamic studies as part of their standard of care provide a unique opportunity for validation of non-invasive MRI derived measurements. In this chapter we present pilot data for a planned larger scale study. Using the same PCMRI methods from our normal volunteer study, we determine the feasibility of the imaging protocol in patients, evaluate the consistency of flow measurements and present preliminary invasive validation data. We explore the relationship between invasive and non-invasive PCMRI measurements before characterising differences in PCMRI haemodynamic measurements in patients with chronic liver disease. Finally, we demonstrate the potential of our PCMRI methods for evaluation of pharmacological and interventional therapies in patients with chronic liver disease undergoing treatment for portal hypertension.

8.2 AUTHOR CONTRIBUTIONS

In fulfilment of the aims in this chapters, I: (a) implemented clinical PCMRI protocols developed previously (Chapter 5); (b) performed invasive validation studies, including transjugular measurement of hepatic venous pressure gradient (HVPG) and drawing of hepatic venous samples for measurement of ICG clearance; (c) developed, procured, secured and maintained ethical approval for patient recruitment; (d) recruited and transported patients from the recruitment site to the hospital where the scanner was located; (e) supervised the scanning of all patients; (f) collected and analysed all the data; (g) prepared all the material contained within this chapter.

Proprietary clinical PCMRI sequences were adapted by Alan Bainbridge for hepatic applications, with additional input from David Atkinson. All HVPG measurements were performed with the supervision of Raj Mookerjee. Indocyanine green (ICG) clearance quantification was undertaken by Helen Jones. Recruitment of TIPSS patients was facilitated by David Patch. Ethical approvals for this study were sought under the supervision of Shonit Punwani. All clinical scans were conducted by MRI radiographers. Statistical power calculations were undertaken by Paul Bassett.

8.3 BACKGROUND

Optimisation for PCMRI scanning protocols used during normal volunteer studies was tailored around meeting the potential challenges when scanning patients – we review some of these adaptations briefly. Firstly, velocity encoding settings of 40, 60, 60, 80 and 120 cm/s for PV, HA, proximal IVC, distal IVC and aortic root flow measurements were used respectively, based on prior experience. Two-dimensional PCMRI studies were planned in exactly the same way as for normal volunteers, to ensure vessel orthogonality (figures 5.19 and 5.20). All anatomical imaging was obtained in expiratory breath-hold. Chronic liver disease is associated with macrovascular anatomical change, including cavernous transformation of the portal vein, the presence of large perihepatic porto-systemic shunts, the potential for PV and hepatic venous thrombus and increased vessel tortuosity [458]. Anatomical images were carefully reviewed for these complications and planning was adjusted accordingly (figure 8.1).

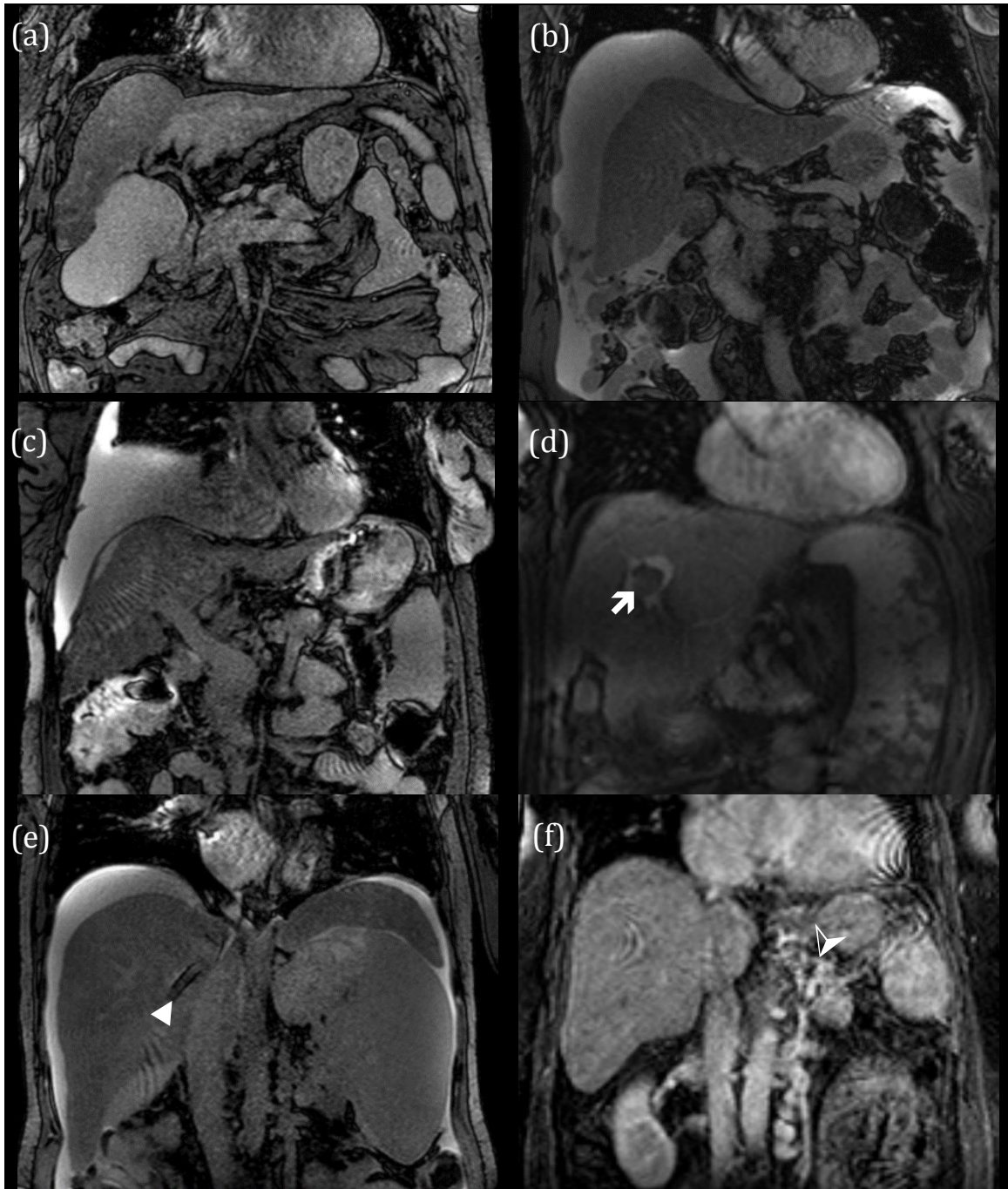


Figure 8.1: Additional anatomical considerations when planning PCMRI studies in patients with chronic liver disease

Imaged cirrhotic livers were (a) commonly atrophic and of irregular outline; (b) were associated with ascites, as demonstrated by the high perihepatic signal; (c) were associated with pleural effusions, as demonstrated by the high signal in the right hemithorax; (d) occasionally PV thrombus was identified, as shown but the low intravascular signal (↑, white) in the right portal vein; (e) TIPSS stents (▲, white) were not associated with significant artefact and (f) multiple extra-hepatic shunts, as shown by the tortuous vessels (▲, white) were commonly identified.

All PCMRI data was acquired at the same resolution as previously (336 x 336 matrix size, 5 mm slice thickness, field-of-view 271 x 210 mm and consequent in-plane spatial resolution of 0.808 x 0.625 mm²) and undertaken in expiratory breath-hold. Given that patients with liver disease are likely to have higher heart rates and smaller breath-hold capacity, the decision was made to use a low temporal resolution PCMRI acquisition with only seven phases through the cardiac cycle. This enabled measurements to be completed within a single breath-hold (< 15 seconds). To mitigate the potential sampling errors that might arise as a result of the lower temporal resolution acquisition and other factors, all measurements were performed in triplicate and recorded measurements were averaged across three acquisitions. Pulse oximetry was used for cardiac gating. Prior to scanning, all patients were instructed on the breath-hold protocol to maximise compliance with instructions while in the scanner.

In order to validate PCMRI measurements, all patients included in the study underwent invasive transjugular haemodynamic studies. Measurements of hepatic venous pressure gradient (HVPG) [15, 23, 34] and indocyanine green (ICG) clearance [39, 40] were obtained after hepatic venous catheterisation and based on the principles described in section 1.2.3.

To study the ability of PCMRI to detect differences and changes in haemodynamic parameters in patients, data was collected at baseline and post-treatment in patients enrolled on a phase II trial of obeticholic acid (OCA) or following a transjugular intrahepatic porto-systemic shunt (TIPSS) procedure. Obeticholic acid is an agonist of the farnesoid-X-receptor (FXR), a transcription factor expressed in several tissues, including the liver [459]. FXR is activated by bile acids and is known to regulate the expression of multiple genes including those responsible for bile acid homeostasis, carbohydrate and lipid metabolism, vasoregulation and possibly even fibrosis [460-464]. There have been a number of proposed mechanisms for the vasoactive effects of FXR activation, including reduced asymmetric dimethyl-arginine (ADMA) levels (with resultant increases in endothelial nitric oxide synthetase (eNOS)) [465, 466]. Preclinical studies using in-situ perfused BDL mouse livers have demonstrated reductions in portal pressure and intrahepatic resistance in response to treatment [467]. Clinical studies performed in patients with portal hypertension have also demonstrated post-treatment reductions in HVPG [468].

TIPSS procedures can be used to treat secondary complications of portal hypertension with indications ranging from acute management of variceal bleeds to elective management of refractory ascites [24, 469]. The principle of creating a large

physical shunt between the hepatic and portal veins, has been shown to have profound effects on hepatic haemodynamics, with previously demonstrated changes in portal and azygous venous flow using PCMRI [194].

With this in mind, in this section we aim to (a) demonstrate the feasibility of using our newly developed PCMRI methods to measure haemodynamic parameters in patients with chronic liver disease, (b) assess the agreement and explore the relationship between PCMRI and invasive haemodynamic measurements, (c) characterise differences between cirrhotic patients with significant portal hypertension and normal volunteers using PCMRI and (d) demonstrate the potential of PCMRI in measuring post-treatment changes in patients (i) participating in a phase II OCA trial and (ii) undergoing TIPSS procedures.

8.4 METHODS

8.4.1 SUBJECTS AND PREPARATION

Local ethics committee approval was obtained and all participants provided informed written consent. Participant information sheets and consent form copies can be found in Appendix F. Histologically confirmed cirrhotic patients requiring elective invasive transjugular studies were identified from the hepatology outpatient clinic ($n = 9$) (most of which were subsequently screened for recruitment into the phase II OCA trial, $n = 7$) and elective TIPSS lists for refractory ascites ($n = 5$). Subjects were contacted by post with participation confirmed after follow-up telephone call. There were eleven male (aged 50.27 ± 3.311 years) and four female (aged 53.50 ± 3.663 years) patients recruited into the study. Subjects were excluded if (a) they had any contraindication to standard MR imaging, (b) were unable to give consent, (c) were allergic to Gd-DOTA (gadoterate dimeglumine), (d) had deranged renal function, with estimated glomerular filtration rate < 30 ml/min or (e) were allergic to ICG. Participants were asked to remain fasted for six hours prior to imaging with ad libitum consumption of water but not caffeinated fluids.

8.4.2 SAMPLE SIZE

Correlation of PCMRI TLBF with ICG clearance was prioritised for calculation of sample size. At the time of planning the study, it was unclear if formal ICG clearance measurements were to be undertaken (therefore yielding measurements in units other than ml/min/100g). Studies were therefore planned based on Pearson's correlation analysis. Power calculations were undertaken for a statistical power of 90% and a 5% significance level. Assuming a correlation coefficient $r \geq 0.6$ as clinically useful, a sample of $n = 25$ subjects would be advised.

8.4.3 TWO-DIMENSIONAL CINE PCMRI

Imaging was performed as previously, using a 3.0T scanner (Achieva, Philips Healthcare, Best, Netherlands) with a 16 channel body coil (SENSE XL-Torso, Philips Healthcare, Best, Netherlands). The coil was positioned over the lower thorax and upper abdomen and subjects were monitored using digital pulse oximetry and bellows.

Initial scouts were performed to ensure inclusion of the entire cardiac and liver volume within the field-of-view. Coronal images of the upper abdomen and lower thorax, and sagittal images including the abdominal great vessels were obtained with successive expiratory breath-holds using a gradient echo sequence. Localisation of the vascular structures of interest was performed as described previously (section 5.5.1), with

additional anatomical imaging through the PV. PCMRI studies were planned through the PV, common HA, proximal IVC, distal IVC and aortic root in succession. Where HA anatomical variations were noted ($n = 3$), measurements were made as close as possible to the aortic origin and measurements were obtained from more than one vessel where necessary. Studies were performed in expiratory breath-hold and cardiac gated using peripheral pulse oximetry and settings listed previously (table 5.3). Before each scan, subject heart rate was recorded on the scanner console software to optimise the arrhythmia rejection window. Acquisition time for each measurement was less than 20 seconds. Each PCMRI study was repeated three times in succession. All PCMRI measurements, including planning time were usually completed within 20 minutes. Quantitation was performed using the freely available software package, Segment (Medviso, Lund, Sweden).

8.4.4 VOLUMETRIC ASSESSMENT AND BULK FLOW NORMALISATION

All PCMRI bulk flow measurements were normalised to liver volume. Liver volume was measured using 5 mm slice thickness gradient echo coronal anatomical images. Segmentation was performed manually using Amira (Amira Resolve RT, Visage Imaging, Berlin, Germany). A tissue density of 1.0 g/ml was assumed [193].

8.4.5 CAVAL SUBTRACTION PCMRI CONSISTENCY STUDIES

Caval subtraction PCMRI consistency studies were undertaken as previously (section 5.5). To measure the consistency of estimated TLBF using subtracted PCMRI IVC flows, comparison was made with bulk inflow PCMRI measurements at the PV and common HA. Comparisons between caval subtraction PCMRI estimated and directly measured HA flow and HA fractions were also studied.

8.4.6 INVASIVE VALIDATION STUDIES

After ultrasound guided cervical puncture of the right internal jugular vein (Sonosite Titan, SonoSite Inc, Washington, USA), the right hepatic vein was cannulated under fluoroscopic guidance (Axiom Artis Zee, Siemens Healthcare, Munich, Germany) using a balloon-tipped catheter (Cordis, Roden, Netherlands). Care was taken to advance the catheter into a wedged position, with no collateral run-off, as confirmed using digital subtraction angiography (Omnipaque, Amersham Health, Little Chalfont, UK). Wedged and free hepatic venous pressure measurements were made with the balloon inflated and deflated respectively. Pressure traces were monitored continuously to confirm stability of the recordings and paired pressure readings were performed in triplicate. HVPG was calculated as the difference between free and wedge hepatic venous pressure. Average measurements were recorded for final analysis.

Total liver blood flow was measured invasively using a weight-based primed and subsequent continuous infusion of ICG (Pulsion Medical Systems, Munich, Germany). Simultaneous paired samples, following radial artery puncture at the wrist and from the hepatic vein (following cannulation for HVPG measurement) were collected. ICG extraction was then calculated in accordance with the Fick principle [39, 470]. ICG TLBF measurements were normalised to anatomical MRI derived liver volumes for comparison with PCMRI measurements.

For ICG and PCMRI measurements of TLBF (L/min), intra-hepatic resistance (IHR, dynes.sec/cm⁵) was calculated from HVPG (mmHg) using the following equation [471-473]:

$$\text{IHR} = \frac{\text{HVPG} \cdot 80}{\text{TLBF}}$$

(Equation 8.1)

Validation of PCMRI estimated TLBF and IHR was undertaken using ICG-derived TLBF and IHR.

8.4.7 HAEMODYNAMIC CHARACTERISATION STUDIES

To investigate the ability of PCMRI to characterise differences between patients, data was stratified using invasive HVPG measurements. Cirrhotic patients with HVPG measurements ≥ 12 mmHg were deemed as higher risk portal hypertensive patients as they are known to be at higher risk of developing variceal bleeds [474-476]. To control for the presence of cirrhosis, comparison with PCMRI flow parameters obtained from normal volunteers at baseline was also undertaken. Subject recruitment and methods for this cohort are described in section 5.5.2.

8.4.8 BASELINE AND POST-TREATMENT STUDIES

For patients recruited into the efficacy cohort of the phase II OCA trial, both MRI and invasive studies were undertaken before and following a 12 day course of 25 mg oral OCA. All MRI studies were performed within 6 days of the invasive studies.

For patients undergoing TIPSS procedures, MRI studies were undertaken before and after a single invasive procedure. Pre-TIPSS HVPG measurements were recorded for correlation with baseline measurements. Post-TIPSS MRI studies took place within two days of the TIPSS procedure.

8.4.9 STATISTICAL ANALYSIS

Kolmogorov-Smirnov tests were used to confirm normality of variable distributions. Consistency and validation studies were assessed using paired t-tests, Bland-Altman analysis of agreement with calculation of the coefficient of repeatability and assessment of correlation between measurements using Pearson's correlation coefficient. The relationship between HVPG and PCMRI haemodynamic parameters was investigated using Pearson's correlation coefficient. Differences between normal volunteer controls, cirrhotics (HVPG < 12 mmHg) and cirrhotics (HVPG ≥ 12 mmHg) were assessed using one-way analysis of variance (ANOVA) with corrections for non-sphericity. Post-hoc Tukey's tests were conducted where significant differences were identified. Given the small sample sizes, baseline and post-OCA treatment differences were analysed using Wilcoxon matched pairs signed rank tests. The threshold of statistical significance was defined to be $p < 0.05$.

8.5 RESULTS

8.5.1 COHORT FEATURES

A total of $n = 14$ patients were recruited into the MRI study, with $n = 7$ patients derived from the phase II OCA trial, $n = 5$ from elective TIPSS lists and $n = 2$ requiring invasive haemodynamic assessment from hepatology outpatient clinic. All patients had established alcoholic cirrhosis, with the exception of one patient with chronic hepatitis C cirrhosis (baseline TIPSS cohort) and another patient with non-alcoholic steatohepatitis cirrhosis (hepatology clinic, but non-OCA trial). Post-treatment MRI scans were performed in $n = 8$ patients ($n = 4$ post-OCA, $n = 4$ post-TIPSS), but full paired data sets were only available for $n = 5$ patients ($n = 4$ OCA trial, $n = 1$ post-TIPSS). A total of 19 scans were performed. Cohort features are summarised in table 8.1.

Table 8.1: Cohort numbers for clinical studies

	BASELINE	POST-TREATMENT
<i>Phase II OCA trial</i>	7	4 (all paired)
<i>Elective TIPSS</i>	2	4 ($n = 1$ paired)
<i>Hepatology outpatient clinic</i>	2	-

Exclusions included one subject who developed an urticarial reaction to ICG, following baseline invasive flow studies. Post-OCA ICG measurements were therefore not undertaken in this subject. HVPG data was recorded prior to and just after TIPSS insertion, but because of inconsistencies in the methodology of post-TIPSS HVPG recordings, this data was excluded. ICG clearance studies were not undertaken in patients undergoing TIPSS procedures because of logistical considerations.

8.5.2 PCMRI FEASIBILITY

PCMRI flow studies in cirrhotic patients demonstrated physiological (figure 8.2) and pathological flow profiles through the PV (figure 8.3), common HA, proximal IVC, distal IVC and aortic root.

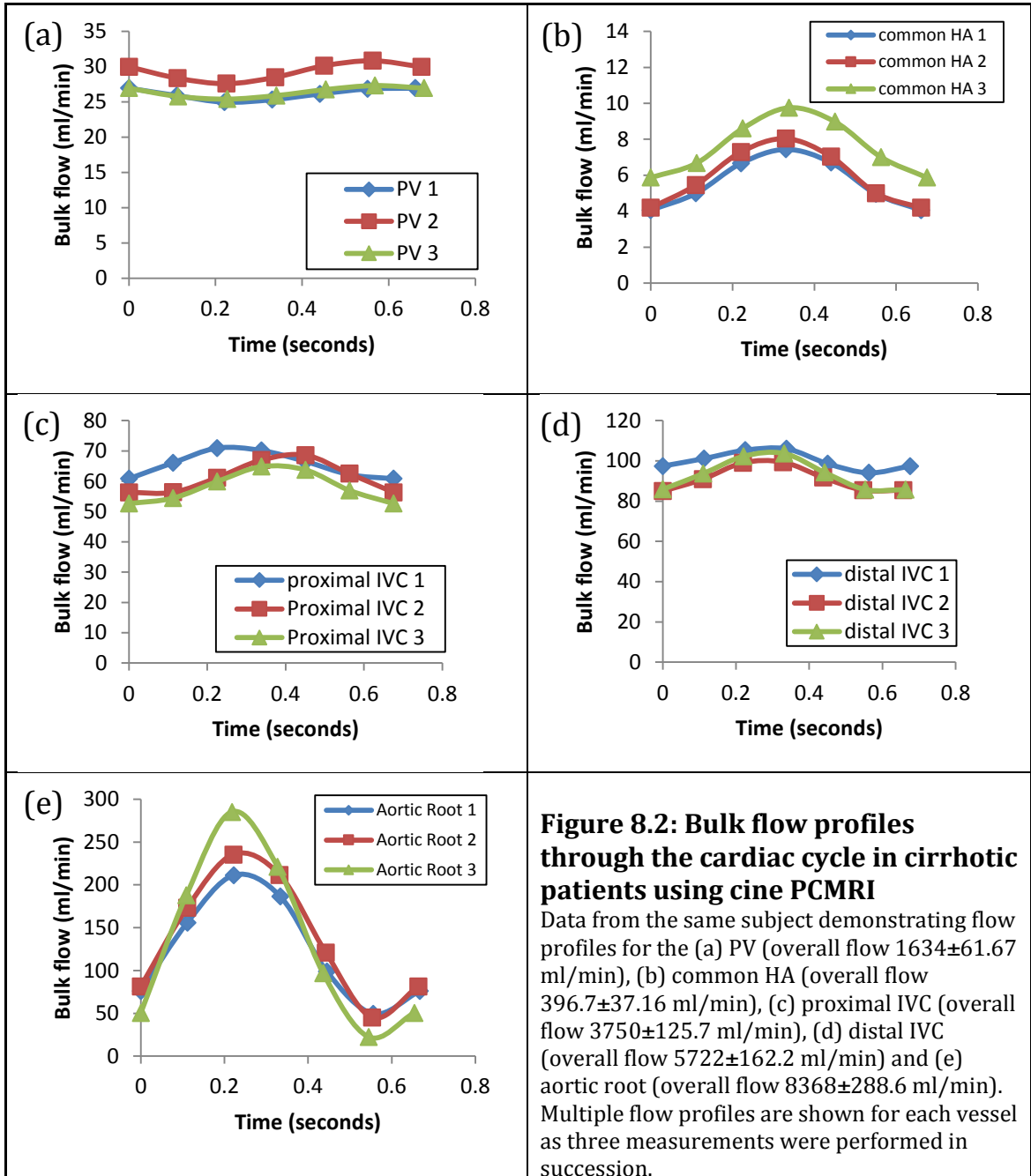
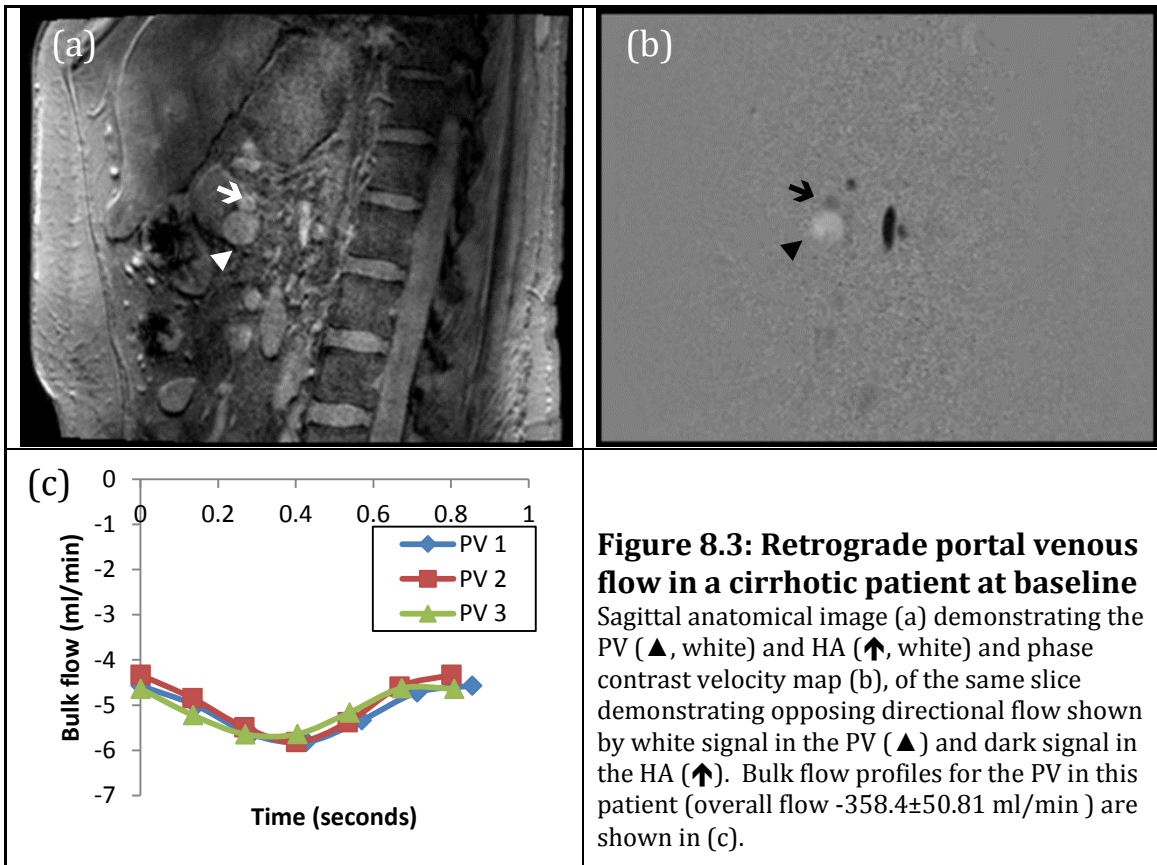


Figure 8.2: Bulk flow profiles through the cardiac cycle in cirrhotic patients using cine PCMRI

Data from the same subject demonstrating flow profiles for the (a) PV (overall flow 1634 ± 61.67 ml/min), (b) common HA (overall flow 396.7 ± 37.16 ml/min), (c) proximal IVC (overall flow 3750 ± 125.7 ml/min), (d) distal IVC (overall flow 5722 ± 162.2 ml/min) and (e) aortic root (overall flow 8368 ± 288.6 ml/min). Multiple flow profiles are shown for each vessel as three measurements were performed in succession.

Retrograde PV flow, a well-documented phenomenon in chronic liver disease, was observed in one subject both pre and post-OCA (figure 8.3). The presence of retrograde PV flow had implications for the calculation of PCMRI estimated HA flow, TLBF and HA fraction, which we explore in the discussion.



Compliance with breath-holds was more of an issue in patients (figure 8.4), but because of the volume of blood flow underpinning phase contrast signal, quantification was not necessarily problematic.

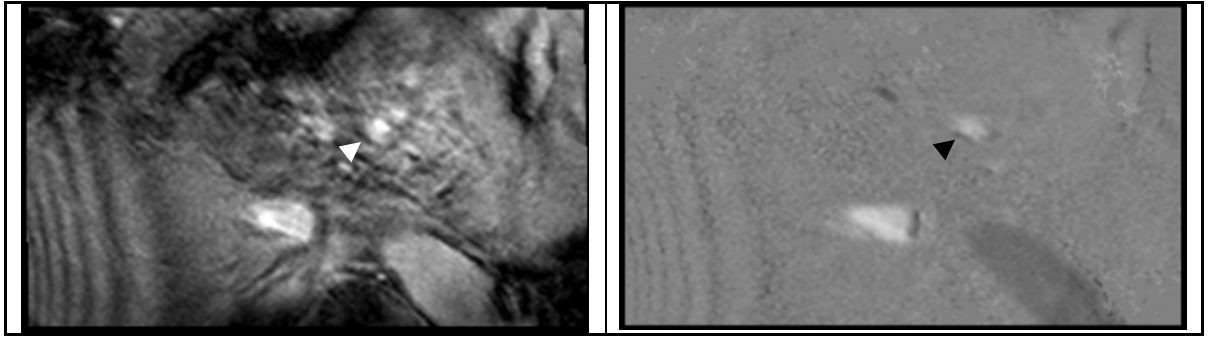


Figure 8.4: Motion artefact during measurement of portal venous flow in a cirrhotic patient at baseline

Oblique anatomical image (a) demonstrating the PV (▲, white) and phase contrast velocity map (b), of the same slice demonstrating flow signal from the PV (▲). In spite of the corruption by motion artefact best appreciated in (a), bulk PV flow was still quantifiable. The triplicate measurement average for this patient was 550.8 ± 19.94 ml/min.

8.5.3 CAVAL SUBTRACTION PCMRI CONSISTENCY

Consistency of caval subtraction PCMRI was assessed by comparison of (a) estimated TLBF with the sum of directly measured PV and HA flow, (b) estimated HA flow with directly measured HA flow and (c) estimated HA fraction with directly measured HA fraction. Agreement was assessed in patients ($n = 14$), at baseline and post-treatment using a total of nineteen measurements. Patients from all three cohorts were pooled into baseline and post-treatment categories for analysis.

Paired t-tests demonstrated a non-significant difference between estimated TLBF and directly measured TLBF at baseline (mean difference 7.327 ± 4.478 ml/min/100g; $p = 0.1328$) and an almost significant difference post-treatment (mean difference 11.01 ± 4.841 ml/min/100g; $p = 0.0571$). The coefficient of variation was higher for caval subtraction PCMRI measurements at baseline (58.49% vs 49.50%; estimated TLBF vs directly measured TLBF) but not post-treatment (40.39% vs 49.97%; estimated TLBF vs directly measured TLBF). Graphical analysis (figure 8.5b) showed significant and strong correlations between estimated and directly measured TLBF using PCMRI ($r = 0.9712$; $p < 0.0001$).

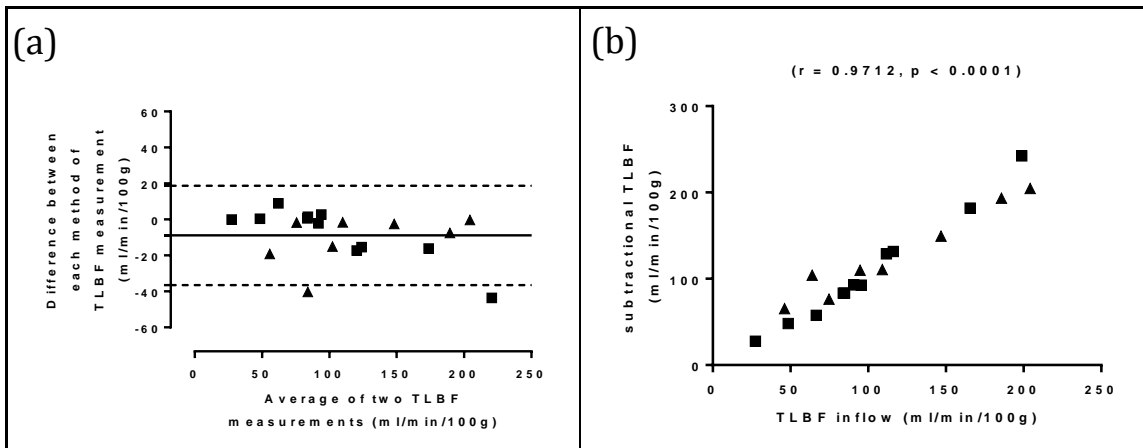


Figure 8.5: Agreement between estimated TLBF derived from caval subtraction PCMRI and inflow TLBF measured directly with PCMRI in patients with cirrhosis

Strong correlations and encouraging agreements between estimated TLBF and directly measured TLBF were demonstrated at baseline (■) and post-treatment (▲). The coefficient of repeatability between measurement methods for the entire dataset was 27.64 ml/min/100g.

Because a fixed quantity (PCMRI PV flow) was subtracted from estimated and directly measured TLBF, paired t-tests for estimated and directly measured HA flow demonstrated the same mean differences and significance levels as previously. The coefficient of variation was higher for estimated HA flow measurements at baseline (78.32% vs 70.74%; estimated vs directly measured HA flow), but similar post-treatment (32.71% vs 31.81%; estimated vs directly measured HA flow). Graphical analysis (figure 8.6b) showed significant correlations between estimated and directly measured HA flow using PCMRI ($r = 0.7927$; $p < 0.0001$).

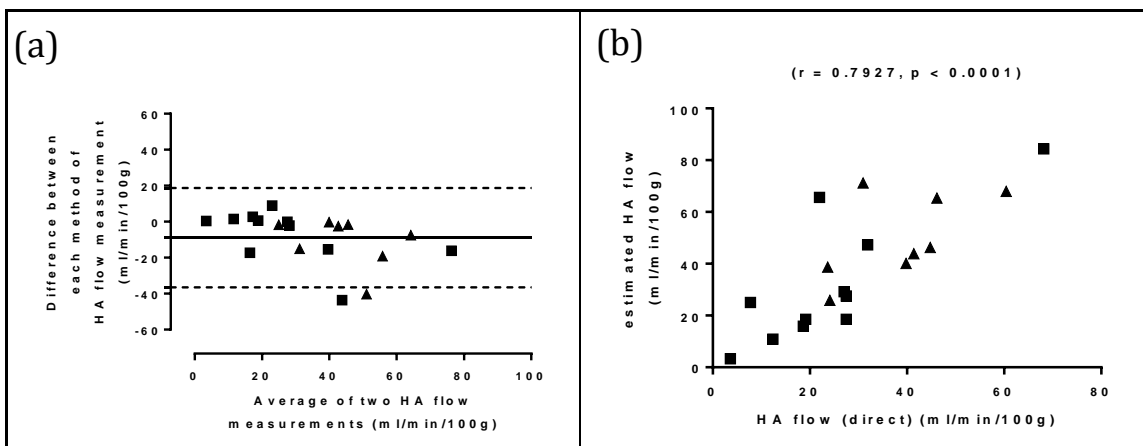


Figure 8.6: Agreement between estimated HA flow derived from caval subtraction PCMRI and HA flow measured directly with PCMRI in patients with cirrhosis

Although strong correlations were observed between estimated and directly measured HA flow at baseline (■) and post-treatment (▲), the coefficient of repeatability between measurement methods for the entire dataset was 27.64 ml/min/100g, which was large in view of absolute HA flow.

Paired t-tests demonstrated a non-significant difference between estimated and directly measured HA fraction at baseline (mean difference $2.959 \pm 2.399\%$; $p = 0.2486$) and post-treatment (mean difference $5.217 \pm 2.776\%$; $p = 0.1092$). The coefficient of variation for estimated HA fraction was smaller than when measured directly at baseline (46.86% vs 57.11%; estimated vs directly measured HA fraction), but larger than when measured directly post-treatment (40.30% vs 30.09%; estimated vs directly measured HA fraction). Graphical analysis (figure 8.7b) showed significant correlations between estimated and directly measured HA fraction using PCMRI ($r = 0.8581$; $p < 0.0001$).

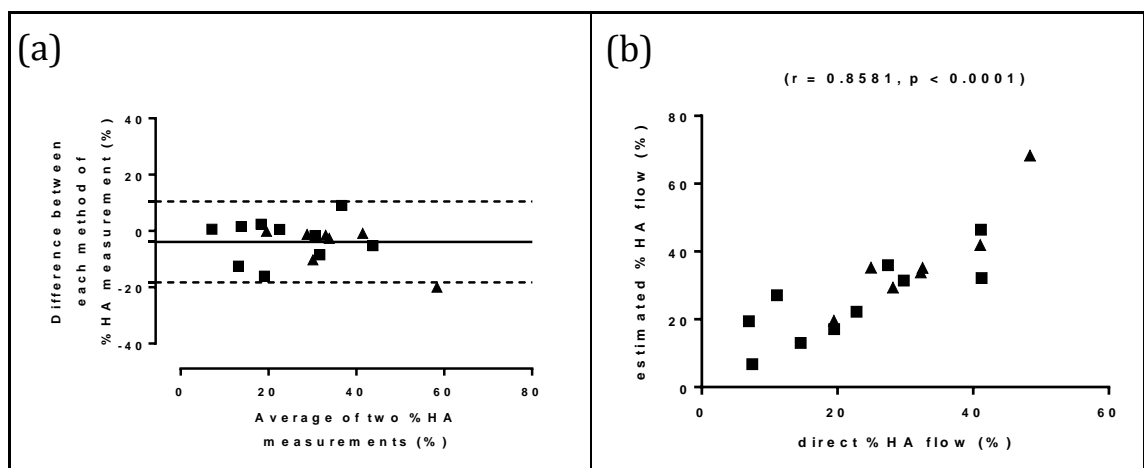


Figure 8.7: Agreement between estimated HA fraction derived from caval subtraction PCMRI and HA fraction measured directly with PCMRI in patients with cirrhosis

Strong correlations were observed between estimated and directly measured HA fraction at baseline (■) and post-treatment (▲). The coefficient of repeatability between measurement methods for the entire dataset was 14.39%.

8.5.4 CAVAL SUBTRACTION PCMRI VALIDATION

Validation of PCMRI measurements of TLBF and PCMRI (combined with HVP) derived IHR was undertaken using measurements of TLBF and IHR determined using ICG. Patients from all three cohorts were pooled into baseline and post-treatment categories for analysis. Agreement was assessed in patients at baseline ($n = 5$) and post-treatment ($n = 3$). Given the small numbers in each cohort, baseline and post-treatment pairs were pooled for analysis. TLBF measurements using PCMRI and ICG were significantly different (mean difference -35.78 ± 12.28 ml/min/100g; $p = 0.0226$). The coefficient of variation was slightly lower for PCMRI TLBF (42.98% vs 50.77%; PCMRI TLBF vs ICG TLBF). Graphical analysis (figure 8.8b) demonstrated modest positive correlation between the two methods, that approached significance ($r = 0.6436$; $p = 0.0851$).

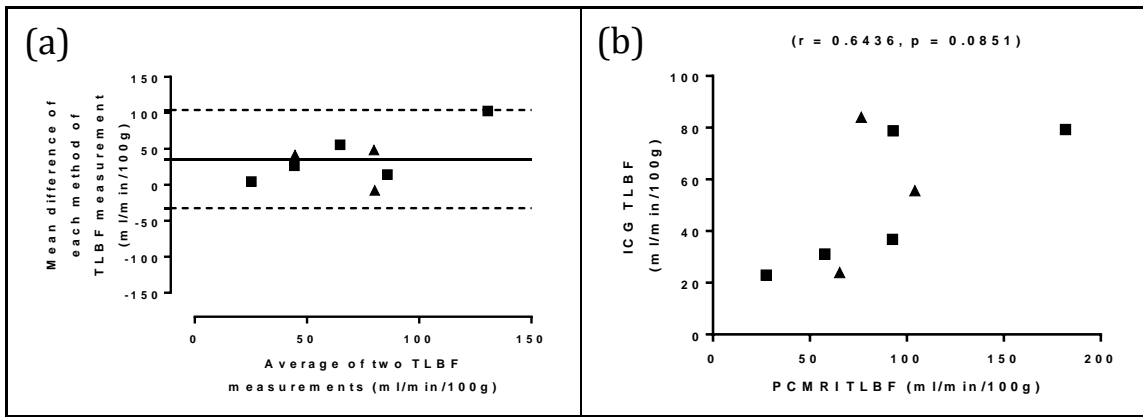


Figure 8.8: Validation of PCMRI TLBF with ICG clearance in cirrhotic patients

Despite small sample size ($n = 8$), encouraging positive correlation between PCMRI estimated TLBF and invasive methods was demonstrated at baseline (■) and post-treatment (▲). The coefficient of repeatability between measurement methods for the entire dataset was a large 68.10 ml/min/100g.

Mean differences between paired PCMRI IHR and ICG IHR measurements were also significantly different (mean difference -729.0 ± 177.5 dynes.sec/cm⁵; $p = 0.0045$). The coefficient of variation was considerably smaller for PCMRI IHR (50.02% vs 86.24%; PCMRI IHR vs ICG IHR). Graphical analysis (figure 8.9b) showed an encouraging positive and significant correlation between the two methods ($r = 0.8382$; $p = 0.0094$).

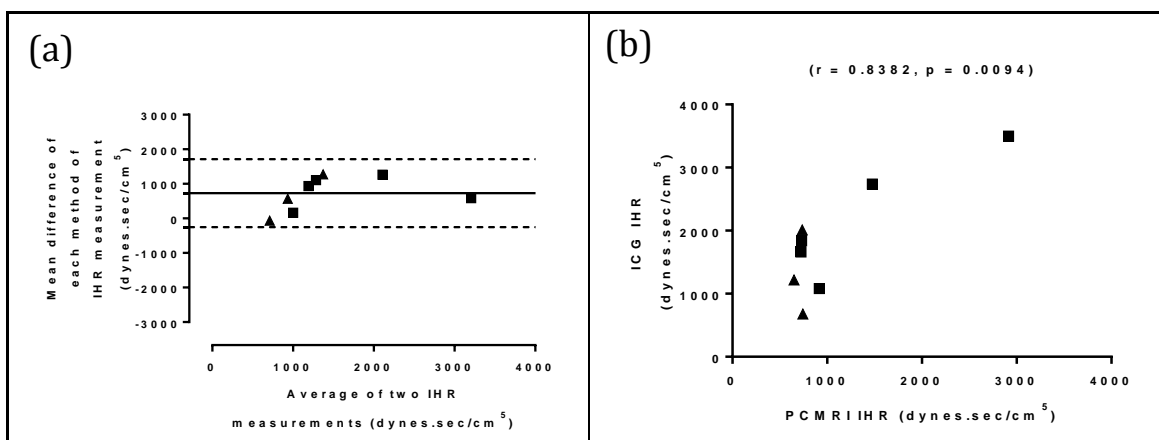


Figure 8.9: Validation of PCMRI IHR using ICG IHR in cirrhotic patients

An encouraging and strong positive correlation between PCMRI and invasive methods was demonstrated at baseline (■) and post-treatment (▲). The coefficient of repeatability between measurement methods for the entire dataset was a large 984.2 dynes.sec/cm⁵.

8.5.5 NON-INVASIVE AND INVASIVE HAEMODYNAMIC PARAMETER RELATIONSHIPS

The relationship between HVPG and PCMRI haemodynamic parameters was evaluated in ten patients, at baseline ($n = 10$) and post-treatment ($n = 5$) using a total of fifteen measurements. Poor and non-significant correlations were demonstrated across the entire cohort between HVPG and PV flow ($r = 0.1216$, $p = 0.6660$), HVPG and estimated TLBF ($r = 0.2576$, $p = 0.3539$), HVPG and estimated HA flow ($r = 0.2658$, $p = 0.3384$) and HVPG and HA fraction ($r = 0.3582$, $p = 0.2293$). Interestingly both baseline estimated HA

flow (figure 8.10c) and HA fraction (figure 8.10d) demonstrated positive correlations with HVPG, which though just above significance for estimated HA flow ($r = 0.6251$, $p = 0.053$), were significant for HA fraction ($r = 0.7755$, $p = 0.0141$).

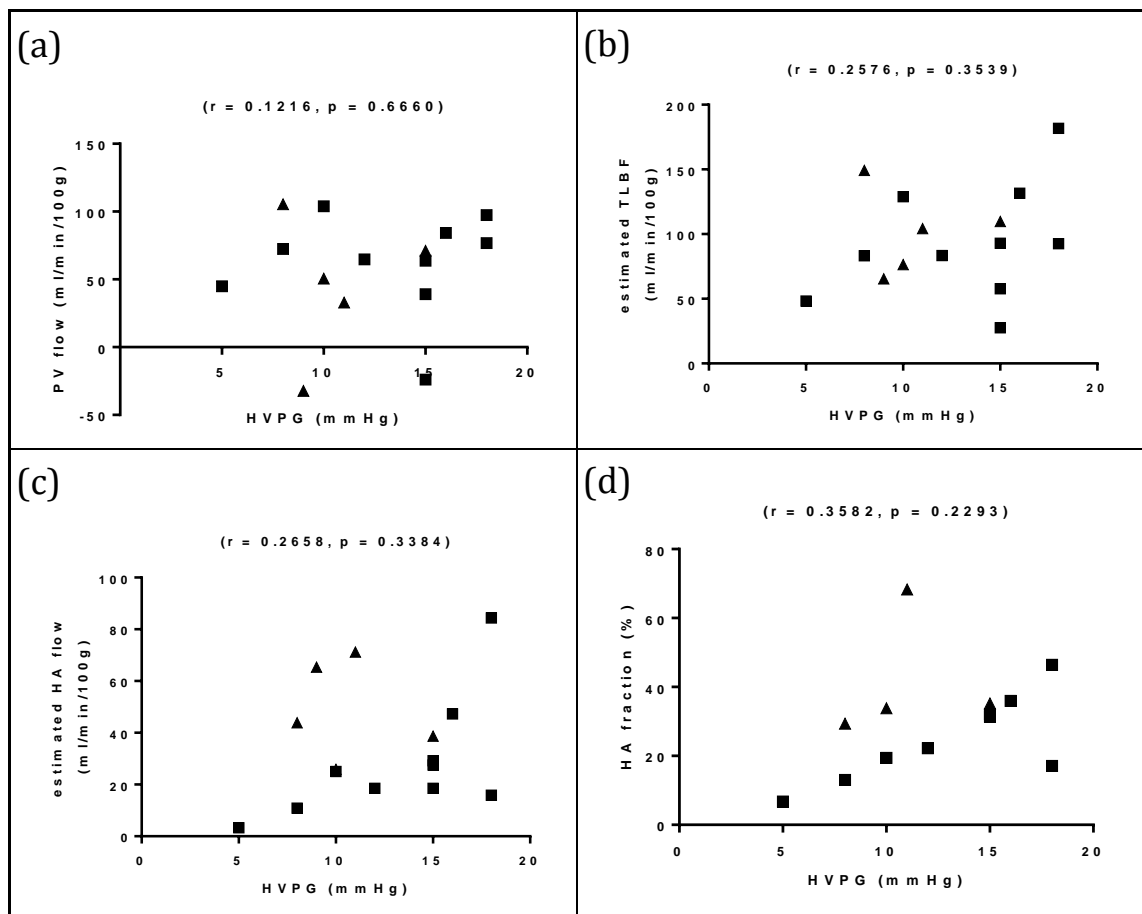


Figure 8.10: HVPG correlations with hepatic PCMRI flow parameters in cirrhotic patients

Encouraging correlations were detected between baseline (■) estimated HA flow and HVPG ($r = 0.6251$, $p = 0.053$) and baseline HA fraction and HVPG ($r = 0.7755$, $p = 0.0141$). Poor HVPG correlations were demonstrated for pooled baseline (■) and post-treatment (▲) PV flow, TLBF, HA flow and HA fraction data.

No HVPG correlations were demonstrated for estimated TLBF as a percentage of cardiac output ($r = -0.4009$, $p = 0.1386$) or estimated HA flow as a percentage of cardiac output ($r = -0.01486$, $p = 0.9581$). Interestingly, a weak but just non-significant positive correlation was demonstrated for baseline HA flow as a percentage of cardiac output and HVPG ($r = 0.5778$, $p = 0.0802$).

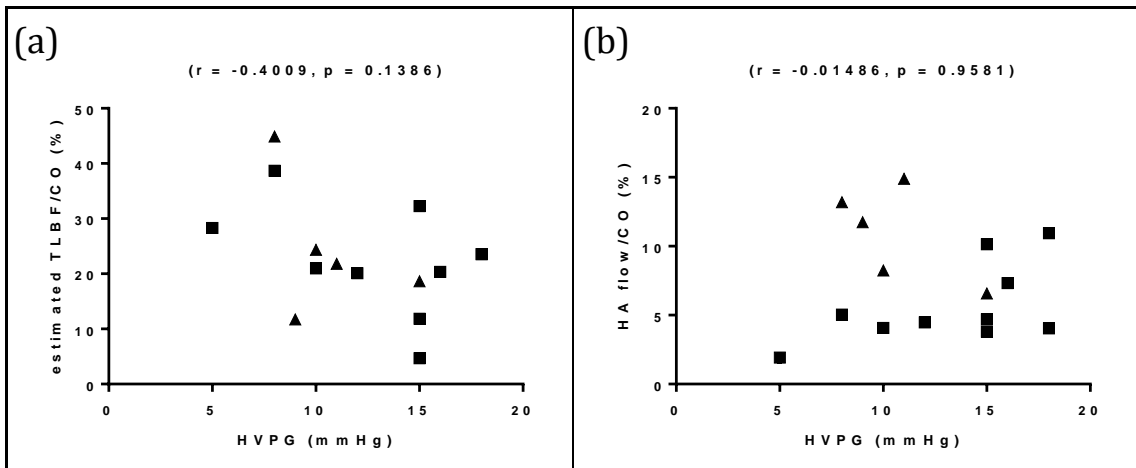


Figure 8.11: HVPG correlations with cardiac output normalised hepatic PCMRI flow parameters in cirrhotic patients

A weak correlation but just non-significant was detected between baseline (■) estimated HA flow as percentage of cardiac output and HVPG ($r = 0.5778$, $p = 0.0802$). Poor HVPG correlations were demonstrated for pooled baseline (■) and post-treatment (▲) TLBF and HA flow as a percentage of cardiac output.

The strongest HVPG correlation across pooled data was demonstrated using cardiac output ($r = 0.571$, $p = 0.0260$) (figure 8.12).

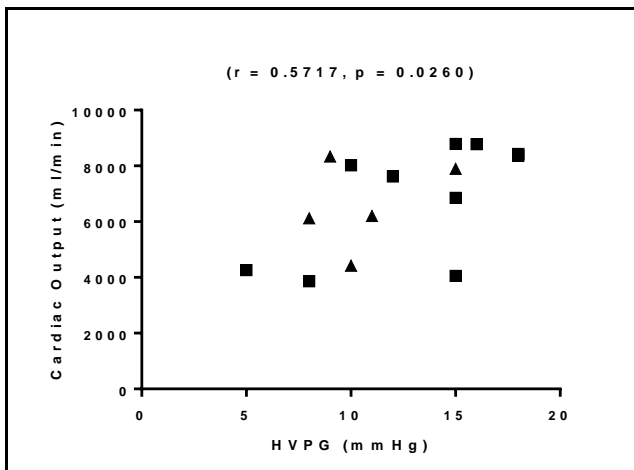


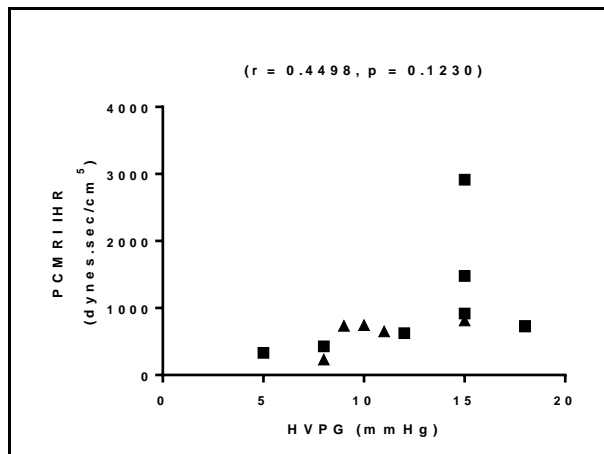
Figure 8.12: HVPG correlation with cardiac output in cirrhotic patients

A weak but significant positive correlation was detected between pooled baseline (■) and post-treatment (▲) cardiac output and HVPG.

It is worth noting that the calculation for IHR includes HVPG (equation 8.1), so a positive correlation would be expected between these two variables. In the absence of the baseline outlier (HVPG 15 mmHg, IHR 2913 dynes.sec/cm⁵), a modest but significant positive correlation was detected ($r = 0.6177$, $p = 0.0323$).

Figure 8.13: HVPG correlation with PCMRI IHR in cirrhotic patients

No correlation was detected between pooled baseline (■) and post-treatment (▲) data. Significant correlations were detected in the absence of the outlier (HVPG 15 mmHg, IHR 2913 dynes.sec/cm⁵).



8.5.6 HAEMODYNAMIC CHARACTERISATION STUDIES

Comparisons were undertaken between patients ($n = 11$) and controls (normal volunteers, $n = 13$). Data collected in patients at baseline ($n = 11$) and post-treatment ($n = 4$) was pooled together before further stratification into datasets with HVPG < 12 mmHg ($n = 3$ baseline, $n = 3$ post-treatment) and those with HVPG ≥ 12 mmHg ($n = 8$ baseline, $n = 1$ post-treatment).

Unpaired t-tests demonstrated an expected significant difference in HVPG between the two cirrhotic cohorts (HVPG <12 mmHg: mean 8.833 ± 0.8724 mmHg; HVPG ≥ 12 mmHg: mean 15.50 ± 0.6814 mmHg; $p < 0.0001$) (figure 8.14a). IHR in the cirrhotic HVPG ≥ 12 mmHg cohort (non-normally distributed, median 772.6 dynes.sec/cm⁵) was higher than in the cirrhotic HVPG <12 mmHg cohort (median 563.3 dynes.sec/cm⁵), but this difference was just above statistical significance ($U = 9.000$, $p = 0.0593$) (figure 8.14b).

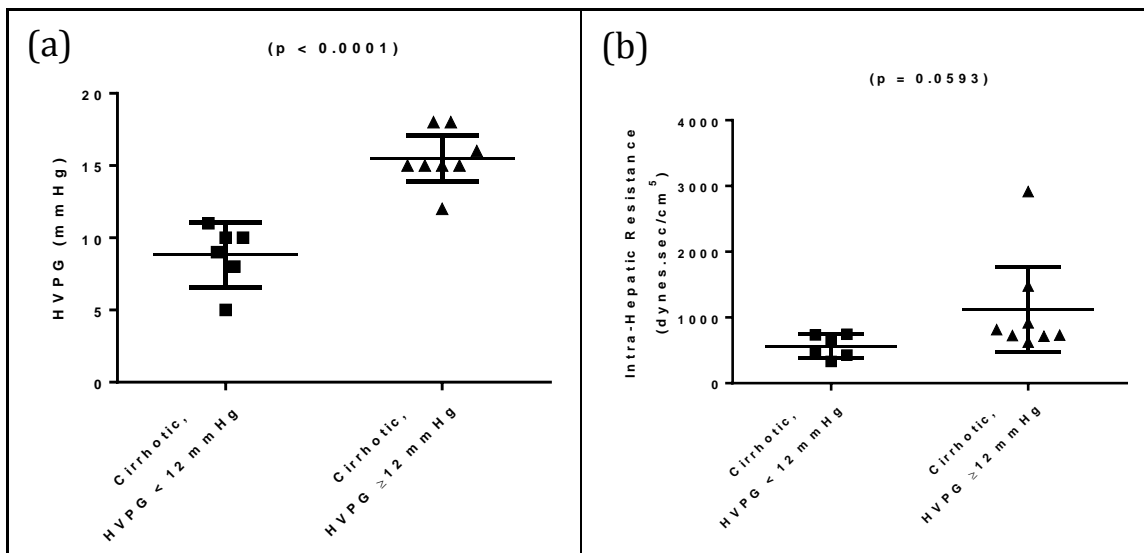


Figure 8.14: HVPG and PCMRI IHR in cirrhotic portal hypertensive patients

An expected significant difference was noted in HVPG, with differences in PCMRI derived IHR approaching significance. IHR was higher in cirrhotics with more severe portal hypertension, as expected by the mathematical derivation of this parameter.

Liver volume was found to be significantly different across all three cohorts ($F(2, 24) = 4.725$; $p = 0.0186$), however significant differences on post-hoc testing were only identified between control and cirrhotic patients with $HVPG < 12 \text{ mmHg}$. No significant difference in liver volume was recorded between less and more severely portal hypertensive cirrhotics (figure 8.15).

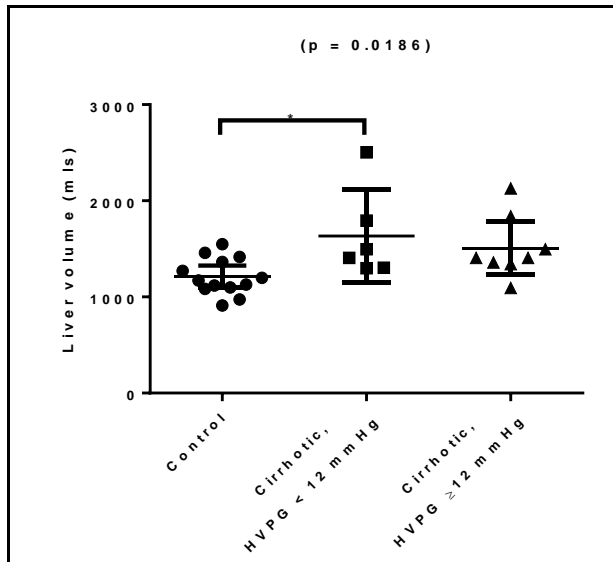


Figure 8.15: Liver volume in cirrhotic portal hypertensive patients

A significant increase in mean volume was detected between controls and cirrhotics with $HVPG < 12 \text{ mmHg}$. Mean liver volume declined in more severely portal hypertensive patients with significant difference in relation to the other two cohorts. p-value quoted for one-way ANOVA test.

No significant difference in PV flow was detected across all three cohorts ($F(2,25) = 0.9861$; $p = 0.3871$) (figure 8.16a). Differences between estimated TLBF however did approach significance ($F(2, 25) = 3.177$; $p = 0.0590$), with post-hoc tests demonstrating a significant difference between controls (mean TLBF 68.85 ± 4.737 ml/min/100g) and cirrhotics with $HVPG \geq 12$ mmHg (mean TLBF 113.3 ± 21.69 ml/min/100g) (figure 8.16b). Estimated HA flow was also significantly different across all three cohorts ($F(2,25) = 4.432$; $p = 0.0227$), with significantly higher HA flow in cirrhotics with $HVPG \geq 12$ mmHg (mean HA flow 38.41 ± 7.846 ml/min/100g) relative to controls (mean HA flow 11.99 ± 4.821 ml/min/100g) (figure 8.16c). No significant differences in HA fraction were detected across the three cohorts ($F(2,23) = 1.736$; $p = 0.1986$) (figure 8.16d).

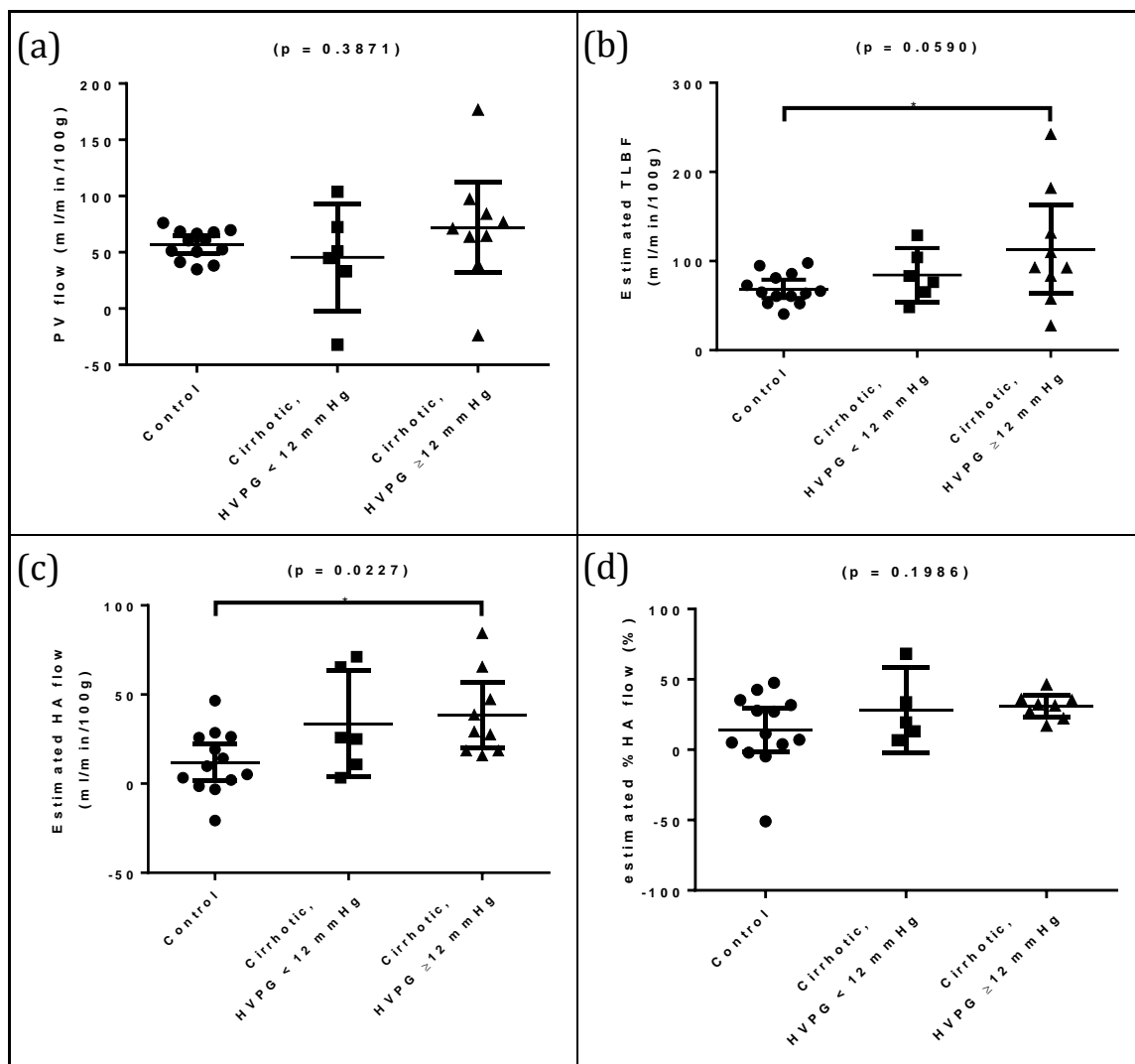


Figure 8.16: PCMRI hepatic haemodynamic parameters in cirrhotic portal hypertensive patients

p-values are quoted for one-way ANOVA tests. Post-hoc test differences in TLBF and HA flow were demonstrated between cirrhotics with $HVPG > 12$ mmHg and controls, but not between cirrhotic patients with differing severities of portal hypertension.

No significant differences were detected between the three cohorts for estimated TLBF as a percentage of cardiac output ($F(2, 24) = 0.7723$; $p = 0.4731$) or estimated HA flow as a percentage of cardiac output ($F(2, 24) = 1.695$; $p = 0.2049$) (figure 8.17).

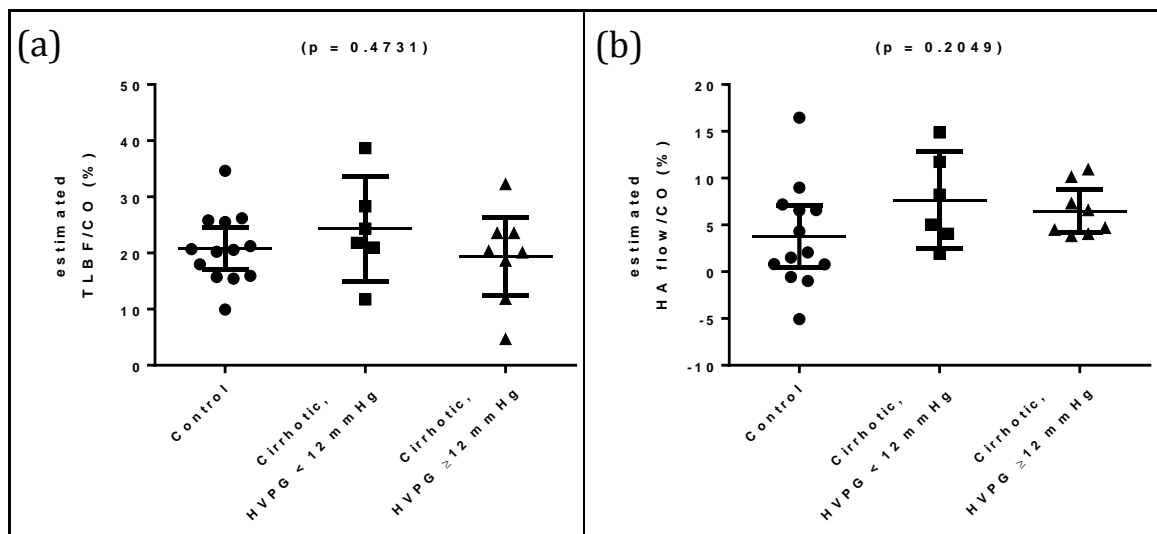


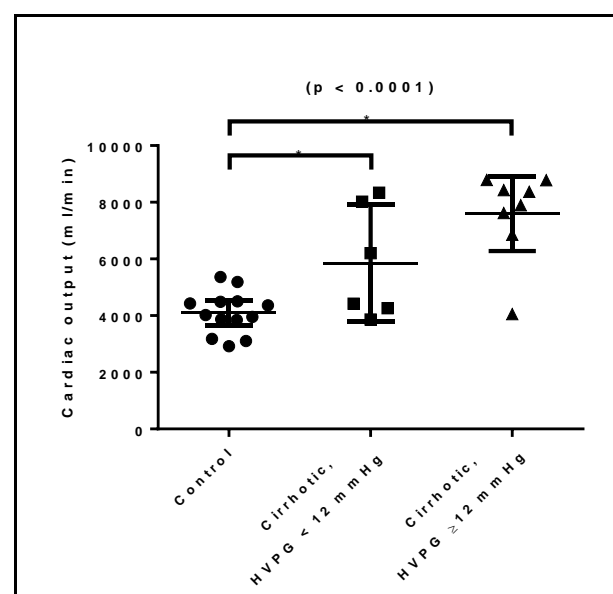
Figure 8.17: PCMRI hepatic haemodynamic parameters relative to cardiac output in cirrhotic portal hypertensive patients

p-values are quoted for one-way ANOVA tests. No significant differences between the three cohorts were identified.

Cardiac output was significantly different across all three cohorts ($F(2, 24) = 17.01$; $p < 0.0001$), with significant differences on post-hoc testing between cardiac output in controls (4094 ± 206.1 ml/min) and the elevated cardiac output recorded in cirrhotic patients with $HVPG < 12$ mmHg (5851 ± 806.6 ml/min) and cirrhotic patients with $HVPG \geq 12$ mmHg (7598 ± 556.1 ml/min). No significant differences were detected on post-hoc testing between cirrhotic cohorts (figure 8.18).

Figure 8.18: Cardiac output in cirrhotic portal hypertensive patients

p-values are quoted for one-way ANOVA tests. Significant differences on post-hoc testing were identified between diseased and control cohorts, but no significant difference was recorded between cirrhotics with varying severity of portal hypertension.



8.5.7 POST-TREATMENT HAEMODYNAMIC RESPONSE

Of the seven patients included in the MRI study screened for participation in the phase II OCA trial, one subject was found to have a baseline HVPG of 10 mmHg. This patient did not participate in the trial (as determined by trial exclusion criteria) and was therefore excluded from our haemodynamic response study. MRI data was obtained at baseline ($n = 6$), with post-OCA measurements obtained for four patients.

Mean baseline PV flow (56.25 ± 17.97 ml/min/100g) declined post-treatment (30.63 ± 22.33 ml/min/100g), but this difference was not significant (median difference -10.76 ml/min/100g, $W = -10.00$, $p = 0.1250$) (figure 8.19a). Mean baseline estimated TLBF (97.39 ± 22.21 ml/min/100g) was similar post-OCA (88.69 ± 10.71 ml/min/100g) and this difference was found to be not significant (median difference 10.69 ml/min/100g, $W = 4.000$, $p = 0.6250$) (figure 8.19b). Estimated HA flow at baseline (37.15 ± 10.47 ml/min/100g) increased post-OCA (50.28 ± 10.78 ml/min/100g), but this difference was also non-significant (median difference 17.25 ml/min/100g, $W = 4.000$, $p = 0.6250$) (figure 8.19c). Estimated HA fraction at baseline ($32.61 \pm 4.706\%$) also increased post-treatment ($45.80 \pm 11.27\%$), but this difference was also non-significant (median difference 2.392%, $W = 4.000$, $p = 0.5000$) (figure 8.19d).

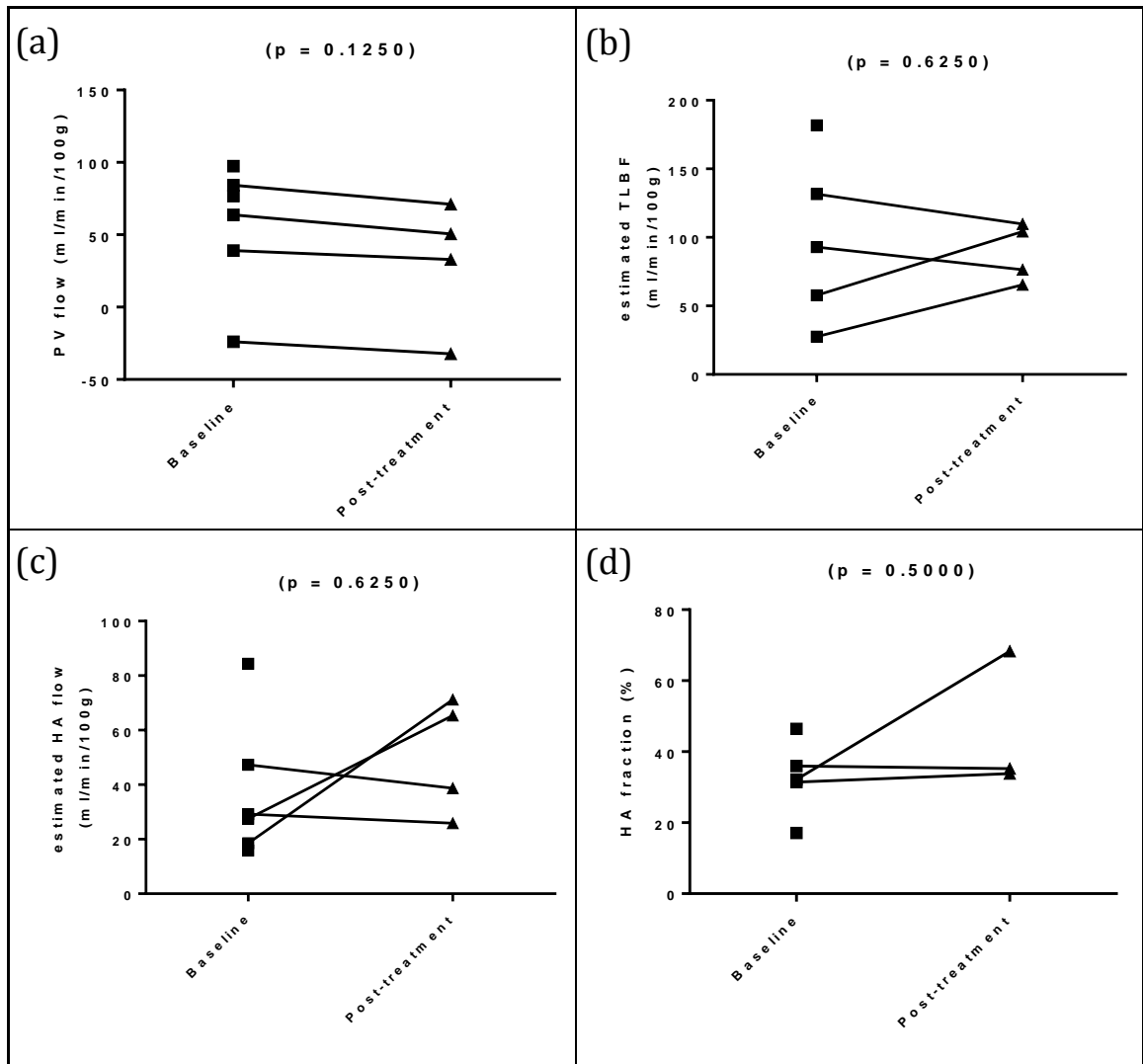


Figure 8.19: PCMRI hepatic haemodynamic parameters in cirrhotic patients at baseline and following treatment with OCA

p-values are quoted for one-way ANOVA tests. Post-hoc test differences in TLBF and HA flow were demonstrated between cirrhotics with HVPg > 12 mmHg and controls, but not between cirrhotic patients with differing severities of portal hypertension.

Mean estimated TLBF as a percentage of cardiac output at baseline ($19.39 \pm 3.980\%$) was similar post-treatment ($19.14 \pm 2.729\%$) and this difference was shown to be non-significant (median difference 2.669%, $W = 2.000$, $p = 0.8750$) (figure 8.20a). Estimated HA flow as a percentage of cardiac output at baseline ($6.824 \pm 1.287\%$) increased post-OCA treatment ($10.36 \pm 1.855\%$), but this difference was also shown to be non-significant (median difference 3.152%, $W = 4.000$, $p = 0.6250$) (figure 8.20b).

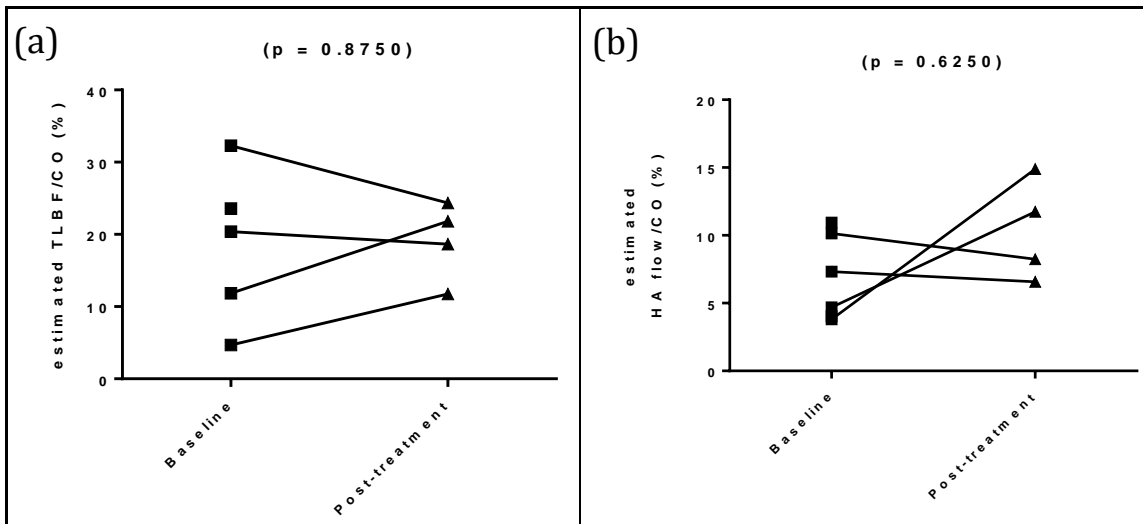


Figure 8.20: PCMRI hepatic haemodynamic parameters relative to cardiac output in cirrhotic patients at baseline and following treatment with OCA
 p-values are quoted for one-way ANOVA tests. No significant differences between the three cohorts were identified.

Average cardiac output at baseline (7545 ± 757.6 ml/min) declined post-treatment (6711 ± 892.2 ml/min), but this difference was non-significant (median difference -551.6 ml/min, $W = -8.000$, $p = 0.2500$) (figure 8.21).

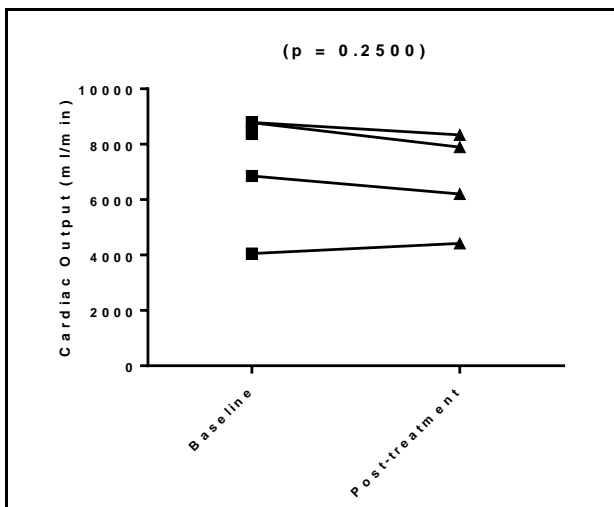


Figure 8.21: Cardiac output in cirrhotic patients at baseline and following treatment with OCA
 p-values are quoted for one-way ANOVA tests. No significant differences between the three cohorts were identified.

Mean HVPg at baseline (16.17 ± 0.6009 mmHg) was also reduced post-treatment (11.25 ± 1.315 mmHg), but this difference was also non-significant (median difference -4.500 mmHg, $W = -10.00$, $p = 0.1250$). Mean PCMRI IHR at baseline (1246 ± 354.1 dynes.sec/cm⁵) also declined post-OCA treatment (736.3 ± 33.59 dynes.sec/cm⁵) but given the lack of post-treatment significant differences for any of the variables used to calculate it, no significant difference in post-treatment IHR was detected (median difference -500.5 dynes.sec/cm⁵, $W = -8.000$, $p = 0.2500$).

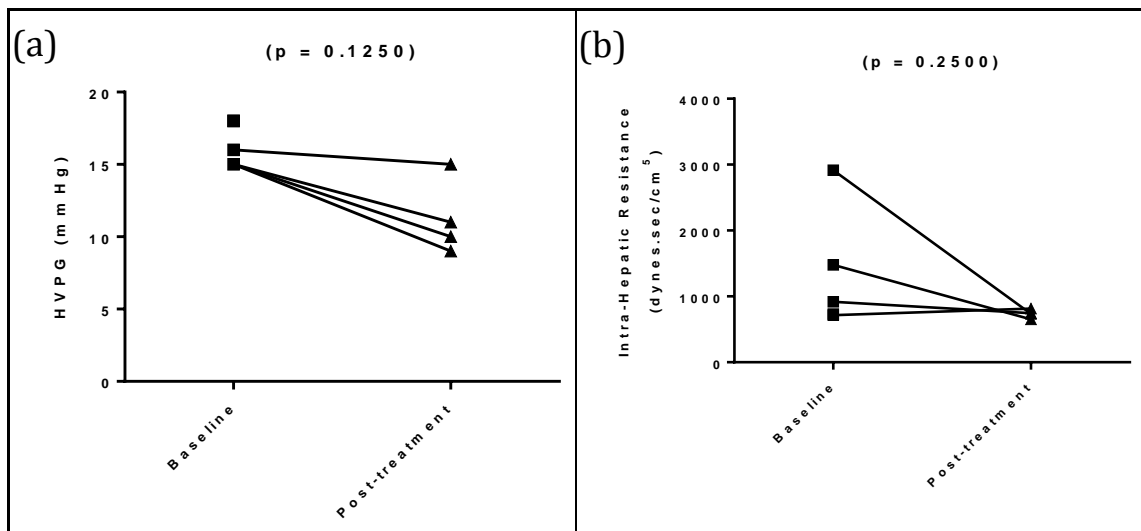


Figure 8.22: HVPG and PCMRI IHR in cirrhotic patients at baseline and following treatment with OCA

An expected significant difference was noted in HVPG, with differences in PCMRI derived IHR approaching significance. IHR was higher in cirrhotics with more severe portal hypertension, as expected by the mathematical derivation of this parameter.

Only five patients were recruited into the TIPSS cohort, and of the two datasets at baseline, only one of these was paired with post-treatment data (table 8.1). Statistical analysis was therefore deemed inappropriate, but as proof-of-principle of the ability of PCMRI to detect haemodynamic changes post-TIPSS, we present the data from the single patient in whom both baseline and post-TIPSS MRI measurements were made.

Post-TIPSS increases were noted in PV flow (+40.65 ml/min/100g), estimated HA flow (+25.34 ml/min/100g), estimated TLBF (+66.00 ml/min/100g) and also HA fraction (+7.135%). Increases in estimated TLBF as a percentage of cardiac output (+24.76%) and estimated HA flow as a percentage of cardiac output were also recorded (+8.713%). A decline in cardiac output was observed (-1499 ml/min) (table 8.2).

Table 8.2: Haemodynamic parameters at baseline and post-TIPSS (n = 1)

	BASELINE	POST-TIPSS
<i>PV flow (ml/min/100g)</i>	64.79	105.4
<i>Estimated TLBF (ml/min/100g)</i>	83.34	149.3
<i>Estimated HA flow (ml/min/100g)</i>	18.55	43.89
<i>Estimated HA fraction (%)</i>	22.26	29.39
<i>Estimated TLBF/CO (%)</i>	20.11	44.88
<i>Estimated HA flow/CO (%)</i>	4.477	13.19
<i>Cardiac output (ml/min)</i>	7618	6119
<i>HVPG (mmHg)</i>	12	8
<i>IHR (dynes.sec/cm⁵)</i>	626.5	233.1

8.6 DISCUSSION

We have demonstrated that adapted standard clinical cine PCMRI protocols to measure bulk vessel flow in upper abdominal vessels can be used in cirrhotic patients. While this in itself is not novel, we have applied the methods we have developed for estimating TLBF and HA flow and for the first time in these patients and used them to non-invasively investigate haemodynamic parameters in chronic liver disease. The application of these methods in cirrhotic patients has identified specific clinical considerations which we explore in this section.

8.6.1 FEASIBILITY

Retrograde PV flow represents a significant pathological derangement of bulk flow that can readily occur in cirrhotic patients with portal hypertension. Using the system of equations based on the principle of conservation of mass presented in section 5.3, we would argue that the following expression in this exceptional situation does not hold true:

$$Q_{TLBF} = Q_{distal\ IVC} - Q_{proximal\ IVC} \quad (\text{Equation 8.2})$$

Where ' Q_{TLBF} ' represents estimated total liver blood flow and ' $Q_{distal\ IVC}$ ' and ' $Q_{proximal\ IVC}$ ' represent flow in the supra-hepatic, sub-cardiac IVC and infra-hepatic, supra-renal IVC respectively.

We would argue instead however, that the presence of retrograde PV flow represents a special instance of the principle of conservation of mass because regardless of the pathological state of the liver, the inflow and outflow from the liver must always be equivalent. The following expression, for example, still holds true, given that PV flow (Q_{PV}) is a negative term:

$$Q_{PV} + Q_{HA} = Q_{distal\ IVC} - Q_{proximal\ IVC} \quad (\text{Equation 8.3})$$

The only difference is that hepatofugal PV flow must represent an outflow and therefore for expressed in terms of the principle of conservation of mass:

$$\begin{aligned} Q_{in} &= Q_{out} \\ Q_{HA} &= Q_{distal\ IVC} - Q_{proximal\ IVC} - Q_{PV} \end{aligned} \quad (\text{Equation 8.4})$$

While this finding is implicit, an important consequence of it is that in this situation TLBF must equate to HA flow alone (and not the sum of PV and HA contributions). This would

make sense as the only afferent blood to the liver in the presence of retrograde PV flow would be from the HA itself:

$$Q_{TLBF} = Q_{HA} \quad \text{(Equation 8.5)}$$

It therefore follows that in this exceptional situation, HA fraction is by default 100%, and the estimated TLBF as a percentage of cardiac output and estimated HA flow as a percentage of cardiac output are equal. For the single case with baseline and post-OCA retrograde PV flow, data was processed using these modifications. We would argue that inclusion of HA fraction data of 100% would erroneously skew the small samples available for analysis and for this reason HA fraction data from the patient with retrograde PV flow was not included. It is worth noting that good consistency of PCMRI inflow and outflow measurements was observed using these modifications both at baseline and post-OCA in the patient with hepatofugal PV flow.

A major concern with the implementation of abdominal quantitative MRI protocols in patients is compliance with breath-hold instructions during the scan. Our data have demonstrated that consistent and coherent data can be obtained, even in patients with poor compliance. A major strength of our protocol is the use of triplicate-averaged measurements, and a reliance on large high flow volume vessels for quantification. The amount of phase contrast signal from a vessel is reliant on the difference between the V_{enc} setting and the velocity of flowing spins within the vessel itself. Loss of signal from V_{enc} overestimation is particularly troublesome in a smaller vessel such as the HA (where there are fewer spins to begin with), which in combination with motion artefact can have ruinous effects on quantification [182].

Finally important considerations for patients scanned post-TIPSS, include clinical safety and any artefacts arising from the TIPSS stent that may compromise quantification. Because of concerns over heating effects, particularly at higher field strengths, all post-TIPSS scans were only performed after ensuring the stent manufacturer had confirmed 3T MRI compatibility [477]. No adverse effects were reported by patients or radiographers. We endeavoured to measure PV and caval flow at sites where the stent was not visualised so at no point did stent artefact compromise quantification. Previous PCMRI studies at lower field strength planned through the stents have however confirmed adequate quantification in spite of possible artefact [194, 478].

8.6.2 CONSISTENCY AND VALIDATION

As with previous normal volunteer data, we used analysis of agreement between independently measured PCMRI inflow and outflow to confirm the consistency of these

and derived measurements. This demonstrated very good agreement between each measurement method, with a coefficient of repeatability of 27.64 ml/min/100g for TLBF and HA flow estimations. This was larger than the coefficient of repeatability between PCMRI inflow and outflow measurements in normal volunteers (22.77 ml/min/100g), and may be a result of greater motion artefact in the patient data affecting quantification. Contrastingly, the coefficient of repeatability between direct and estimated PCMRI HA fraction was 14.39% in cirrhotic patients, compared with 29.57% in normal volunteers. Percentage error was calculated in the same way as previously (table 8.3) and for estimated TLBF was encouraging. The percentage error associated with HA flow (22.62±8.247%) was however much larger than for TLBF, as a result of the same coefficient of repeatability for the measurement of a smaller absolute value. Interestingly, no negative estimations of HA flow were made using the caval subtraction method, indicative of the generally higher HA flows recorded in cirrhotic patients. The percentage error associated with estimated HA flow in patients was also smaller than in normal volunteers (28.32±18.38%). Similarly, HA fraction was associated with a much more acceptable coefficient of repeatability between measurement methods of 14.39% (compared with 29.57% in normal volunteers), a likely consequence of the greater magnitude of measured values rather than any inherent difference in quality of data acquired (table 8.3).

Table 8.3: Error estimation for PCMRI derived flow measurements in cirrhotic patients

	GLOBAL MEAN*	MEAN DIFFERENCE TO 'GOLD STANDARD'	ESTIMATED PERCENTAGE ERROR
<i>Caval subtraction PCMRI TLBF</i>	115.0±13.13 ml/min/100g	8.878±3.236 ml/min/100g [†]	7.720±2.814%
<i>Caval subtraction PCMRI HA flow</i>	39.24±5.275 ml/min/100g	8.878±3.236 ml/min/100g [†]	22.62±8.247%
<i>Caval subtraction PCMRI HA fraction</i>	30.29±3.468%	3.889±1.781% [†]	12.84±5.880%

(*pooled mean across baseline and post-treatment measurements; [†]direct inflow PCMRI measurements gold standard)

As with previous preclinical and normal volunteer data, application of the caval subtraction method to estimate TLBF and HA flow suffers from error propagation. Errors in the measurement of distal and proximal IVC flows summate in the estimation of TLBF, and estimation of HA flow suffers from the additional error associated with PV flow. In this preliminary study we used a small sample of gold-standard invasive measurements of ICG clearance to validate PCMRI TLBF measurements and PCMRI derived IHR measurements. ICG TLBF was consistently less than PCMRI estimated TLBF, and the coefficient of repeatability was large (68.10 ml/min/100g) with an estimated percentage

error for PCMRI TLBF measurements of $36.81 \pm 12.63\%$ (table 8.4). The difference between the methods identifies an important distinction in the implications of the parameters measured by each quantification method. For ICG clearance, hepatic plasma flow (HPF) (subsequently converted into TLBF using the haematocrit) is inversely related to the difference between arterial and hepatic venous ICG concentrations (ICG_A and ICG_{HV} , respectively) (equation 8.6):

$$HPF = \frac{E}{ICG_A - ICG_{HV}} \quad \text{(Equation 8.6)}$$

Where ' E ' represents 'splanchnic turnover rate', a function of ICG infusion rate, body mass, urinary excretion (assumed to be zero) and change in arterial concentration between timed samples (assumed to be 0.0001, across all datasets based on previous data) [450, 468]. Implicit to equation 8.6, is that a reduction in TLBF will be reflected in an increase in the difference between arterial and hepatic venous concentration. ICG however is selectively taken up by hepatocytes (a property which is essential for blood flow quantification), but which also implies that the arterial-venous difference is dependent on the hepatocyte capacity to take up the dye (and therefore their function). In this sense, ICG derived TLBF is measure of 'effective' blood flow, dependent on bulk flow but also on the integrity and state of the hepatic tissue that is being perfused. This is especially relevant in cirrhosis where not only is there potential for impaired hepatocyte uptake of ICG, but also intra-hepatic shunting whereby blood can circulate through the hepatic vascular bed without perfusing hepatocytes. This contrasts starkly to PCMRI, which purely measures bulk flow in afferent or efferent vessels around the liver. In a cirrhotic liver, one would therefore expect to have lower 'effective' blood flow than the actual volume of blood flow circulating through the liver. This could certainly explain the observed persistent overestimation of TLBF by PCMRI. It also adds weight to the implications of the positive (but just above not-significant) correlation recorded between PCMRI and ICG TLBF ($r = 0.6436$, $p = 0.0851$).

Finally, IHR measured using PCMRI and HVPG demonstrated a large coefficient of repeatability ($984.2 \text{ dynes}\cdot\text{sec}/\text{cm}^5$) and estimated percentage error ($95.43 \pm 23.24\%$) (table 8.4). Although suggestive of substantial differences between the methods, these observations could be explained by the differing implications of each the TLBF measurement methods (as discussed previously). The positive (and significant) correlation between the methods ($r = 0.8382$, $p = 0.0094$) is encouraging.

Table 8.4: Error estimation for PCMRI derived haemodynamic measurements in cirrhotic patients

	GLOBAL MEAN*	MEAN DIFFERENCE TO ICG GOLD STANDARD	ESTIMATED PERCENTAGE ERROR
<i>Caval subtraction PCMRI TLBF</i>	97.20±12.60 ml/min/100g	-35.78±12.28 ml/min/100g [†]	36.81±12.63%
<i>Caval subtraction PCMRI estimated IHR</i>	763.9±164.7 dynes.sec/cm ⁵	-729.0±177.5 dynes.sec/cm ⁵ [†]	95.43±23.24%

(*pooled mean across baseline and post-treatment measurements)

8.6.3 HAEMODYNAMIC PARAMETER RELATIONSHIPS

Measurement of HVPG is invasive but essential in the diagnosis and management of portal hypertension. Hepatic pressure and flow parameters are linked by resistance, as given by the expression for IHR (equation 8.1). The investigation of any trends between flow parameters and HVPG are valuable because they can be used to inform our understanding of the pathophysiology of portal hypertension and because strong associations with non-invasive parameters have the potential to independently predict HVPG and IHR. Unlike previously published clinical studies, we have recorded a comprehensive range of non-invasive hepatic haemodynamic parameters for each subject, including PV flow, HA flow, HA fraction, cardiac output and composite variables such as IHR. We review the implications of our findings for each of these in turn.

In the normal volunteer cohort, it would be reasonable to assume that PV flow equates to splanchnic blood flow as all blood draining the GI tract is physiologically diverted to the liver before entering the systemic circulation. In cirrhotic patients with portal hypertension however, efferent splanchnic blood passes into the portal vein but is also diverted via extra-hepatic shunts bypassing the liver and into the systemic circulation at the sites of porto-systemic anastomosis (commonly lower oesophageal, superior rectal, umbilical, etc). Consequently, while a relationship between HVPG and splanchnic blood flow is likely to exist, any relationship between HVPG and PV flow in cirrhotic patients is likely to be weak, as demonstrated by our data (HVPG vs PV flow $r = 0.1216$, $p = 0.6660$) and previously published findings in the literature [192, 193, 195, 200, 382]. Previously presented data (Chapters 4, 5 and 7) demonstrating lower PV flow in BDL rats which were noted to have relatively absent macrovascular extra-hepatic shunts would also support this hypothesis, as PV flow in these subjects is likely to be representative of splanchnic blood flow.

Given the contribution of PV flow to TLBF, the absence of any relationship between HVPG and estimated TLBF in our data is therefore not unexpected ($r = 0.2576$, $p = 0.3539$). In support of this, previously acquired data at our institution has shown a very weak

relationship between ICG derived TLBF and HVPG in patients with stable cirrhosis, with reductions in ICG TLBF recorded only in decompensated or ACLF patients [450].

More interestingly, the demonstration of a lesser role of PV flow serves only to underscore the importance of HA flow in chronic liver disease. Even when allowing for the small cohort size, the correlations at baseline between estimated HA flow ($r = 0.6251$, $p = 0.053$) and HA fraction ($r = 0.7755$, $p = 0.0141$) are telling of the significance of HA flow in the vascular pathophysiology of portal hypertension. It is perhaps even more interesting that post-treatment measurements of estimated HA flow and HA fraction, though small in number seem to challenge the trend.

A positive correlation between cardiac output and HVPG in stable cirrhotic patients has previously been reported at our institution and highlights the importance of the heart in the pathophysiology of haemodynamic dysfunction in liver disease [450]. Although a mild positive, just non-significant HVPG correlation was demonstrated for baseline HA flow as a percentage of cardiac output ($r = 0.5778$, $p = 0.0802$), in the presence of a positive HVPG correlation of both cardiac output and HA flow, a stronger correlation could be achieved by the product of these two variables. The physiological significance of this variable would be uncertain but highlights an interesting point around the use of multivariate regression and mathematical modelling. In this case, the small sample size precluded multivariate regression analysis, but it would be anticipated that once large datasets were accrued, such analysis would be an important step towards prediction of HVPG using purely non-invasive parameters.

Finally, it is worth noting that poor correlations were demonstrated between HVPG and PCMRI IHR ($r = 0.4498$, $p = 0.1230$). This was disappointing given that HVPG is a term in the calculation of IHR. Given the small sample size, and apparent single outlier (HVPG 15 mmHg, IHR 2913 dynes.sec/cm⁵), the analysis was repeated after exclusion of this point to yield a significant positive correlation ($r = 0.6177$, $p = 0.0323$). Interestingly, the outlying measurement was observed in the subject with retrograde PV flow at baseline.

8.6.4 HAEMODYNAMIC CHARACTERISATION STUDIES

Using HVPG to stratify cirrhotic portal hypertensive patients at higher risk of developing complications, we characterised differences in PCMRI haemodynamic parameters between normal volunteer controls and cirrhotics with differing risk profiles. We review these findings alongside previous differences demonstrated in preclinical subjects (sections 5.4 and 7.4) where appropriate.

We demonstrated expected differences between cirrhotic cohorts in HVPG, and just non-significant differences in IHR (mean difference 554.1 ± 325.0 dynes.sec/cm⁵, $U = 9.000$, $p = 0.0593$). The latter is an especially disappointing result as it implies that the addition of flow data to HVPG measurement in the computation of IHR generates a parameter with poorer discriminatory value (for complication risk) than HVPG alone. The borderline significance however does not exclude the possibility of a type II error, and a difference in IHR may become more apparent in a better powered study.

We demonstrated that there were significant differences in liver volumetry, with an increase in liver volume in lower risk cirrhotics, but interestingly no difference between cirrhotic cohorts or higher risk cirrhotics and controls. This would confirm the development of hepatomegaly in less advanced disease, with similar or reduced liver volume in higher risk patients suggestive of atrophy/shrinkage observed in more advanced disease [479]. Such a pattern of volumetric change would be in keeping with the predominantly alcoholic aetiology of chronic liver disease in the patient cohort.

It is worth noting that previously presented preclinical data demonstrated consistently elevated liver mass in BDL rats. Although mechanistic factors in the aetiology of disease could explain this phenomenon, preclinical studies of course have the advantage of much greater homogeneity within the cohort and better control of confounding disease related variables. The important implication of this difference however, is when comparing preclinical and clinical volume normalised flow parameters discussed below.

In support of the earlier discussion of splanchnic blood flow, we found no difference in PV flow between control and cirrhotic cohorts. Interestingly, a significant difference in estimated TLBF was demonstrated on post-hoc testing between controls and higher risk portal hypertensive cirrhotics. On initial inspection, this result is not supported by previously presented preclinical data, which consistently showed lower estimated TLBF in hydrated and non-hydrated BDL rats. Absolute, non-normalised estimated TLBF measurements in rats however, demonstrate a significantly greater TLBF in BDL rats (figure 5.17, replicated in figure 8.23b). This therefore highlights the confounding effect of heterogeneous liver volumetry in cirrhotic patients.

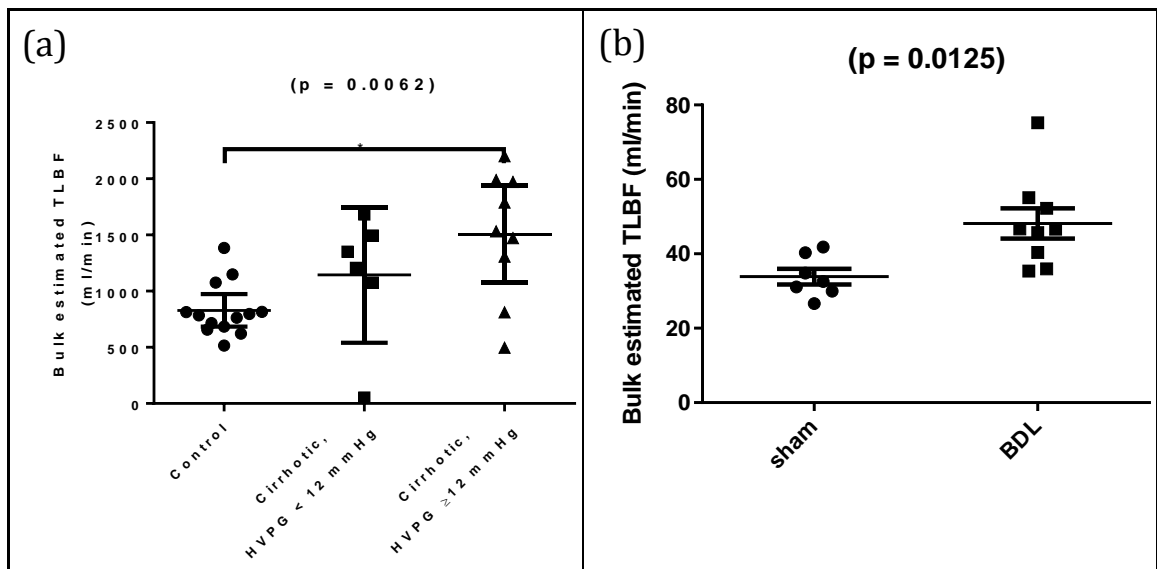


Figure 8.23: Comparison of bulk estimated TLBF in humans and rats

Significant differences in bulk estimated TLBF (non-normalised to liver volume) were demonstrated in (a) patients ($p = 0.0062$) and (b) non-hydrated rats ($p = 0.0125$), with significant differences on post-hoc testing in the human study between normal volunteers and high risk cirrhotic portal hypertensive patients.

We did however demonstrate significant differences in estimated HA flow across control and higher and lower risk portal hypertensive cirrhotic patients. Unfortunately, post-hoc differences were only detected between control and higher risk cirrhotic patients, but the finding of elevated HA flow in cirrhosis is supported by previous measurements in non-hydrated BDL rats. This finding once again highlights the importance of HA flow in the chronic liver disease.

Interestingly, a significant difference in HA fraction was not detected between control and cirrhotic patients, a finding that was corroborated by previous data from hydrated sham and BDL rats. Comparison of cardiac output demonstrated significant differences between cirrhotic patients and normal volunteers, but not between higher and lower risk portal hypertensive cirrhotics. This finding is supported by published clinical data confirming hyperdynamic circulation in cirrhosis [450, 452, 453, 455] but also by previously presented preclinical data in non-hydrated and hydrated BDL rats. Neither normalisation of estimated TLBF or estimated HA flow to cardiac output demonstrated any differences between normal volunteers and cirrhotic patients. The failure to demonstrate any difference in these parameters was corroborated by data in non-hydrated and hydrated BDL rats.

There are several important methodological observations which we acknowledge may compromise the interpretation of some of these analyses. Firstly, the decision to stratify the cirrhotic cohort into patients with a HVPg cut off of 12 mmHg is arguably too conservative. Clinically significant portal hypertension is diagnosed when HVPg > 10

mmHg, and therefore stratification at this level would be more justifiable clinically [19, 475]. Although we argue the 12 mmHg threshold on the basis of complication risk, moving the threshold to 12 mmHg would place only two datasets in the low risk cirrhotic cohort rendering quantitative analysis inappropriate.

Secondly, analysis should ideally be performed using baseline data only but in this study we included post-OCA treatment datasets ($n = 4$) because of the small sample sizes. In the cirrhotic HVPG<12 mmHg cohort, three of the six datasets were obtained post-treatment while in the cirrhotic HVPG \geq 12 mmHg cohort, only one of the datasets was not obtained at baseline. Previous analysis of the relationship between HVPG and haemodynamic parameters identified post-treatment data as outliers to the preliminary baseline data trend demonstrated by HA flow, HA fraction and HA flow as a percentage of cardiac output. Arguably, this data could have contaminated potential differences between the lower and higher risk cirrhotic cohorts.

Finally, comparisons were made with both hydrated and non-hydrated preclinical data on the basis that although patients were fasted before each scan, they were advised to consume water ad libitum. It is therefore impossible to define if patients were indeed hydrated/non-hydrated at the time of scanning. Importantly, no haemodynamic parameter trends between normal volunteers and cirrhotic patients were recorded that disagreed with those observed in sham and BDL rats.

8.6.5 POST-TREATMENT STUDIES

Small sample size compromised the evaluation of haemodynamic changes post-OCA and post-TIPSS. No significant changes were demonstrated for any of the non-invasive or invasive haemodynamic parameters post-OCA, although eyeballing individual patient trends, it is clear that some patients recorded profound differences post-treatment. Preliminary findings from the larger group of patients recruited into the phase II trial stratified patients into responders (post-OCA HVPG<12 mmHg or HVPG reduction >15%; $n = 9$) and non-responders ($n = 5$) [468]. Only one of our MRI study subjects was classed as a non-responder. Interestingly, ICG TLBF data from six trial subjects demonstrated a median 25% increase post-OCA. This finding was not supported by PCMRI estimated TLBF measured in four subjects.

Unfortunately, haemodynamic parameters for post-treatment patients recruited into the TIPSS study were not paired with invasive HVPG measurements ($n = 4$). These measurements were to be undertaken immediately after the TIPSS stent was sited, but because of inconsistencies in the methodology of the HVPG measurements, these were not included in post-treatment analyses. Data from the single subject who underwent baseline

and post-TIPSS non-invasive studies demonstrates the potential for PCMRI in demonstrating post-therapeutic changes in this context. Further studies with larger patient numbers are planned.

8.6.6 GENERAL CRITICISMS

A major criticism of this study is the small sample size used. Invasive measurements and patient recruitment took place at a different site to the MRI scanner, so that logistical factors often restricted patient involvement or enthusiasm. There were also important omissions to the imaging protocol, which have arisen as a result of progressive development of the methodology rather than a deliberate omission. For example, although only bulk flow PCMRI haemodynamic measurements were recorded, DCE MRI and cardiac cine MRI measurements would be important to include in future planned studies. As demonstrated by the data presented in section 7.4, evaluation of tissue perfusion and cardiac systolic function are important aspects of haemodynamic state, which taken together with PCMRI provide much more comprehensive understanding of haemodynamic phenomena in disease.

8.6.7 FUTURE DIRECTIONS

An essential focus of future work would be to reinforce the findings in this study with the recruitment of greater patient numbers. Larger numbers of invasive validation data using ICG clearance would be invaluable in confirming the accuracy of PCMRI estimated TLBF measurements and securing credibility for more widespread use of the technique in the clinical community. Larger size data sets from the OCA trial would also provide insight into haemodynamic changes post-treatment but also demonstrate the potential application of PCMRI in clinical trials. Studies of the TIPSS cohort would be amenable to much larger scale studies, thereby providing a solid platform for demonstrating the sensitivity of PCMRI methods, but also investigating the complex haemodynamic phenomena that occur pre and post-TIPSS insertion.

Our data has also demonstrated ample new opportunities for protocol refinement and development. Inclusion of cardiac cine MRI for the assessment of systolic but also use of cardiac PCMRI for measuring diastolic function would also be important in using our methods to improve our understanding of cardiac dysfunction in the pathophysiology of portal hypertension. Finally DCE MRI, with the refinements introduced in Chapter 6, ASL and potentially dynamic hepatocyte-specific contrast enhanced (DHCE) MRI have the ability to not only inform tissue perfusion but also quantify intrahepatic shunting in disease.

The quantification of splanchnic shunting is an important challenge in non-invasive assessment, particularly as there is an intuitive correlation between the volume of shunting and the severity of portal hypertension. PCMRI has already been used by others to quantify azygous flow in chronic liver disease (section 1.3.6), but the absence of well-designed and well-powered studies of azygous flow have to date compromised both clinical data and enthusiasm.

Massive extrahepatic shunting as seen in the presence of retrograde PV flow, is a unique (and possibly separate) pathological phenotype as identified by this study. The very occurrence of retrograde PV flow has important ramifications for our understanding of the haemodynamic pathophysiology underpinning portal hypertension and the significance of some of the measurements made using PCMRI. Assessing this phenomenon using the principle of conservation of mass, for example, there is the theoretical possibility of ‘caval steal’ – net retrograde hepatic venous flow. The occurrence of this phenomenon is not inconceivable, especially in congestive hepatopathy of cardiac cirrhosis, but also in the presence of cirrhotic cardiomyopathy. As the only afferent supply to the liver in patients with hepatofugal PV flow is from the hepatic artery, these patients are also likely to be especially vulnerable to changes in systemic perfusion induced by inflammation as seen in ACLF. Caval subtraction PCMRI measurements could readily be used to study these phenomena.

The measurement of renal blood flow is also pertinent particularly in the context of hepato-renal syndrome (HRS). Although feasibility studies have not been undertaken, caval subtraction MRI could theoretically be applied quite easily in the measurement of renal blood flow, at the added expense of only a single additional PCMRI study of the infra-renal proximal IVC.

As a final point, the most robust and well-documented index of chronic liver disease is HVPG. Combining HVPG with flow, we can estimate IHR, and only once equipped with all three of these variables can we comprehensively assess hepatic haemodynamics. The measurement of HVPG requires hepatic venous cannulation and it is difficult to argue a clinical role for MRI derived flow measurements if at the time of HVPG measurement, ICG clearance can be easily ascertained. The real value-added from imaging will emerge when protocols are developed that can be used to non-invasively measure sinusoidal pressure alongside those developed for the assessment flow and perfusion. There has been growing interest in the investigation of the relationship between HVPG and biomechanical imaging (MR and ultrasound elastography) quantification. It can be argued that both acute (humoral) and chronic (microarchitectural) changes likely to drive

alterations in HVPG are also likely to have a physical impact on tissue stiffness. Early data has demonstrated encouraging correlations with liver and splenic stiffness measured using transient elastography, particularly at lower HVPG values (< 10 mmHg) [250, 480]. MR elastography data has to date been less convincing [296, 297, 481], but the ultimate goal would be the development of a single 'one-stop' imaging protocol in which PCMRI, DCE MRI (with PCMRI correction) and MRE are performed in succession. Hepatic sinusoidal 'pressure maps' generated from MRE data could then be used in conjunction with DCE MRI perfusion maps to generate maps of intra-hepatic resistance. These in turn could be used to predict sites of intrahepatic shunting, identify segmental areas affected more severely affected by disease, qualify focal hepatic parenchymal lesions, and be used to inform therapeutic interventions ranging from optimising the position of TIPSS stents to planning and enhancing surgical outcomes.

8.7 CONCLUSION

In this section, we have demonstrated the feasibility of using PCMRI to measure haemodynamic parameters in patients with chronic liver disease. We have (i) adapted previous methods to deal with the eventuality of retrograde PV flow, (ii) demonstrated that we can acquire useful quantitative data even in the presence of motion artefact and poor compliance with breath-hold instructions and (iii) shown that patients with TIPSS stents can be imaged safely and without compromising any PCMRI quantification.

We have demonstrated good consistency of estimated (caval subtraction) PCMRI TLBF with directly measured PCMRI TLBF in the same subject and shown improved consistency of estimated HA flow and estimated HA fraction with their directly measured counterparts relative to normal volunteers. Preliminary validation with invasive ICG clearance demonstrated encouraging correlations between ICG and PCMRI TLBF and PCMRI IHR but poor agreement. The latter may be secondary to differences in the implications of TLBF quantification using ICG rather than intrinsic PCMRI measurement error.

We have investigated the relationship between PCMRI haemodynamic parameters and invasive pressure measurements, to identify estimated HA flow, HA fraction and cardiac output as important correlative parameters with HVPG. We have also characterised differences in haemodynamic parameters between normal volunteer controls and cirrhotics with lower and higher risk of developing portal hypertensive complications. These comparisons have demonstrated differences between normal volunteers and lower risk cirrhotics in liver volume and cardiac output, and differences between normal volunteers and higher risk cirrhotics in estimated TLBF, estimated HA flow and cardiac output.

Finally, we applied PCMRI methods to measure changes in hepatic haemodynamic parameters in a small sample of patients post-OCA and post-TIPSS. Although PCMRI demonstrated profound haemodynamic changes in certain subjects, no significant post-OCA haemodynamic parameter changes were recorded.

8.8 CLOSING COMMENTS

This chapter represents the culmination of previous preclinical and clinical work, defined by ultimate translation to the bedside, with investigational studies in patients with chronic liver disease. In this chapter, we have shown how adapted protocols can be applied in the clinical setting to obtain useful quantitative information and shown that the novel caval subtraction PCMRI method proposed in this thesis is still consistent in patients and has credible potential for invasive validation.

Building on previous preclinical and normal volunteer data, we have confirmed relative passivity of the liver to changes in PV flow and underscored the importance of HA flow and cardiac output in the pathophysiology of portal hypertension. Finally, we have demonstrated the potential of our PCMRI methods in the evaluation of pharmacological and interventional therapies in cirrhotic patients with portal hypertension.

The conclusions of this chapter are preliminary – the study findings are restricted both in terms of size and scope. The importance of this chapter is however paramount. While being the final chapter in this thesis, it is in many ways the first chapter in the drive toward bringing MR haemodynamic modelling into the clinic as a viable tool in the management of patients with chronic liver disease.

SUMMARY OF FINDINGS

“...from you,
dark monarch,
giver of syrups and of poisons,
regulator of salts,
from you I hope for justice:
I love life: Do not betray me! Work on!
Do not arrest my song.”

- Ode to the liver [2].

The findings presented in this thesis are broad, extending across the preclinical and clinical remit, including outcomes from developmental/validation work for different MR techniques and findings with implications for our understanding of the pathophysiology of chronic liver disease.

In reflection of this, findings have been arranged in two tables (table 9.1 and 9.2), with conclusions from preclinical and clinical experiments matched where they pertain to similar investigational objectives.

Figure 9.1: Summary of development and validation findings

PRECLINICAL

CLINICAL

a) DCE MRI:

- DCE MRI can be used to estimate hepatic perfusion in healthy rats at 9.4T.
 - Though repeatable, measurements, show large variance and poor agreement with invasive TTUS validation.
 - Effective refinements to DCE MRI methods at 9.4T include use of the inversion recovery method for T1 measurement, improved VIF sampling through use of a syringe driver and a dual bolus approach to contrast agent delivery.
 - Implementation of DCE MRI protocols in larger animals (as would be required for studies of animals with disease) was unsuccessful because of lack of a robust strategy to deal with inflow effects.
- Clinical DCE MRI can be used to quantify perfusion at 3.0T in normal volunteers.
- Pharmacokinetic modelling of DCE MRI data with alternative models can have significant effect on quantification.
 - We propose use of the dual input single compartment model with 'constrained free modelling of pre-estimated VIF delays' as a novel strategy to derive physiologically meaning estimates of VIF delays.
- Using seven-day reproducibility data we propose the use of dual input single compartment pharmacokinetic modelling with the following novel post-processing refinements for quantification:
 - 'constrained free modelling of pre-estimated VIF delays'
 - correction of arterial input functions using PCMRI aortic flow measurements
 - the use of PCMRI caval subtraction measurements of TLBF to correct DCE MRI quantification.

Figure 9.1: Summary of development and validation findings (continued)

PRECLINICAL

CLINICAL

b) PCMRI:

- Two-dimensional respiratory, but non-cardiac gated PCMRI can be used to measure PV flow in rats at 9.4T. These measurements are repeatable and preliminarily reproducible with good agreement with invasive validation using TTUS.
- Fixed delay multiphase cardiac gating can be implemented using pulse oximetry to measure pulsatile vessel flow.
- We propose 'caval subtraction PCMRI', a novel method for measurement of TLBF and HA flow using 2D PCMRI measurements of IVC and PV flow.
- Using cine PCMRI, this method can be used to measure haemodynamic parameters in sham and BDL rats at 9.4T.
- Caval subtraction PCMRI measurements in conjunction with direct measurements of PV flow and cardiac output can be used to evaluate effects of haemodynamic stress.
- We have translated 'caval subtraction PCMRI', a novel method for measurement of TLBF and HA flow using 2D PCMRI measurements of IVC and PV flow.
- Using cine PCMRI, this method can be used to measure haemodynamic parameters in normal volunteers and cirrhotic patients at 3.0T.
- We propose an adaptation of the caval subtraction method to qualify flow parameters in the context of retrograde PV flow
- Caval subtraction PCMRI measurements in conjunction with direct measurements of PV flow and cardiac output can be used to evaluate effects of treatments for portal hypertension.

Figure 9.1: Summary of development and validation findings (continued)

PRECLINICAL

CLINICAL

b) PCMRI (continued):

- Good agreement between PCMRI aortic root flow and cardiac cine MR cardiac output was demonstrated in sham and BDL rats.
- Good agreement between PCMRI PV flow and invasive TTUS was demonstrated in sham rats.
- Reasonable agreement between PCMRI HA fraction and fluorescent microsphere HA fraction was demonstrated.
- Measurements of estimated caval subtraction HA flow and fraction suffer from error propagation.
- Cine PCMRI PV flow measurements are repeatable.
- Good agreement between PCMRI aortic root flow and cardiac cine MR cardiac output was demonstrated in normal volunteers.
- Good consistency between caval subtraction PCMRI and directly measured PCMRI PV and HA flow was demonstrated in normal volunteers and cirrhotic patients.
- Preliminary validation of caval subtraction PCMRI TLBF with invasive ICG clearance in cirrhotic patients demonstrated encouraging correlations, but poor agreement between methods.
- Measurements of estimated caval subtraction HA flow and fraction suffer from error propagation.
- Good seven-day reproducibility of cine PCMRI PV flow and estimated TLBF was demonstrated.
- Seven-day reproducibility of PCMRI estimated HA flow and fraction was inferior to seven-day reproducibility of directly measured PCMRI HA flow and fraction

c) ASL:

- FAIR ASL can be used to estimate hepatic perfusion in sham and BDL rats at 9.4T.
- Look-Locker hepatic parenchymal T1 measurements demonstrate good repeatability.
- Analysis of agreement with caval subtraction PCMRI TLBF demonstrated a tendency for ASL to underestimate hepatic parenchymal perfusion.

Figure 9.2: Summary of pathophysiological findings

PRECLINICAL

CLINICAL

- PV ligation is detected using DCE MRI but fails to demonstrate the hepatic arterial buffer response.
- BDL rats demonstrate higher hepatic parenchymal T1 relative to their sham counterparts

- Caval subtraction PCMRI demonstrates reduced TLBF and HA fraction at baseline in BDL rats.
- Both sham and BDL rats demonstrate reductions in PV flow in response to terlipressin, with failure of the hepatic arterial buffer response in BDL animals.
- Hydrated BDL rats demonstrate reductions in estimated TLBF, reduced PV flow and impaired hepatic arterial buffer response.
- Sham and BDL rats demonstrate relative passivity to changes in PV flow, with impaired regulation of HA flow in BDL rats.

- Post-prandial studies in normal volunteers demonstrate expected rises in PCMRI PV flow, TLBF and a negative hepatic arterial buffer response.

- PCMRI estimated TLBF and estimated HA flow (but not PV flow) are increased in higher risk portal hypertensive patients.

- BDL rats demonstrate features of cirrhotic cardiomyopathy: hyperdynamic circulation, elevated systolic function at rest and poor reserve under stress.
- In spite of having a hyperdynamic circulation, BDL livers fail to place a comparable demand on systemic circulation despite increased organ:body mass ratio.

- We have demonstrated that PCMRI HA flow, HA fraction and cardiac output are important correlative parameters with HVPG.

- PCMRI cardiac output is increased in lower and higher risk portal hypertensive patients.

- Liver volume is increased in lower risk, but not higher risk portal hypertensive patients.

- ACLF is characterised by reductions in TLBF and HA flow, absence of normal sepsis-induced hepatic hyperaemia and blunted cardiac systolic response to sepsis.

- Preliminary investigation in a cohort of portal hypertensive patients undergoing treatment with obeticholic acid did not demonstrate any significant haemodynamic difference post-treatment.

~ 459 ~

APPENDIX A

L-NAME AND TERLIPRESSIN DOSAGE REGIME EXPERIMENTS

AIM:

To determine a safe and ideal doses of L-NAME and terlipressin to achieve reductions in portal flow for periods suitable for imaging

METHODS:

1. Sprague-Dawley rats ($n = 4$, 265-710g), anaesthetised with isoflurane.
2. Jugular venous line sited.
3. Laparotomy with siting of TTUS probe around the portal vein.
4. Animal allowed to stabilise for 10 minutes before baseline flow measurement recording.
5. Bolus drug dose given intravenously followed by 1 ml hepsal flush.
6. Flow changes recorded until flow trends suggested a return to baseline, unless limited by time constraint.
7. For L-N^G-nitro arginine methyl ester (L-NAME), studies were performed in $n = 2$ using 10 mg/kg and 20 mg/kg doses.
8. For terlipressin (Glypressin, Ferring Pharmaceuticals, UK), studies were performed in $n = 2$, using bolus doses titrated up from 0.1 μ g to 100 μ g.

RESULTS:

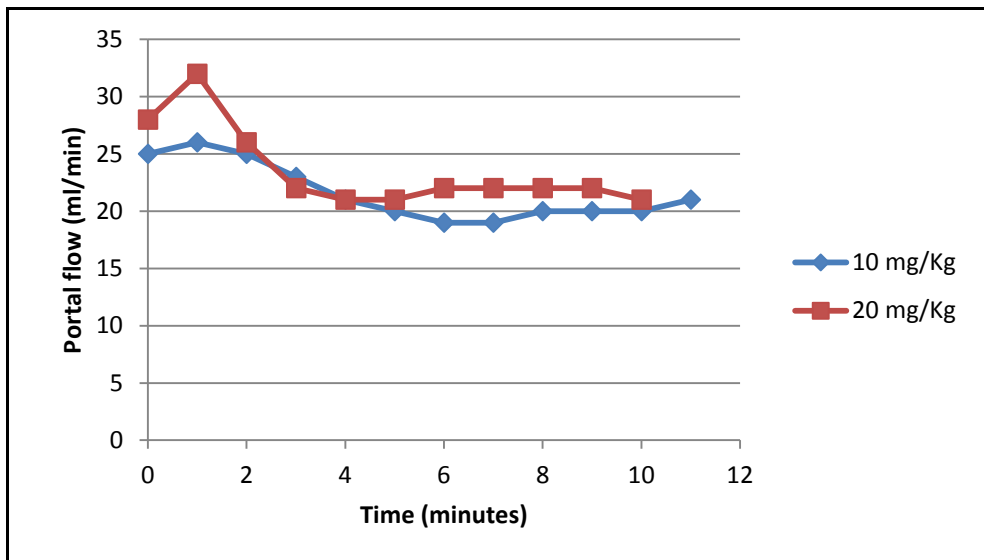
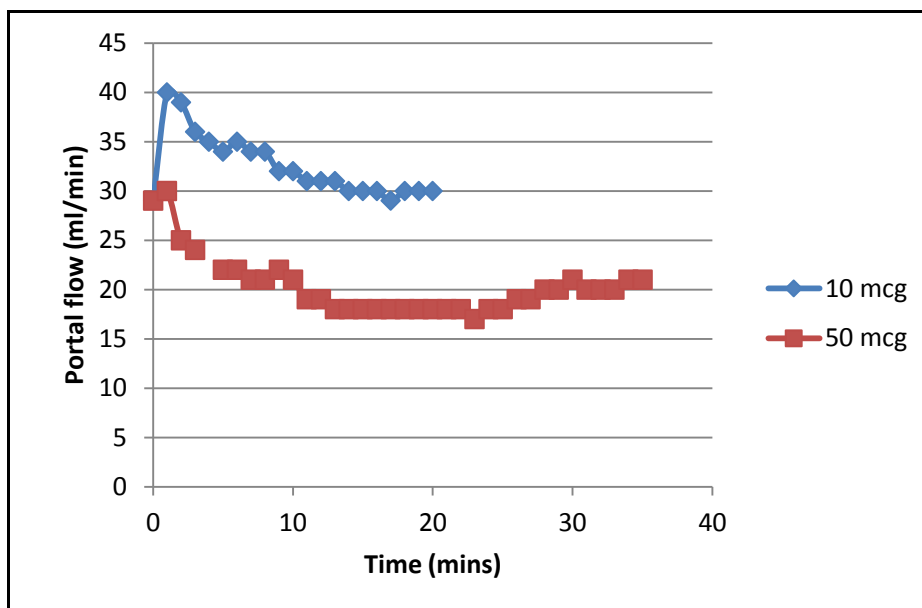


Figure A.1
PV flow response to L-NAME
Data is presented from two subjects.

No response was observed following boluses of 0.1 µg, 0.5 µg and 5 µg doses of terlipressin.

Figure A.2
PV flow response to terlipressin
Data is presented from two subjects.



Normalised to animal weight, the 10µg dose equated to 19.6 µg/kg and the 50 µg dose equated to 98.23 µg/kg. At all doses used, no adverse effects were identified using either drug.

DISCUSSION/CONCLUSION:

Using this data, it was decided that a bolus dose of 10 mg/kg would be suitable for L-NAME studies and a bolus dose of 100 µg/kg would be suitable for terlipressin studies.

TERLIPRESSIN DOSAGE REGIME EXPERIMENTS

AIM:

To determine a safe and ideal terlipressin infusion dose to deliver a sustained reduction in portal venous flow for imaging.

METHODS:

1. Sprague-Dawley rats ($n = 2$, 417g and 521g), anaesthetised with isoflurane.
2. Jugular venous line sited.
3. Laparotomy with siting of TTUS probe around the portal vein.
4. Animal allowed to stabilise for 10 minutes before baseline flow measurement recording.
5. Forty minute infusion initiated, with flow changes recorded after the infusion was stopped, until flow trends suggested a return to baseline.
6. Terlipressin (Glypressin, Ferring Pharmaceuticals, UK) studies were performed using infusion rates of $4\mu\text{g}/\text{min}$ and $9\mu\text{g}/\text{min}$.

RESULTS:

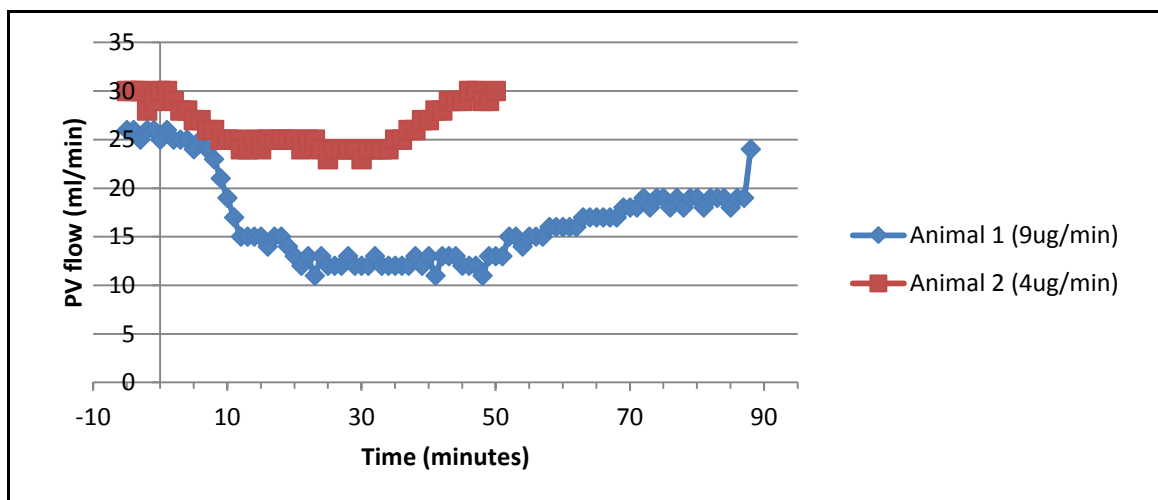


Figure B.1: PV flow response to terlipressin infusion

Data is presented from two subjects. The terlipressin infusion was started at zero minutes and stopped after 40 minutes.

Normalised to animal weight, the $4\mu\text{g}/\text{min}$ dose equated to $8.4\mu\text{g}/\text{kg}/\text{min}$ and the $9\mu\text{g}/\text{min}$ dose equated to $17.5\mu\text{g}/\text{kg}$. The animal receiving the $9\mu\text{g}/\text{min}$ died after 90 minutes. No adverse effects were observed when using the $4\mu\text{g}/\text{min}$ infusion.

DISCUSSION/CONCLUSION:

The $8.4\mu\text{g}/\text{kg}/\text{min}$ appeared to show a sustained PV response, which responded almost immediately when terlipressin was stopped. This was not the case at the higher $17.5\mu\text{g}/\text{kg}/\text{min}$ dose. A sustained response was required for approximately 30-40 minutes to enable acquisition of a full 'post-terlipressin' haemodynamic dataset. It was therefore decided that this could be achieved using an infusion dose of $10\mu\text{g}/\text{kg}/\text{min}$. Given that sustained PV flow reduction seemed to only last 20-25 minutes, a loading bolus dose of $100\mu\text{g}/\text{kg}$ (based on data presented in Appendix A) would be used, to achieve a more immediate reduction, followed by the $10\mu\text{g}/\text{kg}/\text{min}$ infusion.

PRECLINICAL VALIDATION, REPEATABILITY AND STUDIES OF THE HEPATIC ARTERIAL BUFFER RESPONSE – SUBJECT PARTICIPATION DETAILS

SHAM COHORT:

	1	2	3	4	5	6	7	8	9	10	11	12	13
BASILINE TTUS	✓	✓	✓	✓	✓	✓	✓	✓	✓	✓	✓	✓	✓
BASILINE MICROSPHERES			✓	✓	✓	✓	✓	✓	✓	✓	✓	✓	✓
BASILINE PV FLOW PCMRI	✓	✓	✓	✓	✓	✓	✓	✓	✓	✓	✓	✓	✓
BASILINE CAVAL SUBTRACTION PCMRI			✓	✓	✓	✓	✓	✓	✓	✓	✓	✓	✓
BASILINE CARDIAC CINE MRI	✓	✓	✓	✓	✓	✓	✓	✓	✓	✓	✓	✓	✓
BASILINE AORTIC ROOT FLOW PCMRI		✓	✓	✓	✓	✓	✓	✓	✓	✓	✓	✓	✓
REPEATABILITY PV FLOW				✓	✓	✓	✓	✓	✓	✓	✓	✓	✓
TERLIPRESSIN INFUSION				✓	✓	✓	✓	✓	✓	✓	✓	✓	✓
POST-TERLIPRESSIN PCMRI				✓	✓	✓	✓	✓	✓	✓	✓	✓	✓
POST-TERLIPRESSIN TTUS				✓	✓	✓	✓	✓	✓	✓	✓	✓	✓
POST-TERLIPRESSIN MICROSPHERES				✓	✓	✓	✓	✓	✓	✓			

BDL COHORT:

	1	2	3	4	5	6	7	8	9	10	11	12
BASILINE MICROSPHERES	✓	✓	✓	✓	✓	✓	✓	✓	✓	✓	✓	✓
BASILINE PV FLOW PCMRI	✓	✓	✓	✓	✓	✓	✓	✓	✓	✓	✓	✓
BASILINE CAVAL SUBTRACTION PCMRI	✓	✓	✓	✓	✓	✓	✓	✓	✓	✓	✓	✓
BASILINE CARDIAC CINE MRI	✓	✓	✓	✓	✓	✓	✓	✓	✓	✓	✓	✓
BASILINE AORTIC ROOT FLOW PCMRI		✓	✓	✓	✓	✓	✓	✓	✓	✓	✓	✓
REPEATABILITY PV FLOW							✓	✓	✓	✓	✓	✓
TERLIPRESSIN INFUSION	✓	✓	✓	✓	✓	✓	✓	✓	✓	✓	✓	✓
POST-TERLIPRESSIN PCMRI		✓	✓	✓		✓	✓	✓	✓	✓	✓	✓
POST-TERLIPRESSIN MICROSPHERES		✓	✓	✓		✓	✓	✓				

For both cohorts, greyed areas of the table represent data that was acquired but not usable, because of problems errors with the PCMRI sequence that was used. In the sham cohort, subjects 1-3 did not experience the full protocol, as developmental issues were still being addressed. In the BDL cohort, subjects 1 and 5 expired prematurely before the protocol was complete. For BDL subject 6, difficulties with gating while imaging the distal IVC resulted in artefact so that quantification of TLBF could not take place. For both sham and BDL cohorts, shortages of microspheres towards the end of the study resulted in baseline but not post-terlipressin injections taking place. Baseline data is presented as “non-hydrated” data in section 7.4. No other data presented in this section, was or will be incorporated into the main results presented at any other point in this thesis.



Imaging Department
UCL Hospitals
University College Hospital
235 Euston Road
London
NW1 2BU
Telephone: 020 3456 7890 ext 79324
Web-site: www.uclh.org

UCLH Project ID number: 07/Q0502/15
Information sheet version: 6, 30th April 2012

1. Study title

Development of novel magnetic resonance techniques using volunteer participants.

2. Invitation paragraph

You are being invited to take part in a research study. Before you decide it is important for you to understand why the research is being done and what it will involve. Please take time to read the following information carefully and discuss it with others if you wish. Ask us if there is anything that is not clear or if you would like more information. Take time to decide whether or not you wish to take part.

3. What is the purpose of the study?

We are a group of doctors and medical scientists performing research using a medical imaging technique called magnetic resonance imaging (MRI). Our work involves developing new ways to use MRI to acquire images of the body and computers to analyse those images. In due course, we hope that the methods we are developing will lead to new techniques for diagnosis and treatment. However, at this stage we are carrying out preliminary studies to provide data for our research.

4. Why have I been chosen?

We are looking for healthy adult volunteers from University College London and University College London Hospital or patients at University College London Hospital to participate in this study.

5. Do I have to take part?

It is up to you to decide whether or not to take part. If you do decide to take part you will be given this information sheet to keep and be asked to sign a consent form. If you decide to take part you are still free to withdraw at any time and without giving a reason. A decision to withdraw at any time, or a decision not to take part, will not affect the standard of care you receive.



UCL Hospitals is an NHS Trust incorporating the Eastman Dental Hospital, Elizabeth Garrett Anderson & Obstetric Hospital, The Heart Hospital, Hospital for Tropical Diseases, The Middlesex Hospital, National Hospital for Neurology & Neurosurgery, The Royal London Homoeopathic Hospital and University College Hospital.

6. What is involved in the study?

Participation involves either a single visit to the MRI unit at UCLH for a research scan, or an extension to a clinical session. The scanner operator will go through a standard checklist to ensure that it is safe to perform an MR scan. You may be asked to change your outer clothes for a hospital gown, because some clothes contain metal which would affect the MRI scan, or to remove items of jewellery. We may attach a few small, self-adhesive markers to your skin, which we would be able to see in the scans.

You will be asked to lie inside a magnetic resonance scanner while images are acquired. The scanner consists of a large magnet with a tunnel, and you will be inside this tunnel. Devices known as 'RF coils' will be placed on or next to your body. These coils are used to transmit and receive radiowaves (just like the waves used in radio or television broadcasts) as part of the imaging process. While the scanner is acquiring images it is very noisy, so you will be given earplugs and/or headphones to wear: these will protect your ears from the noise, and also allow you to hear what the scanner operator says. There is also a microphone so that you can talk to the operator.

If your study involves the administration of contrast, at the time of the scan we will place a small plastic tube (cannula) in your arm. We will then give you an injection of a standard MRI contrast agent ("gadolinium") which helps highlight blood vessels. It is unlikely you will notice anything during this injection, although some people get a sweet taste in their mouth.

If your study involves a consumer food or drink product prior to the scanning session, you will be asked to consume a normal quantity prior to scanning. You may be asked to fast before consuming the food or drink product up to a maximum period of 8 hours, but may drink water during that time.

The imaging procedure may last for up to an hour, sometimes a little longer. During this time you will usually be asked to remain quite still, although in some cases you may be asked to move in a specified way for part of the time, as our research includes studying and correcting for the effects of motion on MR images. Sometimes you may be asked to hold your breath for one or more short periods during scanning. The exact details of the procedure in your specific case will be explained to you before we begin. If you are participating as an extension to a clinical session, the additional time will be agreed with you before the session and will not normally exceed 20 minutes.

You can stop the examination at any time by talking to the operator.

7. What is the drug or procedure that is being tested?

Magnetic resonance imaging is a well-established technique for imaging the body. It was introduced into hospitals in the mid-1980s, and has been used at UCLH for many years. We are developing new, more advanced ways of acquiring and using MR images.

There are no drugs being tested in this study.

8. What are known risks of the study or the side effects of any treatment received?

MRI has been used to image millions of patients worldwide with no ill effects. Although the possibility of long-term effects cannot be completely ruled out, the weight of experience and opinion is against this.

University College London Hospitals

NHS Foundation Trust

research institutes and companies (possibly outside the European Union) we collaborate with. Parts of the anonymised data may also be published in scientific journals and related media.

11. Studies on tissue

No tissue samples or genetic information will be collected for this study.

12. Gene Studies

No genetic information will be studied in this project.

13. What happens when the research study stops?

You are not affected by the end of the research study, since we only acquire images and do not give any treatment.

14. What will happen if the findings may affect the subject personally?

The findings of the study will not affect you personally.

15. What if something goes wrong?

Complaints:

If you have any concerns or wish to complain about any aspect of the way you have been approached or treated as part of this study, you should initially contact the researchers who will do their best to answer your questions. Their contact details are at the end of this information sheet. If you remain unhappy, you can contact the UCLH Patient Advice and Liaison Service (PALS) in person between 9.00 and 16.00 Monday to Friday (excluding public holidays) at the PALS Office, Ground Floor Atrium at University College Hospital, 235 Euston Road, London NW1 2BU or by telephone. From within the hospital dial extension 73018 or 73002 or from outside the hospital ring the direct line 020 3447 3042 or e-mail to PALS@uclh.nhs.uk. If you remain unhappy and wish to complain formally, you can do this through the NHS Complaints Procedure. Details can be obtained from UCLH or PALS. You can also contact the Research Governance Sponsor of this study, University College London (UCL). Please write to: Joint UCLH/UCL Biomedical Research Unit, R&D Directorate, Rosenheim Wing, Ground Floor, 25 Grafton Way, London WC1E 5DB quoting reference BRD/07/071.

Harm:

The study is considered to be low risk, every care will be taken to ensure your safety during the course of the study and UCL has indemnity (insurance) arrangements in place for non-negligent harm, in the event that something does go wrong and you are harmed as a result of taking part in the research study. If you are harmed due to someone's negligence, then you may have grounds for legal action but you may have to pay for it. Regardless of this, if you the normal National Health Service complaints mechanisms should be available to you.

16. What will happen to the results of the research study?

We hope to publish the results of this study in a medical or scientific journal (either electronically or in paper format). We also hope to present the results at a medical or scientific conference. You cannot be identified in any publication.



UCL Hospitals is an NHS Trust incorporating the Eastman Dental Hospital, Elizabeth Garrett Anderson & Obstetric Hospital, The Heart Hospital, Hospital for Tropical Diseases, The Middlesex Hospital, National Hospital for Neurology & Neurosurgery, The Royal London Homoeopathic Hospital and University College Hospital.

17. Who is organising and funding the research?

The study is funded by research grants. Several different bodies fund different aspects of the research.

18. Inducements

You will not receive any inducement (including payment) for taking part in this study.

19. Withdrawal from the study

Your participation in the trial is entirely voluntary. You can change your mind and withdraw from the study at any time, before or during the scan, and without giving a reason. If you choose not to be part of this study, either before or during the scan, it will in no way affect your future medical care. Participation in this study will in no way affect your legal rights.

20. Who has reviewed the study?

The University College London Hospital Research Ethics Committee has reviewed the study.

21. Contact for further information

For more information, contact the researcher who has asked you to participate, and whose name will appear on your consent form.

You could also contact Heather Fitzke:

Telephone: 020 3447 9094

Email: Heather.Fitzke@uclh.nhs.uk

You will be given a copy of this information sheet.

Department of Imaging
UCL Hospitals NHS Trust
235 Euston Road
London NW1 2BU

Volunteer's name:

UCLH Project ID number: 07/Q0502/15
Form version: 4, 30th April 2012

CONSENT FORM

Title of project: Development of novel magnetic resonance techniques using volunteer participants.
Name of Principal Investigator: Dr. Margaret Hall-Craggs

Please initial box

1. I confirm that I have read and understood the information sheet dated 30th April 2012 (version 6) for the above study and have had the opportunity to ask questions.
2. I confirm that I have had sufficient time to consider whether or not want to be included in the study.
3. I understand that my participation is voluntary and that I am free to withdraw at any time, without giving any reason, without my medical care or legal rights being affected.
4. I agree to the administration of a contrast agent for this research.
5. I understand that this research scan is not intended for diagnostic purposes. In the unlikely event that something on the scan suggests a need for medical follow-up, I understand that a radiologist will inform me, and may contact my GP if appropriate.

(continued overleaf)



UCL Hospitals is an NHS Foundation Trust incorporating the Eastman Dental Hospital, Elizabeth Garrett Anderson & Obstetric Hospital, The Heart Hospital, Hospital for Tropical Diseases, The Middlesex Hospital, National Hospital for Neurology & Neurosurgery and University College Hospital.

6. I agree to allow any MRI data acquired during my scan to be used, anonymised so that I cannot be identified, for research or teaching.

7. I agree to take part in the above study.

UCLH Project ID number: 07Q0502/15
Form version: 4, 30th April 2012

CONSENT FORM

Title of project: Development of novel magnetic resonance techniques using volunteer participants.
Name of Principal Investigator: Dr. Margaret Hall-Craggs

This study has no diagnostic purpose and is not intended for screening or diagnostic purposes. However, in the unlikely event that something on the scans suggests a need for medical follow-up, a radiologist will review the images and inform you. They may also contact your GP. (You don't need to enter your GP details again if we already have a consent form including them from a previous visit and they haven't changed since then.)

GP's name
and address:

Name of volunteer

Date

Signature

Name of person taking consent

Date

Signature

Name of researcher (if different)

Date

Signature

Name of medically qualified staff
providing approval (for patient participants,
contrast agent administration, or food or
drink consumption with/without fasting)

Date

Signature

Researcher to contact if there are any problems (name, organisation, and telephone number):

Comments or concerns during the study

If you have any comments or concerns you may discuss these with the investigator. If you wish to go further and complain about any aspect of the way you have been approached or treated during the course of the study, you should write or get in touch

with the Complaints Manager, UCL hospitals. Please quote the UCLH project number at the top this consent form.

1 form for volunteer; 1 to be kept as part of the study documentation.

APPENDIX E

BLOOD FLOW STUDIES IN CHRONIC LIVER DISEASE – PRECLINICAL STUDIES – SUBJECT PARTICIPATION DETAILS

SHAM COHORT:

	1	2	3	4	5	6	7	8	9	10	11
BASELINE CARDIAC CINE MRI	✓	✓	✓	✓	✓	✓	✓	✓	✓	✓	✓
BASELINE CAVAL SUBTRACTION PCMRI	✓	✓	✓	✓	✓	✓	✓	✓	✓	✓	✓
BASELINE ASL	✓	✓	✓	✓	✓	✓	✓	✓	✓	✓	✓
LPS INFUSION	✓	✓	✓	✓	✓	✓	✓	✓	✓	✓	✓
POST-LPS PCMRI	✓	✓	✓	✓	✓	✓	✓	✓	✓	✓	✓
POST-LPS ASL	✓	✓	✓	✓	✓	✓	✓	✓	✓	✓	✓
POST-LPS CARDIAC CINE MRI	✓	✓	✓	✓	✓	✓	✓	✓	✓	✓	✓

BDL COHORT:

	1	2	3	4	5	6	7	8	9	10	11
BASELINE CARDIAC CINE MRI	✓	✓	✓	✓	✓	✓	✓	✓	✓	✓	✓
BASELINE CAVAL SUBTRACTION PCMRI	✓	✓	✓	✓	✓	✓	✓	✓	✓	✓	✓
BASELINE ASL	✓	✓	✓	✓	✓	✓	✓	✓	✓	✓	✓
LPS INFUSION	✓	✓	✓	✓	✓	✓	✓	✓	✓	✓	✓
POST-LPS PCMRI	✓	✓	✓	✓	✓	✓	✓	✓	✓	✓	✓
POST-LPS ASL	✓	✓	✓	✓	✓	✓	✓	✓	✓	✓	✓
POST-LPS CARDIAC CINE MRI			✓	✓	✓			✓	✓	✓	✓

For both cohorts, the greyed areas of the table represent data that was acquired but not usable. For the sham cohort, problems with gating compromised subject 11 and distal IVC PCMRI flow measurements for subject 10. For the BDL cohort, problems with jugular venous cannulation in subjects 10 and 11 meant that it was impossible to determine if correct doses of fluid resuscitation or LPS had been given. These datasets had to be discarded. For subject 7-9, problems with gating resulted in artefacted and unusable PCMRI and ASL quantification. Cardiac cine data in subjects 8 and 9 was however, still usable. Subjects 1, 2, 6 and 7 expired before the imaging protocol was complete.

APPENDIX F

Version 5

Date: January 2012

Project ID: 08/H0724/35

INFORMATION SHEET: Transjugular liver study patients

Full Title: MRI assessment of liver blood flow characteristics – a correlation with standard liver assessment.

Short Title: MRI assessment of liver haemodynamics

You are being invited to take part in a research study. Before you decide it is important for you to understand why the research is being done and what it will involve. Please take time to read the following information carefully and discuss it with others if you wish. Ask us if there is anything that is not clear or if you would like more information. Take time to decide whether or not you wish to take part.

1. What is the purpose of the study?

The liver is a special organ in that its blood supply is organised in a unique way. Despite having several scanning techniques, we are still unable to accurately measure blood supply and flow through the liver. MRI scanning is a safe and non-invasive way of imaging the body and may be able to provide us with detailed information about changes in blood flow that occur both in health and disease. This study will compare information on the liver obtained from MRI scanning with ultrasound scanning, blood tests, direct liver blood pressure measurements and liver biopsy results. This will help us to develop an accurate way of measuring liver blood flow non-invasively in the future.

2. Why have I been chosen?

You have been chosen because you are due to have a trans-jugular liver study. This will mean we will have information about the pressure inside your liver and nearby blood vessels. At the time of the study, your Doctor may also want a liver biopsy. You may go onto receive a specific treatment after your transjugular study and if this is the case, we may contact you in the near future to participate in the study for a second time. Taking part in the study will NOT mean liver or tissue will be removed purely for research.



The Royal Free Hospital



The Royal National Throat,
Nose and Ear Hospital

The Royal Free Hampstead NHS Trust

Dominic Dodd, chairman; David Sloman, chief executive; www.royalfree.nhs.uk Tel: 020 7794 0500 Fax: 020 7830 2468

3. Do I have to take part?

It is up to you to decide whether or not to take part. If you do decide to take part you will be given this information sheet to keep and be asked to sign a consent form around the time of your first transjugular study before your MRI scan. If you decide to take part you are still free to withdraw at any time. You are free to withdraw from the study at any point and without giving a reason. A decision to withdraw at any time, or a decision not to take part, will not affect your future medical care.

4. What will happen to me if I take part?

Your doctor has requested for the liver study to occur via the trans-jugular route.

a. *MRI scan:*

Around the same time you have this done, we will arrange for you to have an MRI scan of liver. At the time of the scan, we will place a small plastic tube (cannula) in your arm. We will take 3-4 small tubes of blood samples (each about the same as a teaspoon) before the scan takes place. We will then give you an injection of a special MRI contrast agent ("gadolinium") which helps highlight blood vessels. This will be followed by a very slow injection (infusion) through the same plastic tube of a little more contrast during the remainder of the scan. It is unlikely you will notice anything during any of these injections, although some people get a sweet taste in their mouth. We may also go on to scan other parts of your body including your head/neck and lower abdomen. It will take around 90 minutes to complete the scan and this may occur before and/or after the trans-jugular liver biopsy.

b. *Trans-jugular liver study:*

When the study is being performed, we will also study how well your liver removes a chemical ("indocyanine green") from your blood stream. In order to do this test, we will need to place two needles in your wrist or leg. Indocyanine green will be given through one needle and blood samples will be taken from the other needle and from the trans-jugular site at timed intervals over an hour. Once the needles are sited, taking blood samples will not cause any additional pain or discomfort.

c. *Ultrasound:*



The Royal Free Hospital



The Royal National Throat,
Nose and Ear Hospital

The Royal Free Hampstead NHS Trust

Dominic Dodd, chairman; David Sloman, chief executive; www.royalfree.nhs.uk Tel: 020 7794 0500 Fax: 020 7830 2468

Once this complete, we may offer you an ultrasound scan. At the time of the ultrasound scan, we will also use the line to give you a special ultrasound contrast agent (“sonovue”), which also helps highlight blood vessels. Much like the previous injection, it is unlikely you will notice anything during this injection. The ultrasound probe is also used to estimate blood flow in the liver (“Doppler ultrasound”). This may prolong the procedure by around 15 minutes, but is non-invasive and will not cause any discomfort.

We will then analyse your MRI scan and compare it with the results of the biopsy and blood tests as soon as these are available.

5. What do I have to do?

If you agree to take part, we will arrange a convenient time slot for you to attend hospital to have your MRI scan done before the biopsy. You will have a MRI scan with contrast injection and possibly an additional blood test. At the time of biopsy, you may also have ultrasound assessment of your liver blood supply.

On the day on which the MRI scan and/or biopsy is due to take place, we would ask that you remain fasted for 6 hours before the scan. You may take water, but no food or liquids other than water.

The MRI scan may take place on a different day to the day of the transjugular study. If this is the case, you should keep receipts of all travel expenses incurred for travel between your home and the hospital on that day. We will then arrange for the expenses to be reimbursed.

6. If I choose to participate at the time of a future transjugular study, what will happen?

We will follow the same procedure as for the first scan outlined above, but will not be repeating part 4 (b), the indocyanine green clearance test. We will contact you with this information and ask you for signed consent on the day of the scan.

7. How long will it take?

We will try and arrange for the MRI scan and transjugular study to take place on the same day. If this is not the case, you should allow half-a-day for the additional hospital visit. You should allow the same amount of time around the time of the second transjugular study, should you choose to participate at this time.

8. What is the procedure that is being tested?



The Royal Free Hospital



The Royal National Throat,
Nose and Ear Hospital

The Royal Free Hampstead NHS Trust

Dominic Dodd, chairman; David Sloman, chief executive; www.royalfree.nhs.uk Tel: 020 7794 0500 Fax: 020 7830 2468

MRI is an established imaging test and is increasingly used to look at changes in the liver. We are still not completely sure how to best use MRI to accurately and reliably assess liver blood flow. This study will allow us to decide what is the best way to use the MRI scanner to give us precise information about liver blood flow.

9. What are known risks of the study or the side effects of any treatment received ?

The injections we give during your MRI have been used in day to day practice for a long time and are very safe. You will receive gadolinium contrast if you take part in the study, but we will not give you any more than the recommend maximum dose. Allergy to the gadolinium contrast is possible but very rare. Mild reactions (nausea, transient rash etc) occur in less than 3% of patients and more serious reactions are much less common than this. Allergy to indocyanine green is also possible, but rare.

The possible side effects of ultrasound contrast are also minor (dizziness, nausea and vomiting). In a large study of side effects to the contrast over 21000 patients were evaluated and 29 incidences of side effects were found. Two allergic reactions (0.00009%) took place and that required treatment. Twenty three incidences of mild side effects as mentioned earlier (0.001%) and three moderate (0.0001%) and one severe (0.00005%) took place. These occurred in the following few minutes after contrast injection and the moderate and severe categories had symptoms similar to an allergic reaction. Overall, the risk of an allergic reaction is reported to be less than that for common antibiotics or painkillers.

However, in the rare event that you should develop a mild reaction, we would ask you remain for at least 30 minutes after the event to ensure your safety. Should you develop a severe reaction (extremely rare), we will treat this in according to established guidelines from the UK resuscitation council (oxygen via face mask, a small plastic tube (cannula) in your arm for administering anti-histamines, steroids and/or fluids).

You are encouraged to contact the Dr Manil Chouhan (research doctor) in the x-ray dept on 08451555000 ext 73225 or via e-mail (m.chouhan@ucl.ac.uk) if you have any problems after the scan.

10. What are the possible disadvantages and risks of taking part?

The MRI scan will mainly look at the liver. However we will also obtain imaging information about the other organs in your abdomen such as bowel, kidneys etc. We may theoretically therefore detect an incidental abnormality in one of these organs which may need further investigation to clarify its nature. The vast majority of such findings are incidental to and of little importance. Your doctor will be informed of the finding via the clinical report we will provide for the MRI scan. If you have private medical insurance you are advised to check with the company before agreeing to take part in the trial, or you may request Dr



The Royal Free Hospital



The Royal National Throat,
Nose and Ear Hospital

The Royal Free Hampstead NHS Trust

Dominic Dodd, chairman; David Sloman, chief executive; www.royalfree.nhs.uk Tel: 020 7794 0500 Fax: 020 7830 2468

Manil Chouhan (research doctor) in the x-ray dept on 08451555000 ext 73225 or via e-mail (m.chouhan@ucl.ac.uk) to check this for you.

11. Is there any reason why I may not be able to take part?

Because we are not totally sure if MRI is completely safe in the early stages of pregnancy, we asked pregnant women not to take part in the study. Women who are at risk of pregnancy may be asked to have a pregnancy test before taking part to exclude the possibility of pregnancy.

If you have any permanent metallic object in your body (e.g. shrapnel, pacemaker, metallic implant), this too will prevent you taking part. This is because MRI is reliant on magnets, which can interfere with metal objects.

The MRI scanner will involve lying on a bed in a closed space for some time. Some people find the thought of a closed space upsetting and if this is the case, we would advise you not to participate in the study.

12. What are the possible benefits of taking part?

You will receive no direct benefit from allowing us to scan you, but the information from this will be of use for patients in the future.

13. What if new information becomes available?

Sometimes during the course of a research project, new information becomes available about the treatment that is being studied. If this happens, your research doctor will tell you about it and discuss with you whether you want to continue in the study. If you decide to withdraw your research doctor will make arrangements for your care to continue. If you decide to continue in the study you will be asked to sign an updated consent form.

Also, on receiving new information your research doctor might consider it to be in your best interest to withdraw you from the study. He/she will explain the reasons and arrange for your care to continue.

14. What happens when the research study stops?

After the study is complete we will aim to analyse the results, write them up in medical journals and hopefully change to way we interpret scans. We hope to use the information to start further studies looking at how liver blood flow changes in liver disease.



The Royal Free Hospital



The Royal National Throat,
Nose and Ear Hospital

The Royal Free Hampstead NHS Trust

Dominic Dodd, chairman; David Sloman, chief executive; www.royalfree.nhs.uk Tel: 020 7794 0500 Fax: 020 7830 2468

15. What if something goes wrong?

If you have a specific complaint against your treatment by a member of staff (doctors, nurses, etc) you have the right to complain using the usual UCLH complaints procedure.

If you are harmed by taking part in this research project, there are no special compensation arrangements. If you are harmed due to someone's negligence, then you may have grounds for a legal action but you may have to pay for it. Regardless of this, if you wish to complain, or have any concerns of this study, the normal National Health Service complaints mechanisms should be available to you.

16. Will my taking part in this study be kept confidential?

All information which is collected about you during the course of the research will be kept strictly confidential. Any information about you which leaves the hospital/surgery will have your name and address removed so that you cannot be recognised from it. We will need to look at your hospital notes, blood results and past x-ray tests, but only medically qualified doctors at UCH involved in this study will do this.

With your permission, we will tell your GP that you are taking part in the trial and we will tell them the results of your MRI scan if you want them to know. The results of the MRI scan will be available to your GP and other hospital doctors looking after you by the usual hospital results system. Please tell us if you do not want your GP to be informed.

17. Your data

We will create a database for the trial. The data will be anonymised such that your name, hospital number date of birth and address will be fully removed and you will be given a unique trial identification number. The list of identification numbers will be held on a password protected secure computer separate from the database controlled by trial principal investigator (Dr Shonit Punwani). We will store basic information such as your age, as well as results of previous imaging/blood tests, the results of your MRI scan, ultrasound and pathology reports. The database will be stored on a password protected computer drive held by UCL who will collect, store, handle and process the data. Only the trial principal investigator (Dr Shonit Punwani) will have access to the data base and will be responsible for the safety and security of the data. With your permission we may use your data for future studies, although again it will be anonymised as handled as explained above. For this reason we expect to keep the database for 5 years. The study does not involve storage of any body tissue over and above your normal clinical care.



The Royal Free Hospital



The Royal National Throat,
Nose and Ear Hospital

The Royal Free Hampstead NHS Trust

Dominic Dodd, chairman; David Sloman, chief executive; www.royalfree.nhs.uk Tel: 020 7794 0500 Fax: 020 7830 2468

18. What will happen to the results of the research study?

We aim to recruit around 30 patients having this procedure for the study. When we have analysed the results we will write them up and publish them in medical journals. It will probably take about a year from completing the trial to publishing the results. Your doctor at UCH will be able to tell you about the results when they are published so you can get a copy if you wish. You will not be identified in any report/publication.

19. Who is organising and funding the research?

The research is being funded via a research grants from the Radiology Research Trust.

No doctor is being paid for conducting the research.

20. Who has reviewed the study?

The study has been reviewed by RNOH/IOMS Research Ethics Committee.

21. Contact for Further Information

You may contact Dr Manil Chouhan, Radiology Registrar on 07779783511 if you require further information about the study or have any questions.

Thank you very much for considering taking part in the study. If you agree to take part we will provide you with copies of this information sheet and the consent form we will ask you to sign.



The Royal Free Hospital



The Royal National Throat,
Nose and Ear Hospital

The Royal Free Hampstead NHS Trust

Dominic Dodd, chairman; David Sloman, chief executive; www.royalfree.nhs.uk Tel: 020 7794 0500 Fax: 020 7830 2468

Centre Number: 02 UCLH Project ID number: 08/H0724/35
Patient Identification Number for this study: Version 2, December 2008

CONSENT FORM

Title of project: **MRI assessment of liver blood flow characteristics – a correlation with standard liver assessment**

Short title: **MRI assessment of liver haemodynamics**

Name of Principal investigator : Dr Shonit Punwani

Please initial box

1. I confirm that I have read and understood the information sheet dated August 2011 (version 4) for the above study and have had the opportunity to ask questions.
2. I confirm that I have had sufficient time to consider whether or not want to be included in the study
3. I understand that my participation is voluntary and that I am free to withdraw at any time, without giving any reason, without my medical care or legal rights being affected.
4. I understand that sections of any of my medical notes may be looked at by responsible individuals from regulatory authorities where it is relevant to my taking part in research. I give permission for these individuals to have access to my records.
5. I agree to take part in the above study.
6. I agree to my anonymised data being used in future research.
7. I agree to my GP being informed of my participation in the trial



The Royal Free Hampstead NHS Trust

Dominic Dodd, chairman; David Sloman, chief executive; www.royalfree.nhs.uk Tel: 020 7794 0500 Fax: 020 7830 2468

APPENDIX G

ORAL PRESENTATIONS

Chouhan M, Punwani S, Bainbridge A, Davies N, Mookerjee R, Jalan R, Taylor S. Initial experiences evaluating the hepatic arterial buffer response with DCE-MRI in healthy rats at 9.4T. ISMRM, Montreal 2011.

Chouhan M, Punwani S, Bainbridge A, Davies N, Mookerjee R, Jalan R, Taylor S. Initial experiences evaluating the hepatic arterial buffer response with DCE-MRI in healthy rats at 9.4T. Royal College of Radiologists Annual Scientific Meeting, London 2011.

Chouhan M, Bainbridge A, Sharma V, Davies N, Mookerjee R, Jalan R, Punwani S, Taylor S. Invasive validation and repeatability of Phase Contrast MR portal venous flow measurements in healthy rats at 9.4T. British Chapter ISMRM, Bristol 2012.

Chouhan M, Bainbridge A, Davies N, Mookerjee R, Jalan R, Walker-Samuel S, Lythgoe M, Punwani S, Taylor S. Initial experiences evaluating changes in portal venous flow using phase-contrast MRI in healthy rats at 9.4T. RSNA, Chicago 2012.

Chouhan M, Bainbridge A, Davies N, Mookerjee R, Jalan R, Walker-Samuel S, Lythgoe M, Punwani S, Taylor S. Differential portal venous flow response to terlipressin in normal and cirrhotic rats – non-invasive assessment using phase-contrast MRI. ECR, Vienna 2013.

Chouhan M, Bainbridge A, Walker-Samuel S, Lythgoe M, Punwani S, Taylor S, Davies N, Jalan R, Mookerjee R. Altered Portal Venous flow response to terlipressin in BDL rats, measured non-invasively using phase-contrast MRI. Royal Free Division of Medicine Postgraduate Day, London 2013.

POSTERS

Chouhan M, Bainbridge A, Punwani S, Davies N, Mookerjee R, Jalan R, Taylor S. Combined Phase-Contrast and Dynamic Contrast Enhanced MRI – a novel approach for robust quantitation of rat liver blood flow at 9.4T. British Chapter ISMRM, Bristol 2012.

Chouhan M, Bainbridge A, Sharma V, Davies N, Mookerjee R, Jalan R, Punwani S, S Halligan, Taylor SA. Validation and repeatability of portal venous flow measurement using phase-contrast MRI in healthy rats at 9.4T. ESGAR, Edinburgh 2012.

Chouhan M, Bainbridge A, Davies N, Mookerjee R, Jalan R, Punwani S, Halligan S, Taylor SA. Initial experiences evaluating changes in portal venous flow using phase-contrast MRI in healthy rats at 9.4T. ESGAR, Edinburgh 2012.

Chouhan M, Bainbridge A, Davies N, Mookerjee R, Jalan R, Walker-Samuel S, Lythgoe M, Punwani S, Taylor S. Invasive validation and assessment of baseline portal venous flow in normal and cirrhotic rats using phase-contrast MRI at 9.4T. ECR, Vienna 2013.

Chouhan M, Bainbridge A, Davies N, Jalan R, Mookerjee R, Walker-Samuel S, Lythgoe MF, Punwani S, Taylor SA. Differential portal venous flow response to terlipressin in normal and cirrhotic rats – non-invasive assessment using phase contrast MRI. ISMRM, Salt Lake City 2013.

Chouhan M, Ramasawmy R, Campbell-Washburn A, Bainbridge A, Wells JA, Davies N, Pedley RB, Mookerjee R, Punwani S, Taylor SA, Walker-Samuel S, Lythgoe MF. Measurement of bulk liver perfusion: initial assessment of agreement between ASL and phase-contrast MRI at 9.4T. ISMRM, Salt Lake City 2013.

Chouhan M, Bainbridge A, Navies N, Jalan R, Mookerjee R, Walker-Samuel S, Lythgoe MF, Punwani S, Taylor SA. Measurement of portal venous flow using phase-contrast MRI at 9.4T: preliminary repeatability, reproducibility and invasive validation studies. ISMRM, Salt Lake City 2013.

GRANTS AND AWARDS

March 2009 - UCL/Medical Research Council – M3I pump priming scheme - £17000

June 2009 - Radiology Research Trust – Small Projects Grant - £10000

August 2010 - Wellcome Trust – Research Training Fellowship - £202130

March 2013 - European Congress of Radiology – Travel Bursary - £250

July 2013 - Royal Free Division of Medicine Postgraduate Day – Prize for best presentation
- £150

REFERENCES

1. Group NCRGW. Animal research: reporting in vivo experiments: the ARRIVE guidelines. *The Journal of physiology*. 2010;588(Pt 14):2519-21.
2. Neruda P, Peden MS. *Elemental odes*. London: Libris, 1990.
3. Bhogal H, Sterling RK. Staging of liver disease: which option is right for my patient? *Infectious disease clinics of North America*. 2012;26(4):849-61.
4. Castera L. Noninvasive methods to assess liver disease in patients with hepatitis B or C. *Gastroenterology*. 2012;142(6):1293-302 e4.
5. Germani G, Burroughs AK, Dhillon AP. The relationship between liver disease stage and liver fibrosis: a tangled web. *Histopathology*. 2010;57(6):773-84.
6. Martinez SM, Crespo G, Navasa M, Forns X. Noninvasive assessment of liver fibrosis. *Hepatology*. 2011;53(1):325-35.
7. Degos F, Lebrun L, Perez P, Durand-Zaleski I. Methods and interest of noninvasive assessment of liver fibrosis are still in debate. *Hepatology*. 2011;53(5):1781; author reply 82-3.
8. Yoshioka K, Hashimoto S. Can non-invasive assessment of liver fibrosis replace liver biopsy? *Hepatology research : the official journal of the Japan Society of Hepatology*. 2012;42(3):233-40.
9. Zhou K, Lu LG. Assessment of fibrosis in chronic liver diseases. *Journal of digestive diseases*. 2009;10(1):7-14.
10. Afdhal NH, Nunes D. Evaluation of liver fibrosis: a concise review. *Am J Gastroenterol*. 2004;99(6):1160-74.
11. Manning DS, Afdhal NH. Diagnosis and quantitation of fibrosis. *Gastroenterology*. 2008;134(6):1670-81.
12. Berzigotti A, Ashkenazi E, Reverter E, Abraldes JG, Bosch J. Non-invasive diagnostic and prognostic evaluation of liver cirrhosis and portal hypertension. *Dis Markers*. 2011;31(3):129-38.
13. Calvaruso V, Burroughs AK, Standish R, Manousou P, Grillo F, Leandro G, et al. Computer-assisted image analysis of liver collagen: relationship to Ishak scoring and hepatic venous pressure gradient. *Hepatology*. 2009;49(4):1236-44.
14. Abraldes JG, Araujo IK, Turon F, Berzigotti A. Diagnosing and monitoring cirrhosis: Liver biopsy, hepatic venous pressure gradient and elastography. *Gastroenterol Hepatol*. 2012;35(7):488-95.
15. Merkel C, Montagnese S. Hepatic venous pressure gradient measurement in clinical hepatology. *Dig Liver Dis*. 2011;43(10):762-7.
16. Merkel C, Montagnese S. Should we routinely measure portal pressure in patients with cirrhosis, using hepatic venous pressure gradient (HVPG) as guidance for prophylaxis and treatment of bleeding and re-bleeding? Yes! *European journal of internal medicine*. 2011;22(1):1-4.
17. Williams R. Global challenges in liver disease. *Hepatology*. 2006;44(3):521-6.
18. Fleming KM, Aithal GP, Soleymani-Dodaran M, Card TR, West J. Incidence and prevalence of cirrhosis in the United Kingdom, 1992-2001: a general population-based study. *J Hepatol*. 2008;49(5):732-8.
19. Garcia-Tsao G, Bosch J, Groszmann RJ. Portal hypertension and variceal bleeding--unresolved issues. Summary of an American Association for the study of liver diseases and European Association for the study of the liver single-topic conference. *Hepatology*. 2008;47(5):1764-72.
20. Gines P, Quintero E, Arroyo V, Teres J, Bruguera M, Rimola A, et al. Compensated cirrhosis: natural history and prognostic factors. *Hepatology*. 1987;7(1):122-8.
21. D'Amico G, Morabito A, Pagliaro L, Marubini E. Survival and prognostic indicators in compensated and decompensated cirrhosis. *Dig Dis Sci*. 1986;31(5):468-75.

22. Ripoll C, Groszmann R, Garcia-Tsao G, Grace N, Burroughs A, Planas R, et al. Hepatic venous pressure gradient predicts clinical decompensation in patients with compensated cirrhosis. *Gastroenterology*. 2007;133(2):481-8.
23. Bosch J, Abraldes JG, Berzigotti A, Garcia-Pagan JC. The clinical use of HVPG measurements in chronic liver disease. *Nat Rev Gastroenterol Hepatol*. 2009;6(10):573-82.
24. Monescillo A, Martinez-Lagares F, Ruiz-del-Arbol L, Sierra A, Guevara C, Jimenez E, et al. Influence of portal hypertension and its early decompression by TIPS placement on the outcome of variceal bleeding. *Hepatology*. 2004;40(4):793-801.
25. Ripoll C, Banares R, Rincon D, Catalina MV, Lo Iacono O, Salcedo M, et al. Influence of hepatic venous pressure gradient on the prediction of survival of patients with cirrhosis in the MELD Era. *Hepatology*. 2005;42(4):793-801.
26. Pandharipande PV, Krinsky GA, Rusinek H, Lee VS. Perfusion imaging of the liver: current challenges and future goals. *Radiology*. 2005;234(3):661-73.
27. Vollmar B, Menger MD. The hepatic microcirculation: mechanistic contributions and therapeutic targets in liver injury and repair. *Physiol Rev*. 2009;89(4):1269-339.
28. Adams DH, Eksteen B. Aberrant homing of mucosal T cells and extra-intestinal manifestations of inflammatory bowel disease. *Nature reviews Immunology*. 2006;6(3):244-51.
29. Friedman SL. Mechanisms of hepatic fibrogenesis. *Gastroenterology*. 2008;134(6):1655-69.
30. Mookerjee RP. Acute-on-chronic liver failure: the liver and portal haemodynamics. *Curr Opin Crit Care*. 2011;17(2):170-6.
31. Aoki T, Imamura H, Kaneko J, Sakamoto Y, Matsuyama Y, Kokudo N, et al. Intraoperative direct measurement of hepatic arterial buffer response in patients with or without cirrhosis. *Liver Transpl*. 2005;11(6):684-91.
32. Pinzani M, Rosselli M, Zuckermann M. Liver cirrhosis. *Best Pract Res Clin Gastroenterol*. 2011;25(2):281-90.
33. Rappaport AM, MacPhee PJ, Fisher MM, Phillips MJ. The scarring of the liver acini (Cirrhosis). Tridimensional and microcirculatory considerations. *Virchows Arch A Pathol Anat Histopathol*. 1983;402(2):107-37.
34. Groszmann RJ, Wongcharatrawee S. The hepatic venous pressure gradient: anything worth doing should be done right. *Hepatology*. 2004;39(2):280-2.
35. Perello A, Escorsell A, Bru C, Gilibert R, Moitinho E, Garcia-Pagan JC, et al. Wedged hepatic venous pressure adequately reflects portal pressure in hepatitis C virus-related cirrhosis. *Hepatology*. 1999;30(6):1393-7.
36. Thalheimer U, Leandro G, Samonakis DN, Triantos CK, Patch D, Burroughs AK. Assessment of the agreement between wedge hepatic vein pressure and portal vein pressure in cirrhotic patients. *Dig Liver Dis*. 2005;37(8):601-8.
37. Keiding S, Vilstrup H. Intrahepatic heterogeneity of hepatic venous pressure gradient in human cirrhosis. *Scand J Gastroenterol*. 2002;37(8):960-4.
38. Thalheimer U, Mela M, Patch D, Burroughs AK. Targeting portal pressure measurements: a critical reappraisal. *Hepatology*. 2004;39(2):286-90.
39. Leevy CM, Mendenhall CL, Lesko W, Howard MM. Estimation of hepatic blood flow with indocyanine green. *J Clin Invest*. 1962;41:1169-79.
40. Uusaro A, Ruokonen E, Takala J. Estimation of splanchnic blood flow by the Fick principle in man and problems in the use of indocyanine green. *Cardiovasc Res*. 1995;30(1):106-12.
41. Lisotti A, Azzaroli F, Buonfiglioli F, Montagnani M, Cecinato P, Turco L, et al. Indocyanine green retention test as a noninvasive marker of portal hypertension and esophageal varices in compensated liver cirrhosis. *Hepatology*. 2014;59(2):643-50.
42. Wissler EH. Identifying a long standing error in single-bolus determination of the hepatic extraction ratio for indocyanine green. *Eur J Appl Physiol*. 2011;111(4):641-6.

43. Molino G, Cavanna A, Avagnina P, Ballare M, Torchio M. Hepatic clearance of D-sorbitol. Noninvasive test for evaluating functional liver plasma flow. *Dig Dis Sci*. 1987;32(7):753-8.
44. Ercolani G, Grazi GL, Calliva R, Pierangeli F, Cescon M, Cavallari A, et al. The lidocaine (MEGX) test as an index of hepatic function: its clinical usefulness in liver surgery. *Surgery*. 2000;127(4):464-71.
45. Henderson JM, Kutner MH, Bain RP. First-order clearance of plasma galactose: the effect of liver disease. *Gastroenterology*. 1982;83(5):1090-6.
46. Helmke S, Colmenero J, Everson GT. Noninvasive assessment of liver function. *Current opinion in gastroenterology*. 2015.
47. Everson GT, Hoefs JC, Niemann CU, Olthoff KM, Dupuis R, Lauriski S, et al. Functional elements associated with hepatic regeneration in living donors after right hepatic lobectomy. *Liver Transpl*. 2013;19(3):292-304.
48. Everson GT, Shiffman ML, Hoefs JC, Morgan TR, Sterling RK, Wagner DA, et al. Quantitative liver function tests improve the prediction of clinical outcomes in chronic hepatitis C: results from the Hepatitis C Antiviral Long-term Treatment Against Cirrhosis Trial. *Hepatology*. 2012;55(4):1019-29.
49. Christie JH, Chaudhuri TK. Measurement of hepatic blood flow. *Seminars in nuclear medicine*. 1972;2(2):97-107.
50. Bolton RP, Mairiang EO, Parkin A, Ware F, Robinson P, Losowsky MS. Dynamic liver scanning in cirrhosis. *Nuclear medicine communications*. 1988;9(3):235-47.
51. Maughan J, Parkin A, Smith AH, Barker MC, Robinson PJ, Finan P, et al. Hepatic perfusion index: a multicentre trial. *Nuclear medicine communications*. 1992;13(3):161-7.
52. el-Khalily H, Hoeffken H, von Wichert P, Joseph K. Hepatic perfusion scintigraphy. Relationship of liver perfusion and ascites in patients with liver cirrhosis. *Clinical nuclear medicine*. 1996;21(2):132-5.
53. Bennink RJ, Tulchinsky M, de Graaf W, Kadry Z, van Gulik TM. Liver function testing with nuclear medicine techniques is coming of age. *Seminars in nuclear medicine*. 2012;42(2):124-37.
54. Krishnamurthy S, Krishnamurthy GT. Technetium-99m-iminodiacetic acid organic anions: review of biokinetics and clinical application in hepatology. *Hepatology*. 1989;9(1):139-53.
55. Geisel D, Ludemann L, Gebauer B, Froling V, Prasad V, Heimann U, et al. Optimized separation of left and right liver lobe in dynamic Tc-mebrofenin hepatobiliary scintigraphy using a hybrid SPECT-CT scanner. *Annals of nuclear medicine*. 2014.
56. de Graaf W, Hausler S, Heger M, van Ginhoven TM, van Cappellen G, Bennink RJ, et al. Transporters involved in the hepatic uptake of (99m)Tc-mebrofenin and indocyanine green. *J Hepatol*. 2011;54(4):738-45.
57. Wang H, Cao Y. Spatially resolved assessment of hepatic function using 99mTc-IDA SPECT. *Medical physics*. 2013;40(9):092501.
58. Erdogan D, Heijnen BH, Bennink RJ, Kok M, Dinant S, Straatsburg IH, et al. Preoperative assessment of liver function: a comparison of 99mTc-Mebrofenin scintigraphy with indocyanine green clearance test. *Liver Int*. 2004;24(2):117-23.
59. Marshall JS, Green AM, Pensky J, Williams S, Zinn A, Carlson DM. Measurement of circulating desialylated glycoproteins and correlation with hepatocellular damage. *J Clin Invest*. 1974;54(3):555-62.
60. Sawamura T, Kawasato S, Shiozaki Y, Sameshima Y, Nakada H, Tashiro Y. Decrease of a hepatic binding protein specific for asialoglycoproteins with accumulation of serum asialoglycoproteins in galactosamine-treated rats. *Gastroenterology*. 1981;81(3):527-33.
61. Kwon AH, Ha-Kawa SK, Uetsuji S, Inoue T, Matsui Y, Kamiyama Y. Preoperative determination of the surgical procedure for hepatectomy using technetium-99m-galactosyl human serum albumin (99mTc-GSA) liver scintigraphy. *Hepatology*. 1997;25(2):426-9.
62. Sasaki N, Shiomi S, Iwata Y, Nishiguchi S, Kuroki T, Kawabe J, et al. Clinical usefulness of scintigraphy with 99mTc-galactosyl-human serum albumin for prognosis of

cirrhosis of the liver. *Journal of nuclear medicine : official publication, Society of Nuclear Medicine*. 1999;40(10):1652-6.

63. Ohkura Y, Mizuno S, Kishiwada M, Hamada T, Usui M, Sakurai H, et al. Benefit of technetium-99m galactosyl human serum albumin scintigraphy instead of indocyanine green test in patients scheduled for hepatectomy. *Hepatology research : the official journal of the Japan Society of Hepatology*. 2014;44(10):E118-28.

64. Mao Y, Du S, Ba J, Li F, Yang H, Lu X, et al. Using Dynamic T -GSA SPECT/CT Fusion Images for Hepatectomy Planning and Postoperative Liver Failure Prediction. *Annals of surgical oncology*. 2014.

65. Okabe H, Beppu T, Hayashi H, Mima K, Nakagawa S, Kuroki H, et al. Rank classification based on the combination of indocyanine green retention rate at 15 min and (99m)Tc-DTPA-galactosyl human serum albumin scintigraphy predicts the safety of hepatic resection. *Nuclear medicine communications*. 2014;35(5):478-83.

66. Yoshida M, Shiraiishi S, Sakamoto F, Beppu T, Utsunomiya D, Okabe H, et al. Assessment of hepatic functional regeneration after hepatectomy using (99m)Tc-GSA SPECT/CT fused imaging. *Annals of nuclear medicine*. 2014;28(8):780-8.

67. Kwon AH, Matsui Y, Ha-Kawa SK, Kamiyama Y. Functional hepatic volume measured by technetium-99m-galactosyl-human serum albumin liver scintigraphy: comparison between hepatocyte volume and liver volume by computed tomography. *Am J Gastroenterol*. 2001;96(2):541-6.

68. Iwasa M, Nakamura K, Nakagawa T, Watanabe S, Katoh H, Kinoshita Y, et al. Single photon emission computed tomography to determine effective hepatic blood flow and intrahepatic shunting. *Hepatology*. 1995;21(2):359-65.

69. Kato-Azuma M. TC-99m(Sn)-N-pyridoxylamines: a new series of hepatobiliary imaging agents. *Journal of nuclear medicine : official publication, Society of Nuclear Medicine*. 1982;23(6):517-24.

70. Khan AU, Irfanullah J, Shah SQ, Fatima S. Tc-phytate trans-splenic portal scintigraphy in the diagnosis of cirrhotic portal hypertension and compensatory circulation. *Abdominal imaging*. 2014.

71. Sorensen M, Mikkelsen KS, Frisch K, Bass L, Bibby BM, Keiding S. Hepatic galactose metabolism quantified in humans using 2-18F-fluoro-2-deoxy-D-galactose PET/CT. *Journal of nuclear medicine : official publication, Society of Nuclear Medicine*. 2011;52(10):1566-72.

72. Sorensen M, Mikkelsen KS, Frisch K, Villadsen GE, Keiding S. Regional metabolic liver function measured in patients with cirrhosis by 2-[(1)(8)F]fluoro-2-deoxy-D-galactose PET/CT. *J Hepatol*. 2013;58(6):1119-24.

73. Fulop A, Szijarto A, Harsanyi L, Budai A, Pekli D, Korsos D, et al. Demonstration of metabolic and cellular effects of portal vein ligation using multi-modal PET/MRI measurements in healthy rat liver. *PloS one*. 2014;9(3):e90760.

74. McNaughton DA, Abu-Yousef MM. Doppler US of the liver made simple. *Radiographics*. 2011;31(1):161-88.

75. Berzigotti A, Piscaglia F. Ultrasound in portal hypertension--part 1. *Ultraschall Med*. 2011;32(6):548-68; quiz 69-71.

76. Robinson KA, Middleton WD, Al-Sukaiti R, Teefey SA, Dahiya N. Doppler sonography of portal hypertension. *Ultrasound Q*. 2009;25(1):3-13.

77. Sacerdoti D, Gaiani S, Buonamico P, Merkel C, Zoli M, Bolondi L, et al. Interobserver and interequipment variability of hepatic, splenic, and renal arterial Doppler resistance indices in normal subjects and patients with cirrhosis. *J Hepatol*. 1997;27(6):986-92.

78. Wood MM, Romine LE, Lee YK, Richman KM, O'Boyle MK, Paz DA, et al. Spectral Doppler signature waveforms in ultrasonography: a review of normal and abnormal waveforms. *Ultrasound Q*. 2010;26(2):83-99.

79. Moriyasu F, Nishida O, Ban N, Nakamura T, Sakai M, Miyake T, et al. "Congestion index" of the portal vein. *AJR Am J Roentgenol*. 1986;146(4):735-9.

80. Berzigotti A, Piscaglia F. Ultrasound in portal hypertension--part 2--and EFSUMB recommendations for the performance and reporting of ultrasound examinations in portal hypertension. *Ultraschall Med.* 2012;33(1):8-32; quiz 30-1.
81. Tarzamni MK, Somi MH, Farhang S, Jalilvand M. Portal hemodynamics as predictors of high risk esophageal varices in cirrhotic patients. *World J Gastroenterol.* 2008;14(12):1898-902.
82. Annet L, Materne R, Danse E, Jamart J, Horsmans Y, Van Beers BE. Hepatic flow parameters measured with MR imaging and Doppler US: correlations with degree of cirrhosis and portal hypertension. *Radiology.* 2003;229(2):409-14.
83. Baik SK, Kim JW, Kim HS, Kwon SO, Kim YJ, Park JW, et al. Recent variceal bleeding: Doppler US hepatic vein waveform in assessment of severity of portal hypertension and vasoactive drug response. *Radiology.* 2006;240(2):574-80.
84. Kim MY, Baik SK, Park DH, Lim DW, Kim JW, Kim HS, et al. Damping index of Doppler hepatic vein waveform to assess the severity of portal hypertension and response to propranolol in liver cirrhosis: a prospective nonrandomized study. *Liver Int.* 2007;27(8):1103-10.
85. Kim SY, Jeong WK, Kim Y, Heo JN, Kim MY, Kim TY, et al. Changing waveform during respiration on hepatic vein Doppler sonography of severe portal hypertension: comparison with the damping index. *J Ultrasound Med.* 2011;30(4):455-62.
86. Solhjoo E, Mansour-Ghanaei F, Moulaei-Langorudi R, Joukar F. Comparison of portal vein doppler indices and hepatic vein doppler waveform in patients with nonalcoholic fatty liver disease with healthy control. *Hepat Mon.* 2011;11(9):740-4.
87. Doi R, Inoue K, Kogire M, Sumi S, Takaori K, Suzuki T, et al. Simultaneous measurement of hepatic arterial and portal venous flows by transit time ultrasonic volume flowmetry. *Surg Gynecol Obstet.* 1988;167(1):65-9.
88. Jakab F, Rath Z, Schmal F, Nagy P, Faller J. The interaction between hepatic arterial and portal venous blood flows; simultaneous measurement by transit time ultrasonic volume flowmetry. *Hepatogastroenterology.* 1995;42(1):18-21.
89. Omori S, Ishizaki Y, Sugo H, Yoshimoto J, Imamura H, Yamataka A, et al. Direct measurement of hepatic blood flow during living donor liver transplantation in children. *J Pediatr Surg.* 2010;45(3):545-8.
90. Hubner GH, Steudel N, Kleber G, Behrmann C, Lotterer E, Fleig WE. Hepatic arterial blood flow velocities: assessment by transcutaneous and intravascular Doppler sonography. *J Hepatol.* 2000;32(6):893-9.
91. Kleber G, Steudel N, Behrmann C, Zipprich A, Hubner G, Lotterer E, et al. Hepatic arterial flow volume and reserve in patients with cirrhosis: use of intra-arterial Doppler and adenosine infusion. *Gastroenterology.* 1999;116(4):906-14.
92. Zipprich A, Steudel N, Behrmann C, Meiss F, Sziegoleit U, Fleig WE, et al. Functional significance of hepatic arterial flow reserve in patients with cirrhosis. *Hepatology.* 2003;37(2):385-92.
93. Albrecht T, Blomley MJ, Cosgrove DO, Taylor-Robinson SD, Jayaram V, Eckersley R, et al. Non-invasive diagnosis of hepatic cirrhosis by transit-time analysis of an ultrasound contrast agent. *Lancet.* 1999;353(9164):1579-83.
94. Goyal N, Jain N, Rachapalli V, Cochlin DL, Robinson M. Non-invasive evaluation of liver cirrhosis using ultrasound. *Clinical radiology.* 2009;64(11):1056-66.
95. Blomley MJ, Lim AK, Harvey CJ, Patel N, Eckersley RJ, Basilico R, et al. Liver microbubble transit time compared with histology and Child-Pugh score in diffuse liver disease: a cross sectional study. *Gut.* 2003;52(8):1188-93.
96. Lim AK, Taylor-Robinson SD, Patel N, Eckersley RJ, Goldin RD, Hamilton G, et al. Hepatic vein transit times using a microbubble agent can predict disease severity non-invasively in patients with hepatitis C. *Gut.* 2005;54(1):128-33.
97. Searle J, Mendelson R, Zelesco M, Sanford J, Cheng W, McKinstry C, et al. Non-invasive prediction of the degree of liver fibrosis in patients with hepatitis C using an ultrasound contrast agent. A pilot study. *Journal of medical imaging and radiation oncology.* 2008;52(2):130-3.

98. Hohmann J, Muller C, Oldenburg A, Skrok J, Frericks BB, Wolf KJ, et al. Hepatic transit time analysis using contrast-enhanced ultrasound with BR1: A prospective study comparing patients with liver metastases from colorectal cancer with healthy volunteers. *Ultrasound in medicine & biology*. 2009;35(9):1427-35.
99. Li N, Ding H, Fan P, Lin X, Xu C, Wang W, et al. Intrahepatic transit time predicts liver fibrosis in patients with chronic hepatitis B: quantitative assessment with contrast-enhanced ultrasonography. *Ultrasound in medicine & biology*. 2010;36(7):1066-75.
100. Staub F, Tournoux-Facon C, Roumy J, Chaigneau C, Morichaut-Beauchant M, Levillain P, et al. Liver fibrosis staging with contrast-enhanced ultrasonography: prospective multicenter study compared with METAVIR scoring. *European radiology*. 2009;19(8):1991-7.
101. Kim MY, Suk KT, Baik SK, Kim HA, Kim YJ, Cha SH, et al. Hepatic vein arrival time as assessed by contrast-enhanced ultrasonography is useful for the assessment of portal hypertension in compensated cirrhosis. *Hepatology*. 2012;56(3):1053-62.
102. Berzigotti A, Nicolau C, Bellot P, Abraldes JG, Gilibert R, Garcia-Pagan JC, et al. Evaluation of regional hepatic perfusion (RHP) by contrast-enhanced ultrasound in patients with cirrhosis. *J Hepatol*. 2011;55(2):307-14.
103. Hubner GH, Steudel N, Reissmann A, Kuhne I, Kleber G, Scharff K, et al. Hepatic arterial doppler sonography in patients with cirrhosis and controls: observer and equipment variability with use of the ultrasonic contrast agent SHU 508A. *Zeitschrift fur Gastroenterologie*. 2005;43(7):639-45.
104. Gauthier TP, Muhammad A, Wasan HS, Abel PD, Leen EL. Reproducibility of quantitative assessment of altered hepatic hemodynamics with dynamic contrast-enhanced ultrasound. *J Ultrasound Med*. 2012;31(9):1413-20.
105. Axel L. Cerebral blood flow determination by rapid-sequence computed tomography: theoretical analysis. *Radiology*. 1980;137(3):679-86.
106. Miles KA. Measurement of tissue perfusion by dynamic computed tomography. *The British journal of radiology*. 1991;64(761):409-12.
107. Miles KA, Hayball M, Dixon AK. Colour perfusion imaging: a new application of computed tomography. *Lancet*. 1991;337(8742):643-5.
108. Miles KA, Hayball MP, Dixon AK. Functional images of hepatic perfusion obtained with dynamic CT. *Radiology*. 1993;188(2):405-11.
109. Blomley MJ, Coulden R, Dawson P, Korman M, Donlan P, Bufkin C, et al. Liver perfusion studied with ultrafast CT. *Journal of computer assisted tomography*. 1995;19(3):424-33.
110. Tsushima Y, Unno Y, Koizumi J, Kusano S. Measurement of human hepatic and splenic perfusion using dynamic computed tomography: a preliminary report. *Computer methods and programs in biomedicine*. 1998;57(1-2):143-6.
111. Winterdahl M, Sorensen M, Keiding S, Mortensen FV, Alstrup AK, Hansen SB, et al. Hepatic blood perfusion estimated by dynamic contrast-enhanced computed tomography in pigs: limitations of the slope method. *Investigative radiology*. 2012;47(10):588-95.
112. D'Onofrio M, De Robertis R, Ruzzenente A, Mantovani W, Puntel G, Crosara S, et al. Time-to-peak values can estimate hepatic functional reserve in patients undergoing surgical resection: a comparison between perfusion CT and indocyanine green retention test. *Journal of computer assisted tomography*. 2014;38(5):733-41.
113. Ziegler SI, Haberkorn U, Byrne H, Tong C, Kaja S, Richolt JA, et al. Measurement of liver blood flow using oxygen-15 labelled water and dynamic positron emission tomography: limitations of model description. *European journal of nuclear medicine*. 1996;23(2):169-77.
114. Materne R, Van Beers BE, Smith AM, Leconte I, Jamart J, Dehoux JP, et al. Non-invasive quantification of liver perfusion with dynamic computed tomography and a dual-input one-compartmental model. *Clinical science*. 2000;99(6):517-25.
115. Van Beers BE, Leconte I, Materne R, Smith AM, Jamart J, Horsmans Y. Hepatic perfusion parameters in chronic liver disease: dynamic CT measurements correlated with disease severity. *AJR Am J Roentgenol*. 2001;176(3):667-73.

116. Materne R, Annet L, Dechambre S, Sempoux C, Smith AM, Corot C, et al. Dynamic computed tomography with low- and high-molecular-mass contrast agents to assess microvascular permeability modifications in a model of liver fibrosis. *Clinical science*. 2002;103(2):213-6.
117. Kobayashi S, Kitamura A, Matsushita T, Nishiura M, Murase K. Usefulness of a dual-input single-compartment model for quantitative evaluation of thioacetamide-induced acute liver injury in rats using dynamic contrast-enhanced computed tomography. *Radiological physics and technology*. 2012;5(1):27-33.
118. Miles KA, Griffiths MR. Perfusion CT: a worthwhile enhancement? *The British journal of radiology*. 2003;76(904):220-31.
119. Waguri N, Suda T, Kamura T, Aoyagi Y. Heterogeneous hepatic enhancement on CT angiography in idiopathic portal hypertension. *Liver*. 2002;22(3):276-80.
120. Wang X, Xue HD, Jin ZY, Su BY, Li Z, Sun H, et al. Quantitative hepatic CT perfusion measurement: Comparison of Couinaud's hepatic segments with dual-source 128-slice CT. *Eur J Radiol*. 2013;82(2):220-6.
121. Dugdale PE, Miles KA. Hepatic metastases: the value of quantitative assessment of contrast enhancement on computed tomography. *Eur J Radiol*. 1999;30(3):206-13.
122. Leggett DA, Kelley BB, Bunce IH, Miles KA. Colorectal cancer: diagnostic potential of CT measurements of hepatic perfusion and implications for contrast enhancement protocols. *Radiology*. 1997;205(3):716-20.
123. Cuenod C, Leconte I, Siauve N, Resten A, Dromain C, Poulet B, et al. Early changes in liver perfusion caused by occult metastases in rats: detection with quantitative CT. *Radiology*. 2001;218(2):556-61.
124. Fournier LS, Cuenod CA, de Bazelaire C, Siauve N, Rosty C, Tran PL, et al. Early modifications of hepatic perfusion measured by functional CT in a rat model of hepatocellular carcinoma using a blood pool contrast agent. *European radiology*. 2004;14(11):2125-33.
125. Lodhia N, Kader M, Mayes T, Mantry P, Maliakkal B. Risk of contrast-induced nephropathy in hospitalized patients with cirrhosis. *World J Gastroenterol*. 2009;15(12):1459-64.
126. Weinmann HJ, Brasch RC, Press WR, Wesbey GE. Characteristics of gadolinium-DTPA complex: a potential NMR contrast agent. *AJR Am J Roentgenol*. 1984;142(3):619-24.
127. Tofts PS, du Boulay EP. Towards quantitative measurements of relaxation times and other parameters in the brain. *Neuroradiology*. 1990;32(5):407-15.
128. Tofts PS, Kermode AG. Measurement of the blood-brain barrier permeability and leakage space using dynamic MR imaging. 1. Fundamental concepts. *Magnetic resonance in medicine : official journal of the Society of Magnetic Resonance in Medicine / Society of Magnetic Resonance in Medicine*. 1991;17(2):357-67.
129. Johnson G, Ormerod IE, Barnes D, Tofts PS, MacManus D. Accuracy and precision in the measurement of relaxation times from nuclear magnetic resonance images. *The British journal of radiology*. 1987;60(710):143-53.
130. Tofts PS, Berkowitz BA. Measurement of capillary permeability from the Gd enhancement curve: a comparison of bolus and constant infusion injection methods. *Magnetic resonance imaging*. 1994;12(1):81-91.
131. Tofts PS, Brix G, Buckley DL, Evelhoch JL, Henderson E, Knopp MV, et al. Estimating kinetic parameters from dynamic contrast-enhanced T(1)-weighted MRI of a diffusible tracer: standardized quantities and symbols. *Journal of magnetic resonance imaging : JMRI*. 1999;10(3):223-32.
132. Kermode AG, Tofts PS, Thompson AJ, MacManus DG, Rudge P, Kendall BE, et al. Heterogeneity of blood-brain barrier changes in multiple sclerosis: an MRI study with gadolinium-DTPA enhancement. *Neurology*. 1990;40(2):229-35.
133. Larsson HB, Tofts PS. Measurement of blood-brain barrier permeability using dynamic Gd-DTPA scanning--a comparison of methods. *Magnetic resonance in medicine :*

- official journal of the Society of Magnetic Resonance in Medicine / Society of Magnetic Resonance in Medicine. 1992;24(1):174-6.
134. Scharf J, Zapletal C, Hess T, Hoffmann U, Mehrabi A, Mihm D, et al. Assessment of hepatic perfusion in pigs by pharmacokinetic analysis of dynamic MR images. *Journal of magnetic resonance imaging : JMRI*. 1999;9(4):568-72.
135. Scharf J, Kemmling A, Hess T, Mehrabi A, Kauffmann G, Groden C, et al. Assessment of hepatic perfusion in transplanted livers by pharmacokinetic analysis of dynamic magnetic resonance measurements. *Investigative radiology*. 2007;42(4):224-9.
136. Jackson A, Haroon H, Zhu XP, Li KL, Thacker NA, Jayson G. Breath-hold perfusion and permeability mapping of hepatic malignancies using magnetic resonance imaging and a first-pass leakage profile model. *NMR in biomedicine*. 2002;15(2):164-73.
137. Miyazaki K, Collins DJ, Walker-Samuel S, Taylor JN, Padhani AR, Leach MO, et al. Quantitative mapping of hepatic perfusion index using MR imaging: a potential reproducible tool for assessing tumour response to treatment with the antiangiogenic compound BIBF 1120, a potent triple angiokinase inhibitor. *European radiology*. 2008;18(7):1414-21.
138. Totman JJ, O'Gorman R L, Kane PA, Karani JB. Comparison of the hepatic perfusion index measured with gadolinium-enhanced volumetric MRI in controls and in patients with colorectal cancer. *The British journal of radiology*. 2005;78(926):105-9.
139. White MJ, O'Gorman RL, Charles-Edwards EM, Kane PA, Karani JB, Leach MO, et al. Parametric mapping of the hepatic perfusion index with gadolinium-enhanced volumetric MRI. *The British journal of radiology*. 2007;80(950):113-20.
140. Materne R, Smith AM, Peeters F, Dehoux JP, Keyeux A, Horsmans Y, et al. Assessment of hepatic perfusion parameters with dynamic MRI. *Magnetic resonance in medicine : official journal of the Society of Magnetic Resonance in Medicine / Society of Magnetic Resonance in Medicine*. 2002;47(1):135-42.
141. Hagiwara M, Rusinek H, Lee VS, Losada M, Bannan MA, Krinsky GA, et al. Advanced liver fibrosis: diagnosis with 3D whole-liver perfusion MR imaging--initial experience. *Radiology*. 2008;246(3):926-34.
142. Kim H, Booth CJ, Pinus AB, Chen P, Lee A, Qiu M, et al. Induced hepatic fibrosis in rats: hepatic steatosis, macromolecule content, perfusion parameters, and their correlations--preliminary MR imaging in rats. *Radiology*. 2008;247(3):696-705.
143. Cao Y, Wang H, Johnson TD, Pan C, Hussain H, Balter JM, et al. Prediction of liver function by using magnetic resonance-based portal venous perfusion imaging. *International journal of radiation oncology, biology, physics*. 2013;85(1):258-63.
144. Wang H, Cao Y. Correction of arterial input function in dynamic contrast-enhanced MRI of the liver. *Journal of magnetic resonance imaging : JMRI*. 2012;36(2):411-21.
145. Gill AB, Black RT, Bowden DJ, Priest AN, Graves MJ, Lomas DJ. An investigation into the effects of temporal resolution on hepatic dynamic contrast-enhanced MRI in volunteers and in patients with hepatocellular carcinoma. *Physics in medicine and biology*. 2014;59(12):3187-200.
146. Aronhime S, Calcagno C, Jajamovich GH, Dyvorne HA, Robson P, Dieterich D, et al. DCE-MRI of the liver: effect of linear and nonlinear conversions on hepatic perfusion quantification and reproducibility. *Journal of magnetic resonance imaging : JMRI*. 2014;40(1):90-8.
147. Bultman EM, Brodsky EK, Horng DE, Irrarrazaval P, Schelman WR, Block WF, et al. Quantitative hepatic perfusion modeling using DCE-MRI with sequential breathholds. *Journal of magnetic resonance imaging : JMRI*. 2014;39(4):853-65.
148. Van Beers BE, Materne R, Annet L, Hermoye L, Sempoux C, Peeters F, et al. Capillarization of the sinusoids in liver fibrosis: noninvasive assessment with contrast-enhanced MRI in the rabbit. *Magnetic resonance in medicine : official journal of the Society of Magnetic Resonance in Medicine / Society of Magnetic Resonance in Medicine*. 2003;49(4):692-9.
149. Hartono S, Thng CH, Ng QS, Yong CX, Yang CT, Shi W, et al. High temporal resolution dynamic contrast-enhanced MRI at 7 Tesla: a feasibility study with mouse liver

- model. Conference proceedings : Annual International Conference of the IEEE Engineering in Medicine and Biology Society IEEE Engineering in Medicine and Biology Society Conference. 2011;2011:2788-91.
150. Koh TS, Thng CH, Hartono S, Kwek JW, Khoo JB, Miyazaki K, et al. Dynamic contrast-enhanced MRI of neuroendocrine hepatic metastases: A feasibility study using a dual-input two-compartment model. *Magnetic resonance in medicine : official journal of the Society of Magnetic Resonance in Medicine / Society of Magnetic Resonance in Medicine*. 2011;65(1):250-60.
 151. Koh TS, Thng CH, Lee PS, Hartono S, Rumpel H, Goh BC, et al. Hepatic metastases: in vivo assessment of perfusion parameters at dynamic contrast-enhanced MR imaging with dual-input two-compartment tracer kinetics model. *Radiology*. 2008;249(1):307-20.
 152. Gandhi SN, Brown MA, Wong JG, Aguirre DA, Sirlin CB. MR contrast agents for liver imaging: what, when, how. *Radiographics*. 2006;26(6):1621-36.
 153. Van Beers BE, Pastor CM, Hussain HK. Primovist, Eovist: what to expect? *J Hepatol*. 2012;57(2):421-9.
 154. Dahlqvist Leinhard O, Dahlstrom N, Kihlberg J, Sandstrom P, Brismar TB, Smedby O, et al. Quantifying differences in hepatic uptake of the liver specific contrast agents Gd-EOB-DTPA and Gd-BOPTA: a pilot study. *European radiology*. 2012;22(3):642-53.
 155. Reimer P, Schneider G, Schima W. Hepatobiliary contrast agents for contrast-enhanced MRI of the liver: properties, clinical development and applications. *European radiology*. 2004;14(4):559-78.
 156. Ringe KI, Husarik DB, Sirlin CB, Merkle EM. Gadoxetate disodium-enhanced MRI of the liver: part 1, protocol optimization and lesion appearance in the noncirrhotic liver. *AJR Am J Roentgenol*. 2010;195(1):13-28.
 157. Schuhmann-Giampieri G, Schmitt-Willich H, Press WR, Negishi C, Weinmann HJ, Speck U. Preclinical evaluation of Gd-EOB-DTPA as a contrast agent in MR imaging of the hepatobiliary system. *Radiology*. 1992;183(1):59-64.
 158. Planchamp C, Montet X, Frossard JL, Quadri R, Stieger B, Meier PJ, et al. Magnetic resonance imaging with hepatospecific contrast agents in cirrhotic rat livers. *Investigative radiology*. 2005;40(4):187-94.
 159. Pastor CM, Wissmeyer M, Millet P. Concentrations of Gd-BOPTA in cholestatic fatty rat livers: role of transport functions through membrane proteins. *Contrast media & molecular imaging*. 2013;8(2):147-56.
 160. Planchamp C, Gex-Fabry M, Becker CD, Pastor CM. Model-based analysis of Gd-BOPTA-induced MR signal intensity changes in cirrhotic rat livers. *Investigative radiology*. 2007;42(7):513-21.
 161. Ryeom HK, Kim SH, Kim JY, Kim HJ, Lee JM, Chang YM, et al. Quantitative evaluation of liver function with MRI Using Gd-EOB-DTPA. *Korean J Radiol*. 2004;5(4):231-9.
 162. Nilsson H, Nordell A, Vargas R, Douglas L, Jonas E, Blomqvist L. Assessment of hepatic extraction fraction and input relative blood flow using dynamic hepatocyte-specific contrast-enhanced MRI. *Journal of magnetic resonance imaging : JMRI*. 2009;29(6):1323-31.
 163. Nilsson H, Blomqvist L, Douglas L, Nordell A, Jonas E. Assessment of liver function in primary biliary cirrhosis using Gd-EOB-DTPA-enhanced liver MRI. *HPB : the official journal of the International Hepato Pancreato Biliary Association*. 2010;12(8):567-76.
 164. Nilsson H, Blomqvist L, Douglas L, Nordell A, Jacobsson H, Hagen K, et al. Dynamic gadoxetate-enhanced MRI for the assessment of total and segmental liver function and volume in primary sclerosing cholangitis. *Journal of magnetic resonance imaging : JMRI*. 2014;39(4):879-86.
 165. Chen BB, Hsu CY, Yu CW, Wei SY, Kao JH, Lee HS, et al. Dynamic contrast-enhanced magnetic resonance imaging with Gd-EOB-DTPA for the evaluation of liver fibrosis in chronic hepatitis patients. *European radiology*. 2012;22(1):171-80.
 166. Sourbron S, Sommer WH, Reiser MF, Zech CJ. Combined quantification of liver perfusion and function with dynamic gadoxetic acid-enhanced MR imaging. *Radiology*. 2012;263(3):874-83.

167. Saito K, Ledsam J, Sourbron S, Otaka J, Araki Y, Akata S, et al. Assessing liver function using dynamic Gd-EOB-DTPA-enhanced MRI with a standard 5-phase imaging protocol. *Journal of magnetic resonance imaging : JMRI*. 2013;37(5):1109-14.
168. Yamada A, Hara T, Li F, Fujinaga Y, Ueda K, Kadoya M, et al. Quantitative evaluation of liver function with use of gadoxetate disodium-enhanced MR imaging. *Radiology*. 2011;260(3):727-33.
169. Takao H, Akai H, Tajima T, Kiryu S, Watanabe Y, Imamura H, et al. MR imaging of the biliary tract with Gd-EOB-DTPA: effect of liver function on signal intensity. *Eur J Radiol*. 2011;77(2):325-9.
170. Kukuk GM, Schaefer SG, Fimmers R, Hadizadeh DR, Ezziddin S, Spengler U, et al. Hepatobiliary magnetic resonance imaging in patients with liver disease: correlation of liver enhancement with biochemical liver function tests. *European radiology*. 2014;24(10):2482-90.
171. Verloh N, Haimerl M, Zeman F, Schlabeck M, Barreiros A, Loss M, et al. Assessing liver function by liver enhancement during the hepatobiliary phase with Gd-EOB-DTPA-enhanced MRI at 3 Tesla. *European radiology*. 2014;24(5):1013-9.
172. Onishi H, Theisen D, Dietrich O, Reiser MF, Zech CJ. Hepatic steatosis: effect on hepatocyte enhancement with gadoxetate disodium-enhanced liver MR imaging. *Journal of magnetic resonance imaging : JMRI*. 2014;39(1):42-50.
173. Jang YJ, Cho SH, Bae JH, Kim GC, Ryeom H, Kim HJ, et al. Noninvasive assessment of hepatic fibrosis using gadoxetate-disodium-enhanced 3T MRI. *Annals of hepatology*. 2013;12(6):926-34.
174. Nojiri S, Kusakabe A, Fujiwara K, Shinkai N, Matsuura K, Iio E, et al. Noninvasive evaluation of hepatic fibrosis in hepatitis C virus-infected patients using ethoxybenzyl-magnetic resonance imaging. *J Gastroenterol Hepatol*. 2013;28(6):1032-9.
175. Wibmer A, Prusa AM, Nolz R, Gruenberger T, Schindl M, Ba-Ssalamah A. Liver failure after major liver resection: risk assessment by using preoperative Gadoteric acid-enhanced 3-T MR imaging. *Radiology*. 2013;269(3):777-86.
176. Bickelhaupt S, Studer P, Kim-Fuchs C, Candinas D, Froehlich JM, Patak MA. Gadoteric uptake as a possible marker of hepatocyte damage after liver resection-preliminary data. *Clinical radiology*. 2013;68(11):1121-7.
177. Haimerl M, Verloh N, Fellner C, Zeman F, Teufel A, Fichtner-Feigl S, et al. MRI-based estimation of liver function: Gd-EOB-DTPA-enhanced T1 relaxometry of 3T vs. the MELD score. *Scientific reports*. 2014;4:5621.
178. Kamimura K, Fukukura Y, Yoneyama T, Takumi K, Tateyama A, Umanodan A, et al. Quantitative evaluation of liver function with T1 relaxation time index on Gd-EOB-DTPA-enhanced MRI: comparison with signal intensity-based indices. *Journal of magnetic resonance imaging : JMRI*. 2014;40(4):884-9.
179. Oechsner M, Muhlhausler M, Ritter CO, Weininger M, Beissert M, Jakob PM, et al. Quantitative contrast-enhanced perfusion measurements of the human lung using the prebolus approach. *Journal of magnetic resonance imaging : JMRI*. 2009;30(1):104-11.
180. Utz W, Greiser A, Niendorf T, Dietz R, Schulz-Menger J. Single- or dual-bolus approach for the assessment of myocardial perfusion reserve in quantitative MR perfusion imaging. *Magnetic resonance in medicine : official journal of the Society of Magnetic Resonance in Medicine / Society of Magnetic Resonance in Medicine*. 2008;59(6):1373-7.
181. Moran PR. A flow velocity zeugmatographic interlace for NMR imaging in humans. *Magnetic resonance imaging*. 1982;1(4):197-203.
182. Lotz J, Meier C, Leppert A, Galanski M. Cardiovascular flow measurement with phase-contrast MR imaging: basic facts and implementation. *Radiographics*. 2002;22(3):651-71.
183. Singer JR. Blood Flow Rates by Nuclear Magnetic Resonance Measurements. *Science*. 1959;130(3389):1652-3.
184. Edelman RR, Zhao B, Liu C, Wentz KU, Mattle HP, Finn JP, et al. MR angiography and dynamic flow evaluation of the portal venous system. *AJR Am J Roentgenol*. 1989;153(4):755-60.

185. Tamada T, Moriyasu F, Ono S, Shimizu K, Kajimura K, Soh Y, et al. Portal blood flow: measurement with MR imaging. *Radiology*. 1989;173(3):639-44.
186. Finn JP, Edelman RR, Jenkins RL, Lewis WD, Longmaid HE, Kane RA, et al. Liver transplantation: MR angiography with surgical validation. *Radiology*. 1991;179(1):265-9.
187. Finn JP, Kane RA, Edelman RR, Jenkins RL, Lewis WD, Muller M, et al. Imaging of the portal venous system in patients with cirrhosis: MR angiography vs duplex Doppler sonography. *AJR Am J Roentgenol*. 1993;161(5):989-94.
188. Nghiem HV, Winter TC, 3rd, Mountford MC, Mack LA, Yuan C, Coldwell DM, et al. Evaluation of the portal venous system before liver transplantation: value of phase-contrast MR angiography. *AJR Am J Roentgenol*. 1995;164(4):871-8.
189. Sadek AG, Mohamed FB, Outwater EK, El-Essawy SS, Mitchell DG. Respiratory and postprandial changes in portal flow rate: assessment by phase contrast MR imaging. *Journal of magnetic resonance imaging : JMRI*. 1996;6(1):90-3.
190. Burkart DJ, Johnson CD, Morton MJ, Wolf RL, Ehman RL. Volumetric flow rates in the portal venous system: measurement with cine phase-contrast MR imaging. *AJR Am J Roentgenol*. 1993;160(5):1113-8.
191. Burkart DJ, Johnson CD, Ehman RL, Weaver AL, Ilstrup DM. Evaluation of portal venous hypertension with cine phase-contrast MR flow measurements: high association of hyperdynamic portal flow with variceal hemorrhage. *Radiology*. 1993;188(3):643-8.
192. Kashitani N, Kimoto S, Tsunoda M, Ito T, Tsuji T, Ono A, et al. Portal blood flow in the presence or absence of diffuse liver disease: measurement by phase contrast MR imaging. *Abdominal imaging*. 1995;20(3):197-200.
193. Kuo PC, Li K, Alfrey EJ, Jeffrey RB, Garcia G, Dafoe DC. Magnetic resonance imaging and hepatic hemodynamics: correlation with metabolic function in liver transplantation candidates. *Surgery*. 1995;117(4):373-9.
194. Debatin JF, Zahner B, Meyenberger C, Romanowski B, Schopke W, Marincek B, et al. Azygos blood flow: phase contrast quantitation in volunteers and patients with portal hypertension pre- and postintrahepatic shunt placement. *Hepatology*. 1996;24(5):1109-15.
195. Sugano S, Yamamoto K, Sasao K, Watanabe M. Portal venous blood flow while breath-holding after inspiration or expiration and during normal respiration in controls and cirrhotics. *J Gastroenterol*. 1999;34(5):613-8.
196. Nanashima A, Shibasaki S, Sakamoto I, Sueyoshi E, Sumida Y, Abo T, et al. Clinical evaluation of magnetic resonance imaging flowmetry of portal and hepatic veins in patients following hepatectomy. *Liver Int*. 2006;26(5):587-94.
197. Jin N, Lewandowski RJ, Omary RA, Larson AC. Respiratory self-gating for free-breathing abdominal phase-contrast blood flow measurements. *Journal of magnetic resonance imaging : JMRI*. 2009;29(4):860-8.
198. Yzet T, Bouzerar R, Baledent O, Renard C, Lumbala DM, Nguyen-Khac E, et al. Dynamic measurements of total hepatic blood flow with Phase Contrast MRI. *Eur J Radiol*. 2010;73(1):119-24.
199. Yzet T, Bouzerar R, Allart JD, Demuyneck F, Legallais C, Robert B, et al. Hepatic vascular flow measurements by phase contrast MRI and doppler echography: a comparative and reproducibility study. *Journal of magnetic resonance imaging : JMRI*. 2010;31(3):579-88.
200. Gouya H, Vignaux O, Sogni P, Mallet V, Oudjit A, Pol S, et al. Chronic liver disease: systemic and splanchnic venous flow mapping with optimized cine phase-contrast MR imaging validated in a phantom model and prospectively evaluated in patients. *Radiology*. 2011;261(1):144-55.
201. Stankovic Z, Frydrychowicz A, Csatar Z, Panther E, Deibert P, Euringer W, et al. MR-based visualization and quantification of three-dimensional flow characteristics in the portal venous system. *Journal of magnetic resonance imaging : JMRI*. 2010;32(2):466-75.
202. Stankovic Z, Csatar Z, Deibert P, Euringer W, Blanke P, Kreisel W, et al. Normal and altered three-dimensional portal venous hemodynamics in patients with liver cirrhosis. *Radiology*. 2012;262(3):862-73.

203. Morisaka H, Motosugi U, Ichikawa T, Sano K, Ichikawa S, Araki T, et al. MR-based Measurements of Portal Vein Flow and Liver Stiffness for Predicting Gastroesophageal Varices. *Magnetic resonance in medical sciences : MRMS : an official journal of Japan Society of Magnetic Resonance in Medicine*. 2013.
204. Jajamovich GH, Dyvorne H, Donnerhack C, Taouli B. Quantitative liver MRI combining phase contrast imaging, elastography, and DWI: assessment of reproducibility and postprandial effect at 3.0 T. *PloS one*. 2014;9(5):e97355.
205. Wilson DJ, Ridgway JP, Evans JA, Robinson P. Measurement of hepatic arterial flow using phase contrast magnetic resonance imaging. *Physics in medicine and biology*. 2009;54(19):N439-49.
206. Lomas DJ, Hayball MP, Jones DP, Sims C, Allison ME, Alexander GJ. Non-invasive measurement of azygos venous blood flow using magnetic resonance. *J Hepatol*. 1995;22(4):399-403.
207. Ng WH, Chan YL, Sung JY, Lee YT, Lee SF, Chung SS. Comparison of breath-hold 2D phase-contrast with non breath-hold cine phase-contrast MRA in the assessment of azygos venous blood flow in portal hypertension. *Magma*. 2004;16(5):211-7.
208. Steinman DA, Ethier CR, Rutt BK. Combined analysis of spatial and velocity displacement artifacts in phase contrast measurements of complex flows. *Journal of magnetic resonance imaging : JMRI*. 1997;7(2):339-46.
209. Hamilton CA. Correction of partial volume inaccuracies in quantitative phase contrast MR angiography. *Magnetic resonance imaging*. 1994;12(7):1127-30.
210. Tang C, Blatter DD, Parker DL. Accuracy of phase-contrast flow measurements in the presence of partial-volume effects. *Journal of magnetic resonance imaging : JMRI*. 1993;3(2):377-85.
211. Bakker CJ, Hooigeveen RM, Viergever MA. Construction of a protocol for measuring blood flow by two-dimensional phase-contrast MRA. *Journal of magnetic resonance imaging : JMRI*. 1999;9(1):119-27.
212. Frydrychowicz A, Landgraf BR, Niespodzany E, Verma RW, Roldan-Alzate A, Johnson KM, et al. Four-dimensional velocity mapping of the hepatic and splanchnic vasculature with radial sampling at 3 tesla: a feasibility study in portal hypertension. *Journal of magnetic resonance imaging : JMRI*. 2011;34(3):577-84.
213. Markl M, Frydrychowicz A, Kozerke S, Hope M, Wieben O. 4D flow MRI. *Journal of magnetic resonance imaging : JMRI*. 2012;36(5):1015-36.
214. Johnson KM, Markl M. Improved SNR in phase contrast velocimetry with five-point balanced flow encoding. *Magnetic resonance in medicine : official journal of the Society of Magnetic Resonance in Medicine / Society of Magnetic Resonance in Medicine*. 2010;63(2):349-55.
215. Barger AV, Peters DC, Block WF, Vigen KK, Korosec FR, Grist TM, et al. Phase-contrast with interleaved undersampled projections. *Magnetic resonance in medicine : official journal of the Society of Magnetic Resonance in Medicine / Society of Magnetic Resonance in Medicine*. 2000;43(4):503-9.
216. Gu T, Korosec FR, Block WF, Fain SB, Turk Q, Lum D, et al. PC VIPR: a high-speed 3D phase-contrast method for flow quantification and high-resolution angiography. *AJNR American journal of neuroradiology*. 2005;26(4):743-9.
217. Roldan-Alzate A, Frydrychowicz A, Niespodzany E, Landgraf BR, Johnson KM, Wieben O, et al. In vivo validation of 4D flow MRI for assessing the hemodynamics of portal hypertension. *Journal of magnetic resonance imaging : JMRI*. 2013;37(5):1100-8.
218. Frydrychowicz A, Francois CJ, Turski PA. Four-dimensional phase contrast magnetic resonance angiography: potential clinical applications. *Eur J Radiol*. 2011;80(1):24-35.
219. Dyvorne H, Knight-Greenfield A, Jajamovich G, Besa C, Cui Y, Stalder A, et al. Abdominal 4D Flow MR Imaging in a Breath Hold: Combination of Spiral Sampling and Dynamic Compressed Sensing for Highly Accelerated Acquisition. *Radiology*. 2014:140973.

220. Landgraf BR, Johnson KM, Roldan-Alzate A, Francois CJ, Wieben O, Reeder SB. Effect of temporal resolution on 4D flow MRI in the portal circulation. *Journal of magnetic resonance imaging : JMRI*. 2014;39(4):819-26.
221. Buxton RB, Frank LR, Wong EC, Siewert B, Warach S, Edelman RR. A general kinetic model for quantitative perfusion imaging with arterial spin labeling. *Magnetic resonance in medicine : official journal of the Society of Magnetic Resonance in Medicine / Society of Magnetic Resonance in Medicine*. 1998;40(3):383-96.
222. Golay X, Hendrikse J, Lim TC. Perfusion imaging using arterial spin labeling. *Topics in magnetic resonance imaging : TMRI*. 2004;15(1):10-27.
223. Reiser MF, Semmler W, Hricak H, (Eds.). *Magnetic Resonance Tomography*. Berlin: Springer-Verlag, 2008.
224. Petersen ET, Zimine I, Ho YC, Golay X. Non-invasive measurement of perfusion: a critical review of arterial spin labelling techniques. *The British journal of radiology*. 2006;79(944):688-701.
225. Gach HM, Li T, Lopez-Talavera JC, W. KA, editors. Liver perfusion MRI using arterial spin labeling. *Proc Intl Soc Mag Reson Med*; 2002.
226. Hirshberg B, Qiu M, Cali AM, Sherwin R, Constable T, Calle RA, et al. Pancreatic perfusion of healthy individuals and type 1 diabetic patients as assessed by magnetic resonance perfusion imaging. *Diabetologia*. 2009;52(8):1561-5.
227. Ramasawmy R, Campbell-Washburn A, Johnson SP, Wells JA, Pedley RB, Walker-Samuel S, et al., editors. Multi-slice Look-Locker FAIR for hepatic arterial spin labelling. *Proc Intl Soc Mag Reson Med*; 2013.
228. Johnson SP, Ramasawmy R, Campbell-Washburn A, Robson M, Wells JA, Rajkumar V, et al., editors. Comparison of arterial spin labelling and R2* as predictive response biomarkers for vascular targeting agents in liver metastases. *Proc Intl Soc Mag Reson Med*; 2013.
229. Katada Y, Shukuya T, Kawashima M, Nozaki M, Imai H, Natori T, et al. A comparative study between arterial spin labeling and CT perfusion methods on hepatic portal venous flow. *Japanese journal of radiology*. 2012;30(10):863-9.
230. Chouhan M, Ramasawmy R, Campbell-Washburn A, Bainbridge A, Wells JA, Davies ND, et al., editors. Measurement of bulk liver perfusion: initial assessment of agreement between ASL and phase-contrast MRI at 9.4T. *Proc Intl Soc Mag Reson Med*; 2013.
231. Hoad C, Costigan C, Marciani L, Kaye P, Spiller R, Gowland PA, et al., editors. Quantifying blood flow and perfusion in liver tissue using phase contrast angiography and arterial spin labelling. *Proc Intl Soc Mag Reson Med*; 2011.
232. Cox EF, Ghezzi A, Bennet A, Patel M, Jackson A, Harman D, et al., editors. A novel MRI protocol to examine haemodynamic compartments in compensated liver cirrhosis. *Proc Intl Soc Mag Reson Med*; 2013.
233. Foley LM, Picot P, Thompson RT, Yau MJ, Brauer M. In vivo monitoring of hepatic oxygenation changes in chronically ethanol-treated rats by functional magnetic resonance imaging. *Magnetic resonance in medicine : official journal of the Society of Magnetic Resonance in Medicine / Society of Magnetic Resonance in Medicine*. 2003;50(5):976-83.
234. Barash H, Gross E, Matot I, Edrei Y, Tsarfaty G, Spira G, et al. Functional MR imaging during hypercapnia and hyperoxia: noninvasive tool for monitoring changes in liver perfusion and hemodynamics in a rat model. *Radiology*. 2007;243(3):727-35.
235. Barash H, Gross E, Edrei Y, Pappo O, Spira G, Vlodayvsky I, et al. Functional magnetic resonance imaging monitoring of pathological changes in rodent livers during hyperoxia and hypercapnia. *Hepatology*. 2008;48(4):1232-41.
236. Jin N, Deng J, Chadashvili T, Zhang Y, Guo Y, Zhang Z, et al. Carbogen gas-challenge BOLD MR imaging in a rat model of diethylnitrosamine-induced liver fibrosis. *Radiology*. 2010;254(1):129-37.
237. Sorensen A, Holm D, Pedersen M, Tietze A, Stausbol-Gron B, Duus L, et al. Left-right difference in fetal liver oxygenation during hypoxia estimated by BOLD MRI in a fetal sheep model. *Ultrasound in obstetrics & gynecology : the official journal of the International Society of Ultrasound in Obstetrics and Gynecology*. 2011;38(6):665-72.

238. Fan Z, Elzibak A, Boylan C, Noseworthy MD. Blood oxygen level-dependent magnetic resonance imaging of the human liver: preliminary results. *Journal of computer assisted tomography*. 2010;34(4):523-31.
239. Haque M, Koktzoglou I, Li W, Carbray J, Prasad P. Functional MRI of liver using BOLD MRI: effect of glucose. *Journal of magnetic resonance imaging : JMRI*. 2010;32(4):988-91.
240. Choi JW, Kim H, Kim HC, Lee Y, Kwon J, Yoo RE, et al. Blood Oxygen Level-dependent MRI for Evaluation of Early Response of Liver Tumors to Chemoembolization: an Animal Study. *Anticancer research*. 2013;33(5):1887-92.
241. Jhaveri KS, Cleary SP, Fischer S, Haider MA, Pargoankar V, Khalidi K, et al. Blood oxygen level-dependent liver MRI: can it predict microvascular invasion in HCC? *Journal of magnetic resonance imaging : JMRI*. 2013;37(3):692-9.
242. Lerner R.M PKJ, editor. Sonoelasticity in ultrasonic tissue characterization and echographic imaging. *Proc Eur Commun Worksh; 1987 7th October 1987; Nijmegen*.
243. Lerner R.M PKJ. Sonoelasticity imaging. In: L.W. K, editor. *Acoustic Imaging*. The Netherlands 1988. p. 317-27.
244. Sandrin L, Fourquet B, Hasquenoph JM, Yon S, Fournier C, Mal F, et al. Transient elastography: a new noninvasive method for assessment of hepatic fibrosis. *Ultrasound in medicine & biology*. 2003;29(12):1705-13.
245. Sandrin L, Tanter M, Gennisson JL, Catheline S, Fink M. Shear elasticity probe for soft tissues with 1-D transient elastography. *IEEE transactions on ultrasonics, ferroelectrics, and frequency control*. 2002;49(4):436-46.
246. Torr GR. The acoustic radiation force. *American Journal of Physics*. 1984;52:402-08.
247. Nightingale KR, Kornguth PJ, Walker WF, McDermott BA, Trahey GE. A novel ultrasonic technique for differentiating cysts from solid lesions: preliminary results in the breast. *Ultrasound in medicine & biology*. 1995;21(6):745-51.
248. Nightingale K. Acoustic Radiation Force Impulse (ARFI) Imaging: a Review. *Current medical imaging reviews*. 2011;7(4):328-39.
249. Rizzo L, Attanasio M, Pinzone MR, Berretta M, Malaguarnera M, Morra A, et al. A new sampling method for spleen stiffness measurement based on quantitative acoustic radiation force impulse elastography for noninvasive assessment of esophageal varices in newly diagnosed HCV-related cirrhosis. *BioMed research international*. 2014;2014:365982.
250. Rockey DC. Noninvasive assessment of liver fibrosis and portal hypertension with transient elastography. *Gastroenterology*. 2008;134(1):8-14.
251. Carrion JA, Navasa M, Bosch J, Bruguera M, Gilibert R, Forns X. Transient elastography for diagnosis of advanced fibrosis and portal hypertension in patients with hepatitis C recurrence after liver transplantation. *Liver Transpl*. 2006;12(12):1791-8.
252. Vizzutti F, Arena U, Romanelli RG, Rega L, Foschi M, Colagrande S, et al. Liver stiffness measurement predicts severe portal hypertension in patients with HCV-related cirrhosis. *Hepatology*. 2007;45(5):1290-7.
253. Augustin S, Millan L, Gonzalez A, Martell M, Gelabert A, Segarra A, et al. Detection of early portal hypertension with routine data and liver stiffness in patients with asymptomatic liver disease: a prospective study. *J Hepatol*. 2014;60(3):561-9.
254. Berzigotti A, Seijo S, Arena U, Abraldes JG, Vizzutti F, Garcia-Pagan JC, et al. Elastography, spleen size, and platelet count identify portal hypertension in patients with compensated cirrhosis. *Gastroenterology*. 2013;144(1):102-11 e1.
255. Bureau C, Metivier S, Peron JM, Selves J, Robic MA, Gourraud PA, et al. Transient elastography accurately predicts presence of significant portal hypertension in patients with chronic liver disease. *Aliment Pharmacol Ther*. 2008;27(12):1261-8.
256. Hong WK, Kim MY, Baik SK, Shin SY, Kim JM, Kang YS, et al. The usefulness of non-invasive liver stiffness measurements in predicting clinically significant portal hypertension in cirrhotic patients: Korean data. *Clinical and molecular hepatology*. 2013;19(4):370-5.

257. Kitson MT, Roberts SK, Colman JC, Paul E, Button P, Kemp W. Liver stiffness and the prediction of clinically significant portal hypertension and portal hypertensive complications. *Scand J Gastroenterol.* 2015;1-8.
258. Schwabl P, Bota S, Salzl P, Mandorfer M, Payer BA, Ferlitsch A, et al. New reliability criteria for transient elastography increase the number of accurate measurements for screening of cirrhosis and portal hypertension. *Liver Int.* 2015;35(2):381-90.
259. Shi KQ, Fan YC, Pan ZZ, Lin XF, Liu WY, Chen YP, et al. Transient elastography: a meta-analysis of diagnostic accuracy in evaluation of portal hypertension in chronic liver disease. *Liver Int.* 2013;33(1):62-71.
260. Colecchia A, Montrone L, Scaioli E, Bacchi-Reggiani ML, Colli A, Casazza G, et al. Measurement of spleen stiffness to evaluate portal hypertension and the presence of esophageal varices in patients with HCV-related cirrhosis. *Gastroenterology.* 2012;143(3):646-54.
261. Sharma P, Kirnake V, Tyagi P, Bansal N, Singla V, Kumar A, et al. Spleen stiffness in patients with cirrhosis in predicting esophageal varices. *Am J Gastroenterol.* 2013;108(7):1101-7.
262. Calvaruso V, Bronte F, Conte E, Simone F, Craxi A, Di Marco V. Modified spleen stiffness measurement by transient elastography is associated with presence of large oesophageal varices in patients with compensated hepatitis C virus cirrhosis. *Journal of viral hepatitis.* 2013;20(12):867-74.
263. Goldschmidt I, Brauch C, Poynard T, Baumann U. Spleen stiffness measurement by transient elastography to diagnose portal hypertension in children. *Journal of pediatric gastroenterology and nutrition.* 2014;59(2):197-203.
264. Stefanescu H, Grigorescu M, Lupsor M, Procopet B, Maniu A, Badea R. Spleen stiffness measurement using Fibroscan for the noninvasive assessment of esophageal varices in liver cirrhosis patients. *J Gastroenterol Hepatol.* 2011;26(1):164-70.
265. Fraquelli M, Giunta M, Pozzi R, Rigamonti C, Della Valle S, Massironi S, et al. Feasibility and reproducibility of spleen transient elastography and its role in combination with liver transient elastography for predicting the severity of chronic viral hepatitis. *Journal of viral hepatitis.* 2014;21(2):90-8.
266. Singh S, Eaton JE, Murad MH, Tanaka H, Iijima H, Talwalkar JA. Accuracy of spleen stiffness measurement in detection of esophageal varices in patients with chronic liver disease: systematic review and meta-analysis. *Clinical gastroenterology and hepatology : the official clinical practice journal of the American Gastroenterological Association.* 2014;12(6):935-45 e4.
267. Robic MA, Procopet B, Metivier S, Peron JM, Selves J, Vinel JP, et al. Liver stiffness accurately predicts portal hypertension related complications in patients with chronic liver disease: a prospective study. *J Hepatol.* 2011;55(5):1017-24.
268. Colecchia A, Colli A, Casazza G, Mandolesi D, Schiumerini R, Reggiani LB, et al. Spleen stiffness measurement can predict clinical complications in compensated HCV-related cirrhosis: a prospective study. *J Hepatol.* 2014;60(6):1158-64.
269. Castera L, Pinzani M, Bosch J. Non invasive evaluation of portal hypertension using transient elastography. *J Hepatol.* 2012;56(3):696-703.
270. Thabut D, Moreau R, Lebrech D. Noninvasive assessment of portal hypertension in patients with cirrhosis. *Hepatology.* 2011;53(2):683-94.
271. Llop E, Berzigotti A, Reig M, Erice E, Reverter E, Seijo S, et al. Assessment of portal hypertension by transient elastography in patients with compensated cirrhosis and potentially resectable liver tumors. *J Hepatol.* 2012;56(1):103-8.
272. Elkrief L, Rautou PE, Ronot M, Lambert S, Dioguardi Burgio M, Francoz C, et al. Prospective Comparison of Spleen and Liver Stiffness by Using Shear-Wave and Transient Elastography for Detection of Portal Hypertension in Cirrhosis. *Radiology.* 2014;141210.
273. Procopet B, Berzigotti A, Abraldes JG, Turon F, Hernandez-Gea V, Garcia-Pagan JC, et al. Real-time shear-wave elastography: applicability, reliability and accuracy for clinically significant portal hypertension. *J Hepatol.* 2014.

274. Rifai K, Cornberg J, Bahr M, Mederacke I, Potthoff A, Wedemeyer H, et al. ARFI elastography of the spleen is inferior to liver elastography for the detection of portal hypertension. *Ultraschall Med.* 2011;32 Suppl 2:E24-30.
275. Salzl P, Reiberger T, Ferlitsch M, Payer BA, Schwengerer B, Trauner M, et al. Evaluation of portal hypertension and varices by acoustic radiation force impulse imaging of the liver compared to transient elastography and AST to platelet ratio index. *Ultraschall Med.* 2014;35(6):528-33.
276. Vermehren J, Polta A, Zimmermann O, Herrmann E, Poynard T, Hofmann WP, et al. Comparison of acoustic radiation force impulse imaging with transient elastography for the detection of complications in patients with cirrhosis. *Liver Int.* 2012;32(5):852-8.
277. Gao J, Ran HT, Ye XP, Zheng YY, Zhang DZ, Wang ZG. The stiffness of the liver and spleen on ARFI Imaging pre and post TIPS placement: a preliminary observation. *Clinical imaging.* 2012;36(2):135-41.
278. Ran HT, Ye XP, Zheng YY, Zhang DZ, Wang ZG, Chen J, et al. Spleen stiffness and splenoportal venous flow: assessment before and after transjugular intrahepatic portosystemic shunt placement. *J Ultrasound Med.* 2013;32(2):221-8.
279. Furuichi Y, Moriyasu F, Taira J, Sugimoto K, Sano T, Ichimura S, et al. Noninvasive diagnostic method for idiopathic portal hypertension based on measurements of liver and spleen stiffness by ARFI elastography. *J Gastroenterol.* 2013;48(9):1061-8.
280. Bota S, Sporea I, Sirli R, Focsa M, Popescu A, Danila M, et al. Can ARFI elastography predict the presence of significant esophageal varices in newly diagnosed cirrhotic patients? *Annals of hepatology.* 2012;11(4):519-25.
281. Bota S, Sporea I, Sirli R, Popescu A, Danila M, Sendroiu M, et al. Spleen assessment by Acoustic Radiation Force Impulse Elastography (ARFI) for prediction of liver cirrhosis and portal hypertension. *Medical ultrasonography.* 2010;12(3):213-7.
282. Han JY, Cho JH, Kwon HJ, Nam KJ. Predicting portal hypertension as assessed by acoustic radiation force impulse: correlations with the Doppler ultrasound. *The British journal of radiology.* 2012;85(1016):e404-9.
283. Takuma Y, Nouse K, Morimoto Y, Tomokuni J, Sahara A, Toshikuni N, et al. Measurement of spleen stiffness by acoustic radiation force impulse imaging identifies cirrhotic patients with esophageal varices. *Gastroenterology.* 2013;144(1):92-101 e2.
284. Karlas T, Lindner F, Troltsch M, Keim V. Assessment of spleen stiffness using acoustic radiation force impulse imaging (ARFI): definition of examination standards and impact of breathing maneuvers. *Ultraschall Med.* 2014;35(1):38-43.
285. Muthupillai R, Ehman RL. Magnetic resonance elastography. *Nature medicine.* 1996;2(5):601-3.
286. Muthupillai R, Lomas DJ, Rossman PJ, Greenleaf JF, Manduca A, Ehman RL. Magnetic resonance elastography by direct visualization of propagating acoustic strain waves. *Science.* 1995;269(5232):1854-7.
287. Venkatesh SK, Ehman RL. Magnetic resonance elastography of abdomen. *Abdominal imaging.* 2014.
288. Venkatesh SK, Ehman RL. Magnetic resonance elastography of liver. *Magnetic resonance imaging clinics of North America.* 2014;22(3):433-46.
289. Venkatesh SK, Yin M, Ehman RL. Magnetic resonance elastography of liver: clinical applications. *Journal of computer assisted tomography.* 2013;37(6):887-96.
290. Venkatesh SK, Yin M, Ehman RL. Magnetic resonance elastography of liver: technique, analysis, and clinical applications. *Journal of magnetic resonance imaging : JMRI.* 2013;37(3):544-55.
291. Yin M, Chen J, Glaser KJ, Talwalkar JA, Ehman RL. Abdominal magnetic resonance elastography. *Topics in magnetic resonance imaging : TMRI.* 2009;20(2):79-87.
292. Hamhaber U, Grieshaber FA, Nagel JH, Klose U. Comparison of quantitative shear wave MR-elastography with mechanical compression tests. *Magnetic resonance in medicine : official journal of the Society of Magnetic Resonance in Medicine / Society of Magnetic Resonance in Medicine.* 2003;49(1):71-7.

293. Hirsch S, Beyer F, Guo J, Papazoglou S, Tzschentsch H, Braun J, et al. Compression-sensitive magnetic resonance elastography. *Physics in medicine and biology*. 2013;58(15):5287-99.
294. Hirsch S, Guo J, Reiter R, Papazoglou S, Kroencke T, Braun J, et al. MR elastography of the liver and the spleen using a piezoelectric driver, single-shot wave-field acquisition, and multifrequency dual parameter reconstruction. *Magnetic resonance in medicine : official journal of the Society of Magnetic Resonance in Medicine / Society of Magnetic Resonance in Medicine*. 2014;71(1):267-77.
295. Hirsch S, Guo J, Reiter R, Schott E, Buning C, Somasundaram R, et al. Towards compression-sensitive magnetic resonance elastography of the liver: sensitivity of harmonic volumetric strain to portal hypertension. *Journal of magnetic resonance imaging : JMRI*. 2014;39(2):298-306.
296. Nedredal GI, Yin M, McKenzie T, Lillegard J, Luebke-Wheeler J, Talwalkar J, et al. Portal hypertension correlates with splenic stiffness as measured with MR elastography. *Journal of magnetic resonance imaging : JMRI*. 2011;34(1):79-87.
297. Yin M, Kolipaka A, Woodrum DA, Glaser KJ, Romano AJ, Manduca A, et al. Hepatic and splenic stiffness augmentation assessed with MR elastography in an in vivo porcine portal hypertension model. *Journal of magnetic resonance imaging : JMRI*. 2013;38(4):809-15.
298. Ronot M, Lambert S, Elkrief L, Doblas S, Rautou PE, Castera L, et al. Assessment of portal hypertension and high-risk oesophageal varices with liver and spleen three-dimensional multifrequency MR elastography in liver cirrhosis. *European radiology*. 2014;24(6):1394-402.
299. Guo J, Buning C, Schott E, Kroncke T, Braun J, Sack I, et al. In Vivo Abdominal Magnetic Resonance Elastography for the Assessment of Portal Hypertension Before and After Transjugular Intrahepatic Portosystemic Shunt Implantation. *Investigative radiology*. 2015.
300. Morisaka H, Motosugi U, Ichikawa S, Sano K, Ichikawa T, Enomoto N. Association of splenic MR elastographic findings with gastroesophageal varices in patients with chronic liver disease. *Journal of magnetic resonance imaging : JMRI*. 2015;41(1):117-24.
301. Sun HY, Lee JM, Han JK, Choi BI. Usefulness of MR elastography for predicting esophageal varices in cirrhotic patients. *Journal of magnetic resonance imaging : JMRI*. 2014;39(3):559-66.
302. Talwalkar JA, Yin M, Venkatesh S, Rossman PJ, Grimm RC, Manduca A, et al. Feasibility of in vivo MR elastographic splenic stiffness measurements in the assessment of portal hypertension. *AJR Am J Roentgenol*. 2009;193(1):122-7.
303. Asrani SK, Talwalkar JA, Kamath PS, Shah VH, Saracino G, Jennings L, et al. Role of magnetic resonance elastography in compensated and decompensated liver disease. *J Hepatol*. 2014;60(5):934-9.
304. Yin M, Talwalkar JA, Glaser KJ, Venkatesh SK, Chen J, Manduca A, et al. Dynamic postprandial hepatic stiffness augmentation assessed with MR elastography in patients with chronic liver disease. *AJR Am J Roentgenol*. 2011;197(1):64-70.
305. Shin SU, Lee JM, Yu MH, Yoon JH, Han JK, Choi BI, et al. Prediction of esophageal varices in patients with cirrhosis: usefulness of three-dimensional MR elastography with echo-planar imaging technique. *Radiology*. 2014;272(1):143-53.
306. Almeida-Melo CR, Grimaud JA, Andrade ZA. Changes in the rat liver induced by total portal vein ligation. *Brazilian journal of medical and biological research = Revista brasileira de pesquisas medicas e biologicas / Sociedade Brasileira de Biofisica [et al]*. 1983;16(1):49-53.
307. Miquel M, Bartoli R, Odena G, Serafin A, Cabre E, Galan A, et al. Rat CCl₄-induced cirrhosis plus total portal vein ligation: a new model for the study of hyperammonaemia and brain oedema. *Liver Int*. 2010;30(7):979-87.
308. D'Almeida MS, Cailmail S, Lebrec D. Validation of transit-time ultrasound flow probes to directly measure portal blood flow in conscious rats. *The American journal of physiology*. 1996;271(6 Pt 2):H2701-9.

309. Leach KG, Karran SJ, Wisbey ML, Blumgart LH. In vivo assessment of liver size in the rat. *Journal of nuclear medicine : official publication, Society of Nuclear Medicine*. 1975;16(5):380-5.
310. Peeters F, Annet L, Hermoye L, Van Beers BE. Inflow correction of hepatic perfusion measurements using T1-weighted, fast gradient-echo, contrast-enhanced MRI. *Magnetic resonance in medicine : official journal of the Society of Magnetic Resonance in Medicine / Society of Magnetic Resonance in Medicine*. 2004;51(4):710-7.
311. Dale BM, Jesberger JA, Lewin JS, Hillenbrand CM, Duerk JL. Determining and optimizing the precision of quantitative measurements of perfusion from dynamic contrast enhanced MRI. *Journal of magnetic resonance imaging : JMRI*. 2003;18(5):575-84.
312. Miyazaki S, Murase K, Yoshikawa T, Morimoto S, Ohno Y, Sugimura K. A quantitative method for estimating hepatic blood flow using a dual-input single-compartment model. *The British journal of radiology*. 2008;81(970):790-800.
313. Sourbron SP, Buckley DL. On the scope and interpretation of the Tofts models for DCE-MRI. *Magnetic resonance in medicine : official journal of the Society of Magnetic Resonance in Medicine / Society of Magnetic Resonance in Medicine*. 2011;66(3):735-45.
314. Araki M, Inaba H, Mizuguchi T. Differential effects of halothane, enflurane, isoflurane, and sevoflurane on the hemodynamics and metabolism in the perfused rat liver in fasted rats. *Journal of anesthesia*. 1995;9(1):52-7.
315. Debaene B, Goldfarb G, Braillon A, Jolis P, Lebrec D. Effects of ketamine, halothane, enflurane, and isoflurane on systemic and splanchnic hemodynamics in normovolemic and hypovolemic cirrhotic rats. *Anesthesiology*. 1990;73(1):118-24.
316. Gatecel C, Losser MR, Payen D. The postoperative effects of halothane versus isoflurane on hepatic artery and portal vein blood flow in humans. *Anesthesia and analgesia*. 2003;96(3):740-5, table of contents.
317. Grundmann U, Zissis A, Bauer C, Bauer M. In vivo effects of halothane, enflurane, and isoflurane on hepatic sinusoidal microcirculation. *Acta anaesthesiologica Scandinavica*. 1997;41(6):760-5.
318. Cray SH, Crawford MW, Khayyam N, Carmichael FJ. Effects of hypoxia and isoflurane on liver blood flow: the role of adenosine. *British journal of anaesthesia*. 2001;86(3):425-7.
319. Schmidt R, Hoetzel A, Baechle T, Loop T, Humar M, Bauer M, et al. Isoflurane pretreatment lowers portal venous resistance by increasing hepatic heme oxygenase activity in the rat liver in vivo. *J Hepatol*. 2004;41(5):706-13.
320. Christian TF, Rettmann DW, Aletras AH, Liao SL, Taylor JL, Balaban RS, et al. Absolute myocardial perfusion in canines measured by using dual-bolus first-pass MR imaging. *Radiology*. 2004;232(3):677-84.
321. Risse F, Semmler W, Kauczor HU, Fink C. Dual-bolus approach to quantitative measurement of pulmonary perfusion by contrast-enhanced MRI. *Journal of magnetic resonance imaging : JMRI*. 2006;24(6):1284-90.
322. Ding Y, Rao SX, Meng T, Chen C, Li R, Zeng MS. Usefulness of T1 mapping on Gd-EOB-DTPA-enhanced MR imaging in assessment of non-alcoholic fatty liver disease. *European radiology*. 2014;24(4):959-66.
323. Haimerl M, Verloh N, Zeman F, Fellner C, Muller-Wille R, Schreyer AG, et al. Assessment of clinical signs of liver cirrhosis using T1 mapping on Gd-EOB-DTPA-enhanced 3T MRI. *PloS one*. 2013;8(12):e85658.
324. Katsube T, Okada M, Kumano S, Hori M, Imaoka I, Ishii K, et al. Estimation of liver function using T1 mapping on Gd-EOB-DTPA-enhanced magnetic resonance imaging. *Investigative radiology*. 2011;46(4):277-83.
325. Pujol J. The solution of nonlinear inverse problems and the Levenberg-Marquardt method. *Geophysics*. 2007;72(4):W1-W16.
326. Dobre MC, Ugurbil K, Marjanska M. Determination of blood longitudinal relaxation time (T1) at high magnetic field strengths. *Magnetic resonance imaging*. 2007;25(5):733-5.
327. Sarkar SK, Clark RK, Rycyna RE, Mattingly MA, Greig R. 9.4-T NMR microimaging studies of hepatic metastases of human colorectal tumors in nude mice. *Magnetic*

- resonance in medicine : official journal of the Society of Magnetic Resonance in Medicine / Society of Magnetic Resonance in Medicine. 1989;12(2):268-73.
328. Zhang X, Petersen ET, Ghariq E, De Vis JB, Webb AG, Teeuwisse WM, et al. In vivo blood T1 measurements at 1.5 T, 3 T, and 7 T. *Magnetic resonance in medicine : official journal of the Society of Magnetic Resonance in Medicine / Society of Magnetic Resonance in Medicine*. 2013;70(4):1082-6.
329. Silvennoinen MJ, Kettunen MI, Kauppinen RA. Effects of hematocrit and oxygen saturation level on blood spin-lattice relaxation. *Magnetic resonance in medicine : official journal of the Society of Magnetic Resonance in Medicine / Society of Magnetic Resonance in Medicine*. 2003;49(3):568-71.
330. Kim YR, Rebro KJ, Schmainda KM. Water exchange and inflow affect the accuracy of T1-GRE blood volume measurements: implications for the evaluation of tumor angiogenesis. *Magnetic resonance in medicine : official journal of the Society of Magnetic Resonance in Medicine / Society of Magnetic Resonance in Medicine*. 2002;47(6):1110-20.
331. Nazarpour M. Effect of concentration of contrast agent on the inflow effect for measuring absolute perfusion by use of inversion recovery T(1)-weighted TurboFLASH images. *Radiological physics and technology*. 2012;5(1):86-91.
332. Christian TF, Aletras AH, Arai AE. Estimation of absolute myocardial blood flow during first-pass MR perfusion imaging using a dual-bolus injection technique: comparison to single-bolus injection method. *Journal of magnetic resonance imaging : JMRI*. 2008;27(6):1271-7.
333. Kershaw LE, Cheng HL. A general dual-bolus approach for quantitative DCE-MRI. *Magnetic resonance imaging*. 2011;29(2):160-6.
334. Wu O, Ostergaard L, Koroshetz WJ, Schwamm LH, O'Donnell J, Schaefer PW, et al. Effects of tracer arrival time on flow estimates in MR perfusion-weighted imaging. *Magnetic resonance in medicine : official journal of the Society of Magnetic Resonance in Medicine / Society of Magnetic Resonance in Medicine*. 2003;50(4):856-64.
335. Buckler AJ, Bresolin L, Dunnick NR, Sullivan DC, Group. A collaborative enterprise for multi-stakeholder participation in the advancement of quantitative imaging. *Radiology*. 2011;258(3):906-14.
336. Ivancevic MK, Zimine I, Foxall D, Lecoq G, Righetti A, Didier D, et al. Inflow effect in first-pass cardiac and renal MRI. *Journal of magnetic resonance imaging : JMRI*. 2003;18(3):372-6.
337. Ivancevic MK, Zimine I, Montet X, Hyacinthe JN, Lazeyras F, Foxall D, et al. Inflow effect correction in fast gradient-echo perfusion imaging. *Magnetic resonance in medicine : official journal of the Society of Magnetic Resonance in Medicine / Society of Magnetic Resonance in Medicine*. 2003;50(5):885-91.
338. Carr JC, Carr JC, Carroll TJ, SpringerLink. *Magnetic resonance angiography [electronic resource] : principles and applications*. New York: Springer Science+Business Media, 2012.
339. McRobbie DW. *MRI from picture to proton*. 2nd ed. Cambridge, UK.: Cambridge University Press, 2007.
340. Richter S, Mucke I, Menger MD, Vollmar B. Impact of intrinsic blood flow regulation in cirrhosis: maintenance of hepatic arterial buffer response. *Am J Physiol Gastrointest Liver Physiol*. 2000;279(2):G454-62.
341. Nishimura DG, Jackson JI, Pauly JM. On the nature and reduction of the displacement artifact in flow images. *Magnetic resonance in medicine : official journal of the Society of Magnetic Resonance in Medicine / Society of Magnetic Resonance in Medicine*. 1991;22(2):481-92.
342. Lagerstrand KM, Lehmann H, Starck G, Vikhoff-Baaz B, Ekholm S, Forssell-Aronsson E. Method to correct for the effects of limited spatial resolution in phase-contrast flow MRI measurements. *Magnetic resonance in medicine : official journal of the Society of Magnetic Resonance in Medicine / Society of Magnetic Resonance in Medicine*. 2002;48(5):883-9.

343. Lagerstrand KM, Vikhoff-Baaz B, Starck G, Forssell-Aronsson E. Quantitative phase-contrast flow MRI measurements in the presence of a second vessel closely positioned to the examined vessel. *Journal of magnetic resonance imaging : JMRI*. 2006;23(2):156-62.
344. Lagerstrand KM, Vikhoff-Baaz B, Starck G, Forssell-Aronsson E. Contrast agent influences MRI phase-contrast flow measurements in small vessels. *Magnetic resonance in medicine : official journal of the Society of Magnetic Resonance in Medicine / Society of Magnetic Resonance in Medicine*. 2010;64(1):42-6.
345. Lorenz R, Bock J, Snyder J, Korvink JG, Jung BA, Markl M. Influence of eddy current, Maxwell and gradient field corrections on 3D flow visualization of 3D CINE PC-MRI data. *Magnetic resonance in medicine : official journal of the Society of Magnetic Resonance in Medicine / Society of Magnetic Resonance in Medicine*. 2013.
346. Rigsby CK, Hilpiper N, McNeal GR, Zhang G, Boylan EE, Popescu AR, et al. Analysis of an automated background correction method for cardiovascular MR phase contrast imaging in children and young adults. *Pediatric radiology*. 2014;44(3):265-73.
347. Giese D, Haeberlin M, Barmet C, Pruessmann KP, Schaeffter T, Kozerke S. Analysis and correction of background velocity offsets in phase-contrast flow measurements using magnetic field monitoring. *Magnetic resonance in medicine : official journal of the Society of Magnetic Resonance in Medicine / Society of Magnetic Resonance in Medicine*. 2012;67(5):1294-302.
348. Alemayehu A, Lock KR, Coatney RW, Chou CC. L-NAME, nitric oxide and jejunal motility, blood flow and oxygen uptake in dogs. *British journal of pharmacology*. 1994;111(1):205-12.
349. Asfar P, Radermacher P, Cales P, Oberti F. The effects of vasopressin and its analogues on the liver and its disorders in the critically ill. *Curr Opin Crit Care*. 2010;16(2):148-52.
350. Harry D, Anand R, Holt S, Davies S, Marley R, Fernando B, et al. Increased sensitivity to endotoxemia in the bile duct-ligated cirrhotic Rat. *Hepatology*. 1999;30(5):1198-205.
351. Coll M, Rodriguez S, Raurell I, Ezkurdia N, Brull A, Augustin S, et al. Droxidopa, an oral norepinephrine precursor, improves hemodynamic and renal alterations of portal hypertensive rats. *Hepatology*. 2012;56(5):1849-60.
352. Houdijk AP, Teerlink T, Visser JJ, van Lambalgen AA, van Leeuwen PA. Arginine deficiency in bile duct-ligated rats after surgery: the role of plasma arginase and gut endotoxin restriction. *Gastroenterology*. 1997;113(4):1375-83.
353. Lin HC, Huang YT, Wei HC, Yang YY, Lee TY, Wang YW, et al. Hemodynamic effects of one week of carvedilol administration on cirrhotic rats. *J Gastroenterol*. 2006;41(4):361-8.
354. Lanzer P, Botvinick EH, Schiller NB, Crooks LE, Arakawa M, Kaufman L, et al. Cardiac imaging using gated magnetic resonance. *Radiology*. 1984;150(1):121-7.
355. Pelc NJ, Herfkens RJ, Shimakawa A, Enzmann DR. Phase contrast cine magnetic resonance imaging. *Magnetic resonance quarterly*. 1991;7(4):229-54.
356. Latt WW, Legare DJ, d'Almeida MS. Adenosine as putative regulator of hepatic arterial flow (the buffer response). *The American journal of physiology*. 1985;248(3 Pt 2):H331-8.
357. Richter S, Olinger A, Hildebrandt U, Menger MD, Vollmar B. Loss of physiologic hepatic blood flow control ("hepatic arterial buffer response") during CO₂-pneumoperitoneum in the rat. *Anesthesia and analgesia*. 2001;93(4):872-7.
358. Covey AM, Brody LA, Maluccio MA, Getrajdman GI, Brown KT. Variant hepatic arterial anatomy revisited: digital subtraction angiography performed in 600 patients. *Radiology*. 2002;224(2):542-7.
359. Hiatt JR, Gabbay J, Busuttil RW. Surgical anatomy of the hepatic arteries in 1000 cases. *Annals of surgery*. 1994;220(1):50-2.
360. Song SY, Chung JW, Yin YH, Jae HJ, Kim HC, Jeon UB, et al. Celiac axis and common hepatic artery variations in 5002 patients: systematic analysis with spiral CT and DSA. *Radiology*. 2010;255(1):278-88.

361. Gray H, Carter HV. Gray's anatomy. 2nd ed. London: Arcturus, 2010.
362. Winbladh A. Microdialysis in liver ischemia and reperfusion injury. Linköping: Department of Clinical and Experimental Medicine, Linköping University, 2011.
363. Hockings PD, Busza AL, Byrne J, Patel B, Smart SC, Reid DG, et al. Validation of MRI measurement of cardiac output in the dog: the effects of dobutamine and minoxidil. *Toxicology mechanisms and methods*. 2003;13(1):39-43.
364. James SH, Wald R, Wintersperger BJ, Jimenez-Juan L, Deva D, Crean AM, et al. Accuracy of right and left ventricular functional assessment by short-axis vs axial cine steady-state free-precession magnetic resonance imaging: inpatient correlation with main pulmonary artery and ascending aorta phase-contrast flow measurements. *Canadian Association of Radiologists journal = Journal l'Association canadienne des radiologistes*. 2013;64(3):213-9.
365. Kondo C, Caputo GR, Semelka R, Foster E, Shimakawa A, Higgins CB. Right and left ventricular stroke volume measurements with velocity-encoded cine MR imaging: in vitro and in vivo validation. *AJR Am J Roentgenol*. 1991;157(1):9-16.
366. Rudolph AM, Heymann MA. The circulation of the fetus in utero. Methods for studying distribution of blood flow, cardiac output and organ blood flow. *Circulation research*. 1967;21(2):163-84.
367. Van Oosterhout MF, Prinzen FW, Sakurada S, Glenn RW, Hales JR. Fluorescent microspheres are superior to radioactive microspheres in chronic blood flow measurements. *The American journal of physiology*. 1998;275(1 Pt 2):H110-5.
368. Van Oosterhout MF, Willigers HM, Reneman RS, Prinzen FW. Fluorescent microspheres to measure organ perfusion: validation of a simplified sample processing technique. *The American journal of physiology*. 1995;269(2 Pt 2):H725-33.
369. Riegler J, Cheung KK, Man YF, Cleary JO, Price AN, Lythgoe MF. Comparison of segmentation methods for MRI measurement of cardiac function in rats. *Journal of magnetic resonance imaging : JMRI*. 2010;32(4):869-77.
370. Houdijk AP, van Lambalgen AA, Thijs LG, van Leeuwen PA. Gut endotoxin restriction improves postoperative hemodynamics in the bile duct-ligated rat. *Shock*. 1998;9(4):282-8.
371. Steeden JA, Atkinson D, Taylor AM, Muthurangu V. Split-acquisition real-time CINE phase-contrast MR flow measurements. *Magnetic resonance in medicine : official journal of the Society of Magnetic Resonance in Medicine / Society of Magnetic Resonance in Medicine*. 2010;64(6):1664-70.
372. Lee SS, Girod C, Brailion A, Hadengue A, Lebrec D. Hemodynamic characterization of chronic bile duct-ligated rats: effect of pentobarbital sodium. *The American journal of physiology*. 1986;251(2 Pt 1):G176-80.
373. Glenn RW, Bernard S, Brinkley M. Validation of fluorescent-labeled microspheres for measurement of regional organ perfusion. *Journal of applied physiology*. 1993;74(5):2585-97.
374. Rajekar H, Chawla Y. Terlipressin in hepatorenal syndrome: Evidence for present indications. *J Gastroenterol Hepatol*. 2011;26 Suppl 1:109-14.
375. British Medical A, Royal Pharmaceutical Society of Great B. BNF : British national formulary. London: British Medical Association, 2014.
376. Chang FC, Huang YT, Lin HC, Hong CY, Lin JG, Chen KJ. Beneficial effects of combined terlipressin and tetramethylpyrazine administration on portal hypertensive rats. *Canadian journal of physiology and pharmacology*. 1999;77(8):618-24.
377. Chen CT, Chu CJ, Lee FY, Chang FY, Wang SS, Lin HC, et al. Splanchnic hyposensitivity to glypressin in a hemorrhage-transfused common bile duct-ligated rat model of portal hypertension: role of nitric oxide and bradykinin. *Hepatology*. 2009;56(94-95):1261-7.
378. Martins HS, Koike MK, Velasco IT. Effects of terlipressin and naloxone compared with epinephrine in a rat model of asphyxia-induced cardiac arrest. *Clinics*. 2013;68(8):1146-51.

379. Dewachter P, Jouan-Hureaux V, Lartaud I, Bello G, de Talance N, Longrois D, et al. Comparison of arginine vasopressin, terlipressin, or epinephrine to correct hypotension in a model of anaphylactic shock in anesthetized brown Norway rats. *Anesthesiology*. 2006;104(4):734-41.
380. Moreau R, Durand F, Poynard T, Duhamel C, Cervoni JP, Ichai P, et al. Terlipressin in patients with cirrhosis and type 1 hepatorenal syndrome: a retrospective multicenter study. *Gastroenterology*. 2002;122(4):923-30.
381. Berzigotti A, De Gottardi A, Vukotic R, Siramolpiwat S, Abraldes JG, Garcia-Pagan JC, et al. Effect of meal ingestion on liver stiffness in patients with cirrhosis and portal hypertension. *PloS one*. 2013;8(3):e58742.
382. Burkart DJ, Johnson CD, Reading CC, Ehman RL. MR measurements of mesenteric venous flow: prospective evaluation in healthy volunteers and patients with suspected chronic mesenteric ischemia. *Radiology*. 1995;194(3):801-6.
383. Iwao T, Toyonaga A, Oho K, Sakai T, Tayama C, Masumoto H, et al. Postprandial splanchnic hemodynamic response in patients with cirrhosis of the liver: evaluation with "triple-vessel" duplex US. *Radiology*. 1996;201(3):711-5.
384. Stanley AJ, Forrest EH, Redhead DN, Bouchier IA, Hayes PC. Direct measurement of post-prandial portal haemodynamics in cirrhotic patients with a transjugular intrahepatic portosystemic stent-shunt. *Eur J Gastroenterol Hepatol*. 1998;10(5):393-7.
385. Hines CD, Lindstrom MJ, Varma AK, Reeder SB. Effects of postprandial state and mesenteric blood flow on the repeatability of MR elastography in asymptomatic subjects. *Journal of magnetic resonance imaging : JMRI*. 2011;33(1):239-44.
386. Albillos A, Banares R, Gonzalez M, Catalina MV, Pastor O, Gonzalez R, et al. The extent of the collateral circulation influences the postprandial increase in portal pressure in patients with cirrhosis. *Gut*. 2007;56(2):259-64.
387. Fisher AJ, Paulson EK, Kliewer MA, DeLong DM, Nelson RC. Doppler sonography of the portal vein and hepatic artery: measurement of a prandial effect in healthy subjects. *Radiology*. 1998;207(3):711-5.
388. Numata K, Tanaka K, Kiba T, Morita K, Saito S, Fujii T, et al. Hepatic arterial resistance after mixed-meal ingestion in healthy subjects and patients with chronic liver disease. *Journal of clinical ultrasound : JCU*. 1999;27(5):239-48.
389. Vermeulen MA, Ligthart-Melis GC, Buijsman R, Siroen MP, van de Poll MC, Boelens PG, et al. Accurate perioperative flow measurement of the portal vein and hepatic and renal artery: a role for preoperative MRI? *Eur J Radiol*. 2012;81(9):2042-8.
390. Raju S, Sanford P, Herman S, Olivier J. Postural and ambulatory changes in regional flow and skin perfusion. *European journal of vascular and endovascular surgery : the official journal of the European Society for Vascular Surgery*. 2012;43(5):567-72.
391. Orton MR, Miyazaki K, Koh DM, Collins DJ, Hawkes DJ, Atkinson D, et al. Optimizing functional parameter accuracy for breath-hold DCE-MRI of liver tumours. *Physics in medicine and biology*. 2009;54(7):2197-215.
392. Makanyanga J, Punwani S, Taylor SA. Assessment of wall inflammation and fibrosis in Crohn's disease: value of T1-weighted gadolinium-enhanced MR imaging. *Abdominal imaging*. 2012;37(6):933-43.
393. Mendichovszky IA, Cutajar M, Gordon I. Reproducibility of the aortic input function (AIF) derived from dynamic contrast-enhanced magnetic resonance imaging (DCE-MRI) of the kidneys in a volunteer study. *Eur J Radiol*. 2009;71(3):576-81.
394. Parker GJ, Roberts C, Macdonald A, Buonaccorsi GA, Cheung S, Buckley DL, et al. Experimentally-derived functional form for a population-averaged high-temporal-resolution arterial input function for dynamic contrast-enhanced MRI. *Magnetic resonance in medicine : official journal of the Society of Magnetic Resonance in Medicine / Society of Magnetic Resonance in Medicine*. 2006;56(5):993-1000.
395. Yang C, Karczmar GS, Medved M, Oto A, Zamora M, Stadler WM. Reproducibility assessment of a multiple reference tissue method for quantitative dynamic contrast enhanced-MRI analysis. *Magnetic resonance in medicine : official journal of the Society of*

- Magnetic Resonance in Medicine / Society of Magnetic Resonance in Medicine. 2009;61(4):851-9.
396. Just N, Koh DM, D'Arcy J, Collins DJ, Leach MO. Assessment of the effect of haematocrit-dependent arterial input functions on the accuracy of pharmacokinetic parameters in dynamic contrast-enhanced MRI. *NMR in biomedicine*. 2011;24(7):902-15.
397. McGrath DM, Bradley DP, Tessier JL, Lacey T, Taylor CJ, Parker GJ. Comparison of model-based arterial input functions for dynamic contrast-enhanced MRI in tumor bearing rats. *Magnetic resonance in medicine : official journal of the Society of Magnetic Resonance in Medicine / Society of Magnetic Resonance in Medicine*. 2009;61(5):1173-84.
398. Meng R, Chang SD, Jones EC, Goldenberg SL, Kozlowski P. Comparison between population average and experimentally measured arterial input function in predicting biopsy results in prostate cancer. *Academic radiology*. 2010;17(4):520-5.
399. De Naeyer D, Debergh I, De Deene Y, Ceelen WP, Segers P, Verdonck P. First order correction for T2*-relaxation in determining contrast agent concentration from spoiled gradient echo pulse sequence signal intensity. *Journal of magnetic resonance imaging : JMRI*. 2011;34(3):710-5.
400. Kleppesto M, Larsson C, Groote I, Salo R, Vardal J, Courivaud F, et al. T2*-correction in dynamic contrast-enhanced MRI from double-echo acquisitions. *Journal of magnetic resonance imaging : JMRI*. 2014;39(5):1314-9.
401. Ingrisich M, Maxien D, Schwab F, Reiser MF, Nikolaou K, Dietrich O. Assessment of pulmonary perfusion with breath-hold and free-breathing dynamic contrast-enhanced magnetic resonance imaging: quantification and reproducibility. *Investigative radiology*. 2014;49(6):382-9.
402. Kino A, Takahashi M, Ashiku SK, Decamp MM, Lenkinski RE, Hatabu H. Optimal breathing protocol for dynamic contrast-enhanced MRI of solitary pulmonary nodules at 3T. *Eur J Radiol*. 2007;64(3):397-400.
403. Maxien D, Ingrisich M, Meinel FG, Reiser M, Dietrich O, Nikolaou K. Quantification of Pulmonary Perfusion with Free-Breathing Dynamic Contrast-Enhanced MRI - A Pilot Study in Healthy Volunteers. *RoFo : Fortschritte auf dem Gebiete der Rontgenstrahlen und der Nuklearmedizin*. 2013.
404. Melbourne A, Atkinson D, Hawkes D. Influence of organ motion and contrast enhancement on image registration. *Medical image computing and computer-assisted intervention : MICCAI International Conference on Medical Image Computing and Computer-Assisted Intervention*. 2008;11(Pt 2):948-55.
405. Rajaraman S, Rodriguez JJ, Graff C, Altbach MI, Dragovich T, Sirlin CB, et al. Automated registration of sequential breath-hold dynamic contrast-enhanced MR images: a comparison of three techniques. *Magnetic resonance imaging*. 2011;29(5):668-82.
406. Hamy V, Dikaos N, Punwani S, Melbourne A, Latifoltojar A, Makanyanga J, et al. Respiratory motion correction in dynamic MRI using robust data decomposition registration - application to DCE-MRI. *Medical image analysis*. 2014;18(2):301-13.
407. Dieringer MA, Deimling M, Santoro D, Wuerfel J, Madai VI, Sobesky J, et al. Rapid parametric mapping of the longitudinal relaxation time T1 using two-dimensional variable flip angle magnetic resonance imaging at 1.5 Tesla, 3 Tesla, and 7 Tesla. *PloS one*. 2014;9(3):e91318.
408. Hurley SA, Yarnykh VL, Johnson KM, Field AS, Alexander AL, Samsonov AA. Simultaneous variable flip angle-actual flip angle imaging method for improved accuracy and precision of three-dimensional T1 and B1 measurements. *Magnetic resonance in medicine : official journal of the Society of Magnetic Resonance in Medicine / Society of Magnetic Resonance in Medicine*. 2012;68(1):54-64.
409. Treier R, Steingoetter A, Fried M, Schwizer W, Boesiger P. Optimized and combined T1 and B1 mapping technique for fast and accurate T1 quantification in contrast-enhanced abdominal MRI. *Magnetic resonance in medicine : official journal of the Society of Magnetic Resonance in Medicine / Society of Magnetic Resonance in Medicine*. 2007;57(3):568-76.

410. Voigt T, Nehrke K, Doessel O, Katscher U. T1 corrected B1 mapping using multi-TR gradient echo sequences. *Magnetic resonance in medicine : official journal of the Society of Magnetic Resonance in Medicine / Society of Magnetic Resonance in Medicine*. 2010;64(3):725-33.
411. Rohrer M, Bauer H, Mintorovitch J, Requardt M, Weinmann HJ. Comparison of magnetic properties of MRI contrast media solutions at different magnetic field strengths. *Investigative radiology*. 2005;40(11):715-24.
412. Carstensen B. *Comparing clinical measurement methods : a practical guide*. Chichester: Wiley, 2010.
413. Baxter S, Wang ZJ, Joe BN, Qayyum A, Taouli B, Yeh BM. Timing bolus dynamic contrast-enhanced (DCE) MRI assessment of hepatic perfusion: Initial experience. *Journal of magnetic resonance imaging : JMRI*. 2009;29(6):1317-22.
414. Patel J, Sigmund EE, Rusinek H, Oei M, Babb JS, Taouli B. Diagnosis of cirrhosis with intravoxel incoherent motion diffusion MRI and dynamic contrast-enhanced MRI alone and in combination: preliminary experience. *Journal of magnetic resonance imaging : JMRI*. 2010;31(3):589-600.
415. Leporq B, Pilleul F, Dumortier J, Guillaud O, Lefort T, Michael S, et al. Liver perfusion quantification with MR-DCE imaging at 3.0 T for liver fibrosis assessment in patients with chronic liver diseases. *Proc Intl Soc Mag Reson Med*. 2013;21:1.
416. Banerjee R, Pavlides M, Tunnicliffe EM, Piechnik SK, Sarania N, Philips R, et al. Multiparametric magnetic resonance for the non-invasive diagnosis of liver disease. *J Hepatol*. 2014;60(1):69-77.
417. de Bazelaire CM, Duhamel GD, Rofsky NM, Alsop DC. MR imaging relaxation times of abdominal and pelvic tissues measured in vivo at 3.0 T: preliminary results. *Radiology*. 2004;230(3):652-9.
418. Lu H, Clingman C, Golay X, van Zijl PC. Determining the longitudinal relaxation time (T1) of blood at 3.0 Tesla. *Magnetic resonance in medicine : official journal of the Society of Magnetic Resonance in Medicine / Society of Magnetic Resonance in Medicine*. 2004;52(3):679-82.
419. Nichols MB, Paschal CB. Measurement of longitudinal (T1) relaxation in the human lung at 3.0 Tesla with tissue-based and regional gradient analyses. *Journal of magnetic resonance imaging : JMRI*. 2008;27(1):224-8.
420. Barnes A, Morgan C, Bainbridge A, Smith L, Rice S, Atkinson D, et al. Repeatability of whole-body T1 mapping using B1 corrected T1 mDIXON imaging. *Proc Intl Soc Mag Reson Med*. 2014:3241.
421. Kanal E, Maravilla K, Rowley HA. *Gadolinium Contrast Agents for CNS Imaging: Current Concepts and Clinical Evidence*. AJNR American journal of neuroradiology. 2014.
422. Shen Y, Snyder C, Goerner F, Moritz R, Runge V. Accurate T1 Relaxivities (r1) of Gadolinium-based Magnetic Resonance Contrast Agents (GBCAs) in Human Whole Blood at 1.5T and 3T. *Radiological Society of North America 2013 Scientific Assembly and Annual Meeting*. 2013.
423. Hormuth DA, 2nd, Skinner JT, Does MD, Yankeelov TE. A comparison of individual and population-derived vascular input functions for quantitative DCE-MRI in rats. *Magnetic resonance imaging*. 2014;32(4):397-401.
424. Bandula S, Banypersad SM, Sado D, Flett AS, Punwani S, Taylor SA, et al. Measurement of Tissue interstitial volume in healthy patients and those with amyloidosis with equilibrium contrast-enhanced MR imaging. *Radiology*. 2013;268(3):858-64.
425. Levitt DG. The pharmacokinetics of the interstitial space in humans. *BMC clinical pharmacology*. 2003;3:3.
426. Zhang JL, Rusinek H, Bokacheva L, Chen Q, Storey P, Lee VS. Use of cardiac output to improve measurement of input function in quantitative dynamic contrast-enhanced MRI. *Journal of magnetic resonance imaging : JMRI*. 2009;30(3):656-65.
427. Stewart GN. Researches on the Circulation Time and on the Influences which affect it. *The Journal of physiology*. 1897;22(3):159-83.

428. Hamilton WF, Remington JW. Comparison of the time concentration curves in arterial blood of dye injected at a constant rate with that of dye injected intravenously. *Federation proceedings*. 1946;5(1 Pt 2):41.
429. Lawson RS. Application of mathematical methods in dynamic nuclear medicine studies. *Physics in medicine and biology*. 1999;44(4):R57-98.
430. Campbell-Washburn AE, Price AN, Wells JA, Thomas DL, Ordidge RJ, Lythgoe MF. Cardiac arterial spin labeling using segmented ECG-gated Look-Locker FAIR: variability and repeatability in preclinical studies. *Magnetic resonance in medicine : official journal of the Society of Magnetic Resonance in Medicine / Society of Magnetic Resonance in Medicine*. 2013;69(1):238-47.
431. Kim SG. Quantification of relative cerebral blood flow change by flow-sensitive alternating inversion recovery (FAIR) technique: application to functional mapping. *Magnetic resonance in medicine : official journal of the Society of Magnetic Resonance in Medicine / Society of Magnetic Resonance in Medicine*. 1995;34(3):293-301.
432. Kwong KK, Chesler DA, Weisskoff RM, Donahue KM, Davis TL, Ostergaard L, et al. MR perfusion studies with T1-weighted echo planar imaging. *Magnetic resonance in medicine : official journal of the Society of Magnetic Resonance in Medicine / Society of Magnetic Resonance in Medicine*. 1995;34(6):878-87.
433. Library MKA. N0027732 Diagram of human liver. Wellcome Images: Wellcome Images; 2014.
434. Look DCLDR. Time Saving in Measurement of NMR and EPR Relaxation Times. *The Review of scientific instruments*. 1970;41(2):250-51.
435. Ramasawmy R, Campbell-Washburn A, Johnson SP, Wells JA, Pedley RB, Lythgoe MF, et al. Repeatability and Variability of Pre-Clinical Hepatic Arterial Spin Labelling. *Proc Intl Soc Mag Reson Med*. 2014;22:2725.
436. Bauer WR, Hiller KH, Roder F, Rommel E, Ertl G, Haase A. Magnetization exchange in capillaries by microcirculation affects diffusion-controlled spin-relaxation: a model which describes the effect of perfusion on relaxation enhancement by intravascular contrast agents. *Magnetic resonance in medicine : official journal of the Society of Magnetic Resonance in Medicine / Society of Magnetic Resonance in Medicine*. 1996;35(1):43-55.
437. Belle V, Kahler E, Waller C, Rommel E, Voll S, Hiller KH, et al. In vivo quantitative mapping of cardiac perfusion in rats using a noninvasive MR spin-labeling method. *Journal of magnetic resonance imaging : JMRI*. 1998;8(6):1240-5.
438. Rice GC, Ryan CJ, Leiberman DP, Mathie RT, McGhee E, Harper AM, et al. Measurement of liver blood flow in the rat using an 85Krypton clearance technique. *British journal of experimental pathology*. 1977;58(3):236-42.
439. Waller C, Kahler E, Hiller KH, Hu K, Nahrendorf M, Voll S, et al. Myocardial perfusion and intracapillary blood volume in rats at rest and with coronary dilatation: MR imaging in vivo with use of a spin-labeling technique. *Radiology*. 2000;215(1):189-97.
440. Waller C, Hiller KH, Voll S, Haase A, Ertl G, Bauer WR. Myocardial perfusion imaging using a non-contrast agent MR imaging technique. *The international journal of cardiovascular imaging*. 2001;17(2):123-32.
441. Deichmann RH, A. Quantification of T1 values by SNAPSHOT-FLASH NMR imaging. *J Magn Reson*. 1992;96(3):608-12.
442. Balasubramanian V, Dhar DK, Warner AE, Vivien Li WY, Amiri AF, Bright B, et al. Importance of Connexin-43 based gap junction in cirrhosis and acute-on-chronic liver failure. *J Hepatol*. 2013;58(6):1194-200.
443. Gunther M, Bock M, Schad LR. Arterial spin labeling in combination with a look-locker sampling strategy: inflow turbo-sampling EPI-FAIR (ITS-FAIR). *Magnetic resonance in medicine : official journal of the Society of Magnetic Resonance in Medicine / Society of Magnetic Resonance in Medicine*. 2001;46(5):974-84.
444. Mathie RT, Leiberman DP, Harper AM, Blumgart LH. The solubility of 85Krypton in the regenerating liver of the rat. *British journal of experimental pathology*. 1977;58(3):231-5.

445. Jalan R, Gines P, Olson JC, Mookerjee RP, Moreau R, Garcia-Tsao G, et al. Acute-on-chronic liver failure. *J Hepatol.* 2012;57(6):1336-48.
446. Moreau R, Arroyo V. Acute on Chronic Liver Failure: A New Clinical Entity. *Clinical gastroenterology and hepatology : the official clinical practice journal of the American Gastroenterological Association.* 2014.
447. Moreau R, Jalan R, Gines P, Pavesi M, Angeli P, Cordoba J, et al. Acute-on-chronic liver failure is a distinct syndrome that develops in patients with acute decompensation of cirrhosis. *Gastroenterology.* 2013;144(7):1426-37, 37 e1-9.
448. Kumar A, Das K, Sharma P, Mehta V, Sharma BC, Sarin SK. Hemodynamic studies in acute-on-chronic liver failure. *Dig Dis Sci.* 2009;54(4):869-78.
449. Garg H, Kumar A, Garg V, Kumar M, Kumar R, Sharma BC, et al. Hepatic and systemic hemodynamic derangements predict early mortality and recovery in patients with acute-on-chronic liver failure. *J Gastroenterol Hepatol.* 2013;28(8):1361-7.
450. Mehta G, Mookerjee RP, Sharma V, Jalan R. Systemic inflammation is associated with increased intrahepatic resistance and mortality in alcohol-related acute-on-chronic liver failure. *Liver Int.* 2014.
451. Jacob G, Nassar N, Hayam G, Ben-Haim S, Edoute Y, Better OS, et al. Cardiac function and responsiveness to beta-adrenoceptor agonists in rats with obstructive jaundice. *The American journal of physiology.* 1993;265(2 Pt 1):G314-20.
452. Ma Z, Lee SS. Cirrhotic cardiomyopathy: getting to the heart of the matter. *Hepatology.* 1996;24(2):451-9.
453. Wiese S, Hove JD, Bendtsen F, Moller S. Cirrhotic cardiomyopathy: pathogenesis and clinical relevance. *Nat Rev Gastroenterol Hepatol.* 2014;11(3):177-86.
454. Haddadian Z, Eftekhari G, Mazloom R, Jazaeri F, Dehpour AR, Mani AR. Effect of endotoxin on heart rate dynamics in rats with cirrhosis. *Autonomic neuroscience : basic & clinical.* 2013;177(2):104-13.
455. Moller S, Hove JD, Dixen U, Bendtsen F. New insights into cirrhotic cardiomyopathy. *International journal of cardiology.* 2013;167(4):1101-8.
456. Caudron J, Fares J, Bauer F, Dacher JN. Evaluation of left ventricular diastolic function with cardiac MR imaging. *Radiographics.* 2011;31(1):239-59.
457. Russell WMS, Burch RL, Hume CW. The principles of humane experimental technique. Special ed. ed. Potters Bar: Universities Federation for Animal Welfare, 1992.
458. Cho KC, Patel YD, Wachsberg RH, Seeff J. Varices in portal hypertension: evaluation with CT. *Radiographics.* 1995;15(3):609-22.
459. Gadaleta RM, van Erpecum KJ, Oldenburg B, Willemsen EC, Renooij W, Murzilli S, et al. Farnesoid X receptor activation inhibits inflammation and preserves the intestinal barrier in inflammatory bowel disease. *Gut.* 2011;60(4):463-72.
460. Fiorucci S, Antonelli E, Rizzo G, Renga B, Mencarelli A, Riccardi L, et al. The nuclear receptor SHP mediates inhibition of hepatic stellate cells by FXR and protects against liver fibrosis. *Gastroenterology.* 2004;127(5):1497-512.
461. Lefebvre P, Cariou B, Lien F, Kuipers F, Staels B. Role of bile acids and bile acid receptors in metabolic regulation. *Physiol Rev.* 2009;89(1):147-91.
462. Vanwijngaerden YM, Wauters J, Langouche L, Vander Perre S, Liddle C, Coulter S, et al. Critical illness evokes elevated circulating bile acids related to altered hepatic transporter and nuclear receptor expression. *Hepatology.* 2011;54(5):1741-52.
463. Wang YD, Chen WD, Wang M, Yu D, Forman BM, Huang W. Farnesoid X receptor antagonizes nuclear factor kappaB in hepatic inflammatory response. *Hepatology.* 2008;48(5):1632-43.
464. Gracia-Sancho J, Hernandez-Gea V, Garcia-Pagan JC. Obeticholic acid: a new light in the shadows treating portal hypertension? *Hepatology.* 2014;59(6):2072-3.
465. Hu T, Chouinard M, Cox AL, Sipes P, Marcelo M, Ficorilli J, et al. Farnesoid X receptor agonist reduces serum asymmetric dimethylarginine levels through hepatic dimethylarginine dimethylaminohydrolase-1 gene regulation. *J Biol Chem.* 2006;281(52):39831-8.

466. Li J, Wilson A, Kuruba R, Zhang Q, Gao X, He F, et al. FXR-mediated regulation of eNOS expression in vascular endothelial cells. *Cardiovasc Res.* 2008;77(1):169-77.
467. Verbeke L, Farre R, Trebicka J, Komuta M, Roskams T, Klein S, et al. Obeticholic acid, a farnesoid X receptor agonist, improves portal hypertension by two distinct pathways in cirrhotic rats. *Hepatology.* 2014;59(6):2286-98.
468. Mookerjee R, Rosselli M, Pieri G, Beecher-Jones T, Hooshmand-Rad R, Chouhan M, et al. Effects of the FXR agonist Obeticholic Acid on hepatic venous pressure gradient (HVPG) in alcoholic cirrhosis: a proof of concept phase 2A study. *J Hepatol.* 2014;60(Suppl):S1-22.
469. Chen RP, Zhu Ge XJ, Huang ZM, Ye XH, Hu CY, Lu GR, et al. Prophylactic use of transjugular intrahepatic portosystemic shunt aids in the treatment of refractory ascites: meta-regression and trial sequential meta-analysis. *J Clin Gastroenterol.* 2014;48(3):290-9.
470. Henriksen JH, Winkler K. Hepatic blood flow determination. A comparison of ^{99m}Tc-diethyl-IDA and indocyanine green as hepatic blood flow indicators in man. *J Hepatol.* 1987;4(1):66-70.
471. Bellis L, Berzigotti A, Abraldes JG, Moitinho E, Garcia-Pagan JC, Bosch J, et al. Low doses of isosorbide mononitrate attenuate the postprandial increase in portal pressure in patients with cirrhosis. *Hepatology.* 2003;37(2):378-84.
472. Turnes J, Hernandez-Guerra M, Abraldes JG, Bellot P, Oliva R, Garcia-Pagan JC, et al. Influence of beta-2 adrenergic receptor gene polymorphism on the hemodynamic response to propranolol in patients with cirrhosis. *Hepatology.* 2006;43(1):34-41.
473. Zafra C, Abraldes JG, Turnes J, Berzigotti A, Fernandez M, Garcia-Pagan JC, et al. Simvastatin enhances hepatic nitric oxide production and decreases the hepatic vascular tone in patients with cirrhosis. *Gastroenterology.* 2004;126(3):749-55.
474. Feu F, Garcia-Pagan JC, Bosch J, Luca A, Teres J, Escorsell A, et al. Relation between portal pressure response to pharmacotherapy and risk of recurrent variceal haemorrhage in patients with cirrhosis. *Lancet.* 1995;346(8982):1056-9.
475. Garcia-Tsao G, Sanyal AJ, Grace ND, Carey W, Practice Guidelines Committee of the American Association for the Study of Liver D, Practice Parameters Committee of the American College of G. Prevention and management of gastroesophageal varices and variceal hemorrhage in cirrhosis. *Hepatology.* 2007;46(3):922-38.
476. Jalan R, Hayes PC. UK guidelines on the management of variceal haemorrhage in cirrhotic patients. *British Society of Gastroenterology. Gut.* 2000;46 Suppl 3-4:III1-III15.
477. Busch M, Vollmann W, Bertsch T, Wetzler R, Bornstedt A, Schnackenburg B, et al. On the heating of inductively coupled resonators (stents) during MRI examinations. *Magnetic resonance in medicine : official journal of the Society of Magnetic Resonance in Medicine / Society of Magnetic Resonance in Medicine.* 2005;54(4):775-82.
478. Owen JW, Fowler KJ, Saad NE, Priatna A, Crowley M, Narra VR. Volumetric Phase Contrast Imaging of the Hepatic Vasculature. *Proc Intl Soc Mag Reson Med.* 2014;22:3868.
479. Brant WE, Helms CA. *Fundamentals of diagnostic radiology.* 4th ed. ed. Philadelphia, Pa. ; London: Lippincott Williams & Wilkins, 2012.
480. Castera L, Forns X, Alberti A. Non-invasive evaluation of liver fibrosis using transient elastography. *J Hepatol.* 2008;48(5):835-47.
481. Huang SY, Abdelsalam ME, Harmoush S, Ensor JE, Chetta JA, Hwang KP, et al. Evaluation of liver fibrosis and hepatic venous pressure gradient with MR elastography in a novel swine model of cirrhosis. *Journal of magnetic resonance imaging : JMRI.* 2014;39(3):590-7.